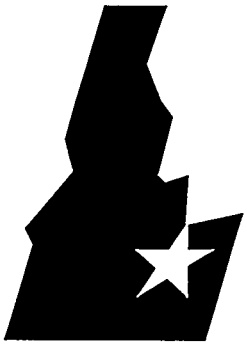

Idaho
National
Engineering
Laboratory

CONF-9509218--

September 1995

Proceedings
2nd IEA International Workshop on Beryllium Technology for Fusion

September 6-8, 1995
Jackson Lake Lodge, Wyoming

Glen R. Longhurst

Lockheed
Idaho Technologies Company

CONF-9509218

PROCEEDINGS
2ND IEA INTERNATIONAL WORKSHOP ON BERYLLIUM TECHNOLOGY FOR FUSION

September 6-8, 1995
Jackson Lake Lodge, Wyoming

Glen R. Longhurst

Lockheed Martin Idaho Technologies
P.O. Box 1625
Idaho Falls, ID 83415

FOREWORD

The 2nd IEA International Workshop on Beryllium Technology for Fusion was held September 6-8, 1995 at Jackson Lake Lodge, Wyoming. Forty-four participants took part in the workshop representing Europe, Japan, the Russian Federation, and the United States including representatives from both government laboratories and private industry. Co-chairs of the workshop were G. R. Longhurst of the Idaho National Engineering Laboratory (INEL) and M. Dalle Donne of Forschungszentrum Karlsruhe (FzK), Germany. This is the second workshop in this area conducted under the auspices of the International Energy Agency (IEA). The first was at Karlsruhe, Germany in October of 1993. Prior to IEA sponsorship, similar workshops were held at the INEL in 1988 and at Clearwater Beach, Florida in 1991.

The workshop was divided into six technical sessions and a "town meeting' panel discussion. Technical sessions addressed the general topics of: (a) Thermomechanical Properties, (b) Manufacturing Technologies, (c) Radiation Effects, (d) Plasma/Tritium Interactions, (e) Safety, Applications, and Design, and (f) Joining and Testing.

This volume contains the majority of the papers presented at the workshop. In some instances, the authors of the papers could not be present at the workshop, and the papers were given by others, sometimes in summary form and in some instances combined with others. The full papers are included here in the sequence in which they would have been given. In other instances, presentations were made but no papers were submitted for publication. Those papers do not appear here.

In summary, the workshop was very successful. The main objectives of bringing key members of the fusion beryllium community together was certainly met. Forty-four participants registered, and 35 papers were presented. Considerable work has been done since the last workshop, but there are still major research needs for the community to pursue. This is the first beryllium workshop in this series at which the Russian Federation has been represented, and they added greatly to its succes.

The organizers express appreciation to all who helped make this workshop a useful and worthwhile experience. In particular, we express appreciation to the International Energy Agency under whose kind auspices this workshop was held. Also, a number of U.S. agencies provided support for visitors from the Russian Federation, and the Russian nuclear agency, MINATOM, was also generous in their support. To sponsors and authors who took the trouble to attend, we offer our thanks. We hope this series will continue to provide a useful forum for communicating the results of research in this field.

Glen R. Longhurst
Mario Dalle Donne

CONTENTS

THERMAL FATIGUE OF BERYLLIUM

E. DEKSNIS, D. CIRIC, H. FALTER, C. IBBOTT, A. PEACOCK
JET Joint Undertaking, Abingdon, OX14 3EA, UK

Thermal fatigue life of S65c beryllium castellated to a geometry 6 x 6 x (8-10)mm deep has been tested for steady heat fluxes of 3 MW/m^2 to 5 MW/m^2 and under pulsed heat fluxes (10-20 MW/m^2) for which the time averaged heat flux is 5 MW/m^2. These tests were carried out in the JET neutral beam test facility A test sequence with peak surface temperatures ≤ 600°C produced no visible fatigue cracks. In the second series of tests, with T_{max} ≤750°C evidence for fatigue appeared after a minimum of 1350 stress cycles. These fatigue data are discussed in view of the observed lack of thermal fatigue in JET plasma operations with beryllium PFC. JET experience with S65b and S65c is reviewed; recent operations with Φ = 25 MW/m^2 and sustained melting/resolidification are also presented. The need for a failure criterion for finite element analyses of Be PFC lifetimes is discussed.

1. INTRODUCTION

The requirements for beryllium plasma facing components specify that the beryllium cladding sustain steady heat fluxes of 5 MW/m^2 under normal conditions and steady heat fluxes of 20 MW/M^2 under off-normal conditions. The proposed designs envision a thick cladding of beryllium (6-10 mm) onto an actively cooled heat sink, i.e. a CuCrZr substrate. The stresses in the beryllium part of such a duplex component comprise, in addition to the singular stresses that obtain at the free edge of the brazed joint a concentrated stress field near the irradiated surface and another one near the brazed interface (away from the vicinity of the singularity).

The extensive JET experience with inertial PFC made out of S65 and S65c Beryllium has produced data for the thermal fatigue of S65c for heat fluxes S-25 MW/M^2, $T_{surface}$ up to and including melting. Careful experiments in a controlled test-bed environment on S65c material for JET applications have been carried out by SNLA (1) and partially by JET (2). More recent ITER emergency tasks investigated the fatigue lifetime of S65c beryllium material under pulsed, transient heating conditions. The aim of the study was to understand the effect of peak surface temperature upon the fatigue characteristics of S65c material (3). Somewhat surprisingly there appears to be a temperature threshold of 600-750°C for the development of large invisible permanent thermal distortions @ 10^3 cycles of Φ max ≈ 10- 15 MW/M^2.

More recently JET has examined as an ITER task the thermal mechanical response of thick beryllium cladding of a CuCr vapotron. These results are still being examined and will be presented in full in a forthcoming conference (4). However, visual observations indicate that resolidified S65c material under these actively cooled conditions and that looks to be different to the appearance typical of inertial tiles show a markedly different appearance. Finite element results will be presented in this paper to investigate the possible reasons for this difference.

Very recent JET tokamak experience with inertial tiles that have been deliberately melted in tokamak operation (5) shows that extreme events, giant ELM's producing 200-400 MW/m^2 localized heat fluxes, can be sustained without apparent low-cycle fatigue failure. Sustained

melting experiments @ 25 MW/m^2 liquified (and displaced) up to 3mm of tile material without apparent prejudice to the mechanical integrity of the inertial tiles.

2. CONTROLLED HIGH HEAT FLUX TESTING

Irradiation of beryllium tiles at flux densities of 5-25 MW/m^2 has been carried out in the past for several designs of the JET Mark I beryllium target plates in a dedicated test rig located within the JET Neutral Beam Test bed. For the ITER emergency task only one tile of beryllium was irradiated at a time. Adjacent areas (originally up to four tiles could be tested simultaneously) were covered by copper tiles. A copper shutter, seen schematically in Figure 2, was designed to allow selected areas of the irradiated tile to be exposed to different flux histories.

Initially the shutter was located at its highest position which allowed nearly all of the beryllium tile to be illuminated. As the shutter is lowered the irradiated area became less. The pulse history of castellations accumulated as the shutter was lowered. 'Me design of the shutter did not permit raising of the shutter without a full exchange of the beryllium test-rig. This latter is a time consuming process (of the order of two days), largely due to delays in receiving safety checks for the absence of contamination due to beryllium dust.

Calorimetry (for diagnostic purposes) of the applied beam was achieved through eleven individual calorimeters located at the lower edge of the shutter, i.e. the copper castellations in the shutter cf. in Figure 2.

Surface temperature of the beryllium component was measured by an AGA IR camera. The emissivity of the surface and transmission factors for the windows is measured by observing the cooldown of the beryllium tile heated to ~200°C. Thermocouples embedded in the tile allow calibration of the IR camera. Heat loss from the tile is principally by conduction to the holders and through black body radiation. A change in bulk tile temperature of ~100°C was found to occur within five minutes. Thus the bulk temperature of a tile under repeated tests, i.e. cycling with intervals of three - five minutes came quickly to an equilibrium value ~50°C.

The testing sequence for both tiles was similar. With the shutter in the top position a flux density of ~5 MW/m^2 was applied over the entire beryllium tile face. For series I tests pulse lengths were adjusted for all shutter positions such that the maximum surface temperature did not exceed 600°C. An interlock alarm was set up between the IR camera and the plasma source allowing the source to be switched off (within 50 ms) if the measured temperature approached to within 10° of the set level. For the second series of tests the corresponding set point was raised to 750°C.

As part of this study beryllium tiles made of S65c material with overall dimensions 32 x 79 x 49mm deep, T-shaped in cross-section with surface castellations, as shown schematically in Figure 1, were irradiated in the JET neutral beam test-bed (6). In order to maximize the results of this experiment it was decided to (a) consider a pulse train that has a time average flux density of 5 MW/m^2 instead of steady long pulses of 5 MW/m^2 and (b) to shadow parts of the tile under different loading conditions so as to study the evolution of fatigue induced deformations (if any) with the number of applied heating cycles. Two blocks of material were available for the study and the difference between the two series of tests was the end temperature to which the surface was heated, i.e.≤600°C for series 1, ≤750°C for series 2 (7).

3. FATIGUE TEST RESULTS

Table 1 above gives a summary of the irradiation conditions for the various positions of shielding plate in both series of experiments.

The power deposition profile can be seen in figure I where the isotherms are shown for a tile in test series 2. For technical reasons the line of sight to the central vertical row of castellations was obscured. The maximum temperatures reached there show a continuation of the footprint without any areas of concentrated heat flux. Figure 2 shows two rows of tiles where typically 2 laterally adjacent castellations (nearly identical heat irradiation history) show distinctly evidence for dimensional change.

An elevation view of the areas showing signs of thermal fatigue is seen in figure 3. There is substantial vertical growth of the central surface region of a castellation accompanied by anticlastic inwards bowing of material near the tip of the top corners. There is no visible evidence for fatigue cracking akin to that cf (5) and shown in figure 4.

Table 2 below shows a compendium of thermal fatigue data for beryllium tiles castellated typically with a groove of 0.5 mm rounded bottom. Failed means that vertical cracks developed in the test piece centered on irradiated castellated surfaces. These propagated some 2-5 cm and it appeared that they would propogate without bound.

Table 2. JET experience with castellated S65c material

Castellation mm	Φ MW/m^2	Cycles
6 x 6 x 8	≤ 20	~ 2 x 10^4
10 x 14 x 6	≤ 18	failed
10 x 12 x 12	≤ 16	failed

JET has used S65 revision b powder to produce belt limiter tiles. All other inertial components for PFC applications has been HIP product using S65 revision c material. A small amount of S200 material is used for RF screens.

The outcome of these investigations is that JET Mark I beryllium tiles were castellated to roughly 7 x 6.5 x 8 mm deep size with a very considerable cost incurred by the requirement of having to hide each comer of each castellation. Typically there are ~ 8000 tiles each of which is subdivided into 55 castellations.

4. CASTELLATION STRATEGY

All of the beryllium PFC components installed on JET have been castellated to improve their fatigue lifetime. In fact all of these components have been partially melted due to accidental exposure (e.g. belt limiter tile edges JET) or deliberately (ISX-B (7) and more recently JET (5)). It can be said that the castellation strategy has not proved itself to improve JET PFC lifetimes.

Prior to the deliberate melting experiments a series of plasma events, giant ELM's caused localized melting of a small fraction of the MKI beryllium tile surface. Typically 1MJ (total) energy was deposited for ~10ms leading to localized flux densities of 200-400 MW/m^2 onto the surface of castellations. The onset of melting occurs within the time scale of the event itself. Mechanical computations show that strain rates of 10-100/sec are likely to have been sustained and that the entire top 1-1.5mm of castellations plastified to ~ 2-5% per event. However, this layer at least has been subsequently melted and little trace is likely to be found in detailed metallurgical examinations of these tiles.

The most recent JET experiments with deliberate melting of beryllium have shown that inertial tiles castellated per the results of the JET fatigue tests, i.e. approximately 6.5 x 7mm, up to 8mm deep, of 0.5mrn width castellations, 0.25mm radius, have shown no signs of low cycle thermal fatigue at flux densities of ~25MW/m^2, 4Hz (swept plasmas). For unswept plasmas severe surface melting obtains 0.25mm radius, have shown no signs of low cycle thermal fatigue at flux densities of ~25MW/m2,

4Hz (swept plasmas). For unswept plasmas severe surface melting obtains at a similar flux density. It is estimated that ~200 cycles have been carried out in recent JET experiments with no evidence for large thermal fatigue cracks under these conditions.

Figure 3 shows a view of the S65c Mark I beryllium tiles in the region where strong melting has been sustained. In fact nearly 3mm of material has been melted and displaced laterally to solidify as large drops of beryllium. The largest of these drops is nearly 8mm in diameter. The character of the melted surface due to tokomak operation is markedly different, cf figure 4 for a view of a thermal fatigue test tile with ~ 10^3 pulses at $\Phi \leq 25$ MW/m^2. Detailed metallurgical investigation of the MKI tiles is to search for lateral cracks hidden by resolidified layers or developed at the root of castellations.

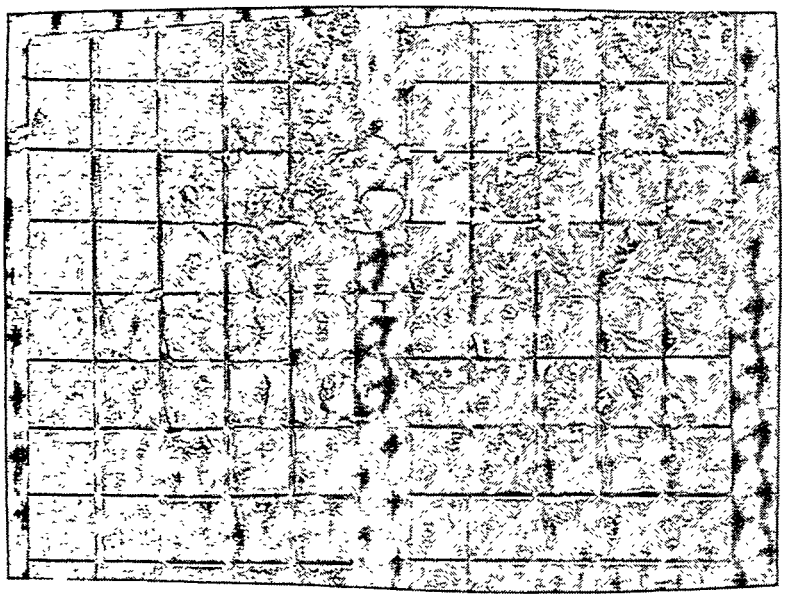

Figure 3: MkI Beryllium tiles

5. BE CLAD PFC

The JET testing programme for thin claddings 2-3mm Be onto CuCr vapotrons, has been extensively documented, (6). All of these tests have relied upon S200, also S200H material. More recently work has been done for thick 10mm layers of S65c clad to a vapotron. Details of this testing are to be presented elsewhere (4). However, the non-destructive part of this work, i.e. avoidance of surface melting showed that for S65c cladding, some 100 cycles at 5 MW/m^2 were sustained with $T_{surface} \leq 600°C$ and with no evidence of surface failure. These claddings are 27mm x 27mm. Experience from previous JET testing of inertial tiles would have predicted lateral cracking of the irradiated surface at 5MW/m^2. This was not observed to be the case.

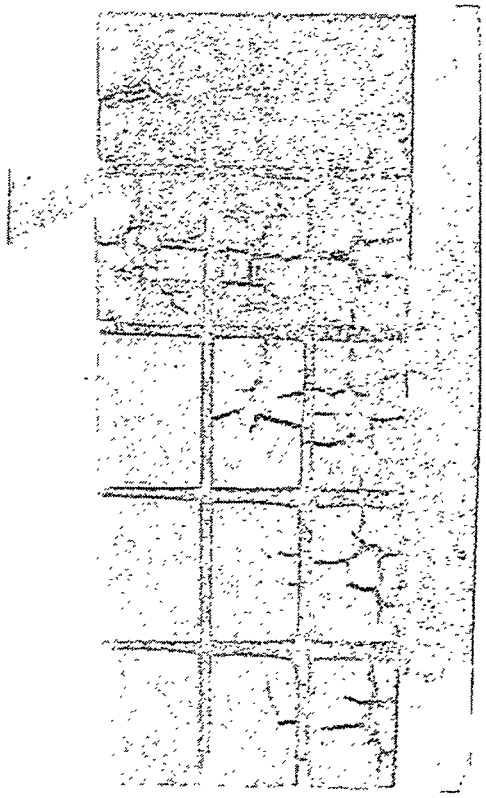

Figure 4: Reference fatigue tests

The confirmation of finite element analyses is subject to the lack of a failure criterion for thermal fatigue in Beryllium. It is noted that there is no published data for the fatigue of any grade of beryllium at elevated temperatures (8). Recent results, reported later in this conference

Table 1. S65c fatigue tests, flux densities MW/m^2

Series 1

shutter position	peak power density				number of		on time per pulse		modulation	
	max	min	average	std	pulses	cycles	average	std	on time ms	off time ms
1	5.55	3.21	4.61	0.45	112	112	2.40	0.80		
2	12.87	4.62	11.04	0.98	112	1041	0.93	0.17	108	142
3	19.73	13.63	15.00	0.98	86	700	1.00	0.98	110	190
4	21.06	16.35	18.70	0.86	93	827	1.07	1.00	96	231

Series 2

shutter position	peak power density				number of		on time per pulse		modulation	
	max	min	average	std	pulses	cycles	average	std	on time ms	off time ms
1	7.69	4.09	5.39	0.55	98	98	3.60	0.89		
2	12.01	7.75	9.63	0.77	60	1236	2.34	0.75	104	108
3	15.57	9.63	13.43	0.96	51	823	1.86	0.33	107	189
4	19.65	7.91	18.40	1.56	71	800	1.91	0.60	146	273

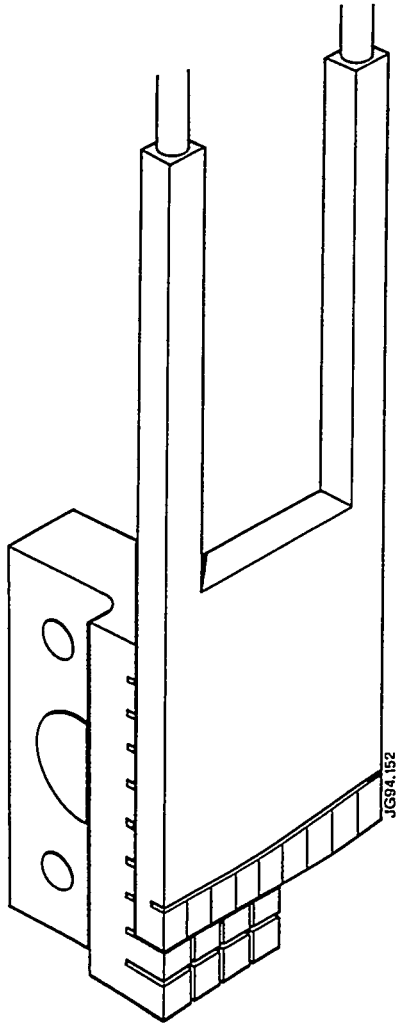

Figure 1: Shadowing of irradiated tile

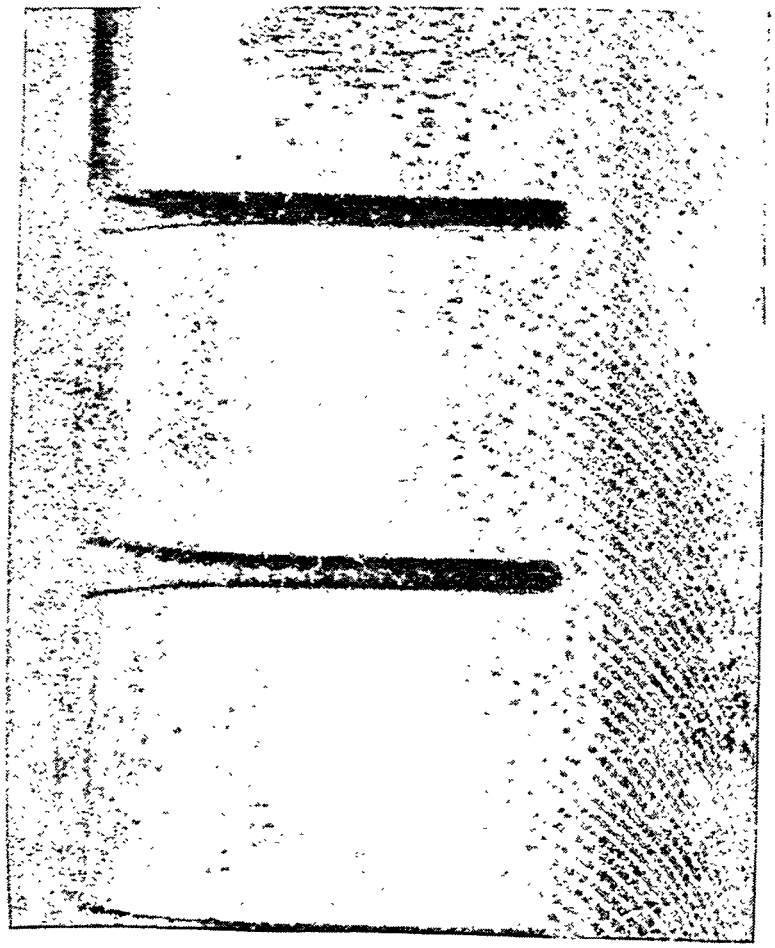

Figure 2: Edge view after irradiation of S65c castellated tiles

(9), suggest that S65c is superior to S200 in terms of resistance to cracking due to thermal shock. Modelling of these latter experiments confirms the need for a model of the plastic behavior of beryllium under thermal loadings.

6 CONCLUSIONS

The data presented here suggest that there is a substantial reduction in the fatigue lifetime of S65c for temperatures in excess of 600°C. In attempting to model this effect the sparseness of the database on material properties is noted. In particular, in view of ITER requirements, the need is clear for material properties at all temperatures up to the melting temperature of beryllium.

The principal mechanism for the fatigue failure seen in these experiments is anticlastic bending of material along diagonal vertical edges of castellations. Modelling shows that the location of peak plastic strain in finite element analyses is sensitive to the value of Poisson's ratio, particularly the value of this quantity at elevated temperatures. The little data that has been published is contradictory for the temperature evolution of Poisson's ratio for any grade of beryllium (8).

7. ACKNOWLEDGEMENTS

Peter Miodurszewski of Oak Ridge National Laboratory, R.D. Watson of Sandia National Laboratory for transparencies used in oral presentation.

REFERENCES

[1] M.F. Smith et al, Thermomechanical testing of beryllium for limiters in ISX-B and JET, Fusion Technology, Vol 8, July 1985, p 1174-1183

[2] E. Deksnis et al, Fatigue of inertial beryllium elements for JET MKI pumped divertor, Proceedings 17th SOFT, Vol 1, p 242-246, 1993

[3] E. Deksnis, D. Ciric, H. Falter, D. Martin, Report on ITER emergency task fatigue studies of S65c beryllium, JET report (1994)

[4] H. Falter, High heat flux tests on 10mm beryllium tiles brazed to an actively cooled vapotron made by CuCr, to be published (1995)

[5] B. Tubbing et al, First results with JET Beryllium melting experiment, EPS conference, Bournemouth, UK, July 1995 (to appear)

[6] H. Falter etal, Thermal test results of the JET divertor plates, Proceedings SPIE, Vol 1739, pp 167-172, 1992

[7] P. Mioduszewski et al, Joint JET-ISX-B Beryllium Limiter Experiment, Final Report, ORNL, July 1986

[8] D.E.Dombrowski, E.B.Deksnis, M.Pick, Thermomechanical Properties of Beryllium,IAEA Handbook in Properties of PFC materials, Vienna 1995

[9] R.D. Watson, D.I. Youchison, D.E. Dombrowski, R.N. Guiniatouline, Low cyclethermal fatigue testing of Beryllium grades for ITER PFC, 2nd IEA Int'l Workshop on Beryllium Technology for Fusion, Sept 6-8, 1995

Low Cycle Thermal Fatigue Testing of Beryllium Grades for ITER Plasma Facing Components

R.D. Watson[a], D.L. Youchison[a], D.E. Dombrowski[b], R.N. Guiniatouline[c], I.B. Kupriynov[d]

[a]*Sandia National Laboratories, MS-1129, P.O. Box 5800, Albuquerque, NM 87185*
[b]*Brush Wellman, Inc., 17876 St. Clair Ave, Cleveland, OH 44110*
[c]*Efremov Institute, P.O. Box 42, St. Petersburg, Russia 189631*
[d]*Russian Institute of Inorganic Materials, 5 Rogov St., Moscow, 123060, Russia, Box 369*

Abstract

A novel technique has been used to test the relative low cycle thermal fatigue resistance of different grades of US and Russian beryllium, which is proposed as plasma facing armor for fusion reactor first wall, limiter, and divertor components. The 30 kW electron beam test system at Sandia National Laboratories was used to sweep the beam spot along one direction at 1 Hz. This produces a localized temperature "spike" of 750 °C for each pass of the beam. Large thermal stresses in excess of the yield strength are generated due to very high spot heat flux, 250 MW/m^2. Cyclic plastic strains on the order of 0.6% produced visible cracking on the heated surface in less than 3000 cycles. An *in-vacuo* fiber optic borescope was used to visually inspect the beryllium surfaces for crack initiation. Grades of US beryllium tested included: S-65C, S-65H, S-200F, S-200F-H, SR-200, I-400, extruded high purity, HIP'd spherical powder, porous beryllium (94% and 98% dense), Be/30% BeO, Be/60% BeO, and $TiBe_{12}$. Russian grades included: TGP-56, TShGT, DShG-200, and TShG-56. Both the number of cycles to crack initiation, and the depth of crack propagation, were measured. The most fatigue resistant grades were S-65C, DShG-200, TShGT, and TShG-56. Rolled sheet Be (SR-200) showed excellent crack propagation resistance in the plane of rolling, despite early formation of delamination cracks. Only one sample showed no evidence of surface melting, Extruded (T). Metallographic and chemical analyses are provided. Good agreement was found between the measured depth of cracks and a 2-D elastic-plastic finite element stress analysis.

1. Introduction

Beryllium has been used successfully as limiters for protecting the first wall and vacuum vessel of tokamak physics experiments since 1984 when beryllium was first used as a rail limiter on the UNITOR tokamak [1]. Subsequent use on both the ISX-B tokamak [2] and the Joint European Torus (JET) tokamak [3] has demonstrated the positive effects on plasma performance. Beryllium, with its low atomic number (Z=4), excellent capability in gettering oxygen, and high thermal heat capacity and conductivity, has resulted in lower plasma impurity levels, reduced plasma dilution, enhanced wall pumping, reduced density limit disruptions, and reduced runaway electron events, despite occurrences of local melting and cracking [3,4].

Beryllium is proposed as a protective armor material on plasma facing components (PFC's) for the next generation of tokamak experiments, including the International Thermonuclear Experimental Reactor (ITER). This deuterium-tritium burning machine, with a fusion power = 1500 MW, and long-pulse operation, 1000 s, will subject the PFC's to heat fluxes in the range of 1-20 MW/m^2 for up to 10,000 cycles. Long-pulse operation will require active cooling to maintain steady-state surface temperatures of the 5-10 mm thick armor tiles in the range of 600-800 °C. Beryllium tiles must be permanently bonded to a water cooled copper alloy heat sink to provide adequate cooling.

Critical issues for using beryllium in ITER include: (1) thermal fatigue cracking, (2) tritium inventory, loss of melt layers during plasma disruptions, (3) reliable bonding to the copper heat sink, and (4) neutron damage effects. However, in this paper, we will focus only on the issue of thermal fatigue cracking. Thermal stresses, due to the large temperature difference across the tile, can be quite large due to the large coefficient of thermal expansion (CTE) and elastic modulus (E). Large thermal stresses, when combined with the inherently low ductility of beryllium (3-5% for S-65C at 25 °C), can result in thermal fatigue cracking in a relatively low number of cycles.

Cracking should be avoided if it leads to: (1) erosion of material, (2) a reduction in thermal conductivity if cracks run across the direction of heat flow, or (3) a water leak if the cracks propagate through the tile and into the copper heat sink. Cracking is expected to be worse in neutron-irradiated beryllium, due to the embrittling effect of (n,alpha) helium gas bubbles in both the matrix and along grain boundaries, which causes a severe loss of ductility.

Grades of beryllium other than S-65C have been proposed for use in ITER. In this paper, we will describe how the SNL e-beam test facility was used to rapidly produce low cycle fatigue damage on 14 different grades of beryllium and 3 other beryllium materials. The goal was to rank the relative resistance to crack initiation and propagation of the various grades, in an attempt to help select the best for ITER PFC's. This work was performed in support of the ITER technology R&D task, T-221, "Beryllium and Other Armor Materials".

The primary motivation for developing this new screening technique is to reduce the high costs associated with traditional methods of fatigue testing of beryllium at elevated temperature, especially combined thermo-mechanical fatigue testing. For this reason, the e-beam spot heat loads used in our tests were much larger than expected in ITER operation. This allowed us to accelerate the rate of damage accumulation, and, hence, minimize the time needed to complete a large number of cycles. This technique could easily be used for testing neutron-irradiated samples in a hot cell e-beam facility, such as the JUDITH facility at KFA in Juelich, Germany.

2. Literature Review

No references were found on fatigue properties of modern grades of beryllium using standard ASTM rotating bar or round bar tensile test geometries.

Previous studies by the fusion community on the thermal fatigue cracking of beryllium using electron or ion-beam test facilities have shown a wide variety of behaviors, depending on the geometry, heat flux, and pulse length.

Sandia National Laboratories (SNL) in preparation for the ISX-B tokamak experiment in 1984, performed thermal cycling with a rastered e-beam of a 2.54 cm cube of S-65B beryllium at a heat flux of 25 MW/m^2 for 0.3 second pulses [5,6]. These tests showed that a fine network of microcracks developed on the heated surface after only 25 cycles, when viewed in the SEM. Cracks visible to the naked eye were observed after 500 cycles. Finally, a large single crack ran down through the bulk of the cube to a depth of 7 mm after 800 cycles. Additional cycling to a total of 1500 cycles produced no further growth. Chemical etching of the surface did not prevent cracking. Finite element analysis predicted a cyclic plastic strain of 0.5% at the heated surface [5].

Examination of the beryllium limiter tiles after 3600 tokamak shots in ISX-B, showed a similar pattern of surface microcracks [2].

In preparation for the use of beryllium limiter tiles in JET, e-beam testing of a prototype S-65B limiter tile was performed at SNL in 1986 [7]. At a surface heat flux of 2.5 MW/m^2 for 15 s pulses, a large array of surface microcracks were observed with the naked eye after 3000 cycles. After 10,000 cycles, these vertical cracks had grown to a depth of 4 mm. The rate of crack growth decreased as the crack depth increased *(presumably due to the lower cyclic stresses at greater depths)*. Finite element analysis indicated a cyclic plastic strain of 0.15% at the heated surface.

Subsequent e-beam tests on a new set of S-65B tiles at higher heat loads, 4-5 MW/m^2 for 10 s pulses, showed dramatically different results [8]. Cracking of unslotted tiles was characterized by a single, wide crack growing to a depth of 20-30 mm after a few thousand cycles. Also, so-called "lateral" cracks (e.g. parallel to the heated surface) were observed, for the first time, in both slotted and unslotted tiles at a depth of 3-4 mm from the heated surface, growing from the free edge towards the bulk.

High heat flux testing of S-65B beryllium "Mark I" divertor target tiles was done in 1992 at JET using their Neutral Beam Test Bed [9]. Testing on tiles 10 mm x 15 mm with castellations 10 mm deep produced a pattern of cross-shaped vertical cracks after 1000 cycles at 14 MW/m^2 for 0.1 s pulses. After a total of 5000 cycles, the tiles were inspected and found to also have lateral cracks running parallel to the heated surface at a depth of approximately 1 mm. Local melting above the lateral cracks was observed *(presumably due to the lack of good heat conduction)*. Subsequent testing of smaller tiles, 6 mm x 6 mm, showed no evidence of macroscopic cracks after 10,000 pulses at 18 MW/m^2 for 0.1 s pulses. A final test sequence on a third set of tiles at 25 MW/m^2 for 0.1 s pulses showed local melting due to lateral cracks growing from the four corner edges. No evidence of

vertical cracks was seen. These tests found that increasing the initial temperature from 100 °C to 250 °C improved the fatigue lifetime from 1000 to 5000 cycles *(presumably due to the improved ductility of beryllium at higher temperatures).* The issue of anisotropic thermal expansion in the remelted zone, with columnar grains, above the lateral cracks was raised by the authors as possibly contributing to the formation of lateral cracks. Finite element analyses showed cyclic plastic strains developing at the heated surface. Also, tensile stresses were predicted along the free vertical edges at the approximate location where lateral cracks were located

High heat flux testing of S-65B beryllium tiles brazed to a water cooled copper hypervapotron heat sink was performed at JET in 1993 [10]. Three different tile thicknesses were tested: 1.5 mm, 2 mm, and 3 mm. No evidence of surface cracking was observed after 1000 cycles at 12.5 MW/m^2 for 1 and 2 s pulses. However, melting of a few tiles was observed after failure of the braze joint occurred [11, 12].

Electron beam testing at SNL in 1994 was performed on 5 mm thick Russian TGP-56 beryllium tiles diffusion bonded to a water-cooled dispersion strengthened copper alloy heat sink [13]. No evidence of fatigue cracking on the surface of the beryllium was observed after 9200 cycles at 5 MW/m^2 for 15 s pulses. The test was terminated after debonding occurred at the Be/Cu interface. Finite element analyses predicted that cyclic plastic strains were zero.

In summary, beryllium plasma facing components can develop cracks from cyclic high heat flux irradiation. Both vertical and lateral cracks have been observed. Key controlling factors include the heat flux, pulse length, and degree of geometrical constraint. A critical controlling parameter appears to be the level of cyclic plastic strain, with higher values leading to shorter numbers of cycles to crack initiation.

3. Finite Element Analysis

The low cycle fatigue geometry is shown in Figures 1 and 2. In our experiment, we stacked 14 tiles side-by-side so that many different samples would be subjected to the same heat flux history. The tiles were clamped on both sides by water-cooled copper blocks, including a Papyex graphite paper gasket, to remove the time-averaged heat deposition and prevent thermal ratcheting.

3.1 Finite element model

A 2-D finite element mesh of the beryllium tile was generated with PATRAN [16], and analysed with a general-purpose finite element code, ABAQUS 5.4 [17], running on a HP 735/125 UNIX workstation. Because the tile is thin (5 mm) relative to its other dimensions (25.4 mm), we felt that a 2-D plane stress model would provide a reasonable approximation. First, a transient thermal analysis was performed, and then the resulting temperatures were then applied to an elastic-plastic stress analysis. Fig. 3 shows the mesh that was used. It consists of 3804 nodes and 1221 8-noded isoparametric quad elements (DC2D8 for thermal, and CPS8 for stress). A smaller mesh size was used in the region where the steepest gradients were expected, i.e. underneath the beam spot. The size of the smallest elements was 0.2 mm x 0.2 mm. In ABAQUS, the direction labeled "1" corresponds to the X-direction, and "2" to the Y-direction. Table 1 lists the temperature-dependent thermal properties of S-65C that were used in the analysis [7].

To simulate in ABAQUS the heating during one complete cycle at 1 Hz sweep frequency, a constant heat flux = 80 MW/m^2 was applied over a 2 mm wide spot for a pulse length = 0.06 seconds. Subsequently, the heat flux is turned off for 0.94 seconds. The heat flux was determined by taking the e-gun power, 1300 W, times an estimated absorption factor, 0.6, and then dividing by the heated area of a single tile, 2 mm x 5 mm. This gives 80 MW/m^2. The pulse length was determined by taking the fraction of the total cycle time, 1 s, which is spent traversing the width of a single tile, (5 mm/84 mm x 1 s = 0.06 s). We assumed that the velocity of the beam spot (v = 84 mm/s) was sufficiently fast that the peak beam spot heat flux (250 MW/m^2) was effectively spread out over the entire width of one tile.

The general 3-D thermal response of a rapidly moving spot heat source on a copper plate has been modeled analytically by Sheng and Howell [15] for an e-beam moving a 200 meters/s with a beam power of 1000 W. Fig. 4 shows the general shape of the surface temperature profile for a Gaussian e-beam spot profile. The rapid drop-off in temperature of the leading edge can easily be seen because the spot's velocity is much greater than the velocity of a thermal diffusion wave in copper.

In our experiments, however, the spot velocity is 3 orders of magnitude slower, only 0.084 meters/s (84 mm/s) for a 14-tile stackup length of 84 mm and 1

sweep Hz frequency. This is very close to the velocity of the thermal diffusion wave in beryllium. This implies that significant "pre-heating" will occur 1-2 mm out in front of the beam spot. This effect was actually observed in our tests; (1) both the heat affected zone (HAZ) was wider at the beam's exit from the sample that at the beam's entrance, and (2) more melting was observed at the beam's exit than entrance. Only with a detailed 3-D thermal analysis, including the small beam spot (diameter = 2 mm) traversing the thicker tile (5 mm), would a more accurate analysis of the real temperature response be obtained. The 2-D model used in this paper is intended only to predict the qualitative thermo-mechanical response.

3.2 Thermal analysis results

Fig. 5 shows the temperature response for a single on/off cycle at the hottest point on the surface of the beryllium tile directly underneath the beam spot. The peak temperature rises from 25 °C to 750 °C during the 0.06 s time that the heat flux is on. This agrees reasonably well with what was observed experimentally. The hot spot has cooled back down to 35 °C at the end of the 1 s cycle, indicating that only a small amount of thermal ratcheting would occur with multiple cycles. Fig. 6 shows the contours of constant temperature at the end of the heating pulse (t=0.06 s). The very steep temperature gradient is confined to a region roughly 2 mm deep. Fig. 7 plots the temperature as a function of distance from the heated surface (in cm) along a line drawn parallel to the Y-axis, through the symmetry line of the tile (path A-A' in Fig. 3). Fig. 8 shows the temperature profile at t=0.06 s along a line following the heated surface from left side to right side of the tile (path B-B'(cm) in Fig. 3).

3.3 Stress analysis results

The same mesh used for the thermal analysis was subsequently used for the stress analysis. No mechanical constraint was applied to the tile in ABAQUS since the copper cooling blocks clamped to the sides applied little actual force. The complete transient temperature history for the first heating/cooling cycle was applied to each cycle of the stress model.

Table 2 lists the temperature-dependent mechanical properties for S-65C that were used [7]. A bi-linear stress/strain curve was used, as shown in Fig. 9. Kinematic hardening was used. No attempt was made to adjust the material properties for the other grades of beryllium, despite the fact that the yield behavior, and anisotropy vary widely among them.

Initially, only an elastic analysis was performed. Peak stress in the X-direction, σ_x, at the heated surface was found to be -1270 MPa. This exceeds the yield strength of S-65C beryllium at 750 C by approximately 14 times, clearly that indicating plastic yielding would occur during heating. Subsequently, all calculations were performed using the elastic-plastic model described earlier. We will report centroidal-averaged results for element #1086, which is located at the heated surface along the symmetry plane of the model. Element #1086 also experiences the highest temperature swings.

Fig. 10 shows the deformed mesh plot (magnified by 200 times) at the end of the 0.06 s heating pulse. The thermal expansion is confined to the region of highest temperature rise. Fig. 11 shows the contours of σ_x at the end of the heating pulse. Peak compressive stresses equal to -260 MPa are located on either side of the hot spot. At the center of the hot spot, a lower compressive stress is found, -130 MPa, due to the fact that the higher temperatures are causing a lower yield strength. There is a peak tensile stress in the bulk of the beryllium equal to 114 MPa.

Fig. 12 shows contours of plastic strain in the X-direction, ε_{px}, at the end of the heating pulse. The plastic strain is concentrated in the region directly underneath the heated spot, and extends to a region only about 2 mm wide by 2 mm deep. The peak plastic strain, -1.0 %, occurs at element #1086.

Fig. 13 shows the time evolution of σ_x for the first on/off cycle for element #1086. The compressive stress increases rapidly up to a maximum value of -260 MPa during the first 3 milliseconds when the temperature has risen about 100 °C. Then, with increasing temperature up to 750 °C, plastic yielding occurs, and the peak compressive stress decreases to -130 MPa. Next, the heat flux is turned off, and the temperature gradient relaxes. The σ_x stress reverses sign and becomes tensile, first elastically, then plastically, as the yield strength is exceeded during cooldown. Within about 0.2 s, the temperature pulse has relaxed sufficiently that only small changes in the peak tensile stress of 240 MPa occur from 0.2 to 1 s.

Fig. 14 plots the time evolution of the plastic strain in the X-direction, ε_{px}, during the first on/off cycle for element #1086. The compressive plastic strain increases continuously up to a peak value of

-0.9 % at the end of the 0.06 s heating pulse. This value then decreases as the temperature pulse decays during the cooldown, leaving a permanent "residual" compressive plastic strain of -0.3% at the end of the first cycle.

Fig. 15 shows the deformed shape (magnified by 200) at the end of the cycle (t=1 s). The residual plastic strain produces a small "bump" on the surface. Fig. 16 shows the contours of σ_x at the end of the cycle. Peak tensile stresses of 250 MPa occur on either side of the hot spot, with a value of 210 MPa in the center (element #1086). Also, a peak residual compressive stress equal to -180 MPa is located about 2 mm below the surface. Figs. 46-49 show zoomed-in plots of Figs. 6, 11, 12, and 16, respectively

Next, a total of 12 on/off cycles was applied to the model, using the same transient temperature history shown in Fig. 5. Fig. 18 shows the combined stress vs plastic strain curves for element #1086. Shakedown to a stable response occurs during the first 6-8 cycles. The cyclic plastic strain for this element, i.e. the difference in plastic strain between the end of the heating pulse and the end of the cooling cycle, is 0.65%. Kinematic hardening is used in this case. This figure also shows the large stress swing that element #1086 undergoes each cycle, from -260 MPa to +240 MPa, a stress swing $\Delta\sigma_x$ equal to 500 MPa.

Fig. 19 shows the equivalent hysteresis loop for isotropic hardening. Clearly, convergence to a stable loop has not happened, and the growth in gross plastic strain appears to be proportional to the number of cycles. Such a response, similar to "plastic ratcheting", may explain the large bump on top of the samples. The cyclic plastic strain, 0.5%., is smaller than with kinematic hardening. However, the cyclic stress has increased to 650 MPa.

Fig. 20 shows the time evolution of the plastic strain, ε_{px}, for element #1086 with kinematic hardening. Fig. 21 shows the same variable for isotropic hardening.

Fig. 22 plots the stress, σ_x , as function of distance from the surface (along path A-A' in cm), at the end of the heating pulse, and at the end of the cooling cycle. The difference between these two curves is equal to the cyclic stress, $\Delta\sigma_x$. The distribution of cyclic stress remains rather constant for the first 1 mm, but then decays rapidly to zero at a depth of about 2 mm. This would indicate that fatigue cracks, once initiated, should grow rapidly through the first 1 mm, but then slow down at they approach a depth of 2 mm. The cyclic stress range, $\Delta\sigma_x$, is sufficiently high, 500 MPa, that rapid crack growth would be anticipated.

Fig. 23 plots the plastic strain, ε_{px} , as a function of distance from the surface (along path A-A' in cm), at the end of the heating pulse, and at the end of the cooling cycle. The difference between these two curves is equal to the cyclic plastic strain, $\Delta\varepsilon_{px}$. The distribution of cyclic plastic strain decays rapidly to zero at a depth of 0.8 mm. This would indicate that fatigue crack initiation should be concentrated in a region than 0.8 mm deep. With peak cyclic plastic strain values exceeding 0.6%, crack initiation should be expected to occur rather quickly.

A full 3-D analysis should be performed next in order to properly understand the magnitude of the out-of-plane stresses, which could be significant. Inclusion of the finite thickness in a 3-D model will most likely increase the levels of plastic strain.

4. Experimental Procedure

The matrix of test samples consisted of 14 different grades of beryllium metal, 2 types of Be/BeO composites, and 1 type of beryllide. We decided to include the widest possible range of processing conditions in order to cover all of the modern grades of beryllium.

Table 3 lists the various grades of beryllium that were obtained from Brush Wellman and from the Efremov Institute. Five samples of each grade were provided. Some experimental materials were also provided by Brush Wellman: 94% dense Be, 98% dense Be, Be + 30% BeO, Be+ 60% BeO, and titanium beryllide, $TiBe_{12}$. Each tile was 2.54 cm x 2.54 cm x 0.5 cm for the US grades, and 0.6 cm thick for the Russian grades. All of the US samples were chemically etched after machining, and degreased with an industrial grade, water based degreaser, then rinsed with acetone and methanol. Some of the Russian samples have a silvery, reflective finish which may be a the result of electropolishing.

4.1 Description of Brush Wellman materials

S-200F is a vacuum hot pressed (VHP) beryllium grade made from impact ground beryllium powder. It is the most commonly used structural grade, has medium BeO content and anisotropic properties.

S-200F-H is a hot isostatically pressed (HIP) beryllium grade made from impact ground beryllium powder. It is the most commonly used structural grade, has medium BeO content and isotropic properties.

S-65C is a vacuum hot pressed (VHP) beryllium grade made from impact ground beryllium powder. This grade has the lowest metallic impurity concentration level and lowest BeO content of the Brush Wellman structural grades. It has anisotropic properties and the highest high temperature elongation of all the Brush Wellman grades.

S-65H is a hot isostatically pressed (HIP) beryllium grade made from impact ground beryllium powder. This grade has the lowest metallic impurity concentration level and lowest BeO content of the Brush Wellman structural grades. It has isotropic properties.

SR-200 is a vacuum hot pressed (VHP) beryllium grade made from impact ground beryllium powder. The sheet is made by cross-rolling a billet at elevated temperatures while encased in a steel can. It has medium BeO content and highly anisotropic properties.

I-400 is an instrument (I) grade made by vacuum hot pressing (VHP) powder that has been impact ground and then ground in a ball mill. It has one of the highest microyield strengths of the instrument grades and has a very high (4.25% min.) BeO content.

HIP'd Spherical Powder Beryllium is usually made from comminuted powder which is either platelike in shape or blocky. This new spherical powder grade is made by inert gas atomization of molten beryllium to minus 325 mesh spheres followed by hot isostatic pressing. It has among the lowest oxide content of the Brush Wellman grades, isotropic properties, and shows indications of enhanced fracture toughness.

Special BWI Extrusion Extruded beryllium has very anisotropic properties and grain shape. This particular extrusion used an experimental high purity beryllium grade with very low (0.38wt%) BeO content.

Be/30wt% BeO Composite This experimental material is made by hot isostatic pressing from powders. It is tailored for electronics heat sink applications due to the high thermal conductivity and low electrical conductivity of the BeO. The composite has a low CTE.

Be/60wt% BeO Composite This experimental material is made by hot isostatic pressing from powders. It is tailored for electronics heat sink applications due to the high thermal conductivity and low electrical conductivity of the BeO. The composite has a low CTE.

94 and 98 % Dense CIP/Sinter S-65 These were made from S-65 grade beryllium powder by cold isostatic pressing (CIP) followed by sintering. The porosity can act to block crack propagation. There is data indicating that maximum beryllium fracture toughness is obtained with 95% dense material.

Titanium Beryllide This is $TiBe_{12}$, an intermetallic compound with a melting point (1593 °C) significantly higher than beryllium (1289 °C) . It has good oxidation resistance, but low thermal conductivity.

Table 4 lists some mechanical properties of US beryllium grades, taken from material certification sheets provided by Brush Wellman for our samples. The grain size was measured by the linear intercept method.

4.2 Russian Federation (RF) materials

TGP-56 This is a technical purity grade with 0.9-1.3 wt% BeO made from minus 56 micron beryllium powder by punched hot pressing. It has quasi-isotropic mechanical properties.

TShGT This is a technical purity grade with 1.2 wt% BeO made from beryllium powder by hot pressing to partial density and then punching to full density.

DShG-200 This is a high purity distilled grade which is made by taking minus 200 micron distilled beryllium powder and hot pressing it to partial density and then punching to full density. It has about 0.9-1.3wt% BeO. It has highly anisotropic properties and the best high temperature elongation of all the RF grades. Properties in transverse direction are generally superior to the longitudinal direction. There is 0 % elongation in the longitudinal direction until 300 °C is reached.

TShG-56 This is a technical purity grade with 1.3 wt% BeO made from minus 56 micron beryllium powder by hot pressing to partial density and then punching to full density. It has anisotropic mechanical properties.

Table 5 lists the chemical composition of US and RF beryllium grades. All analyses were performed in August, 1995 by Brush Wellman on the actual tiles used in this experiment. All grades typically have BeO contents on the order of 1 wt%, with the exception of I-400, which has 6 wt% BeO. The distilled grade, DShG-200, is not significantly purer than the other two technical grades. There is significant variation in the Cu and Ni concentrations within each of the RF samples. Of the 4 Russian samples, TShG-56 has significantly lower impurity content.

4.3 Electron beam test setup

The 30 kW Electron Beam Test System (EBTS) was used to apply a highly concentrated heat pulse to the surface of each beryllium tile. This system, described in more detail in [14], consists of a 30 kV, 1 amp (max) electron beam that can be rastered in X- and Y-directions at frequencies up to 10 kHz. For this experiment we chose to raster the beam only in one direction at a frequency of 1 Hz over a total length of 8.4 cm. The concentrated heat flux produces a large temperature "spike" underneath the beam spot, which decays rapidly before the next traverse of the beam. This technique was originally developed at Argonne National Laboratories [15]. They used an e-beam welder rastered at 1000 Hz for fatigue testing of high strength copper alloy heat sinks used in synchrotron radiation sources. It was quite successful in creating fatigue damage in a short amount of time.

The power level of the EBTS was selected to be in the range of 1000-3000 W in order to cause a temperature rise on each tile of 400-800 °C during each pass of the beam spot. This temperature spike roughly follows the same range of temperatures expected during thermal cycling of actual ITER plasma facing components.

Although we did not measure the e-beam size, post-test examination of the heat affected zone indicated that the beam FWHM was approximately 2 mm wide. The raster control was programmed to be a sawtooth pattern, with a constant velocity in one direction along the length of the 14 tiles, with a quick (20 times faster) return back to the beginning. The total length of the raster pattern, approximately 84 mm, was adjusted so that the beam spot completely fell off the ends of the first (#1) and last (14) tiles.

Diagnostics for the EBTS consisted of a scanning IR camera, and two spot IR (1-color) pyrometers, covering the range of 150-550 C, and 300-1300 C, respectively. Emissivity was set at the lowest value, 0.1, because the beryllium was initially very shiny and reflective. No attempt was made to calibrate the emissivity as the surfaces changed during the tests, hence, only qualitative temperature information was obtained. The rapid changes in the surface due to oxidation, microcracking, and melting makes accurate pyrometry a difficult and time-consuming procedure. No attempt to calibrate the emissivity was made.

However, visual observation of the color of the hot spot, after the beam had moved on to the next tile, indicate peak temperatures of at least 600 °C. Darkening of the surface occurred rapidly (less than 100 seconds) and left a clear visual indication of the path of the e-beam. In many cases, clear evidence of melting was also observed.

Initially, the EBTS beam power was set to 2700 W. Two different cases (#1 and 2) were run, where each "case" represents a different set of 14 tiles stacked in the holder. However, it was clear that melting was occurring before cracking. For this reason, we reduced the gun power to 1300 W. At this level, we estimated that the peak heat flux of the beam spot (if it was stationary) was 250 MW/m^2. Any spot on the beryllium surface in the path of the beam would be exposed to this peak heat flux for a time pulse of roughly 20 milliseconds, repeated once every second (at 1 Hz).

Three more cases (#3, 4, and 5) at 1300 W gun power. Each tile was inspected after every 100 cycles with an *in-vacuo* fiber optic borescope for any evidence of cracking or melting. Cycling was then continued on all 14 tiles until the last sample of the set had cracked. In only one instance was a tile removed before completing the entire sequence because it had broken into many pieces ($TiBe_{12}$). If a grade performed well in case #3, another sample of the same grade was included in case #4. Likewise, the best performers from case #4 were replaced with fresh tiles and included in case #5

A total of 56 different samples were tested in all five cases. However, we will focus only on the results from cases #3, 4, and 5 for the remainder of the paper. These cases used the same beam parameters.

5. Experimental Results

5.1 Crack initiation lifetime

Our criteria for determining crack initiation was whether or not a crack was visible when looking through the *in-vacuo* fiber optic borescope. We estimated that cracks had to be at least 1 mm long and 20 microns wide on the surface in order to be seen by the borescope. Fig. 24 summarizes the number of cycles required to produce visible cracks for cases 3, 4, and 5. The uncertainty is ~100 cycles, since that was the frequency of observation. The sample of $TiBe_{12}$ cracked into many small pieces within only a few shots, and was subsequently removed from test sequence #3. We realize that the statistics are rather poor (only one sample per case, and, at most, three repeats). Hence, the data shown is intended to indicate only qualitative trends, not absolutely accurate results. The scatter in some of the grades is quite large. This is typical of fatigue testing, and up to 7 identical tests are often used to get adequate statistics. Fig. 25 shows the same data averaged over the 3 cases.

The samples with the best resistance to crack initiation were:

- S-65C (L)
- DShG-200
- S-65C (T)
- TShGT
- S-65H
- TShG-56

The samples with the worst resistance to crack initiation were:

- TiBe12
- Be/60wt% BeO
- Be/30wt% BeO
- I-400 (L)
- SR-200
- 94% S-65

5.2 Macroscopic examination of heat affected zone

There are a number of common features among the samples. Looking down on the heated surface (top view) there is a clearly defined heat affected zone (HAZ) which is usually dark brown or black, with parallel bands of lighter color. It has the appearance of heavily oxidized metal. Many of the samples have a single major crack running down the middle of the HAZ parallel to the beam path, but rolled sheet and extruded samples have major cracks perpendicular to it.

The HAZ is typically 2 mm wide. In most samples, the HAZ is wider, and the damage was more severe, on the side where the beam exited the sample. Surface melting was also observed, more so on the beam's exit side. On many samples, the tile's width is narrower in the HAZ, more on the beam exit side than on the entrance side, by as much as 0.4 mm. Some tiles that cracked perpendicular to the beam's path expanded in width, rather than contracting.

Looking perpendicular to the heated surface (side view), all samples show a elliptical-shaped discolored area underneath the beam spot, consisting of both darker and lighter bands. The sharp change in color from dark brown to a light grey may be caused by different thicknesses and morphology of the BeO layer [13]. All samples have a raised hump in the material which is tallest directly underneath the center of the beam path. The height of the hump is typically 0.2-0.4 mm tall. This hump is also characterized by a network of many fine cracks which are tens of microns long. Many samples showed evidence of surface melting. Some showed evidence of net erosion of material, especially the samples with high BeO content.

Many samples show a single thin, straight crack descending from the highest point of the hump perpendicular to the heated surface. Crack depths range from 0.1 mm to 2.0 mm, with the average being about 1.0 mm. These cracks were usually deeper on the side of the tile where the beam exited the sample. On some samples this single crack curved over roughly 90° into a "J" shape. A few samples showed lateral cracks running parallel to the heated surface at a depth of approximately 0.1 mm below the surface.

Surface melting is another measure or indicator of poor thermal performance, among the various grades of beryllium metal, since it must be related to the number, size, and direction of cracks which effectively hinder the good flow of heat. The samples which showed no evidence of surface melting are:

- SR-200 (case 4 only)

- S-65 (T) (case 4 only)
- Extruded (T) (cases 4 & 5)

5.3 Macrographs of selected samples

Figures 26-39 show photomacrographs of selected samples. A wide range of crack morphology can be seen.

5.4 Microscopic examination of selected fatigue cracks

Figures 40-43 show microphotographs of selected samples. The mean grain size was measured using the linear intercept method on selected tiles from case #5 after cycling. The measurement was taken approximately 5 mm away from the HAZ. The US grades showed a range of mean grain size from 5-12 microns. The mean grain size for DShG-200, 18.8 microns, is roughly twice as large as typical US grades. Also, the RF grade, TShG-56, showed an unusually large range of grain sizes, from 8 to 105 microns, within one sample.

5.6 Crack propagation depths

The cracks tended to fall into two categories: either straight, narrow and long or blunt, wide and short. The blunt, wide and short crack morphology was correlated with the best crack initiation resistance. Only one sample had both types of cracks: S-65C with the transverse direction parallel to the heated surface. This sample shows a long, straight, narrow crack propagation from one of the blunt cracks. There was no strong correlation with microstructural features such as grain size and inclusion concentration, but there was a complicated relationship with texture. The highly textured grades (sheet and extrusion) performed worse than partially textured grades such as VHP. HIP grades, which have minimal texture, performed worse than VHP grades.

Table 6 lists the crack depths measured from the side for all samples in cases 4 and 5. Samples in case 4 all received 2700 cycles, and 2400 cycles for case 5. The average length of all the samples was 0.8 mm (excluding $TiBe_{12}$). Typically, the cracks on the beam's exit side were 20% longer than on the beam's entrance side. Crack depths for case 5 were 24% longer than case 4, on average. The average crack depths are shown in Fig. 44.

The samples with the shortest cracks are:

- SR-200*
- TShGT
- S-65C (L)
- DShG-200
- Be/60% BeO
- TShG-56

*The length of the delamination crack is 0.6 mm deep.

The samples with the longest cracks are:

- $TiBe_{12}$
- Extruded (L)
- S-200F (L)
- I-400 (T)
- TGP-56

6. Discussion

6.1 Fatigue resistance

There are two significant components to life of a material in low cycle thermal fatigue: crack initiation and crack propagation. Although crack initiation resistance is an important characteristic to use in material selection, actual in-system use will not be limited by the initiation of a ten micron long crack. The limit on use will be propagation of that crack (1) to the extent that the beryllium spalls off, (2) the extent to which heat transfer is decreased by a laterally spreading cracks, or (3) the crack penetrates to the water cooled substrate causing a water leak.

Fig. 45 summarizes the experimental results; it shows both the crack initiation cycles and crack propagation depths. $TiBe_{12}$ is not shown, because the crack depths are off the scale (16 mm). If we look at just the grades of beryllium metal with isotropic and near-isotropic properties (S-65C, S-65H, S-200F, S-200F-H, 94% S-65, 98% S-65, I-400, TGP-56), we see an obvious trend. Samples in this group with high number of cycles to crack initiation also have low crack propagation depths, and visa-versa. This could be because they are tougher, or simply because there haven't been many cycles after crack initiation to propagate cracks deeper. Likewise, samples which initiate cracks early on have more time (e.g. cycles) to grow the crack deeper.

Some samples, such as SR-200, Be/30wt% BeO, and Be/60wt% Be), fall outside the trend described above. They show poor resistance to crack initiation,

but excellent resistance to crack propagation. The composites of BeO composites are easy to initiate cracks because they are brittle, but resist growing cracks because the thermal expansion coefficient of BeO is low, which reduces the cyclic thermal stress.

For the case of SR-200 (TShGT also), the low strength and ductility in the direction perpendicular to the plane of rolling explains why these samples formed a delamination crack relatively quickly. However, in-plane, vertical cracks (when viewed from the side), show excellent resistance to growth. This is probably due to the outstanding mechanical properties in the plane of rolling (350 MPa Yield, 550 MPa Ultimate, and 25% elongation, at room temperature for SR-200, from Table 4). Use of beryllium in this form, as sheet "lamellae", bonded to a copper tube with the tube running perpendicular to the plane of the sheet, has been proposed for ITER high heat flux components by Merola, Matera, Federici, and Chiocchio [18].

6.2 Performance of VHP grades versus HIP grades.

The reason why VHP grades performed better than HIP grades is not clear. One hypothesis is that there is more particle movement and hence more abrasion of the surface oxide in VHP compared to HIP, but this has not been confirmed. This hypothesis may help explain the good performance of some of the RF grades which had a wide range in grain size and very high BeO contents. Any forging which may have occurred probably broke up the continuous oxide film of the prior particle boundaries and provided greater total area of metal to metal bonding. TEM photographs also show that HIP grades have a more uniform oxide layer at the grain boundaries. VHP grades have been processed at much higher temperatures and at longer times, which allows the grain boundary oxide to coarsen.

6.3 Effect of Impurity Levels

Note that the two grades with nominally the lowest metallic impurity levels (excluding BeO) performed the best by crack initiation standards. S-65C is the highest purity structural beryllium grade in the Brush Wellman series of alloys, and the DShG-200 is the highest purity grade of the Russian Federation materials. Material purity is a strong controlling parameter given that basic material parameters such as microalloying and grain size are within acceptable limits. However, other factors must be important since there is poor correlation between Brush Wellman parameters and Russian Federation material parameters for the most successful materials: especially impurity concentrations, grain size, BeO content and microalloying appear to be different.

The low cycle fatigue tests indicate that the BeO concentration is not necessarily a robust predictor; the highest BeO concentration grade (I-400) performed identically to the lowest BeO concentration grade (BWI special extrusion).

6.4 Resistance to surface melting

Only three samples resisted surface melting in case 4: SR-200, S-65C, and extruded (T). Only the extruded (T) did not melt in case 5. Case 5 appears to have had a more intense beam spot heat flux. Three observations point to this: (1) melting of more tiles in case 5, (2) shorter number of cycles to initiate a crack (20% fewer cycles on average in case 5), and (3) longer cracks (24% longer on average in case 5). The good resistance to melting of the SR-200 and S-65 correlate well to the short crack depths that was observed. In the case of extruded (T) sample, the lack of melting, despite a deeper crack (1 mm), indicates that the crack was vertical and did not hinder the good heat conduction.

6.5 Comparison with finite element model results

Despite the shortcomings associated with using a 2-D finite element model, relatively good agreement can be found with the experimental observations. The size of the heat affected zone agrees well with the temperature profiles. The large amount of cyclic plastic strain, estimated to be 0.6 %, is consistent with the low number of cycles to crack initiation. The profile of cyclic stress is consistent with the observation of crack depths. The curvature of deeper cracks into a "J" shape that was observed is consistent with the concentration of compressive stress a few millimeters below the heated surface. The formation of a "bump" on top of the surface is predicted by the model. The orientation of the main vertical crack (e.g. parallel to the beam traverse), is consistent with the direction of maximum tensile stresses predicted by ABAQUS. Of course, this doesn't apply to those samples with highly anisotropic properties. Finally, the observation that cracks are open at the heated surface when viewed at room temperature is consistent with the residual tensile stress state developed upon cooldown.

7. Recommendations for Future Work

A metallographic study should be made of samples immediately after crack initiation is made. This would elucidate the crack initiation mechanism, which could aid in optimization of beryllium grade. The SNL low cycle fatigue tests investigated the number of cycles to initiation, but then continued cycling such that most materials had significant crack propagation. In fact, many of the long cracks changed modes by the conclusion of the test. The actual mechanism of crack initiation cannot be determined. Determination of the initiation mechanism may contribute significantly towards grade optimization for use in a tokamak.

The rankings shown here are only done to illustrate the differences in ranking which can result from the two different ranking measurements. The rankings are not statistically significant. Much more data is needed to make these rankings valid because fatigue measurements generally exhibit a large amount of scatter.

The work reported here is an important preliminary step in evaluating materials based upon tokamak thermal fatigue conditions. One obvious need is a calibrated e-beam profile which would allow quantitative comparison with tokamak conditions. Another would be reduce the temperature swing, and , hence, the stress swing, to a level closer to what is expected in ITER designs. This will likely result in longer numbers of cycles to crack initiation. So, one possibility is to increase the sweep frequency to 10 Hz, or to reduce the beam power level. Using 10 Hz will permit a total of 10,000 cycles in less than 20 minutes. The increased beam spot velocity will also help to prevent pre-heating of the tile ahead of the beam spot, which will produce a much more uniform heat affected zone.

More tests using pre-cracked or notched samples could be performed to focus only on the crack propagation aspects. Also, samples which have previously been exposed to simulated plasma disruptions (plasma guns) could be tested. Neutron-irradiated samples could be tested in the JUDITH facility. Finally, samples of plasma sprayed beryllium should be included.

Future efforts in finite element modeling should include : (1) using a 3-D model, with a moving e-beam spot, (2) anisotropic material's properties, (3) improved description of the yield surfaces (e.g. kinematic vs isotropic hardening).

Future work should also include measurements of the fatigue behavior, at a number of temperatures, using standard ASTM-type specimen geometries. Measurements of the fracture toughness, and fatigue crack growth rate curves, is needed, as well.

8. Conclusions

A novel technique has been developed to rapidly and efficiently determine the relative low cycle fatigue resistance of a number of different beryllium materials. Operating the electron beam at 1 Hz produces a localized temperature spike of sufficient intensity such that cyclic plastic strains on the order of 0.6% and cyclic stresses of 500 MPa are created, producing visible cracking in less than 3000 cycles.

A number of features were correctly predicted by a 2-D elastic-plastic finite element analysis, including: peak temperatures, width of the heat affected zone, orientation of the main crack, formation of a bump on the surface, depth of crack propagation, curvature of crack near a compressive zone, and residual tensile stresses causing crack opening upon cooldown. The 2-D, plane stress model did not account for two features: (1) out-of-plane stresses that caused delamination cracks in rolled sheet beryllium, and (2) narrowing of the tile due to plastic deformation.

The most fatigue resistant grades were S-65C, DShG-200, TShGT, and TShG-56. Rolled sheet Be (SR-200) and TShGT showed excellent crack propagation resistance in the plane of rolling, despite early formation of delamination cracks. Only one sample showed no evidence of surface melting, extruded (T), despite cracking. The good thermal conduction is preserved because cracks only grow perpendicular to the heated surface because of the highly aligned grain structure in the extruded form.

The degree and morphology of cracking is strongly dependent on the metallographic texture. Vacuum hot pressed grades generally perform better than hot isostatic pressed grades. Likewise for the longitudinal direction oriented parallel to the heated surface. Lower metallic impurity contents correlates well with increased fatigue resistance, but BeO content does not correlate well. The use of highly textured beryllium, i.e. rolled sheet, in the form of thin "lamellae" proposed by Merola appears to be an attractive concept for improving fatigue lifetime of

high heat flux components. A second round of electron beam experiments is recommended in order to generate better statistics, and to improve our understanding of low cycle fatigue behavior.

Acknowledgments

This work was performed at Sandia National Laboratories, supported by the US Department of Energy, Office of Fusion Energy, under contract DE-AC04-94AL85000. The authors wish to thank Brush Wellman, Inc. for their supply of the beryllium materials, and post-test examination, metallography, and chemical analyses. We wish to also thank Fred Bauer, Ken Trancosa, Jimmie McDonald, LaWonda Wold, and Wynona Sexson for their contributions to operating the electron beam test system and computer network.

References

[1] J. Hackman, J. Uhlenbusch, "Experimental Study of the Compatibility of Beryllium Limiters with a Tokamak Plasma", J. Nucl. Fusion, Vol. 24, No. 5, p. 640 (1984).

[2] P.K. Mioduszewski, et. al., "The Beryllium Limiter Experiment in ISX-B",J. Nuclear Fusion, Vol. 26, No. 9, p. 1171 (1986).

[3] K.J. Dietz, et. al., "Experience with High Heat Flux Components in Large Tokamaks", Fusion Engineering and Design, Vol. 16, p. 229 (1991).

[4] E. Bertolini, et. al., "Impact of JET Experimental Results and Engineering Development on the Definition of the ITER Design Concept", Fusion Engineering an Design, Vol. 27, p. 27 (1995).

[5] R.D. Watson, et. al., "Thermomechanical Testing of Beryllium for the JET/ISX-B Beryllium Limiter Experiment", Proc. 13th Symp. on Fusion Tech. (SOFT), Varese, Italy, p. 1283, Sept. 24-28, (1984).

[6] M.F. Smith, et. al., "Thermomechanical Testing of Beryllium for Limiters in ISX-B and JET", J. Fusion Technology, Vol. 8, p. 1174 (1985).

[7] R.D. Watson and J.B. Whitley, "Thermal Fatigue Tests of a Prototype Beryllium Limiter for JET", J. Nuclear Eng. and Design, Vol. 4, p. 49, (1986).

[8] private communication, R.D. Watson.

[9] E. Deksnis, et. al, "Solid Beryllium Tiles for the JET Pumped Divertor", Proc. SPIE High Heat Flux Engineering, Vol. 1739, p. 173 (1992).

[10] H.D. Falter, et. al, "Testing of Plasma Facing Materials for Divertors in the JET Neutral Beam Test Bed", Proc. SPIE, Vol. 1997 High Heat Flux Engineering-II, p. 170 (1993).

[11] H.D. Falter, et. al, "Thermal Test Results of the JET Divertor Plates", Proc. SPIE, Vol. 1739 High Heat Flux Engineering, p. 163 (1992).

[12] E.B. Deksnis, et. al, "Assessment of Water-Cooled Beryllium Components for Plasma-Facing Applications", Jnl. Nuc. Mat, Vo. 212-215, p. 1266 (1994).

[13] D.L. Youchison, et. al, "Thermal Fatigue Testing of a Diffusion Bonded Beryllium Divertor Mockup under ITER Relevant Conditions", Proc. 18th Symp. on Fusion Technology (SOFT), Aug. 22-26, Karlshrue,Germany, p. 287 (1994).

[14] D.L. Youchison, J.M. McDonald, L.S. Wold, "High Heat Flux Testing Capabilities at Sandia National Laboratories-New Mexico", ASME Heat Transfer in High Heat Flux Systems, HTD-Vol. 301, p. 31 (1994).

[15] I.C. Sheng and J. Howell, "Thermal Analysis of the Crotch Absorber in APS", Proc. SPIE, Vol. 1739 High Heat Flux Engineering, p. 200 (1992).

[16] PDA Engineering, Inc.

[17] Hibbett, Karlsson and Sorenson, Inc.

[18] M. Merola, R. Matera, G. Federici, S. Chiocchio, "Thermomechanical study of a new concept for a beryllium-protected high heat flux component", Fusion Eng. And Design, Vol. 28, p. 97 (1995).

Table 1 Thermal Properties of S-65C beryllium [7]

Temperature (C)	Thermal Conductivity (W/cm-K)	Heat Capacity (J/g-K)	Thermal Diffusivity (cm^2/s)	Density (g/cm^3)
51	1.87	1.91	0.54	1.82
139	1.52	2.24	0.38	1.81
183	1.44	2.35	0.34	1.81
242	1.34	2.44	0.3	1.81
291	1.29	2.53	0.28	1.8
336	1.25	2.61	0.27	1.8
400	1.17	2.67	0.24	1.79
464	1.1	2.73	0.23	1.79
543	1.02	2.78	0.21	1.78
619	0.96	2.86	0.19	1.77
700	0.88	2.94	0.17	1.76
854	(0.76)	(3.09)	0.14	1.74
996 (extrapolated value)	(0.64)	(3.22)	0.12	1.73

Table 2 Mechanical properties of S-65C beryllium [7]

Temperature (C)	Young's Modulus (GPa)	Thermal Expansion Coefficient (x10-6) 1/K	Yield Strength (MPa)	Ultimate Strength (MPa)	Ductility (%)
25	310	10.5	271	435	3-5
100		13.3			
200	300	14.8	233	386	17
300		16.3			
400	290	17.5	178	269	50
500		18.7			
600	230	19.8	120	164	29
700		20.7			
800	97	21.5			
900		22.2			
1000	48	22.7			
1100		23.3			
1200		23.7			
1300		24			
(Poisson's Ratio = 0.08)					

Table 3 List of US and RF beryllium grades

Brush Wellman Grades	Russian Federation Grades	Experimental US Grades
S-65H	TGP-56	Be/30wt% BeO, HIP
S-65C (L) VHP	TShGT	Be/60wt% BeO, HIP
S-65C (T) VHP	DShG-200	98% dense CIP/Sinter S-65
S-200F-H	TShG-56	94% dense CIP/Sinter S-65
S-200F (L) VHP		TiBe12
S-200F (T) VHP		
I-400 (L) VHP		
I-400 (T) VHP		
SR-200 rolled sheet		
HIP'd Spherical Powder		
High Purity Extrusion		

Table 4 Properties of US Beryllium Grades from Certification Sheets

Type	Ave Grain Size (microns)	Density %	Yield Strength (MPa)	Ultimate Strength (MPa)	Elongation (%)
S-65-C	8.1	99.8	284(L),284(T)	383(L), 383 (T)	3.0(L),3.9(T)
S-65-H	7.3	100	288(X),285(Z)	456(X),446(Z)	6.1(X),5.0(Z)
S-200-F	8.9	99.9	279(L),283(T)	373(L),407(T)	3.2(L),5.9(T)
S-200-F H	6	99.9	414(Z)	483(Z)	3.9
SR-200			348(L),363(T)	544(L),545(T)	25.5(L),24.5(T)
I-400	5	99.4		583(T),520(L)	
Extrusion			317(L),328(T)	731(L),414(T)	8.2(L),0.75(T)

Table 5 Chemical composition of US and RF beryllium grades, measured by Brush Wellman, Inc. in August, 1995

Type	Be (wt%)	BeO (wt%)	Fe (wt%)	C (wt%)	Al (wt%)	Mg (wt%)	Si (wt%)	Other Metals (wt%)	Zn	Ni	Mn
S-65C	99.4	0.6	0.07	0.03	0.02	<0.01	0.03	<0.04			
S-65-H	99.5	0.5	0.06	0.03	0.02	<0.01	0.02	<0.04			
S-200-F	99.2	0.9	0.1	0.08	0.04	0.01	0.02	<0.04			
S-200-F H	99.1	0.9	0.1	0.06	0.04	0.06	0.03	<0.04			
SR-200	98.9	0.9	0.08	0.15	0.03	<0.01	0.03	<0.04			
I-400	95.4	6.2	0.13	0.12	0.03	<0.01	0.06	<0.10			
Extrusion	99.76	0.38	785 ppm	0.01	70 ppm	80 ppm	95 ppm				
DShG-200		0.94	1005 ppm	0.028	130 ppm	<5 ppm	105 ppm		<10 ppm	345/235 ppm	25 ppm
TShGT		0.95	1185 ppm	0.031	120 ppm	<5 ppm	130 ppm		<10 ppm	270/410 ppm	45 ppm
TGP-56		1.3	1430 ppm	0.026	120 ppm	<5 ppm	140 ppm		<10 ppm	980/655 ppm	110 ppm
TShG-56		0.75	255 ppm	0.061	40 ppm	15 ppm	40 ppm		<10 ppm	75 ppm	25 ppm

Type	Sc	Cu	Ag	Ti	Co	Pb	Ca	W	U	Mo	Cr	N	Zr	B
DShG-200	<5 ppm	305/140 ppm	<3 ppm	65 ppm	3 ppm	<20 ppm	20 ppm	<100 ppm	<30 ppm	<20 ppm	290 ppm	90 ppm	<10 ppm	<2 ppm
TShGT	10 ppm	190/295 ppm	<3 ppm	70 ppm	5 ppm	<20 ppm	30 ppm	<100 ppm	<30 ppm	<20 ppm	200 ppm	115 ppm	<10 ppm	<2 ppm
TGP-56	<5 ppm	890/500 ppm	<3 ppm	135 ppm	5 ppm	<20 ppm	20 ppm	<100 ppm	<30 ppm	<20 ppm	275 ppm	140 ppm	<10 ppm	<2 ppm
TShG-56	<5 ppm	90 ppm	<3 ppm	5 ppm	3 ppm	<20 ppm	20 ppm	<100 ppm	40 ppm	<20 ppm	60 ppm	125 ppm	<10 ppm	NA

Table 6 Lengths of longest side cracks after cycling.

			Length of Longest Side Crack (mm)				
Case No.	Tile No.	Type	Beam Entrance Side	Beam Exit Side	Average Length	case #4 average	case #5 average
4	none	TiBe12	18	14.8	16.4		
4	3-1	S-200-F-H	1.2	1.2	1.2		
4	3-2	I-400 (T)	1.6	1.11	1.4	1.2	
5	4-14	I-400 (T)	1.1	1.4	1.3		0.6
4	3-3	SR-200	0.1	0	0.1	0.1	
5	4-3	SR-200	0	0.2	0.1		0.1
4	3-4	S-65-H	0.74	1.26	1.0	1	
5	4-4	S-65-H	1.2	1.5	1.4		1.4
4	3-5	Be/30wt%BeO	0.32	0.66	0.5		
4	3-6	98% dense S-65	0.55	0.85	0.7		
5	4-2	98% dense Be	0.32	0.89	0.6		
4	3-7	Be/60wt%BeO	0	0.55	0.3		
4	3-8	94% dense S-65	1.11	1.28	1.2		
4	3-9	Extrusion (T)	0.6	0.77	0.7	0.7	
5	4-1	Extrusion (T)	0.4	1.6	1.0		1
4	3-10	Extrusion (L)	2.04	1.38	1.7	1.7	
5	4-13	Extrusion (L)	2.3	2.3	2.3		2.3
4	3-11	TGP-56	0.91	1.28	1.1	1.1	
5	4-6	TGP-56	1.2	1.2	1.2		1.2
4	3-12	TShGT	0	0.1	0.1	0.1	
5	4-7	TShGT	0.3	0.35	0.3		0.3
4	3-13	S-65-C (T)	0.3	0.3	0.3	0.3	
5	4-5	S-65-C (T)	0.57	1.3	0.9		0.9
5	4-10	S-65-C (L)	0.34	0.21	0.3		
5	4-8	DShG-200	0.32	0.3	0.3		
5	4-9	TShG-56	0.7	0	0.4		
5	4-11	S-200-F (L)	1.4	1.4	1.4		
5	4-12	S-200-F (T)	0.85	1.2	1.0		
		Average Length (mm)	0.76	0.91	0.83	0.78	0.98

Note: The figures for this paper appear out of order to effect economies in reproduction.

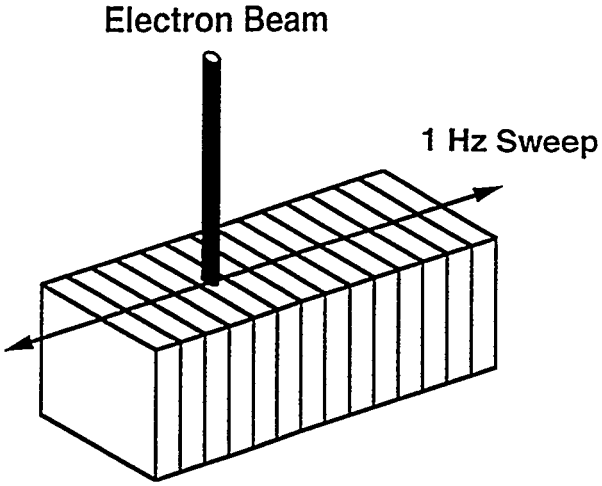

Fig. 1 Conceptual drawing of using a small electron beam spot swept back and forth across the surface of many samples to create low cycle fatigue damage.

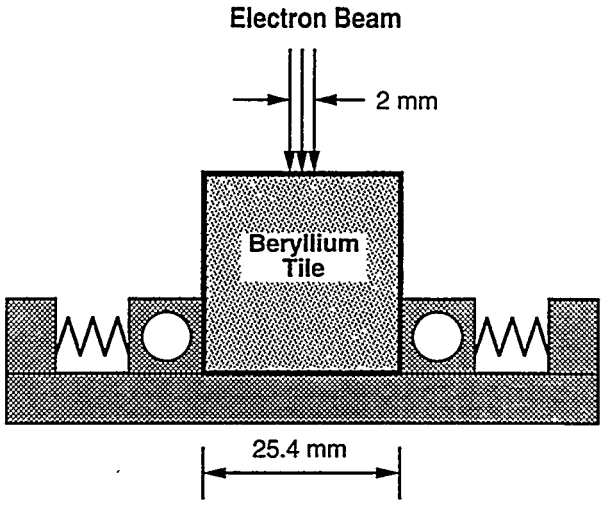

Fig. 2 End view of experimental setup for low cycle e-beam tests. The beryllium tiles are clamped by water cooled copper blocks with Papyex interlayer.

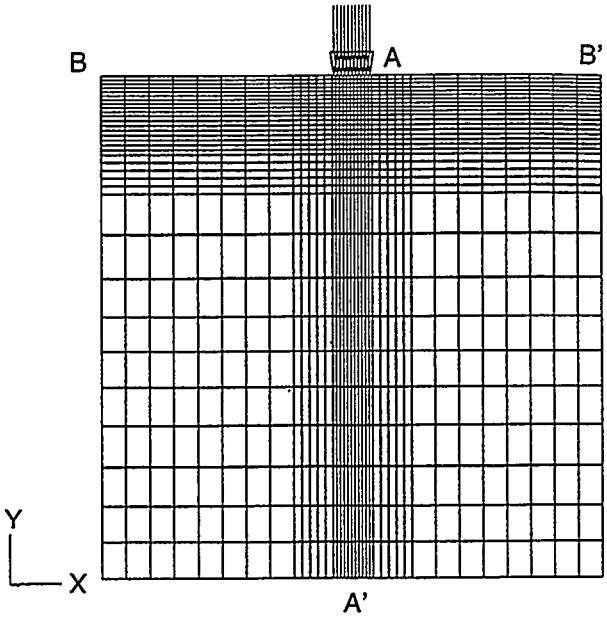

Fig. 3 Finite element mesh of beryllium tile made by PATRAN mesh generator. A finer mesh is used underneath the beam spot.

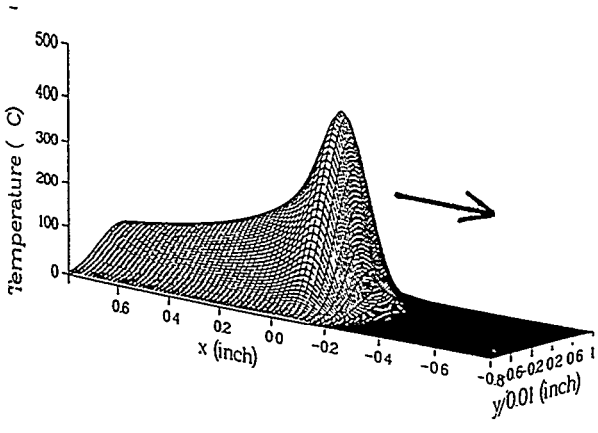

Fig. 4 Surface temperature distribution of a copper plate heated by 1000 W Gaussian e-beam spot moving at 200 m/s from left to right [15].

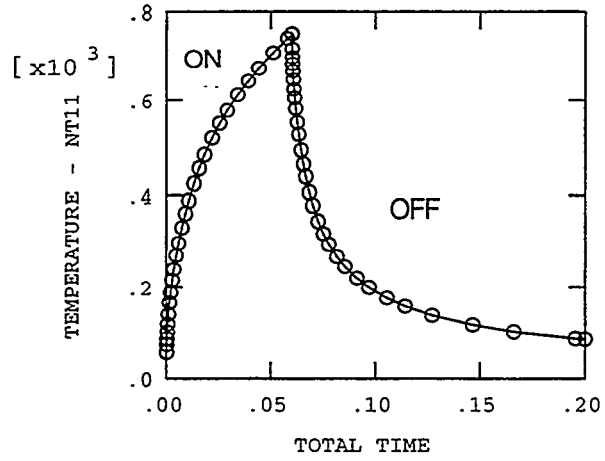

Fig. 5 Temperature (C) vs Time (s) for element #1086. Peak temperature = 750 °C at end of heating pulse, t = 0.06 s. Cooldown within 0.2 s to < 50 °C

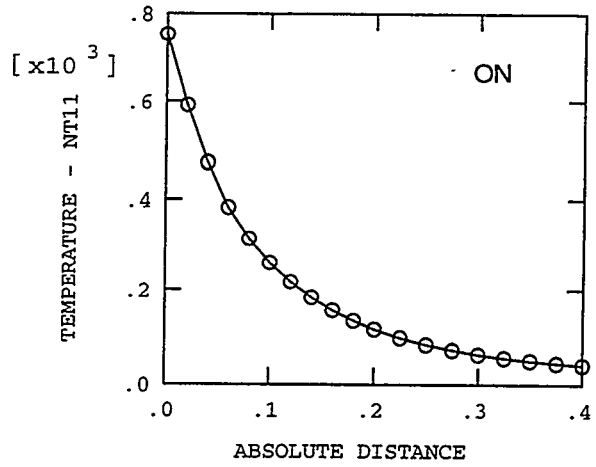

Fig. 7 Temperature profile (C) through thickness of tile at t=0.06 s along path A-A' (cm). Temperature has decayed to 10% of peak over a distance of 3 mm.

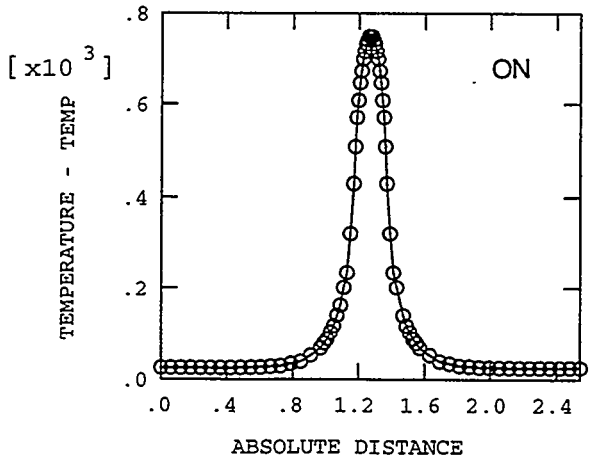

Fig. 8 Temperature profile (C) at t=0.06 s along a line following the heated surface from left side to right following path B-B'. Distance units in cm.

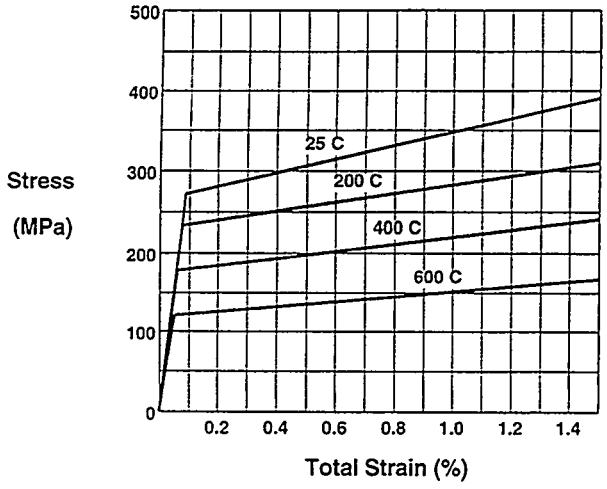

Fig. 9 Bi-linear stress/strain model used in ABAQUS finite element analysis code for S-65C beryllium [7].

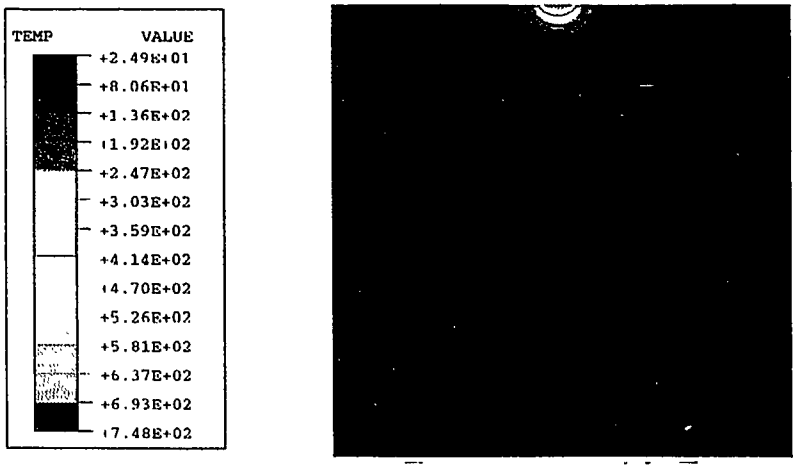

Fig. 6 Contours of constant temperature (C) at the end of the heating pulse, t=0.06 s. Peak temperature = 750 C.

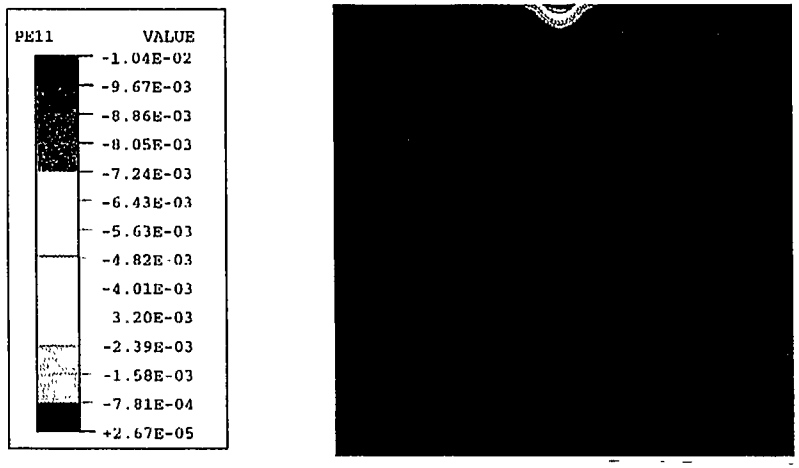

Fig. 12 Contours of constant plastic strain in the X-direction at the end of the heating pulse, t=0.06 s. Peak plastic strain = -1.0 %.

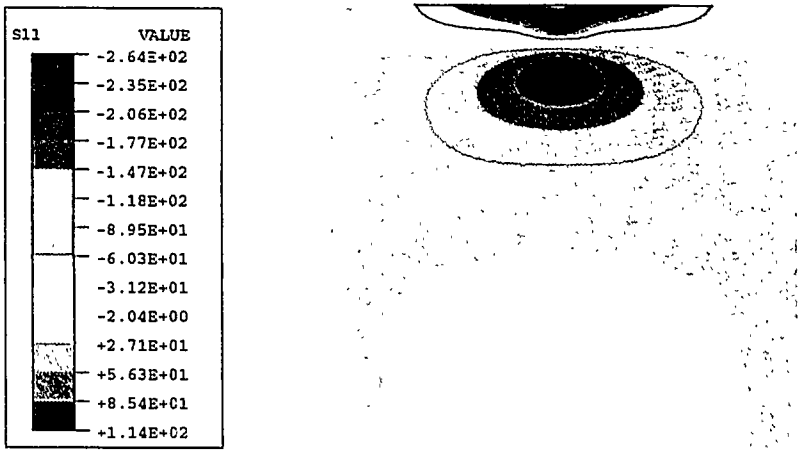

Fig. 11 Contours of contant stress (MPa) in the X-direction at the end of the heating pulse, t=0.06 s. Peak compressive stress = -260 MPa, peak tensile stress = 110 MPa.

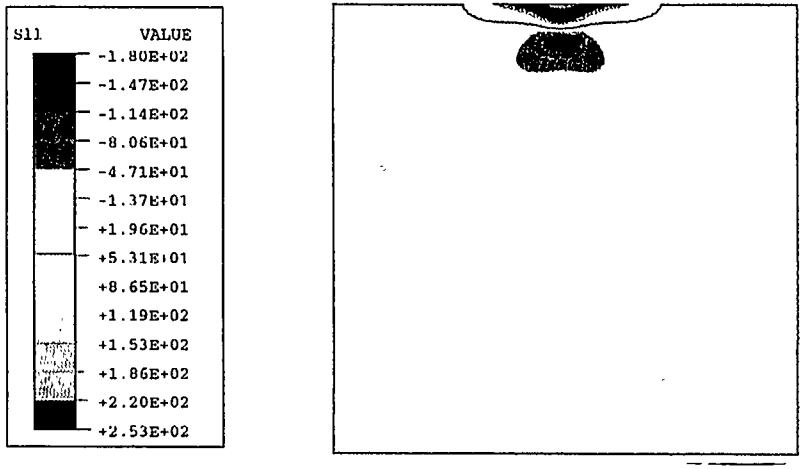

Fig. 16 Contours of contant stress (MPa) in the X-direction at the end of the cycle, t=1.0 s. Peak compressive stress = -180 MPa, peak tensile stress = 250 Mpa.

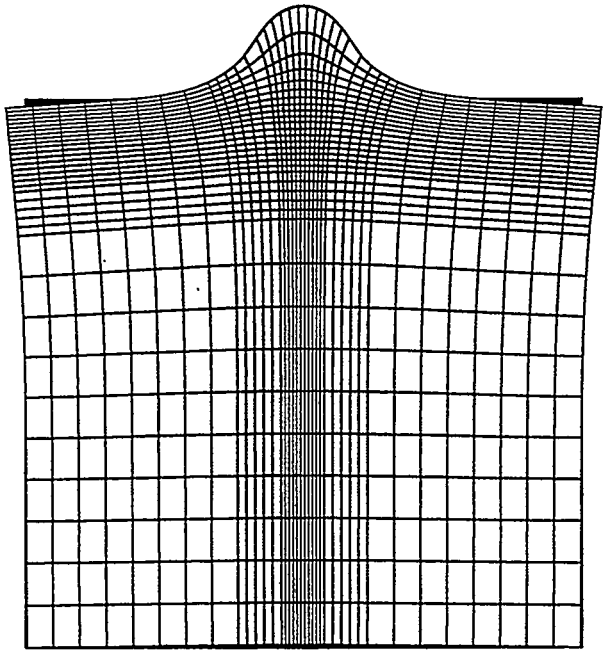

Fig. 10 Deformed mesh (magnified by 200 x) at the end of heating pulse, t=0.06 s. The expansion is greatest in the region of highest temperature rise.

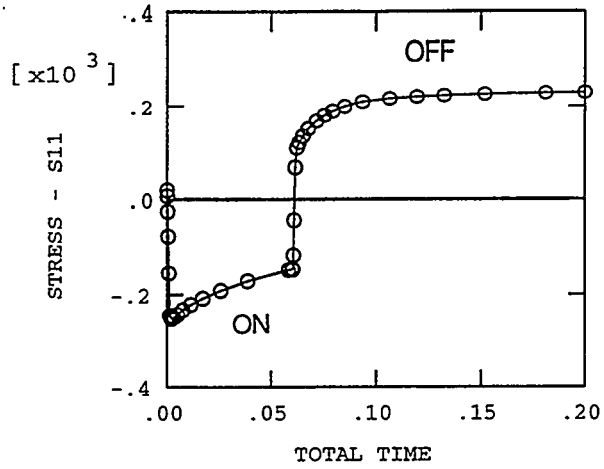

Fig. 13 Time evolution of σ_x stress in the X-direction during the first on/off cycle for element #1086. Peak compressive stress is -260 MPa, peak tensile is 240.

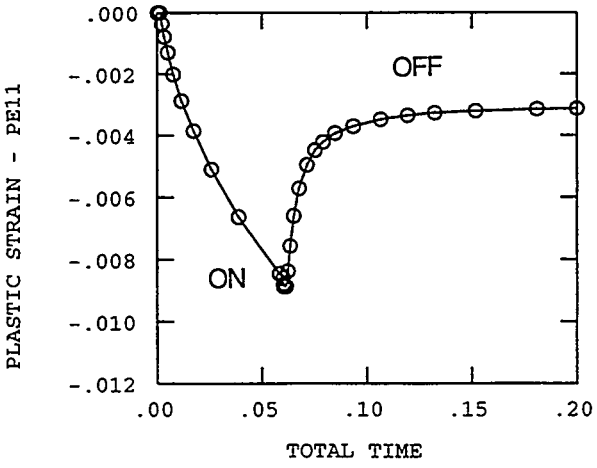

Fig. 14 Time evolution of the plastic strain ε_{px} in the X-direction during the first on/off cycle for element #1086. Peak plastic strain is -0.9% at t=0.06 s.

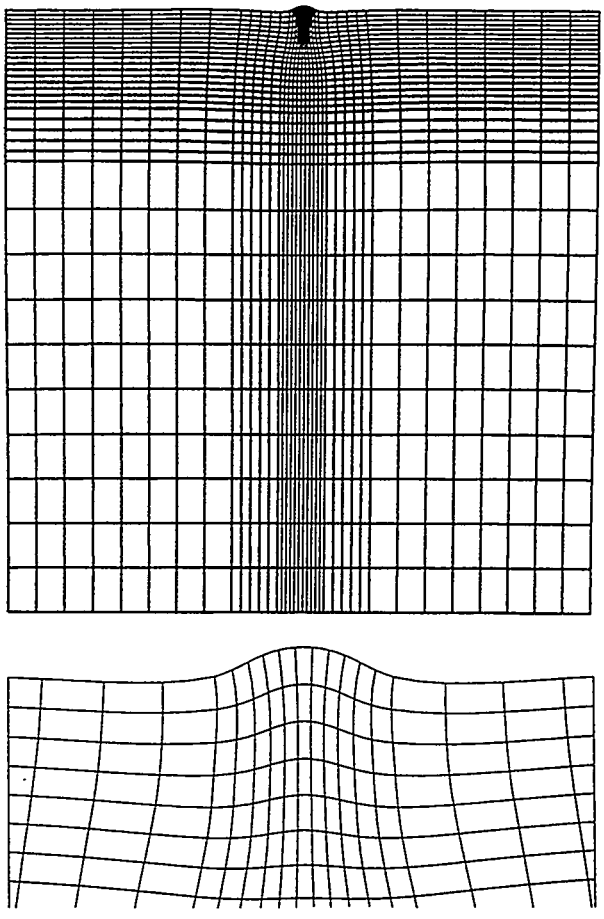

Fig. 15 Deformed mesh (magnified by 200 x) at end of cycle, t=1s. Residual plastic strain produces a small bump on the surface.

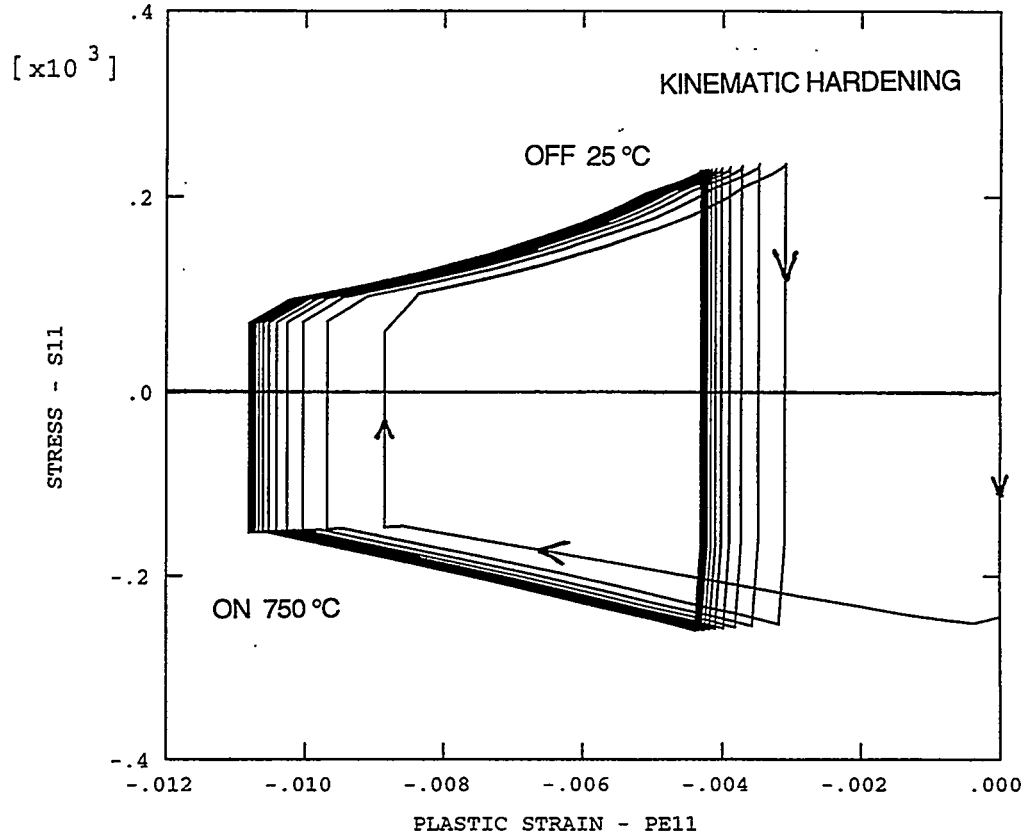

Fig. 18 Combined stress vs plastic strain loops for element #1086 (kinematic hardening) for 12 cycles. Cyclic plastic strain = 0.65%, cyclic stress=500 MPa. Convergence is achieved after 12 cycles.

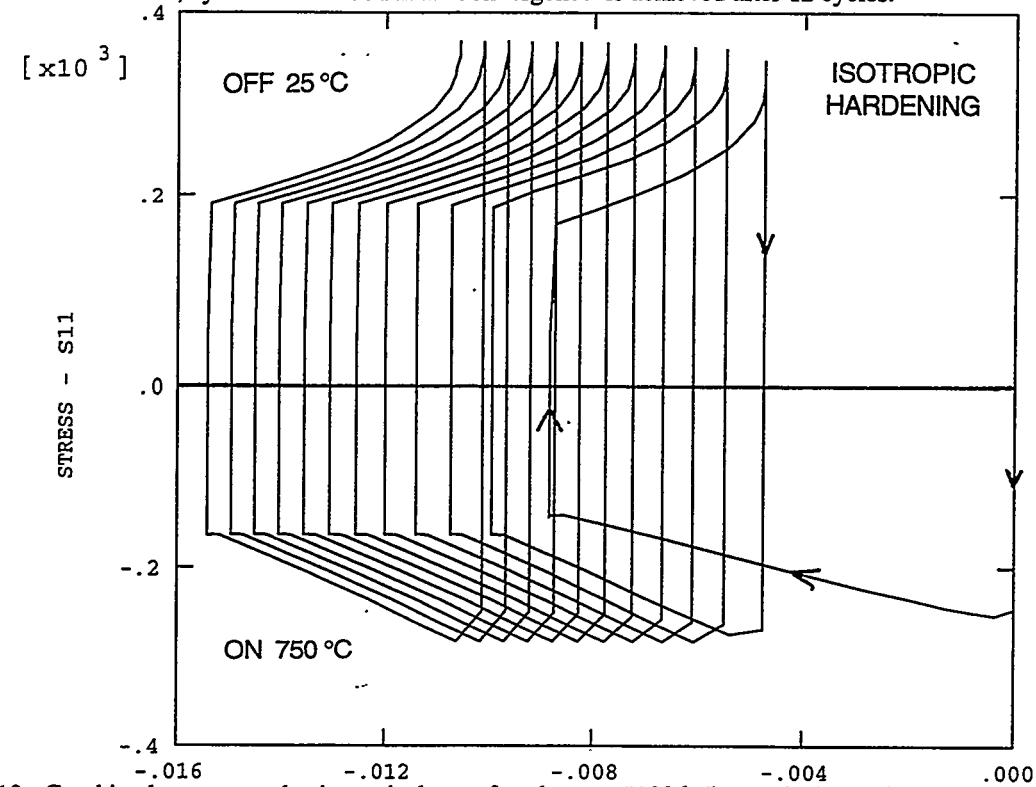

Fig. 19 Combined stress vs plastic strain loops for element #1086 (isotropic hardening) for 12 cycles. Cyclic plastic strain = 0.5%, cyclic stress=650 MPa. Convergence is not achieved after 12 cycles.

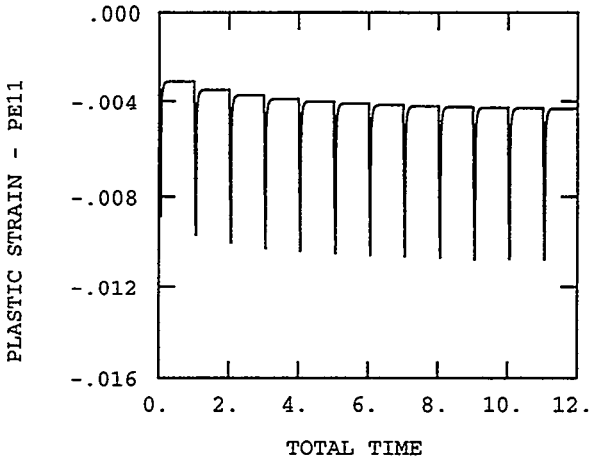

Fig. 20 Time evolution of plastic strain in X-direction for element #1086 with kinematic hardening.

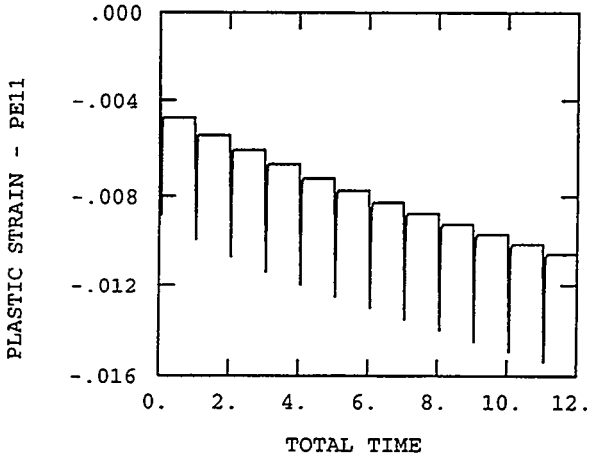

Fig. 21 Time evolution of plastic strain in X-direction for element #1086 with isotropic hardening.

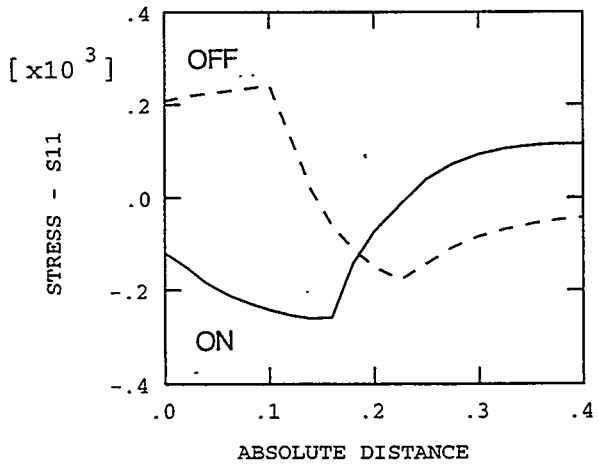

Fig. 22 Profile of σ_x through thickness along path A-A' (cm) at t=0.06 s and at end of cycle (t=1 s). Cyclic stress range, 500 MPa, remains flat for first 1 mm.

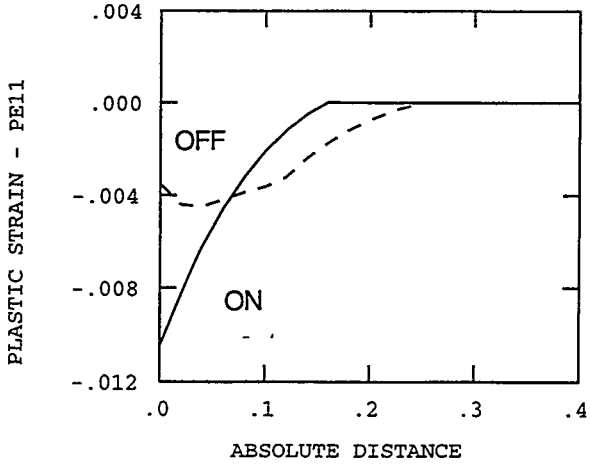

Fig. 23 Profile of ε_{px} through thickness along path A-A' (cm) at t=0.06 s and at end of cycle (t=1 s). Cyclic plastic strain is concentrated in first 0.5 mm.

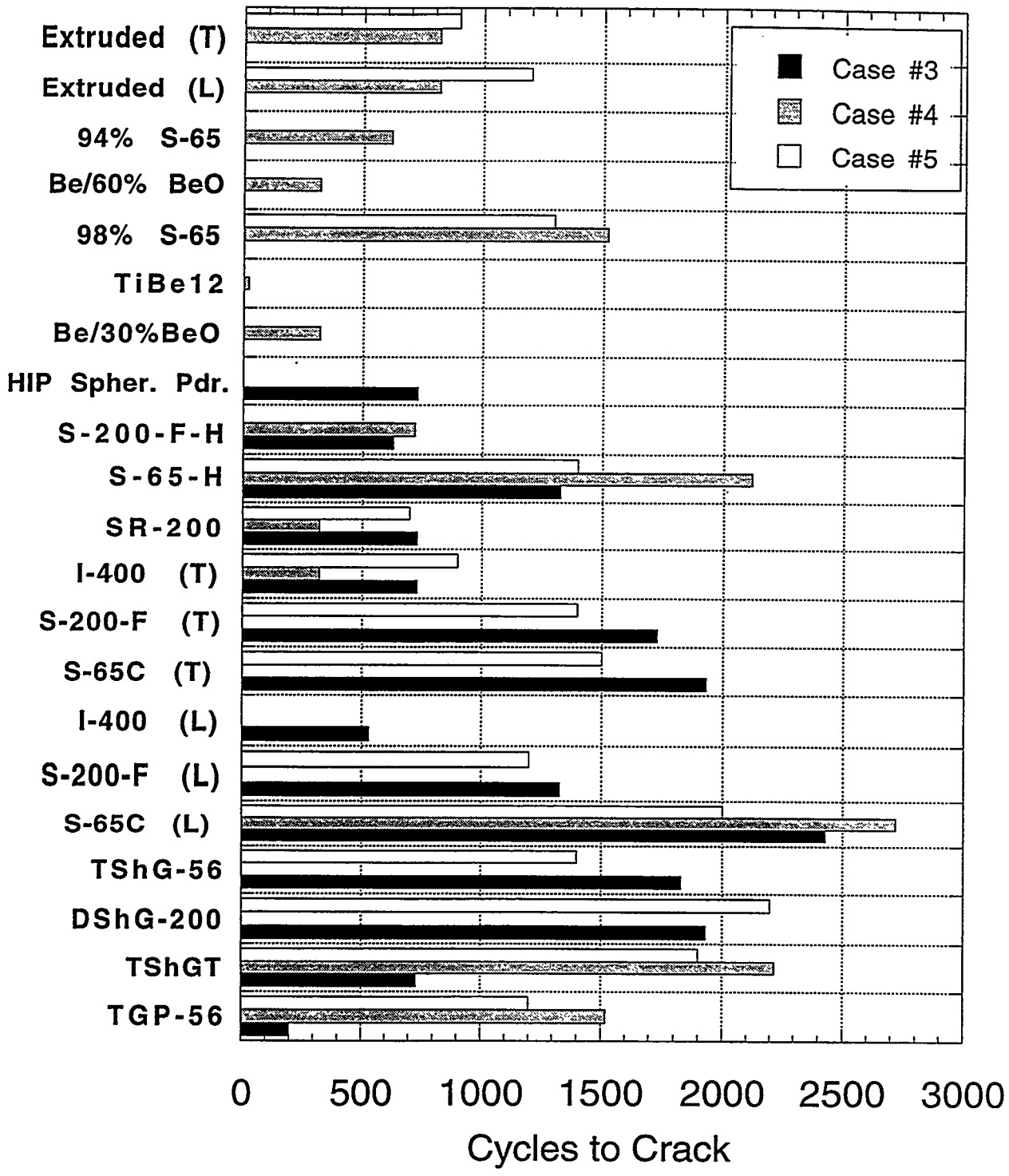

Fig. 24 Number of cycles to crack initiation for cases 3, 4, and 5, as observed by *in-vacuo* fiber optic borescope.

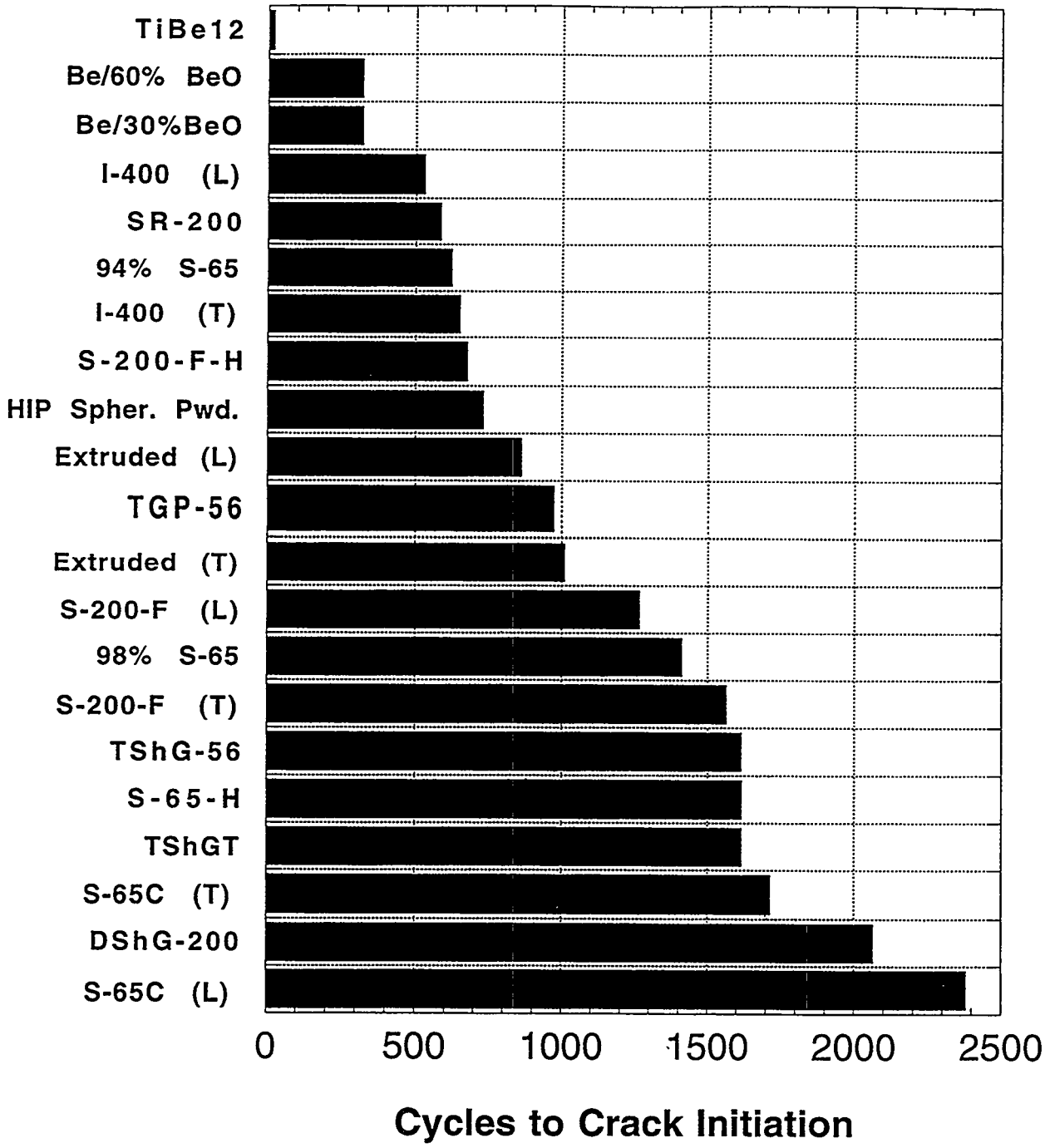

Fig. 25 Number of cycles to crack initiation averaged over cases 3, 4, and 5, as observed by *in-vacuo* borescope

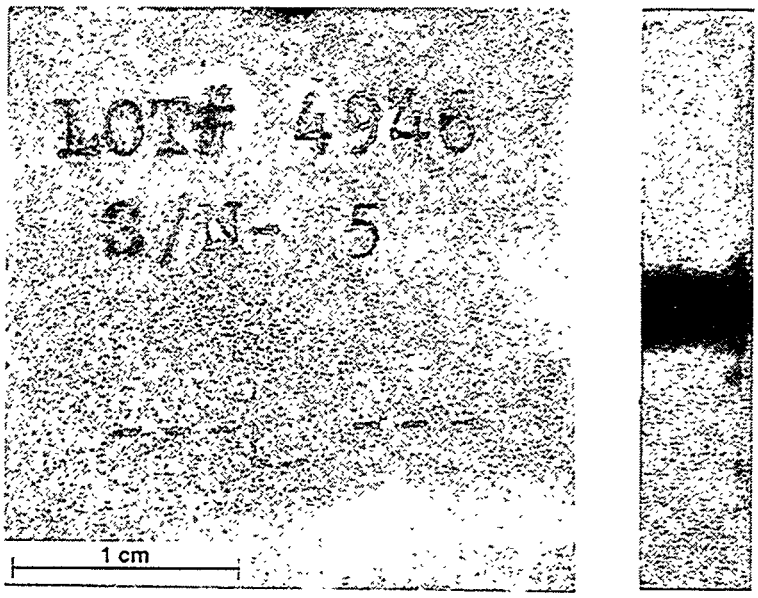

Fig. 26 Macro-photograph of S-65C (L) after 2400 cycles. Longitudinal VHP billet orientation is parallel to heated surface. A small raised bump can be seen on the side view. The top view shows a narrow heat affected zone (HAZ). Tile 4-10. Mag. 3X.

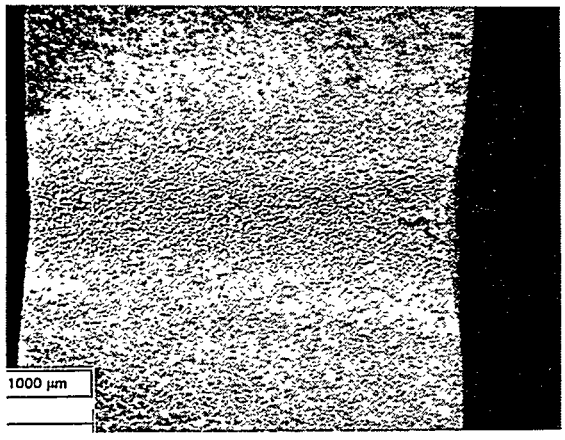

Fig. 27 Top view of S-65C (T) after 2700 cycles. Transverse VHP billet orientation is parallel to heated surface. Rising bread loaf look for 90% of HAZ. Last 10% of HAZ has a series of microcracks in it. Beam traverse from left to right. The tile is narrower in the HAZ. Tile 3-13. Mag. 18X.

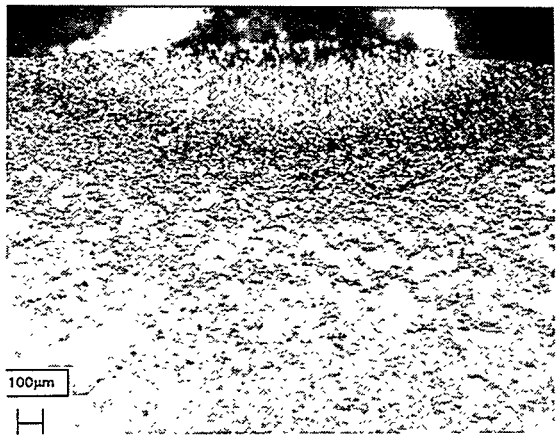

Fig. 28 Side view of S-65C (T) after 2700 cycles. Transverse VHP billet orientation is parallel to heated surface. Beam exit side. Average size HAZ perceptible only as a slight bulging. Other side has very short thin crack off center of HAZ. Tile 3-13. Mag. 47X.

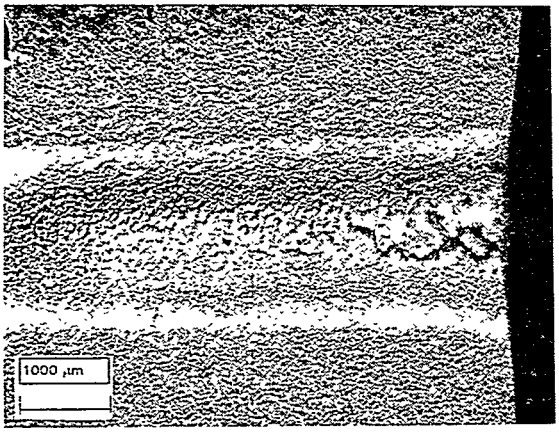

Fig. 29 Top view of RF grade DShG-200 after 2400 cycles. Beam traverse is from left to right. Raised surface separating into cracks and molten globules at one end. No major cracks. Tile 4-8. Mag. 18X.

Fig. 30 Side view of RF grade DShG-200 after 2400 cycles. Beam exit side. Shallow, medium depth HAZ with no crack. Tile 4-8. Mag. 47X.

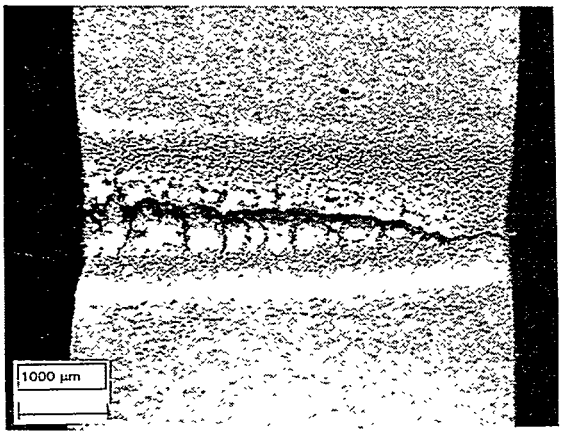

Fig. 31 Top view of S-200F (T) after 2400 cycles. Transverse VHP billet orientation is parallel to heated surface. Beam traverse is from right to left. Wide meandering central crack with molten globules at left end. Tile 4-12. Mag. 18X.

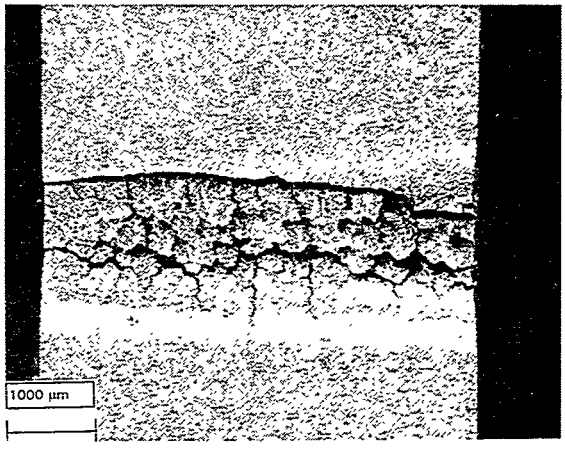

Fig. 32 Top view of I-400 after 2700 cycles. Transverse VHP billet orientation is parallel to heated surface. Beam traverse is from left to right. The top looks like an array of mounds or castellated beryllium which has a few cracks along that top surface that are oriented perpendicular to the beam traverse. Tile 3-2. Mag. 18X.

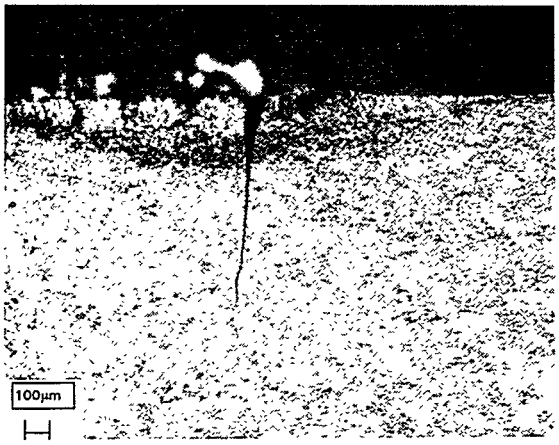

Fig. 33 Side view of I-400 after 2700 cycles. Transverse VHP billet orientation is parallel to heated surface. Beam exit side. Thin, straight crack in center of HAZ. Some lateral cracks about 0.1 mm below surface. Tile 3-2. Mag. 47X..

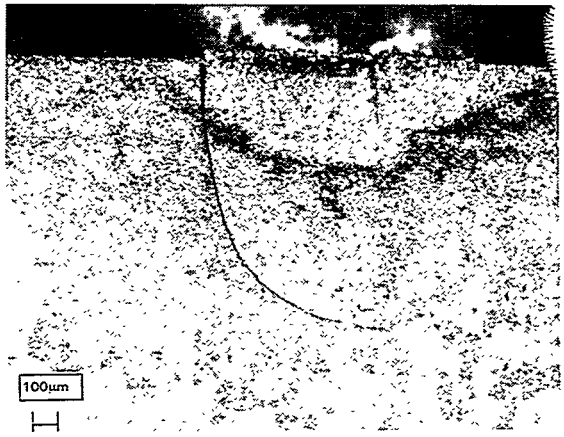

Fig. 34 Side view of I-400 after 2700 cycles. Transverse VHP billet orientation is parallel to heated surface. Beam entrance side. Thin, curved crack starting from edge of HAZ. Tile 3-2. Mag. 47X.

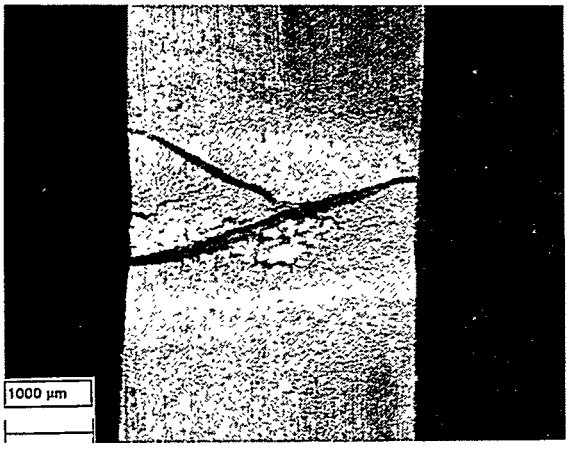

Fig. 35 Top view of high purity extrusion after 2700 cycles. Longitudinal extrusion billet orientation is parallel to heated surface. Beam traverse from right to left. Large, wide, Y-shaped fracture. Surrounding material looks like it has risen above the original surface, and has many microcracks distributed throughout it. Tile 3-10. Mag. 18X.

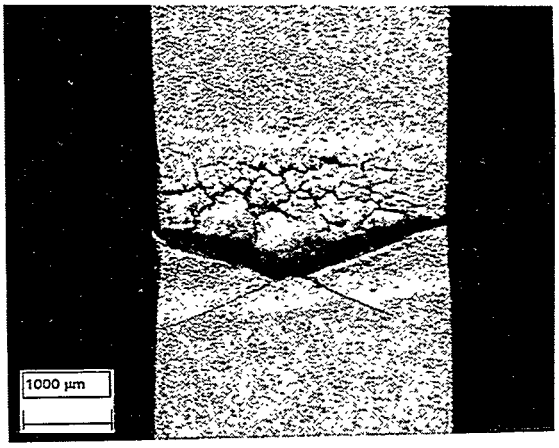

Fig. 36 Top view of high purity extrusion after 2400 cycles. Longitudinal extrusion billet orientation is parallel to heated surface. Beam traverse from right to left. V-shaped crack that is very wide and very deep, with the point of the crack at the center of tile. This crack has a strip of globules/beads on one side. Tile 4-13. Mag. 18X.

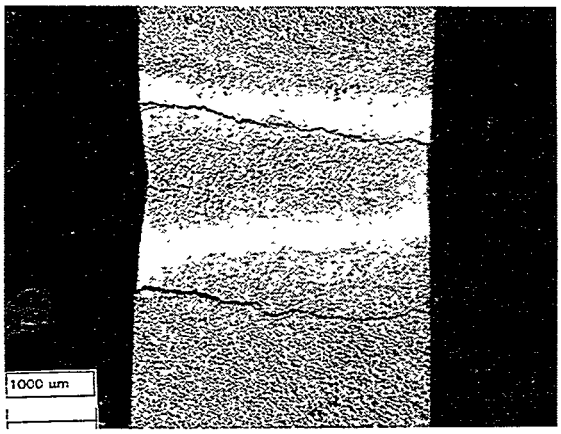

Fig. 37 Top view of high purity extrusion after 2700 cycles. Transverse extrusion billet orientation is parallel to heated surface. Beam traverse from right to left. Very shiny copper colored deposit defining HAZ. Two parallel, narrow cracks at either edge of HAZ. Tile 3-9. Mag. 18X.

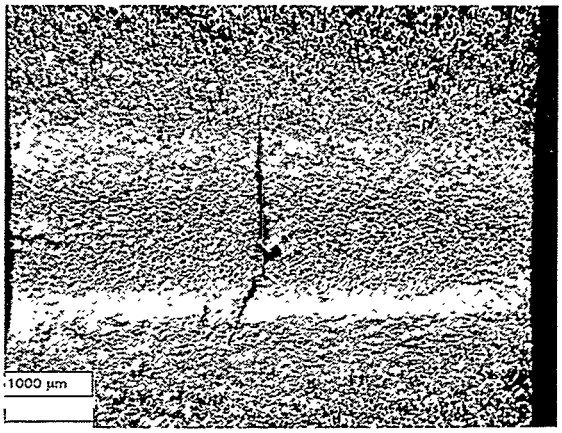

Fig. 38 Top view of RF grade TShGT after 2700 cycles. Longitudinal extrusion billet orientation is parallel to heated surface. Beam traverse from right to left. Rising bread loaf look along beam path. Medium width crack perpendicular to beam path in center of tile. Tile 3-12. Mag. 18X.

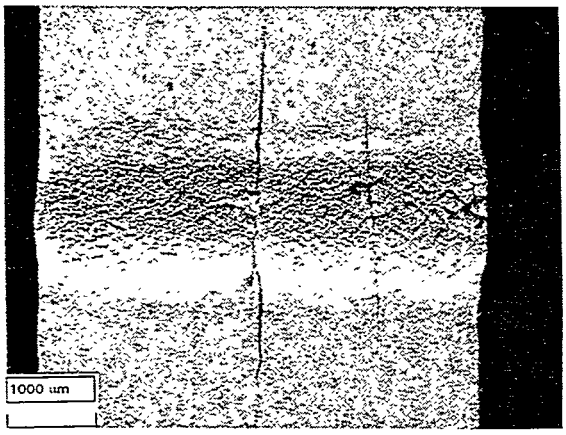

Fig. 39 Top view of SR-200 after 2700 cycles. Longitudinal extrusion billet orientation is parallel to heated surface. Beam traverse from left to right. Two long cracks perpendicular to beam path, one halfway and the other one quarter of the way from the beam exit side. Rest of the surface looks granular. Tile 3-3. Mag. 18X.

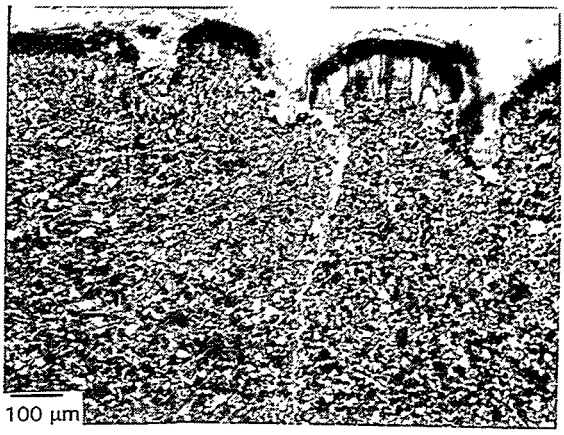

Fig. 40 Photomicrograph of main crack in VHP S-65C (T) tile after 2400 cycles. Transverse direction is parallel to the heated surface. Direction of view is same as Fig. 27 (side view). The major cracks are blunt and short, but also has a secondary crack that is long and narrow. No evidence of lateral cracks. Elongated columnar grains, 100 microns long, in region of melted bumps on top surface. Polarized light. Tile 4-5. Mag. 100X.

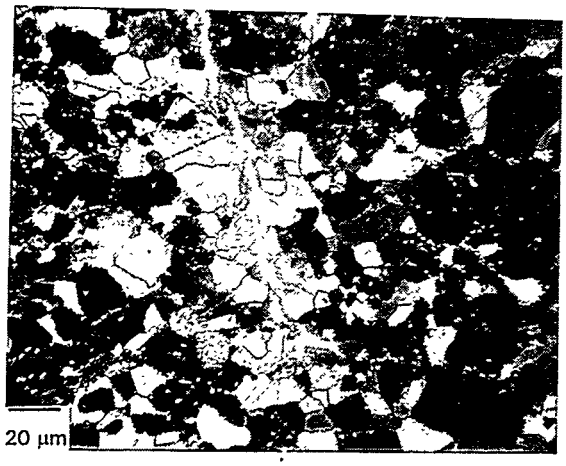

Fig. 41 Photomicrograph of main crack in VHP S-65C (T) tile after 2400 cycles. Transverse direction is parallel to the heated surface. Direction of view is same as Fig. 27 (side view). Focus is on long, narrow crack. Both intergranular and transgranular fracture is evident. Polarized light. Tile 4-5. Mag. 250X.

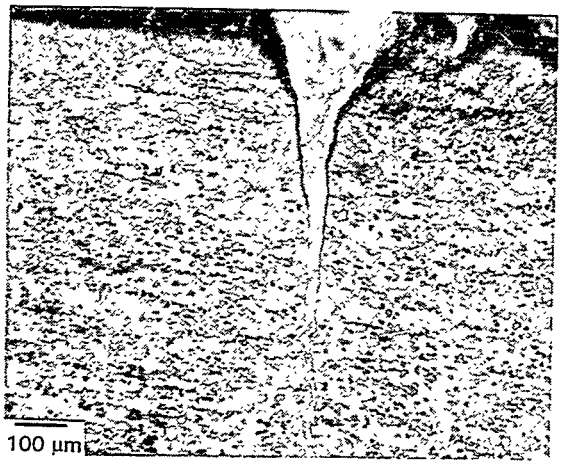

Fig. 42 Photomicrograph of high purity beryllium extrusion after 2400 cycles. Direction of view is same as Fig. 27 (side view). Transverse extrusion direction is parallel to heated surface. Main crack is narrow, long, and relatively straight. Polarized light. Tile 4-13. Mag. 100X.

Fig. 43 Photomicrograph of high purity beryllium extrusion after 2400 cycles. Direction of view is same as Fig. 27 (side view). Transverse extrusion direction is parallel to heated surface. The crack tip looks transgranular. The 90° bend in the crack is probably due to a hard particle of some kind, and is not representative behavior. Polarized light. Tile 4-13. Mag. 250X.

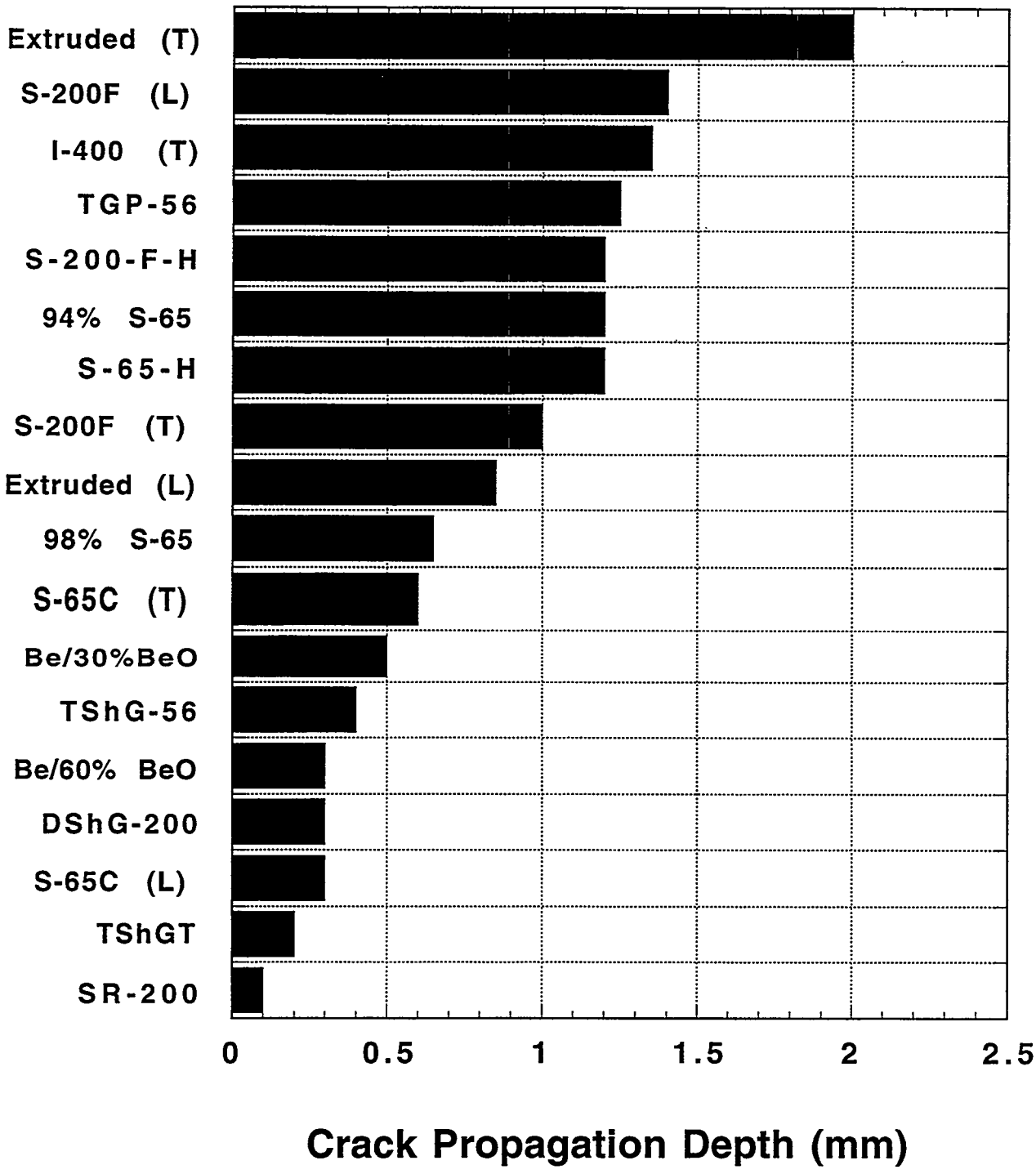

Fig. 44 Summary of crack propagation depths (mm), averaged among cases 4 and 5, both sides.

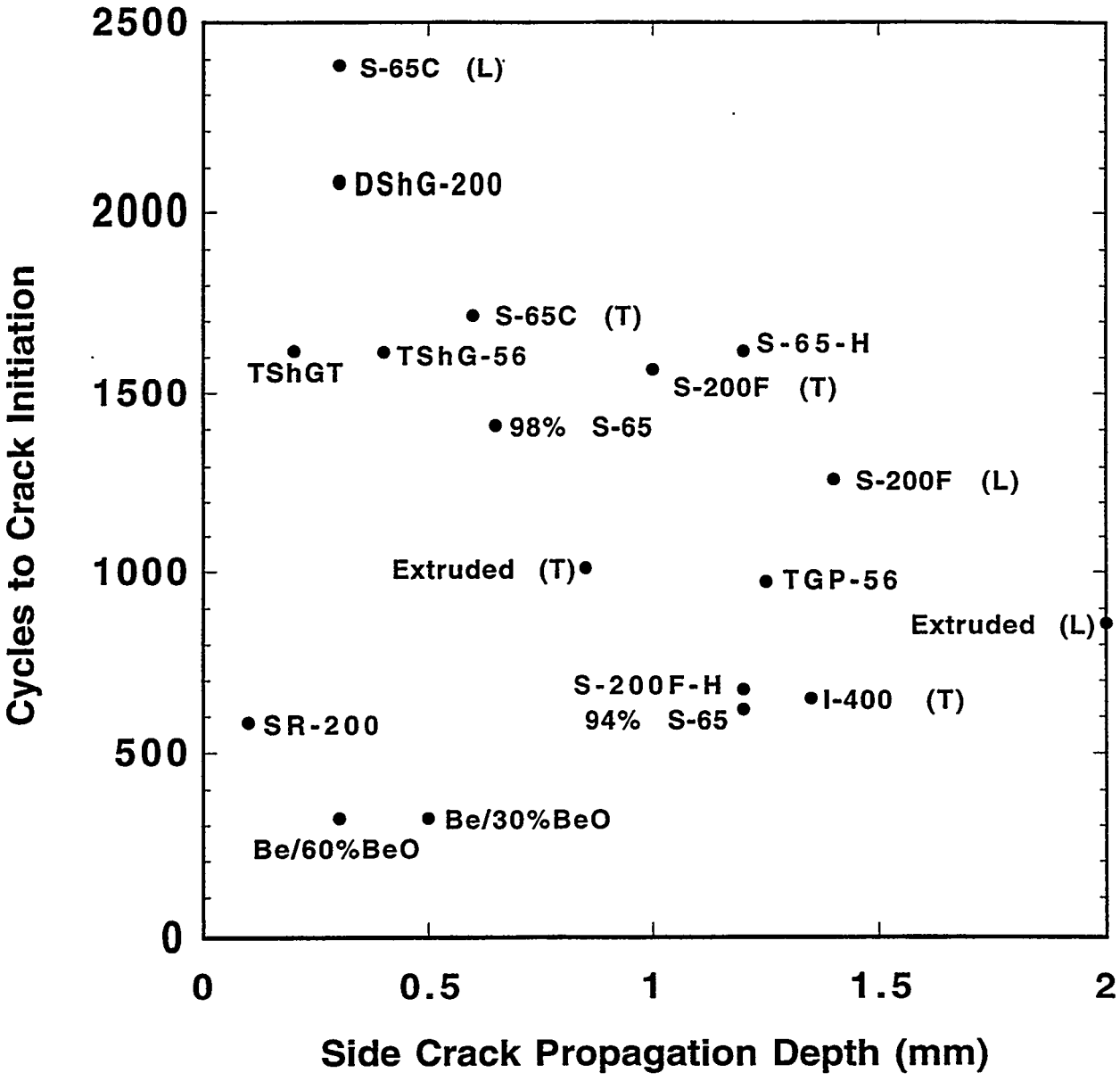

Fig. 45 Summary of experimental results. Crack propagation depths (mm), averaged among cases 4 and 5, both sides are plotted, along with number of cycles to crack initiation. Samples with best overall fatigue resistance would be found in the upper left-hand quadrant of this plot, including S-65C, DShG-200, TShGT, and TShG-56.

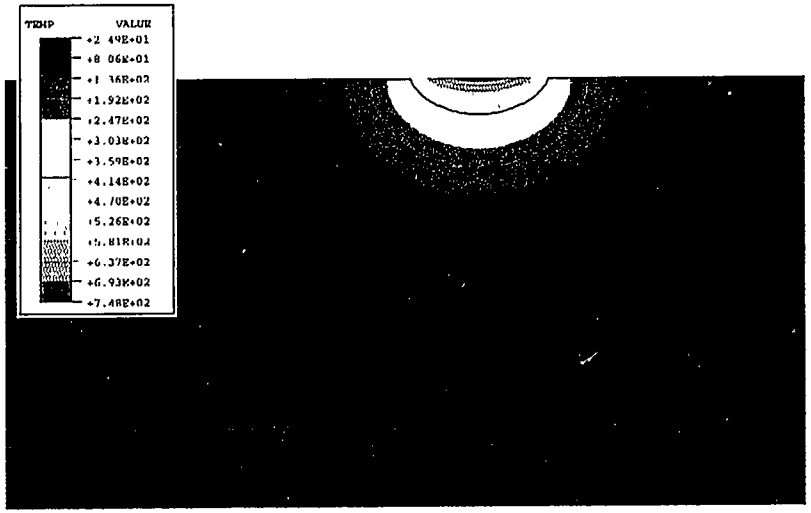

Fig. 46 Contours of constant temperature (C) at the end of the heating pulse, t=0.06 s. Peak temperature = 750 C. Zoomed-in picture.

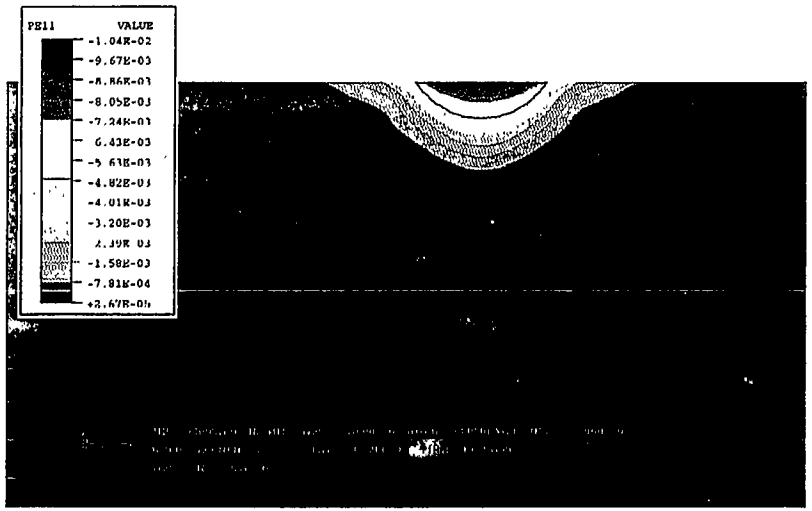

Fig. 48 Contours of constant plastic strain in the X-direction at the end of the heating pulse, t=0.06 s. Peak plastic strain = -1.0 %. Zoomed-in picture.

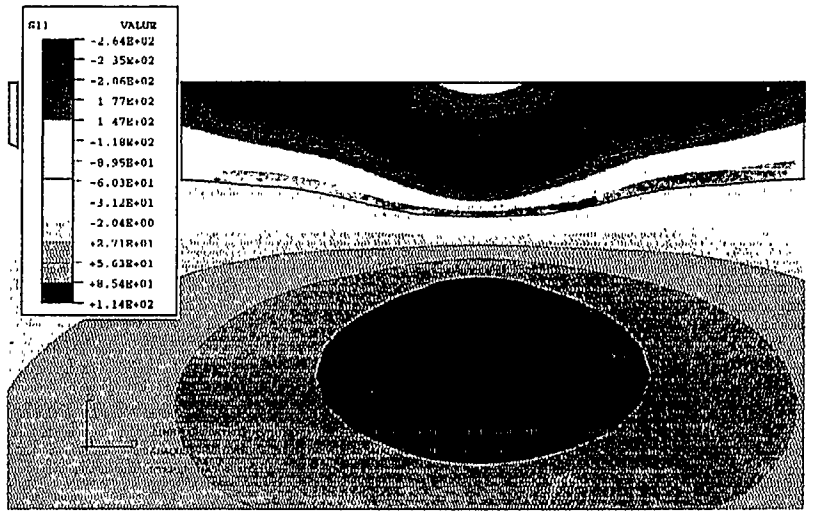

Fig. 47 Contours of contant stress (MPa) in the X-direction at the end of the heating pulse, t=0.06 s. Peak compressive stress = -260 MPa, peak tensile stress = 110 Mpa. Zoomed-in picture.

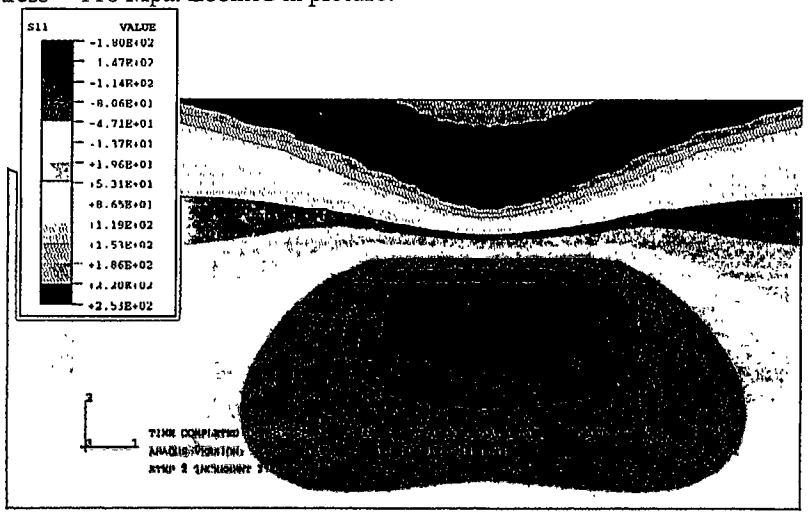

Fig. 49 Contours of contant stress (MPa) in the X-direction at the end of the cycle, t=1.0 s. Peak compressive stress = -180 MPa, peak tensile stress = 250 Mpa. Zoomed-in picture.

Thermal Shock Tests with Beryllium Coupons in the Electron Beam Facility JUDITH

M. Rödig, R. Duwe, A. Gervash*, A.M. Khomutov**, J. Linke, A. Schuster

Forschungszentrum Jülich GmbH, KFA-EURATOM-Association, D-52428 Jülich, Germany

* D.V. Efremov Scientific Research Institute of Electro-Physical Apparatus, 189 631 St. Petersburg, Russia

** Bochvar Institute, 123060 Moscow, Russia

Abstract

Several grades of American and Russian beryllium have been tested in high heat flux tests by means of an electron beam facility. For safety reasons, major modifications of the facility had to be fulfilled in advance to the tests.

The influence of energy densities has been investigated in the range between 1 and 7 MJ/m^2. In addition the influence of an increasing number of shots at constant energy density has been studied. For all samples, surface profiles have been measured before and after the experiments. Additional information has been gained from scanning electron microscopy, and from metallography.

1. Introduction

For the last four years, the electron beam facility JUDITH has been used for high heat flux testing of different kinds of plasma facing materials. Among these materials were CFC's, fine grain graphites, B_4C coatings, tungsten, SiC etc. [1,2,3]. Beryllium samples now have been loaded under thermal shock conditions for the first time in JUDITH. Beside the reference material S65C by Brush Wellman, several Russian beryllium grades have been tested. In the following, first results of these experiments are reported.

2. Experimental Set-up

2.1 Electron Beam Test Facility JUDITH

The facility consists of a modified electron beam welding machine, a vacuum chamber of 800 x 600 x 900 mm^3, and a number of diagnostic devices [4]. The focused electron beam with a diameter of 1 mm can be sweeped in two directions at frequencies up to 100 kHz. The technical data of the machine are as follows:

beam potential:	$\leq$ 150 kV
beam current:	$\leq$ 400 mA
beam power:	$\leq$ 60 kW
pulse duration	$\geq$ 1 ms
beam deflection:	$\pm$ 50 mm (in x- and y-direction)
scanning frequency:	$\leq$ 100 kHz

Short pulses up to 100 ms (as they were used in the thermal shock tests) are produced by means of a charged capacitor. Rise times for these pulses are 100 μs approximately.

The following diagnostic devices have been installed:

- two colour infra-red pyrometers, covering a temperature range between 300°C and 3500°C,
- a fast pyrometer from 1500 to 3500°C (rise time < 10 μs),
- an infra-red camera system (scanner) with cooled detector for temperature monitoring down to room temperature,
- a video camera for visual monitoring of the tests,
- several thermocouples,
- quadrupol mass spectrometer for rest gas analysis.

In addition to these diagnostic devices, it is possible to measure the total electron current through the sample.

The electron beam facility JUDITH is located in a hot cell and has been designed for the testing of neutron irradiated materials. Testing of irradiated materials will start in spring 1996.

2.2 Upgrades for Testing of Beryllium

In the thermal shock tests the evaporation and erosion of beryllium particles had to be taken into consideration, and due to the toxic behaviour of beryllium special safety requirements had to be taken. The safety concept was guided from the considerations to avoid the spreading of beryllium particles in the lab on one hand, and to avoid contamination of the electron gun and of the vacuum chamber on the other hand. The latter demand was seen under the aspect of future experiments with non-toxic materials such as CFC. The electron beam facility JUDITH has been provided with the following modifications (cf. fig. 1):

- insertion of a second containment inside the vacuum chamber being evacuated separately (inner vacuum chamber),
- magnetic electron beam deviation system and aperture to prevent contamination of the electron beam cathode,
- glove box for dust free loading and unloading of samples,
- locking mechanism at the door of the vacuum chamber to allow change of samples without flooding the main chamber with air,
- additional filters in both vacuum systems.

3. Materials

Beryllium S65C produced by Brush Wellman has been chosen as the reference material. Further tested materials are Russian TShG-200, TGP-56, and TR-30, delivered through Efremov Institute St. Petersburg, and a material delivered through Baikov Institute, Moscow (cf. table 1). The TR-30 material has been developed in respect to best neutron irradiation behaviour, i.e. low neutron induced swelling and low material properties degradation. It has got a fine grain structure, but due to high oxygen content it has a relatively poor ductility. TShG-200 is thought to exhibit best thermal shock resistance because of coarse grain structure and is expected to show good neutron irradiation properties, too. The TGP-56 covers an intermediate grain size and is a compromise between TR-30 and TShG-200. On the beryllium delivered through Baikov Institute little informations were available.

4. Performance of Tests

Two different types of test coupons have been used for thermal shock tests (cf. fig. 2):

- Samples "E" (25 x 25 x 10 mm^3) allow application of four spots 5 x 5 mm^2 on the surface without the changing of samples. Hence experimental time is minimised. But no weight loss measurements are possible fore these samples. However from the experience from former CFC tests, profilometry measurements seemed the more promising method of evaluation.
- Samples "F" (12 x 12 x 5 mm^3) in addition to profilometry allow weight loss measurements. These specimens also act as a reference for later tests with neutron irradiated samples.

Surfaces of all samples have been polished.

The loading parameters for the thermal shock tests have been chosen as follows:

- The loaded area was 5 x 5 mm^2. This was achieved by scanning of the electron beam with frequencies of 20 kHz in x-direction and 50 kHz in y-direction, respectively.
- Standard tests were one shot tests. Some additional series with 1, 2, 5, 10 shots have been performed to investigate surface conditioning effects.
- Energy flux density was 1....7 MJ/m^2 per pulse. This energy flux density is a bit lower as it is expected under ITER conditions. But in this first series of experiments it was intended to evaporate not too much beryllium for safety reasons. The variation of energy flux density is realized by variation of the beam current.

Profilometer measurements have been performed by an UBM microfocus laser scanning profilometer before and after e-beam loading to determine maximum depth of erosion craters, maximum height of ejected material, and mean erosion crater depth.

Weight measurements of test coupons have been accomplished before and after electron beam loading to determine the weight loss. Ultrasonic cleaning before measurements had to be applied to remove beryllium dust originating both from transport and from erosion due to the test.

Microphotographs of all samples have been taken before and after electron beam loading to determine surface changes optically. Metallographic pictures have been taken in a plane perpendicular to the surface of samples. Image analysis on sectioned samples for a crack structure analysis is in progress.

Scanning electron microscopy has been performed on several samples to examine oxide layer effects on beryllium test coupons.

5. Results

The maximum crater depth has been shown in fig. 3 as a function of energy flux density in the range between 1 and 7 MJ/m². For S65C in general the craters become deeper with energy flux density. But below 3 MJ/m² a swelling of the material is observed. For higher loadings more and more material is eroded and the crater depth increases with energy density.

Fig. 4 shows microphotographs of the sample surfaces loaded by e-beams shots of 1, 1.44, and 3.8 MJ/m². The profilometer line scans for these samples are shown in fig. 5. At 1 MJ/m² swelling is very homogeneous as can be seen from the line scan. But no influence can be recognised by surface microscopy; even the grinding groves are still visible after loading. At 1.44 MJ/m² for the first time the 5 x 5 mm^2-loading spot appears on the surface, swelling is still very homogeneous. From 2.4 MJ/m² a melting rim appears and from 2.9 MJ/m² a hole formation is visible.

At an energy flux density of 4.8 MJ/m^2 a marked dynamic melting process and whirling of the molten material can be seen. Resolidification may deliver asymmetric formations.

At an energy of 5.8 MJ/m^2 droplet formation has been detected for the first time. Drops spray out of the melt and resolidify on the surface of the material. Dynamical overflooding of the melt before resolidification takes place. Some samples partly show very deep holes, wide borders appear in the profile.

For the beryllium samples the highest applied energy flux density has been chosen as 6,7 MJ/m^2 per pulse. At this energy flux density besides an increase in dynamics no new behaviour has been found.

Scanning Electron Microscopy

Fig. 6 shows the SEM of a S65C sample loaded at 5.8 MJ/m². The brightness distribution of the photographs represents the oxygen distribution of the oxide surface layer on the sample, and, additionally a certain amount of topographic effect. This has been confirmed by EDX measurements. Three different regions can be distinguished: bright areas with a high oxygen

signal, consisting of pure beryllium oxide, dark areas, where signals of oxygen, carbon, silicon and aluminium can be found in approximately equal intensities. These areas are thought to consist of pure beryllium material in metallic form with only a thin oxide layer. The grey areas, consist of a mixed form.[1] The depth of penetration of the used 5 keV electrons in beryllium is approximately 0,3 μm. Therefore the oxide layer in the dark areas cannot be much thicker than this value.

Two kinds of cracks can be recognised:

- Cracks with a clear topography (the rims of these cracks can be clearly recognised), which are real cracks going into the metallic beryllium.
- Cracks without a clear topography which appear only in the surface oxide layer, opening a view on the (black) metallic beryllium.

Metallography

Fig. 7 shows metallographic pictures perpendicular to the surface for a high (5.8 MJ/m²) and a low (2,8 MJ/m²) energy density. At 5.8 MJ/m² melting takes place up to a depth of 200 μm approximately. A columnar grain structure appears for the resolidified material. The concentration of oxygen on the grain surface is thought to be gettered from the residual oxygen of the vacuum chamber. At 2.8 MJ/m² the columnar structure appears less clear, and an additional "S-shaped" structure seems to be overlaid. For this lower energy flux density no melting but a recrystallization has taken place.

For both loading conditions cracks appear perpendicular to the surface and penetrate only as deep as the molten/recrystallized zone. At 5.8 MJ/m² additional small cracks appear at the edge between the molten zone and the bulk material.

Comparison of different beryllium grades:

Fig. 3 in addition to the results of S65C, shows the maximum crater depth for the Russian beryllium grades. The material delivered through Baikov-Institute as well as TShG 200 and TR 30 show a strong influence of energy flux density on crater depth. But TGP 56 shows only slightly deeper craters than S65C.

[1]Beryllium with Z=4 cannot be detected by energy dispersive X-ray analysis (EDX). One is supposed to be concerned with pure beryllium if only the usual background signals of C, Si and Al can be found.

Micrographs for all four Russian beryllium grades loaded at 5.8 MJ/m² are shown in figures 8 to 11. Different to S65C the cracks go beyond the molten zone. This holds even for TGP 56 for which little cracking has been reported in [5]. TR 30 shows severe cracking with cracks moving parallel to the surface (cf. fig. 10). For this material the columnar grain structure can be observed even for low energy densities. This suggests that this grain structure is favoured by a high content of BeO.

Influence of number of pulses

A series of tests has been performed with different numbers of up to 10 pulses at a constant energy flux density of 2.4 MJ/m² (cf. fig. 12). If one leaves apart the values at 2.4 MJ/m² for TShG 200, most Be grades are not influenced by multiple shots. It is assumed that at relatively low energy flux density of 2.4 MJ/m² no evaporation of materials takes place, and thus during the following shots only a re-shaping of the surface without material loss takes place. Hence the crater depth stays more or less constant during the following shots.

The materials TR30 with a high BeO-content of 3 % behaves different, it shows an increasing crater depth with each shot. So it is assumed that no remelting of the surface takes place like for the other materials, but due to the brittleness of TR30 particles are eroded during each shot. This behaviour is similar to the one found for carbon materials [3].

Metallographic pictures of the grade S65C show that for multiple shot experiments, cracks grow into the bulk material beyond the recrystallized or molten zone (cf. fig. 13).

6. Summary

Thermal shock tests for Brush Wellman beryllium S65C and several Russian beryllium grades have been carried out. All materials show a swelling if loaded by a low energy flux density of up to 3 MJ/m² approximately. No melting seems to take place up to this load, but recrystallization is observed. Beyond 3 MJ/m² melting occurs and craters become deeper with increasing energy density. Erosion is lowest for S65C and for TGP 56.

Erosion depth seems not to be influenced by multiple shots (except for the brittle TR 30). This might be different at higher energy densities.

7. Future Activities

The reported results give only an overview on a first series of test on beryllium samples. Future activities in the JUDITH facilities will include:

- Thermal shock tests at higher energy flux densities (beyond 7 MJ/m²).
- Tests with new developed materials, such as plasma sprayed beryllium grades [6]
- Thermal shock tests on hot samples. Under tokamak operating conditions, beryllium tiles most of the time are on high temperatures up to 600 °C. As elongation of most beryllium grades is higher at elevated temperatures, the cracking and erosion behaviour might be different.
- Thermal shock tests after neutron irradiation. Neutron irradiations at 350°C and 700°C up to fluences of 0.5 dpa are carried out in the High Flux Reactor (HFR) at Petten [7]. Testing of irradiated samples will start by summer 1996.

References

[1] J van der Laan, G. Schnedecker, E.V. van Osch, R. Duwe, J. Linke: "Plasma sprayed boron carbide coatings for first wall protection in ITER", J. Nucl. Mater. 211, 1994, 135-140[1]

[2] P. G. Valentiene, P.W. Trester, J. Winter, J. Linke, R. Duwe, E. Wallura, V. Philipps: "Boron carbide based coatings on graphite for plasma facing components", J. Nucl. Mater. 212-215, 1994, 1146

[3] H. Bolt, H. Hoven, K. Koizlik, J. Linke, H. Nickel, E. Wallura: "Materials for High Heat Flux Components of the First Wall in Fusion Reactors", KFA-report Jül-2002 (1985)

[4] R. Duwe, W. Kühnlein, H. Münstermann: "The New Electron Beam Facility for Materials Testing in Hot Cells - Design and Preliminary Experience"", 18th Symposium on Fusion Technology (SOFT), Karlsruhe, 22. - 26.8.94

[5] R. D. Watson, D. L. Youchison, D. E. Dombrowski, R. N. Guiniatouline: "Low Cycle Thermal Fatigue Testing of Be Grades for ITER Plasma Facing Components", 2nd Int. Workshop on Beryllium Technology for Fusion, Jackson Lake Lodge, Wyoming (USA), Sept. 6 - 8, 1995

[6] R. Castro, P. W. Stanek, K. E. Elliot, A. D. Bartlett, R. D. Watson, D. L. Youchison, D. S. Walsh: "Structure, Properties, and Performance of Plasma-Sprayed Beryllium for Fusion Applications", 2nd Int. Workshop on Beryllium Technology for Fusion, Jackson Lake Lodge, Wyoming (USA), Sept. 6 - 8, 1995

[7] J. Linke, R. Duwe, A. Gervash, W. Kühnlein, M. Roedig, A. Schuster, Nakamura, A. Peacock: "Pre-irradiation Testing of Actively Cooled Be/Cu Divertor Modules", 2nd Int. Workshop on Beryllium Technology for Fusion, Jackson Lake Lodge, Wyoming (USA), Sept. 6 - 8, 1995

	production process	BeO content [%]	hardness HV 20	UTS (RT) [Mpa]	elong. (RT) [%]	elong.(600°C) [%]
S65-C	PM vacuum hot pressed	< 1	171	454	5,4	26 (long.) 31 (transv.)
TShG 200	PM punched	0.8	134	146 (long.) 259 (transv.)	0 (long.) 0.5 (transv.)	29.5 (long.) 29.5 (transv.)
TGP 56	PM sintered, hot pressed	0.9	173	236 (long.) 356 (transv.)	0 (long.) 1.2 (transv.)	29.5 (long.) 30.6 (transv.)
TR 30	PM punched	3.1	250	589 (long.) 691 (transv.)	0.2 (long.) 1.9 (transv.)	9.3 (long.) 14.9 (transv.)
cond. Be (Efremov)	condensed from Be vapour	0.15		140 (transv.)	3.5 (transv.)	
Baikov		<1	173			

Table 1: Description of tested beryllium grades

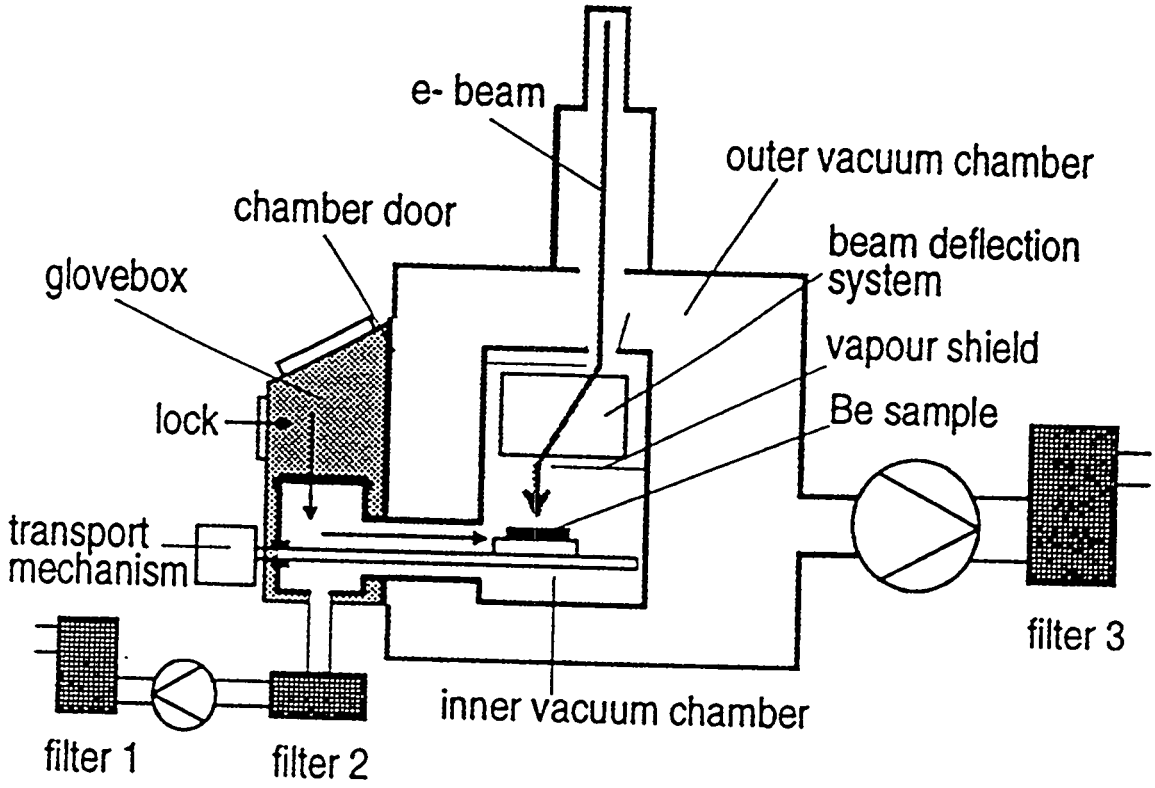

Fig. 1: Modifications of JUDITH for thermal shock testing of beryllium samples

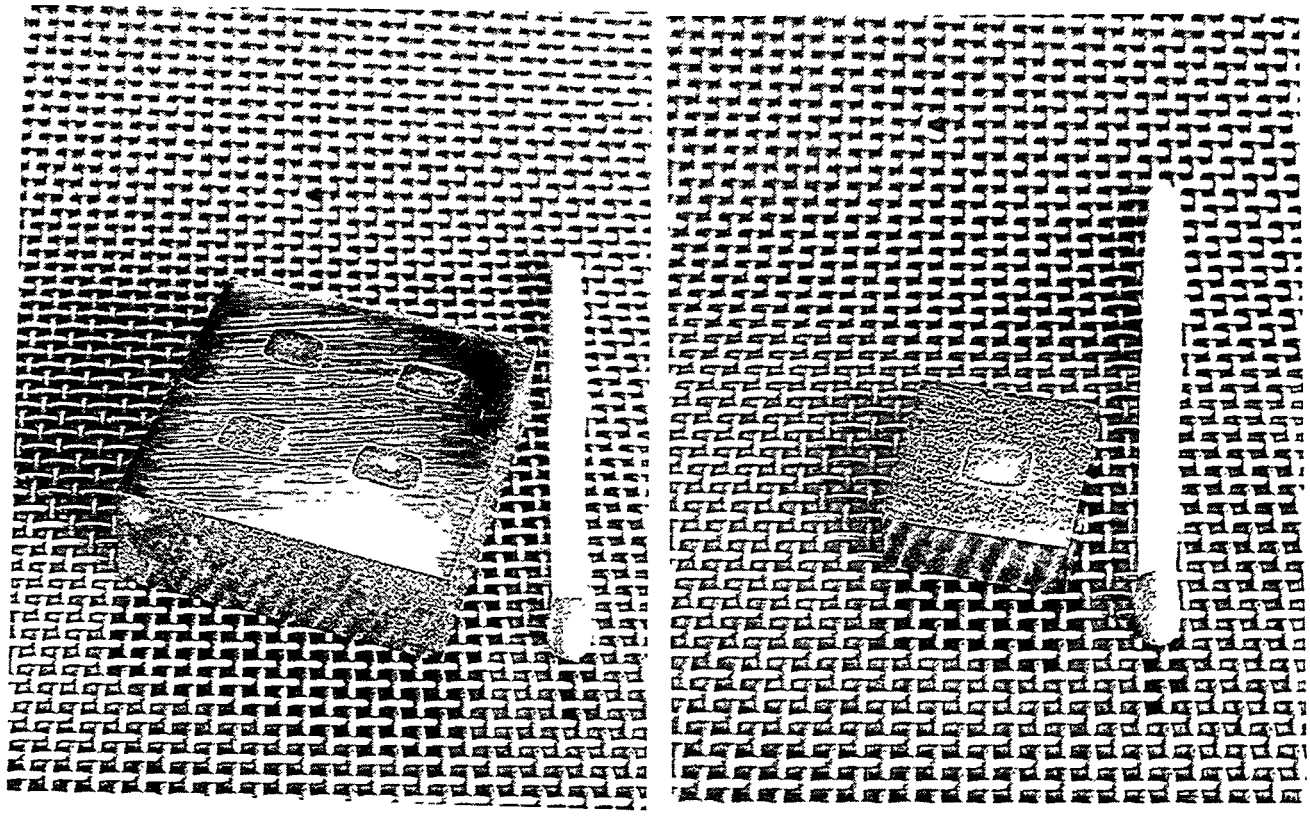

Fig. 2: Thermal shock samples used in the experiments. Sample "E" (left) allows four shots, sample "F" (right) one shot on each sample

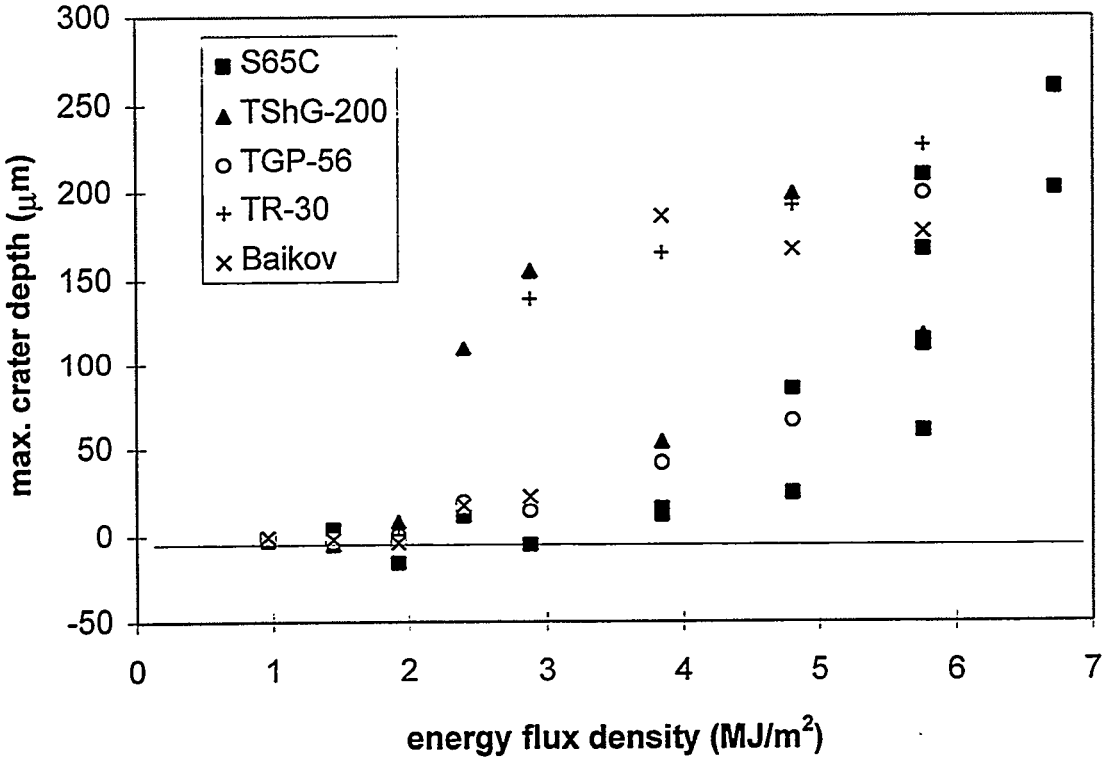

Fig. 3: Maximum crater depth as a function of energy flux density for different grades of beryllium (sample type "F", Δt = 5 ms, single shots)

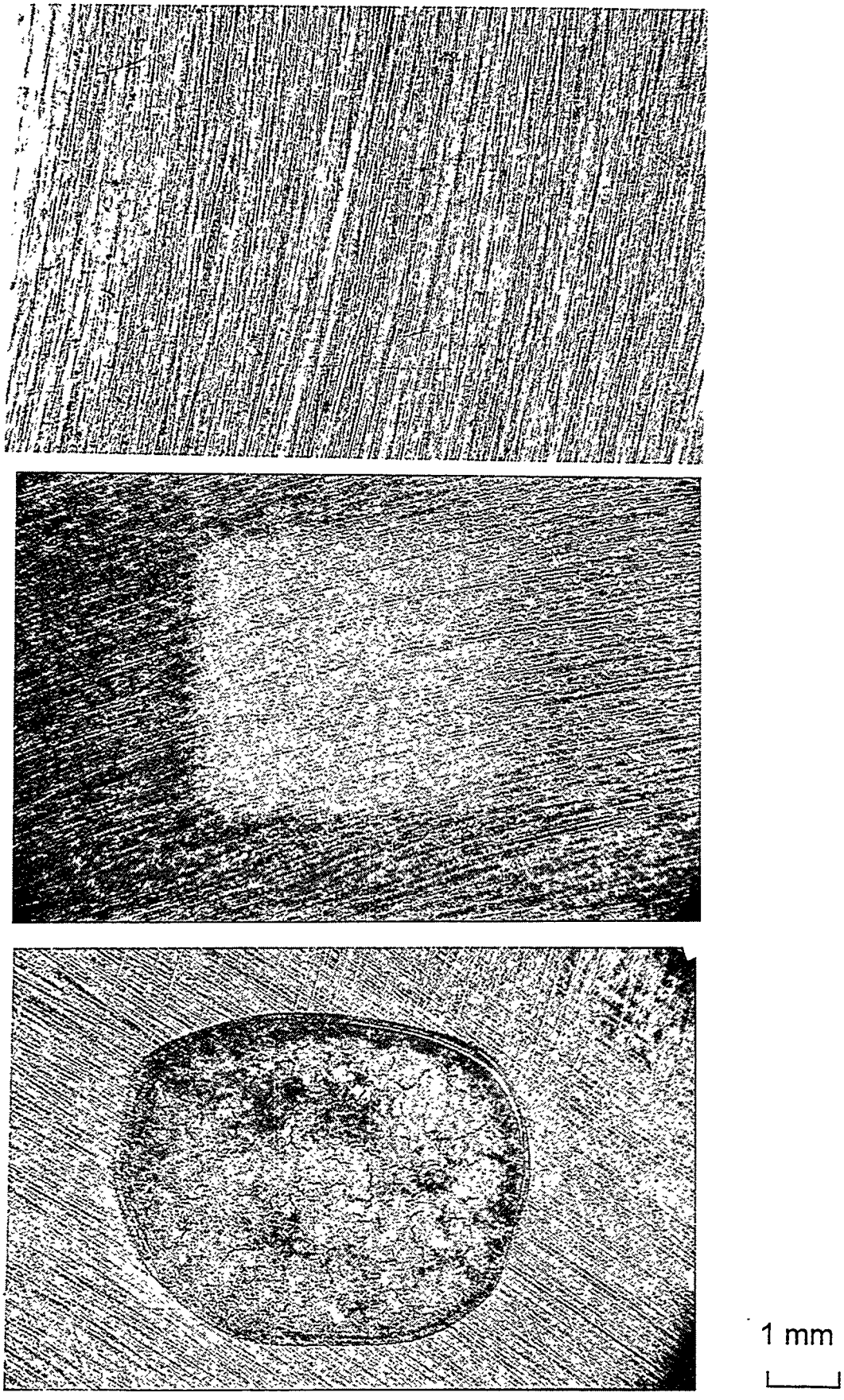

Fig. 4: Microscopic pictures of sample surfaces loaded at 1.0, 1.4 and 3.8 MJ/m², (Δt = 5 ms, single shots).

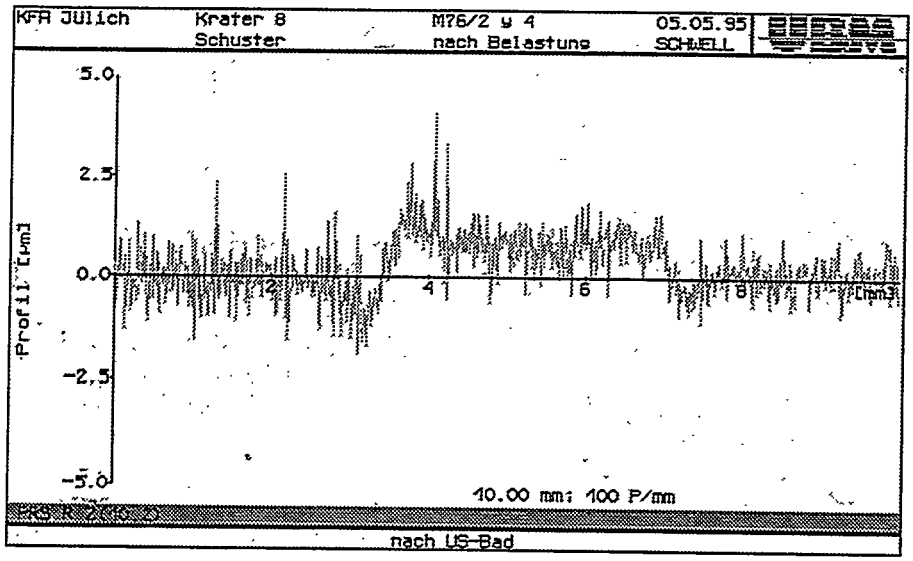

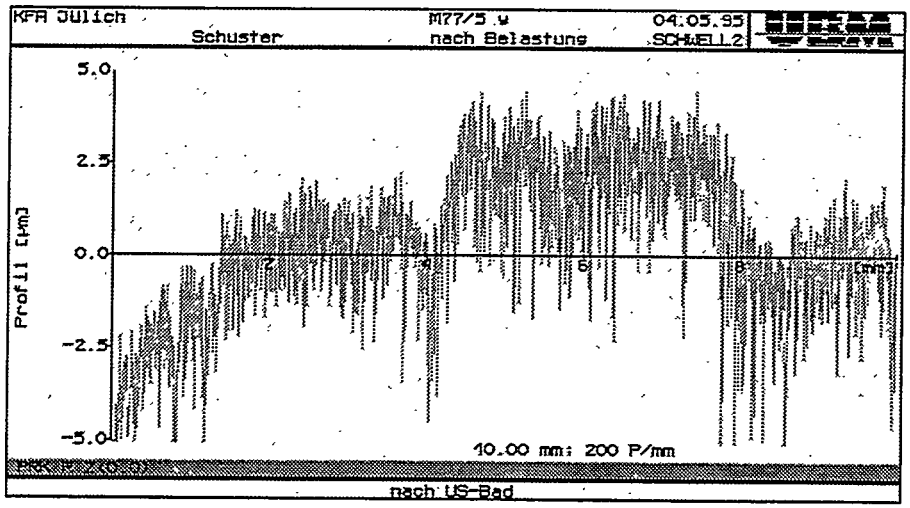

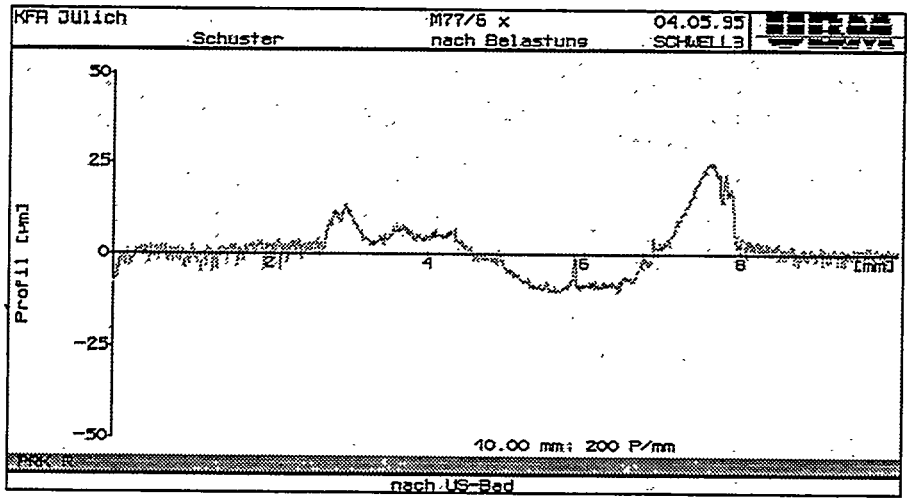

Fig. 5: Profilometer line scans for samples loaded at 1.0, 1.4 and 3.8 MJ/m², (Δt = 5 ms, single shots)

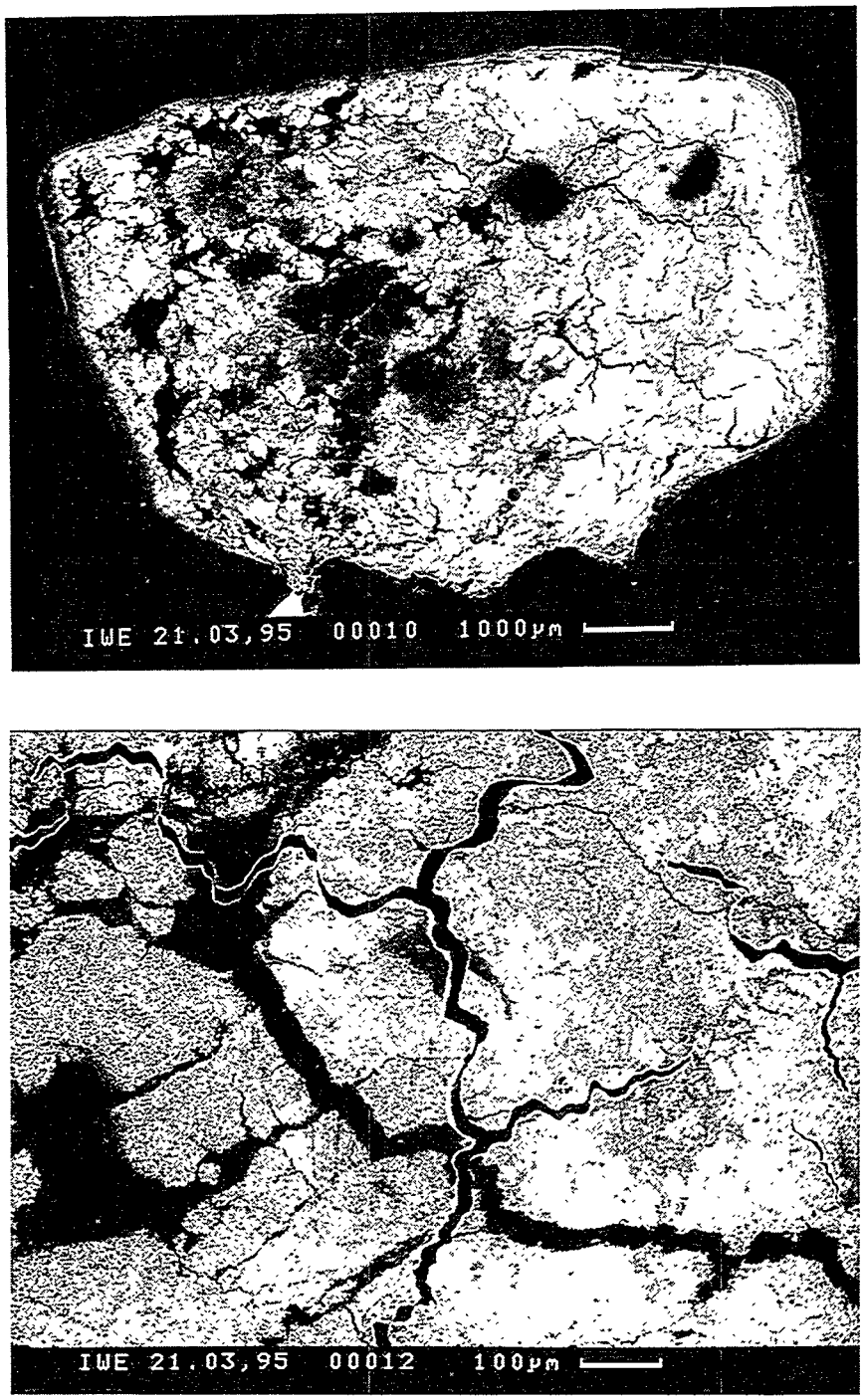

Fig. 6: Scanning electron micrograph of a sample loaded at 5.8 MJ/m² (S65C, Δt = 5 ms, n = 1)

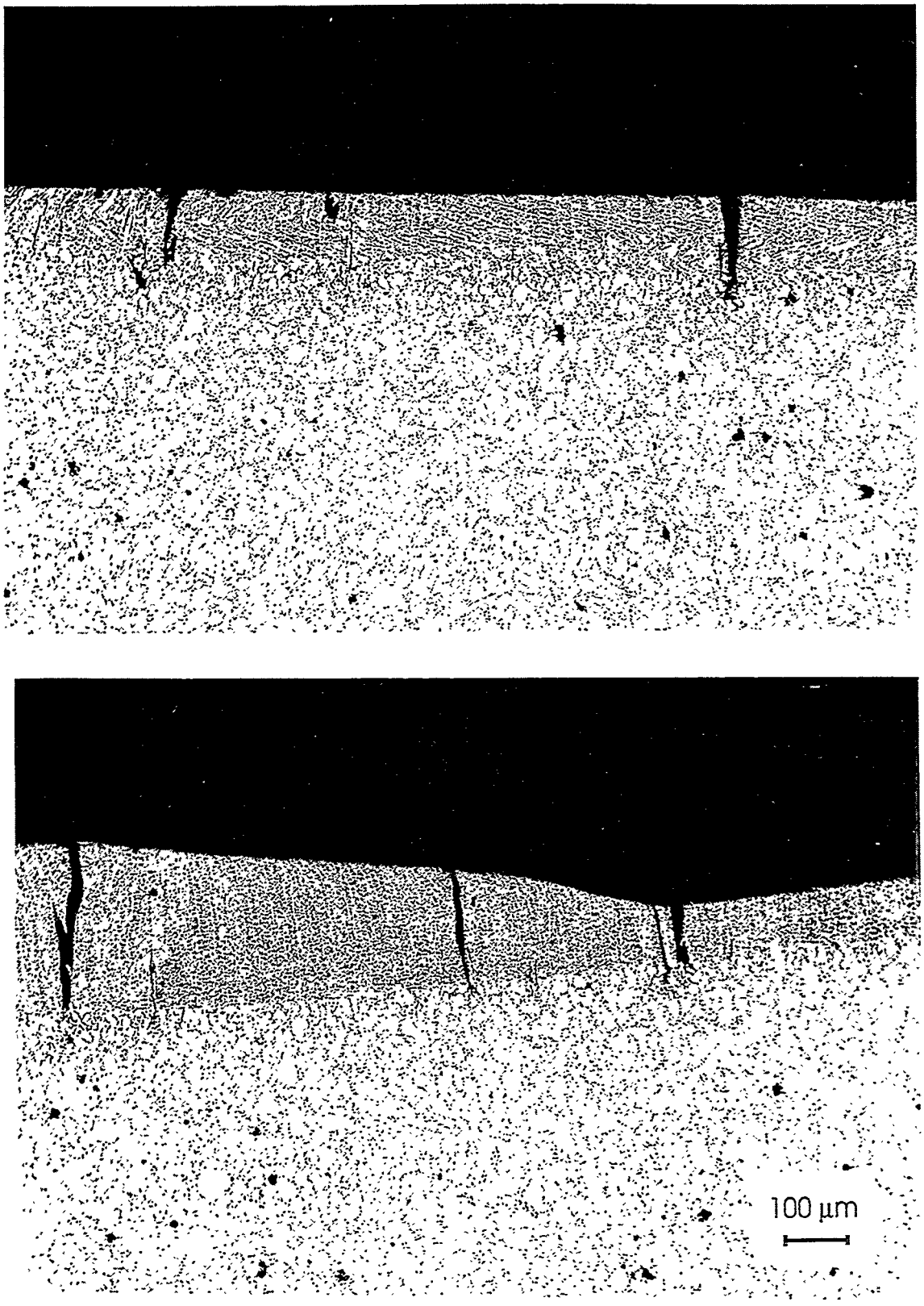

Fig. 7: Metallography of S65C loaded at energy densities of 2.8 MJ/m² (above) and 5.8 MJ/m² (below)

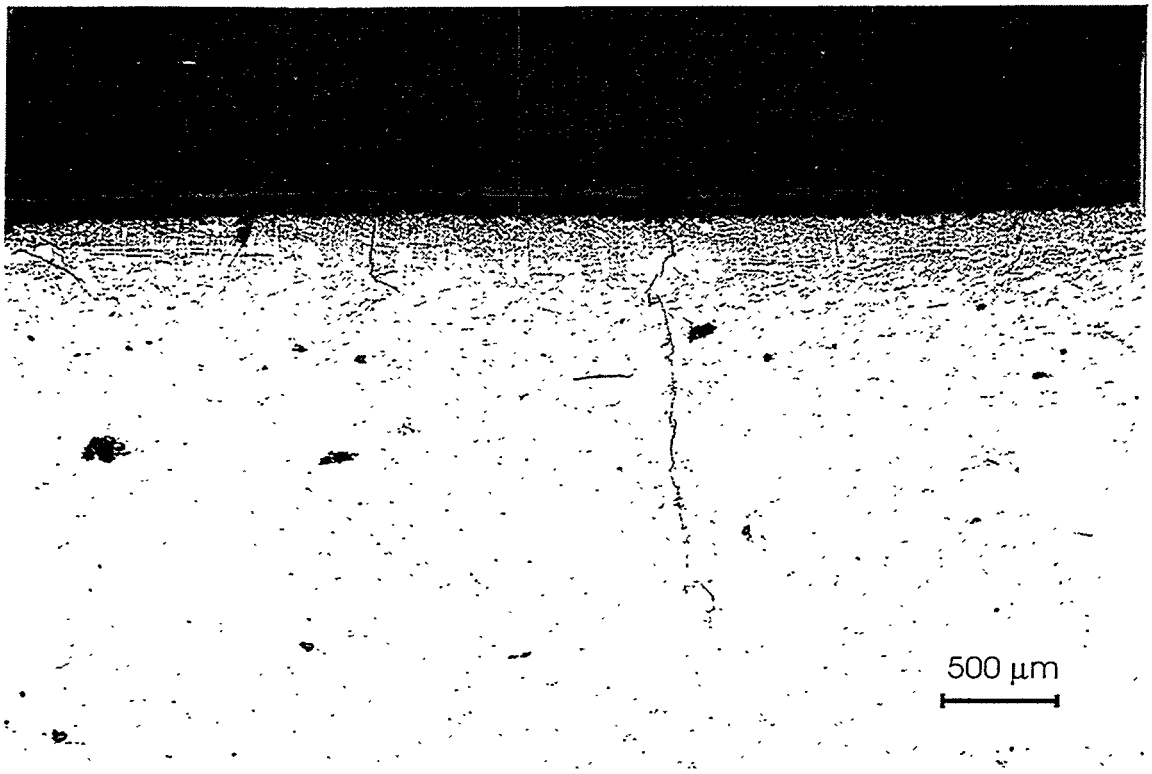

Fig. 8: Metallography of TShG 200 loaded at an energy density of 5.8 MJ/m², (Δt = 5 ms, single shots)

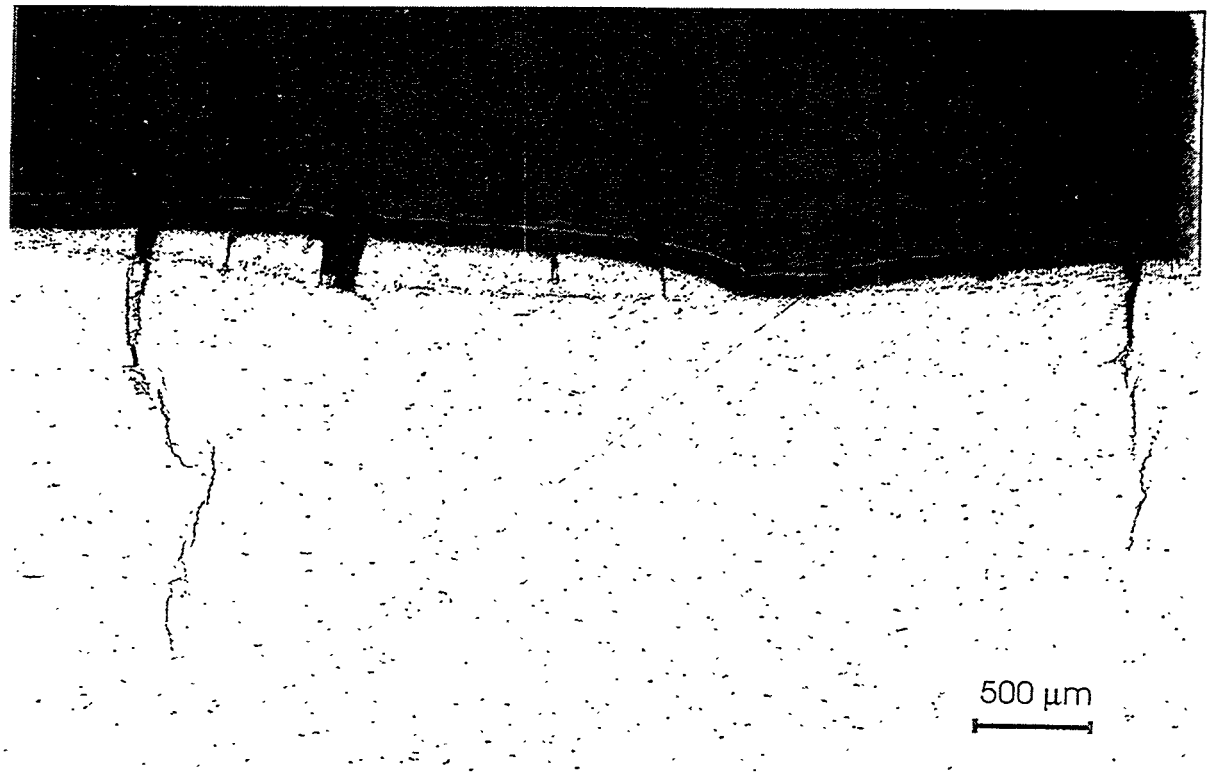

Fig. 9:

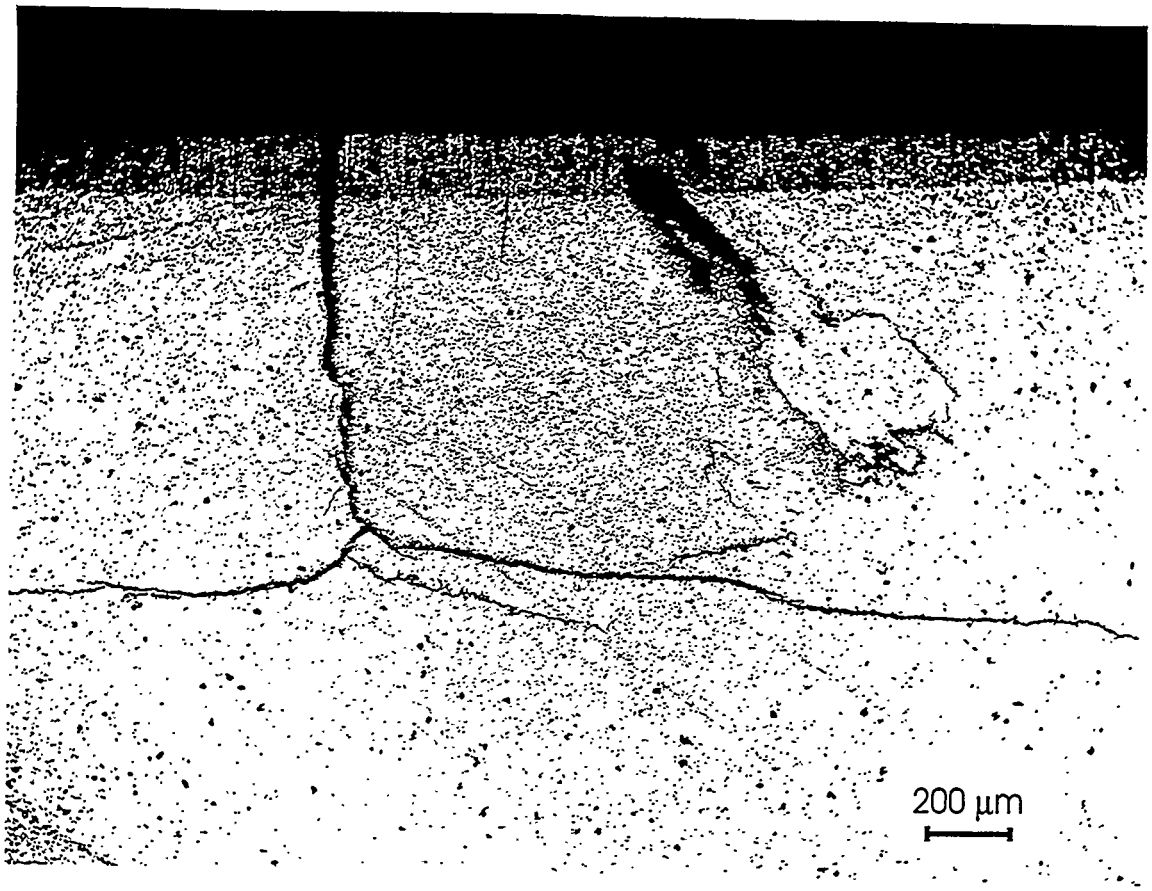

Fig. 10: Metallography of TR 30 loaded at an energy density of 5.8 MJ/m², (Δt = 5 ms, single shots)

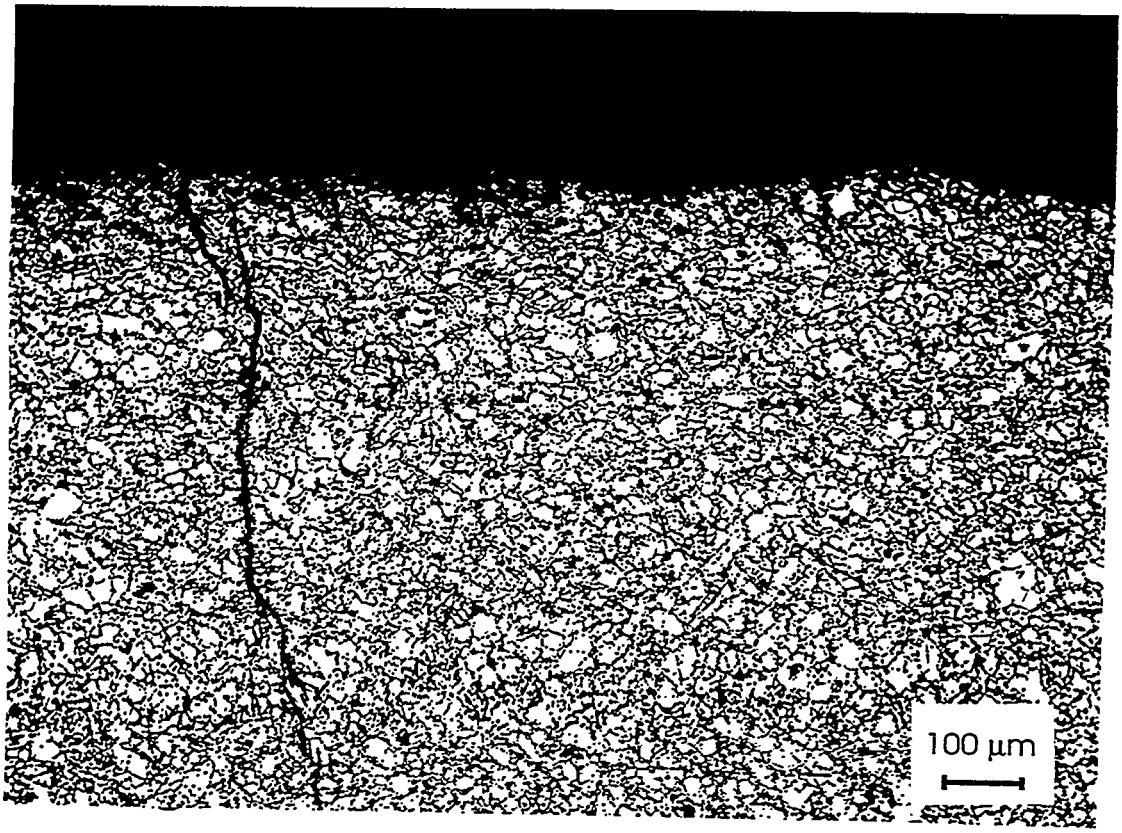

Fig. 11: Metallography of Baikov beryllium loaded at an energy density of 5.8 MJ/m², (Δt = 5 ms, single shots)

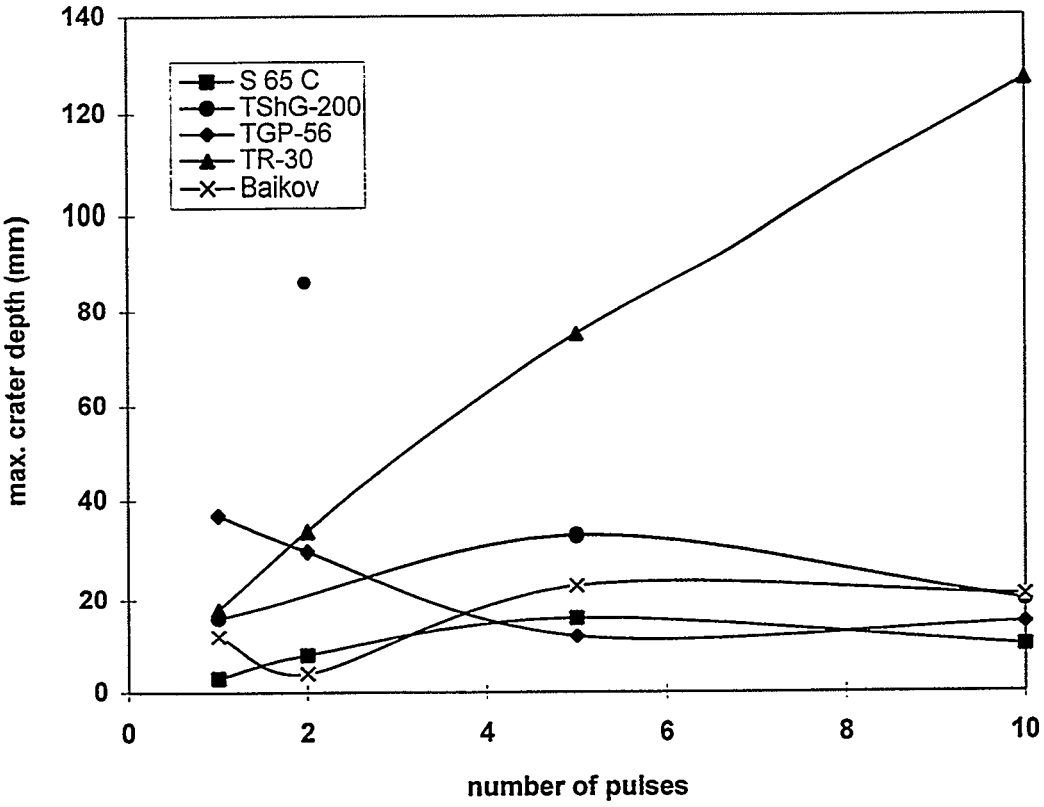

Fig. 12: Max. crater depth in multiple shot experiments (E = 2.8 MJ/m², Δt = 5 ms)

ELEVATED TEMPERATURE STRESS STRAIN BEHAVIOR OF BERYLLIUM POWDER PRODUCT

S.P. Abeln*, M.C. Mataya**, R. Field*

* Los Alamos National Laboratory, MST-6, G770, Los Alamos, New Mexico 87545
** Safe Sites of Colorado, Rocky Flats Enviromental Technology Site, Golden, Colorado 80402-0464

Several grades of beryllium powder product were tested under isothermal conditions in compression over a temperature range of room temperature to 1000°C and a strain rate range from 0.00 1 s^{-1} to 1 s^{-1}. Samples were compressed to a total strain of 1 (64% reduction in height). It is shown that all the grades are strain rate sensitive and that strain rate sensitivity increases with temperature. Yield points were exhibited by some grades up to a temperature of 500°C, and appeared to be primarily dependent on prior thermal history which determined the availability of mobile dislocations. Serrated flow in the form of stress drops was seen in all the materials tested and was most pronounced at 500°C. The appearance and magnitude of the stress drops were dependent on accumulated strain, strain rate, sample orientation, and composition. The flow stress and shape of the flow curves differed significantly from grade to grade due to variations in alloy content, the size and distribution of BeO particles, aging precipitates, and grain size. The ductile-brittle transition temperature (DBTT) was determined for each grade of material and shown to be dependent on composition and thermal treatment. Structure/property relationships are discussed using processing history, microscopy (light & transmission), and property data.

INTRODUCTION

Figure-1 shows the variation of ultimate tensile strength and elongation for a wrought, fine grained, high purity beryllium product over a temperature range from 300°C to 1000°C (the strain rate was not reported)(1). The smooth curves demonstrate that this high purity material is well behaved and predictable.

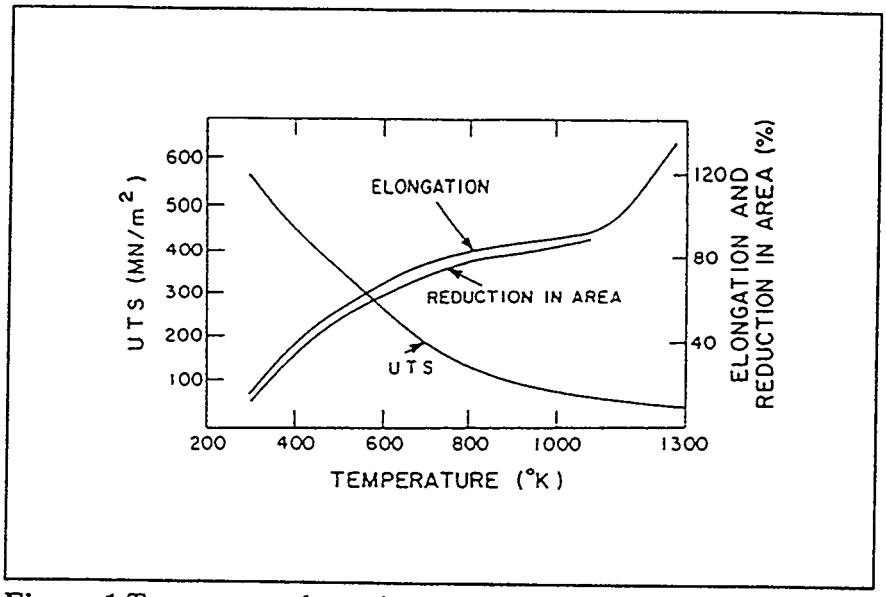

Figure 1 Temperature dependence of the mechanical properties for a fine grained, high purity wrought product.

Conventional beryllium powder product is considerably less pure and its properties are affected by processing and impurity content. Some examples of reported discrepancies from ideally simple behavior include: yield points, serrated flow, ductility minimums, superplastic behavior, and anisotropy associated with texture.

Metal flow is typically thermally activated and therefore temperature and strain rate sensitive. Thus, the characterization of material deformation at high temperature must include the stress-strain behavior as a function of temperature and strain rate. The majority of data in the

literature pertains only to specific operational requirements, and is therefore limited.

The objective of this study is to establish a high temperature stress-strain data-base for beryllium powder product and provide structure/property information. The data-base spans a range of beryllium microalloyed materials made to different specifications to provide insight into the effects of chemistry, processing history and starting microstructure on high temperature stress-strain behavior. The data-base goes beyond normal structural performance requirements (in both temperature and strain rate) and provides information to the metallurgist interested in the shaping of beryllium components via various forming and consolidation operations.

BACKGROUND (Structure/Properties)

Impurities or microalloy content play a major role in the stress-strain behavior of beryllium. The principle impurities that affect stress-strain behavior are BeO, Al, and Fe, and are introduced during the manufacturing process. Several variables, such as, consolidation technique, impurity concentration/solubility, and heat treat can affect the distribution and morphology of these elements. The origin and microstructural evolution of these impurities during processing, and their effect on elevated temperature properties, are discussed below.

BeO

The oxide, BeO, forms on all exposed surfaces of powder during the comminution process. Oxide levels in powder product, compared to cast and wrought product, are therefore inherently higher due to the high total surface area of the combined powder particles. The oxide layer is altered during the consolidation process to produce discrete particles.

Webster et al(2) found BeO at two locations in hot pressed beryllium block; 1) along the grain boundaries, and 2) at isolated clusters within the grain. Oxide growth at these two locations was observed to differ. The growth of BeO at high angle grain boundaries was found to be accelerated by higher concentrations of Al, Mg, and Si, and higher consolidation temperatures. The growth of BeO within the matrix was found to be negligible, regardless of

purity or processing temperature. The discrepancy between oxide growth rate within the grain boundaries and matrix demonstrates that the low melting impurities (Al, Si, Mg), which segregate preferentially to the grain boundaries, are the principle controlling factors for grain boundary oxide distribution and morphology. The BeO particles within the matrix are unaffected because the low melting impurities are not soluble within the matrix.

The presence of liquid phases at particle/grain boundaries, which can form at relatively low temperatures if impurities are present, can further enhance diffusion of Be and oxygen causing rapid coarsening of BeO. In addition to the low melting phases, the pressure-temperature cycle during consolidation was also found to influence BeO size and distribution.

Webster et al(2) found that when pressure was applied early in the pressing cycle, the extent of oxide coarsening was reduced. This apparently results from different diffusivities between free surfaces in the compact and particles which are in contact or bonded.

The relationship between BeO size and distribution, and consolidation temperature implies that the distribution of BeO can be controlled through appropriate processing. In fact, variations in oxide morphology and distribution have been observed with different consolidation techniques(3). The two principle consolidation techniques utilized for beryllium powder product are hot isostatic pressing (HIP) and vacuum hot pressing (VHP). HIP employs higher pressures while VHP pressures are limited by die material constraints. The lower pressure associated with VHP requires higher consolidation temperatures to achieve full density. Typical consolidation

parameters for HIP and VHP are as follows:

- HIP- 1000^{0}C/15ksi/3 hrs
- VHP- 1050-1150^{0}C/2ksi/36 hrs

The difference in oxide size and distribution between the same material consolidated by these two different techniques is primarily in the grain boundary because matrix BeO is not affected by consolidation. The HIP process typically produces a fine (0.05-0.1μm) uniform dispersion along the grain boundaries and the VHP process a coarsened (0.1-0.50μm), relatively heterogeneous dispersion.(3)

The effect of BeO on properties is complex. At elevated temperatures, BeO behaves similarly to a fine dispersoid in dispersion strengthened materials in that it inhibits grain growth and stabilizes the microstructure. At elevated temperatures, stable grain size, improves creep properties. At lower temperatures, BeO particles act as stress concentrators which can initiate cracks under certain conditions.

Al-Fe

It has been established that control of the levels of certain microalloy elements, combined with proper heat treating cycles, can dramatically change the mechanical properties of beryllium, particularly at elevated temperature(4). The principle microalloy elements have been identified as Fe and Al, which together interact synergistically. Their interaction can best be described as follows:(4)

$$Al + \overset{Fe}{\underset{FeBe_{11}}{\updownarrow}} + Be \overset{>850^0C}{\underset{650-850^0C}{\leftrightharpoons}} AlFeBe_4$$

The reaction states that at temperatures greater than 850°C, the ternary compound dissolves leaving free Al at the grain boundaries and Fe in the matrix. The Fe is present in solid solution or the binary precipitate $FeBe_{11}$. At temperatures between 650-850°C the ternary precipitate forms at the grain boundaries. Formation of the ternary requires diffusion of Fe out of the matrix and into the grain boundary, depleting Fe from the matrix.

One of the important aspects of this reaction on the high temperature properties relates to the free Al. Excess free Al at the grain boundaries accounts for observed high temperature ductility minimums or hot shortness in beryllium. Aluminum melts at 660°C and there is a Be-Al eutectic at 645°C. Therefore, material containing excess Al would be expected to fail intergranularly under stress above approximately 650°C. In fact intergranular failure associated with free Al has been observed as low as 350°C(5). The lower limit of free Al at which intergranular failure will occur has been determined to be 200ppm(4). Therefore it is important to control the relative proportions of the Al and Fe, so that sufficient Fe is present to combine with all of the free Al. The atomic weight of Fe is approximately twice that of Al so that the proper proportion is at least twice as much Fe by weight to account for all the Al.

The other important aspect of the above reaction is the quantity and form of Fe within the

matrix. Matrix Fe is dependent on the total Fe content and any depletion which may have occurred due to migration to the grain boundaries during heat treatment. The Fe in the matrix appears either in solid solution or as a precipitate ($FeBe_{11}$). The precipitate forms when the solid solubility is exceeded during heat treat. Precipitation of $FeBe_{11}$ is favored below 650°C. The solubility of Fe in beryllium has been shown by Myers and Smugeresky(6) to depend on the presence of Al. The solubility of Fe in high purity Be is about 1000ppm (0.1wt%) at 500°C and about 10,000ppm (1wt%) at 850°C. In the presence of Al the solubility drops to about 600ppm (0.06wt%) below 850°C.

Beryllium is strengthened by Fe in solid solution. Floyd(7) reported a 2.3 psi increase in room temperature yield stress per ppm of Fe for solutionized beryllium. Aged conditions which precipitate $FeBe_{11}$ also showed strength increases, but were more difficult to define quantitatively. Floyd attributed this to two mechanisms 1)softening by removing Fe from solution (forming $AlFeBe_4$ and $FeBe_{11}$) and 2)hardening by precipitation ($FeBe_{11}$).

Two yield phenomena have been related to the solute atoms or precipitation reactions discussed above, yield points and serrated flow. Yield points have been seen at room temperature and elevated temperatures. Serrated flow is a high temperature phenomenon which is strain rate dependent.

Yield points have been attributed to precipitate pinning. Floyd(7) suggested that yield points were due to $AlFeBe_4$ precipitates while Stonehouse(3) indicated that $FeBe_{11}$ was the

source. In either case, the precipitates are thought to pin dislocations, reducing the number of glissile dislocations sufficiently to require new dislocations to be generated at a higher stress level. Yield points have not been observed above 650°C(3).

Serrated yielding has been observed in a number of different studies(8-10). The most detailed study by Weisz, et al(10) showed serrated yielding occurred between 350 and 550°C in cast-extruded metal in the solutionized condition. They attributed the serrated yielding to Fe in solution for the following reasons:

- Plastic deformation was required prior to the occurrence of the serrations, indicating a probable substitutional element which requires the enhanced diffusion offered by a vacancy rich deformed lattice.
- Serrated yielding was eliminated by heat treatment for 100 hrs at 650°C which precipitated $FeBe_{11}$.

Grain Size

Grain size in powder product beryllium is controlled by the input powder particle size and the consolidation temperature. The smaller the powder particle size and the lower the consolidation temperature the smaller the final grain size will be. This is advantageous from the standpoint that beryllium has been shown to follow the Hall-Petch relationship, where strength is proportional to the inverse square root of the grain size and therefore finer grain size results in

improved strength. A Hall-Petch plot for high purity beryllium block is shown in figure-2(11). Note that a reduction in grain size from 10μ to 5μ results in an approximate increase in Y.S. of 130 Mpa. As grain size is reduced further even greater increases in strength are realized. For example, a reduction in grain size from 5μ to 3μ results in an approximate increase in Y.S. of 160 Mpa. In addition, finer, more isotropic grain size and distribution have led to improved ductility. The improved ductility is attributed to greater slip compatibility within the matrix, reducing the stress concentrations and crack propagation associated with anisotropic orientations. However, reducing the powder particle size also increases the BeO content which in turn reduces ductility. Therefore there is generally a compromise particle size/grain size for optimum strength and ductility.

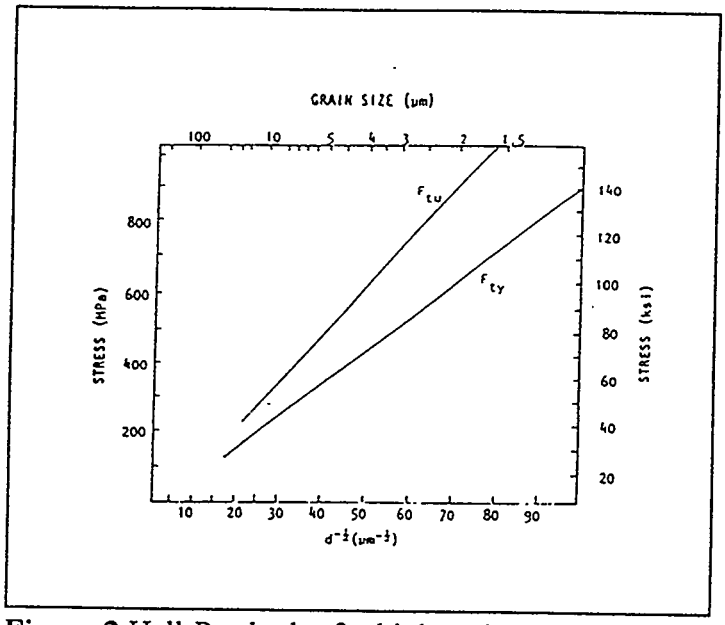

Figure 2 Hall-Petch plot for high purity beryllium block.

Texture

A mild texture is generally found in hot-pressed beryllium. The texture not only relates to nonisotropic consolidation techniques (VHP) but also to the shape of the powder particles. Due to the anisotropic nature of the beryllium single crystal, particles are fractured along basal

planes during comminution which leads to a flat-like powder particle. These particles tend to align themselves during die or can filling. Thus, mild textures are formed even under isotropic consolidation conditions. Basal textures of vacuum hot pressed beryllium in the pressing direction are typically 1.3 to 1.8 random(9). The various textures have little effect on the yield or ultimate strengths, but significantly affect ductility. Typical elongations can vary by a factor of two, with the longitudinal orientation (parallel to the pressing direction) showing lower elongations and transverse (perpendicular to the pressing direction) exhibiting higher elongations. This appears to be due to the higher population of basal planes perpendicular to the stress axis in the longitudinal orientation, and their propensity to generate and propagate cleavage cracks.

EXPERIMENTAL APPROACH

Material

Table-1 shows the matrix of materials evaluated with their associated microalloy concentrations, tensile properties, grain size, and heat treat condition (when known).

Table-1

	CHEMISTRY				PROPERTIES				
MATERIAL	Si	Al	Fe	BeO	YS	UTS	EL%	GS(μ)	HT
	WEIGHT %				(ksi)	(ksi)			
P31664	0.025	0.038	0.09	0.72	35	54	6T,3L	11	OA
S200F(spec)	0.06	0.1	0.13	1.5	35	47	2	<20	
S200E	0.03	0.03	0.06	1.6	38	56T,52L	2T,1L	9.3	NO
RM253939	0.034	0.016	0.058	0.79	41	63	6T,3L	9.4	OA
S65(spec)	0.06	0.06	0.08	1	30	42	3	<15	
S65(cert)	0.02	0.02	0.09	0.6	40	52	7T,3L	12.2	
S65(cert)	0.02	0.03	0.06	0.6	34	54	6T,4L	10.3	
CIP-HIP-1	0.004	0.004	0.018	1.09	35[1]	50[1]	3[1]	9	NO
I250	0.02	0.07	0.07	1.9	76	83	4.3	5	SR
1400	0.05	0.03	0.18	6.2	NR	89T,50L	NR	4.5	NO

1- SPECIFICATION REQUIREMENT

SR- STRESS RELIEF

OA- OVERAGE

NR- NOT REPORTED

NO- NO POST CONSOLIDATION HEAT TREATMENT

Two heat treatments commonly given to beryllium product are stress relief and over aging. The stress relief consists of heating at 1450°F (788°C) for a hold time of one hour per inch of thickness followed by a slow cool of 50°F/hour. The overage heat treatment is a multi step process:

1)heat to 871°C and hold for 4 hours

2)cool to 746°C and hold for 12 hours

3)cool to 728°C and hold for 12 hours

4)cool to 717°C and hold for 12 hours

5)cool to 704°C and hold for 4 hours

6)cool to 690°C and hold for 4 hours

7)remove from furnace and air cool

note: cool down time may be included in the hold time in each step.

The extensive times at temperature for the overage heat treatment are to ensure sufficient diffusion of Fe to the grain boundaries.

This range of material types provides a wide contrast in microstructure and properties for

study. The following is a brief description of each material.

P31664 is a DOE production specification consolidated by VHP and the most commonly used weldable grade of beryllium. The Al/Fe ratio is controlled and the material is overaged to tie up the Al in the grain boundaries as the ternary $AlFeBe_4$. The significance of the heat treat, in addition to tying up the free Al, is that it reduces the matrix Fe to approximately 0.018%.

S200E is an older commercial grade of beryllium which utilizes attritioned powder and is consolidated by vacuum hot pressing (VHP). This particular lot was HIP'ed after VHP, probably to achieve full density.

RM253939 is a DOE production specification for high strength and weldable beryllium. The powder is made by impact grinding and consolidation is by HIP. The Al/Fe ratio is controlled and the material is overaged similarly to the P31664 grade. As a result of heat treat, the matrix Fe is reduced to approximately 0.024%. The higher matrix Fe and smaller grain size of this grade results in a higher yield strength when compared to P31664.

CIP-HIP-1 is a high purity grade derived from electrolytic flake. The powder is made by impact grinding and is hot isostatically pressed. There is little need to heat treat this material due to the high purity.

I250 is a new grade of beryllium which achieves higher strength levels and still maintains

ductility above 3%. The powder is made by impact grinding and is consolidated by HIP. The grain size is much smaller than the previously discussed grades and the BeO and Fe level increases are kept to a minimum.

I400 is an instrument grade made from ball milled powder and is designed to provide a high micro-yield strength. Contaminate levels are higher than conventional structural grades. This material was VHP'ed.

Microstructural Characterization

Light microscopy was used to evaluate grain size and in some cases oxide distribution. The specimens were polished and examined under polarized light. Transmission electron microscopy (TEM) was used to characterize dislocation content, BeO distribution, and precipitation. Microstructure and prior processing history are used to evaluate properties.

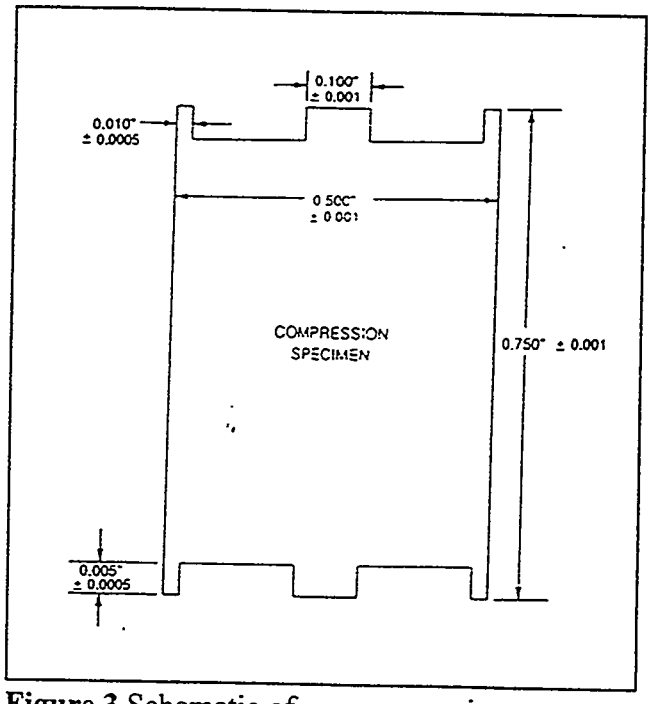

Figure 3 Schematic of compression specimen

Mechanical testing

Cylindrical compression samples (figure-3), 12.7mm diameter (.5") by 19.05 mm high (.75"), were machined from each billet with specimen axis parallel to either

the billet axis (referred to as the longitudinal direction) or the billet radius (transverse). The end faces were recessed to form a lubricant well, an effective technique for constraining lubricant to the sliding face during compression. High temperature (>300^{0}C) specimens had cylindrical wells and low temperature specimens round lubricant wells with blended radii to minimize stress concentrations. A consistent finish machining schedule of 10-5-2-2 (in thousandths of an inch) was utilized to minimize any effects of machining damage.

The hot compression tests were performed on a computerized 250 KN servo-hydraulic testing machine (manufactured by MTS, Inc.) configured with a specialized hot zone as shown in figure-4. The compression load train consists of Astroloy compression rams fitted with silicon nitride compression platens lapped to 8 RMS surface finish with opposite faces parallel to within 0.0127-mm over a 69.85-mm diameter. The platens are held in place on the rams using waspalloy clamps and bolts. The rams are partially hollow and filled with fiberfax insulation to reduce heat loss and decrease heat-up time. The rams are seated in stainless steel water cooled grips which protect the system load cell and actuator.

The heat source is comprised of a three zone Model #2961 (Applied Test Systems Inc.) clamshell resistance furnace capable of temperatures up to 1200^{0}C. The three zones are controlled independently. The center of the furnace is aligned with the top of the bottom platen where the test specimen is placed and heated to temperature. There is also a quartz observation window to view the test. Thermocouples placed in the upper and lower platens as well as touching the sample are used to monitor temperature. Temperature of the dies and specimen are

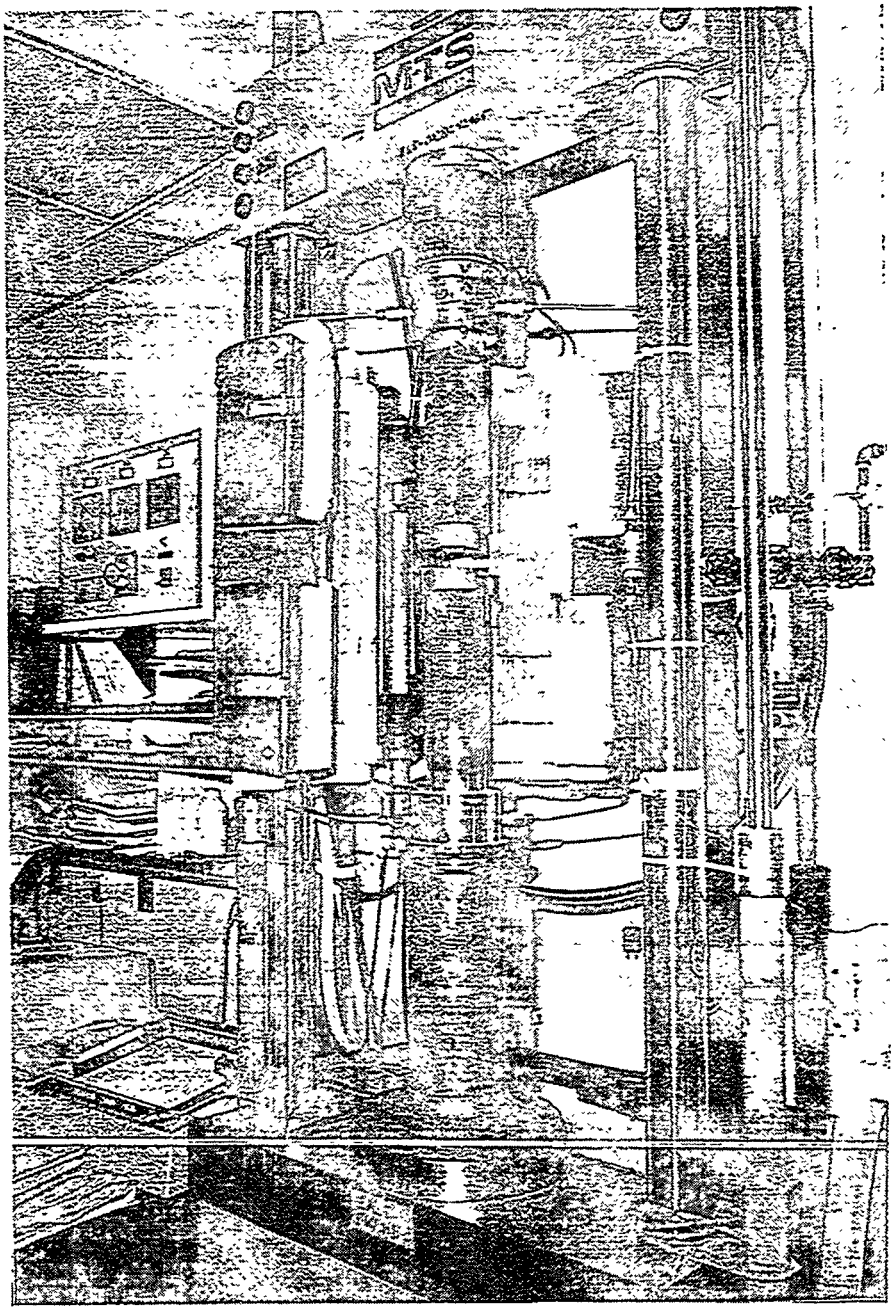

Figure 4 Photograph of hot compression system.

typically within 5^0C during compression.

The test samples were compressed in air at four strain rates (0.001, 0.01, 0.1, and 1 s^{-1}), temperatures from the ductile brittle transition to 1000^0C, and to a total strain of one (ϵ=1). Test samples were coated with glass, which provided lubrication and protection from surface oxidation, loaded onto the bottom die in the furnace in air, held for 10 min. at the test temperature (specimens required approximately 5 min. to reach the furnace temperature), compressed uniaxially, and quenched in water after deformation.

Compliance in the load train resulted in deviations in ϵ and $\dot{\epsilon}$ up to about -5 pct with the maximum occurring at the lowest temperature, at which the greatest loads were encountered. The true flow stress, σ, can be assumed equal to the true average pressure because the coefficient of friction between sample and die is near zero(12). In addition the strain distribution can be assumed uniform throughout the specimen and true strain, ϵ, can be calculated from the change in test specimen height(13). Note, for uniform uniaxial compression the effective or significant stress and strain reduce to the axial normal component of stress and strain, as is the case for tensile testing in the uniform elongation realm(13). Values for σ and ϵ were calculated from the as-measured load and corrected displacement data utilizing conventional relationships(14). Sample dimensions, measured at ambient temperature, were corrected for thermal expansion which occurs on heating to the test temperature. The measured displacement of the sample, obtained with a linear-variable-differential-transformer (LVDT) mounted at the lower end of the moving ram, was corrected for test system compliance. Calculated values of final ϵ, obtained

moving ram, was corrected for test system compliance. Calculated values of final ϵ, obtained from the LVDT displacement and corrected for compliance and for cooling to ambient temperature, were typically within 1 to 2 pct of the measured plastic strain, calculated from the actual initial and final height of the test sample.

Lubrication

Adequate lubrication is required to provide reliable and consistent data. A review of the effects of friction in compression testing is provided in the ASM book Workability Testing Techniques(15). The general characteristics of frictional effects on the compression of a short cylinder are shown in figure-5. Frictional restraint at the end faces retards the outward motion or diametral expansion of the sample at the faces. This causes the sample to have a greater diameter at the mid-height position, giving it a barreled appearance. At greater strain and continued barreling, material that is originally located on the circumferential surface may rotate enough to eventually contact the die face. Barreling introduces a complex stress state and inhomogeneity in strain and strain rate across the cross section of the specimen. In this case, the as-measured stress does not give a true measure of the material's flow stress.

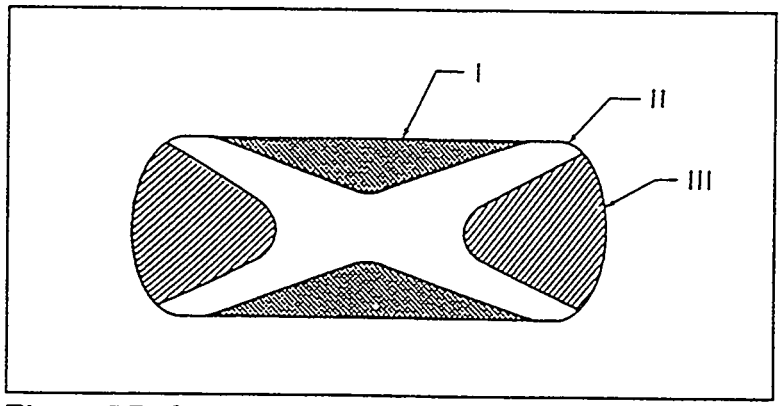

Figure 5 Deformation zones associated with inadequate end lubrication in a cylindrical compression sample

The inhomogeneity associated with friction and barreling results in three distinct zones of deformation as shown in figure-5. Metal in contact with the compression platens remains stationary, resulting in volumes of material, adjacent to the die face, which are relatively undeformed. These volumes are typically referred to as dead metal zones (region I). The most severe deformation is concentrated in zones of shear just outside the dead metal zones (region II). Metal near the outer surface of the cylinder flows or bulges outward but sees little compressive strain due to barreling (region III). Good lubrication is represented by spreading of the end faces resulting in a straight walled cylinder after deformation with a uniform distribution of strain throughout.

The stress-strain response of a material is most accurately described when ideal lubrication is obtained. Because of this, a significant effort was made to find an appropriate lubricant for each test condition that would result in as close to a uniform state of deformation as possible. Figure-6 shows a beryllium compression specimen before deformation and after deformation to a strain of 1. The straight side walls indicate good

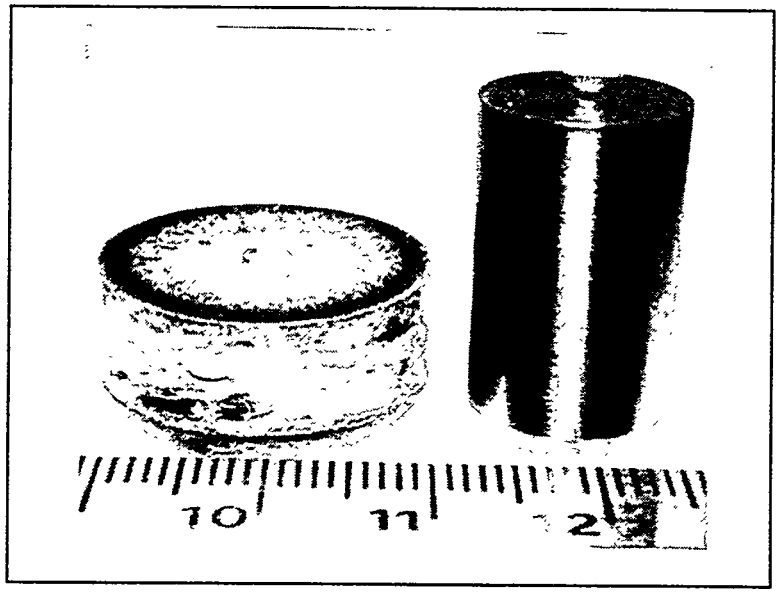

Figure 6 Photograph of a beryllium compression sample before (right) and after (left) testing exhibiting straight side walls and good lubrication. This sample was tested at 600°C and a strain rate 0f 0.1 s^{-1}.

lubrication. In this case the original circumferential lip which holds the lubricant on the sliding surface was observed to have spread to the outer most position of the deformed sample face. In some cases, fairly straight side walls have been observed in conjunction with the lack of spreading of the end face. In these instances, the circumferential surface has barreled, come into contact with the compression platens and become part of the end face of the sample, giving the illusion that good lubrication had been attained when in fact it had not.

During the lubrication study and subsequent testing, a trend was noticed in the flow curves of test samples that had good and bad lubrication. Figure-7 illustrates the difference found at 700°C and a strain rate of 0.1/s. Curve 1 had excellent lubrication and the flow curve remained relatively flat all the way to the end of the test while Curve 2, which exhibited poor lubrication, not only has a higher flow stress but also turns up at the end. It is believed that the increased flow stress is due to the energy required to overcome friction and the turned up flow curve is a result of the barreled surface coming into contact with the platens which increases the

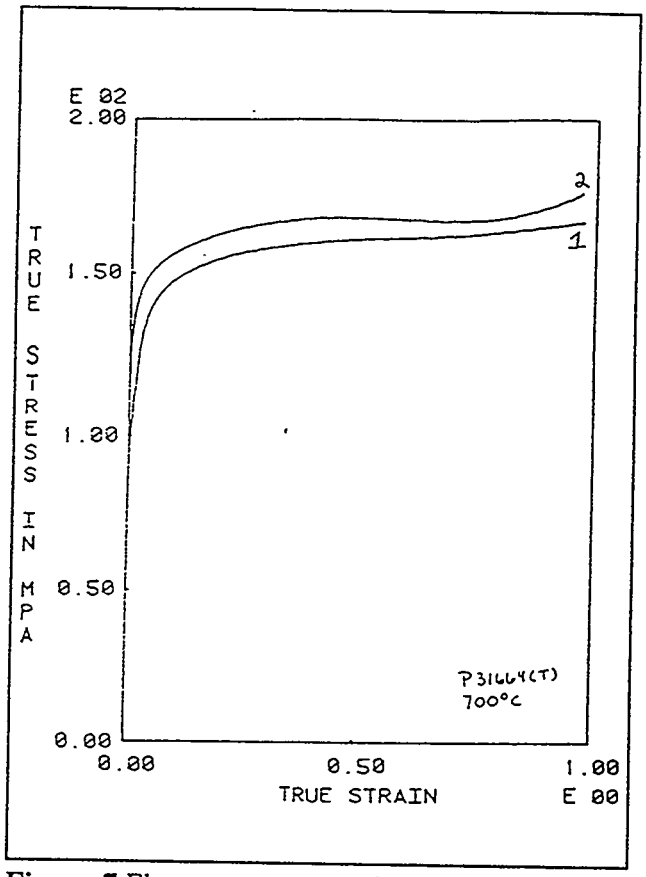

Figure 7 Flow curve comparison between good (curve-1) and poor (curve-2) lubrication. Note the higher flow stress and slope changes associated with the poor lubrication.

surface area of deformation.

Another trend that was noticed during the testing was the effect of temperature on the apparent lubrication of the specimens. As the test temperature increased general lubrication became worse and more dependent on strain rate. In general, at 400 and 500^{0}C lubrication increased with decreasing strain rate, while at and above 600^{0}C the opposite was true. This may be due to the extremely low flow stress of Be at elevated temperatures compared to the force required to overcome friction.

EXPERIMENTAL RESULTS and DISCUSSION

The typical data generated is shown in Figure-8, which gives the stress-strain behavior as a function of strain rate for a specific temperature and material. There are four strain rates shown in each family of curves, 1,0.1,0.01, and 0.001 s^{-1}. Note the higher flow stress associated with

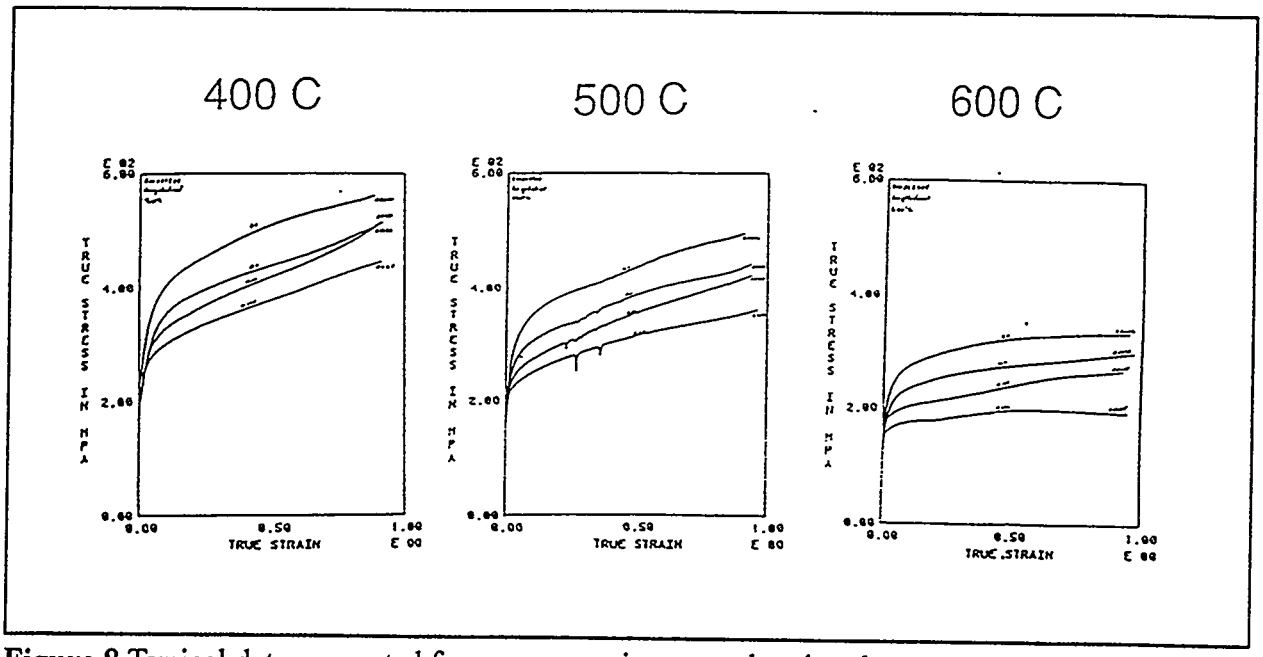

Figure 8 Typical data generated from compression tests showing the stress-strain behavior as a function of strain rate at a constant temperature for RM253939.

the higher strain rates and that data is shown as true stress vs true strain. All specimens were deformed to a strain of 1 (64% reduction in height) unless fracture occurred first. The beryllium stress-strain data shows evidence of yield points, serrated flow, strain rate sensitivity, and ductile-brittle transitions. The occurrence and magnitude of these observations will be shown to

be dependent on chemistry, texture, and prior thermal history. A metallographic/ microstructural evaluation was conducted on all starting material and, where applicable, powder processing history and microstructural characterization is used to rationalize observed properties.

The results and discussion section will be presented as follows:

-Microstructural characterization

-General yield and ductility behavior

-Discrepancies from ideal flow.

The microstructural characterization is discussed first because it supports discussion of structure/property relationships of the different grades of beryllium. The general yield and ductility behavior then provides an overview of properties and processing requirements to achieve strength and ductility. The discrepancies from ideal flow then point out specific material behavior which can result from processing or service environment.

Microstructural characterization

The initial structures of the materials tested were characterized with optical and transmission microscopy. Figures 9-14 show microstructural composites of polarized light and transmission electron photomicrographs of each material tested. Metallographically each material is similar except for the grain size. The grain size in decreasing order is P31664, S200E, RM253939, CIP-HIP-1, I250, and I400. Transmission electron micrographs were taken to reveal the general structure of the matrix and grain boundaries, and delineate any significant

microstructural differences which may correlate to property differences.

The P31664 material (figure-9) displayed a relatively low BeO content, with particles generally confined to the grain boundaries and sub-boundaries. $AlFeBe_4$ was found in the grain boundaries, primarily a triple points. The particles shown residing next to the grain boundaries are oxides. The dislocation density was low.

The S200E material (figure-10) displayed a much higher BeO content, distributed in the grain boundaries and the matrix. It also exhibited a significantly higher dislocation density. No precipitates other than oxides were found.

The RM253939 material (figure-11) showed a low oxide content No significant precipitation of $FeBe_{11}$ was observed. A few grain boundary precipitates of $AlFeBe_4$ were found, an example of which is shown. The particle was identified as $AlFeBe_4$ by EDS and electron diffraction. Some faulting on {111} planes can be seen in the micrograph, consistent with the fcc structure. The dislocation density in this alloy was low, similar to that observed in P31664.

The CIP-HIP-1 material (figure-12) displayed a moderate BeO content, with particles primarily at the grain boundaries and sub-boundaries. The oxide dispersion was very fine, characteristic of hot isostatically pressed material. The grain size was variable, ranging from 3-5μ to over 10μ. The larger grains generally contained sub-boundaries, with relatively high dislocation densities, both in the boundaries themselves and in the surrounding area. Most of the

smaller gains were dislocation free.

The I250 material (figure-13) was similar to the CIP-HIP-1, with a moderate BeO content, mostly restricted to the grain boundaries and sub-boundaries. The BeO size and distribution was very fine, characteristic of hot isostatically pressed material. The dislocation density was low.

The I400 material (figure-14) had a very high BeO content. Much of the BeO appears to be sitting on the surfaces of the foil (left standing proud after the matrix was polished away). The BeO is not necessarily associated with the grain boundaries, but appears distributed throughout the microstructure. The dislocation density was low.

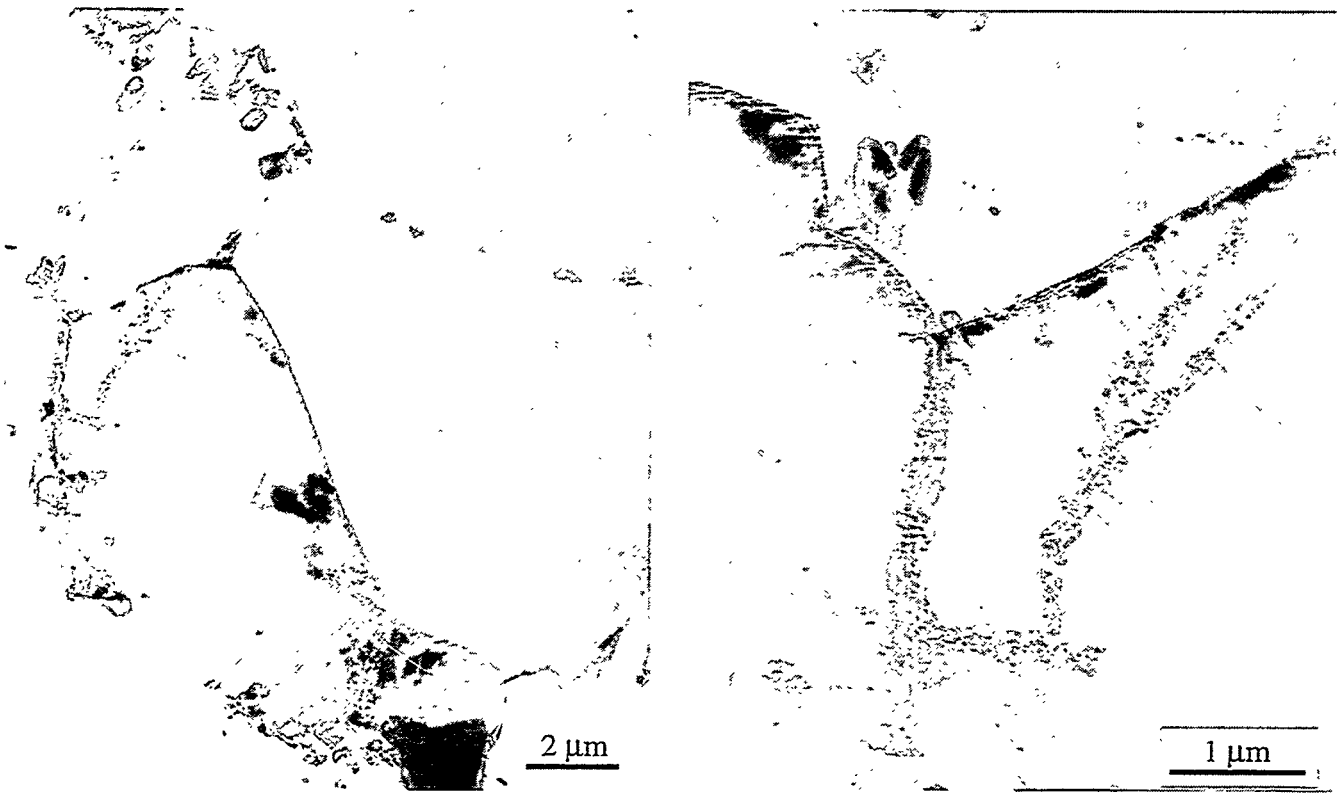

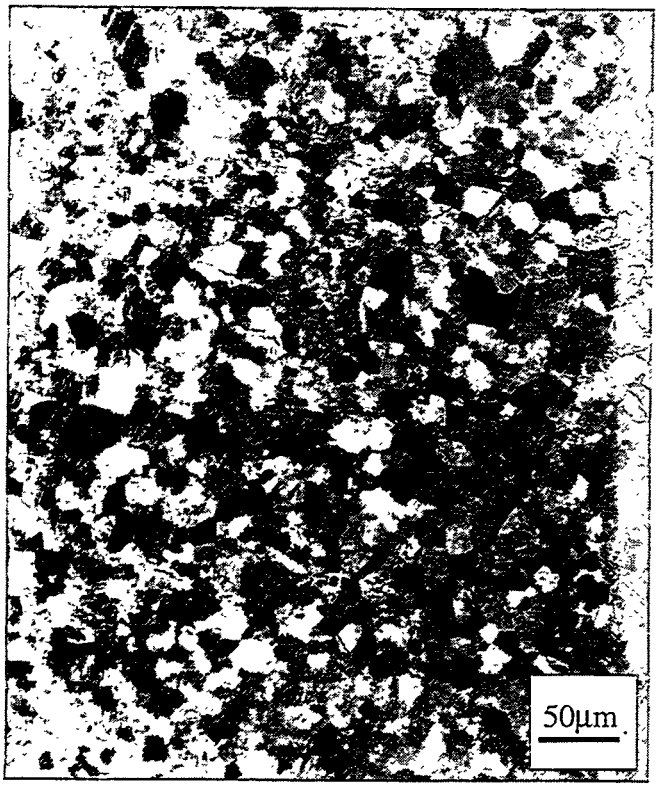

Figure 9 Microstructural composite of P31664 material showing polarized light (left) and TEM (top) photomicrographs.

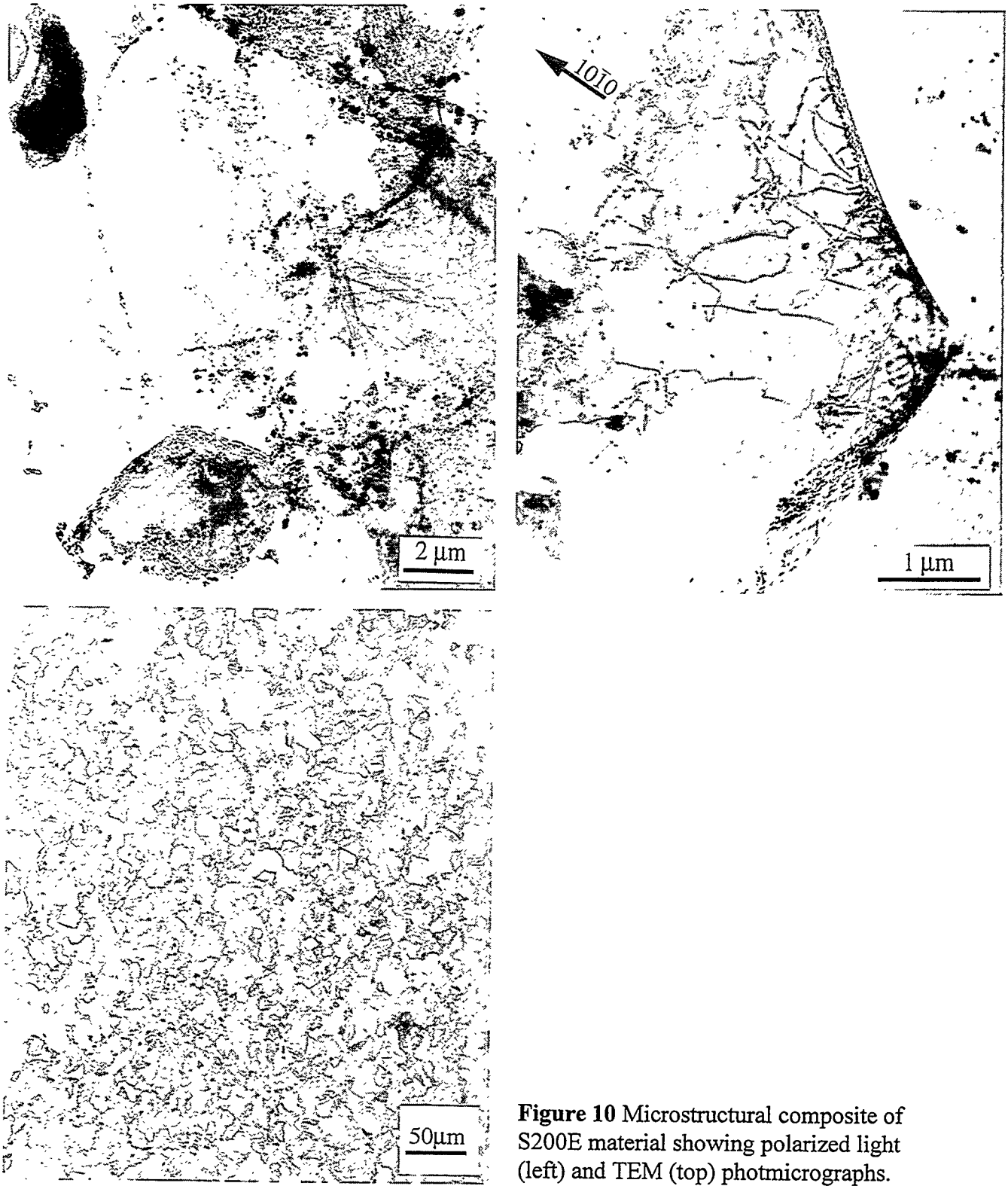

Figure 10 Microstructural composite of S200E material showing polarized light (left) and TEM (top) photmicrographs.

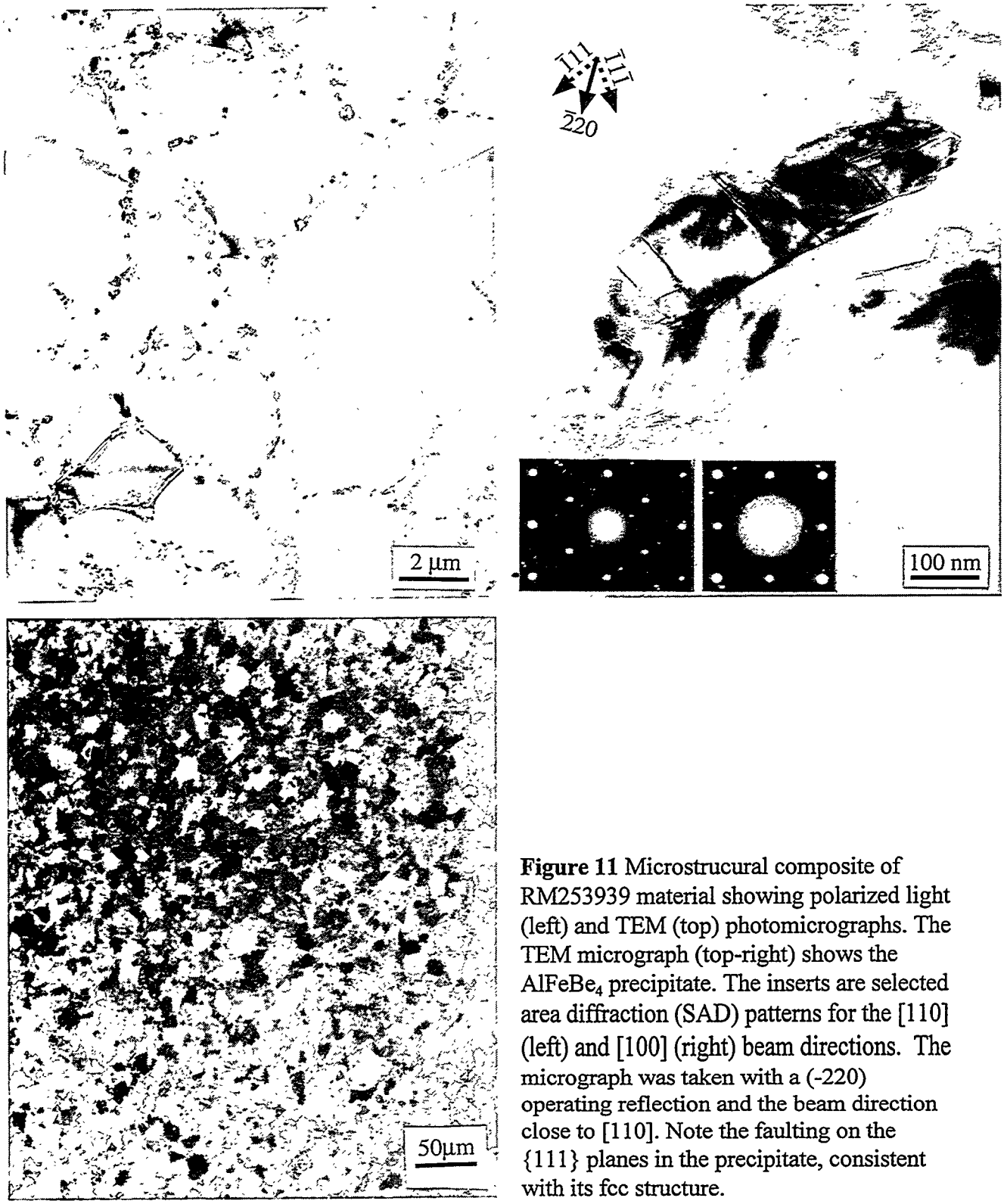

Figure 11 Microstrucural composite of RM253939 material showing polarized light (left) and TEM (top) photomicrographs. The TEM micrograph (top-right) shows the $AlFeBe_4$ precipitate. The inserts are selected area diffraction (SAD) patterns for the [110] (left) and [100] (right) beam directions. The micrograph was taken with a (-220) operating reflection and the beam direction close to [110]. Note the faulting on the {111} planes in the precipitate, consistent with its fcc structure.

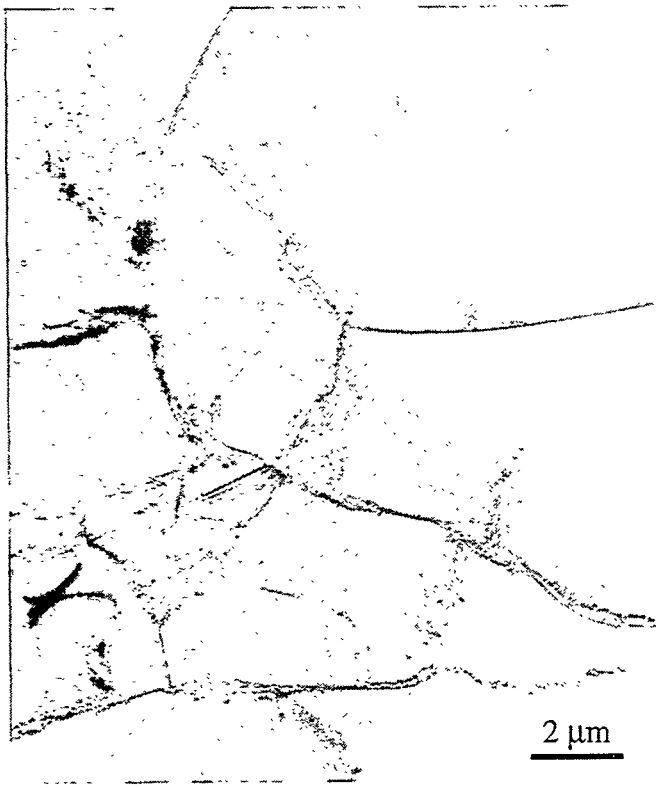

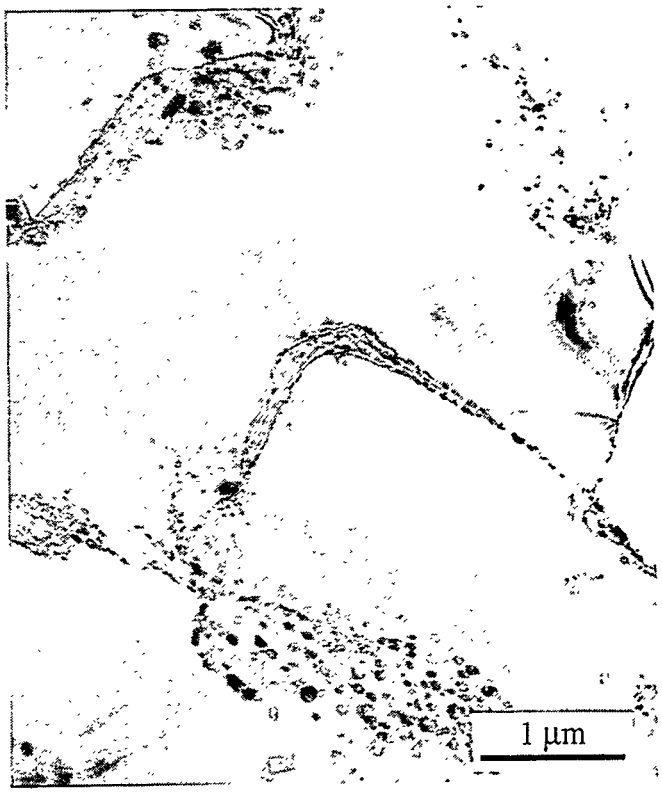

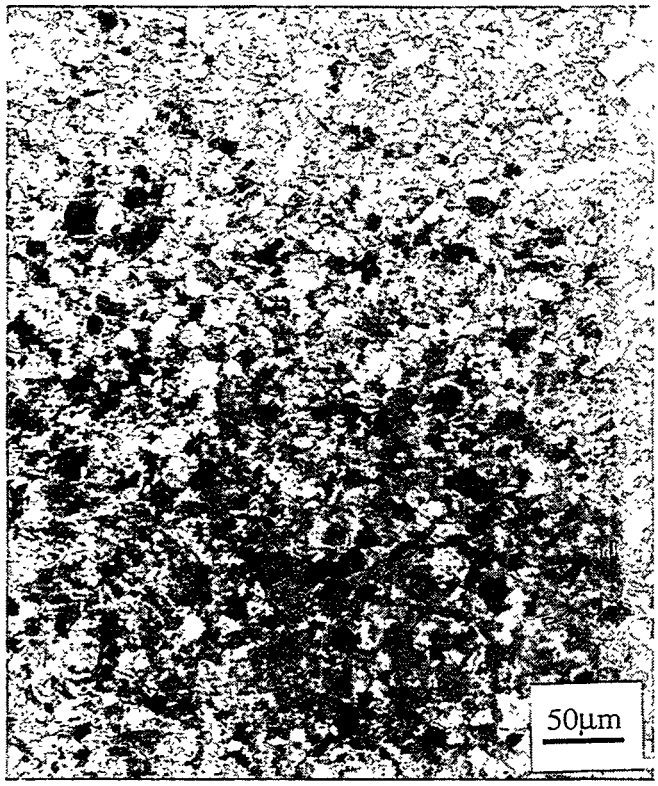

Figure 12 Microstrucural composite of CIP-HIP-1 material showing polarized light (left) and TEM (top) photomicrographs.

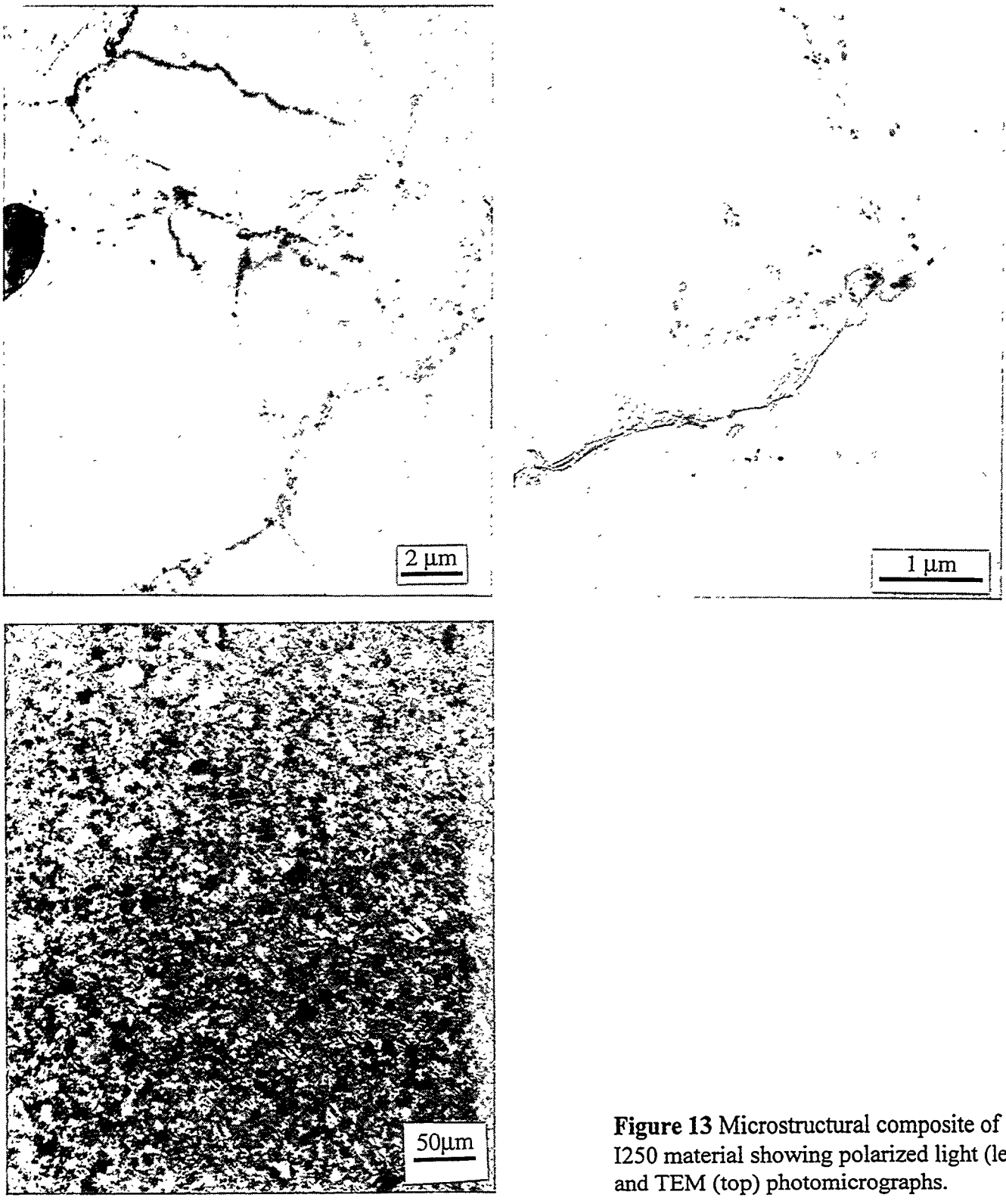

Figure 13 Microstructural composite of I250 material showing polarized light (left) and TEM (top) photomicrographs.

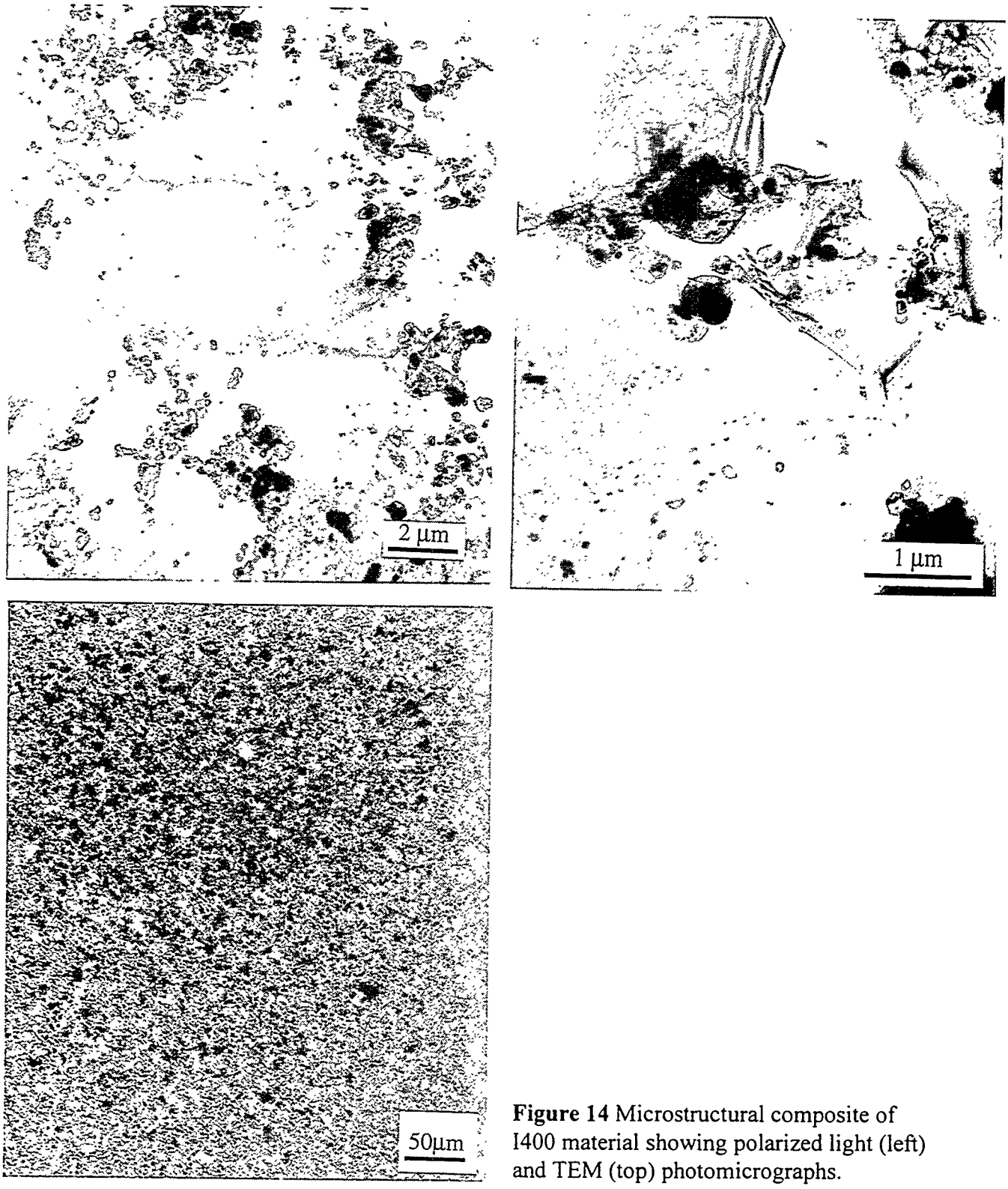

Figure 14 Microstructural composite of I400 material showing polarized light (left) and TEM (top) photomicrographs.

General Yield and Ductility trends

The 0.2 percent yield strength as a function of test temperature is plotted in Figure-15 for the various alloys compressed at a strain rate of 0.001 s^{-1}. From 25°C to 900°C, the I400 and I250 alloys are significantly stronger than the other four alloys. In this range, the yield strengths of I400 and I250 are more sensitive to temperature than the yield strengths of the other alloys. Small differences do persist however giving a strength ranking similar to that observed for the alloys at lower temperature.

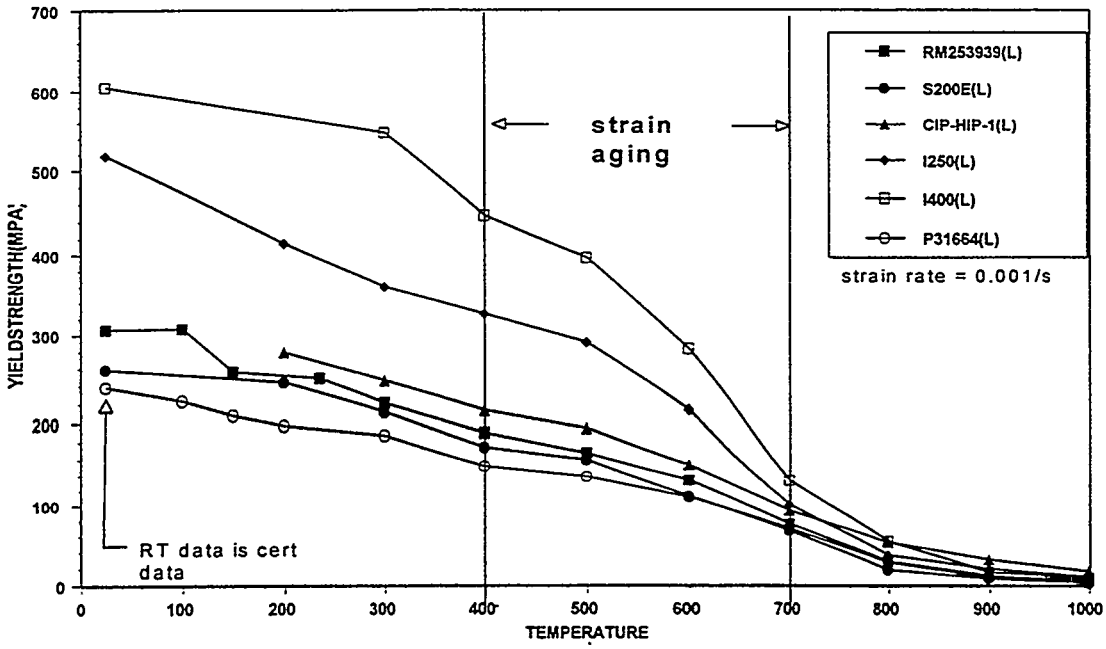

Figure 15 Yield Strength as a function of temperature at a constant strain rate of 0.001 s^{-1} for all materials tested.

It is interesting to note that the CIP-HIP-1 material yield strength surpasses that of the I250 and I400 at the highest temperatures. This is most likely attributed to the high purity of this

alloy. At elevated temperatures free Al and Si at the grain boundaries are molten and would obviously decrease the yield strength. Above 850^{0}C, even the heat treated material which ties up the Al in the ternary phase, would show dissolution and reduced strengths. Therefore the low microalloy (Al,Si) content of CIP-HIP-1 would account for the improved very high temperature strength.

Figure-15 also shows that all of the strength versus temperature curves show a consistent, small increase at 500°C, indicating that another strengthening mechanism may be in operation at this temperature. This is also the temperature at which each alloy demonstrated serrated flow curves, or stress-drops, at strains well beyond yielding.

Compression tests were conducted from 1000°C, down to the DBTT, at strain rates of 1 and 0.001 s^{-1}. The true strain or reduction in sample height at which failure occurs is plotted as a function of test temperature in Figures 16 & 17 for strain rates 0.001 and 1 s^{-1} respectively.

Figure-16 shows that at slow strain rates there is a temperature range of ductile-brittle transition behavior from approximately 400^{0}C down to 100^{0}C depending on the material tested. I400, the strongest material exhibits the highest DBTT. This is followed by a grouping of S200E, CIP-HIP-1, and I250 which show very similar transition temperature. The most ductile materials (showing the lowest DBTT) are the DOE specifications, with the P31664 showing

slightly lower DBTT. All materials tested at this strain rate failed from tensile hoop stresses and cracked axially along the compression specimen surface.

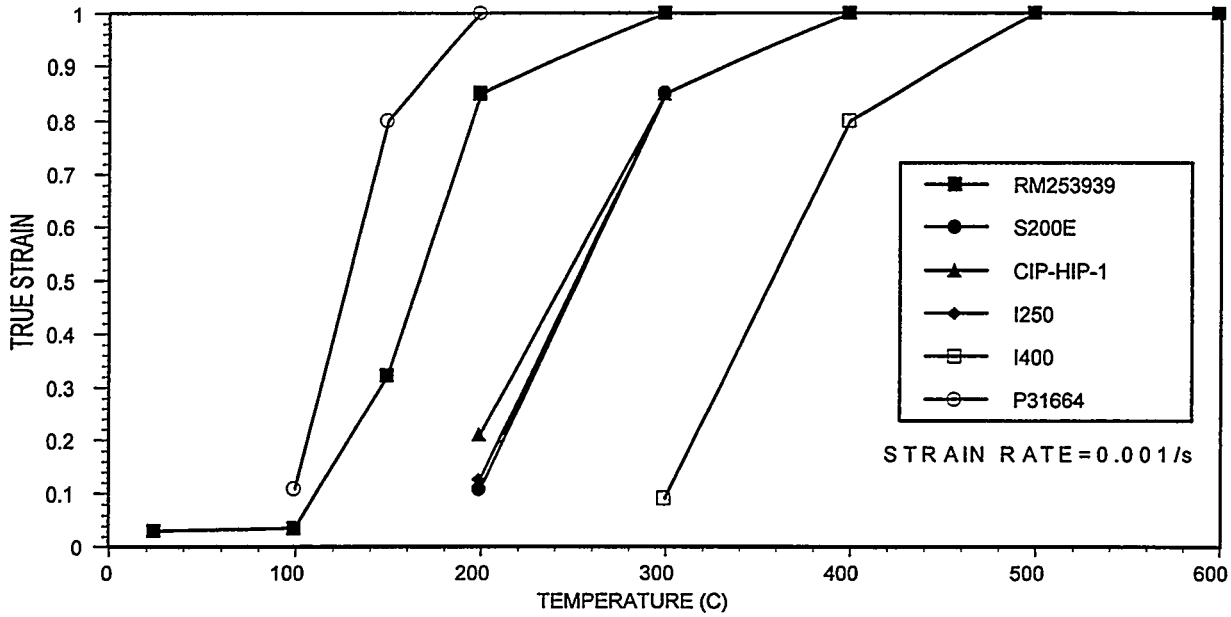

Figure 16 True strain (reduction in height) as a function of temperature at a strain rate of 0.001 s^{-1} for all materials tested.

It's interesting to note that the materials which show the lowest DBTT's are the two which have been overaged. This results in the precipitation of the teranary compound at the grain boundaries. This compound has been shown to reside primarily at triple points and may indicate that triple point grain boundaries may play an important role in fracture. Further microstructural investigation is ongoing to better understand this trend.

Figure-17 shows that at the fast strain rate of 1 s^{-1} the DBTT range is narrowed to approximately 200°C to 400°C. The data trend is similar to the slow strain rate with the high strength I400 showing the highest DBTT followed by a grouping of alloys S200E, CIP-HIP-1, I250, and P31664, and finally the lowest DBTT is shown by alloy RM253939. The general

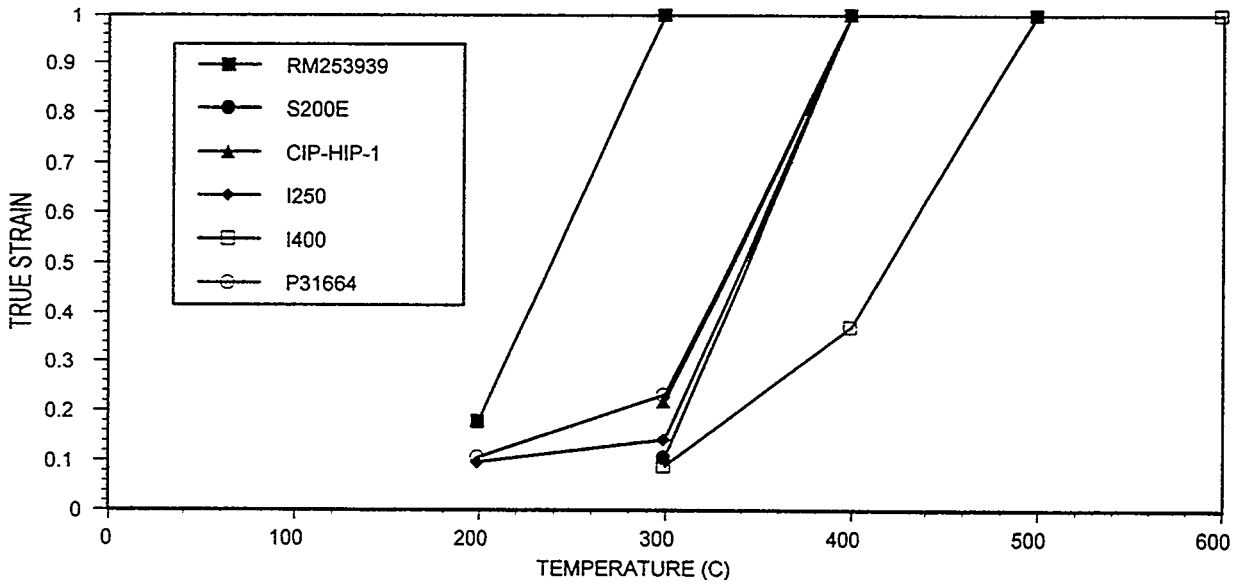

Figure 17 True strain (reduction in height) as a fuction of temperature at a strain rate of 1 s^{-1} for all materials tested.

effect of increasing the strain rate is to shift the DBTT up approximately 100°C. The fracture mode at the higher strain rate also changed from a tensile hoop stress fracture to an adiabatic shear band failure at a 45° plane through the specimen. Adiabatic shear bands develop under conditions of high strain rate when the heat generated by local deformation cannot be dissipated. As a result, the local flow stress decreases and further localized flow is stimulated(16). The fractures are therefore ductile in nature and do not represent true DBTT.

Discrepancies from Ideal Flow

Some of the alloys investigated in this study showed a yield point up to 500°C. Various degrees of yielding were observed and material was noted as having a yield point if there was an inflection or discontinuity in the stress-strain curve at the point of yield, there was a leveling of the flow stress at yield (similar to a Luders' band), or there were the conventional upper and lower yield points. From the DBTT to 500°C, alloys P31664, RM253939, I250, and I400 showed yield points at all strain rates. Alloys S200E and CIP-HIP-1, however, did not exhibit any yield point phenomena. None of the alloys had yield points at or above 600°C.

The number of individual data points used to generate each stress-strain curve is approximately 500 and these are spread evenly over the entire strain range. Therefore the number of data points within the yield point region is limited and only qualitative assessments of the yield point behavior can be made.

Yields points have been observed in many alloys, most notably lightly alloyed alpha-Fe. The yield point, followed by an immediate drop in stress and then usually a period of extensive strain at constant stress known as Luders' elongation has been generally attributed to either of two mechanisms. In the first, dislocations which are pinned by an atmosphere of some impurity or alloying constituent, e.g. C in alpha-Fe, break away from their pinning sites. The avalanche of dislocation movement occurs suddenly and stress drops giving an upper yield point followed by a sharp drop in the flow stress. In the alternate mechanism, existing dislocations are pinned and do not move, but instead at a critical maximum stress, the upper yield point, an avalanche of new

dislocations are emitted from sources.

Although yield points and Luders' elongation was not the subject of this study, some interesting observations have been made. In beryllium micro-alloys, it has been shown that slow-cooled and/or aged conditions typically show the yield point phenomenon. During slow cooling and aging treatments, existing dislocations can be pinned by substitutional elements like Fe or precipitates like $FeBe_{11}$ and $FeAlBe_4$. Upon reloading, an avalanche of dislocations, by one of the two above mechanisms occurs and an upper and lower yield point is formed. Yield points have been eliminated in beryllium alloys by either heating to high temperature and quenching or by pressurization treatments at relatively low temperature (below the aging temperature range). Either treatment induces new mobile dislocations that are free to move under stress in subsequent room temperature deformation testing. Borch(17)found that the large difference in thermal expansion coefficient with crystallographic orientation should cause large thermal stresses on rapid cooling thereby generating mobile dislocations. In pressurization treatments, new dislocations are also thought to be introduced. Once eliminated by these type of treatments, yield points can be reintroduced by heating into the precipitation range and/or by slow cooling from a high temperature allowing either precipitation or solute atom pinning of the dislocations.

Consistent with the results in the literature, the three materials in this study which demonstrate the yield point phenomena are ones which were given either a stress-relief or an over aging heat treatment. Both of the treatments involve time at temperature for diffusion of Fe to dislocations or precipitate formation on dislocations. These materials are the P31664 and

RM253939 alloys, which were overaged, and I250, which was stress relieved. The two other materials which were not given any post-consolidation heat treatment, S200E and CIP-HIP-1, demonstrated a smooth flow curve in the low strain region with no evidence of the yield point phenomena.

The behavior of I400 appears to be an exception to the above results because it was not heat treated but does have a yield point. It could be that cooling after consolidation was slow enough in this particular heat that dislocation pinning was fostered or that the Fe content, which is much higher in this alloy than the others, results in the rapid pinning of dislocations on cooling. The production histories of all of the alloys are being further investigated in the ongoing study for more detail on the cooling and post heating cycles in order to shed light on the origin of the yield point phenomena.

Serrated flow was observed in all materials tested. A follow on study will attempt to model these observations as a means of identifying the operable mechanism. Their presentation here is aimed at raising awareness in relation to the operating environment in ITER and proposing probable mechanisms.

The general characteristics of the serrated flow are shown in figure-18. These type serrations were only observed at 500°C, which is within the operating range for Be plasma facing in ITER. The serrations are peculiar in that the curves generally do not oscillate in stress about a mean value, thus exhibiting upper and lower yield points, but instead serrations are composed solely of intermittent stress-drops. The character of the stress-drops varies with strain rate. Generally, as strain rate is lowered from 1 to .001 s^{-1} the magnitude of the stress-drops increase while their frequency decreases.

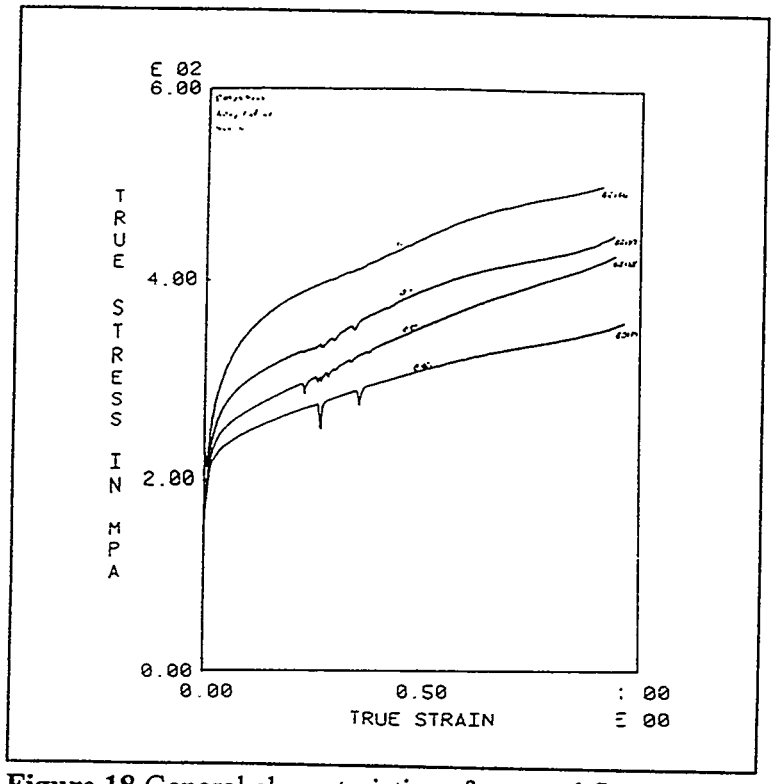

Figure 18 General characteristics of serrated flow observed at 500°C. The material shown is RM253939 at strain rates of 1,0.1,0.01,and 0.001.

Undulations in the flow stress which occur at strains which are well past the yield strain have been referred to as discontinuous yielding, serrated yielding, or jerky flow, and have been attributed largely to dynamic strain aging. During dynamic strain aging, moving dislocations have a velocity which is similar to the diffusing solute. Dislocations become pinned by the solute and then become mobile again after considerable increase in stress. Stress rises due to pinning and falls upon unpinning. For the effect to be observed as a macroscopic effect on the flow curve, large

numbers of dislocations must undergo pinning and release at the same time. This phenomenon is affected by strain rate and temperature. For example, as strain rate increases, the dislocation velocity becomes much greater than the diffusing solute atoms and pinning does not occur. At lower temperatures, the velocity of the diffusing species is retarded, eliminating pinning. At high temperature, the velocity of the pinning species may be fast enough so that the dislocations never break away, but instead the solute exerts a constant drag on the dislocations, and again unpinning may not occur.

In this study, serrated flow was observed in each alloy at a deformation temperature of 500°C. The effect was minimized by increasing strain rate which is consistent with dynamic strain aging. The observed increase in frequency and decrease in amplitude with increasing strain rate may also be consistent with dynamic strain aging, but remains unexplained at this time. Also consistent with typical dynamic strain aging, the serrated flow disappears as temperature is lowered or raised. No serrations were observed in any of the alloys at 400°C, and only occasional small serrations were observed at 600°C. Another interesting aspect of the serrations is that in most of the alloys tested at 500°C, only two major stress drops, serrations, were observed at the lowest strain rate.

Serrated yielding was reported by Gelles and Peterson(9) to occur during tension testing at 476°C and at a strain rate of 0.00064 s^{-1} for various grades of hot-pressed block (HP-10 and HP-21 from KBI, and S-240 from Brush, Inc.). The serrations generally occurred in the strain range between 0.03 and 0.15, and damped out before tensile specimen failure. This strain range

is well below that observed for serrated yielding during compression. In this study, testing at similar temperature and strain rate, 500°C and 0.001 s^{-1}, showed the strain range to vary from about 0.15 to 0.5. This difference in the critical strain for serration nucleation between tension and compression indicates that the mechanism for serrated yielding is inhibited by compression. In general, the fluctuation in the magnitude of the flow stress is much greater while the frequency of serrations is much smaller in compression compared to tension, from qualitative observation of the published tensile curves(9). These observations also appear to be consistent with the above suggestion that compression inhibits serrated yielding. For example, a large potential for the first stress drop may accumulate during the relatively large pre-straining period in compression, with the critical strain ranging from 0.15 to 0.3 in compression versus 0.03 to 0.05 in tension. The large accumulation of strain may then be expected to result in a large stress-drop followed by another period of serration-free flow before a subsequent stress-drop occurs. In tension, serrated flow appears to be unrestricted, starting at a low critical strain and progressing in small bursts at high frequency.

In both tension and compression, serrations were peculiar to the temperatures near 500°C. Tension testing at 370°C and 595°C and compression testing at 400°C and 600°C did not produce serrated yielding, although minor serrations did occur in compression at 600°C in the S200E, I250, and I400 materials.

One notable exception to the general agreement between the tensile study(9) and this study featuring compression testing was that the results on the same grade of beryllium, S200E,

do not agree. Serrated yielding was not observed in tension while large stress-drops, relative to the magnitude of the stress drops observed for the other materials in this work, were observed in compression. The reason for this discrepancy can not be explained at this time. It has been suggested by Weisz et al(10) that a critical strain for serrated flow, assuming a dynamic strain aging mechanism, is related to the achievement of a critical vacancy density which enhances diffusion of the pinning species to a level that the species can move effectively to pin the mobile dislocations. Considering this, one would expect that at higher strain rates, the critical vacancy density would be achieved at a lower measured strain because at the higher rate there would be less time for dynamic annealing of the vacancies as they form. In this case, a reduction in the critical strain should occur with increased strain rate as was generally observed for the materials tested in this study, except for I400. The average velocity of the dislocations would increase with strain rate, but may be moderated by an increase in dislocation density. The role of dislocation velocity and density, and their potential effects on the nature of serrated yielding is beyond the scope of this report and is not considered further.

CONCLUSIONS

In general, the flow curves at high strain rates showed work hardening at the lowest temperatures and work softening at the highest temperatures. HIP'ed material generally showed less work softening. At low strain rates, work hardening was observed at low temperatures. At high temperatures, the flow stress typically achieved a steady state. Between 25 and 700°C and at the strain rate of 0.001 s^{-1} the ranking of the yield stress between materials is consistent. The materials are listed in descending order of strength: I400, I250, CIP-HIP-1, RM253939, S200E, P31664. At 900 and 1000°C CIP-HIP-1 material has the greatest yield strength, followed by I250.

Serrated flow was observed in all the materials tested and was most pronounced at 500°C, showing large drops in the flow stress. Three common factors among all materials tested were:

-serrated flow was not observed until a critical amount of strain was accumulated;

-the magnitude and occurrence of the serrations was strain rate dependent showing greater magnitude serrations at the slowest strain rates and almost complete elimination at the high strain rates;

-serrated flow was only observed within a specific temperature range. Sharp, large serrations were observed at 500°C and minor perturbations in the flow stress up to 700°C.

One material was tested in the transverse direction. Serrations were more pronounced when the test sample axis corresponded to the longitudinal axis of the starting billet material.

Trends in the data related to the observance of yield points were as follows:

-no yield points were observed above 600^{0}C;

-the yield points became more pronounced at higher strain rates when tested at 500^{0}C;

-the yield points became less pronounced at higher strain rates when tested at 400^{0}C;

-both the S200E and CIP-HIP-1 materials did not exhibit yield points.

Strain rate sensitivity was observed in all alloys showing a greater difference in yield and flow stress as temperature was increased. The higher strain rate showed the greater yield and flow stress.

RECOMMENDATIONS

1)Building block material Al/Fe ratio should be controlled and material heat treated to control hot shortness and improve ductility.

2)Aluminum content of plasma spray material should be minimized (<200ppm) to minimize hot shortness.

3)Consideration should be given to writing specifications for ITER applications.

4)ITER Be material should be designed for resistance to thermal fatigue and not based on yield strength data.

REFERENCES:

1)I.I. Papirov and G.F. Tihkinskiy, Structure and mechanical properties of fine-grain deformed beryllium, Phys. Metals Met., (English translation of Fiz. Metal. Metalloved>), 29(5), 167-169, Pergamon Press, London (1971).

2)D. Webster, The effect of low melting phases on the elevated microstructural stability of hot pressed beryllium, Met. Trans. 6A, 803-808 (1975).

3)A.J. Stonehouse, Beryllium science and technology Vol I,pp200-201, Plenum Press, New York and London.

4)R.A. Foos, A.J. Stonehouse, K.A. Walsh, Microalloying Relationships in Beryllium, Brush Wellman Report BBC-TR-456, March 23, 1970.

5)A.B. Brown, F. Morrow, A.J. Martin, An improvement in the ductility of beryllium at high temperatures, Nature 187, 494-496(1960).

6)S.M. Myers, J.E. Smugeresky, Phase Equilibrium in the Be-Al-Fe System Using High Energy Ion Beams, Met Trans 7A, 795-802(1976)

7)D.R. Floyd, Causes of Yield Point Phenomenon in Commercial Beryllium Products, Feb. 1,1974, Rocky Flats Plant Report RFP-2061.

8)A.B. Brown, F Morrow, A.J. Martin, The effect of strain rate, and heat treatment, on the tensile properties of extruded beryllium rods between 25 and 600^{0}C, J. of Less Common Metals, 3,(1961) 62-88.

9)S.H. Gelles, J.H. Peterson, Characteristics of Commercial Vacuum-Hot-Pressed Beryllium, BMI-X-629, Sept. 1972.

10)M. Weisz, J. Mallen, Y. Adda, Study of the portevin Lechatelier Effect in Berylliu of Commercial Purity, Sixth Metallurgy Colloquim of Scalay, July 1962, University Press (1963).

11)G.J. London et al, Grain Size and Oxide Content affect Beryllium's Properties, Metals Eng. Quart.(August, 1976)

12)G.W. Rowe, An introduction to the Principles of Metalworking, Edward Arnold, London, 1965, p.245.

13)G.E. Dieter, Mechanical Metallurgy, 2nd ed., McGraw-Hill inc., New York, NY, 1976, pp72-102.

14)M.C. Mataya, V.E. Sackschewsky, Effect of Internal Heating During Hot Compression on the stress-strain Behavior of Alloy 304L, to be published in Met. Trans.

15)Workability Testing Techniques, American Society For Metals (1984).

16)H.C. Rogers, Ann. Rev. Mater. Sci., 1979, vol.9, pp283-311.

17)R.W. Armstrong, N.R. Borch, Thermal Microstresses in Beryllium and other HCP Metals, Met. Trans. 2, 3070-3077 (1971).

The Elevated Temperature Tensile Properties of S-200E Commercially Pure Beryllium

G. A. Henshall, S. G. Torres, and J. E. Hanafee

Abstract

The tensile properties of commercially pure beryllium are sensitive to temperature, impurity content, texture, grain size, and prior processing. Therefore, tensile tests have been conducted using the commercially pure S-200E Be commonly employed at Lawrence Livermore National Laboratory. These experiments were performed at temperatures ranging from 300 to 1100°C in the longitudinal and transverse orientations at the quasi-static strain rate of 5.5×10^{-4} s^{-1}.

The results of these experiments reveal that the stress-strain curve is smooth, ie. without yield points or serrations, over the entire temperature range studied. The yield stress (YS) and ultimate tensile stress (UTS) decrease monotonically with increasing temperature. Similar strengths were measured for both the longitudinal and transverse orientations, with the latter exhibiting slightly lower YS and UTS values. The measured failure elongation (e_f) vs. temperature curve is complex due to the competing effects of increasing basal-plane fracture stress with increasing temperature combined with the presence of hot shortness at intermediate temperatures. The latter is believed to be caused, at least partially, by the presence of free aluminum impurities at the grain boundaries. This hypothesis is supported by the measured increase in e_f at 700°C following a 100-hr anneal at 750°C, which would remove free Al from the grain boundaries. Texture also was found to influence e_f. The favorable orientation of the basal planes for initiation and propagation of cleavage cracks in longitudinal specimens results in a significantly decreased failure elongation compared with the transverse orientation. The effects of testing temperature and specimen orientation on the reduction in area were found to be similar to those described for e_f. Finally, comparison of the tensile results with the compression data of Abeln *et al.* suggests that the stress-strain response of S-200E Be is not significantly affected by the direction of straining. The only exception to this finding is that serrated flow occurs in compression at 500°C, while the tension curves are smooth at all temperatures. The favorable comparison between the data of Abeln *et al.* and the present study also provides confidence in the results reported here.

I. Introduction

Commercially pure beryllium is a commonly used structural material at Lawrence Livermore National Laboratory (LLNL). Design calculations involving Be typically include finite-element stress analyses using the NIKE [1] structural mechanics code. For the constitutive model most often used within NIKE for these purposes, the yield stress (YS), ultimate tensile stress (UTS), and elongation to failure (e_f) all are needed at one or more quasi-static strain rate. These data are required over the entire range of temperatures to which the component may be exposed in service or in conceivable accident scenarios. Therefore, this full body of data must be available to the design engineer for the grade of Be used in the design.

The YS, UTS, and e_f were not available in the literature over the temperature range of interest for the commercially pure S-200E Be employed at LLNL. Therefore, an experimental investigation of the elevated temperature tensile properties of S-200E Be was undertaken. These experiments were performed using the stock material employed at LLNL so that the data reflect the relevant impurity contents and processing methods. Further, since the mechanical properties of Be are known to be anisotropic [2,3], the tensile properties were evaluated for both the transverse and longitudinal orientations of the stock material. The results of these tests are presented in this report in such a way that the design engineer can make use of them in finite-element analyses.

II. Experimental Materials and Procedures

The commercially pure Be used in this investigation was Brush Wellman grade S-200E. This product is vacuum hot pressed from powder produced by the attrition method. Unlike some other grades of commercially pure Be, no post-consolidation anneal is performed for S-200E [4]. The chemical composition specified for this material is given in Table I. As discussed elsewhere [3-6], the impurities most influential on the mechanical properties are BeO, Al, and Fe.

Table I. Specified chemical composition for S-200E beryllium.

Species	Content (wt. %)
Be	Bal.
BeO	1.6-
Fe	0.06
Al	0.03
C	0.08
Mg	0.01
Si	0.03

The material used in this study was received as a 10-in. (254-mm) diameter cylindrical billet with a length of 30 in. (762 mm). Metallographic sections were taken from the as-received billet in both the longitudinal and transverse orientations. The grain size and microstructure appeared to be identical for both orientations. The average grain size of the as-received material was approximately 27 μm, with a minimum of 6 μm and a maximum of 45 μm. A network of small (about 1 μm) particles, presumably BeO, was observed in the microstructure. A small number of unidentified inclusions with a diameter of about 10 gm also was observed. Annealing the material for 1 hr. at 700°C did not alter the microstructure visibly.

Shoulder-grip tensile specimens were machined from the cylindrical billet by single-point turning followed by polishing of the gage section to remove tool marks. Standard practices for machining Be were employed to reduce surface damage. To verify that surface damage was not significant,. some specimens were annealed for one hour at 700°C in argon and others were chemically milled by etching in a 70°C stirred solution of 750 ml H_3PO_4 (85%), 71 g CrO_3 (99%), 200 ml deionized H_2O, and 30 ml H_2SO_4 (95 to 98%) [7]. Specimens were etched to remove 0.002 to 0.004 in. (0.051 to 0.102 mm) of material from the diameter of the gage section. Two specimen geometries were needed to keep the tensile loads within reasonable limits for the wide range of strengths exhibited over the 300 to 1100°C temperature range. Figure I presents a schematic representations of these geometries. Specimens were machined from the billet with two orientations: (1) longitudinal, with the axis of the specimen parallel to the long axis of the billet, and (2) transverse, with the specimen axis perpendicular to the long axis of the billet. Note that the (0001) basal planes of the Be unit cell tend to be perpendicular to the axis

of the billet in this textured product.

The equipment and procedures used to perform the experiments were described in detail by Torres and Henshall [8], and are summarized briefly here. Tensile testing was performed using a Brew Front-Loading, high vacuum furnace that was mounted between the columns of a screw-driven Instron Model TT-D-L universal testing machine. The temperature was measured using two type S thermocouples (Pt/Pt- 10% Rh) attached to the gage section of the specimen approximately 0.25 inches apart with 0.020 gauge niobium wire. Figure 2 presents a photograph showing the shoulder-grip specimen within the TZM molybdenum grips, the two thermocouples (prior to placement on the sample), the TZM molybdenum pull rods, and the tungsten furnace elements and shielding. Prior to heat-up and testing, the furnace was evacuated to a pressure of approximately 5×10^{-5} torr. In cases for which an inert gas was used, the furnace was purged twice with house argon prior to final evacuation and filling with the desired gas. Tests were performed at a cross-head speed of 0.02 in./min., corresponding to a strain rate of approximately 5.5×10^{-4} s^{-1}. Testing at other rates was beyond the scope of this investigation; the reader is referred to the work of Abeln *et al.* [4] for information on the strain-rate dependence of the flow stress for S-200E Be measured in compression.

Load vs. time data were collected using a Hewlett-Packard data acquisition system. These load and displacement measurements were used to calculate and plot the stress vs. strain results, from which YS (0.2% offset from the elastic line), UTS, and e_f values were determined. In addition, reduction-in-area measurements were performed by measuring the specimen diameter at three different positions (approximately 120° apart) on each half of the fractured specimens using an optical comparator. An average value was used to compute the reduced cross-sectional area at fracture. Finally, for tests in which a clear fracture load was detectable from the load-displacement curve (generally $T \leq 600$°C) the fracture stress was computed by dividing the fracture load by the reduced area at fracture.

III. Experimental Results and Discussion

To test the possible influence of furnace atmosphere and tensile specimen preparation methods on the elevated temperature tensile properties of Be, a small number of tests were performed in the intermediate temperature range of 500-800°C. In this temperature regime the failure elongations are relatively low and, therefore, the tensile properties are most sensitive to the potentially detrimental effects of specimen preparation and furnace atmosphere. Figure 3 shows that the specimen preparation method has little influence on the measured YS. A similarly small effect on the UTS also was observed. Figure 4 reveals that the variation in the measured e_f is significantly larger than that for the strength values, with the annealed specimens consistently exhibiting the largest elongations. However, this finding may not be associated with the "healing" of surface damage but rather a decrease in the amount of free aluminum at grain boundaries caused by annealing [5], as discussed later in this section.

The insensitivity of the tensile results to the surface preparation after machining may be due to the absence of significant machining damage. In addition, the temperature range examined in this study, 300 to 1100°C, lies above the ductile-brittle transition temperature (DBTT); measurements by Abeln *et al.* [4] show that the DBTT for a similar grade of Be is 100-200°C. Surface damage would be expected to significantly influence the tensile properties only below the DBTT. The main point from Fig. 4 is that etching the specimens

prior to testing does not improve the elevated temperature ductility. Based on the results shown in Figs. 3 and 4, subsequent testing was performed using only as-machined specimens.

The effects of furnace atmosphere on the elevated temperature tensile properties of S--200E beryllium are illustrated in Figs. 5 and 6. Figure 5 summarizes the YS data for as-machined, longitudinal specimens tested in house argon (purity not known precisely), high purity argon (99.999%), and vacuum (5 x 10^{-5} torr). Throughout the temperature range studied, there is only a small variation in YS for the various furnace atmospheres. Although these limited data may support a small systematic decrease in YS for specimens tested in vacuum, the deviations are within experimental error, about 15-20%. Similar results were obtained for the UTS. Figure 6 shows that the effects of furnace atmosphere on ductility are not systematic. The relatively large scatter in these data is typical for ef measurements in Be [9]. In summary, the furnace atmosphere was not found to have a significant influence on the elevated temperature tensile properties of Be. This finding is consistent with previous studies showing that oxygen, nitrogen, and hydrogen impurities do not have a large effect on the mechanical properties of Be [5,91.

Tensile tests of S-200E beryllium in the longitudinal and transverse orientations were then performed over the entire temperature range (300 -1100°C) using specimens in the as-machined condition and a high purity argon atmosphere. These data are tabulated in the Appendix. All of the measured stress-strain curves were smooth, with no indications of a yield point or serrated flow. The lack of a yield point in S-200E is consistent with the compression data of Abeln *et al.*[4] for this grade of Be. It is also consistent with the lack of a post-consolidation anneal which could result in the pinning of dislocations by solute diffusion and/or precipitation [4]. Unlike the finding of the present study, Abeln *et al.* found evidence for serrated yielding in compression at 500°C. However, they noted that the results of earlier tensile studies are consistent with our observation of a lack of serrated flow at 500°C. No explanation-currently exists to explain this difference in the tension and compression data [4].

Quantitative comparisons of the tensile stress-strain curves with compression data gathered by Abeln *et al.*[4] at Rocky Flats Plant (RFP) also have been made. Figures 7 and 8 compare our 5.5 x 10^{-4} s^{-1} results at 400 and 500°C with the RFP data of Abeln et al. at the similar strain rate of 1.0 x 10^{-3} s^{-1}. Figure 7 shows that there is relatively little scatter in the LLNL data at 400°C, and that the tensile results are similar to those in compression. Figure 8 shows a favorable comparison of the two data sets at 500°C. For both temperatures, the "flattening" of the tensile curves near the highest strains is associated with plastic instability in tension, and does not indicate a true difference in material behavior compared with compression loading. The compression tests do not suffer from this instability, and the flow stress rises continuously to true strains as large as 0.8.[4] For lower strains, the tensile flow stress is somewhat larger than the compression flow stress at both temperatures. However, this deviation is small considering the differences in testing methods (aside from the loading direction). Therefore, the data suggest that the flow stress of polycrystalline S-200E beryl-lium is not significantly affected by the direction of loading.

The temperature dependence of the tensile properties for S-200E beryllium is presented in Figs. 9-14 for both orientations. (Note that no experiments were performed below 300°C in the present study; the 20°C data shown in

Figs. 9-12 represent values certified by Brush Wellman and are shown only for reference.) Typical of a pure metal, both the YS and UTS decrease monotonically with increasing test temperature. Figures 9 and 10 show that the strength of S-200E beryllium in the transverse orientation generally is slightly less than that for the longitudinal orientation. The overall shapes of the YS and UTS vs. temperature curves are similar for the two orientations. Although elevated temperature tensile data are not available in the literature for S-200E beryllium, some data are available for other grades of vacuum hot pressed commercially pure material. The strength values we have obtained are consistent with these previous investigations [6]. In addition, the compression YS vs. temperature data of Abeln *et al.* [4] for S-200E in the longitudinal orientation are generally consistent with those presented in Fig. 9. While the compression values fall approximately 10% below those given in Fig. 9 for intermediate temperatures, the shape of the YS vs. temperature curve is the same for both investigations.

Compared with the strength data, a much more striking difference in properties between the longitudinal and transverse orientations is exhibited by the tensile failure elongations, Figs. 11 and 12. Again, the shapes of the ductility vs. temperature curves are similar, but the elongations are consistently larger for the transverse orientation. This result is not surprising since the basal planes are more favorably oriented for the initiation and propagation of cleavage cracks in the longitudinal orientation. [2,3] The complex shape of the e_f vs. temperature curves is believed to be associated with the natural increase in the fracture stress of the {0001} basal planes with increasing temperature [3] combined with hot shortness at intermediate temperatures caused by the presence of Al impurities, discussed below.

The S-200E beryllium used in this study contains about 300 ppm Al and 600 ppm Fe (Table I). Al is known to cause hot shortness of beryllium at intermediate temperatures if it is present at the grain boundaries in elemental, i.e. "free," form.[5] The usual remedy for this problem is to anneal the material at temperatures of 650-800°C for roughly 60-200 hours, allowing for diffusion and the formation of $AlFeBe_4$ precipitates upon reaction with Fe. (This may help to, explain the higher ductilities in the annealed material in Fig. 4). To test this hypothesis, a longitudinal S-200E beryllium specimen was annealed in Ti foil for 100 h at 750°C. This specimen was tensile tested at 700°C and the nominal strain rate of 5.5×10^{-4} s^{-1}. As shown in Figs. 9 and 10, annealing reduced the strength of the longitudinally oriented material somewhat; the YS and UTS values are similar to those of the unannealed transverse material. Similarly, Fig. 11 shows that the annealing treatment has increased the tensile elongation to a value more consistent with the unannealed transverse material. Therefore, it appears that the limited ductility of S-200E Be at intermediate temperatures may be caused, at least partially, by the presence of free Al at the grain boundaries.

The temperature dependence of the reduction in area (R. A.) is shown in Fig. 13 for S-200E Be in the longitudinal and transverse orientations. The trends exhibited in Fig. 13 are the same as those shown in Fig. 12 for e_f The reduction in area increases from 300°C to a local maximum at 400°C, then decreases to a local minimum at 700-800°C. Above 800°C, the reduction in area rapidly increases with increasing temperature to the highest temperature tested, 1100°C. Also consistent with the e_f data, the reduction in area for the transverse orientation is generally larger than for the longitudinal orientation.

At high temperatures, typically 700°C and

above, the precise fracture load was not detectable from the digitized load vs. displacement data due to the gradual drop in load nearly to zero prior to specimen failure. However, for $300 \leq T \leq 600$°C specimens typically fractured abruptly, allowing for unambiguous measurement of the fracture load. The fracture stress (FS), calculated from this load and the cross-sectional area at fracture, is shown in Fig. 14 as a function of temperature. For clarity, only the transverse data are compared with the corresponding UTS values; similar results were obtained for the longitudinal orientation, as tabulated in the Appendix. The data in Fig. 14 reveal that the fracture stress is significantly larger than the UTS for temperatures below 600°C. Above 600°C, the fracture stress may be expected to nearly equal the UTS based on the trend shown in Fig. 14. However, additional data would be required to confirm this hypothesis.

IV. Conclusions

Based on the results of elevated temperature (300 to 1100°C) tensile tests using commercially pure S-200E beryllium, the following conclusions have been reached.

1. The furnace atmosphere (vacuum, low purity or high purity argon) and the specimen preparation procedures do not significantly affect the elevated temperature tensile properties of S-200E Be.

2. The stress-strain curves for S-200E tested in tension in the temperature range 300 to 1100°C are smooth, with no yield points or serrated flow.

3. The yield stress (YS) and ultimate tensile stress (UTS) decrease monotonically with increasing temperature. Similar strengths were measured for both the longitudinal and transverse orientations, with the latter exhibiting slightly lower YS and UTS values.

4. The failure elongation (e_f) vs. temperature curve is complex due to the competing effects of an increase in {0001} basal-plane fracture stress with increasing temperature combined with hot shortness at intermediate temperatures. The latter is believed to be caused, at least partially, by the presence of free aluminum impurities at the grain boundaries. This hypothesis is supported by the measured increase in e_f at 700°C following a 100-hr anneal at 750°C, which would remove free Al from the grain boundaries.

5. The favorable orientation of the basal planes for initiation and propagation of cleavage cracks in longitudinal specimens results in a significantly decreased failure elongation compared with the transverse orientation.

6. The reduction-in-area data exhibit the same trends as a function of testing temperature and specimen orientation as measured for e_f.

7. The fracture stress is significantly larger than the UTS for temperatures below about 600°C. Above this temperature, the data suggest that the fracture stress may nearly equal the UTS, though this conclusion has not been confirmed.

8. Comparison of the tensile results with the compression data of Abeln *et al.* suggests that the flow stress of S-200E Be is not significantly affected by the direction of straining.

References

1. B. E. ENGELMANN, "NIKE2D User Manual," University of California - Lawrence Livermore National Laboratory, UCRL-MA-105413 (1991).

2. F. ALDINGER, "Flow and Fracture of Single Crystals," in *Beryllium Science and*

Technology, Vol. 1, D. WEBSTER and G. J. LONDON, eds., Plenum Press, New York, pp. 7-114 (1979).

3. H. J. SAXTON and G. J. LONDON, "Flow and Fracture of Polycrystalline Beryllium," in *Beryllium Science and Technology, VoL 1,* D. WEBSTER and G. J. LONDON, eds., Plenum Press, New York, pp. 1 1 5-144 (1979).

4. S. P. ABELN, M. C. MATAYA, and M. P. RIENDEAU, "Elevated Temperature Stress-Strain Behavior of Beryllium Powder Product," EG&G, Rocky Flats Plant Report, September, 1994.

5. A. J. STONEHOUSE, "Impurity Effects in Beryllium," in *Beryllium Science and Technology, VoL 1,* D. WEBSTER and G. J. LONDON, eds., Plenum Press, New York, pp. 181-206 (1979).

6. N. R. BORCH, "Elevated Temperature Behavior," in *Beryllium Science and Technology*, Vol. 1, D. WEBSTER and G. J. LONDON, eds. Plenum Press, New York, p.307-330 (1979).

7. A. GOLDBERG, J. E. HANAFEE, and R. G. SCOTT, "Mechanical Properties Evaluation of Some Commercial Beryllium Materials," University of California Lawrence Livermore National Laboratory Report No. UCRL-87392(1982).

8. S. G. TORRES and G. A. HENSHALL, "Tensile Properties of 21-6-9 Stainless Steel at Elevated Temperature," University of California - Lawrence Livermore National Laboratory Report, UCRL-ID-114590 (1993).

9. Private communication with D. CROOKS, Lockheed Palo Alto Research Laboratory, February 1994.

Appendix: Tabulated Data

Table A. 1. Tensile data for longitudinal, as-machined S-200E Be.

Temp. (°C)	YS (MPa)	UTS (MPa)	e_f(%)	R. A. (%)	FS (MPa)
300	219.8	304.8	5.300	9.2	328.7
300	202.4	294.8	9.950	16.9	333.0
400	193.8	258.8	15.80	32.2	323.1
400	203.8	261.8	13.15	----	-----
500	185.9	230.4	12.53	22.9	255.9
600	159.6	181.4	6.380	8.5	177.3
600	142.4	159.6	4.150	----	-----
600	161.1	185.9	6.580	----	-----
700	122.4	127.4	3.270	4.0	107.7
700	96.30	102.7	4.080	2.4	104.9
700	112.9	117.9	2.990	3.7	-----
800	52.21	53.00	3.620	3.9	-----
800	34.30	34.80	4.020	1.2	-----
800	48.20	48.20	2.100	4.0	-----
900	15.39	15.70	8.480	----	-----
1000	6.670	6.990	15.98	35.3	-----
1000	2.860	3.070	55.43	37.8	-----
1100	2.600	2.640	64.80	45.3	-----

Table A.2. Tensile data for transverse, as-machined S-200E Be.

Temp. (°C)	YS (MPa)	UTS (MPa)	e_f(%)	R. A. (%)	FS (MPa)
300	197.3	297.3	25.40	39.4	413.8
400	183.9	248.8	30.40	45.7	333.4
500	162.6	196.4	15.16	29.6	237.1
500	158.1	189.6	14.73	22.6	222.0
600	155.1	185.1	9.890	18.9	202.2
700	59.95	60.45	8.870	5.1	-----
700	59.45	60.45	5.340	3.8	-----
700	57.96	59.45	5.820	5.1	-----
800	20.73	21.10	6.580	5.8	-----
900	7.990	8.040	15.18	15.0	-----
1000	2.560	2.900	60.33	39.9	-----
1100	0.690	0.720	114.0	57.6	-----
1100	-----	-----	-----	63.6	-----

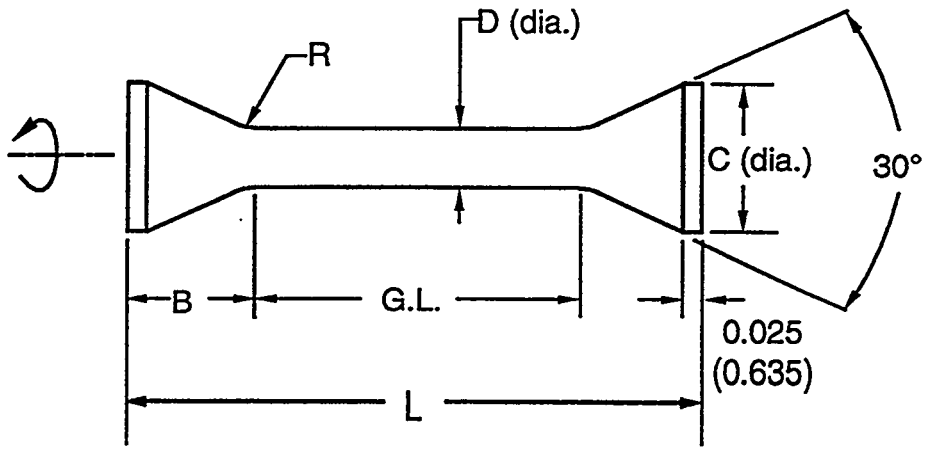

Specimen	D	R	G.L.	L	B	C
Low T	0.134 (3.40)	0.241 (6.12)	0.595 (15.11)	1.195 (30.35)	0.300 (7.62)	0.286 (7.26)
High T	0.250 (6.35)	0.375 (9.52)	0.600 (15.24)	1.570 (39.88)	0.485 (12.32)	0.470 (11.94)

Figure 1. Schematic diagram of the cylindrical tensile specimen geometries for "low" temperature ($T \leq 900$ °C) and "high" temperature ($T > 900$ °C) testing. Dimensions are given in inches with the mm equivalents in parentheses.

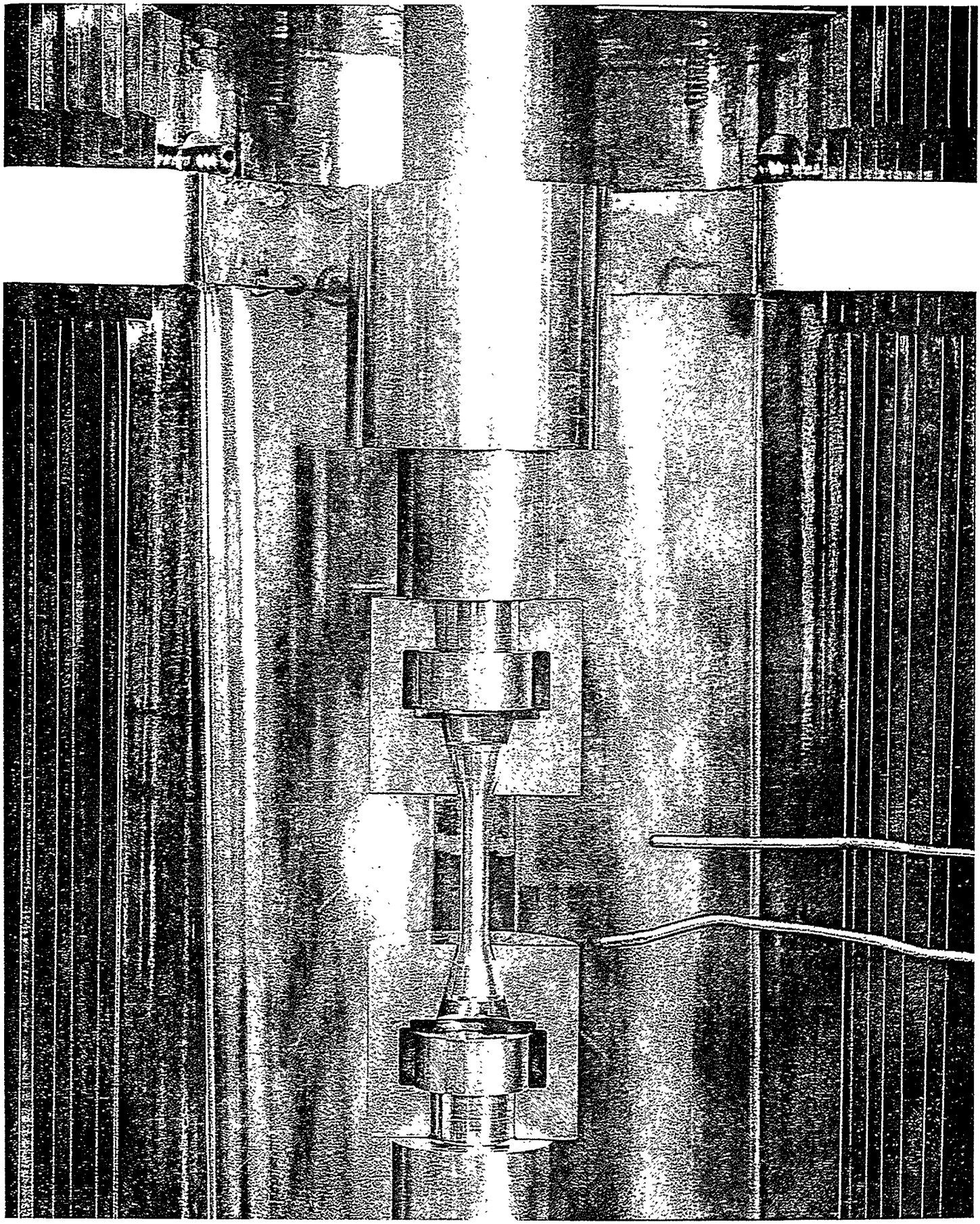

Figure 2. Photograph of the load train showing the furnace elements and shielding, grips, thermocouples, and shoulder-grip tensile specimen.

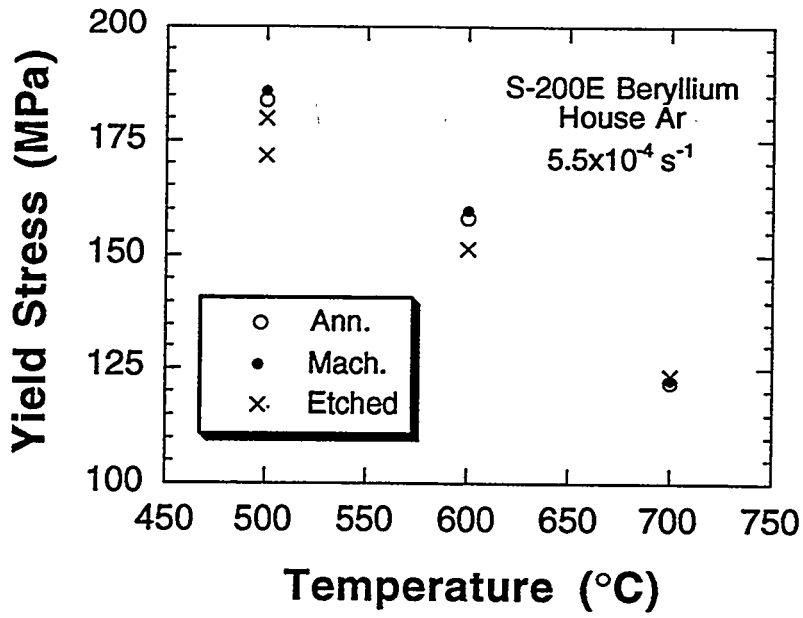

Figure 3. The effect of specimen preparation method on the yield stress of longitudinal S-200E Be at intermediate temperatures.

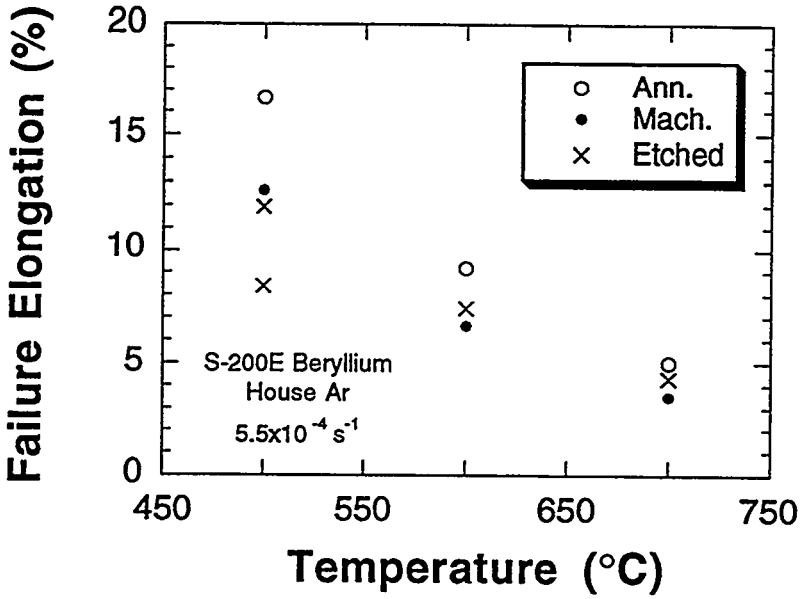

Figure 4. The effect of specimen preparation method on the failure elongation of longitudinal S-200E Be at intermediate temperatures.

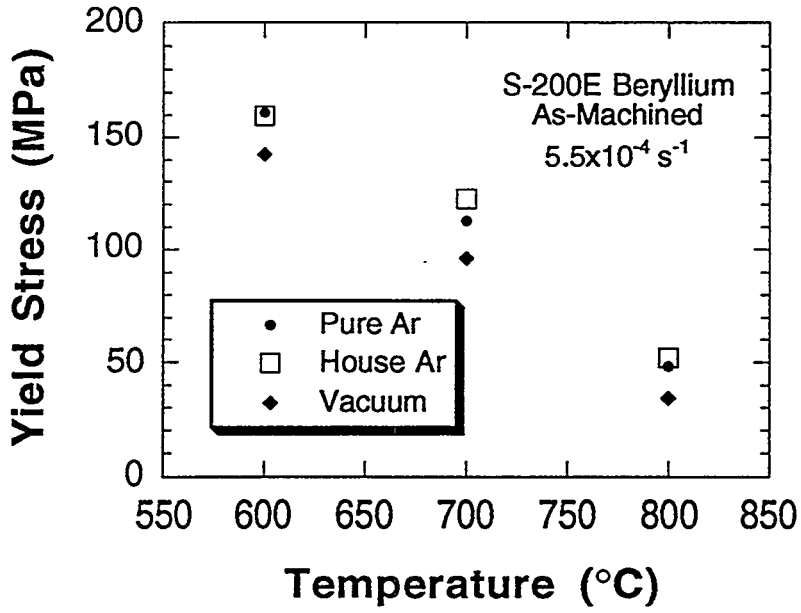

Figure 5. The effect of furnace atmosphere on the yield stress of longitudinal S-200E Be at intermediate temperatures.

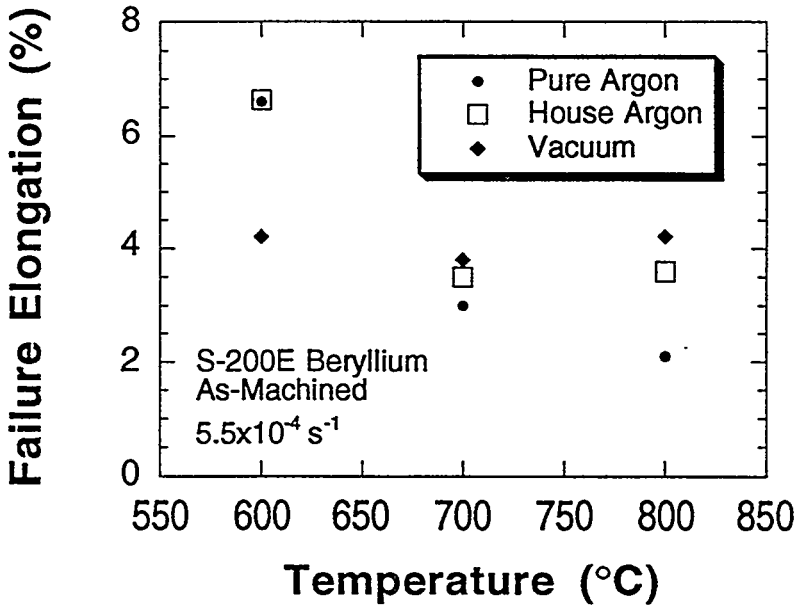

Figure 6. The effect of furnace atmosphere on the failure elongation of longitudinal S-200E Be at intermediate temperatures.

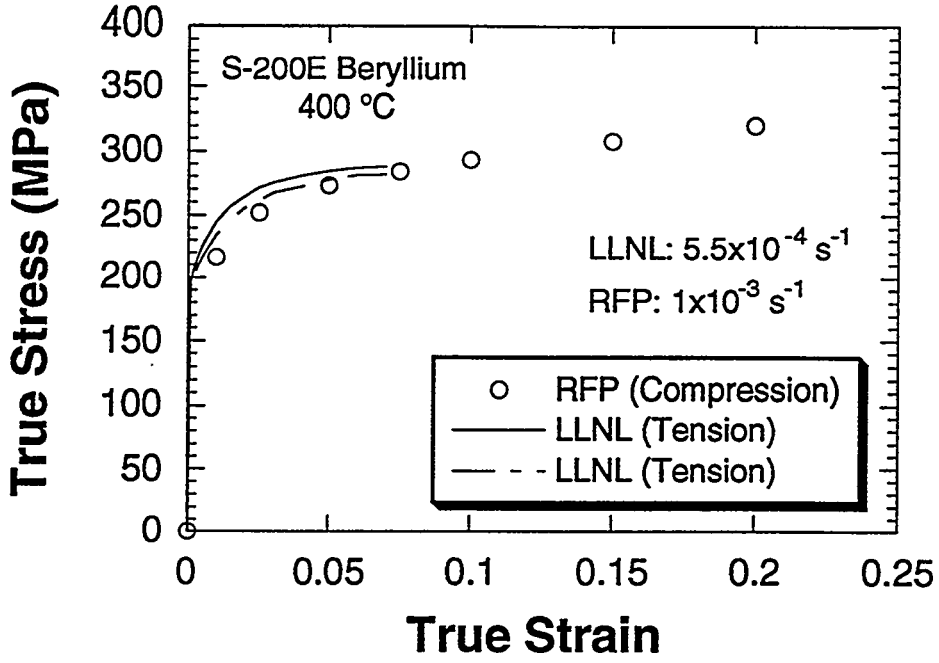

Figure 7. Comparison of the true stress vs. true strain curves in tension (present study) and compression (Abeln *et al.* [4]) at 400 °C and comparable strain rates.

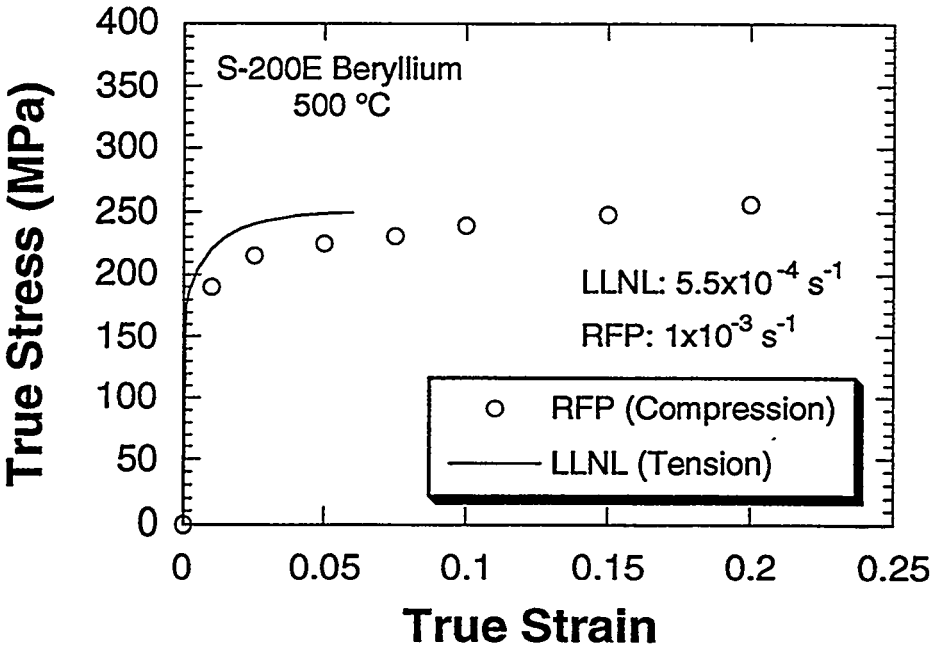

Figure 8. Comparison of the true stress vs. true strain curves in tension (present study) and compression (Abeln *et al.* [4]) at 500 °C and comparable strain rates.

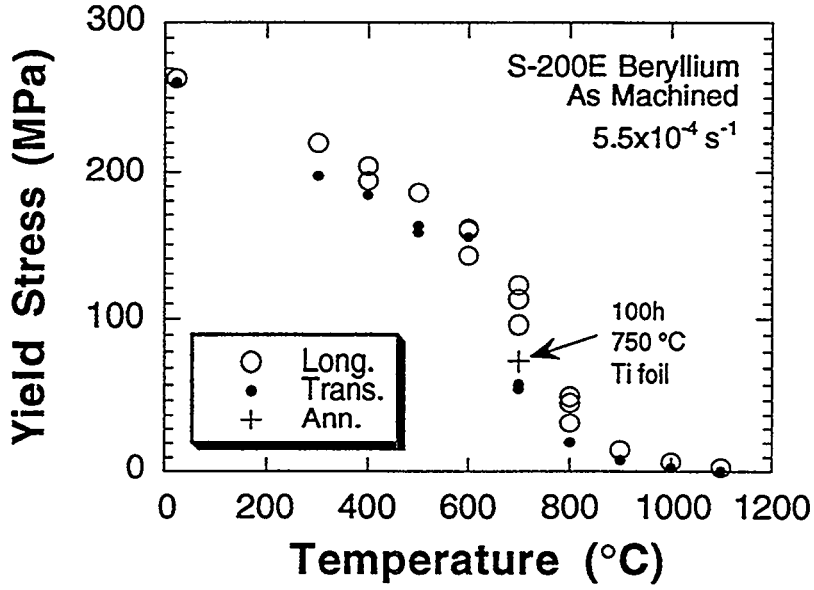

Figure 9. The 0.2%-offset yield stress of S-200E beryllium as a function of test temperature for longitudinal and transverse orientations.

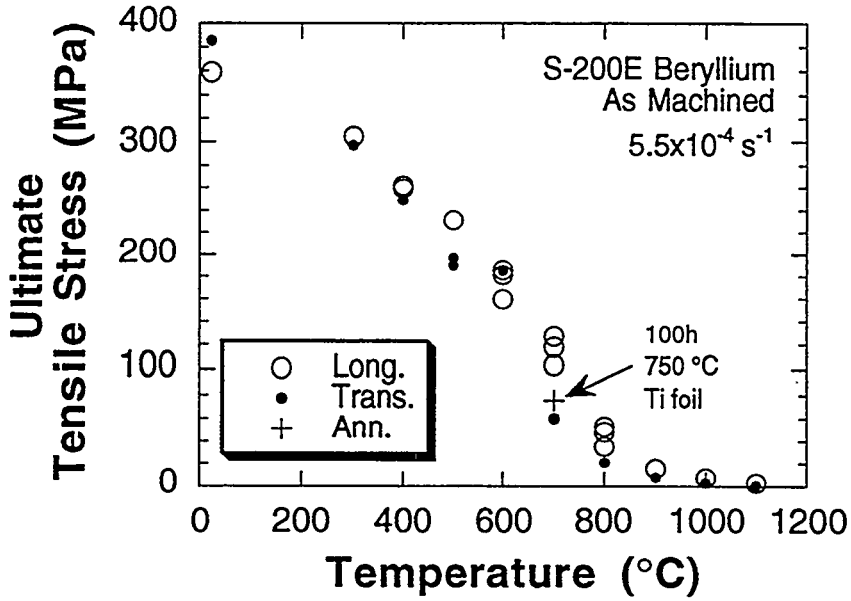

Figure 10. The ultimate tensile stress of S-200E beryllium as a function of test temperature for longitudinal and transverse orientations.

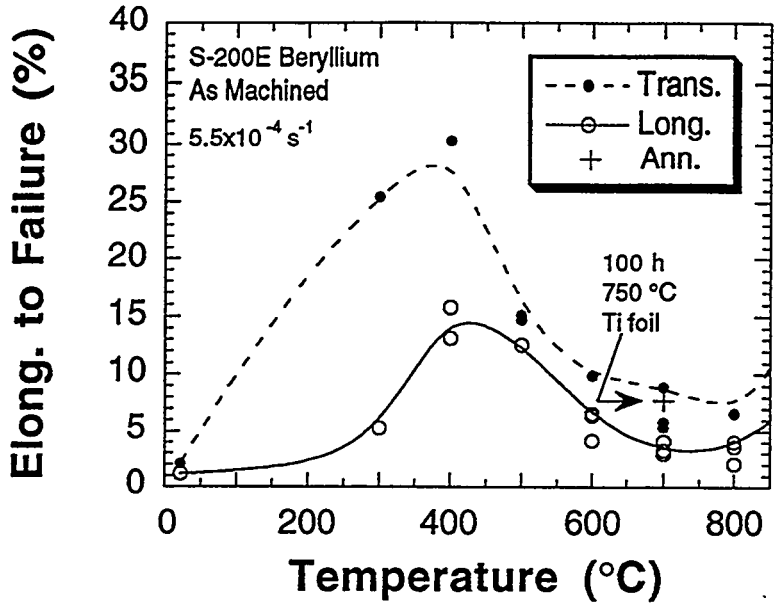

Figure 11. The elongation to failure of S-200E beryllium as a function of test temperature for longitudinal and transverse orientations. Data are shown for temperatures below 900 °C and for a specimen annealed for 100 hr. at 750 °C.

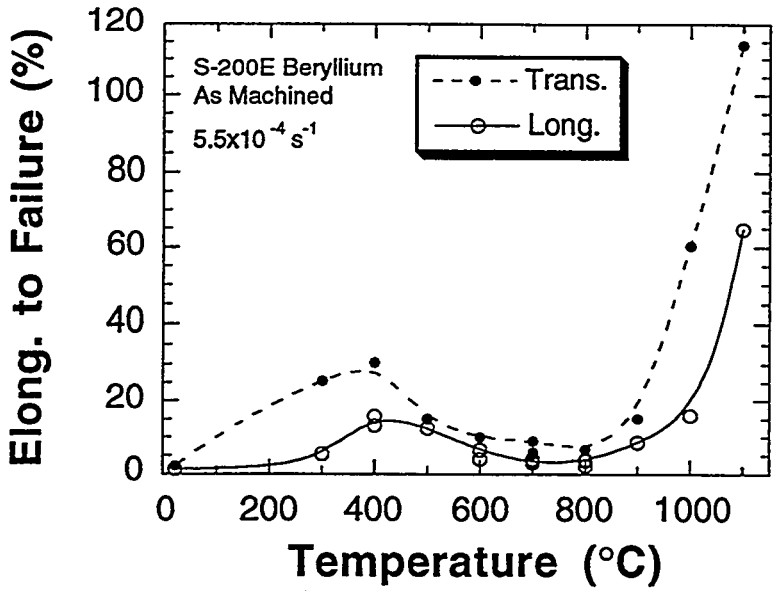

Figure 12. The elongation to failure of S-200E beryllium as a function of test temperature for longitudinal and transverse orientations. Data are shown for all temperatures tested.

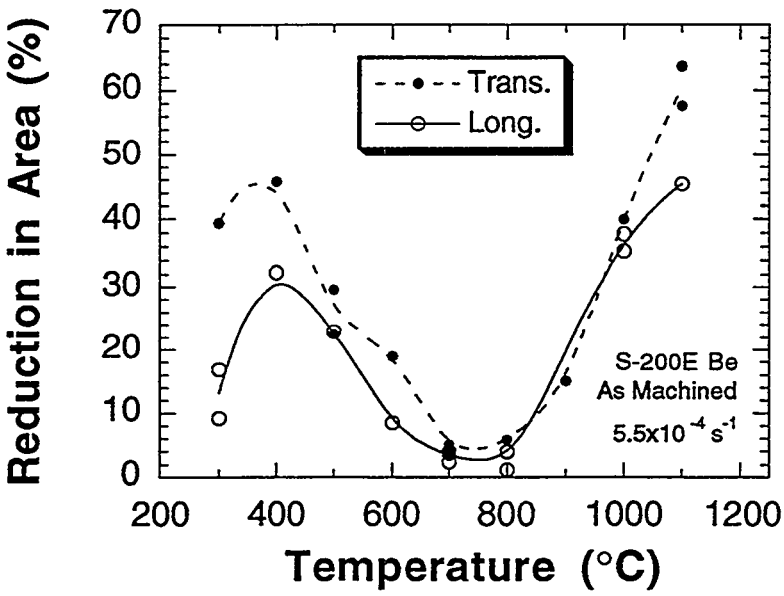

Figure 13. The reduction in area for S-200E beryllium as a function of test temperature for longitudinal and transverse orientations.

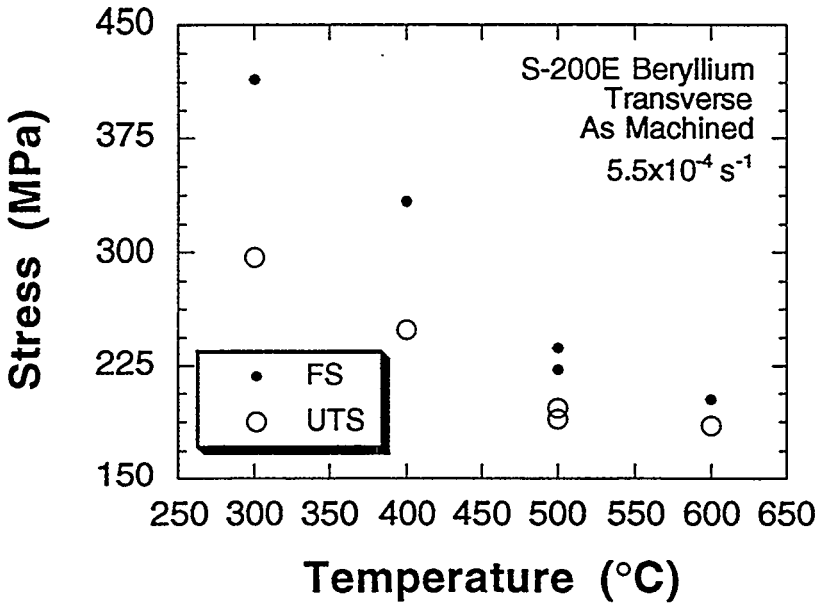

Figure 14. The fracture stress (FS) and ultimate tensile stress (UTS) are shown as a function of test temperature for S-200E beryllium in the transverse orientation.

Pre-Irradiation Testing of Actively Cooled Be-Cu Divertor Modules

J. Linke[a], R. Duwe[a], A. Gervash[b], W. Kühnlein[a], K. Nakamura[c], A. Peacock[d], M. Rödig[a]

a Forschungszentrum Jülich GmbH, KFA-EURATOM-Association, D-52428 Jülich, Germany
b D.V. Efremov Scientific Research Institute of Electro-Physical Apparatus, St. Petersburg, Russia
c Japan Atomic Energy Research Institute, 801-1 Naka-machi, Naka-gun, Ibaraki 311-01, Japan
d JET Joint Undertaking, Abingdon, Oxfordshire OX14 3EA, UK

Abstract:
A set of neutron irradiation tests is prepared on different plasma facing materials (PFM) candidates and miniaturized components for ITER. Beside beryllium the irradiation program which will be performed in the High Flux Reactor (HFR) in Petten, includes different carbon fiber composites (CFC) and tungsten alloys. The target values for the neutron irradiation will be 0.5 dpa at temperatures of 350°C and 700°C, resp.. The post irradiation examination (PIE) will cover a wide range of mechanical tests; in addition the degradation of thermal conductivity will be investigated. To determine the high heat flux (HHF) performance of actively cooled divertor modules, electron beam tests which simulate the expected heat loads during the operation of ITER, are scheduled in the hot cell electron beam facility JUDITH. These tests on a selection of different actively cooled beryllium-copper and CFC-copper divertor modules are performed before and after neutron irradiation; the pre-irradiation testing is an essential part of the program to quantify the zero-fluence high heat flux performance and to detect defects in the modules, in particular in the brazed joints.

1. Introduction

Since neutron irradiation programs on plasma facing materials and components are rather time consuming and expensive, a careful pre-selection is required for all samples to be included in the test. However, a final decision on the material (beryllium, carbon, or tungsten) for the individual plasma facing components (PFC) in ITER is still open. Thus, at the present state of planning, samples and components from all three materials are included in the test program. On the other hand, it seems to be unlikely that all components (divertor targets, dump plates, baffle, first wall, etc.) can be manufactured from the same class of materials; therefore the combination of at least two materials (e.g. Be and C) has to be considered.

To contribute to the establishment of an adequate data base, test samples and components from the above mentioned three materials (Be, C, W) have been selected for thermo-mechanical tests and high heat flux experiments. In the latter group of tests miniaturized actively cooled divertor modules with different materials, different geometries (monoblock, flat tile type, monoliths), and different joining techniques have been supplied by laboratories involved in the ITER PFC activities and by industry. A final decision on the components to be included in the irradiation program will be made following a detailed thermal analysis on a larger number of test coupons.

2. Neutron irradiation program

The neutron irradiation will be performed in the High Flux Reactor (HFR) of the Joint Research Center's "Institute for Advanced Materials" at Petten, The Netherlands [1]. The HFR is one of the most powerful multi-purpose research and test reactors in Europe. This 45 kW light water cooled and moderated reactor provides 19 in-core positions with maximum thermal fluxes up to $1.5 \cdot 10^{18} m^{-2} s^{-1}$; max. fast fluxes in the core center ($E > 0.1$ MeV) are $4.6 \cdot 10^{18} m^{-2} s^{-1}$. The target values of this irradiation program will be 0.5 dpa at 350°C and 700°C, resp.. The test samples will be contained in 8 capsules with a diameter of 67 mm; the mean capsule length is 110 mm. Beside beryllium test specimens made from different CFC materials and tungsten alloys will be irradiated. Fig. 1 shows a cross section of those capsules which will contain the Be samples and components. The post irradiation examination (PIE) on beryllium will cover a wide spectrum of different test:

- tensile tests
- fatigue tests
- fracture toughness tests
- impact bending tests
- shear tests on brazed joints
- thermal conductivity measurements
- thermal shock tests (electron and laser beam loading)
- HHF-tests on actively cooled modules

On those test specimens which will be subjected to non-destructive testing a careful pre-irradiation testing is required to determine the neutron induced degradation of the properties. This pre-irradiation testing has to be performed on all thermal conductivity samples. In addition HHF modules have been subjected to an extensive characterization to quantify the heat removal capability of each individual module and to detect defects in the brazed joints or in the plasma facing Be tiles. However, to avoid any pre-damaging of the modules these tests have been performed at moderate heat loads (i.e. below power density levels of 5.6 MW m^{-2} for quasi-stationary heat loads).

High heat flux thermal shock tests with pulse durations of 5 ms and below have been performed on small non-actively cooled test coupons; test results have been reported elsewhere [2].

3. Hot cell electron beam facility

All HHF testing was done in JUDITH (Juelich Divertor Test Facility in Hot Cells). Fig. 2 shows a schematic drawing of the test device which is installed inside a hot cell [3], [4]. The incident heat fluxes on actively or passively cooled plasma facing materials and components are simulated by energetic electrons ($E \leq 150$ keV) which are scanned in a rectangular frame (max. dimensions of the scanned area: 100 mm x 100 mm). A variety of different diagnostics are available to quantify the response of the test piece to the applied heat load:

- thermo-couples in the PFM/PFC
- integral and two-color pyrometers covering a temperature range from 300°C to 3500°C
- high speed pyrometer for transient heat loads
- infrared scanner (starting at RT)
- strain gauges
- residual gas analyzer
- instrumented high pressure coolant loop (H_2O, $p \leq 4$ MPa).

The specifications and the heat load parameter which have been applies for the pre-irradiation test program on actively cooled Be-Cu-divertor moduls is shown in Table 1.

Layout parameters of JUDITH:	
total power:	60 kW
acceleration voltage:	≤ 150 kV
power density:	≤ 15 GW m^{-2}
loaded area:	4 mm^2 ... 100 cm^2
scanning frequency:	≤ 100 kHz
beam rise time:	130 µs
Loading conditions for pre-irradiation tests:	
acceleration voltage:	120 kV
power density:	1.6 ... 5.6 MWm^{-2}
pulse length:	30 s
loaded area:	≅ Be tile surface
coolant flow rate:	0,63 $l \cdot s^{-1}$

Table 1: Layout data for the electron beam testbed JUDITH and applied heat flux conditions.

Due to the limited volume in the irradiation capsules a miniaturization of the actively cooled test modules has been required [5]. Thus, all neutron irradiation tests will be performed on modules (flat tile or mono-block design) with only 1 (or at least 2) tiles of the plasma facing material brazed to the heat sink. On flat tile modules the coolant tubes for the connection to the coolant loop have heen omitted. To guarantee tigh sealing of the high pressure loop a special clamping mechanism (cf. Fig. 3) has been developed. Two sealing adapters machined from OF copper in combination with O-ring sealings on the cooling pipes provide sufficient safety against water leaks. The mechanism is motor driven and can be operated by remote handling techniques.

sample ID	number of modules	Be grade	surface area for HHF loading	Be tile thickness	heat sink material
FT 25[1)]	2	S65C	15x15 mm^2	5 mm	CuCrZr
FT 29[2)]	8	S65C	25x15 mm^2	3 mm	CuCrZr
FT 30[2)]	8	S65C	25x15 mm^2	8 mm	CuCrZr
FT 31[3)]	2	TPG56	25x15 mm^2	8 mm	CuCrZr

samples supplied by:
1) JAERI
2) JET
3) Efremov Institute

Table 2: Materials and geometries of actively cooled divertor modules

The miniaturized test components with Be as a PFM were all from the flat tile design; the modules supplied by different laboratories had different geometries (cf. Fig. 4). A total of 20 modules were tested. The heat sink of all samples was made from copper; the joining of the Be tiles with thicknesses ranging from 3 to 8 mm to the heat sink was done by brazing (Ag containing brazes for all modules [6], [7]). Details on the sample geometries are listed in Table 2.

To accomodate stresses from the brazing process and/or high heat flux testing the Be tiles of test modules FT29 through FT31 were castellated (size of the castellations ≈6 mm x ≈7 mm).

4. High heat flux tests

Main objective of the pre-irradiation high heat flux tests on the actively cooled Be-Cu divertor modules [8] was the pre-selections of those components which should be included in the irradiation in the HFR reactor. On the other hand a careful quantification of the heat removal efficiency (i.e. temperature increase as a function of incident power density) before neutron degradation was essential.

Any damage to the brazed joint (imperfections in the braze layers, voids or cracks) or in the plasma facing material would result in a localized surface temperature rise. To make these effects visible, a high resolution IR imaging system (12 bit resolution; 5 pixels per mm) with a long focus IR lens has been installed. Figs. 5a and 5b show typical IR images from Be-Cu moduls during e-beam heating. Fig. 5a shows an example of a defect brazed joint (this test has been performed on a test module not listed in Table 2 but otherwise similar geometries without castellation). Even at rather low heat loads (320 Wm^{-2}) significant heating up to approx. 400°C has been detected on the right hand edge of the Be tile. The intact (left hand edge) remains relatively cold (T ≈ 60°C). The resulting thermal gradient along the indicated line (LI01) is shown in the insert.

Surface temperature variation on a 3 mm thick castellated tile (sample ID-number FT 29/1) become visible in Fig. 5b, however, as has been demonstrated by scanning electron microscopy (SEM) the brighter spots which appear to be some ten degrees above the base level can not be attributed to any defects in the braze layer or in the tile material itself. Fig. 6a shows a SEM micrograph from such an area; Cu-deposits (obviously originating from a brass wire which was used for spark erosion cutting of the sample surface) are clearly visible. These deposits result in an increased emissivity ε which mimics the observed temperature rise. The circular hot spots in the IR image (Fig. 5b) have been identified as small Cu droplets (possibly thin Cu-deposits which agglomerated due to the applied heat load) which become visible in the SEM micrograph in Fig. 6b. Since these droplets have only poor contact to the underlying Be-tile, the temperature rise is far beyond that of the Be surface. Evaporated copper from these droplets is re-deposited in a short distance from its origin (white area in Fig. 6b).

The presence of impurity deposits as well as beryllium oxide layers on the surface of the PFC makes surface temperature measurements using imaging IR sensors rather sensitive to the prevailing emissivity ε of the Be tile. Therefore a careful determination of ε has to be performed before HHF testing in JUDITH. To determine a mean emissivity for each surface the modules have been heated homogeneously to a temperature of 100°C in an oven (cf. Fig. 7). The heating cycle was controlled by a graphite sample with a pre-determined emissivity (ε = 0.80). In addition the graphite specimen was instrumented with a thermocouple. After having reached thermal equilibrium the emissivity on the control unit of the IR scanner was adjusted in such a way that the surface temperature within a retangular frame (see Fig. 7) was exactly 100°C. To avoid any influence of hot spots, the median temperature has been selected for this analysis (using the average temperature value will result in minor variations of ε only). The rectangular frame covered approx. 85 % of the tile's surface, i.e. including the castellations which appear to show high emissivity values (due to the black body radiation). The castellations become clearly visible in the line scans (see right column in Fig. 7). For that reason emissivity measurements from the castellated area only result in smaller ε-values (difference in ε approximately 0.05).

Having performed ε-measurements for all Be-Cu modules the thermal response (IR-images, median temperature T_{med}, average temperature T_{avg}) has been determined for incident heat fluxes from 1.6 to 5.6 MW m^{-2} (increment 0.8 MW m^{-2}). To limit the resulting surface temperature to 300°C, all modules with beryllium tiles thicker than 5 mm (FT 30, FT 31) were loaded up to 3.2 MW m^{-2}. Fig. 8 shows IR images from 8 identical modules (sample ID: FT 30; Be tile thickness = 8 mm) at an incident heat load of 3.2 MW m^{-2}. Despite of hot spots and smaller areas with slightly increased surface emissivities due to surface impurities (c.f. Fig. 5b), all samples show temperatures of approx. 245°C

(±25°C). The calculated surface temperatures T_{med} and T_{avg} do not differ significantly.

The thermal response (T_{med} vs. incident power density) for all tested Be-Cu modules is plotted in Fig. 9. All specimens show an almost linear increase of T_{med} with increasing heat fluxes. The smallest temperature increase has been realized for samples FT 25 (approx. 35°C per MW m^{-2} incident heat flux) followed by samples FT 29 (approx. 42°C per MW m^{-2}). The good behavior of the test modul FT 25 which has a Be tile thickness of 5 mm in comparison to module FT 29 with a thickness of only 3 mm is mainly due to the different design of the heat sink (in sample FT 25 the coolant channel is much closer to the braze layer). A fast temperature rise was measured for specimens FT 30 and FT 31 with approx. 70 and 85°C per MW m^{-2} incident power density.

5. Conclusions

To establish a data base for the candidate plasma facing materials (Be, CFC, W) neutron irradiation experiments with ITER relevant parameters are most essential. Beside the degradation of thermo-mechanical parameters the post irradiation high heat flux performance of the divertor has to be investigated. To increase the number of test coupons which can be included in the forth-coming irradiation experiment in the HFR reactor in Petten, a miniaturization process of the actively cooled modules has been successful. A special clamping mechanism guarantees tight sealing of the high pressure coolant loop. It allows a rapid exchange of test pieces and can easily be operated by remote handling techniques on neutron irradiated components.

The available diagnostics are suitable to detect failures in the brazed joint or other defects in the Be-tiles which decrease the heat flux from the loaded surface to the copper heat sink. In addition, the heat removal efficiencies of the unirradiated actively cooled modules have been measured; these data will be required for a comparison with HHF test performed on the n-irradiated samples later. The characterization of the high heat flux performance requires a detailed analysis of the emissivity (and local emissivity variations) in order to avoid disturbing influences of surface contaminants or oxide layers. All modules investigated so far (sample ID-number FT 25 and FT 29 through 31) didn't show any indications of failures and are thus qualified to be used in the forthcoming neutron irradiation program.

6. Literature

1. J. Ahlf, A. Zurita, Report EUR 15151 EN, Luxembourg, 1993
2. M. Rödig,, R. Duwe, A. Gervash, A. Khomutov, J. Linke, A. Schuster, this workshop, 1995
3. R. Duwe, W. Kühnlein, H. Münstermann, Proc. 18th Symposium on Fusion Technology, Karlsruhe, 1994, 355 - 358
4. N. Sakamoto, M. Akiba, H. Kawamura, this workshop, 1995
5. J. Linke, M. Akiba, M. Araki, H. Bolt, G. Breitbach, R. Duwe, K. Nakamura, J.H. You, Fusion Engineering and Design 28, 1995, 72-80
6. C.M. Ibbot, H.D. Falter, P. Meurer, E. Thomson, M.J. Watson, G. Critchlow, D. Ciric, Proc. 18th Symposium on Fusion Technology, Karlsruhe, 1994, 431 - 434
7. G. Humpston, D.M. Jacobson, S.P.S. Sangha, Endeavor, New Science, Vol. 18, No. 2, 1994
8. H.D. Falter, D. Ciric, P. Massmann, C. Ibbot, Report R(93)02, JET, 1993

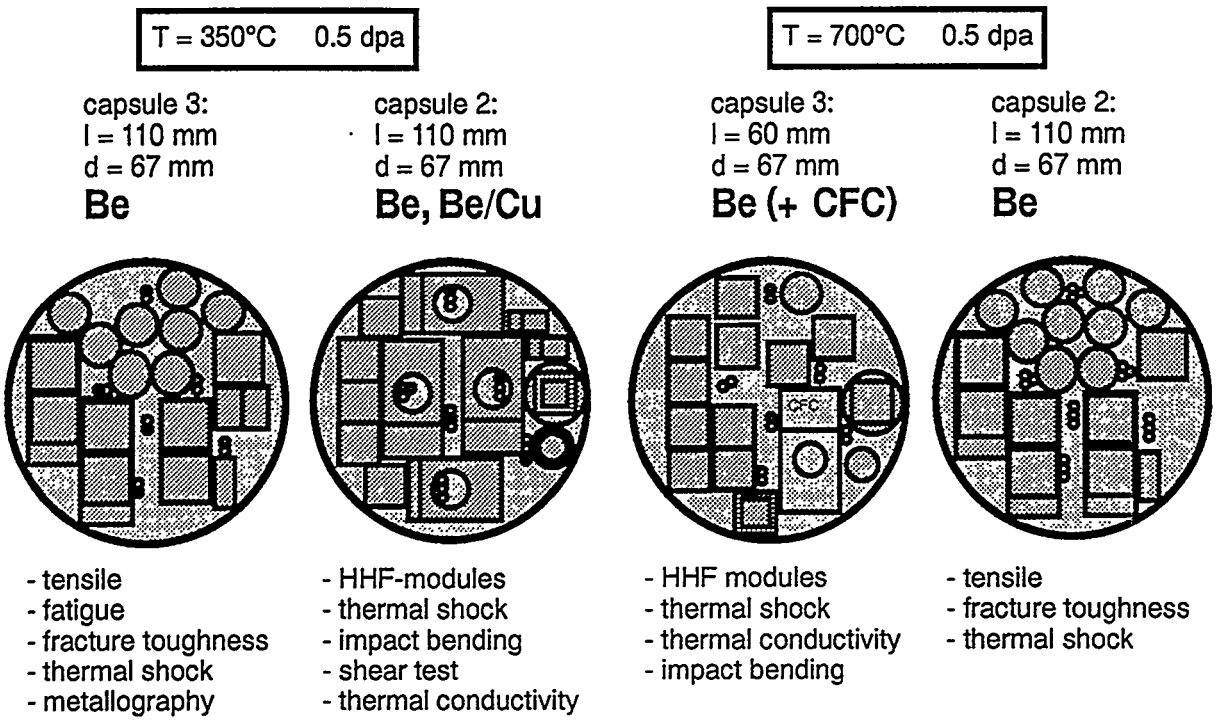

Fig. 1: Cross sections from test samples and capsules (beryllium capsules only) to be irradated in the HFR.

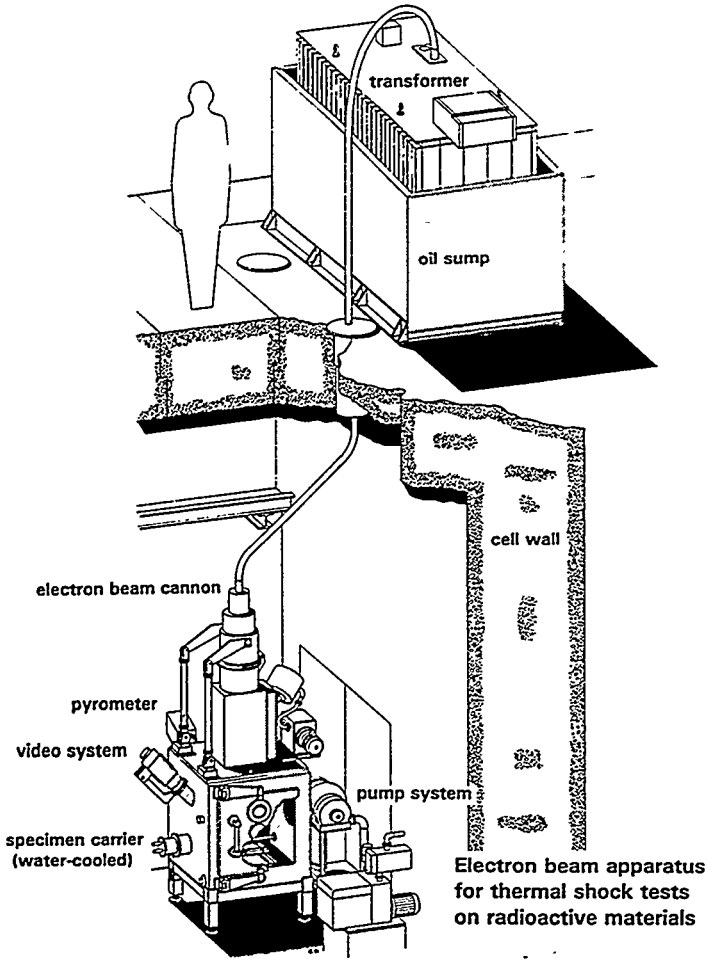

Fig. 2: Schematic drawing of the hot cell electron beam facility JUDITH.

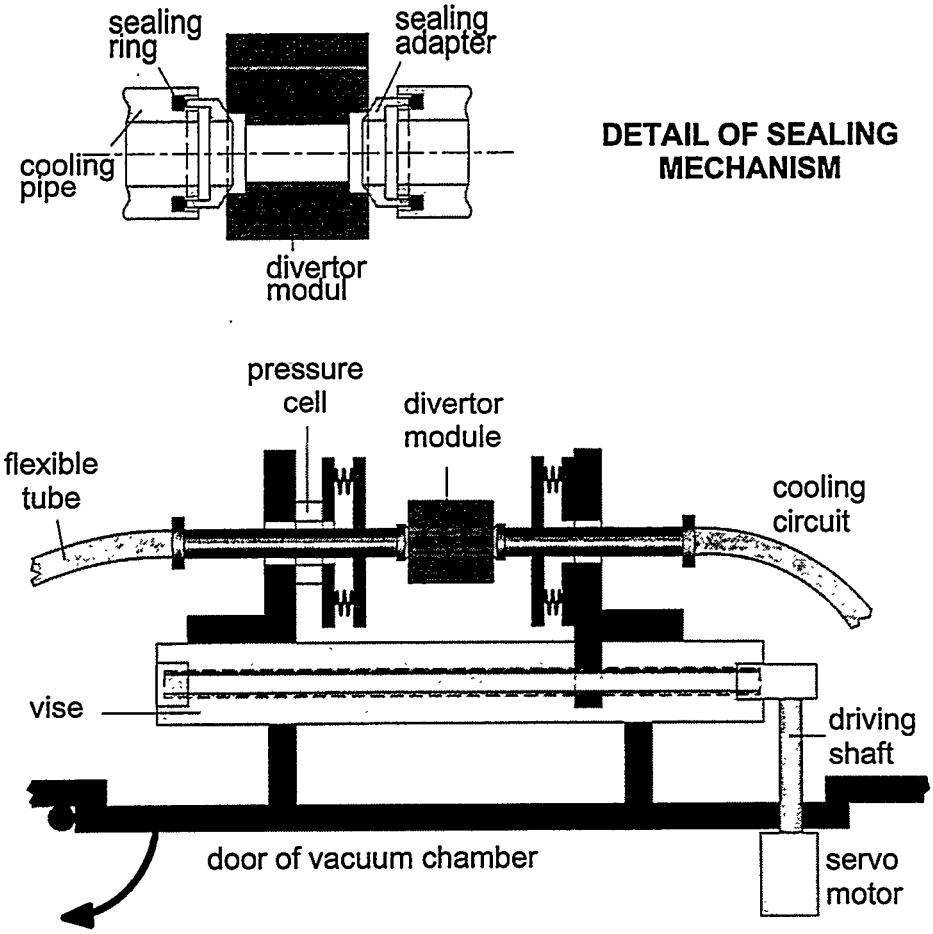

Fig. 3: Clamping mechanism for high heat flux tests on miniaturized actively cooled divertor modules.

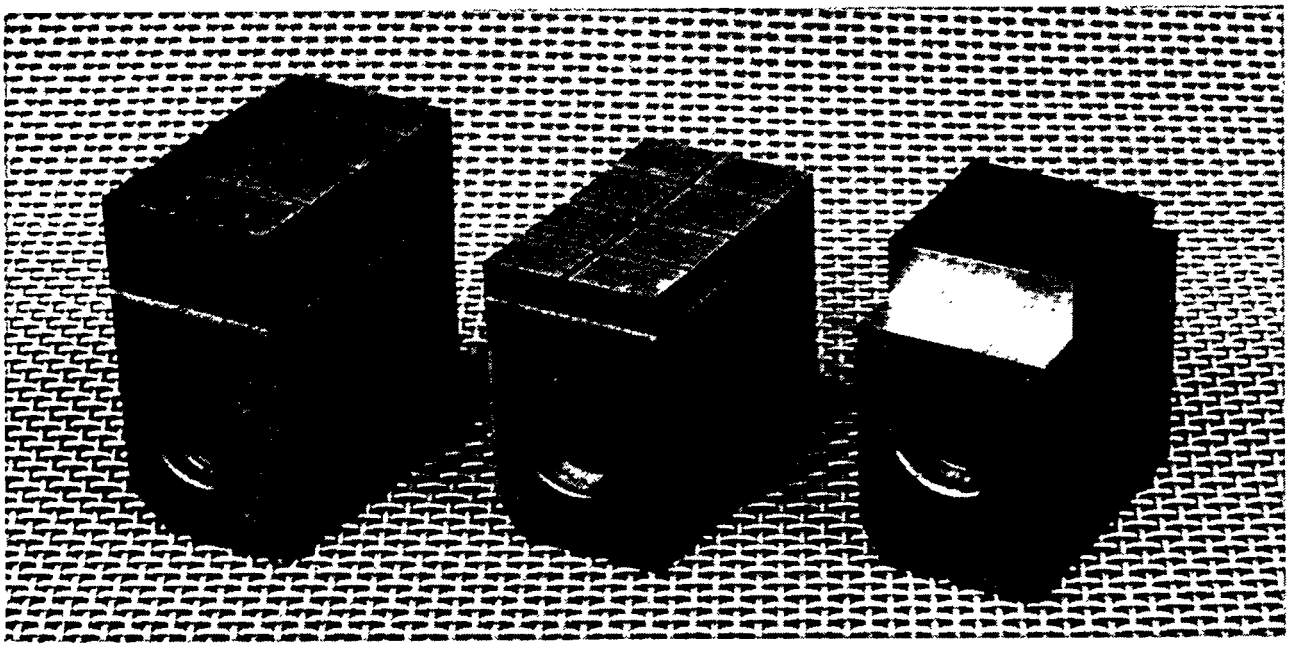

Fig. 4: Miniaturized divertor modules (beryllium tiles brazed to a water cooled copper heat sink).

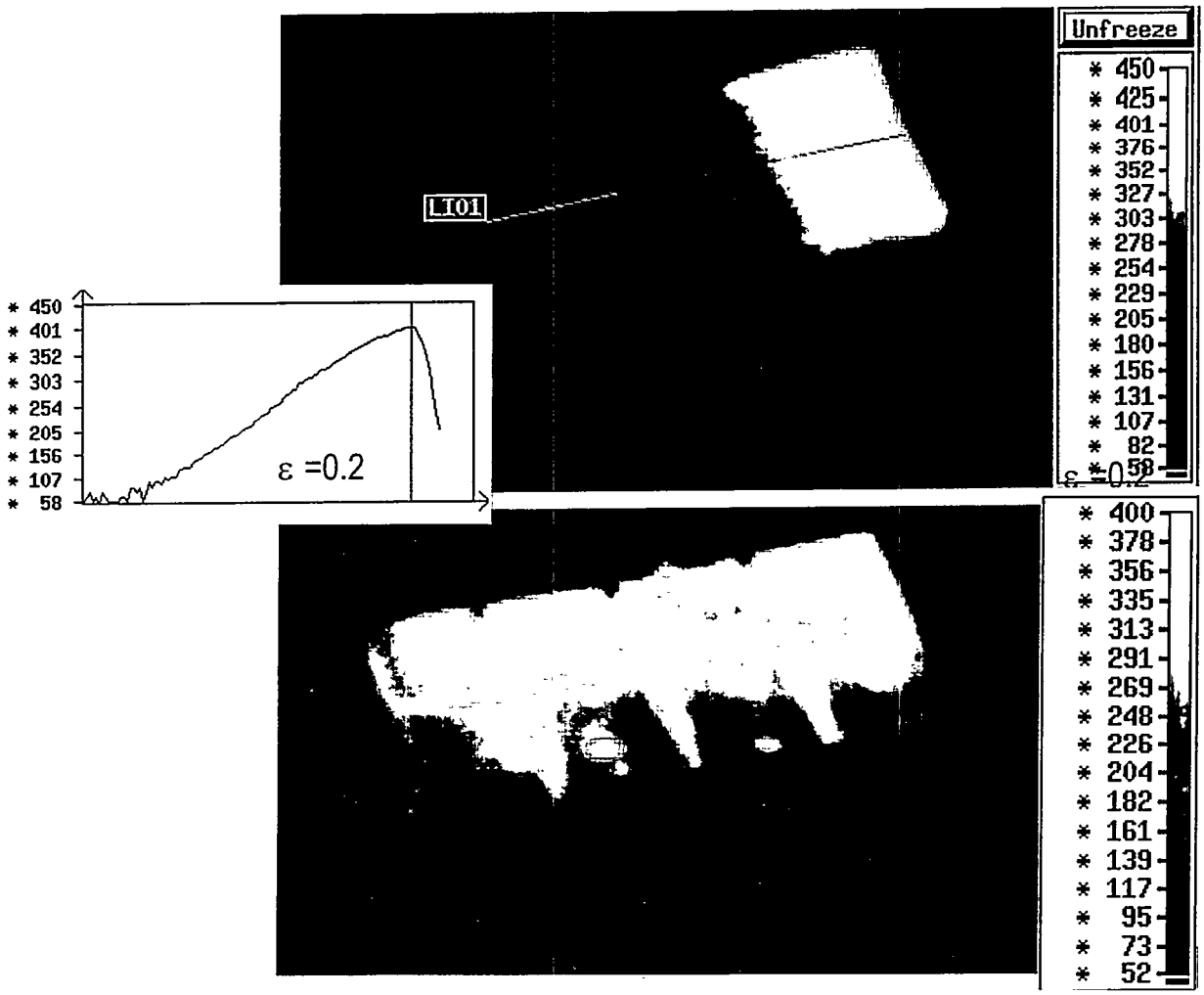

Fig. 5: Infrared images from Be-Cu divertor modules during electron beam loading:
a) defect braze layer at 320 Wm^{-2} (insert shows thermal gradient)
b) hot spots and variations in emissivity due to surface contaminants.

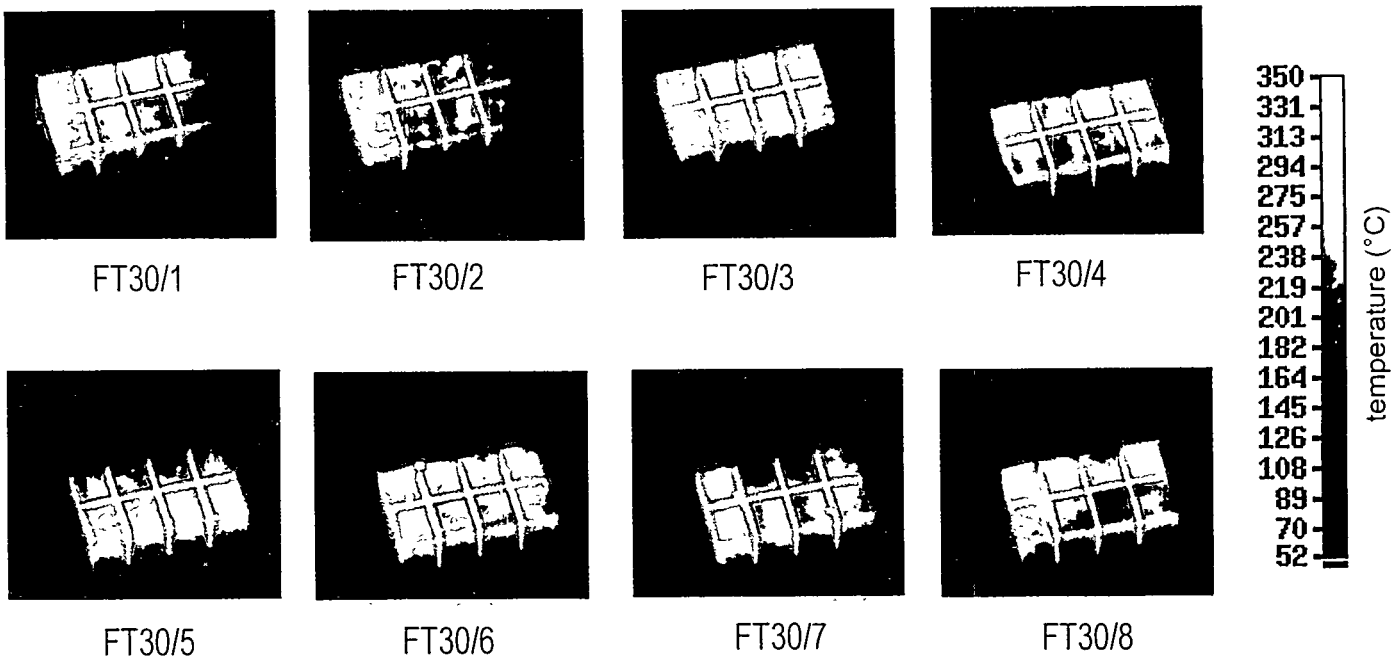

Fig. 8: Infrared images from a set of identical Be-Cu-modules (Be thickness: 8 mm) at a quasi-stationary heat load of 3.2 MW m^{-2}.

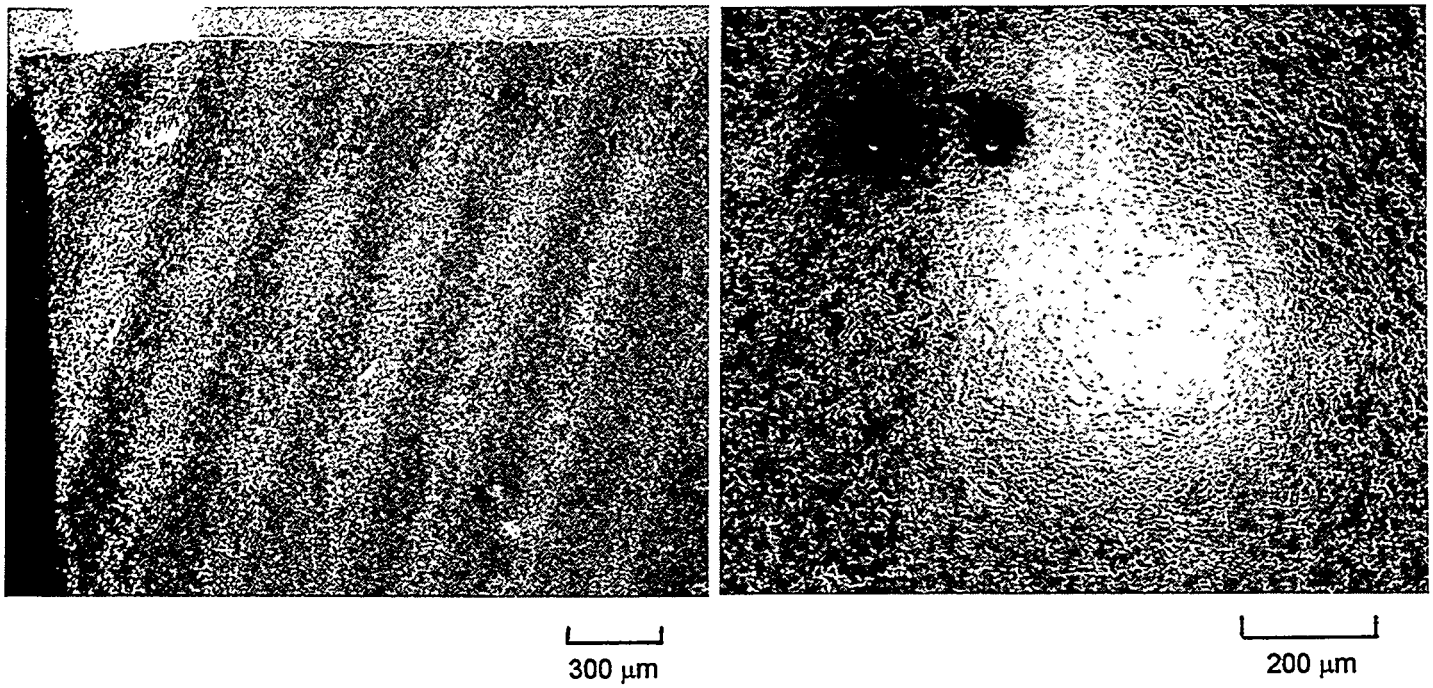

Fig. 6: Scanning electron micrographs of the module shown in Fig. 5b:
a) left: copper deposits (from spark erosion cutting process)
b) right: copper droplet (black) and thin layer of redeposited Cu (white area).

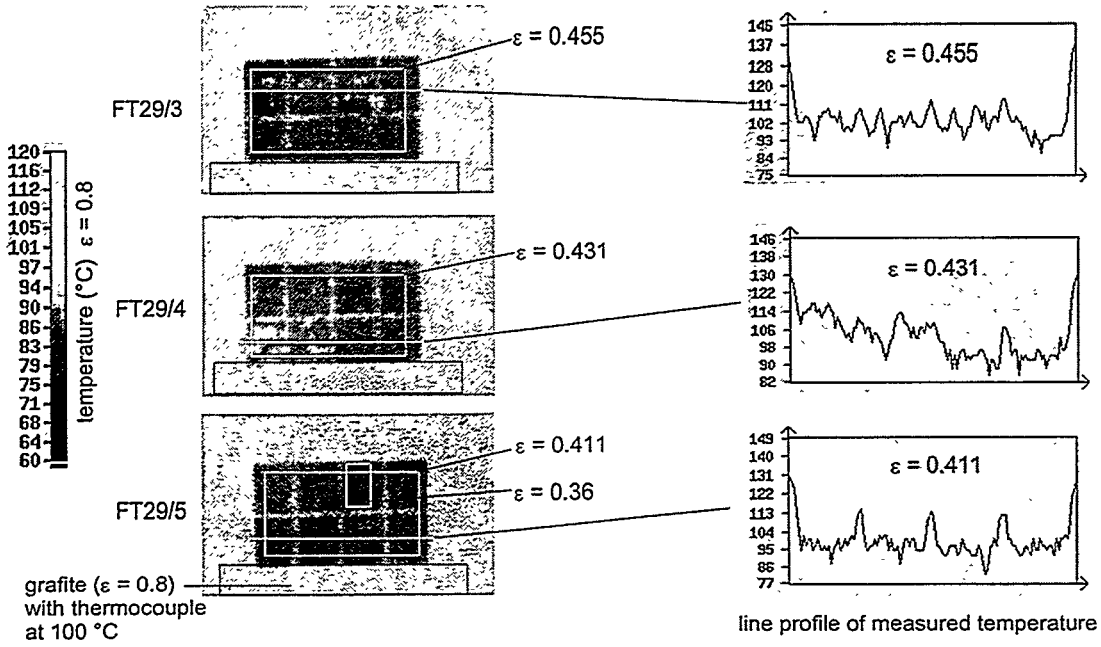

Fig. 7: Measurement of surface emissivity on different castellated beryllium surfaces (homogeneous sample heating to 100°C).

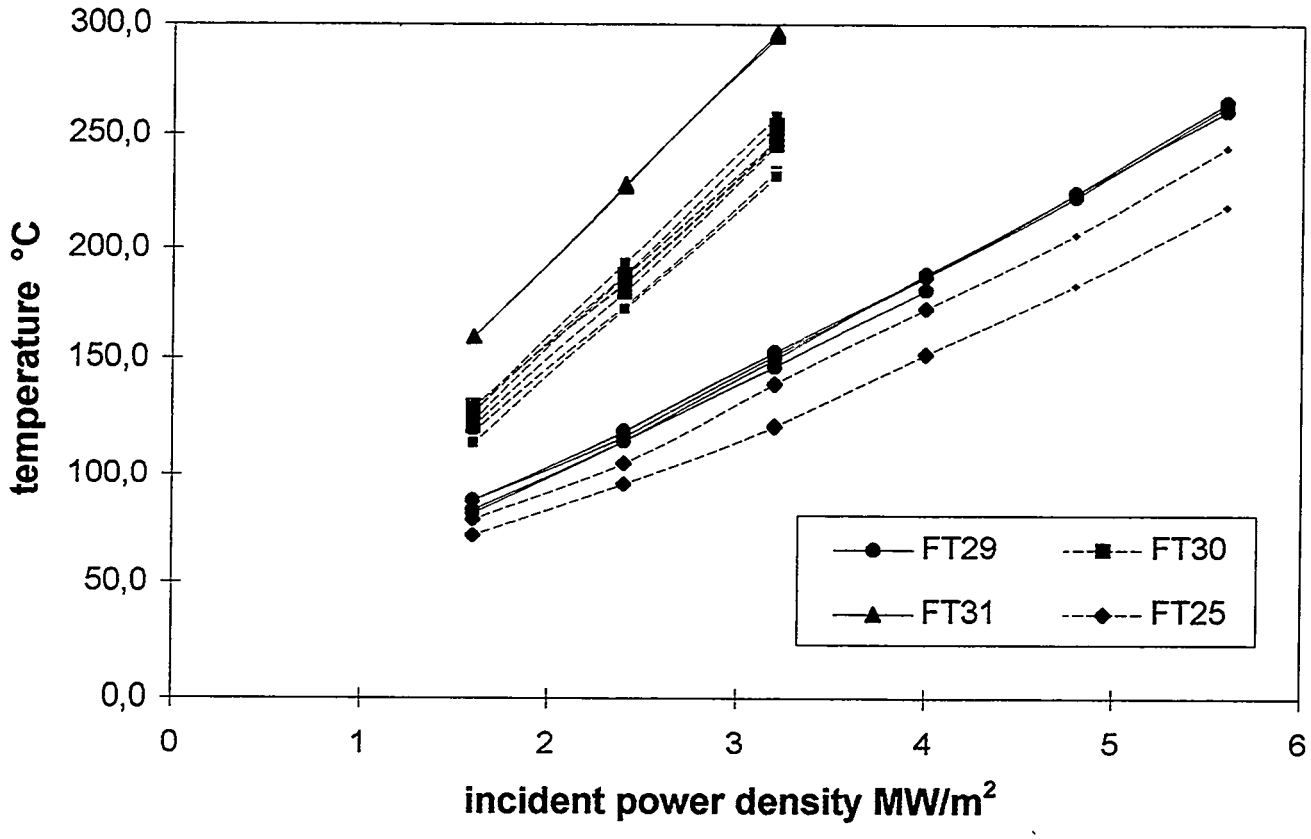

Fig. 9: Surface temperature (T_{med}) vs. incident power density for different Be-Cu-divertor modules.

THE ANALYSIS OF BERYLLIUM-COPPER DIFFUSION JOINT AFTER HHF TEST

R.N.Guiniatouline,[1] I.V.Mazul,[1] A.E.Gorodetskii,[2] R.H.Zalavutdinov,[2] S.Y.Rubkin,[2] V.I.Savenko[2]

[1]Efremov Research Institute, 189631, St.Petersburg, Russia
[2]Institute of Physical Chemistry, Moscow

The development of beryllium-copper joints which can withstand to relevant ITER divertor conditions is one of the important tasks at present time. One of the main problem for beryllium-copper joints is the inter-metallic layers, the strength and life time of joints significantly depends from the width and contents of the intermetallic layers. The objective of this work is to study the diffusion joint of TGP-56 beryllium to OFHC copper after thermal response and thermocyclic tests with beryllium-copper mockup. The HHF test were performed at e-beam facility (EBTS, SNLA). The following methods were used for analyses: the roentgenographic analysis; X-ray spectrum analysis; the fracture graphic analysis. During the investigation the followed studies were done: the analysis of diffusion boundary Be-Cu, which was obtained at the crossection of one of the tiles, the analysis of the debonded surfaces of a few beryllium tiles and corresponding copper parts; the analysis of upper surface of one of the tiles after HHF tests.

The results of this work have showed that:

the joint roentgenographic and elements analyses indicated the following phases 'in the diffusion zone: Cu_2Be (~170 μm), CuBe (~30 μm), $CuBe_2$ (~1 μm) and solid solution of copper in beryllium. The phases Cu_2Be, CuBe and solid solution of copper in beryllium were indicated using quantitative microanalysis and phases CuBe, $CuBe_2$, Cu, Be - by roentgenographic analysis;

the source of fracture (initial crack) is located in the central part of the tiles, the crack caused by the influence of residual stresses during cooling of a mock-up after fabrication and developed under the conditions of slow elastic-plastic growing during the process of thermal fatigue testing.

This analysis gives the important data about joint's quality and also may be used for any type of joints and its comparison for ITER applications.

Introduction.

The specimen under investigation was the diffusion-bonded mock-up after thermal response and thermal fatigue tests (Fig. 1). The objectives of investigation were:

- the diffusion boundary Be-Cu, which was obtained at the crossection of the tile H (this tile was not HHF tested);
- the debonded surfaces of six beryllium tiles A, B, C, D, E, F and corresponding copper parts;
- the porous coating of the MAGT tube after testing.
- upper surface of the tile D after HHF tests;

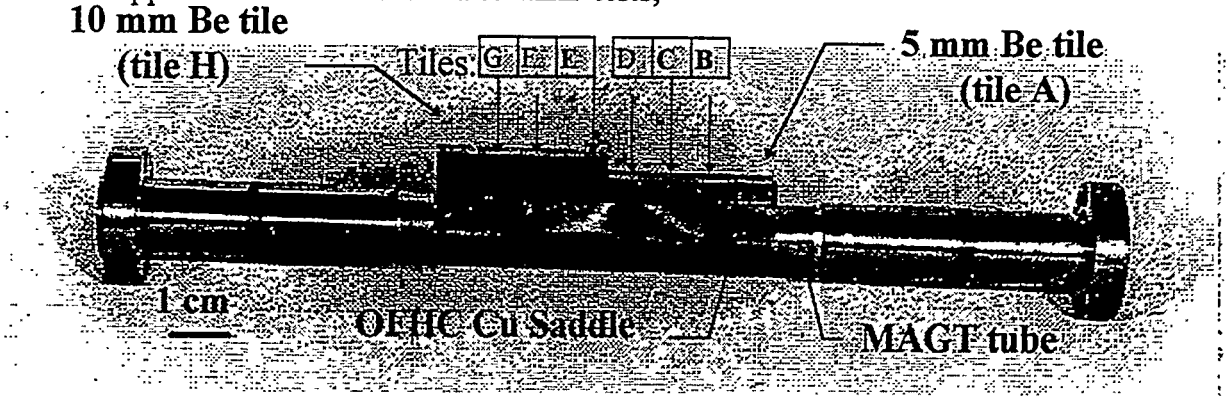

Fig.1. The scheme of mock-up for post-testing analysis.

Experimental procedure.

Mock-up was wire-cut before analysis along the tube, so thin copper plate (≈ 1 mm) with beryllium tiles on it was obtained. At the next step this bimetallic plate was wire-cut along the big sides of beryllium tiles. During the cutting tiles C, D, E, and F debonded. For the tiles E&D it was unexpected, we can assume that it was an effect of relaxation of residual stresses in the sample. Tile H with the copper saddle part was wire-cut along the long middle line and then polished. So, 6 beryllium tiles , 6 copper tiles and one polished crossection were obtained for the investigation.

The following methods and devices were used for analyses:

- the roentgenographic analysis was carried out using X-ray Diffracometer DRON-3 with copper Kα characteristic line λ_{Cu}=0.154 nm;

- X-ray spectrum analysis was done at CAMEBAX, E=20 keV, beam diameter 1 μm;
- the fracture graphic analysis was done at Raster Electron Microscope (REM) "Stereoscan S150" with the system of elements analysis :"LINK 860".

Experimental results.

1. Roentgenographic analysis of the debonded surfaces for Be and Cu tiles.

Four roentgenograms were obtained from beryllium and copper surfaces for the tiles B&D. ASTM tables were used for roentgenograms analysis and the following phases were assumed: Be, BeO, $CuBe_2$, CuBe, Cu, Cu_2O, CuO, Cu_4O_3. All diffraction lines with reflection angles and intensities are presented at the Tables 1&2.

The difractograms of Be surface (from the side of the diffusion boundary) have mostly lines of beryllium and weak lines of BeO and Cu_2Be. The difractograms of copper surface (from the side of the diffusion boundary) have lines $CuBe_2$, CuBe and Cu. The intensity of beryllidies lines are significantly stronger than for copper lines.

So, using the results of the roentgenographic analysis we can assume that the damage of the diffusion joint was occurred along the boundary of beryllium and intermetallic layers.

Table 1. Results of roentgenographic analysis, Tile B.

From the side of copper						
I, %	2ϑ, degree	ϑ, degree	d_{hkl}, Å	d_{hkl}(tab), Å		
				Cu	BeCu	Be_2Cu
2	24.76	12.38	3.596			
13	25.86	12.93	3.445			3.436^{80}
67	33.20	16.6	2.698		2.732^{24}	
12	42.55	21.28	2.124		2.062^{16}	
9	42.80	21.4	2.112			2.101^{100}
9	43.58	21.79	2.077	2.088^{100}		
100	47.7	23.85	1.907		1.931^{100}	
7	50.4	25.2	1.810	1.808^{46}		
9	50.72	25.36	1.799			1.799^{100}
26	59.3	29.65	1.558		1.560^{16}	
8	69.62	34.81	1.350		1.350^{8}	
2	74.66	37.33	1.271	$1,279^{20}$		
18	79.25	39.63	1.208		1.211^{8}	1.211^{80}
22	88.7	44.35	1.102		1.110^{16}	
2	90.65	45.33	1.084	1.091^{17}		
1	95.62	47.81	1.040	1.044^{5}		

Table 1 (continue). Results of roentgenographic analysis, Tile B.

From the side of beryllium					
I, %	2ϑ, degree	ϑ, degree	d_{hkl}, Å	$d_{hkl(tab)}$Å	
				Cu	BeO
1	38.58	12.29	2.334		2.336^{91}
2	43.9	21.95	2.062		2.062^{100}
32	45.72	22.86	1.984	1.980^{30}	
20	50.92	25.46	1.793	1.792^{25}	
100	52.68	26.34	1.737	1.733^{100}	
12	70.8	35.4	1.331	1.330^{9}	
19	84.7	42.35	1.144	1.143^{9}	
14	97.7	48.85	1.024	1.022^{8}	
3	102.1	51.05	0.991	0.990^{1}	
21	106.12	53.06	0.965	0.964^{8}	
17	107.6	53.8	0.955	0.954^{6}	

Table 2. Results of roentgenographic analysis, Tile D.

From the side of copper						
I, %	2ϑ, degree	ϑ, degree	d_{hkl}, Å	d_{hkl}(tab) Å		
				Cu	BeCu	Be_2Cu
11	25.8	12.9	3.453			3.436^{80}
67	33.24	16.62	2.695		2.732^{24}	
10	42.6	21.3	2.122		2.062^{16}	
9	42.86	21.43	2.110			2.101^{100}
14	43.6	21.8	2.075	2.088^{100}		
100	47.9	23.95	1.899		1.931^{100}	
6	50.4	25.2	1.810	1.808^{46}		
11	50.8	25.4	1.797			1.799^{100}
15	59.3	29.65	1.558		1.569^{16}	
10	69.7	34.85	1.349		1.350^{8}	
2	74.6	37.3	1.272	1.279^{20}		
15	79.35	39.68	1.207		1.211^{8}	1.211^{80}
18	88.7	44.35	1.102		1.110^{16}	
2	90.6	45.3	1.084	1.091^{17}		
1	95.78	47.89	1.039	1.044^{5}		

Table2 (continue). Results of roentgenographic analysis, Tile D.

From the side of beryllium						
I, %	**2ϑ, degree**	**ϑ, degree**	**d_{hkl}, Å**	**d_{hkl}(tab), Å**		
				Be	**BeO**	**Be_2Cu**
4	25.9	12.95	3.440			3.436^{80}
5	38.5	19.25	2.338		2.336^{91}	
3	41.1	20.55	2.196		2.188^{61}	
2	42.88	21.44	2.109			2.10^{100}
5	43.9	21.95	2.062		2.062^{100}	
80	45.8	22.9	1.981	1.980^{30}		
57	50.9	25.45	1.793	1.792^{25}		1.799^{100}
100	52.66	26.33	1.738	1.733^{100}		
35	70.86	35.43	1.330	1.330^{9}		
47	84.7	42.35	1.144	1.143^{9}		
39	97.7	48.85	1.024	1.022^{1}		

2. **The analysis of diffusion zone for Be-Cu joint. The analysis of elements content for the damaged beryllium and copper surfaces.**

The scheme of crossection for bimetallic joint of the tile H was obtained using roentgenospectrum analysis, it is shown at Figure 2.

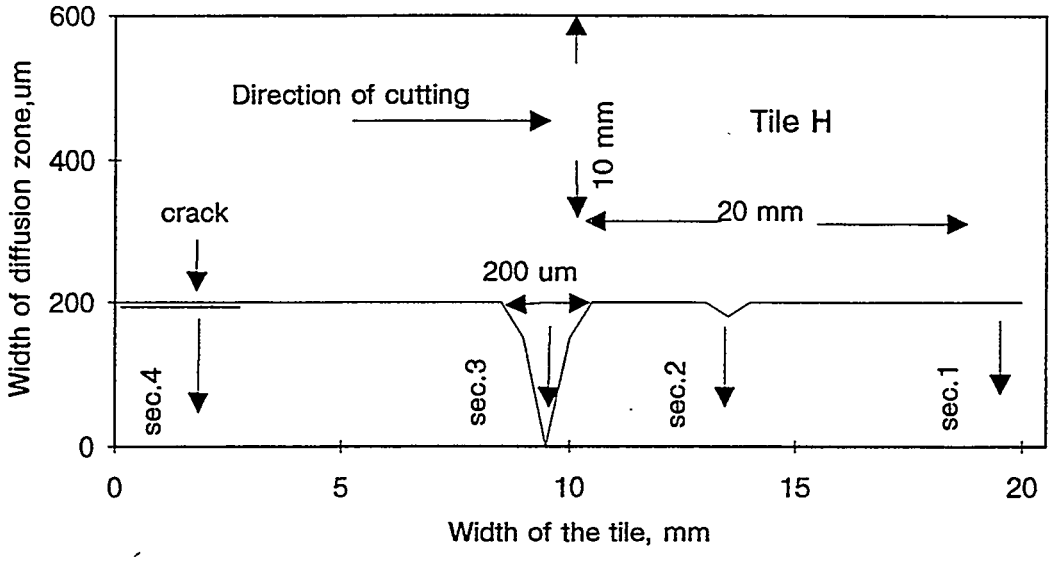

Fig.2. The scheme of crossection for Be-Cu joint (Tile H).

The width of diffusion zone for this joint is about 200 μm along all length of the boundary. There are some local defects of the joint: the narrowing of the diffusion zone in section 2 and disappearance of it in section 3 (Fig.2). Figure 8 shows the electron-microscopic view of the diffusion zone, the zones with different contrast indicate the existing of a few phases.

The profiles of copper radiation intensity K_α for the marked sections are presented at Figurres 3-6.

The intensity profile in the zone without defects (crossection 1) is shown at the Figure 3.

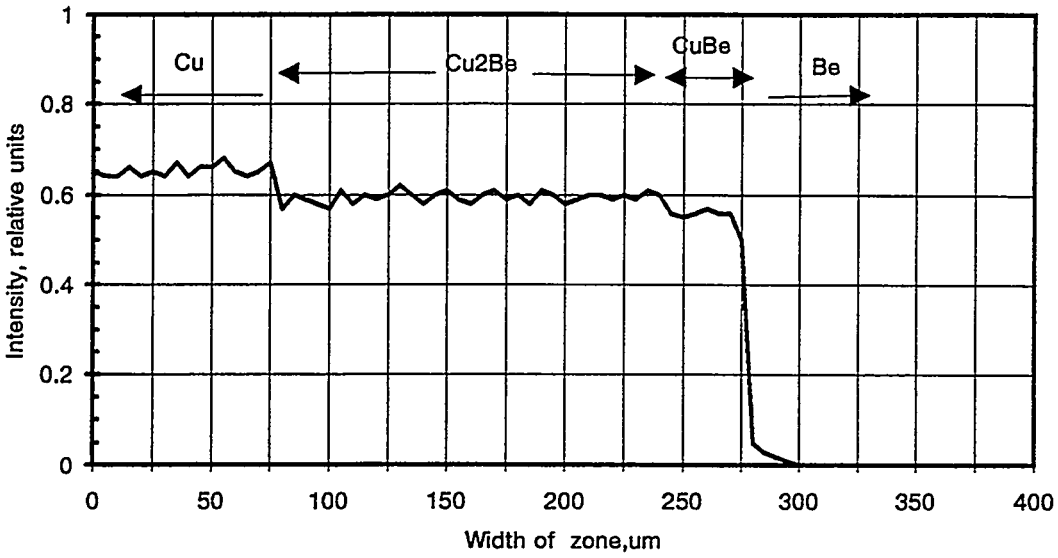

Fig.3. The intensity of copper distribution in diffusion zone for crossection 1.

Copper distribution in the diffusion zone has two regions of constant content, the quantitative analysis shows that there are Cu_2Be and CuBe. The width of Cu_2Be layer is ≈170 μm and of CuBe - ≈30 μm. The phase $CuBe_2$ which was indicated by roentgenographic analysis, is not identified at Figure 3 because its width is near 1 μm (width is comparable to the beam diameter).

Copper distribution in the narrowed zone (crossection 2) is presented at the Figure 4.

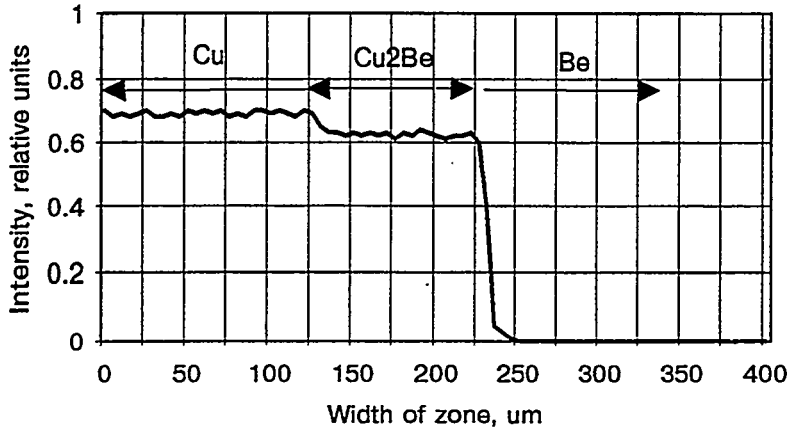

Fig.4. The intensity of copper distribution in diffusion zone for crossection 2.

The width of a boundary is about 100μm and phase CuBe is absent. The diffusion welding was not obtained in crossection 3, there are no inter metallic phases here (Fig.5).

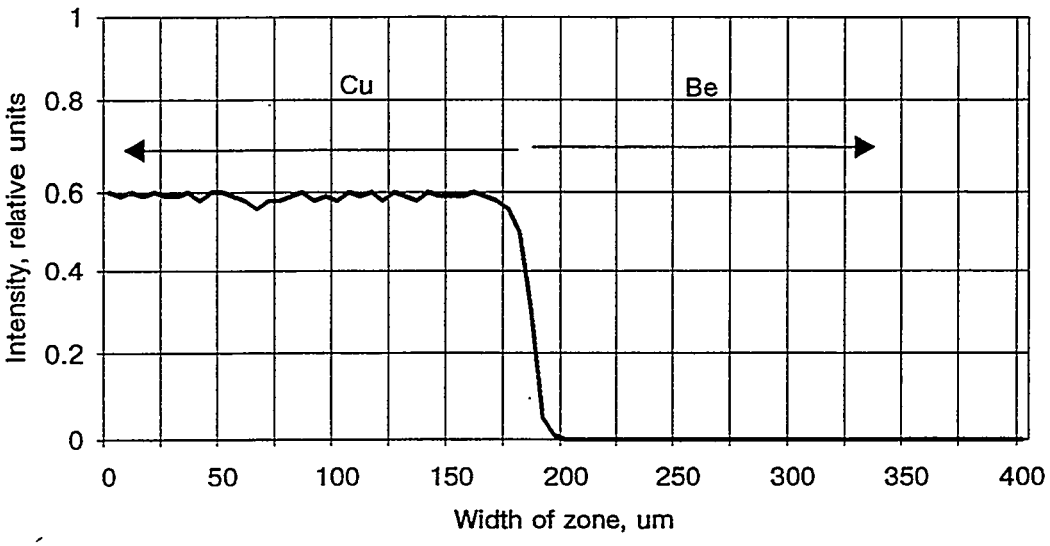

Fig.5. .The intensity of copper distribution in diffusion zone for crossection 3.

The crack in the zone of contact CuBe-Cu is take place at the crossection (FIg.2). This crack is indicated by significant reduce of copper intensity lines at the copper distribution in crossection 4 (Fig.6). The thickness and structure of the diffusion boundary in the crack zone are the same as for Figure 3. It means that the crack appeared during the cool down of the sample after diffusion welding or after wire-cutting as a result of residual stresses influence. The beforemade ultrasonic control did not indicate these defects.

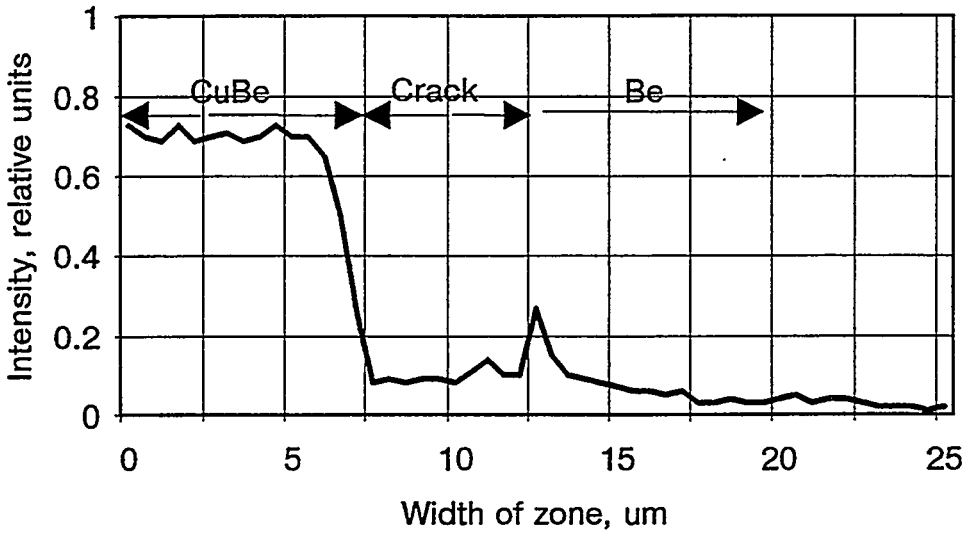

Fig.6. .The intensity of copper distribution in diffusion zone for crossection 4.

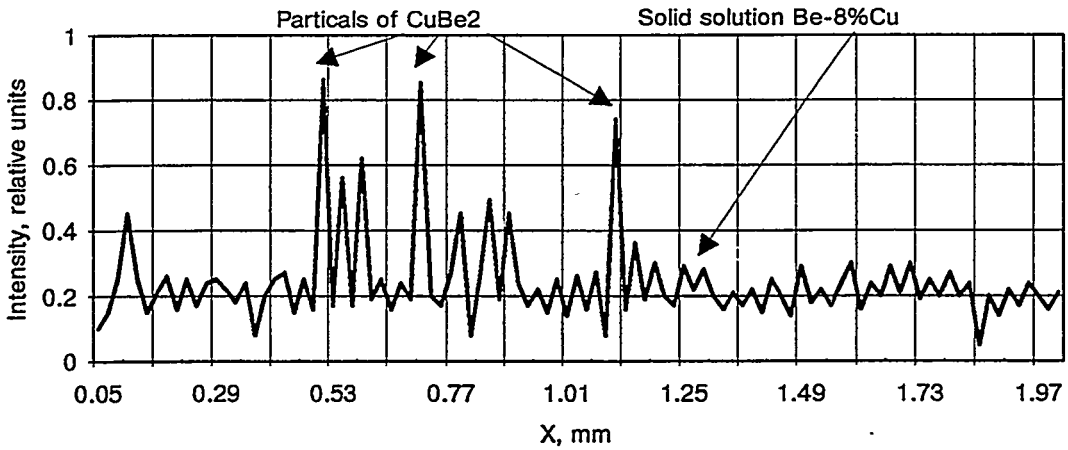

Fig7. Copper distribution at the surface of the beryllium tile B after debonding.

Figure 7 shows copper distribution at the surface of the beryllium tile B after debonding. The quantitative analysis showed that the structure of the surface is correspond to solid solution of Cu in Be. This fact is approved by copper distribution at the Figure 9. Besides, some particles of $CuBe_2$ were detected. These results approve the conclusion of the roentgenographic analysis: the debonding of the diffusion joint during the thermocyclic testing is occurring along the boundary $CuBe_2$-Be.

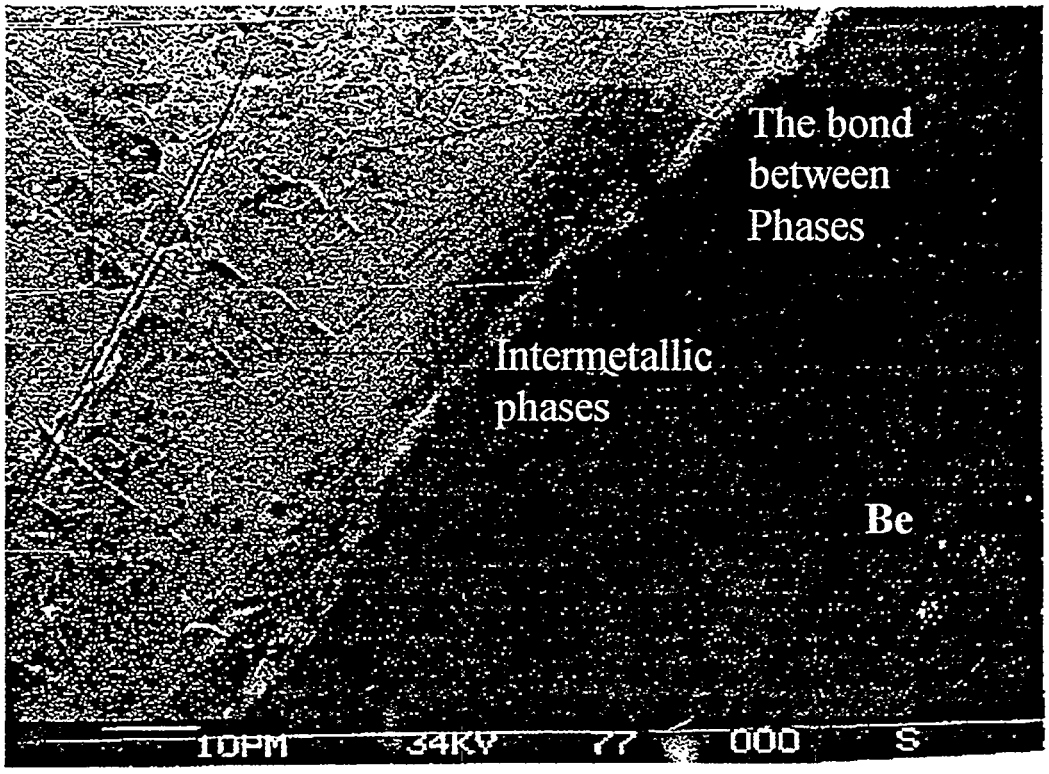

Fig.8: The structure of diffusion zone for Be/Cu joint (tile H).

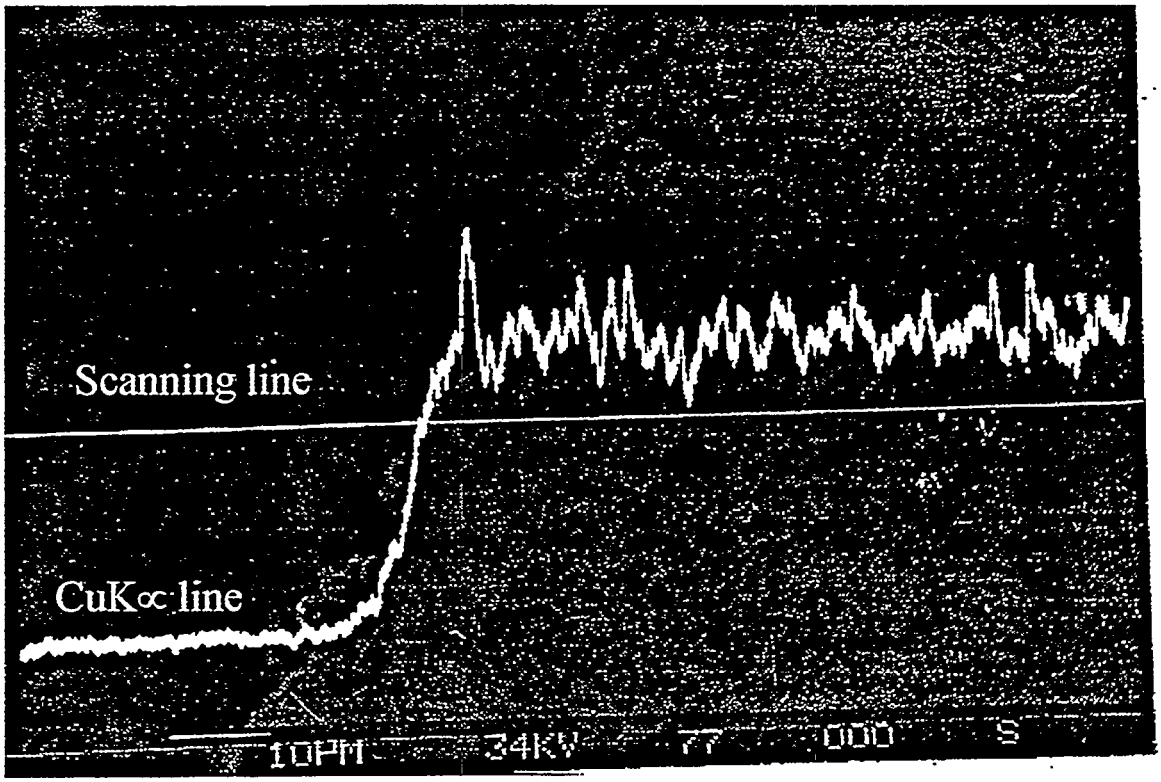

Fig.9. Distribution of Cu along Be/Cu diffusion zone (tile H).

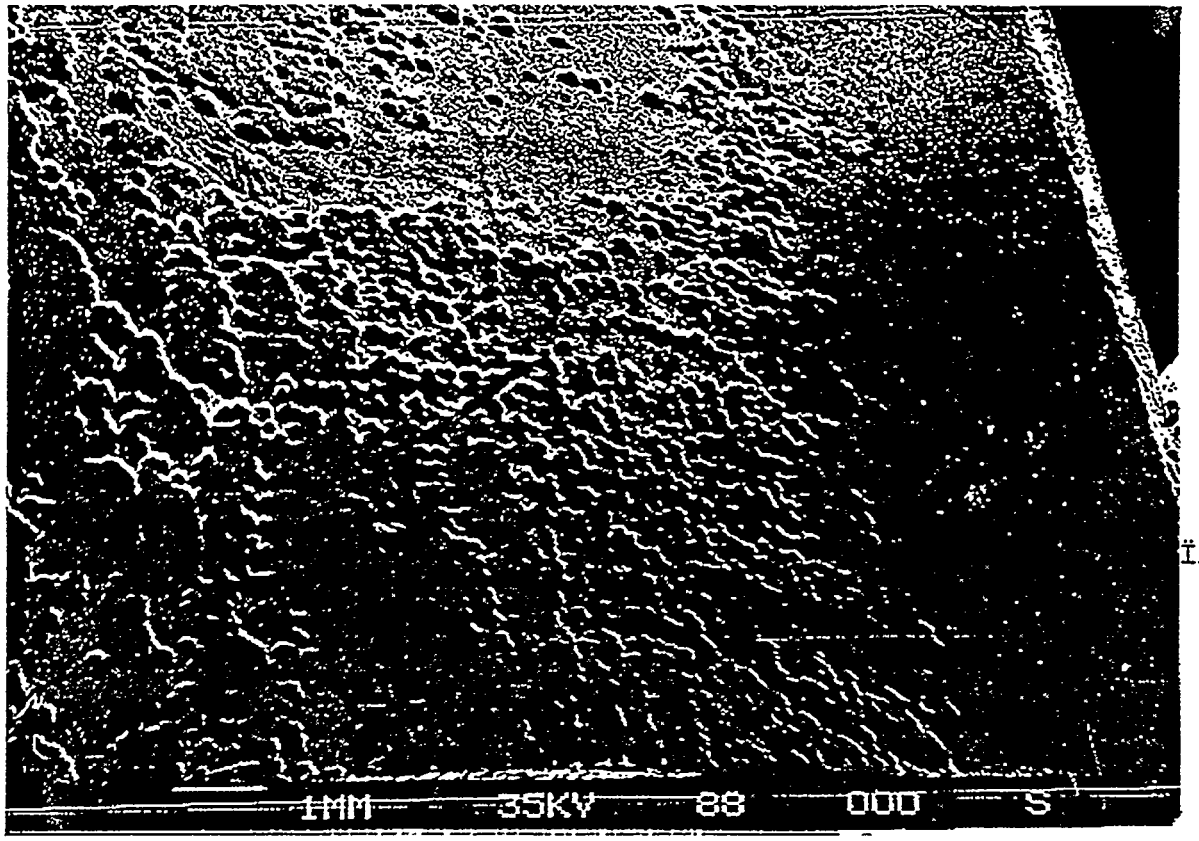

Fig. 10. The view on debonded surface from the side of Cu (tile D).

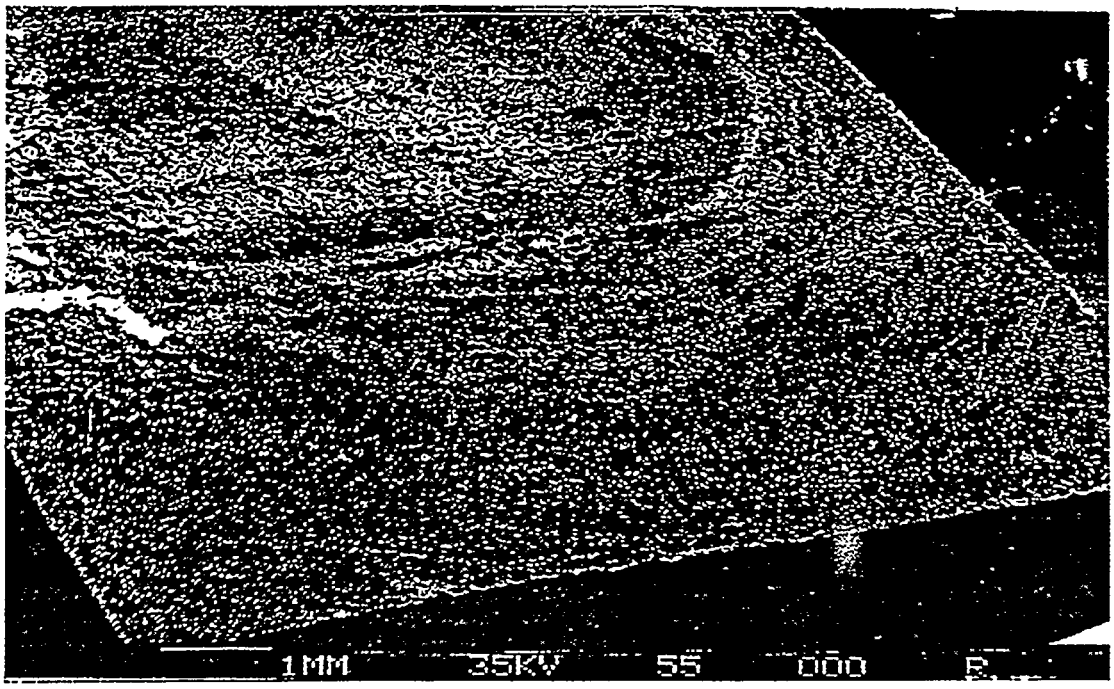

Fig.11. The view on debonded surface from the side of Be (tile D).

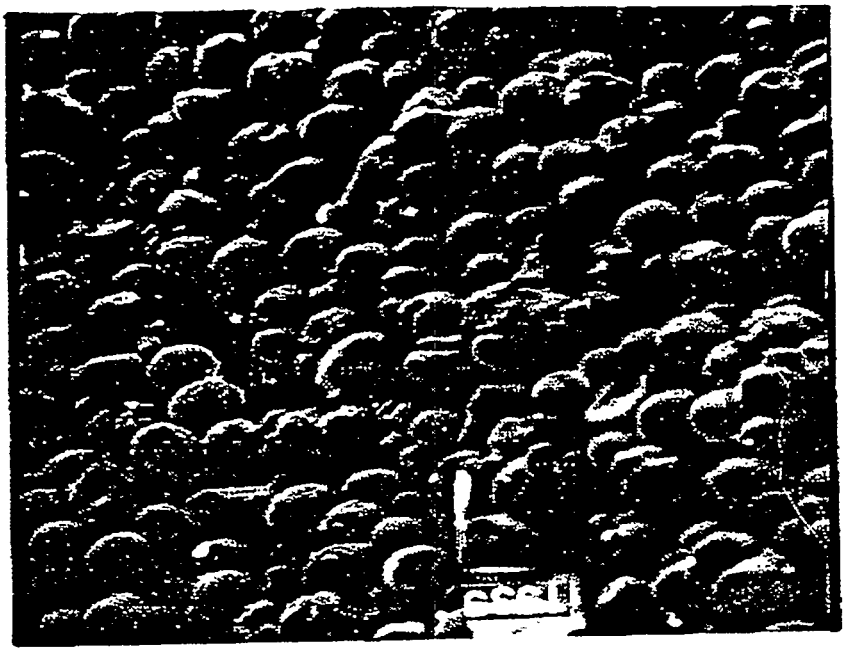

Fig.12. The view of porous coating at inside surface of the tube after HHF tests.

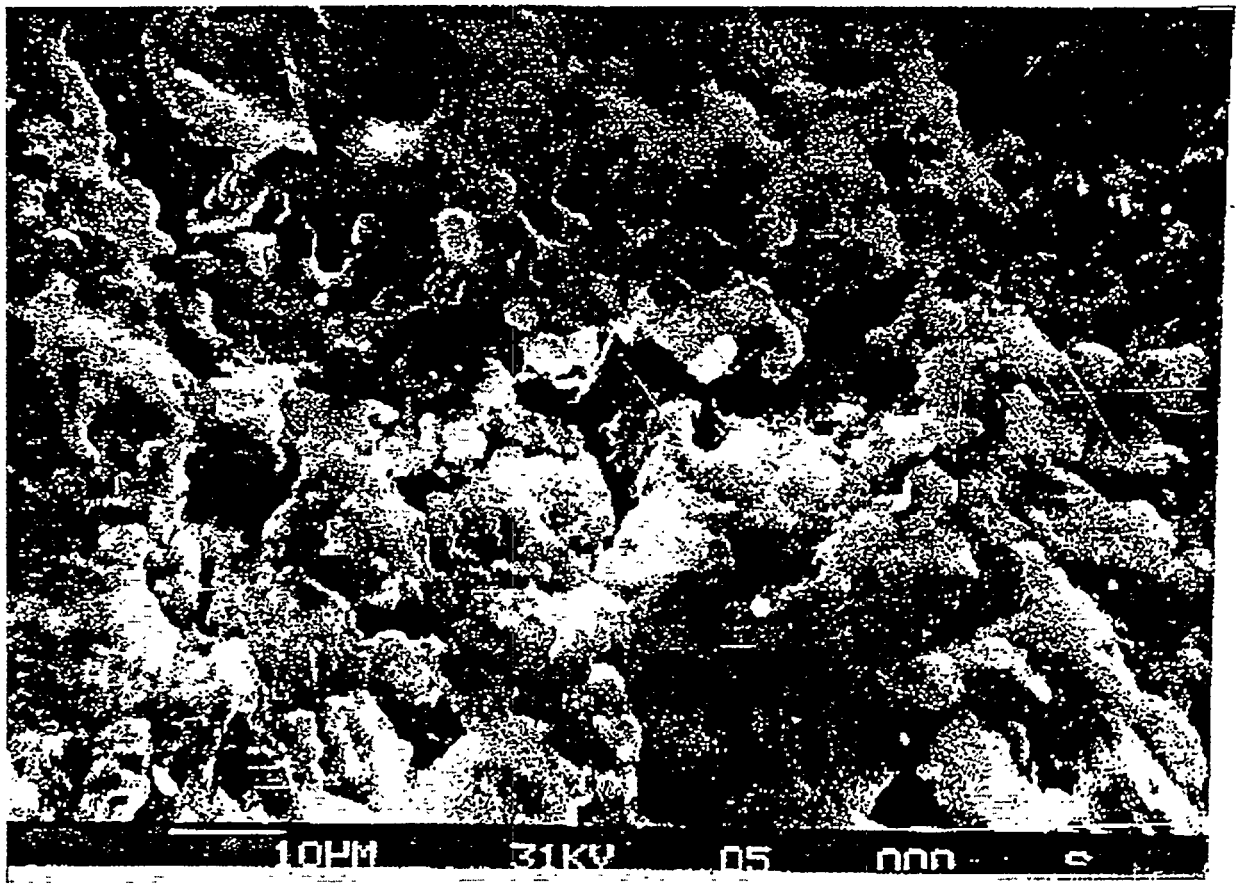

Fig.13. The upper surface of the tile D after HHF tests.

3. Fracturegraphic analysis of the debonded surfaces.

The fracture surface for all beryllium and copper tiles are qualitatively identical and the initial crack spread parallel to the plate of Be-Cu contact. Simple visual or with weak optical magnification analyses give the regions with different macro profiles (Fig.10):

- "central part" with a large plateau in the central part of the tiles;
- "periphery part" with a smooth surface near the edges of the tiles;
- "intermediate part" with branching macro profile between central and periphery parts.

The analysis of the surfaces from different angles (Fig.11) gives the thin lines of oval shape (macro marks) which indicate the slow spreading of the fracture caused by outside or inside extension stresses. The concentric configuration of the macro marks shows the direction of a fracture development: from the central part to the edges of the tile.

The existing of the "central parts" on fracture surfaces for all beryllium and copper tiles allows to make the conclusion that this part oftiles is a source of damage. The absence of great number of secondary fracture sources at the damaged surfaces shows on the fact that debonding development had elastic-plastic deformation character similar to low cyclic fatigue.

4. The results of inside porous coat checking and upper surface of beryllium tile B.

Figure 12 shows that all inside surface of the tube is coated by one uniform layer of copper spheres with diameter 40-70 um. The checking of the coating before testing was not done and it is diffical to say that the part of the porous coating washed out. As known , the exsisting of one spheres layer is enough for itself purposes. So, it may be considered that the reason of surface temperature increasing during the fatigue tests is in damaging of beryllium - copper boundary from cycle to cycle.

Figure 13 shows the upper surface of the tile D after HHF tests. It is seen that the surface of tile became porous but no cracking was observed

Conclusions.

1. The joint roentgenographic and elements analyses indicated the following phases in the diffusion zone: Cu_2Be (~170 μm), CuBe (~30 μ m), $CuBe_2$ (~1 μm) and solid solution of copper in beryllium. The phases Cu_2Be, CuBe and solid solution of copper in beryllium were indicated using quantitative microanalysis and phases CuBe, $CuBe_2$, Cu, Be - by roentgenographic analysis.

2. The total width of the diffusion zone was about 200 μm.

3. The source of fracture (initial crack) is located in the central part of the tiles. The crack caused by the influence of residual stresses during cooling of a mock-up after fabrication and developed under the conditions of slow elastic-plastic growing during the process of thermal fatigue testing.

High Conductivity Be-Cu Alloys for Fusion reactors

Eugene A. Lilley [a], Takao Adachi [b], Yoshiki Ishibashi [b]

[a]*NGK Metals Corporation., Tuckerton Road, P. O. Box 13367, Reading, PA. 19612 USA*
[b]*NGK INSULATORS, LTD., 1 Maegata-cho, Handa-City, Aichi-ken 475, Japan*

Presently, there are many materials under consideration for use as the heat sink in fusion reactors, especially in the ITER(International thermonuclear experimental reactor). The optimum material has not yet been identified.

This will result in heat from plasma to the first wall and divertor. That is, because of cracks and melting by thermal power and shock. Today, it is considered to be some kinds of copper alloys, however, for using, it must have high conductivity. And it is also needed another property, for example, high strength and so on.

We have developed some new beryllium copper alloys with high conductivity, high strength, and high endurance. Therefore, we are introducing these new alloys as suitable materials for the heat sink in fusion reactors.

1. Introduction

NGK is one of the world leading companies in the production of beryllium and beryllium copper alloys and works on positive lines for the development of new alloy.

Beryllium copper alloys are generally classified into two types. One is a high conductivity type and another is a high strength type (Figure1).

The new beryllium copper alloys developed in recent years have been especially focused on improvement of the high conductivity type alloys.

In this paper, the outline of these developments are presented and the suitability of these alloys to the heat sink in the fusion reactor are discussed.

2. Strengths of Beryllium Copper among Copper alloys.

The position of beryllium copper is shown in Figure2 and Figure3 as the relationship between conductivity and strength.

Regarding the high strength type, 25 alloy which is the most popular beryllium copper, has superior mechanical properties to the other typical copper alloys such as brass and phospher bronze. MC-16 alloy was developed for the applications like shell molding dies, and is known for its high wear resistance.

There are several new beryllium copper alloys in high conductivity type, which are 7 alloy, MC-9 alloy, 17510 alloy and 77 Alloy (temporary name at laboratory base). Although the conductivity of these alloys is somewhat below the other high conductivity copper alloy such as Cu-Zr, Cu-Cr, the balance of strength and conductivity of beryllium copper is superior to the others.

3. Outline of development

There are two directions for the development of high conductivity type beryllium copper alloys (Figure4).

Normally in the low beryllium content material (Be<1.0wt%) nickel is added for the development of high conductivity, and strength by the precipitation of BeNi. It is therefore important to research the relationship of Be to Ni ratio with properties and microstructure. The tensile strength diagram verses Be% and Ni% is shown in Figure5.

The chemistry is optimized by making the diagram like Figure5 for various properties such as electrical conductivity and other properties. The addition of other alloying elements such as Fe, Zr, Si, Al, Cr, Sn etc. and the evaluation of process parameters such as heat treatment, cold reduction and so on are introduced in order to achieve the property balance demanded by the market.

3-1 Development of 7 Alloy

High reliability material is required by the electronic industry with the miniaturization, high density, high performance component driven by new technical innovations. Under this circumstances, 7 alloy was developed to have high strength with good formability and electrical conductivity.

The key properties of 7 alloy are shown in Figure6 and the experimental procedure for the development is shown in Figure7.

As mentioned above, this alloy was developed through the selection of the appropriate Be and Ni ratio, and the addition of other alloying elements.

3-2 Development of MC 9 Alloy

MC 9 Alloy was developed as a forged material for casting dies which require high temperature toughness (heat shock) and thermal controllability (Figure8).

The positioning of MC 9 Alloy is shown in Figure9 compared with other typical materials for the casting dies such as steel, Al bronze and so on. It is clear on this figure that MC-9 alloy has a good combination of thermal conductivity and hardness.

3-3 Development of 77 Alloy

The development of 77 alloy was initiated for the purpose of further optimizing both ultimate high strength and conductivity.

This development is still in progress. As of this writing, it is confirmed on a laboratory basis that the material with the tensile strength superior to 680 N/mm^2 and the electrical conductivity superior to 70 IACS% can be obtained by the adjustment of chemical composition and process parameters (The outline is shown in Figure10).

4. Application of High Conductivity Type BeCu to the Sink in Fusion Reactors

4-1 Thermal conductivity at high temperature

The change of thermal conductivity at high temperature is shown in Figure11 concerning 77 alloy, 14 alloy, Oxgen Free Copper (OFC) and Dispersion Strengthened Copper (Cu/Al_2O_3).

As shown in the figure, the thermal conductivity of the age hardening type beryllium copper 77 alloy and 14 alloy increases as the temperature is elevated. OFC and Cu/Al_2O_3 continually lose conductivity as the temperature is elevated. The difference between the alloys becomes quite small above 500℃.

4-2 Mechanical property at high temperature

The change of tensile strength at high temperature is shown in Figure12.

Beryllium copper 77 alloy and 14 alloy keep high strength even at high temperature compared with OFC and Cu/Al_2O_3.

4-3 Diffusion bonding between beryllium and beryllium copper

Recently reactivity testing between Be and BeCu was done at NGK.

In this test, it is recognized that the reactivity between Be and BeCu 14 alloy shows the successive diffusion line profile under conditions such as 500℃ × 300hrs. It seems that the bonding between Be and BeCu 14 alloy has greater potential compared with the other copper alloys.

5. Summary

- Some new beryllium copper alloys of high conductivity type have been developed by the adjustment of chemical composion and process parameters on the base of low beryllium content materials.
  Especially 14 alloy and the recently developed 77 Alloy indicate good combinations of strength and conductivity at high temperature.
  Therefore, we think these BeCu alloys are suitable materials for the heat sink in fusion reactors.

- It is probable that the diffusion bonding of beryllium to beryllium copper will be easier to achieve compared to the other copper alloys.

Figure1

NGK

DEVELOPMENT OF BERYLLIUM COPPER ALLOY BY NGK

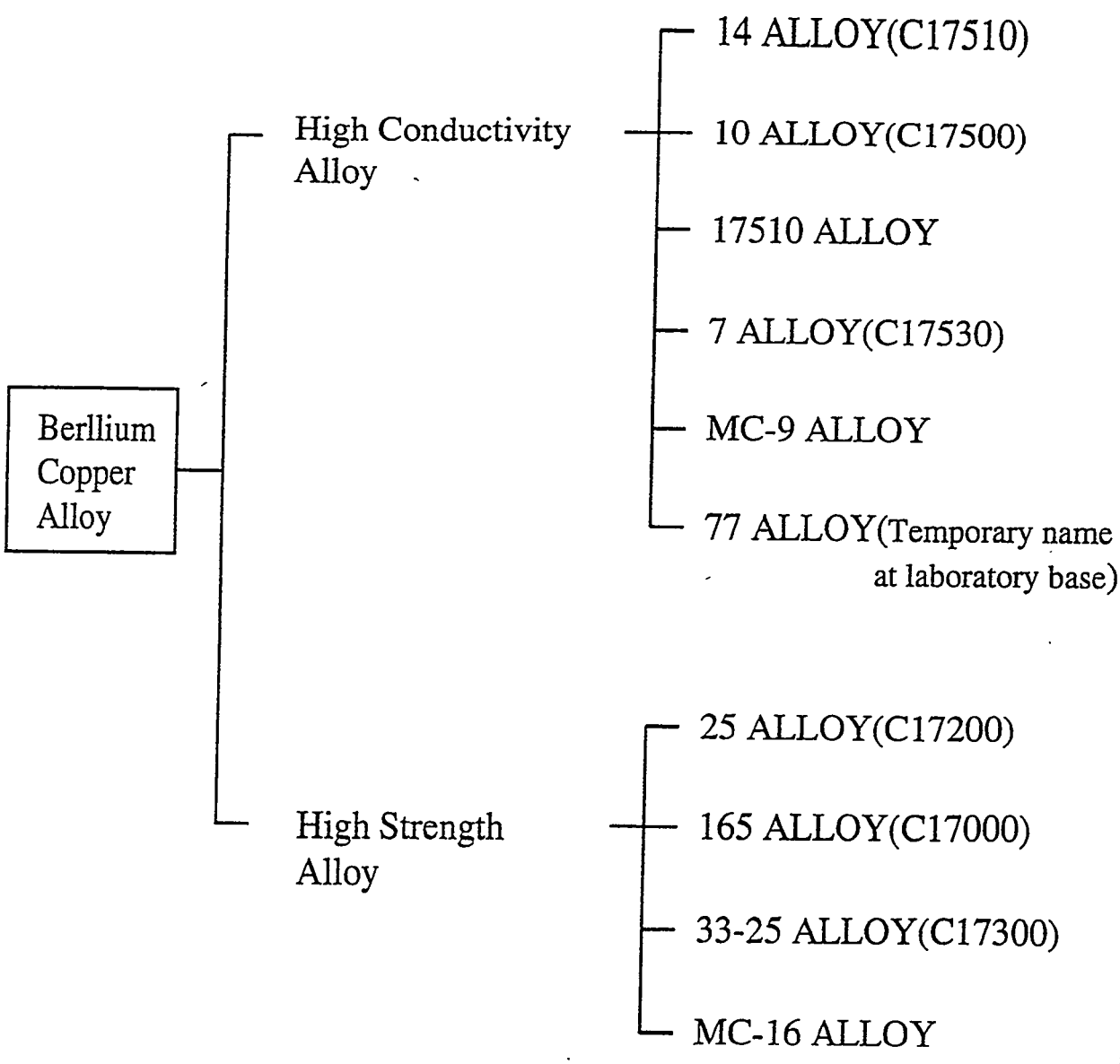

Figure2

NGK

COPPER ALLOY MAP BY RELATIONSHIP BETWEEN CONDUCTIVITY AND STRENGTH

- **High Strength Type**

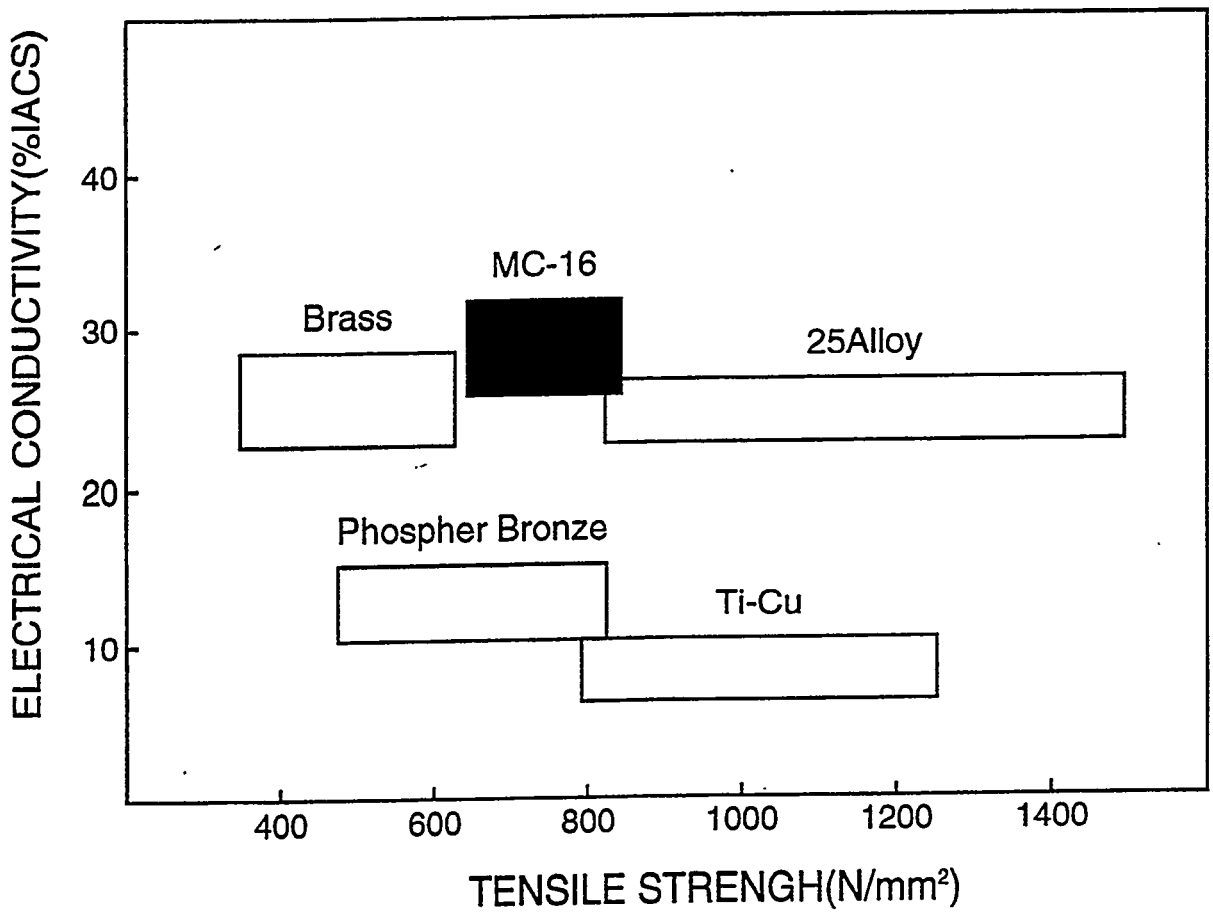

Figure3

NGK

COPPER ALLOY MAP BY RELATIONSHIP BETWEEN CONDUCTIVITTY AND STRENGTH

• High Conductivity Type

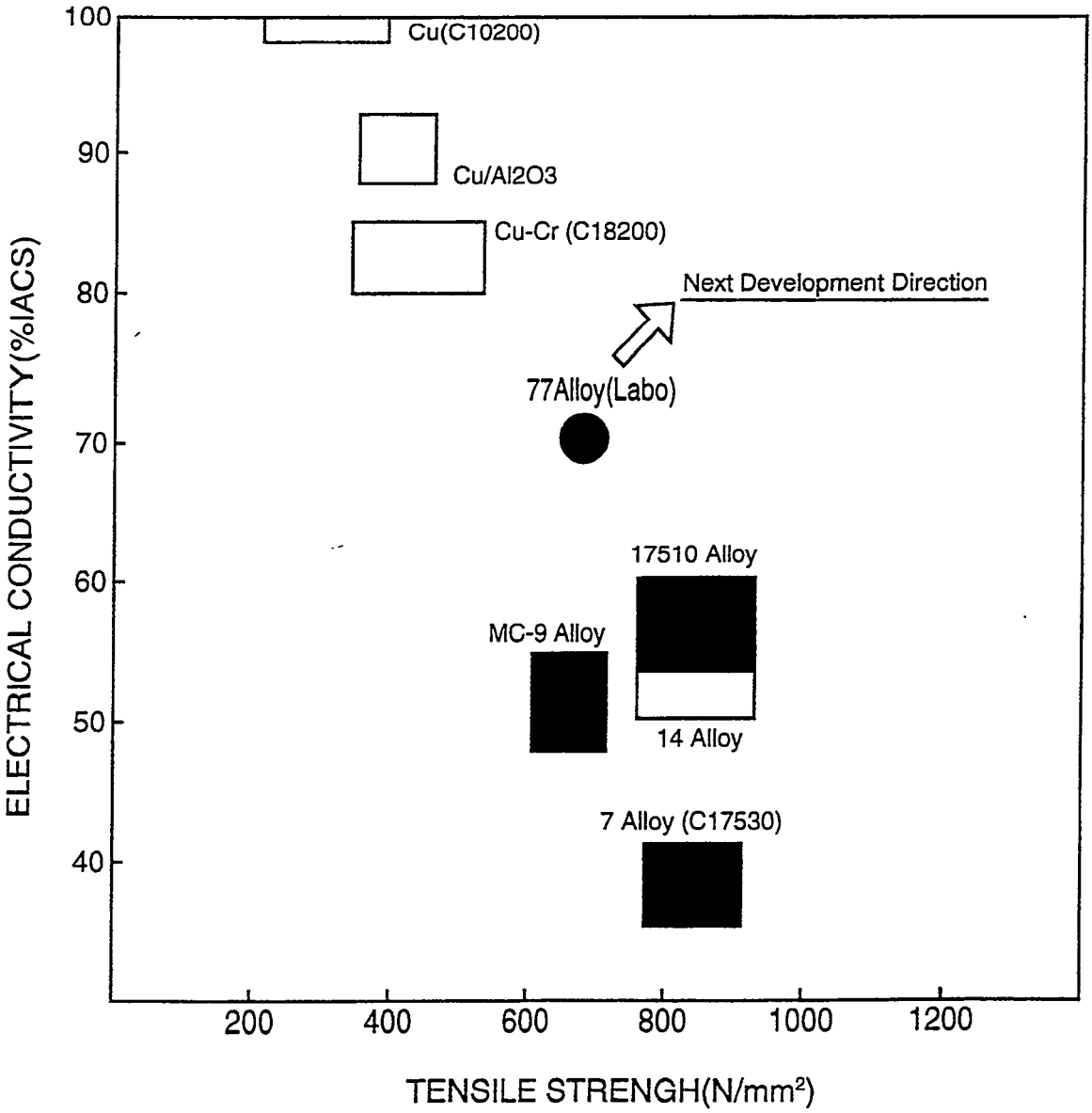

Figure4

NGK

TECHNICAL POINTS FOR THE DEVELOPMENT OF HIGH CONDUCTIVITY TYPE BeCu ALLOY

- **Selection of the appropriate combination of Be% and Ni% and Addition of other elements**

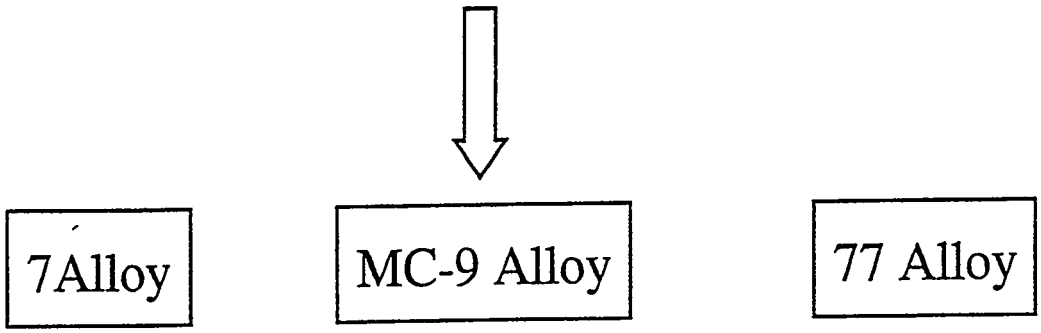

- **Selection of the best process parameters**

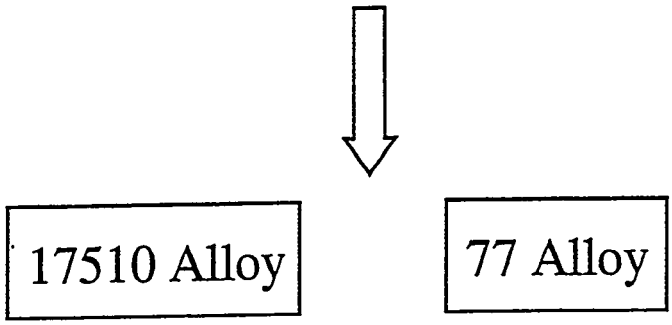

Figure5

NGK

TENSILE STRENGTH DIAGRAM BY Be% AND Ni%

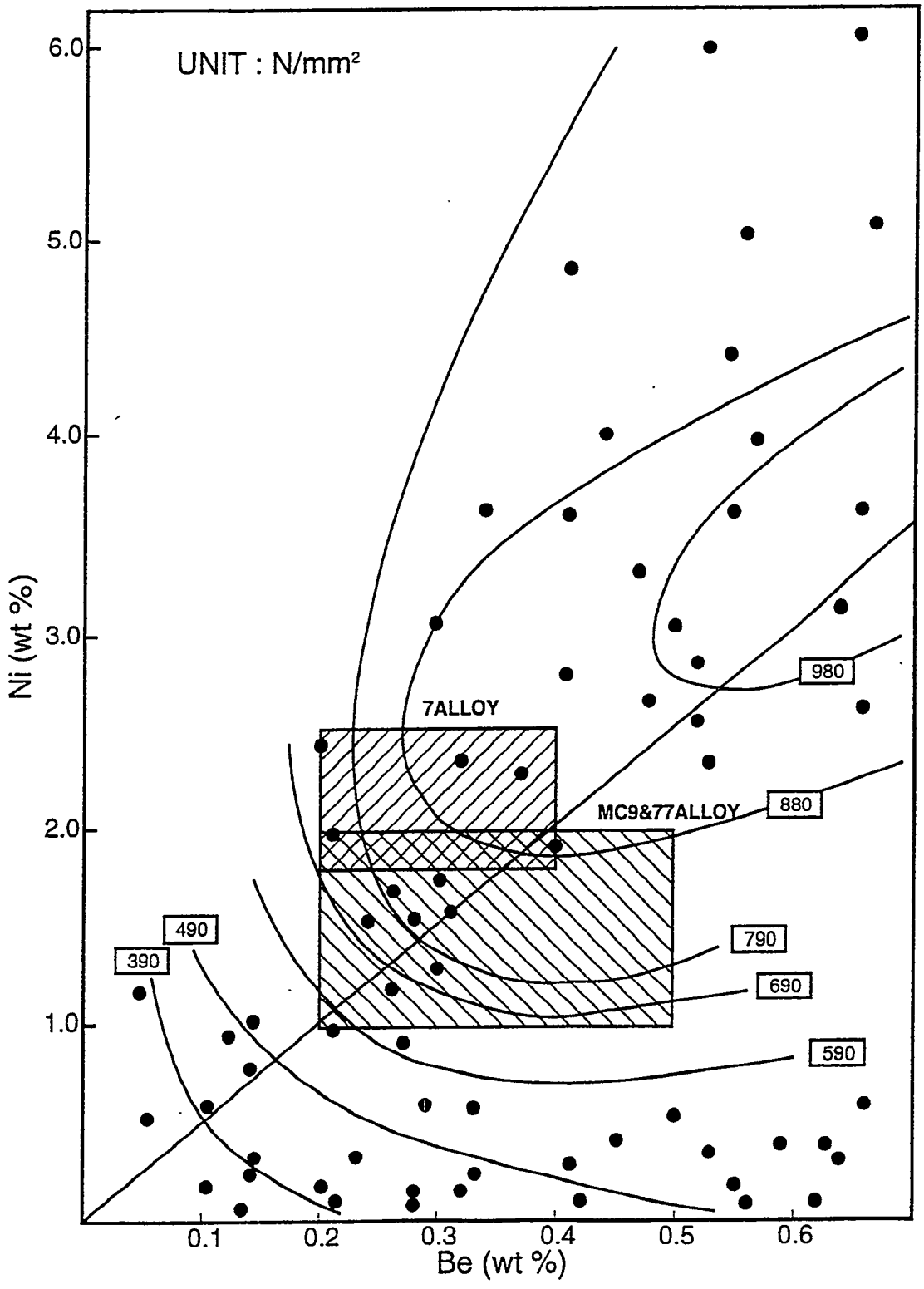

Figure6

NGK

KEY PROPERTIES OF BeCu HIGH CONDUCTIVIT YTYPE ALLOY

Property \ Alloy	7	MC-9	17510	77
Tensile Strength (N/mm^2)	830	685	840	690
Yield Strength (N/mm^2)	740	510	750	590
Elongation (%)	10	23	10	8
Hardness (V.H.N)	240	205	250	210
Electrical Conductivity (%IACS)	37	50	58	70
Formability (R/t*[1] 90°bend)	0.5	———	1.5	———

*1 : 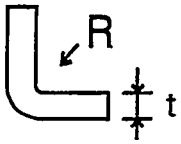

R : Internal Radius
t : thickness

Figure7

NGK

DEVELOPMENT OF 7 ALLOY (C17530)

• Experimental Procedure

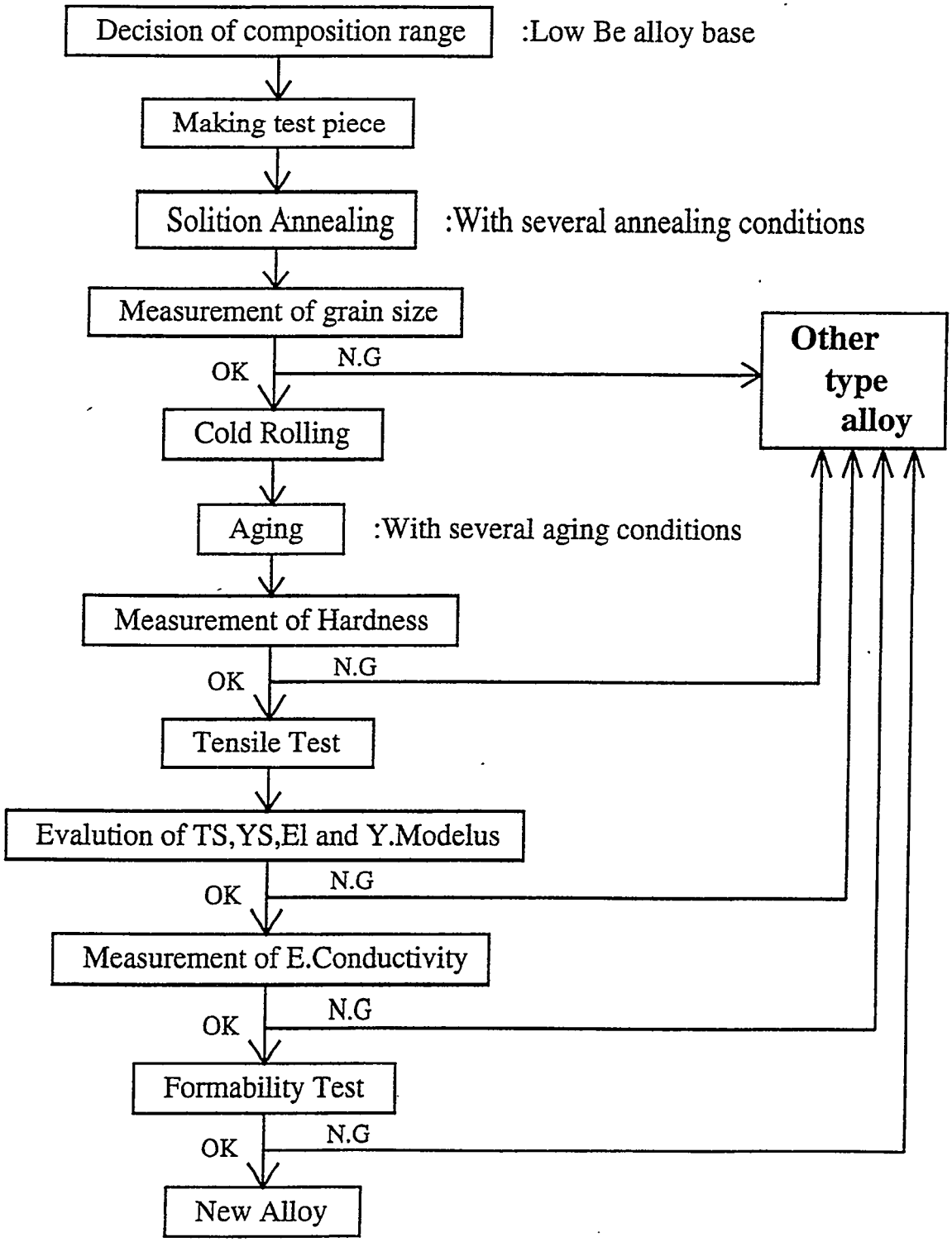

Figure8

NGK

DEVELOPMENT OF MC-9 & MC-16

Cast and Forged New Copper Alloys of Low Be content

Alloy design

Type	Applications	Demands and Technical trend
High Thermal Conductive Alloy (MC9)	Casting Dies ● Al Alloys ● Cu alloys ● Cast iron	● High Temperature Toughness (Heat Shock) ● Thermal Contorollability ⇩ Die Life, High Cycle Casting, Reduction of Shrinkage Defects
High Wear Resistance Alloy (MC16)	● Shell molding Dies ● Plastic Injection Dies	● Thermal Contorollability ● Hardness ● Machinability and Weldability ⇩ Die Life, High Cycle Forming, Reduction of Defects

Characteristic Comparison

Designation	Strength	Conductivity	Wear Resistance	Machining	EDM	TIG Weld
MC9	◎	◎	○	○	×	×
MC16	◎	○	◎	○	○	○
Popular mater. (iron, steel)	×	×	×	◎	◎	◎

Figure9

NGK

MATERIALS MAP OF RELATIONSHIP BETWEEN CONDUCTIVITY AND HARDNESS

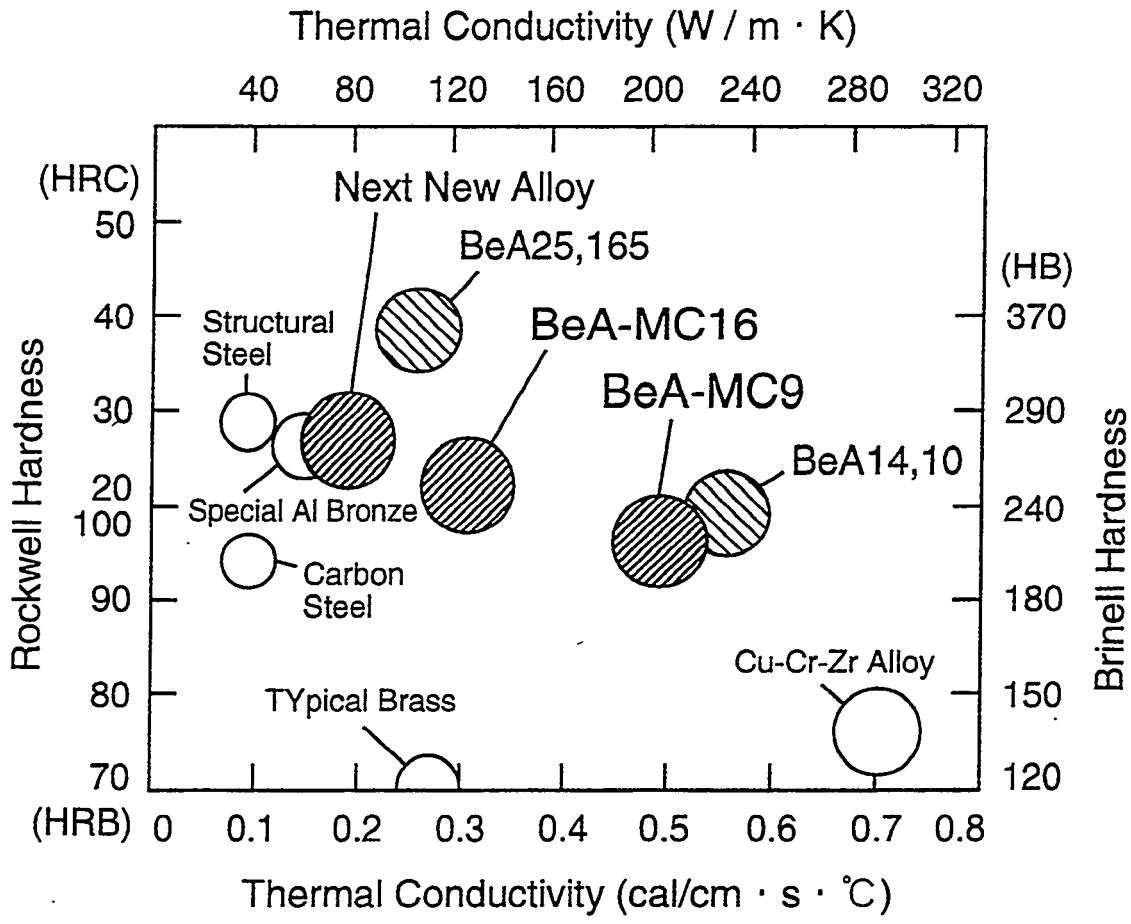

Figure10

NGK

DEVELOPMENT OF NEW COPPER BERYLLIUM ALLOY WITH HIGH CONDUCTIVITY AND HIGH STRENGTH

- **Target Properties**

  Tensile Strength $\geqq 680\ N/mm^2$

  Electrical Conductivity $\geqq 70\%$

- **Experimental Process**

Casting : Low Be alloy base

↓

Cold Rolling

↓

Annealing

↓

Cold Rolling

↓

Annealing : With several annealing conditions

↓

Cold Rolling : With several rolling conditions

↓

Aging : With several aging conditions

- **Results**

At laboratory base, achieved to the target under a certain combination of composion and process parameters.

Figure11

NGK

THEMAL CONDUCTIVITY AT HIGH TEMPERATURE

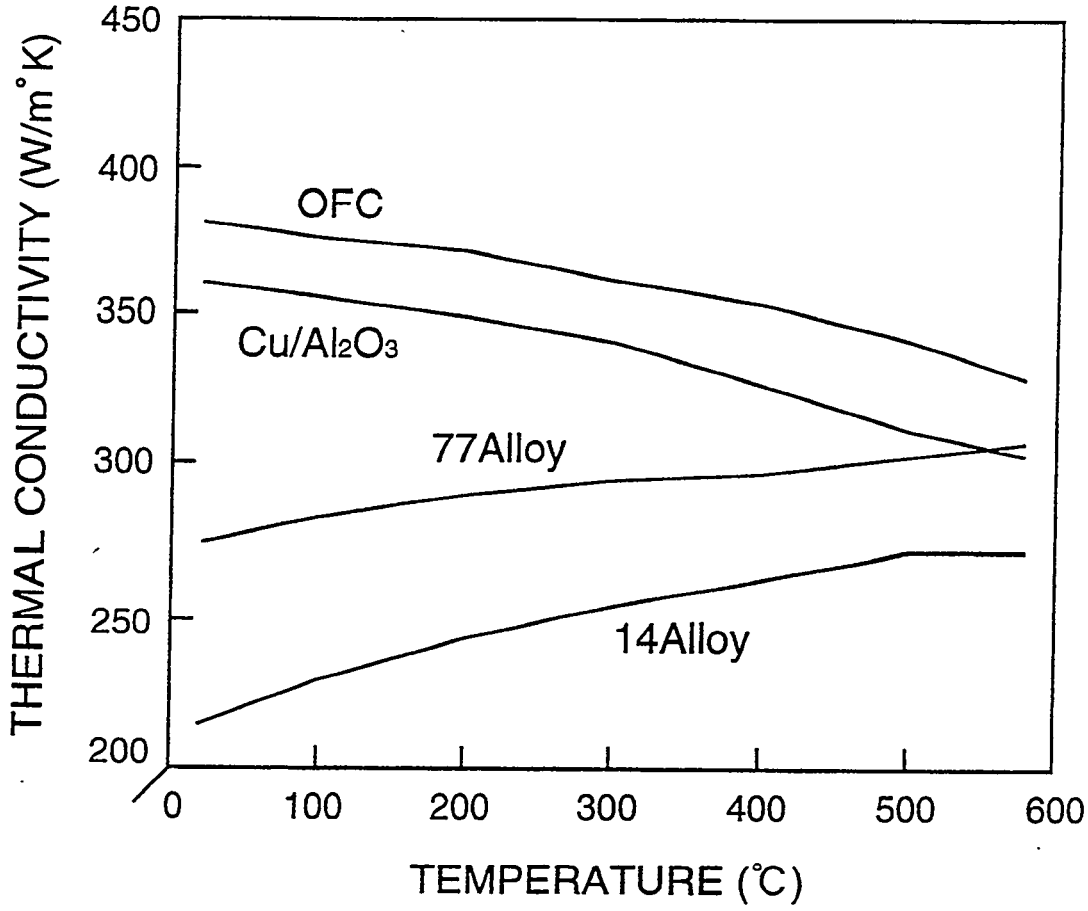

The thermal conductivity of the age hardening type alloy like 14 alloy. and 77 alloy increases as the temperature is elevated.

In case of the work hardening type alloy such as OFC and Cu/Al_2O_3, the thermal conductivity decrease with the elevation of temperature.

Figure12

NGK

MECHANICAL CHARACTERISTICS AT HIGH TEMPERATURE

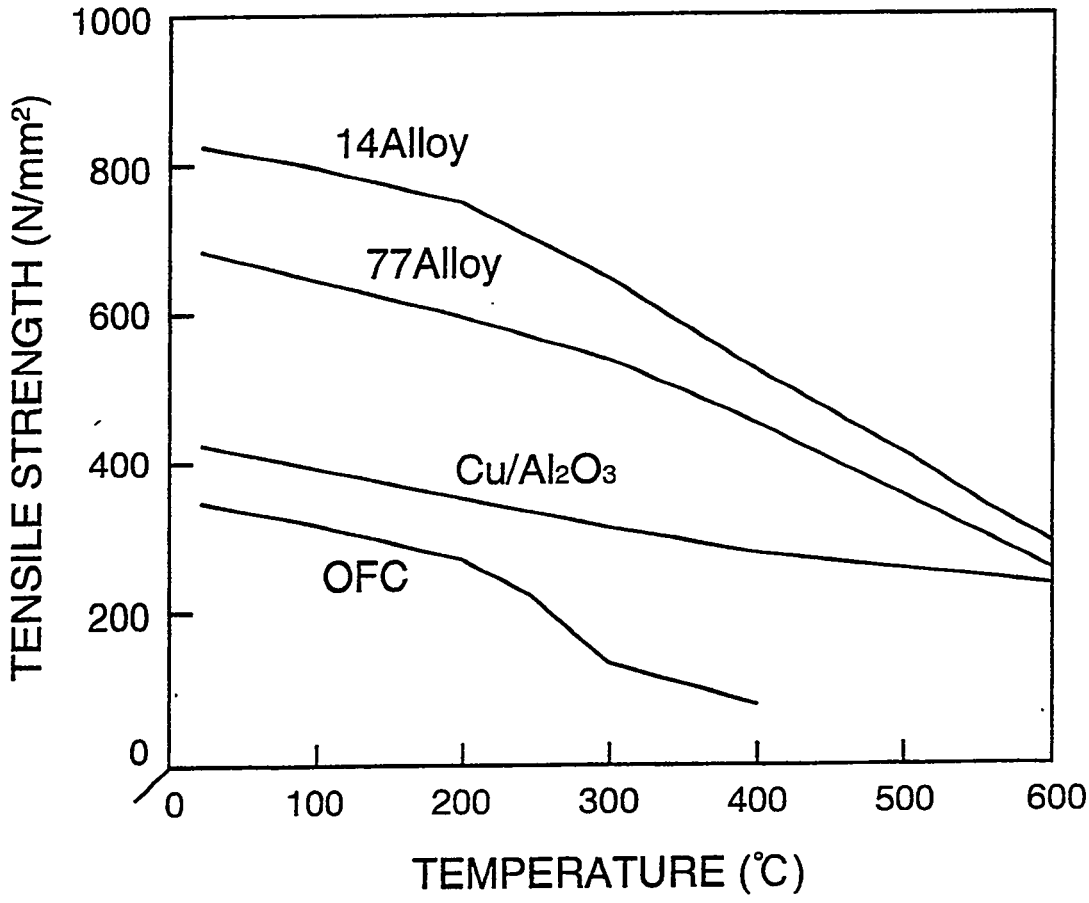

Beryllium copper 14 and 77 alloy keep high strength at high temperature compared with OFC and Cu/Al_2O_3.

The Structure, Properties and Performance of Plasma-Sprayed Beryllium for Fusion Applications

Richard G. Castro, Paul W. Stanek and Keith E. Elliott
Los Alamos National Laboratory, Los Alamos, N.M. 87545, USA

Dennis L. Youchison, Robert D. Watson and David S. Walsh
Sandia National Laboratory, Albuquerque, N.M. 87185, USA

Abstract

Plasma-spray technology is under investigation as a method for producing high thermal conductivity beryllium coatings for use in magnetic fusion applications. Recent investigations have focused on optimizing the plasma-spray process for depositing beryllium coatings on damaged beryllium surfaces. Of particular interest has been optimizing the processing parameters to maximize the through-thickness thermal conductivity of the beryllium coatings. Experimental results will be reported on the use of secondary H_2 gas additions to improve the melting of the beryllium powder and negative transferred-arc cleaning to improve the bonding between the beryllium coatings and the underlying surface. Information will also be presented on thermal fatigue tests which were done on beryllium coated ISX-B beryllium limiter tiles using 10 sec cycle times with 60 sec cooldowns and an International Thermonuclear Experimental Reactor (ITER) relevant divertor heat flux slightly in excess of 5 MW/m^2.

1.0 Introduction

Plasma-spraying of beryllium for coating applications in magnetic fusion energy devices will require extensive research and development in order to qualify this technology for *in situ* and off-site repair. Areas of research which will need to be investigated include; optimization/understanding of the thermal and physical properties of the beryllium coatings under irradiated and non-irradiated conditions, maximizing the adherence of the beryllium plasma-sprayed coatings to underlying beryllium and/or copper surfaces, reclamation and recycling of the beryllium oversprayed powder, remote manipulation to perform *in situ* repair, real-time inspection of the process and the deposited coatings, and technology scale-up. Much of the technology of plasma-spraying has been developed through a trial and error approach. This methodology requires extensive experimental plasma-spray trials and metallographic evaluations to arrive at the optimum conditions for providing the required coatings. Due to the limited facilities available to perform beryllium plasma-spray experiments, development of this

technology for fusion energy applications must rely on the available technology and expertise which has been developed for other material systems.

Current advances in plasma-spray technology such as plasma-spraying under a reduced pressure, transferred-arc cleaning/spraying and use of hydrogen gas additions into the arc gas, are being implemented in the R&D program to improve the overall quality of the beryllium coatings. The benefits of plasma-spraying under a reduced pressure (i.e., vacuum plasma-spraying) has been discussed extensively by a number of researchers [1,2,3,4]. In general, spraying under a reduced pressure, results in increased velocities of the molten particles exiting from the plasma torch. This can improve the impacting and consolidation of the individual molten particles which make up the bulk of the coating. In addition, spraying in an inert atmosphere at a reduced pressure also provides the ability to spray reactive materials such as beryllium.

To coat a beryllium surface via plasma-spraying some type of surface preparation will be required to clean and roughen the surface in order to maximize the coating adherence. Grit-blasting is the conventional method used to prepare most surfaces prior to plasma-spraying but would not apply for preparing damaged plasma facing surfaces inside of a fusion reactor. Negative transferred-arc cleaning provides the ability to clean damaged and contaminated surfaces as a result of the cathodic cleaning that can occur on the surface of the material to be coated. Negative transferred-arc cleaning has been use to clean surfaces of Mo, Ti, Ni [5] and mild steel [6]. The use of this technique has resulted, in many cases, a factor of two increase in the bond strength between the plasma-sprayed coatings and the underlying material [5]. The basic operation of negative transferred-arc cleaning results from establishing a negative or cathodic condition at the substrate. This can be achieved by applying a voltage between the plasma torch nozzle and the surface to be coated, Fig. 1.

The mechanism of cleaning results from the formation of microscopic cathode arc spots on the thin dielectric oxide layer present on the metal surface [7, 8]. Electrons are emitted from the oxide films as a result of the very high electric fields that exist at each cathode arc spot. Melting of the surface oxides results from the high concentration of electric currents (10^8 A/cm^2) that are present at these cathode arc spots. This results in the removal of the oxide surface layer exposing a clean metallic surface. Processing conditions which can effect the performance of the negative transferred-arc process are; the composition of the plasma gas, the torch to substrate distance, power levels associated with the plasma torch and the transferred-arc power supply, and the operating pressure in the plasma-spraying chamber. The negative transferred-arc process is described in more detail in reference [9].

Addition of hydrogen gas into a conventional D.C. argon plasma torch has been commonly used throughout the thermal spray industry to improve the as-deposited density and overall quality of plasma-sprayed deposits. The selection of a plasma generating gas for spraying a given material depends primarily on the gas energy, the gas reactivity and the cost. The relationship between the plasma temperature and gas energy

content is shown in Fig. 2. In this figure it is shown that the energy content of nitrogen and hydrogen is considerably higher then for argon or helium due to the dissociation reactions in the nitrogen and hydrogen prior to ionization. Generally about 1 to 10% hydrogen is mixed with argon to increase the heat content and improve the heat transfer characteristics of the primary arc gas. Hydrogen also acts as a reducing agent in the plasma. The gas selection should provide a plasma source capable of heating the injected particles to a molten or near molten state so that particle flow will occur upon impact.

In this paper, experimental results will be presented on plasma-spraying beryllium with hydrogen gas additions along with the use of negative transferred-arc cleaning to prepare beryllium surfaces prior to depositing beryllium. Discussions will focus on applying beryllium plasma-spray technology for coating beryllium limiter tiles which were used in the ISX-B tokamak experiment at ORNL [11]. Results on the performance of the beryllium coated tiles after thermal cycling the tiles under an ITER relevant heat flux of 5 MW/m^2 will also be discussed.

2.0 Experimental Procedure

2.1 Hydrogen Gas Additions

Commercial grade hydrogen was introduced into the argon plasma using an MKS 147 multi-gas flow controller. Hydrogen gas additions of 1 and 4 standard liters per minute (slm) were used for this investigation. The plasma torch operating parameters used for depositing beryllium are given in Table I. Beryllium deposits produced with hydrogen gas additions were compared to beryllium deposits produced with a secondary gas addition of 10 standard liters per minute of helium. Bell-shaped beryllium deposits 50.8 mm long x 25.4 mm wide x 10.0 mm thick were deposited on stainless steel substrates 6.35 mm thick. The deposits were subsequently removed from the stainless steel substrates by bending the stainless steel until the deposit detached. All beryllium plasma-spray trials were performed in a reduced pressure argon atmosphere at pressures between 400-450 torr. The beryllium spray deposits were mounted and polished and then examined using polarized light microscopy. Porosity levels were determined using image analysis techniques. Thermal diffusivity samples 3 mm thick x 12.7 mm in diameter, were machined from each spray deposit and tested at Virginia Polytechnic Institute, Thermophysical Research Laboratory, Blacksburg, Virginia, using laser flash diffusivity. The thermal conductivity was determined using the following relationship:

$$\kappa = \rho C_p D \qquad (1)$$

where ρ is the density and C_p is the heat capacity and D is the thermal diffusivity. Prior to the thermal conductivity measurements, the density of each sample was determined using a water immersion technique (Archimedes principle). All beryllium plasma spray

trials performed in this investigation were done using a selective size fraction of -38 +10 μm gas atomized beryllium powder produced commercially by Brush Wellman Inc.

2.2 Negative Transferred-Arc Cleaning

The effect of negative transferred-arc cleaning of beryllium surfaces prior to plasma-spraying was investigated by cleaning eight as-received beryllium samples (25.4 mm wide x 12.7 mm long x 3.2 mm thick) which had been sputter coated with 10 to 100 monolayers of tungsten and carbon. This combination of materials was chosen to simulate a contaminated surface similar to what might be expected in the International Thermonuclear Experimental Reactor (ITER) if carbon, tungsten and beryllium are used as plasma-facing materials. The sputter coatings were produced from both tungsten and carbon anodes using 100 eV of Ar and D_2 at a 1:2 ratio, and a current of 100 mA for 30 minutes. The beryllium samples were located 76.2 mm from the sputter targets. Rutherford Backscattering Spectrometry (RBS) using 1.6 MeV He ions was used to characterize the surface of the beryllium before and after negative transferred-arc cleaning. The surface analysis included detection of carbon, tungsten, oxygen, argon and copper. All measurements were done at the centerpoint of each beryllium sample. Processing parameters used for negative transfer-arc cleaning of the eight beryllium samples are given in Table II. Processing variables such as the chamber pressure, the torch to substrate distance and the substrate temperature were varied to observe the effect on cleaning and roughening of the beryllium surfaces.

2.3 Coating of the ISX-B Beryllium Limiter Tiles

ISX-B beryllium limiter tiles previously used in the ISX-B tokamak experiment at ORNL [11] were used to demonstrate the feasibility of coating and repairing beryllium plasma-facing components using plasma-spraying technology. Various types of damaged and undamaged limiter tiles, (which included castellated surfaces), were received from Sandia National Laboratory, Albuquerque, for beryllium plasma-spray investigations, Fig. 3. A plasma-sprayed coating of beryllium was first applied to an undamaged beryllium tile which contained only surface contamination as a result of the ISX-B environment. A second tile which contained a severely melted and microcracked surface, was then coated. In both cases the beryllium coatings were applied to non-castellated tiles. Negative transferred-arc cleaning was used to clean the surfaces prior to depositing the beryllium coatings.

Operating parameters used for negative transferred-arc cleaning and plasma-spraying the ISX-B beryllium limiter tiles are given in Table III. No mechanical surface conditioning was performed on the beryllium tiles prior to plasma-spraying. Plasma-sprayed beryllium coatings approximately 1 to 1.5 mm thick were deposited on the surface of each tile over an area of 25.4 mm wide by 50.8 mm long. Thermal fatigue

testing of the beryllium coated ISX-B tiles was performed at Sandia National Laboratory's Electron Beam Test System (EBTS) Facility. ITER divertor-relevant heat fluxes slightly in excess of 5 MW/m^2 were used with 10 second pulse lengths and 60 second cool-downs.

3.0 Results and Discussion

3.1 The Effect of H_2 Gas Additions

The resulting as-deposited microstructures when plasma-spraying beryllium with 1 and 4 standard liters per minute of hydrogen and 10 standard liters per minute of helium are shown in Figs. 4a, b and c. A substantial difference in the as-deposited grain size is seen with the introduction of the hydrogen gas additions. The beryllium spray deposits produced with 10 slm of helium showed evidence of unmelted beryllium particles which were surrounded by a fine grain beryllium matrix. The as-deposited densities of the deposits produced with helium were approximately 94% of theoretical (1.74 g/cm^3) with a room temperature (RT) thermal conductivity of 115 W/mK. These results are in contrast to the beryllium deposits produced with the 1 slm of hydrogen which had elongated grains on the order of 25 to 50 microns long oriented in the spray direction. The as-deposited density in this case was approximately 96% of theoretical (1.77 g/cm^3) with an increase in the room temperature thermal conductivity of approximately 160 W/mK.

The thermal conductivity as function of temperature (up to 600 °C) was determined for the beryllium deposits produced with 1 slm of hydrogen. These results were compared to other beryllium grades (12) over the same temperature range, Fig. 5. The behavior in thermal conductivity for plasma-sprayed beryllium over the RT to 600 °C temperature range was similar to that observed for the other grades of beryllium. The differences in the thermal conductivity between the beryllium plasma-sprayed coatings and the various grades of beryllium ranged from 85% of the reported values at room temperature to approximately 80% at 600 °C.

For the case of the beryllium deposits produced with 4 standard liters per minute of hydrogen, a more elongated microstructure was observed with grains on the order of 100 to 150 microns which were also oriented in the sprayed direction. The as-deposited density, in this case, was approximately 98% of theoretical (1.81 g/cm^3). Thermal conductivity measurements of these beryllium deposits are currently being completed at Virginia Polytechnic Institute, Blacksburg, Virginia. The thermal conductivity of these deposits over the RT to 600 °C temperature range is expected to lie somewhere between the current reported values for plasma-sprayed beryllium using 1 standard liter per minute of hydrogen and the various beryllium grades.

A chemical analysis of the deposits produced with the 4 standard liters per minute of hydrogen is given in Fig. 6. The analysis showed similar levels of BeO, Fe, Si and W to

the starting beryllium gas atomized powder produced at Brush Wellman Inc. The elevated levels of copper observed in the deposit is a result of the erosion of the copper anode in the plasma torch. The erosion rate of the copper anode has been shown to increase with the introduction of hydrogen as a secondary plasma generating gas. The higher aluminum levels were attributed to cross-contamination of the beryllium source powder which may have occurred when the beryllium powder feeders were calibrated with both aluminum and beryllium-aluminum alloy powders.

3.2 Negative Transferred-Arc Cleaning

Results of the Rutherford Backscattering Analysis (reported in density free units) of the sputtered coated beryllium samples before negative transferred-arc cleaning are given in Table IV. The values reported for the tungsten and carbon correspond to a thickness of 1.0 to 3.5 nm for tungsten, and a thickness of 4.0 to 15.0 nm for carbon at "normal" densities. Of the eight sputtered coated samples, Sample 4 showed the thickest deposit. The detection of argon on the beryllium surface is a result of the argon sputtering process which may also account for the near surface detection of copper. As would be expected oxygen is present as a result of the native oxide that readily forms on the surface of beryllium.

Results of the sputter coated beryllium samples after negative transferred-arc cleaning are given in Table V. Optical viewing of the beryllium surfaces prior to RBS analysis indicated that a cleaning of the beryllium surfaces had occurred. Two samples (5 and 8) showed indications that surface melting from the cleaning process may have resulted. Analysis of these samples were performed away from the apparent melted regions. Results of the RBS analysis showed that both the carbon and argon present on the surface of all eight beryllium samples were no longer detectable (minimum detection limit $\leq 10^{13}$ atoms/cm^2). For most of the beryllium samples, the surface tungsten was also reduced by an order of magnitude. An increase in the amount of copper on the surface of the beryllium was detected which extended beyond the range of the RBS analysis (>4.2 x 10^{18} atoms/cm^2). The elevated levels of copper are a result of the negative transferred-arc cleaning process which utilizes the copper cooled anode of the plasma-torch as one of the electrodes to promote cleaning of the beryllium surface. Oxygen was still present on all the beryllium samples as a result of air exposure to the samples prior to the RBS analysis.

3.3 Thermal Fatigue of Beryllium Coated ISX-B Beryllium Limiter Tiles

Despite the fact that the beryllium plasma spray process was not completely optimized for this demonstration, the coating on an undamaged beryllium limiter tile survived approximately 80 cycles at 5 MW/m^2 for 10 sec pulses before cracking was observed in the coating which led to the formation of hot spots on the surface of the coating. The beryllium coating which was applied to the badly melted ISX-B tile, however, survived

500 cycles before cracking was observed and a total of 680 cycles before the formation of hot spots on the coating surface terminated the tests. A cross-section of each tile is shown in Figs. 7 a and b. The coating which lasted 80 cycles showed thermal fatigue cracks which propagated through the thickness of the beryllium coating and then turned 90° and extended along the interface between the coating and the tile surface. The formation of hot spots on the coating surface was a result of the delamination of the coating from the beryllium tile leading to poor thermal conduction across the coating/tile interface. The microstructural features of the coating showed intermixed regions of columnar grains approximately 15 to 25 microns long adjacent to a fine equiax microstructure. The coating thickness was approximately 1.5 mm thick with a porosity level on the order of 7 percent.

For the case of the beryllium coating which lasted 680 cycles, thermal fatigue cracks which propagated through the thickness of the coating extended into the previously remelted surface region of the damaged beryllium tile and proceeded along the columnar grain boundaries of the remelted zone. There were no indications that any delamination occurred between the beryllium coating and the tile surface. The improved performance of the beryllium coating on the damaged ISX-B tile was attributed to the preferential grain boundary separation that occured along the columnar grains present in the remelted layer on the surface of the damaged tile. The microstructural features of the beryllium coating showed a fine equiax grain structure with no presence of columnar growth indicating that the substrate temperature during spraying might have been lower than what was observed for the beryllium coating on the undamaged beryllium limiter tile. The porosity level of the coating in this case was on the order of 12 percent with a 1 mm thick coating.

Surface temperature measurements done at Sandia National Laboratory during the EBTS high heat flux testing indicated that the coating on the undamaged beryllium surface was lower by approximately 100 °C after the initial thermal cycles. This indicated that the beryllium coating on the undamaged limiter tile was more effective in initially conducting the heat away from the surface during the high heat flux testing. The presence of the intermixed columnar/equiax grain structure, the lower porosity in the coating and a potentially better bond between the coating and the substrate may have contributed to an overall higher thermal conductivity. In general, the beryllium coating on the surface of the damaged beryllium ISX-B limiter tile which lasted 680 cycles, was of lower quality then the coating on the undamaged ISX-B tile which lasted only 80 thermal cycles. Clearly, there are other factors influencing the structural performance than simply the quality of the beryllium coating.

4.0 Conclusions

- Secondary additions of 1 and 4 standard liters per minute of hydrogen gas into the plasma-torch significantly influenced the as-deposited microstructure of plasma-sprayed beryllium resulting in long columnar grains in the direction of spraying. The presence of these columnar grains resulted in a dramatic improvement in the through thickness thermal conductivity of the plasma-sprayed beryllium coatings from 115 W/mK to 160 W/mK.

- Negative transferred-arc cleaning of beryllium was used to remove sputtered coated carbon and tungsten from the beryllium surface. The carbon was reduced below 10^{13} atoms/cm^2 which was the detection limit for the RBS analysis technique and the sputter coated tungsten was reduced by an order of magnitude.

- The performance of the beryllium plasma-sprayed coatings on two ISX-B limiter tiles after thermal cycling the tiles between 10 sec cycle times with 60 sec cooldowns at an ITER relevant divertor heat flux slightly in excess of 5 MW/m^2 were as follows: 1) the beryllium coating on the previously undamaged ISX-B tile lasted 80 thermal cycles before hot spots formed on the coating surface 2) the beryllium coating on the severely melted ISX-B tile lasted 680 thermal cycles before the test was terminated due to the formation of hot spots on the coating surface. Based on the results of the two beryllium coated ISX-B tiles, an improved performance of the beryllium coating on the damaged ISX-B tile was attributed to grain boundary separation along the columnar grains present in the remelted layer on the surface of the damaged tile.

Acknowledgments

The authors would like to thank the following people for their contributions: Dr. Donald Cowgill of Sandia National Laboratory, Livermore CA for sputter coating the beryllium samples, Dr. D.P.H. Hassleman of Virginia Polytechnic Institute for thermal diffusivity measurements, Ann Kelly for metallographic sample preparation and Raul Brunner for machining of thermal diffusivity samples. The authors would also like to acknowledge the DOE Office of Fusion Energy for sponsoring this research.

References

1. Apelian, D., Smith, R.W., Paliwal M., and Schilling, W.R., International Metals Review, **28** (5) (1983) pp. 271-294.
2. Apelian, D., and Wei, D., Thin Solid Films, 118, (1984) pp. 395-407.
3. Wei, D., Ph.D Thesis, "Melting Powder Particles in D.C. and R.F. Plasmas: A Modeling Study" Drexel University, Philadelphia PA, (1987).
4. Smith, M.F., and Dykhuizen, R.C., Surface and Coating Technology, 34, (1988), pp. 25-31.
5. Henne, R., Bradeke, M.V., Schiller, G., Schnurnberger, W., and Weber, W., "Vacuum Plasma Spraying of Oxide Electrocatalytic Materials", Proceeding of 12th International Thermal Spray Conference, (1989).
6. Itoh, A., Takeda, K., Itoh M., and Koga, M., "Pretreatment of Substrates by Using Reversed Transferred Arc in Low Pressure Plasma Spray", Proceeding of the 3rd National Thermal Spray Conference, Long Beach, CA, (1990) pp. 245-251.
7. Guile, A.E., and Juttner, A.E., IEEE Trans on Plasma Science, **PS-8**, (3) (1980). pp. 259-269.
8. Guile, A.E., "Electric Arc-Phenomena", Proc. IEE, IEE Reviews, **118** (9R) (1971) pp. 1131-1154.
9. Muehlberger, E., U.S. Patent No. 4,328,257 (1982).
10. Gerdeman, D.A., and Hecht, N.L., "Arc Plasma Technology in Material Science", Springer-Verlag, New York Wien (1972) pp. 10.
11. Mioduszewski, P.K., et. al., "The Beryllium Limiter Experiment in ISX-B", Nuclear Fusion, **26(9)** (1986) pp. 1171.
12. Barabash, V., "Recommended Data on Be Thermomechanical Properties for Plasma Facing Components: Design Evaluation" ITER Draft Report NG1, First Edition, ITER Garching Joint Work Site, (1994) pp.7.

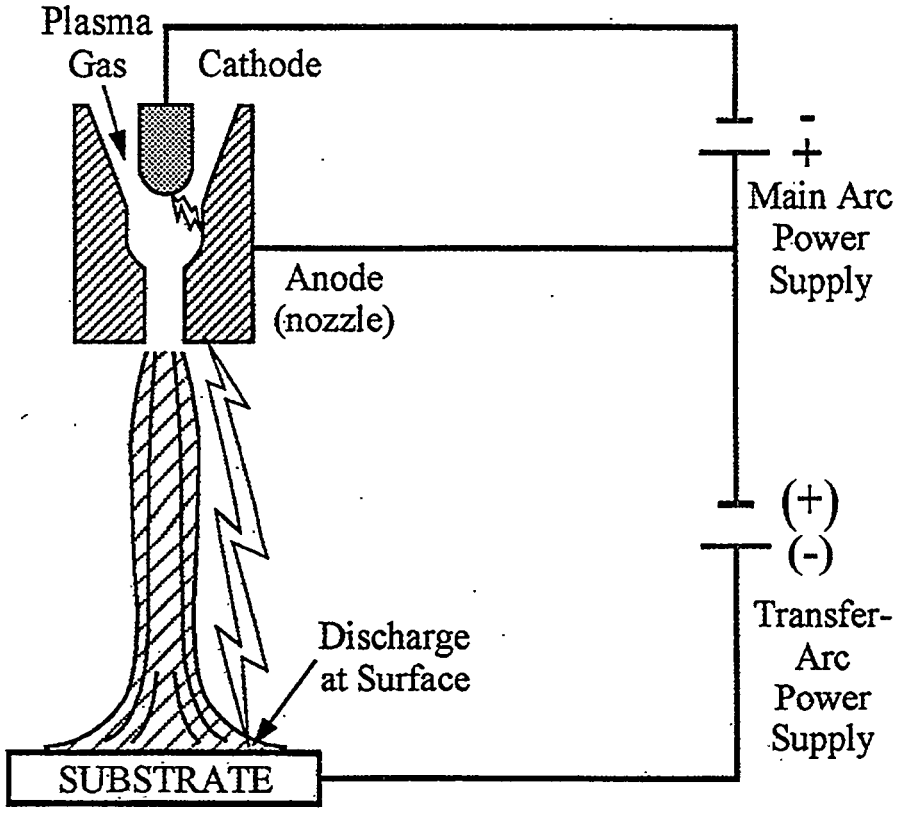

Fig. 1. Basic operation of negative transferred-arc cleaning.

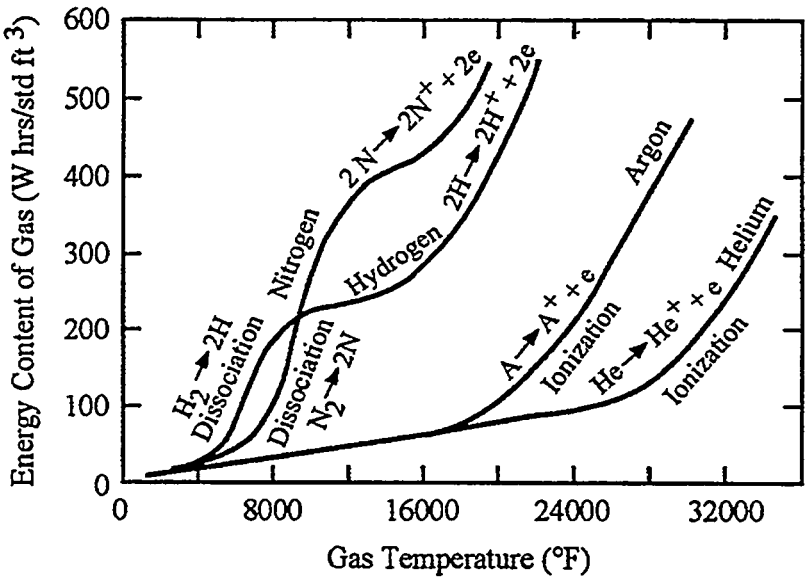

Fig. 2. Plasma temperature as a function of gas energy content at atmospheric pressure [10].

Table I. Operating parameters for plasma-spraying with hydrogen and helium secondary gas additions.

Parameters	**A**	**B**	**C**
Plasma Torch	SG-100	SG-100	SG-100
Primary Gas (Ar)	40 slm	40 slm	40 slm
Secondary Gas (slm)	**1 - H_2**	**4 - H_2**	**10 - He**
Powder Gas (Ar)	1 slm	1 slm	1 slm
Powder Feed Rate (gm/min)	~7.6	~7.6	~7.6
Current (amps)	800	800	800
Volts (V)	22	26	36
Chamber Pressure (torr)	400 - 450	400 - 450	400-450
Substrate temperature (C)	800	900	700
Anode	2083-730	2083-730	2083-730
Cathode	1083A-129	1083A-129	1083A-129
Gas Injector	2083-112	2083-112	2083-112

Table II. Parameters for negative transferred-arc cleaning sputter coated beryllium samples.

Torch operating parameters:		**Transferred-arc parameters:**	
primary gas (Ar)	40 slm	amps	60
amps	100	volts	120
volts	25	pulser	off

Sample	**1**	**2**	**3**	**4**	**5**	**6**	**7**	**8**
distance (cm)	7.62	10.16	7.62	7.62	7.62	7.62	10.16	10.16
chamber pressure (torr)	84	100	30	250	100	100	100	250
substrate temp °C	375	250	500	450	350	410	450	450

Fig.3. Various ISX-B beryllium limiter tiles used for plasma-spraying investigations.

Table III. Parameters used for negative transferred-arc cleaning and plasma-spraying ISX-B beryllium tiles.

T/A Parameters	**Settings**	**Torch Parameters**	**Settings**
current (A)	60	arc gas (Ar)	40 slm
volts	120	secondary gas (H_2)	2.5 slm
pulser (on/off)	(on) 9/130	powder gas (Ar)	1 slm
chamber pressure	40 torr	feed rate (lbs/hr)	~ 1
plasma torch current (A)	550	currrent (A)	800
substrate preheat temp	800 °C	volts	28
distance (cm)	8.89	chamber pressure	400-450 torr
		substrate temp	800 °C
		anode	2083-730
		cathode	1083A-120
		gas injector	2083-12

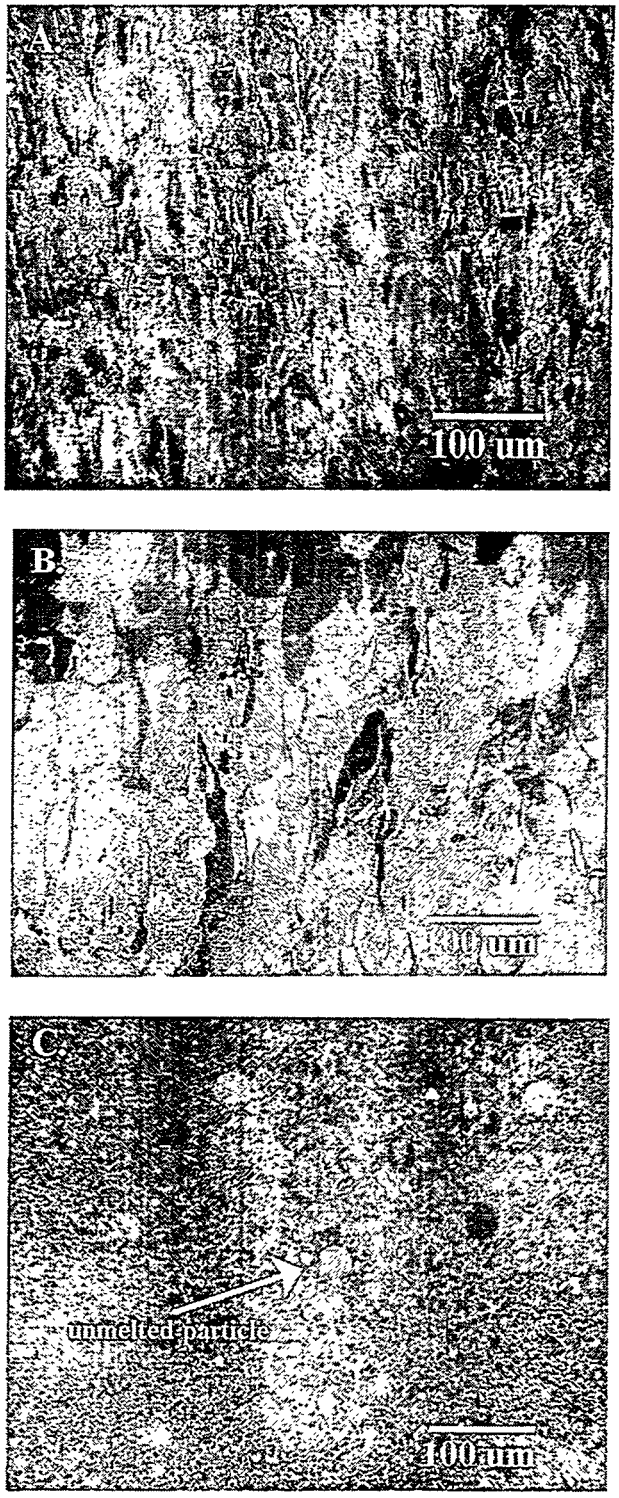

Fig. 4. Plasma-sprayed beryllium deposits using; a) 1 slm of hydrogen, b) 4 slm of hydrogen and c) 10 slm of helium.

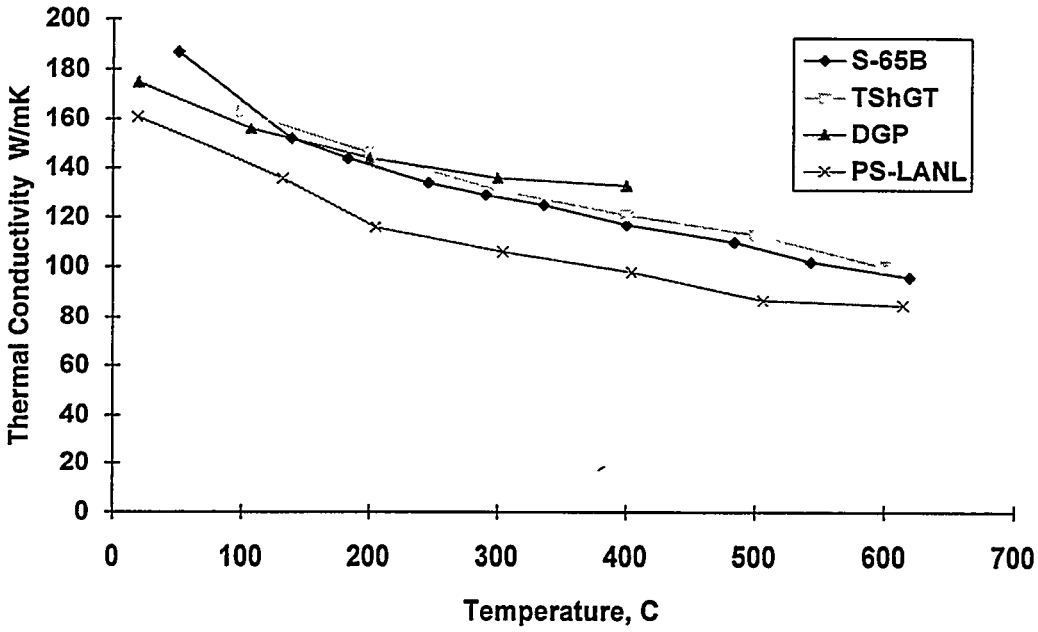

S-65B - Vacuum Hot Pressed
TShGT - Technical Purity, punched from hot pressed product
DGP - Distillation Purity, sintered hot pressed
PS-LANL - Low pressure plasma-sprayed beryllium

Fig. 5. The thermal conductivity of plasma-sprayed beryllium compared to other grades of beryllium [12] from room temperature to 600 °C.

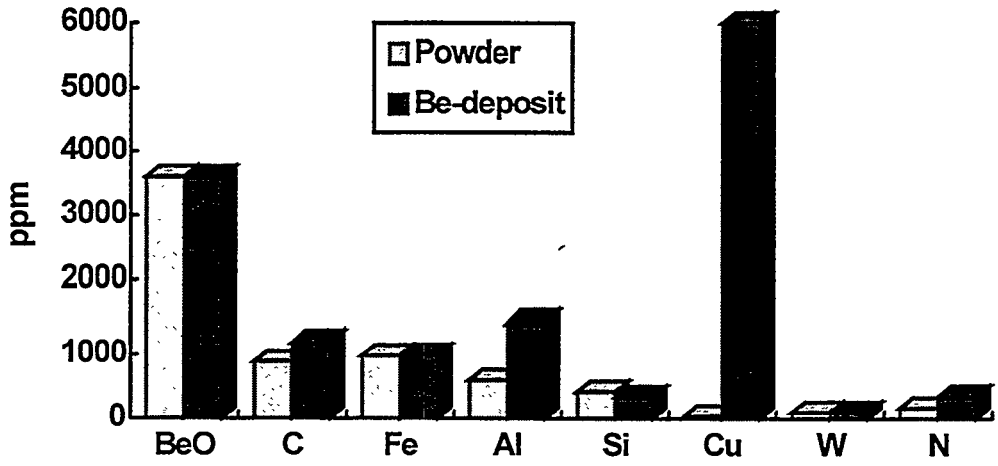

Fig. 6. Results of the chemical analysis comparing the source powder used for plasma-spraying to the as-deposited beryllium coatings when using 4 standard liters per minute of hydrogen.

Table IV. 1.6 MeV He RBS at centerpoint of Be tile samples prior to negative transferred-arc cleaning.

Measured Elemental Areal Density (10^{15} atoms/cm^2)

Sample	C	O	Ar	Cu	W
1	43.49	73.56	0.89	1.28	13.45
2	114.10	149.20	3.35	1.28	15.97
3	50.41	76.00	2.38	0.63	19.12
4	152.10	116.30	1.72	7.72	21.59
5	37.58	79.08	1.84	0.06	17.78
6	96.16	75.05	1.86	0.08	12.73
7	68.55	98.63	1.39	3.45	10.54
8	116.80	83.73	2.02	5.74	6.73

Table V. 1.6 MeV He RBS at centerpoints of Be tile samples following negative transferred-arc cleaning.

Measured Elemental Areal Density (10^{15} atoms/cm^2)

Sample	C	O	Ar	Cu	W
1	n.d	85.00	n.d.	u.d.	1.10
2	n.d	65.00	n.d	u.d.	0.68
3	n.d	55.00	n.d	u.d.	3.00
4	n.d	93.00	n.d	u.d.	0.41
5	n.d	61.00	n.d.	u.d.	7.00
6	n.d.	43.00	n.d.	u.d	9.60
7	n.d.	83.00	n.d.	u.d	0.71
8	n.d	120.00	n.d.	u.d	1.30

n.d. = not detectable

u.d. = present but undetermined quantity

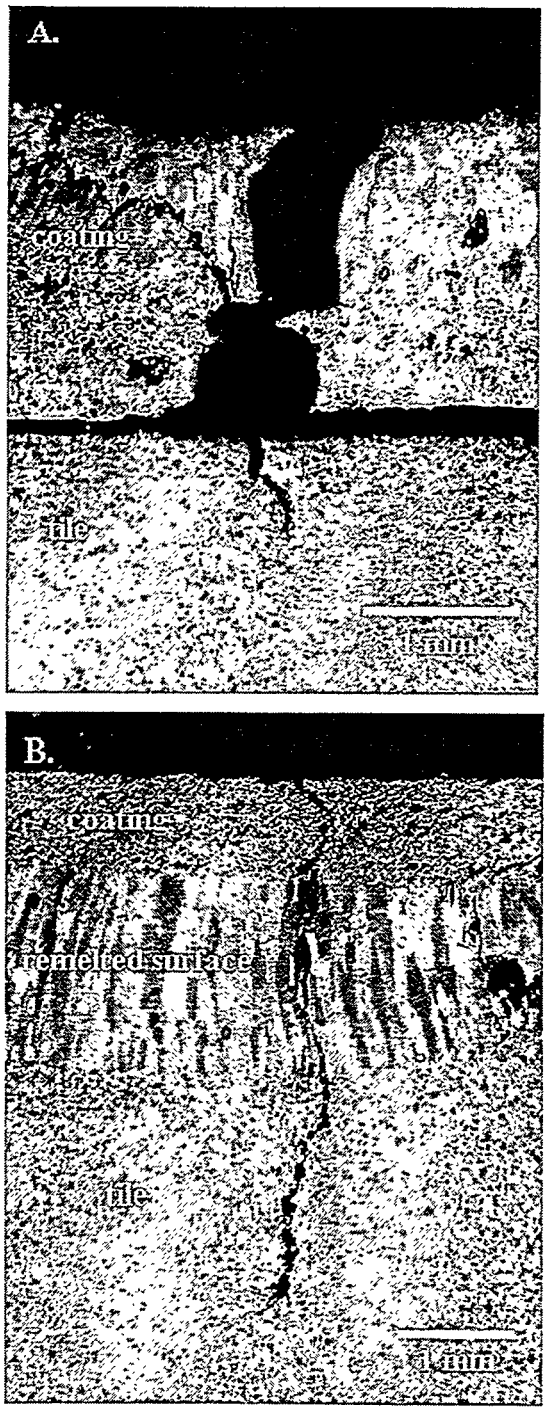

Fig. 7. Cross-sections of beryllium plasma-sprayed coated ISX-B beryllium tiles after high heat flux testing at 5 MW/m^2: a) beryllium coating on undamaged tile which lasted 80 thermal cycles, b) beryllium coating on damaged tile which lasted 680 thermal cycles.

RECENT RESULTS
FOR
BONDING S-65C GRADE Be TO COPPER ALLOYS

David E. Dombrowski

Brush Wellman Inc.
Cleveland, OH

Abstract

Novel processes for bonding beryllium to copper alloys without the use of a silver bonding aid have been developed at Brush Wellman. Tensile strength results will be presented at room temperature and elevated temperatures. A comparison will be made between bond strengths derived from rectangular tensile specimens and reduced section tensile specimens. Failure modes of the specimens at various temperatures will be shown.

RECENT RESULTS
FOR
BONDING S-65C GRADE Be TO COPPER ALLOYS

David E. Dombrowski

Brush Wellman Inc.
Cleveland, OH

Introduction

Bonding beryllium to copper is a critical task for manufacture of both the divertor and First Wall in ITER. A number of processes have been considered and tested, including furnace brazing(1), induction brazing (2), friction welding (1), explosive bonding (3), diffusion bonding by uniaxial pressing in vacuum (4), diffusion bonding by hot isostatic pressing(5-7), and electroplating (4). To date, the most successful process is a silver based vacuum induction brazing process developed by JET (2) which yields high bond strengths from room temperature to 400°C. However, neutron irradiated silver presents an unacceptable radiation hazard (1,4). Until now, no other process has achieved beryllium to copper alloy bond strengths above about 35 MPa.

The results presented here show that the Brush Wellman bonding processes A and B have produced bond strengths significantly above 35 MPa.

Background

The driving force for investigations in bonding beryllium to copper is application of beryllium as water cooled armor for plasma facing components in ITER. The ITER constraints include the following:

1. Bond must not contain any elements which upon neutron irradiation pose a radiation safety hazard equal to or greater than silver.

2. Bond strength should be above 35 MPa and preferably around 100 MPa for the temperature range from room temperature to 400°C.

3. Bonding process must be capable of scale up to production processes.

Table I shows some of the published data on beryllium to copper bonding (2)(5). Also shown is data for common silver free brazing processes (8). This data serves to illustrate several features of the beryllium to copper bonding problem. Although

there is no published specification for bond strength, the ITER community considers the JET process bond strength levels (> 150 MPa) very good and the MSC process bond strength levels (32.5 MPa) unacceptable. The data for diffusion bonding of beryllium to itself (9) indicates that there is no inherent problem with beryllium which prevents bonding. The bond strength shown equals base metal tensile strength of many beryllium grades. The data for zinc based and aluminum based brazing clearly show that although acceptable room temperature bond strengths can be achieved, elevated temperature strengths drop to unacceptable levels. This means that a simple extension of existing silver free beryllium bonding technology is unlikely to meet ITER needs.

One metallurgical rule of thumb often cited for a successful bond is that intermetallics will not be present in a successful bond. However, Hanafee (10) has stated that a dispersion of fine intermetallics may not be deleterious.

Materials

The ITER beryllium reference grade, vacuum hot pressed S-65C, was used for these experiments. Pure copper (C10100) was used as the other half of the joint. This was done so as to minimize the complexity of bond microstructure.

Bonding Processes

Two proprietary processes were used to conduct these bonds: Brush Wellman Processes A and B.

Silver was not used as a bonding aid.

All bonding materials used present less radioactive hazard after neutron irradiation than silver.

Bond Strength Determination

Several methods have been used to measure bond strength of beryllium to copper alloy joints. They include tensile strength, single lap shear tensile tests, double lap shear tensile , bend tests, and the JET shear tests. There is no consensus on testing method. Since investigators are largely looking for experimental vectors at this point and not absolute bond strength values, bond strength values for different types of testing are often compared. For, example, shear tests results are directly compared with tensile test results.

Initial tensile tests have been conducted in a number of studies using a rectangular straight sided tensile specimen without a reduced section. This rectangular straight sided specimen is also specified for some upcoming studies (11). The advantage of this sample is that it is inexpensive to machine, it maximizes the

bond area to be analyzed and thereby averages bond defects over a greater area, and it is not subject to the clamping forces used to make a reduced section specimen. This last advantage is useful when it is suspected that the bonds are weak bonds but semi-quantitative data is needed to direct future experiments.

The typical reduced section tensile specimen is preferred for the usual reasons of controlling the point of strain loading.

This study used both types of specimens. The results with the two specimens are contrasted.

The rectangular specimen used in the present study was 51 mm (2 in) tall by 18.3 mm (0.720 in) wide by 4.78 mm (0.188 in) thick with two 6.4 mm (0.25 in) diameter pin loading holes placed at 9.52 mm (0.375 in) away from each end. The sample was gripped at each end by a 6.4 mm (0.25 in) pin through the pin hole.

The reduced section tensile specimen was made by modifying the above rectangular specimen. A central gauge section which was 17.1 mm (0.675 in) long and 6.4 mm (0.25 in) wide was machined with the bond at its centerpoint. 6.4 mm (0.25 in) radius curves were machined between the gage section and the gripping ends. This sample was also pin loaded.

Tensile tests were conducted at room temperature, 200°C, and 400°C.

Results and Discussion

Table II and Table III show the bond strengths measured using the two different tensile specimens. The results of tensile testing with a rectangular straight sided specimen are shown in Table II. BWI Process A and B both produce nominal bond strengths above 30 MPa at both room temperature and 400°C. Process A clearly produces a stronger bond at both temperatures. The bond strengths at 400°C must be taken as semi-quantitative. As shown in Figures 1 and 2, those specimens failed through the copper pinhole. The bond strength is greater than that of the dead soft pure copper across the 6.4 mm span between pinhole and the specimens. Even if these results are only taken as semi-quantitative figures of merit, further investigation of these processes is justified.

Bond strength measurements using reduced section tensile samples are shown in Table III. These values are roughly twice as large as the values obtained with the straight sided rectangular specimens. The bonds produced by BWI Process A now are shown to have tensile strength above 140 MPa at room temperature and 200° C, and a tensile strength above 90 MPa at 400°C. The 400°C bond strengths have reasonable reproducibility. The bond strengths obtained with Process B are

significantly lower at room temperature and 200°C, but are close to the Process A values at 400°C. The closeness of the Process B bond strengths at 400°C to the Process A bond strengths at 400°C may be a result of the low copper strength at that temperature rather than of actual convergence of bond strength. C10100 copper only has a 100 MPa tensile strength at 400°C. In addition, the 400°C tensile sample for Process A failed completely in the copper rather than in the bond, as shown in Figure 3. Note that the copper side of the tensile is on the bottom. The equivalent sample for Process B failed in the bond, as shown in Figure 4. These bond strength results are again semi-quantitative, because there was some pin hole elongation in the copper as shown in Figures 3 and 4.

Location of the fracture in the tensile specimens can be seen in Figures 3 and 4, and is summarized in Table IV. The appearance of room temperature, 200°C , and 400°C tensile specimens of Process A material after testing is shown in Figure 3. The equivalent Process B specimens are shown in Figure 4. Location of fracture for the reduced section samples varies with temperature and varies to a lesser extent between Processes A and B. In general, weak bonds will fail at the interface between the beryllium and the bond layer. Process A samples showed a progression away from the beryllium/bond interface as the temperature was increased, with the final fracture being in the copper. This latter result indicates that at 400°C the bond is stronger than the copper. It is always a promising sign when the bond is stronger than one of the base metals. Process B showed a similar progression of fracture location that was less sensitive to temperature; the Process B fracture at 400°C was located in a similar position as the Process A fracture at 200°C. The straight sided, rectangular tensile samples failed at the Be/bond interface at room temperature, and in the copper pin holes at 400°C for both Process A and B.

The reduced section bond strength results are significant for several reasons. They indicate that these Brush Wellman processes can produce significantly higher room temperature and elevated temperature strengths than has heretofore been reported for beryllium to copper bonding without silver. The strengths at elevated temperatures also exceed those for beryllium to beryllium bonding using aluminum based and zinc based brazing processes. Bond resistance to degradation during handling and machining is also important. The straight sided, rectangular samples were machined from bonded stock material by electric discharge machining (EDM). EDM is a relatively low stress machining method which does not use much clamping force on the stock material. The reduced section samples were machined from straight sided, rectangular samples by conventional milling. This shows that these bonds can withstand the stresses of conventional machining; they are robust.

The comparison of straight sided, rectangular and reduced section sample geometries produced some significant results. There is clearly a significant effect

of specimen type on the bond strength value; the reduced section values are about twice as high. Since the reduced section values are expected to be more representative of the actual bond strength, is there any value in the use of straight sided, rectangular specimens? The room temperature bond strengths derived from the straight sided, rectangular specimens correctly indicated the significant difference between Processes A and B. The 400°C bond strengths from the straight sided, rectangular specimens are less useful in comparing the two processes. This may be more closely related to the use of a copper with poor elevated temperature strength and non-optimal pin hole design than the strain loading characteristics of this geometry. Nevertheless, it may be prudent to restrict the use of straight sided, rectangular specimens to room temperature testing.

It should be noted that Brush Wellman Bonding Processes A and B are in the development stage. Future work will include optimization of the process parameters. Now that the robust nature of the bond is known, testing will be conducted with thinner but better designed sample geometries. Accurate characterization of elevated temperature bond strength can only be done with copper alloys which have higher elevated temperature strength. The copper alloy of choice should also be thermally stable during the bonding process and there are advantages if the copper alloy is also age hardenable. High heat flux testing of the bonds should be delayed until the bond characteristics are optimized for use with a higher strength copper alloy.

Conclusions

- Brush Wellman Bonding Processes A and B can produce significantly higher room temperature and elevated temperature strengths than have heretofore been reported for beryllium to copper bonding without silver.

- The strengths at elevated temperatures exceed those for beryllium to beryllium bonding using aluminum based and zinc based brazing processes.

- Bond resistance to degradation during handling and machining is good.

- There is a significant difference in measured bond strengths depending on whether straight sided rectangular or reduced section sample geometries are used. Bond strengths measured with reduced section specimens are twice as high as when measured with straight sided, rectangular specimens. Straight sided, rectangular specimens should only be used to indicate room temperature trends.

Recommendations

- Future work should include optimization of the process parameters.
- Now that the robust nature of the bond is known, testing should be conducted with thinner but better designed sample geometries.
- Accurate characterization of elevated temperature bond strength can only be done with copper alloys which have higher elevated temperature strength, are thermally stable during the bonding process and are age hardenable.
- High heat flux testing of the bonds should be delayed until the bond characteristics are optimized for use with a higher strength copper alloy.

References

1. Odegard, C. Cadden, W. Bonivert, S. Robinson, "Joining of Be to Copper for High Heat Flux Components", in Proceedings of Japan-U.S. Workshop P243 on High Heat Flux Components and Plasma Surface Interactions for Next Fusion Devices, eds., T. Hino and M. Ulrickson, Hokkaido University, Sapporo, Japan, January 31 - February 3, 1995

2. Altmann, et. al,"An Analysis of Induction Brazed Beryllium on Copper Alloy Substrates, presented at 15th IEEE Symposium on Fusion Engineering, Hyannis, MA, Oct. 11-15, 1993

3. Butler, D.E. Dombrowski, "Preliminary Results for Explosion Bonding of Beryllium to Copper", presented at The 2nd IEA Workshop on Beryllium Applications in Plasma Facing Components, Jackson Lake,Wyoming, September 6 - 8, 1996

4. Russian Federation Home Team for ITER , as described by R.D. Watson, in "Beryllium joining Development", presented to DOE Technical Evaluation Panel for Use of Beryllium for ITER Plasma Facing Material and Breeder Blanket Material, June 7-8, 1994

5. Floyd, A.L. Liby, W. Weaver, "Solid State Bonding of Beryllium to Copper and Vanadium", presented at IEA Workshop on Beryllium for Fusion Applications, Karlsruhe, Germany, Kernforschungszentrum Karlsruhe document no. KfK 5271, December 1993

6. Franconi et. al, "Development of beryllium bonds for plasma-facing components", Journal of Nuclear Materials, 191-194, 1992, pp. 493-498

7. D.E. Dombrowski, D.H. Hashiguchi, A. Peacock, M. Pick, unpublished research

8. Grant, Chapter 13 in Beryllium Science and Technology , D.R. Floyd, J.N. Lowe, eds., Plenum Press, 1979

9. O'Brien, C.R. Rice, D.L. Olson, "High Strength Diffusion Welding of Silver Coated Base Metal", Weld J. (Miami), vol. 55, 1976, pp. 25-27

10. Hanafee "Joining Beryllium to Itself and Other Metals" presented to the DOE Technical Evaluation Panel for Use of Beryllium for ITER Plasma Facing Material and Breeder Blanket Material, July 1994

11. Odegard, private communication

Table I Bond Strengths (MPa) Achieved in Other Candidate Processes

	Process	Room Temperature	200 °C	400 °C
JET (1993) Be to Cu Alloy	Ag Based Induction Brazing	220 MPa	≈ 215 at 250°C	≈ 157
MSC (1993) Be to Cu Alloy	Ag Sputtered on Be and Cu followed by HIP	32.5	NA	NA
O'Brien, Rice, and Olson (1976) Be to Be	Ag sputtered on Be followed by Diffusion Bonding	434	NA	NA
Be to Be	Al Based Brazing	102	64	NA
Be to Be	Zn Based Brazing	88	52	20

Table II Bond Strength Determination for S-65C grade Be Bonded to Cu (C10100) by Brush Wellman Processes A and B

Rectangular Tensile Samples

	Tensile Strength of Bond (MPa)		
Process	Room Temp.	200°C	400°C
A	73.8	NA	49.6
B	49.6	NA	35.2

Table III Bond Strength Determination for S-65C grade Be Bonded to Cu (C10100) by Brush Wellman Processes A and B

Reduced Section Tensile Samples

	Tensile Strength of Bond (MPa)		
Process	Room Temp.	200°C	400°C
A	142	141	96.5 95.8
B	88.2	112	90.3 94.5

Table IV Summary of Tensile Sample Failure Location

	Process A		Process B	
	Rect.	Reduced Section	Rect.	Reduced Section
Room Temp.	Flat Fracture at Be/Bond Interface	Flat Fracture in Bond	Flat Fracture at Be/Bond Interface	Flat Fracture at Be/Bond Interface
200 °C	NA	Uneven Fracture in Bond	NA	Flat Fracture at Be/Bond Interface
400 °C	Failed In Cu Pin Hole	Failed in Main Body of Cu	Failed In Cu Pin Hole	Uneven Fracture in Bond and at Be/Bond Interface

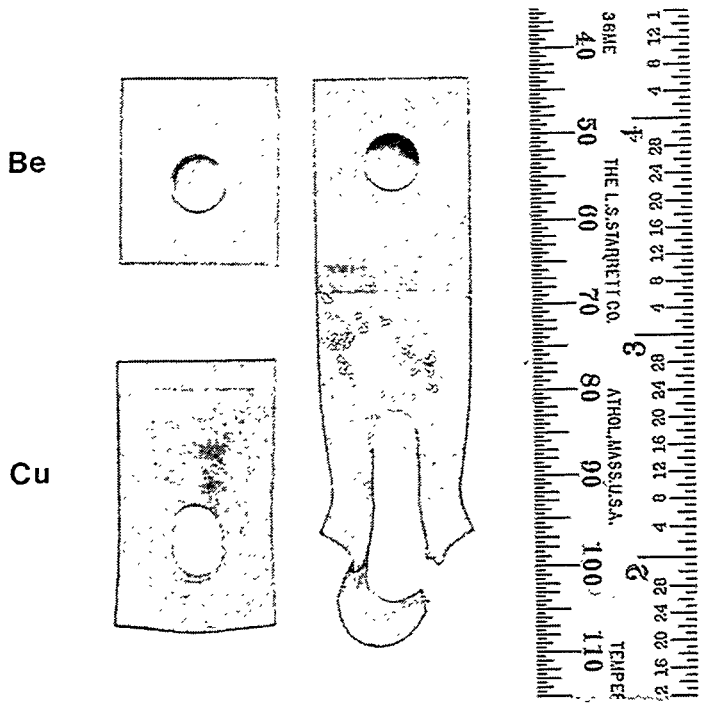

Figure 1 Comparison of Macroscopic Appearance of Room Temperature and 400° C Straight Sided Rectangular Tensile Specimens for BWI Process A

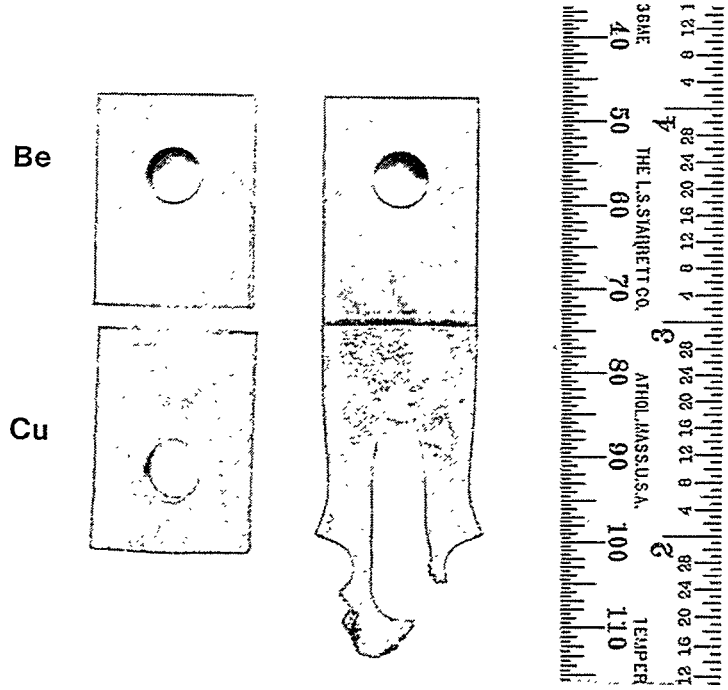

Figure 2 Comparison of Macroscopic Appearance of Room Temperature and 400° C Straight Sided Rectangular Tensile Specimens for BWI Process B

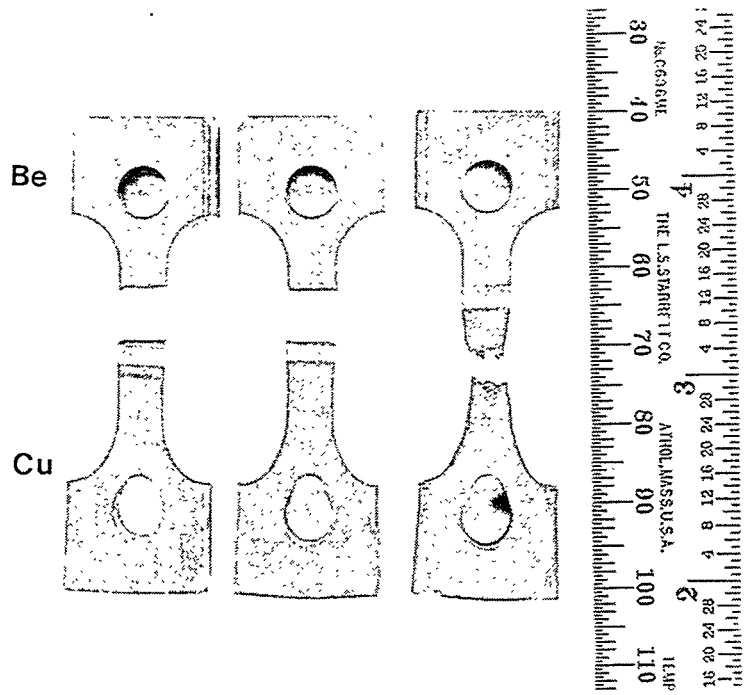

Figure 3 Comparison of Macroscopic Appearance of Room Temperature, 200°C, and 400°C Reduced Section Tensile Specimens for BWI Process A

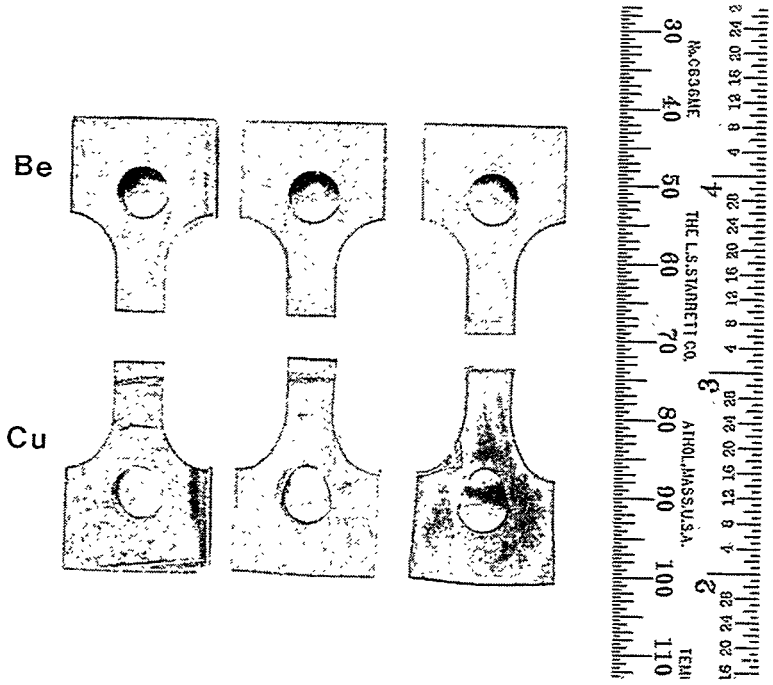

Figure 4 Comparison of Macroscopic Appearance of Room Temperature, 200°C, and 400°C Reduced Section Tensile Specimens for BWI Process B

LASER FABRICATION OF BERYLLIUM COMPONENTS

James E. Hanafee and Terry J. Ramos
Lawrence Livermore National Laboratory
7000 East Ave., P.O. Box 808
Livermore, California 94550

Working with the beryllium industry on commercial applications and using prototype parts, we have found that the use of lasers provides a high-speed, low-cost method of cutting beryllium metal, beryllium alloys, and beryllium–beryllium oxide composites. In addition, we have developed laser welding processes for commercial structural grades of beryllium that do not need a filler metal; i.e., autogenous welds were made in commercial structural grades of beryllium by using lasers.

1. INTRODUCTION

Beryllium and beryllium alloys have several properties—low atomic number, good neutron reflection capability, low density, high modulus of elasticity, high mechanical damping capacity, and high frequency resonance—that make them ideal for a variety of applications. However, fabrication of this material can be difficult, especially machining and welding operations.

Even when care is used, conventional machining can damage these hard, low-ductility beryllium and beryllium alloys and significantly impair their mechanical performance.[1] The damage is in the form of microstructural changes that take place during the machining operation, and the mechanical properties can be seriously degraded. The microstructural changes are in the form of twinning, microcracks, residual stresses, and crystallographic texture.[1] Twinning and a highly worked surface layer can be seen in Figure 1. Evidence suggests that the loss in mechanical properties are primarily due to a strain-hardened oriented surface layer, and that while twinning is the most apparent microstructural feature, it does not play a dominant role.[1] Microcracks, of course, are harmful, but they can usually be detected by nondestructive test methods, and they are also indicative that the

Figure 1. Machining damage in beryllium. Note the distorted grain morphology and twinning extending from the surface to a depth of about 100 μm (200×).

machining operation is out of control and corrective action should be taken. The decrease in mechanical properties is in the ultimate strength and ductility. Typical values are shown in Table 1.[1]

Welding this low-ductility metal and its alloys also presents problems. Conventional welding processes require use of a filler metal, i.e., a different alloy from the metal being welded. For beryllium, the most successful filler metal has been an aluminum–silicon alloy, and this process was developed over thirty years ago. Use of a filler alloy is not desirable for some applications, but autogenous welding—welding without a filler alloy—has been nearly impossible with beryllium.

We have found laser alternatives to the conventional methods of cutting and welding. Working with Brush Wellman, Inc. (BWI), on commercial applications and using prototype parts, we found that the use of lasers provides a high-speed, low-cost method of cutting beryllium metal, beryllium alloys, and beryllium–beryllium oxide composites. In a separate project with Nuclear Metals, Inc. (NMI), and Space Power, Inc. (SPI), we developed laser-welding processes for commercial structural grades of beryllium that do not need a filler metal; i.e., autogenous welds were made in commercial structural grades of beryllium by using lasers.

2. LASER-CUTTING

For unique LLNL applications, we succeeded in cutting thin, high-purity beryllium foil using lasers long ago. However, there was no effort to explore cutting other beryllium based materials at that time. With recent new needs and applications, we saw that the use of lasers might provide a solution to some unique problems in fabricating beryllium base materials. We proposed that lasers be used to cut commercial structural grades of beryllium, beryllium alloys, and a beryllium–beryllium oxide composite. The beryllium alloy was AlBeMet 162, a 62% Be–38% Al alloy from BWI, and the beryllium–beryllium oxide composite was also from BWI. Of several lasers at LLNL approved for use with beryllium, we chose two for our initial study: a 400-W pulsed neodymium:yttrium–aluminum–garnet (Nd:YAG) laser and a 1000-W continuous-wave carbon dioxide (CO_2) laser.

Both the pulsed Nd:YAG and the CO_2 laser penetrated beryllium and AlBeMet sheet. Parameters were developed that cut beryllium sheet and the AlBeMet 162 alloy sheet at thicknesses from 0.5 mm to about 2.5 mm. Table 2 shows typical laser parameters for cutting. The 0.5-mm beryllium sheet was cut at speeds up to 40 mm/s, and 2.0-mm-thick sheet was cut at speeds up to 6 mm/s. The 0.5-mm AlBeMet sheet was also cut at speeds up to 40 mm/s, and

Table 1. Tensile properties of machine-damaged beryllium.

Grade	Condition	UTS MPA (ksi)	YS MPA (ksi)	Elongation (%)	Machining damage
S200E	As-machined	263 (38)	216 (31)	0.7	100 μm deep
	Annealed	343 (50)	230 (33)	3.1	None
	Etched	342 (50)	239 (35)	3.3	None
1319	As-machined	282 (41)	277 (40)	0.7	100 μm deep
	Annealed	381 (54)	235 (34)	3.8	None
	Etched	372 (54)	270 (39)	4.0	None

the maximum cutting speed for the AlBeMet 2.0-mm-thick sheet was 4 mm/s.

Both lasers easily produced acceptable surface finishes of the cut edges (Figure 2). A generic prototype part cut from a large, 0.5-mm-thick beryllium sheet is shown in Figure 3. The part's outline and six holes were cut in 18 s. Most of this time was spent on relocating the part for cutting the holes, rather than the cutting itself. On a microscopic scale, the cut edges were acceptable, and the part easily met tolerance requirements. In laser cutting, the beam size determines the minimum radius possible, which is in the range of 25 μm for our equipment. The smallest holes in the part shown have 1.0-mm radii.

Table 2. Typical beryllium cutting development parameters with a 400-W pulsed Nd:YAG laser.

Thickness of sheet mm (in.)	Cutting speed mm/min (in./min)	Power (W)	Power density (W/mm^2)	Pulse rate (Hz)
0.5 (0.020)	1270 (50)	390	6400	100
0.5 (0.020)	1900 (75)	350	5500	200
0.5 (0.020)	2540 (100)	400	5500	150
2.0 (0.080)	250 (10)	410	6700	50
2.0 (0.080)	380 (15)	410	6700	50
6.4 (0.250)[a]	250 (10)	410	6700	50

[a] Full penetration not achieved.

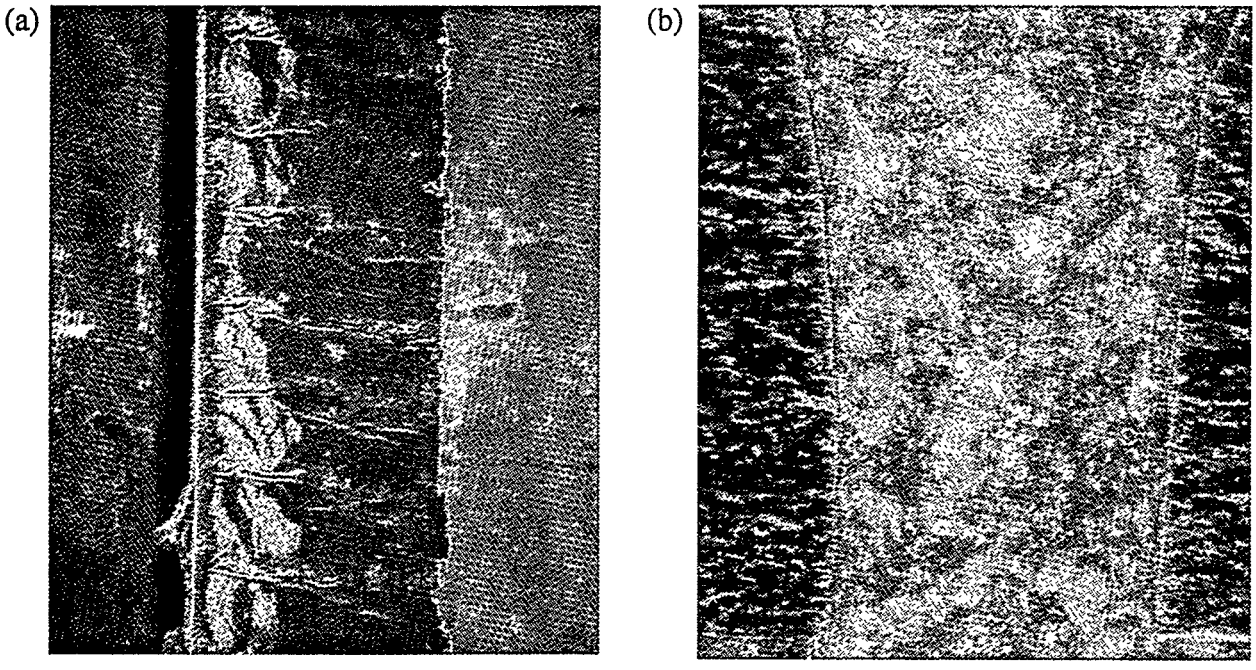

Figure 2. Edge and cross section of pulsed Nd:YAG-laser–cut beryllium sheet. (a) Edge; note evidence of individual laser pulses (60×). (b) Cross section showing grain structure on each side of the laser cut; note absence of machining damage (160×).

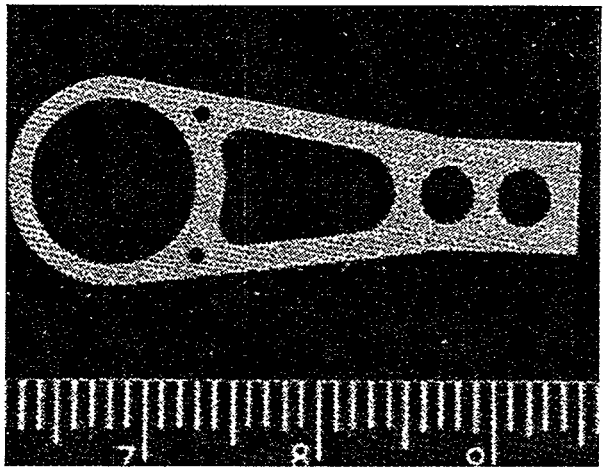

Figure 3. Generic beryllium disk-drive component cut by laser from 0.5-mm sheet in less than 20 seconds. Scale is in centimeters.

The pulsed Nd:YAG laser did not produce acceptable results in cutting the beryllium–beryllium oxide composite, while the CO_2 laser was successful. As expected, the cutting speeds were slower than for the metals, and the maximum speed achieved for the 1.6-mm-thick sheet was 4 mm/s.

There are additional advantages to laser cutting. First, the kerf is small and the parts can be laid out in a very efficient fashion on the sheet. Thus, more parts can be made from a sheet of a given size, and just as important, there is less beryllium waste for disposal. Second, there is no machining damage. This microscopic damage can harm mechanical properties and ordinarily would require additional steps to ensure that it is not a problem. For the laser-cut edges, from microscopic examination, we did not observe any machining damage. We also cut tensile specimens from the same structural beryllium sheet and, without any further treatment after the laser cutting, pulled the tensile specimens to failure. The mechanical properties easily met the mechanical properties expected for powder-origin beryllium sheet, specifically elongation to failure and ultimate strength (Table 3). This confirmed our microscopic observations of no machining damage. Third, for large-scale production, a more powerful laser can be used and the beam split to cut several parts from a sheet at the same time. Fourth, it may be useful to pipe the laser beam into a single designated room for beryllium-cutting operations. This would reduce the possible exposure of personnel to beryllium particulate and reduce the number of formal beryllium workers.

Table 3. Mechanical properties of beryllium sheet.

Condition	UTS MPA (ksi)	YS MPA (ksi)	Elongation (%)	Orientation in sheet
As-laser cut	450 (65.5)	270 (39.4)	13.9	Transverse
As-laser cut	510 (74.0)	330 (47.8)	17.4	Longitudinal
As-laser cut	485 (70.5)	355 (51.4)	20.2	45°
BW S200E spec.	480 (70)	345 (50)	10	—

3. AUTOGENOUS LASER WELDING

Autogenous welding of metals (i.e., no filler metal) is usually preferred. It is a simpler process and would result in a more homogenous part across the junction of the two pieces being welded. In addition, operating temperatures may militate against the use of a lower melting point filler metal. However, many metals and alloys do not lend themselves to autogenous welding, which is basically a complicated high-speed casting process.

The low-strength ingot grade of beryllium can be welded in an autogenous manner, and it has been welded with no filler metal for the past thirty-plus years. For specialized applications in which the welding metallurgist had freedom in the details of the weld design, we have autogenously laser welded thin sheets of ingot beryllium and, in one case, autogenously electron beam welded the structural grade of beryllium. However, generally the more useful high strength powder-origin structural beryllium grades have not been amenable to autogenous welding, with severe cracking prevalent.

Several times over the past few years, we have been asked to make or design specialized beryllium parts for satellites. The various parts have been for such applications as detection of signals from deep space or operation of the satellite. The common requirement for these parts was no foreign material; viz., no filler material in the form of a weld or braze alloy. In the past, we have responded by making very thin braze joints, usually with aluminum or an aluminum alloy. Recently, an application came to our attention in which even a thin braze line with a minimum of non-beryllium material was not satisfactory.

Through NMI, we learned that SPI needed beryllium caps joined to beryllium cylinders to encapsulate a nontoxic hydride. The cylinder would eventually be a component in a power source for a satellite, and the beryllium had to be the higher-strength structural grade. The reason for no filler metal in the weld (i.e., autogenous) was due to two requirements. First, a higher atomic weight element than beryllium would harm the performance of the unit. Second, the cylinder operating temperature was above 600°C, which is above the melting temperature of virtually all welding filler alloys for beryllium. Any filler metal would violate one or both of these requirements.

With our experience in autogenously welding beryllium, albeit very limited, we offered to try laser welding the components. We knew this would be difficult because the application was a circumferential weld, which results in substantial residual stress problems, and beryllium is a low-ductility material that is not amenable to residual stresses.

After considerable experimentation on the exact weld design and laser parameters, we were successful in autogenously welding the cap on the 25-mm-diam cylindrical component. We preferred the pulsed Nd:YAG laser; however, the CO_2 continuous-wave laser is promising. Table 4 shows typical laser parameters for welding. The typical appearance of the laser weld

Table 4. Typical beryllium welding development parameters with a 400-W pulsed Nd:YAG laser.

Thickness of sheet mm (in.)	Cutting speed mm/min (in./min)	Power (W)	Power density (W/mm^2)	Pulse rate (Hz)	Comments
0.35 (0.014)	200 (8)	210	260	10	Good weld
0.30 (0.012)	200 (8)	170	210	10	Poor weld
0.30 (0.012)	200 (8)	135	165	10	Poor weld
0.25 (0.010)	200 (8)	95	115	10	Poor weld

fusion zone is shown in Figure 4. The approach is, in a sense, the opposite of the laser cutting. For the welding, a small amount of energy, gently applied, is necessary to avoid high residual stresses, especially at the weld start and stop. Laser welding does have the advantage that, compared to electron beam welding, the depth of the weld can be more precisely controlled. The individual ridges on the fusion zone reflect the individual laser pulses. There is some columnar epitaxial grain growth in the fusion zone (Figure 4). This is not desired, and we believe we can improve upon the microstructure with refinement of the welding parameters and slightly modifying the weld design.

The sealed cylinder containing the hydride was delivered to SPI, and they reported that the cylinder provided excellent results and there was no leaking above 600°C. This is the first successful application of autogenous laser welding of structural grades of beryllium.

4. SUMMARY

Lasers can be used to cut components to size from beryllium sheet, beryllium alloy sheet, and beryllium–beryllium oxide composite sheet. The cutting can be done at high speeds with tight tolerances and small radii without introducing machining damage. The small size of the laser beam and the use of CNC machines result in high material efficiencies. Lasers can be used to autogenously weld commercial structural grades of beryllium.

ACKNOWLEDGMENTS

The authors are indebted to Calvin D. Anglin and Jim A. Butler for their guidance on laser parameters and operation of the lasers. This work was performed under the auspices of the U.S. Department of Energy by the Lawrence Livermore National Laboratory under Contract No. W-7405-Eng-48.

REFERENCES

1. James E. Hanafee, *J. Appl. Metalworking* **1**, 41 (1980).

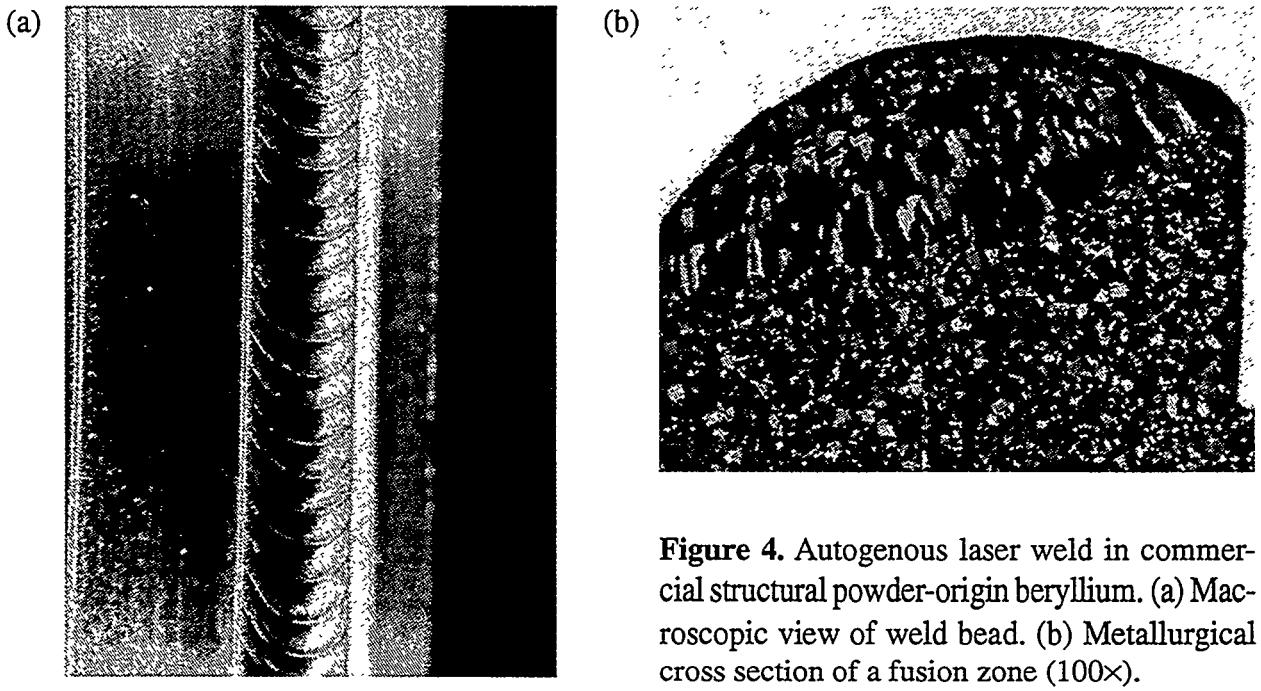

Figure 4. Autogenous laser weld in commercial structural powder-origin beryllium. (a) Macroscopic view of weld bead. (b) Metallurgical cross section of a fusion zone (100×).

Reactivity test between beryllium and copper

H.Kawamura[a] and M.Kato[b]

[a] *Japan Atomic Energy Research Institute, Oarai Research Establishment, Oarai-machi, Higashi Ibaraki-gun, Ibaraki-ken 311-13, Japan*

[b] *NGK INSULATORS,LTD.,1 Maegata-cho, Handa-city, Aichi-ken 475, Japan*

ABSTRACT

Beryllium has been expected for using as plasma facing material on ITER. And, copper alloy has been proposed as heat sink material behind plasma facing components. Therefore, both materials must be joined. However, the elementary process of reaction between beryllium and copper alloy does not clear in detail. For example, other authers reported that beryllium reacted with copper at high temperature, but it was not obvious about the generation of reaction products and increasing of the reaction layer.

In the present work, from this point, for clarifying the elementary process of reaction between beryllium and copper, the out-of-pile compatibility tests were conducted with diffusion couples of beryllium and copper which were inserted in the capsule filled with high purity helium gas (6N). Annealing temperatures were 300, 400, 500, 600 and 700°C, and annealing periods were 100, 300 and 1000h. Beryllium specimens were hot pressed beryllium, and copper specimens were OFC(Oxygen Free Copper) .

1.INTRODUCTION

Beryllium has been indispensable for the fusion reactor material particularly. For example, beryllium has been considered as plasma facing material in the first wall and divertor (plasma facing components) against plasma. On the other hand, copper alloy has been proposed as heat sink material behind plasma facing components. In those using, they will be joined by some kinds of methods, for example, diffusion bonding, brazing and so on. However, disregarding their bonding methods, their materials will be heated at high temperature under the condition of fusion reactor designing. So in the present work, we noted on the chemical interaction between beryllium and copper under the high temperature condition.

As for the interaction between beryllium and copper, Vickers et al.[1] conducted on the diffusion couple test at the temperature of 600°C for 2000h under vacuum atmosphere. As the results, they reported that a few layers were formed on copper side, and identified BeCu and Be2Cu as the reaction products. Baird et al.[2] reported that they reacted from the temperature of 500°C, and the reaction layer was 18μm after annealing at 500°C for 29 days. From the results of Monroe et al.[3], in the condition of annealing at 760°C for 4h, beryllium diffused into copper side remarkably, and both of them were bonded. Recently, V.R.Barabash et al.[4] conducted on diffusion bonding test in the condition at the temperature from 800°C to 850°C for about 5 minutes. From the results, they reported that diffusion bonding could be probably used. Then the reaction layers were consisted of a few layers.

From these reports, though it was cleared that the interaction between beryllium and copper took place above 500°C, they were never clarifying about the generation of reaction products and increasing of the reaction layer. Therefore, for clarifying the elementary process of reaction between beryllium and copper, we conducted the out-of-

pile compatibility tests with diffusion couples of beryllium and copper which were inserted in the capsule filled with high purity helium gas (6N). Annealing temperatures were 300, 400, 500, 600 and 700°C, and annealing periods were 100, 300 and 1000h. Beryllium specimens were hot pressed beryllium, and copper specimens were OFC (Oxygen Free Copper).

2.EXPERIMENT

2.1.Specimens

2.1.1.Beryllium

The beryllium specimens were hot-pressed beryllium disks made by NGK INSULATORS, LTD.. The specimen dimensions were 10.0 mm diameter and 1.0 mm thickness. The purity of the beryllium specimens was almost 99wt.%. The results of a chemical analysis of the beryllium specimens are shown in Table 1. The main impurity of the beryllium specimens was beryllium oxide. Hot-pressed beryllium was wrapped with mild steel(SS41), rolled at 900°C, annealed at high temperature, and then polished until shining condition by $\phi 1\mu m$ diamond on buff cloth. Cleaning of the beryllium specimens was done by ultrasonic washing with acetone.

2.1.2.Copper

The copper specimens were OFC (Oxygen Free Copper) disks. The specimen dimensions were 10.0 mm diameter and 1.0 mm thickness. The purity of the copper specimens was 99.99wt.%. The copper specimens were also polished and cleaned by the same method as beryllium one.

2.2.Procedure

The outline of the capsule is shown in Fig.1. A diffusion couple of beryllium and copper disks was inserted into the capsule made of Zry-2. Then, after filling the capsule with high purity helium gas(6N purity), the capsule was sealed by TIG welding. The diffusion couple was pressed down by tungsten spring to maintain the constant pressure(32.4 N/contacting area) at the interface. The helium leak test was carried out on the assembled capsule, and the leakage rate was less than $1.0 \times 10^{-9} Pa \cdot m^3/s$. The capsules were annealed in the electric furnace. The annealing conditions were 100, 300 and 1000h at the temperatures of 300, 400, 500, 600 and 700°C. After annealing, the interactions between beryllium and copper was evaluated.

As for the evaluation, the thickness of reaction layer was investigated by optical microscope and SEM. Then, the reaction products(phase's formation) on beryllium and copper surfaces were identified by EPMA(Electron Probe Micro Analyzer). Here, accelerating voltage was 15kV, and electron beam diameter was about $\phi 1\mu m$.

3.RESULTS

3.1.Observation of the specimen cross-section

It was observed by SEM that reaction layer formed above 400°C by the interaction between beryllium and copper, and both of them was bonded absolutely above 400°C. Then, the degree of the reaction was remarkable at 700°C. Concerning all reaction layers, there was a micro-line at the center of the reaction layer, and there was brittle area near the beryllium side. Concerning the former, it was considered as the initial contacting interface between beryllium and copper.

3.2.Identification of reaction products

We used quantitative analysis by EPMA not structural characterization by X-ray diffraction as the method of identifying of reaction products(phase's formation) in the reaction layer, because the analysis at the point as small as possible was needed in this test.

SEM photograph of the reaction layer formed between beryllium and OFC after annealing at 600°C for 1000h is shown in Fig.2. From this photograph, the reaction layer consisted of two layers, one was a thin layer(about 10μm), and another layer was much more thick than that. Then, Table 2 shows the result of quantitative point analysis on it. From this result, it appeared that Be2Cu phase was formed at (2), and BeCu phase was formed at (3) and (4).

The result of quantitative analysis across the reaction layer formed between beryllium and OFC after annealing at 700°C for 100h was shown in Fig.3. From this result, Be-Cu(ß) phase whose concentration was almost constant was formed at 700°C in addition to Be2Cu phase and BeCu phase, because the atomic concentration was corresponded to Be-Cu(ß) phase as shown in [5]. And, the plot of Be-Cu(ß) phase concentration was a little scattering, that is, it was considered to transform into BeCu phase and Cu phase by the reason why it was cooled slowly.

4.DISCUSSIONS

4.1.Formation of reaction layer

Changes of the thickness of total reaction layer with annealing temperature for 300h was shown in Fig.4. Reaction layer formed above 400°C, and it consisted of two layers, that is, Be2Cu phase and BeCu phase until 600°C. In this case, the thickness of total reaction layer increased with increasing of annealing temperature.

And additionally, very thick Be-Cu(ß) phase formed at 700°C as shown in Fig.3.

By the way, reaction layer formed by the interaction between beryllium and copper consisted of a few layers whose concentrations were almost constant by SEM and quantitative analysis. The condition of the total reaction layer consisted of each layer was as follows,

(a)Total thickness = Be2Cu phase(about 10μm) + BeCu phase(main)
(400°C≤T≤600°C)

(b)Total thickness = Be2Cu phase(about 10μm) + BeCu phase+Be-Cu(ß) phase(main)
(T>600-700°C)

4.2.The behavior concerning increasing of reaction layer

It was discussed about the behavior concerning increasing of BeCu phase except for Be2Cu phase and Be-Cu(ß) phase.

At first, because the nonreacted diffusion area was not observed, it was considered that beryllium reacted with BeCu phase immediately at Cu/BeCu interface and copper also did the same at Be/BeCu interface. Therefore, the reaction site would be determined at BeCu phase interface. So, the process of increasing of BeCu phase was supposed to be controlled by mass transfer, that is, diffusion of beryllium and copper in BeCu phase.

From the steady-state diffusion of beryllium and copper through BeCu phase after reacting at the initial interface was as follows, concerning for beryllium,

$$J_{Be}=-D_{Be}(dC_{Be}/dX_{Be}) \quad (mol/mm^2\cdot s) \quad (1)$$

Here, J_{Be} is the flux of beryllium to copper side(mol/mm^2·s), D_{Be} is the diffusion constant in BeCu phase(mm^2/s), C_{Be} is the concentration(mol/mm^3) and X_{Be} is the diffusion distance(mm). The next equation was introduced from (1).

$$\Omega(1/A)(dX_{Be}/dt)=-D_{Be}(dC_{Be}/dX_{Be}) \quad (2)$$

Here, Ω is the constant(mol/mm), A is the reaction area(mm^2) and t is the time(sec).

So, because of steady-state, if it was supposed that the difference of beryllium concentration between Cu/BeCu phase interface and Be/BeCu phase interface was constant, gradient of the concentration was introduced to $dC_{Be}/dX_{Be}=\Delta C_{Be}/X_{Be}$. When it was substituted this for (2), as follows,

$$dX_{Be}/dt=-(A\cdot D_{Be}/\Omega)(\Delta C_{Be}/X_{Be})=-k_{Be}/X_{Be} \quad (3)$$

Here, k_{Be} is the diffusion rate constant of beryllium(mm^2/sec). From the initial condition of t=0(sec) and X_{Be}=0(mm),

$$X_{Be}=-k_{Be'}\cdot t^{1/2} \quad (4)$$

From equation (4), the case of copper was the same as,

$$X_{Cu}=k_{Cu'}\cdot t^{1/2} \quad (5)$$

From these relations, the equation (6) was introduced as the total diffusion distance,

$$X=X_{Be}+(-X_{Cu})=-(k_{Be'}+k_{Cu'})\cdot t^{1/2}=-k\cdot t^{1/2} \quad (6)$$

Here, k is the total rate constant(mm/sec$^{1/2}$). In this present, change of electrical and chemical potential between beryllium and copper in BeCu phase was ignored as almost constant, however, BeCu phase might be the form of $Be_{1-x}Cu_{1+x}$ or $Be_{1+x}Cu_{1-x}$ with fine structural change. Therefore, the only driving force of diffusion which was generated between interfaces was taken into consideration.

Change of the thickness of BeCu phase until 600°C with annealing time was shown in Fig.5. From this figure, because change of the thickness was linear relation against a square root of annealing time, the equation (6) was appropriate to this result.

Then, the relation between the total rate constant(k) and annealing temperature(1/T) for 300h was shown in Fig.6. From this figure, because the total rate constant(k) was linear to annealing temperature(1/T), it appeared that the apparent activation energy as for the formation of BeCu phase was calculated as 66300(J/mol). And, the total rate constant(k) was as follows,

$$k=0.588\exp(-66300/RT) \quad R:8.314(J/mol/K) \quad (7)$$

From (6) and (7), the thickness of BeCu phase could be expressed such as (8).

$$X=\{0.588\exp(-66300/RT)\}\cdot t^{1/2} \quad (8)$$

Here, X is the thickness of BeCu phase(mm), R is the constant of 8.314(J/mol/K), T is the temperature(K) and t is the time(sec).

5.CONCLUSIONS

We investigated the interaction between beryllium and copper (OFC), which were promising as fusion reactor material. The summary obtained by this test was as follows;

(1)The reaction layer which consisted of two layers (Be_2Cu phase and BeCu phase) formed above 400°C, and additionally, very thick Be-Cu(ß) phase formed at 700°C.

(2)The thickness of BeCu phase was linear to a square root of annealing time. Therefore, it appeared that the behavior concerning increasing of BeCu phase was controlled by mass transfer, that is, diffusion of beryllium and copper. And, the apparent activation energy as for the formation of BeCu phase was calculated as 66300(J/mol), then the thickness of BeCu phase could be expressed such as $X(mm)=\{0.588\exp(-66300/RT)\}\cdot t^{1/2}$, R:8.314(J/mol/K), T:(K), t:(sec).

ACKNOWLEDGMENTS

The authors express their sincere thanks to Mr.K.Nishida, director in the New Metals Division Metals Business Group in NGK INSULATORS, LTD.. Also, they are thankful to Mr.T.Kikuchi in the Mechanical Engineering Division of JAERI.

REFERENCES

1. W.Vickers et al., "The compatibility of beryllium with various reactor materials" , Proc.Int.Conf.on the metallurgy of beryllium, institute of metals monogragh and report series, No.28,335-349(1961).
2. Baird,J.D. et al., "Proceedings of the Second United Nations Conference on the Peaceful Uses of Atomic Energy, Geneva" , 24,(1958).
3. Monroe, R.E., Martin, D.C. and Voldrich,C.B., "U.S.Atom.En.Comm." , Rep.No. BMI-836,(1953).
4. V.R.Barabash, L.S.Gitarsky et al., "Beryllium-metals joints for application in the plasma-facing components" J. Nucl. Mater., 212-215, 1604-1607(1994).
5. H.Okamoto and L.Tanner, "Phase diagrams of binary beryllium alloys" , ASM International, Be , 60-76(1987).

Table 1 Chemical component of beryllium specimen

Element	Analysis value(wt.%)
Be	99.0
BeO	1.04
C	0.083
N	0.0045
Al	0.053
Fe	0.072
Mg	0.035
Si	0.022
Mn	0.008
Cr	0.008
Ni	0.005
Ca	0.014
Cu	0.005

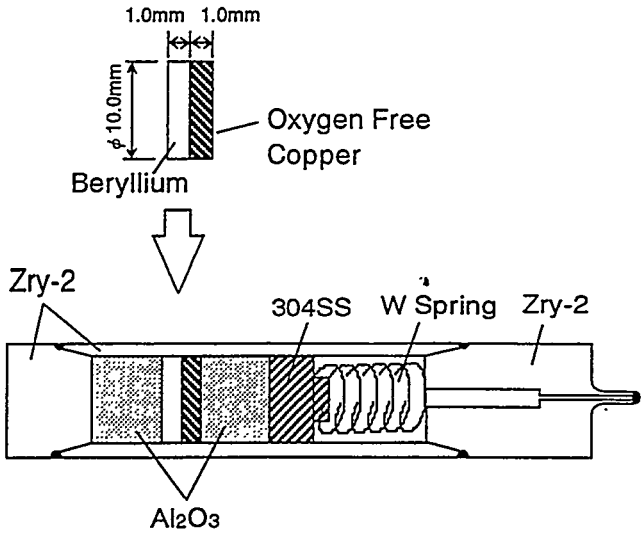

Fig.1 Outline of the capsule

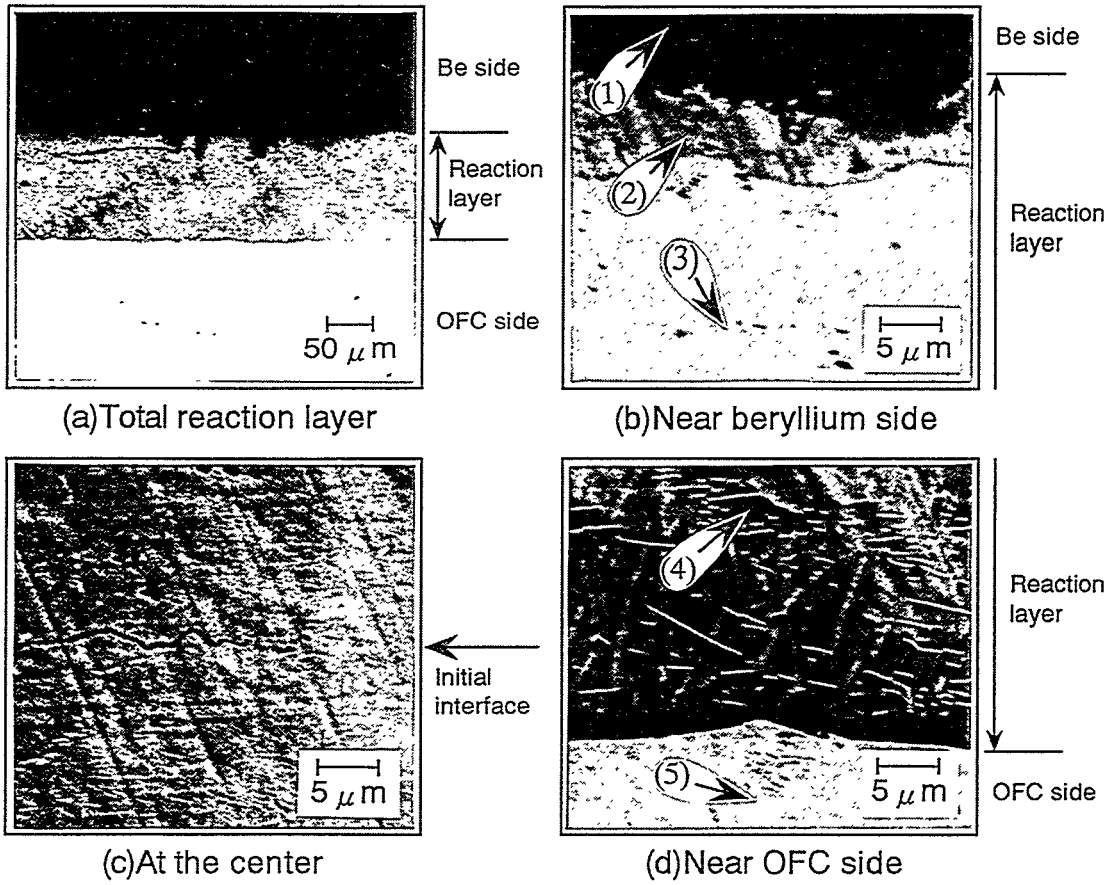

Fig.2 SEM photograph in the reaction layer formed between beryllium and OFC (600℃-1000h).

Table 2 The results of quantitative point analysis in the reaction layer formed between beryllium and OFC (600℃-1000h).
((1)-(5) : see Fig.2)

Position		(1)	(2)	(3)	(4)	(5)
Concentration (at%)	Be	99.9	73.8	50.7	41.5	0
	Cu	0	26.2	49.3	58.5	99.9
Atomic Ratio(Be/Cu)		—	2.82	1.03	0.71	—

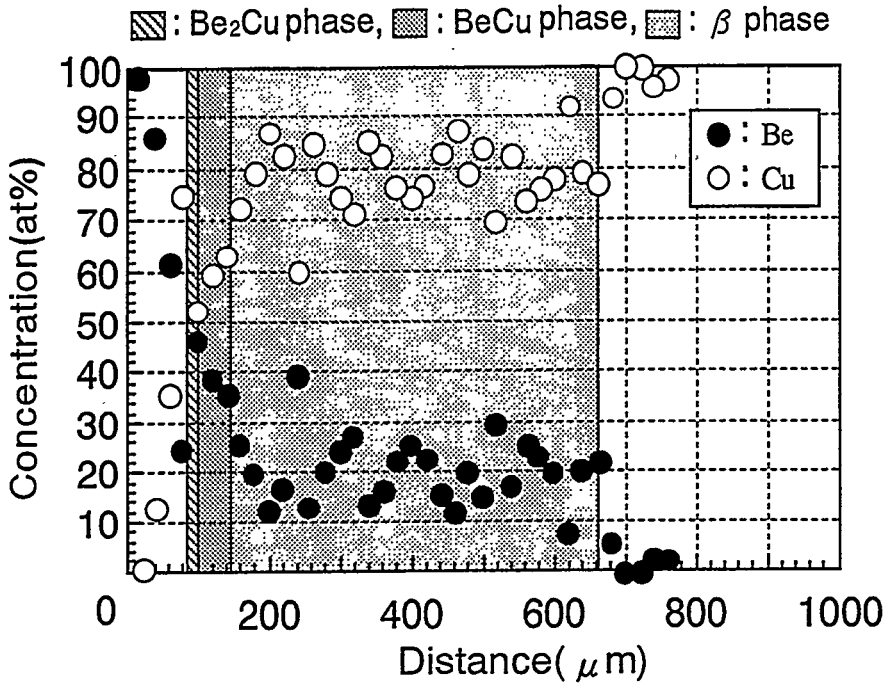

Fig.3 The results of quantitative analysis in the reaction layer formed between beryllium and OFC (700℃-100h).

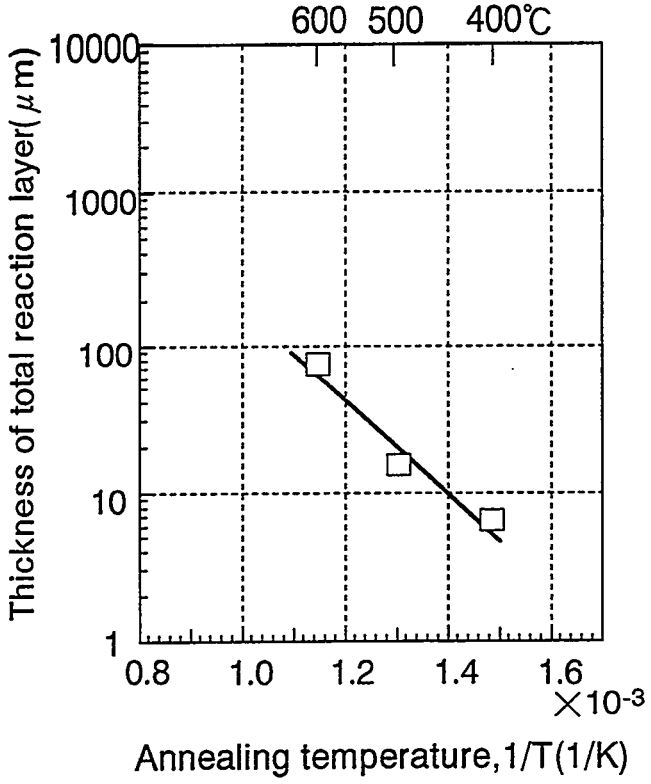

Fig.4 Changes of the thickness of total reaction layer with annealing temperature for 300h.

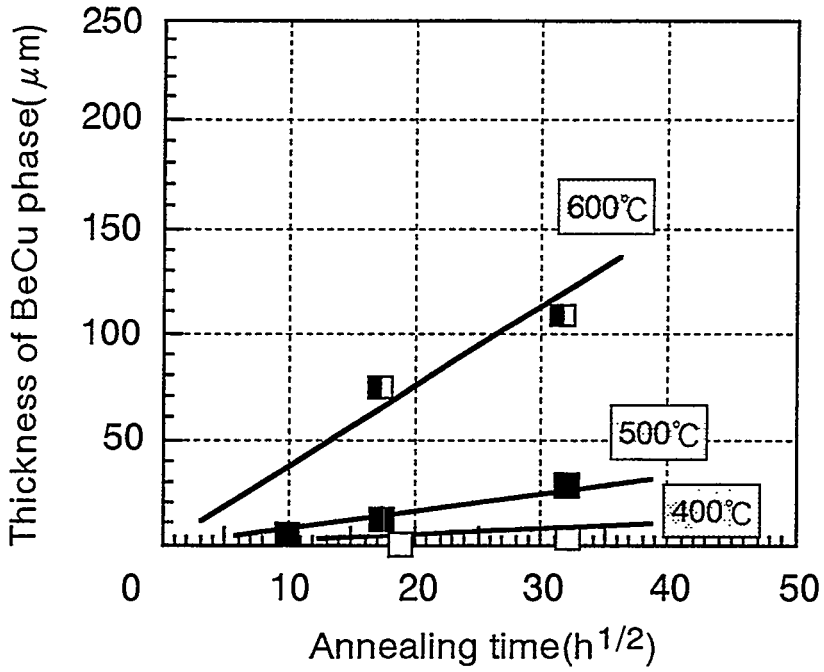

Fig.5 Changes of the thickness of BeCu phase until 600℃ with annealing time.

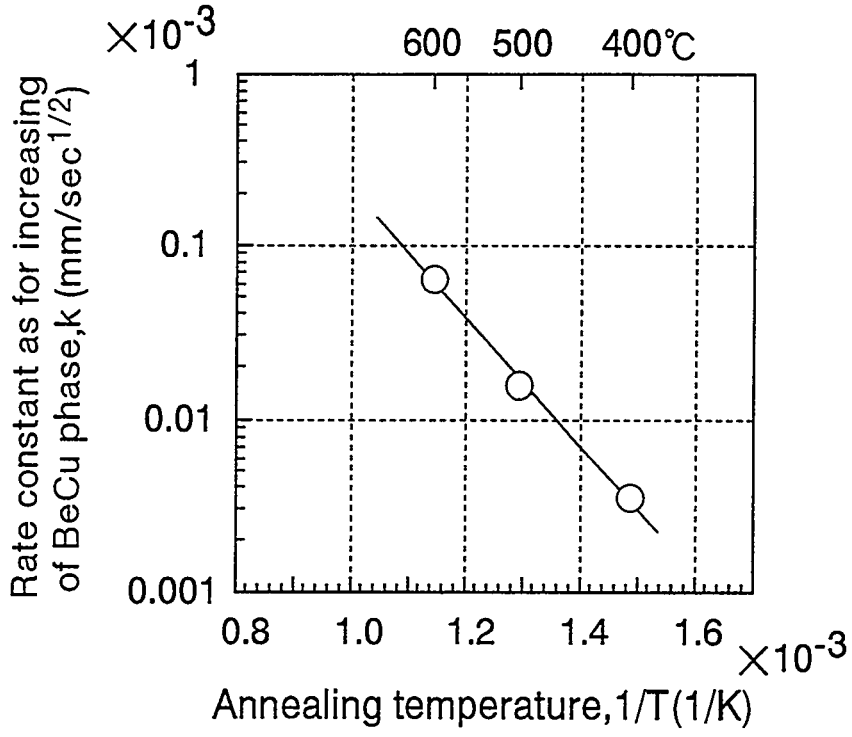

Fig.6 Rate constant as for increasing of BeCu phase(k) with annealing temperature (1/T) for 300h.

PRELIMINARY RESULTS FOR EXPLOSION BONDING OF BERYLLIUM TO COPPER

DONALD J. BUTLER, DAVID E. DOMBROWSKI[+]

Northwest Technical Industries, Inc., 2249 Diamond Point Road, Sequim, WA 98382
[+]Brush Wellman, Inc., 17876 St. Clair Avenue, Cleveland, OH 44110

This program was undertaken to determine if explosive bonding is a viable technique for joining beryllium to copper substrates. The effort was a cursory attempt at trying to solve some of the problems associated with explosive bonding beryllium and should not be considered a comprehensive research effort. There are two issues that this program addressed. Can beryllium be explosive bonded to copper substrates and can the bonding take place without shattering the beryllium? Thirteen different explosive bonding iterations were completed using various thicknesses of beryllium that were manufactured with three different techniques.

Introduction

There has been some apparent success bonding the beryllium to copper, but no mechanical testing of the joint has been completed to confirm the bond strength.

The explosive bonding effort was undertaken by NTI using internal R & D funds. Beryllium, Hycon 3 HP™ copper alloy and metallographic analysis were donated by Brush Wellman. Lawrence Livermore National Laboratory (LLNL) also supplied some beryllium sheet and metallographic analysis funded through a small business technology transfer program.

Materials

LLNL furnished three pieces of 1.3 mm x 76 mm x 152 mm(0.050" x 3" x 6") electrolytically refined beryllium which had been cold isostatically pressed, HIPed then cold rolled. Brush Wellman supplied the following materials:

3 pcs	SR-200E beryllium	1 mm x 76 mm x 152 mm(0.040" x 3" x 6")
3 pcs	SR-200E beryllium	5.1 mm x 76 mm x 152 mm(0.200" x 3" x 6")
4 pcs	S-65C beryllium	5.1 mm x 76 mm x 152 mm(0.200" x 3" x 6")
4 pcs	Hycon 3 HP™ copper	6.4 mm x 76 mm x 152 mm(0.250" x 3" x 6".)

NTI supplied 110 copper alloy for the iterations which did not use Hycon 3 HP™ copper.

Note that there is a significant difference in properties between rolled beryllium sheet (SR-200E and LLNL sheet) and S-65C grade vacuum hot pressed slabs. The rolled sheet has great (>10% elongation) in plane ductility and essentially zero through thickness ductility. Vacuum hot

pressed S-65C can have up to 3% elongation in orthogonal orientations.

Process

All of the bonding work completed during this effort used the explosive bonding process. Explosive bonding is a unique process that takes advantage of the dynamic energy created during an explosive event. This process can metallurgically join similar or dissimilar metals and is considered a solid state bonding process that uses controlled explosive energy to force two or more metals together at high pressures (Fig. 1). During the bonding event, the clad metal is accelerated by the explosive into the base metal. Several atomic layers on the surface of each metal become plasma due to the high velocity impact (200-500 m/s). The collision angle forces the plasma to jet in front of the collision front effectively scrub-cleaning both surfaces that leaves virgin metal on the surface. The remaining thickness of each metal remains near ambient temperature and acts as a huge heat sink. Therefore, the bond line is an abrupt transition from the clad metal to the base metal with virtually no degradation of their initial physical and mechanical properties.

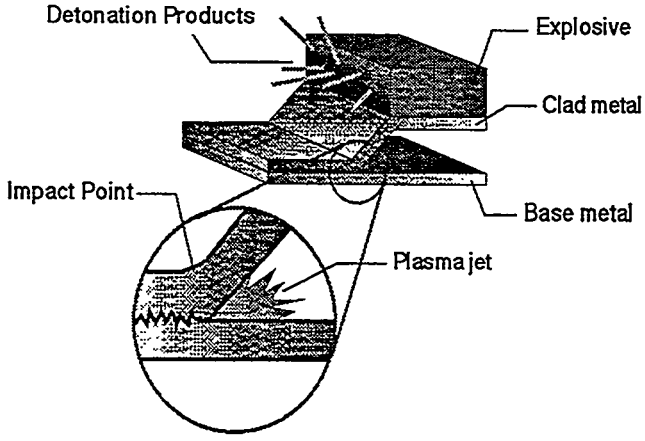

Figure 1: Explosion Bonding During Mid-Event

A multitude of variables can be adjusted.

a) Stand off gap between materials to be bonded
b) Detonation velocity of the explosive c) Density of the explosive
d) Depth of the explosive charge
e) Thickness of the materials to be bonded
f) Temperature of the materials to be bonded
g) Which material is accelerated by the explosive
h) Manufacturing technique of the beryllium

Results

In all of the iterations, the beryllium developed some cracks. In most cases there is apparent bonding between the copper and beryllium. Mechanical tests of the joints have not been performed. NTI does not have the capabilities to perform mechanical testing of beryllium. Metallographic analysis of several of the pieces was performed by LLNL and Brush Wellman.

Figure 2 is a photograph of a sample (traveler #2145) analyzed by LLNL. The beryllium is 1 mm(0.040") thick SR-200E and was furnished by Brush Wellman. The sample was sectioned in three locations marked 1, 2, and 3 in figure 2. Figures 3, 4, and 5 show the bond line at each location. No Be-Cu intermetallic phases were detected through optical microscopy. There was no indication of bond line separation at any location. Cracking was observed in the beryllium. The analysis indicates all cracks were perpendicular to the plane of the sheet,

and 5 show the bond line at each location. No Be-Cu intermetallic phases were detected through optical microscopy. There was no indication of bond line separation at any location. Cracking was observed in the beryllium. The analysis indicates all cracks were perpendicular to the plane of the sheet, with one minor exception. One minor crack (figure 2) was detected parallel to the plane of the sheet. A high density of shear bands was in the beryllium sheet.

Brush Wellman performed metallographic examination of two samples (#2213 and #2216). These samples were fabricated using Brush Wellman's 5.1 mm(0.200") thick SR-200E beryllium rolled sheet.

Sample #2216 was successfully bonded, but cracking was observed in the beryllium. The sample was analyzed in three locations using bright field optical microscopy, secondary electron imaging (SEI), back scattered electron images (BEI) and energy dispersive x-ray analysis (EDS).

The optical microscopy in all three locations showed that a low amplitude wave pattern developed during the bonding event. SEI and BEI analysis showed evidence of intermetallic formation at the bond line near the leading end of the sample. The leading end (LE) is the end of the sample nearest to the detonation point of the explosive. Figures 7, 8, and 9 show the optical microscopy, SEI and BEI photographs from the leading end. Only one intermetallic phase was found. EDS was used to determine the elements in the intermetallic. The intermetallic contains iron and copper and possibly beryllium. Due to beryllium's low atomic number most EDS systems can not detect beryllium. The other two locations showed no evidence of intermetallic formation. Figures 10, 11 and 12 show the optical microscopy, SEI and BEI photographs from the center of the sample. All locations showed that the cracks in the beryllium were perpendicular to the bond line. No cracks were noted parallel to the bond line. The analysis showed that the beryllium and copper were bonded to the edge of the cracks.

The iron intermetallic would not be typical of production scale material. The beryllium on sample #2216 was framed with steel bar during the bonding event. Debris from the steel bar entered the joint during the bonding event. This is not uncommon during explosive bonding near the detonation point. In a production environment extra steps are taken to block the debris from entering the interface between the materials. The other two locations are more representative of a bond generated during a production cycle. Be-Cu intermetallics can be very brittle and would adversely effect the bond strength. The fact that no intermetallics are present in these two locations is very encouraging.

One extreme case was examined to determine the general failure mechanism of the beryllium. Sample #2213 was an unsuccessful trial in which massive cracking of the beryllium was observed and the beryllium did not bond to the copper. Figure 13 shows the badly cracked beryllium. Figure 14 shows an edge with a shear lip. The shear lip indicates primary fracture. The uniform thickness of the shear lip indicates that the crack initiated on one

side of the sheet and propagated through the thickness of the sheet. This is consistent with bending fracture. The surfaces of the fractures are typical for fractured beryllium. Figure 15 is an SEI of a fractured surface. This information should be useful in selecting the best beryllium grade for future work.

The explosive bonding iterations between the S-65C beryllium and Hycon 3 HP™ copper were completed just prior to publication. The analysis of this material has not been completed.

Summary

This very limited number of tests showed that a continuous, intermetallic free bond can be formed between beryllium and copper by explosive bonding. This demonstrates the basic feasibility of the approach. The primary problem was formation of cracks in the beryllium perpendicular to the bonding interface. However, techniques were developed to reduce this cracking. Comparison of the number of cracks in sample #2145 (one of the first iterations) and sample #2216 (one of the last iterations) show a significant difference. Since this very limited number of tests did not optimize the process variables, there is potential for further improvement.

Recommendations

Explosive bonding has more process variables than could be adequately addressed in this small number of tests, and a more comprehensive test matrix is needed. The size of the test matrix can be minimized by holding some variables constant. It is recommended that beryllium thickness, grade, and manufacturing method be held constant. The copper alloy should also be held constant. The matrix should include bond strength determination by shear or tensile methods because the only measure of bond quality in the present investigation was metallographic examination.

References

1. D. E. Dombrowski, Brush Wellman, letter to NTI, March 28, 1995

2. J. E. Hanafee, Lawrence Livermore National Laboratory, letter to NTI, October 12, 1994

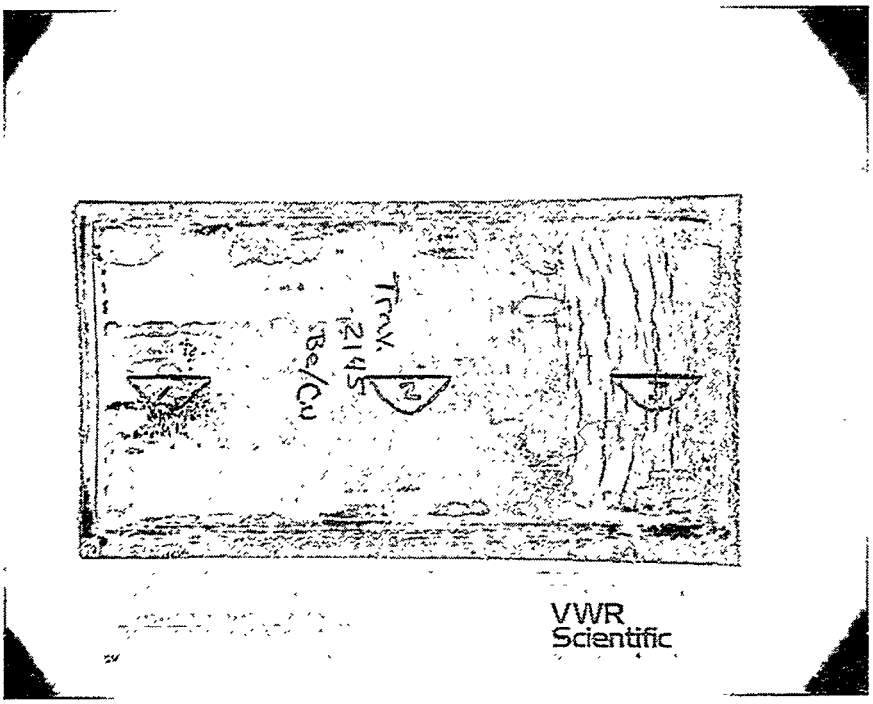

Figure 2 - As bonded beryllium surface, traveler #2145.

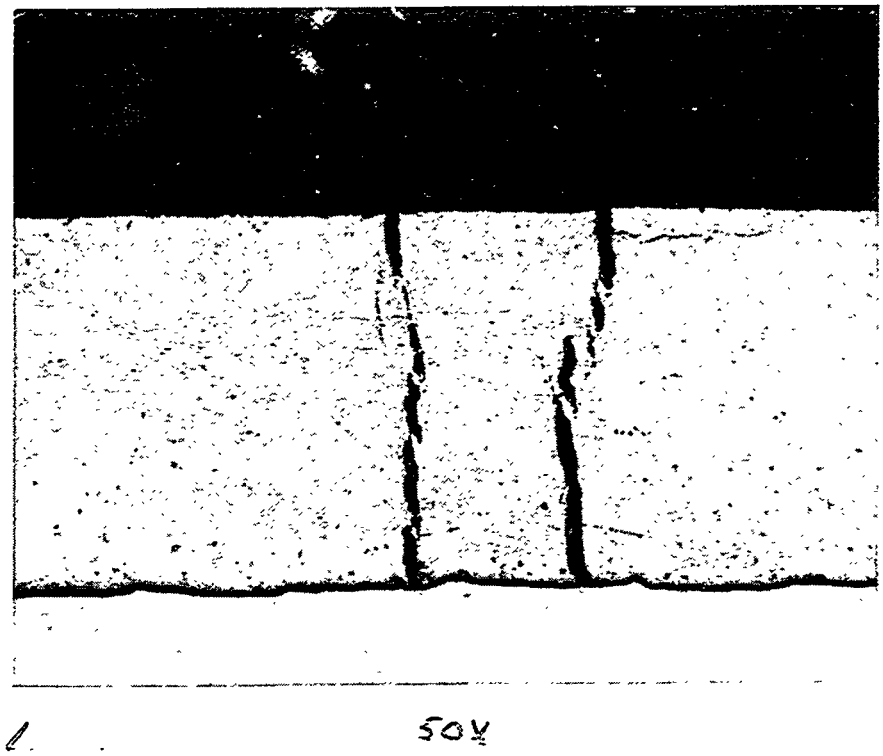

Figure 3 - Be/CU bond line at location 1, traveler #2145. 50x.

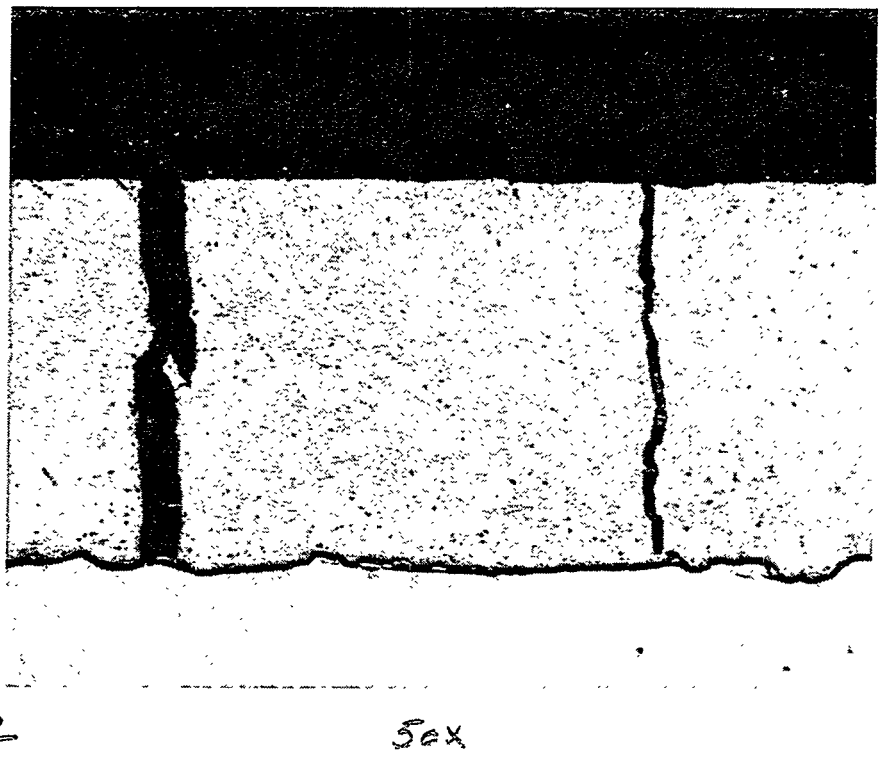

Figure 4 - Be/Cu bond line at location 2, traveler #2145. 50x.

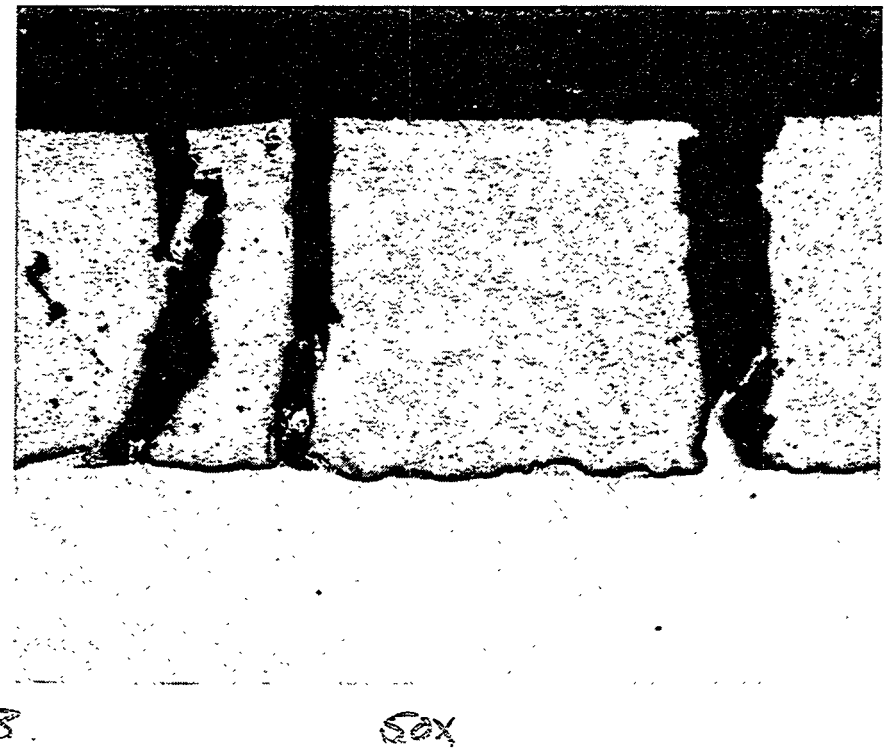

Figure 5 - Be/Cu bond line at location 3, traveler #2145. 50x.

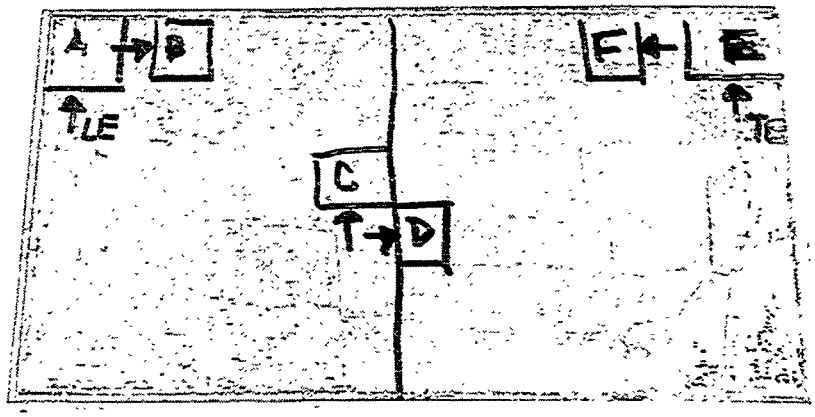

Figure 6 - Photograph of the as bonded beryllium surface, traveler #2216

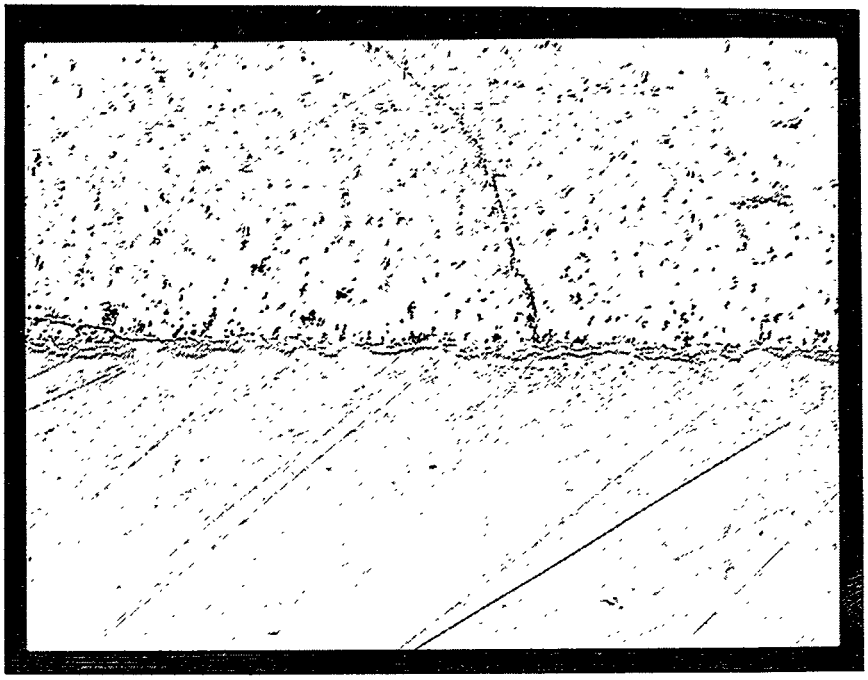

Figure 7 - Nomarski Interference photograph of the Be/Cu interface from traveler #2216. This photograph is from the leading end of the sample. The top pitted phase is Be. The lower phase is copper. 50x.

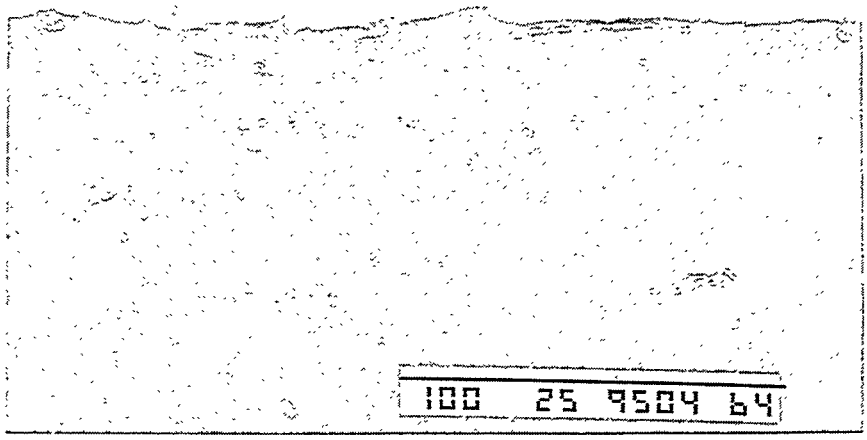

Figure 8 - SEI of the Be/Cu interface of the leading end of traveler #2216. The lighter gray phase in the upper half is copper. The dark gray phase is Be. The medium gray phase on the bond line contains Fe and Cu intermetallics. 500x.

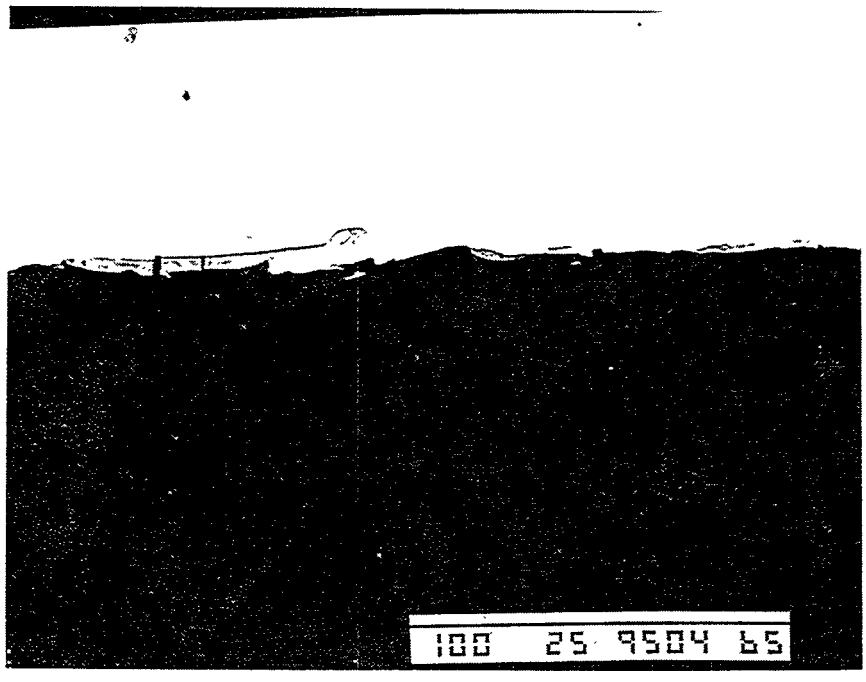

Figure 9 - BEI of the Be/Cu interface of the leading end of traveler #2216. The light phase in the upper half is copper. The dark phase is Be. The gray phase on the bond line contains Fe and Cu intermetallics. 500x.

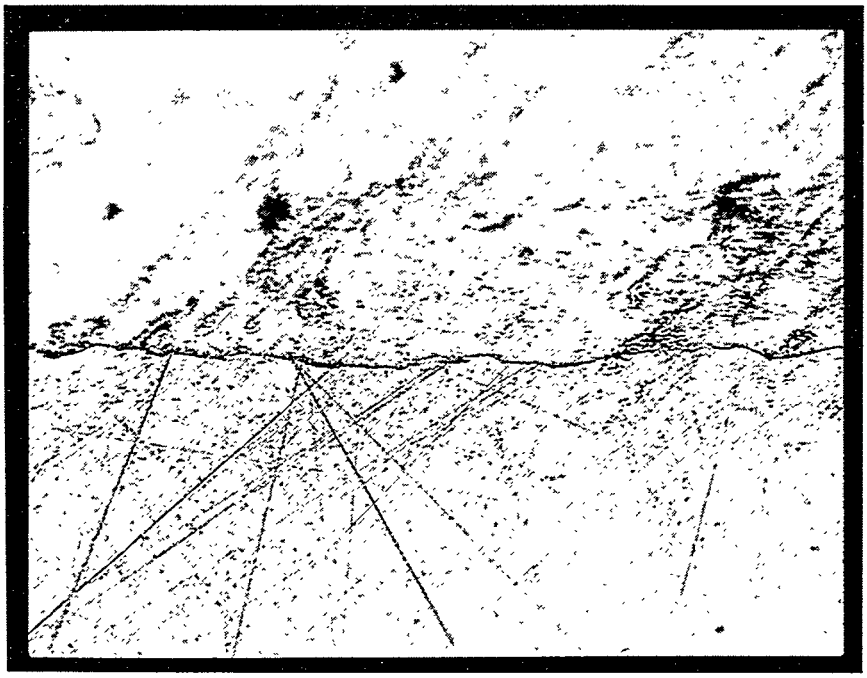

Figure 10 - Nomarski Interference photograph of the Be/Cu interface from traveler #2216. This photograph is from the trailing end of the sample. The top pitted phase is Be. The lower phase is copper. 500x.

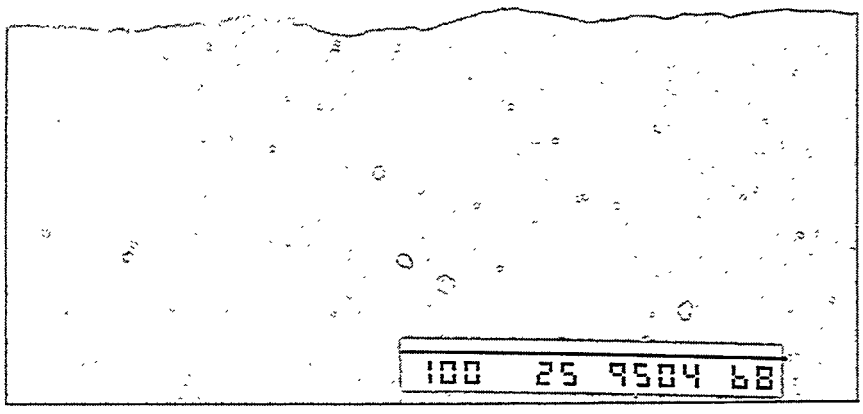

Figure 11 - SEI of the Be/Cu interface of the center of traveler #2216. The lighter gray phase in the upper half is copper. The dark gray phase is Be. 500x.

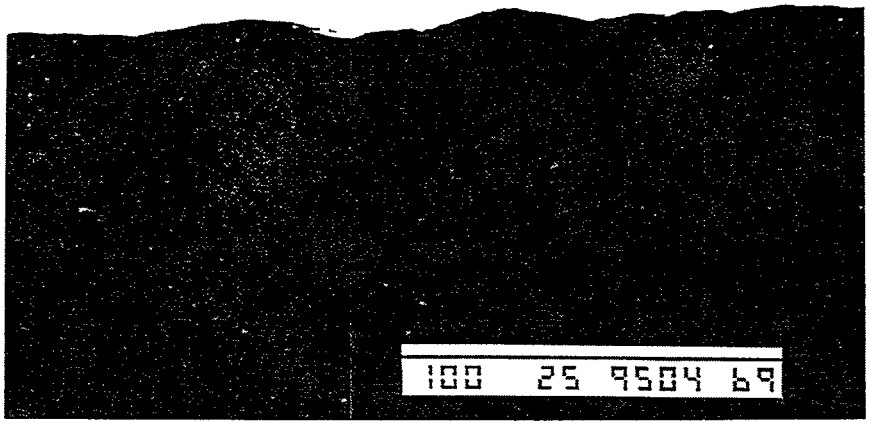

Figure 12 - BEI of the Be/Cu interface of the center of traveler #2216. The light phase in the upper half is copper. The dark phase is Be. 500x.

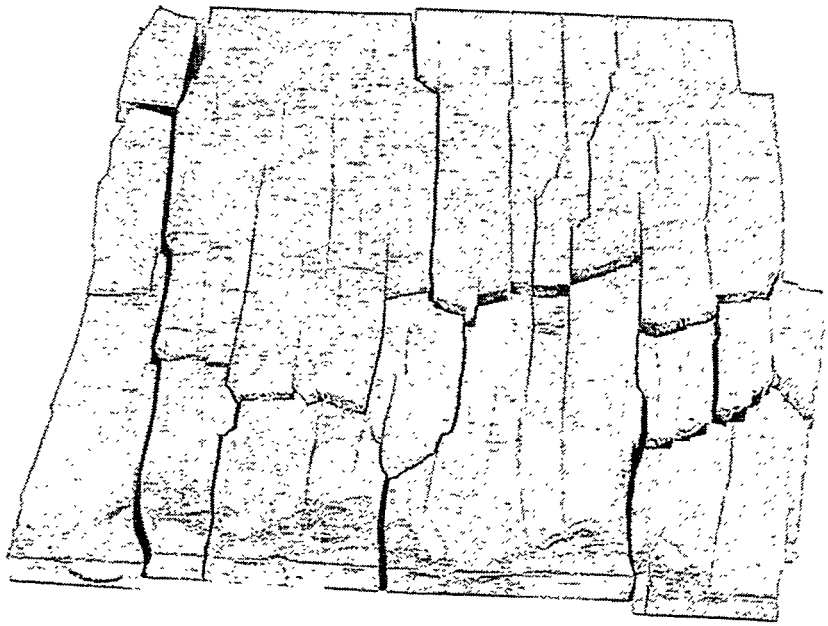

Figure 13 - Macroscopic photograph of cracked Be from traveler #2213.

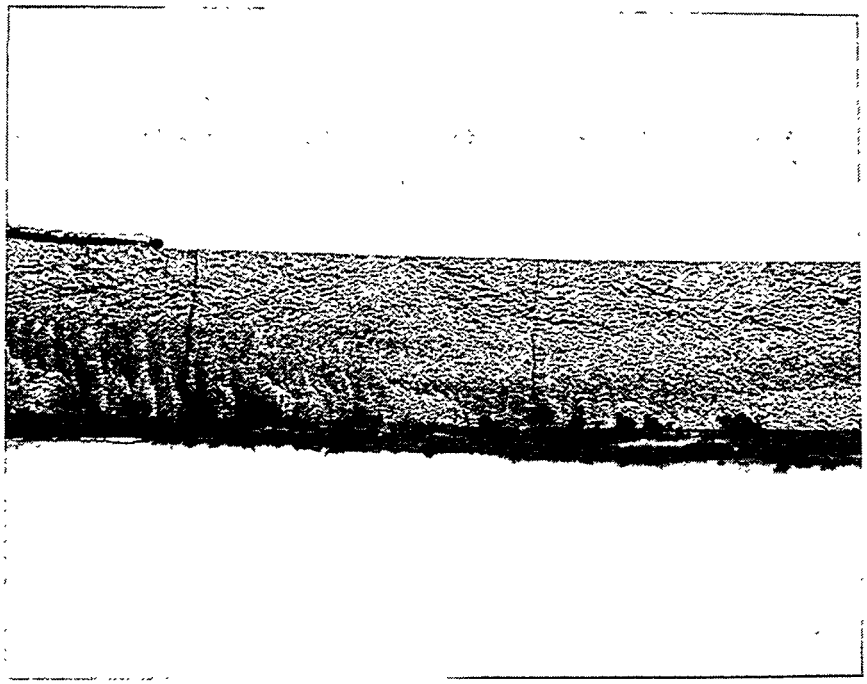

Figure 14 - Edge view of a Be fracture surface from traveler #2213. 5x.

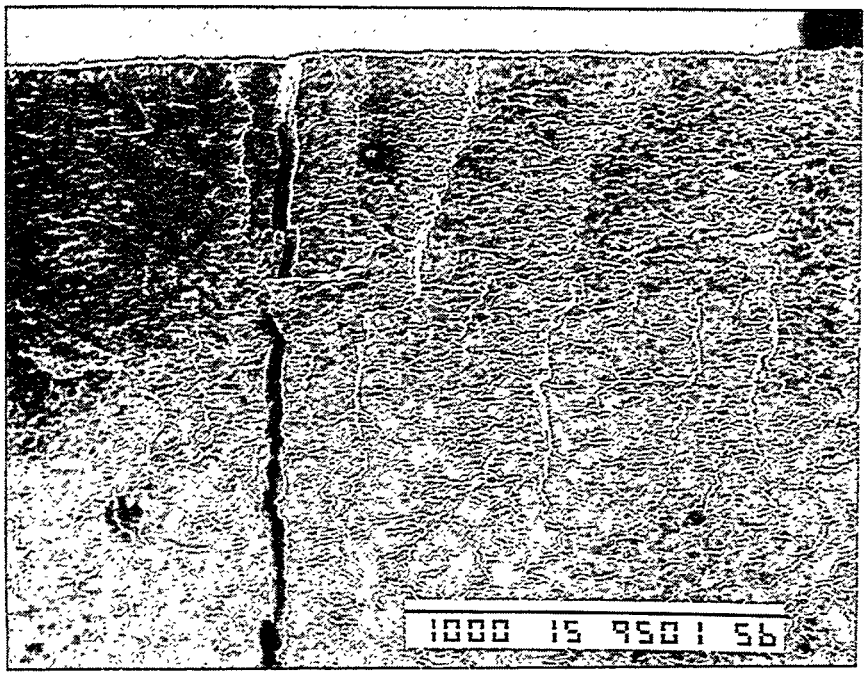

Figure 15 - SEI image of vertical fracture surface for SR-200E sheet from traveler #2213. 50x.

IMPURITIES EFFECT ON THE SWELLING OF NEUTRON IRRADIATED BERYLLIUM

M. Dalle Donne, F. Scaffidi-Argentina
Forschungszentrum Karlsruhe, Institut für Neutronenphysik und Reaktortechnik
Postfach 3640, D-76021 Karlsruhe, F.R.G.

ABSTRACT

An important factor controlling the swelling behaviour of fast neutron irradiated beryllium is the impurity content which can strongly affect both the surface tension and the creep strength of this material. Being the volume swelling of the old beryllium (early sixties) systematically higher than that of the more modern one (end of the seventies), a sensitivity analysis with the aid of the computer code ANFIBE (ANalysis of Fusion Irradiated BEryllium) to investigate the effect of these material properties on the swelling behaviour of neutron irradiated beryllium has been performed.
Two sets of experimental data have been selected: the first one named *Western* refers to quite recently produced Western beryllium, whilst the second one, named *Russian* refers to relatively old (early sixties) Russian beryllium containing a higher impurity rate than the Western one.
The results obtained with the ANFIBE Code were assessed by comparison with experimental data and the used material properties were compared with the data available in the literature. Good agreement between calculated and measured values has been found.

1. INTRODUCTION

In order to generate confidence in the results provided by the code ANFIBE [1] and to assess its prediction capabilities, it was necessary to compare the calculated results with a large number of reliable experimental data [2-11].
The large variety of experimental conditions referring to both in-pile and out-of-pile tests has constituted a reliable benchmark, providing good examples of gas behaviour in beryllium under different steady state and transient conditions and for different metallographic features of the samples.
The proposed analysis is aimed at defining the confidence level of the predictions for the ranges of parameters and the operating conditions to which the code can be applied and to assess the influence of the key variables affecting the overall kinetics and dynamics of gas in beryllium during fast neutron irradiation.
The measured or calculated helium generation rate instead of the neutron flux was taken as the characterizing parameter for the considered swelling experiments. The use of helium content instead of fast fluence is due to the fact that radiation-induced dimensional changes in beryllium subjected to fast neutron irradiation are dominated by helium-bubble swelling.

2. MATERIAL PROPERTIES

The modelling of the experimental results requires a realistic assessment of a number of parameters determining the helium behaviour in beryllium along with physical and mechanical properties of beryllium. The method which has been followed in carrying the swelling analysis deals with experiments where the conditions (i.e. irradiation temperatures, helium generation rates, impurity contents, etc.) were reasonably well known, as well as with the use of a set of experimental physical properties for the material of interest.
Two sets of data have been selected: the first one named *Western* refers to Western beryllium produced quite recently, whilst the second one, named *Russian* refers to relatively old (early sixties) Russian beryllium containing a larger amount of impurities.
Unfortunately, some of the experimental data and material properties crucial to helium modelling in irradiated beryllium are currently very scattered or unavailable. Particular attention has been done in minimizing the number of parameters that can be varied to match the model to the experimental results. The two most important material properties affecting the swelling of beryllium under irradiation are the surface tension and the thermal creep and they are both affected by the amount of impurities in the material.

2.1. Surface tension

In theoretical models of gas-driven swelling in metals, the surface tension of solid material as a function of the temperature is an important variable because it is one of the most important parameters governing the swelling behaviour. This material property is, however, very sensitive to the manufacturing processes and impurity contents, so its experimental value is scattered over a quite large range. It is known that impurities in the metal matrix can strongly affect the surface tension by reducing

its value for the pure material. For this reason particular care has been done in selecting the surface tension equations both for Western and Russian beryllium [12-16].

The experimental data on surface tension of beryllium available from the literature are generally for high temperatures near the melting point. However, if one consider temperatures where the atomic diffusion is significant ($T > 0.5T_m$), the surface tension has the same numerical value as surface free energy [15] and its dependence on temperature may be given by [16-17]:

$$\gamma(T)[N/m] = \gamma(T_m) - K \times (T - T_m) \quad (1)$$

$\gamma(T_m)$ being the surface tension at the melting point and K a constant varying between 0 and 3×10^{-3} [17]. In the present analysis the average value $K=1.5\times10^{-3}$ was assumed for the modern Western beryllium and $\gamma(T_m)$ was chosen equal to 1.96 N/m as given in Ref. [18]. For the Russian beryllium the value γ(973 K) = 0.85 N/m was chosen as reference, close to the value reported in the literature for beryllium produced in the early sixties (like the russian beryllium) [13]. This value is about three times smaller than that for the Western and more modern beryllium. Therefore, for Russian beryllium a surface tension with a temperature dependence similar to that for Western one but having a magnitude about three times smaller has been chosen for the present analysis. The surface tension for Western and Russian beryllium as a function of temperature is shown in Fig. 1.

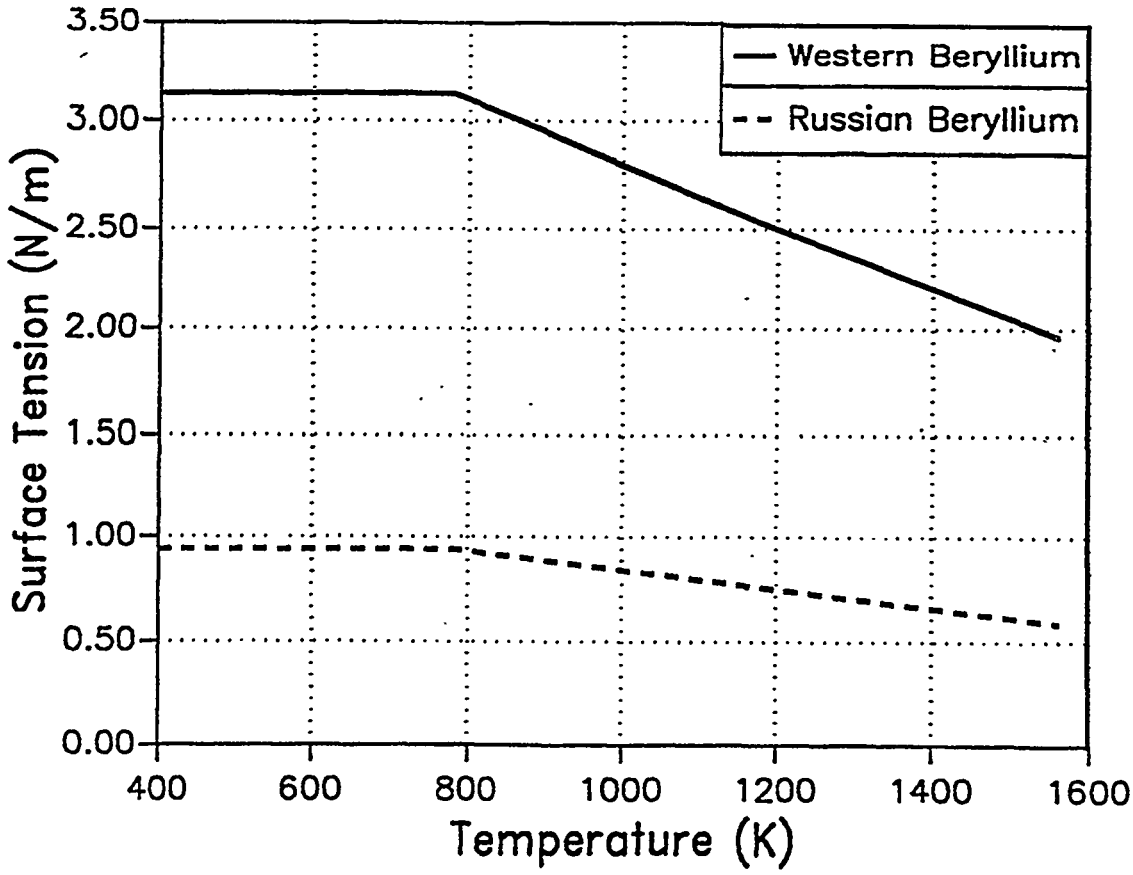

Figure 1: Surface tension for Western and Russian beryllium as a function of temperature.

2.2. Thermal and irradiation creep

Referring to the thermal creep law one must make a distinction between Western and Russian experimental data too. In the former case, in fact, a thermal creep law has been found in the literature and thus used for the analysis [19-20]. In the latter case (and in general for all kind of old beryllium), however, only a very scattered set of data has been found in the literature, which did not directly refer to the considered set of Russian samples irradiated at high temperature [21].

The creep strength of beryllium is controlled by grain size, oxide distribution, initial dislocation density and concentration of certain impurity elements [21]. The most important single factor controlling the creep strength of beryllium is indubitably the impurity content. The principal impurities in beryllium are beryllium oxide, carbon, iron, aluminium, silicon and magnesium. The beryllium oxide impurities have an indirect influence on creep strength through their effects on the recrystallization temperature and grain boundary mobility, whilst iron and carbon appear to have only a minor influence on creep strength. On the contrary, above temperatures of 650-700 °C the beryllium creep strength is considerably reduced by the presence of aluminium, magnesium and silicon, and this reduction becomes more marked as the temperature increases [21-22].

Due to their practical insolubility in beryllium, these three elements (which are normally located on the grain boundaries where they form noncontinuous lenticular globules) can form low-melting phases. Indeed the melting points of aluminium and magnesium are 660 °C and 650 °C respectively, while Al-Si and Al-Mg eutectics melt at temperatures as low as 577 °C and 450 °C respectively [21-22]. Once these liquid phases are formed on the beryllium grain boundaries, due to the impossibility of a shear stress to be transmitted by a liquid, they will act as a cavity so determining a stress concentration at their tips. As a consequence, an accelerated grain boundary shear and cracking will occur around each liquid globule so causing a pronounced grain boundary sliding and an accelerated creep rate.

The difference in creep strength between the weakest and strongest beryllium grades which have been found in the literature was about 20 times and the difference in creep rate was about 8 orders of magnitude [21]. A parametric analysis was thus necessary in order to identify the set of parameters (pre-exponential factor, stress exponent and activation energy for thermal creep) which is able to better match the model to the experimental results. The chosen thermal creep laws are shown in Figs. 2 and 3 for Western and Russian beryllium respectively. The stress exponent for creep law is in both cases equal to 3.6, that is higher than one: this means that creep mechanisms in beryllium entail dislocation climb and cannot be interpreted as a simple diffusional creep phenomenon. The activation energy for creep Q_c has been assumed equal to 216.2 kJ/mol for both Western and Russian beryllium for temperature up to 650 °C. However, for T≥650 °C, corresponding to the melting temperature range of Al and Mg, Q_c has been assumed equal to 710.9 kJ/mol for the Russian beryllium, which is within the range of values given in Ref. [21] for beryllium grades containing impurities.

Referring to the irradiation creep, the mechanism governing this phenomenon in beryllium is at present not well known, thus it is not possible to make a prediction of the enhancement of creep under irradiation in a wide range of temperatures. Only one experiment of irradiation creep in beryllium has been reported in the literature [23] and the corresponding steady state creep rate law has been used for the present calculations. Although this correlation refers to a single experimental test it can be in any case taken as a reference for the evaluation of the irradiation creep rate at all temperatures where self-diffusion is insignificant. In any case, probably the effect of the enhancement of irradiation creep plays only a minor role in governing swelling behaviour of beryllium for temperatures higher than 250 °C due to the prevalence of the thermal creep.

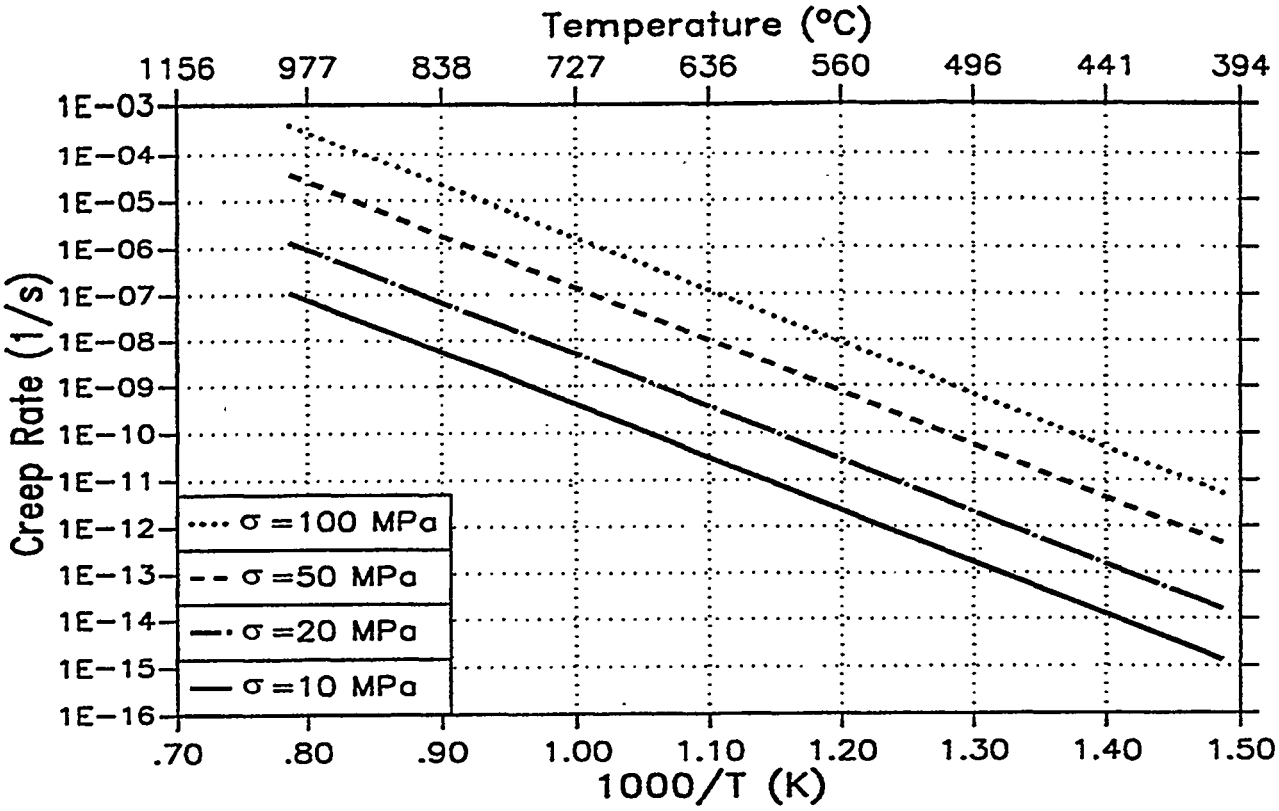

Figure 2: Thermal creep rate for Western beryllium as a function of temperature.

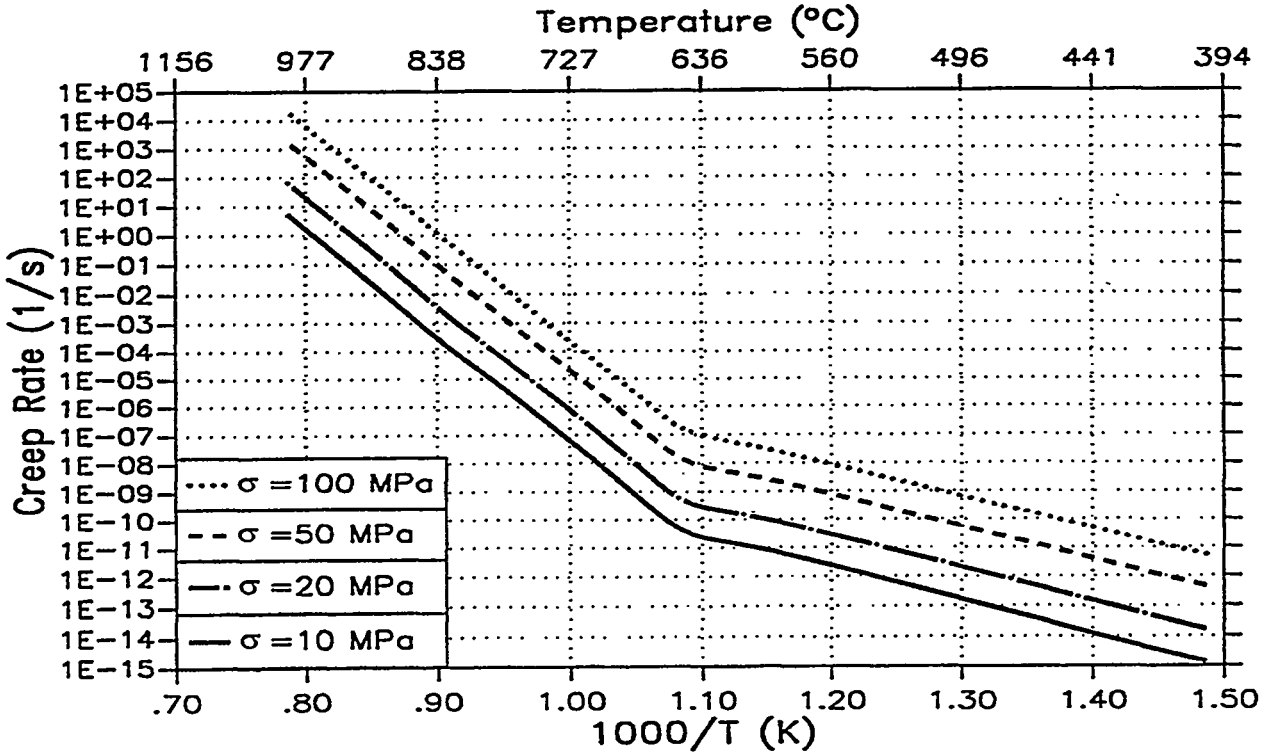

Figure 3: Thermal creep rate for Russian beryllium as a function of temperature.

3. EXPERIMENTAL DATA

Beryllium Western and Russian irradiation experiments carried out in different fission reactors [2-11] at temperatures ranging from 50 to 970 °C and at neutron fluences up to $5.0 \cdot 10^{26}$ m^{-2} (E_n>0.8-1 MeV), with helium contents up to 26100 appm were used for the calibration of ANFIBE code. The major part of the swelling data are, however, for beryllium irradiated both at low temperatures up to very high fluences and at low fluences up to high temperatures [2-5] [7-8] [10]. The only available Western swelling data referring to relatively high irradiation temperature (T=427-487 °C) and, at the same time high fast neutron fluence (up to 10^{26} m^{-2}) come from Beeston's experiments [6]. The other set of well characterized high temperature Western irradiated beryllium refers to specimens irradiated in the SILOE reactor in Grenoble (BEGONIA Experiment) at temperatures up to 700 °C but a relatively low fast neutron fluence (up to $2.5 \cdot 10^{25}$ m^{-2}) [9].
A set of experiments has been found in the literature with reference to Russian beryllium samples irradiated at temperatures up to 970 °C and at fast neutron fluences up to 10^{26} m^{-2} (E_n>0.8-1 MeV) [11].

4. COMPARISON WITH ANFIBE CALCULATIONS

A comparison between calculated and experimental swelling data for in-pile Western irradiated beryllium is shown in Fig. 4 each point of which, classified according to the irradiation temperature, represents the swelling behaviour of a single neutron irradiated beryllium specimen. The agreement between calculated swelling and experimental data is excellent.

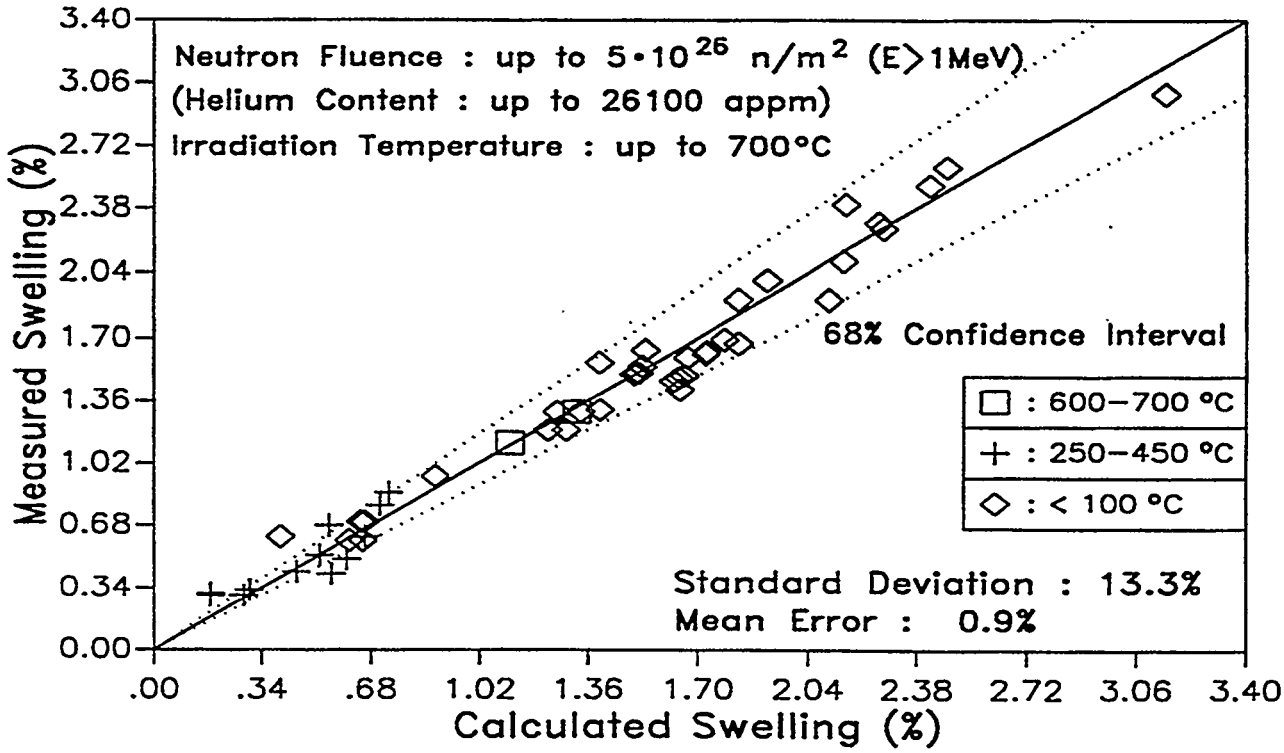

Figure 4: Comparison of calculated and experimental swelling data for in-pile irradiated Western beryllium [2-9].

A comparison between calculated and experimental beryllium swelling data for the available Western experiments referring to relatively high irradiation temperature and, at the same time, relatively high fast neutron fluence [6] [9] is shown in Fig. 5.
Also in this case ANFIBE correctly predicts the experimental results; the discrepancies are due both to the uncertainty in the experimental conditions (i.e. fast flux, helium generation rate, volumetric heat generation, etc.) and in the relevant beryllium properties (i.e. creep law) which are affected by impurity content and manufacturing processes in a stronger way than in the case of low irradiation temperature.

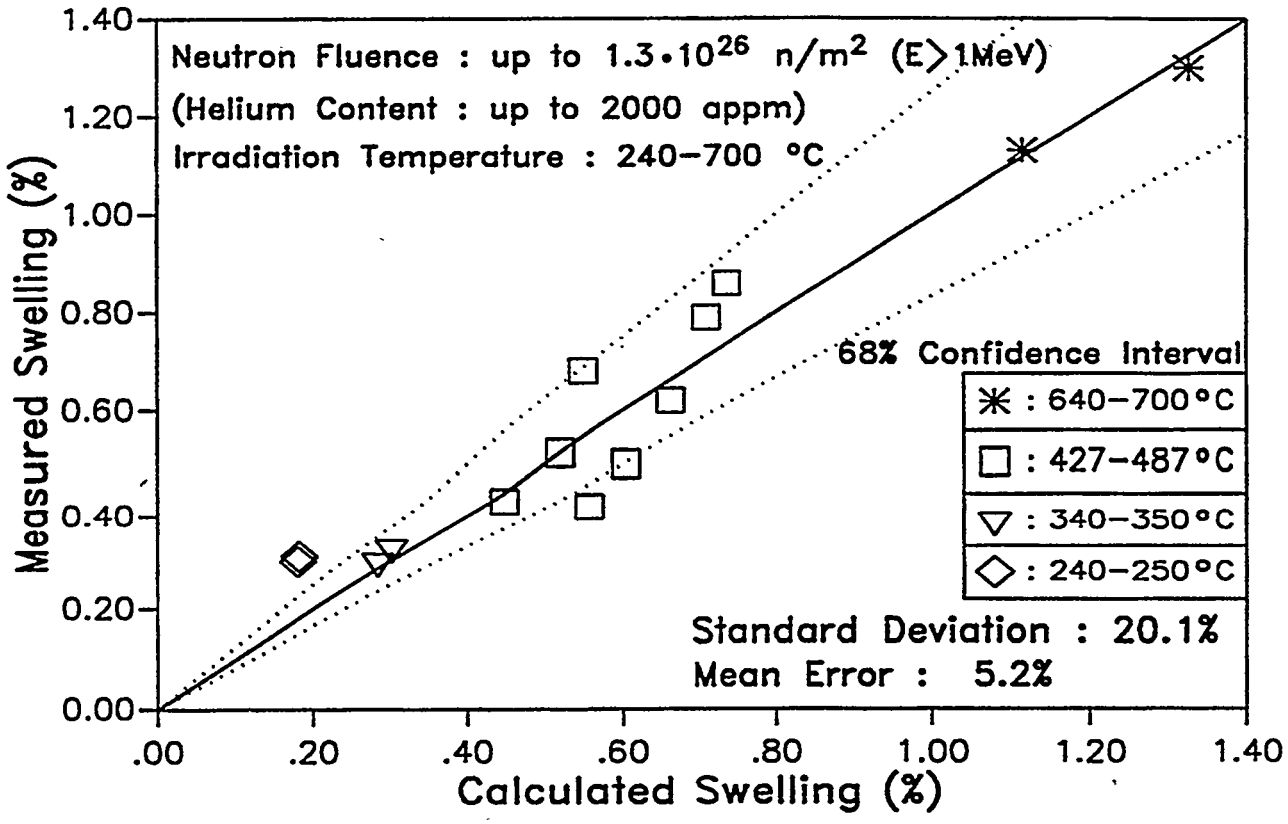

Figure 5: Comparison of calculated and experimental swelling data for high temperature in-pile irradiated Western beryllium [6] [9].

As it has been previously pointed out, another set of experiments refers to Russian beryllium samples irradiated both at high temperature and at high fast neutron fluence [10-11]. However, being these data obtained for a very old beryllium (early sixties) the physical properties of which differ very much from those of the more modern beryllium, an additional calibration analysis was required in order to good characterize these experiments.
For a helium reference creation rate of 4000 appm He per 10^{26} m^{-2} fast neutron fluence cited in the literature [10-11], the measured swelling of Russian beryllium is always higher than that of the more modern Western one containing the same He quantity and subjected to similar irradiation conditions. This fact is clearly illustrated in Fig. 6, which shows the volumetric swelling of beryllium irradiated at temperatures below 100 °C as a function of helium content in comparison with the prediction of the ANFIBE code.

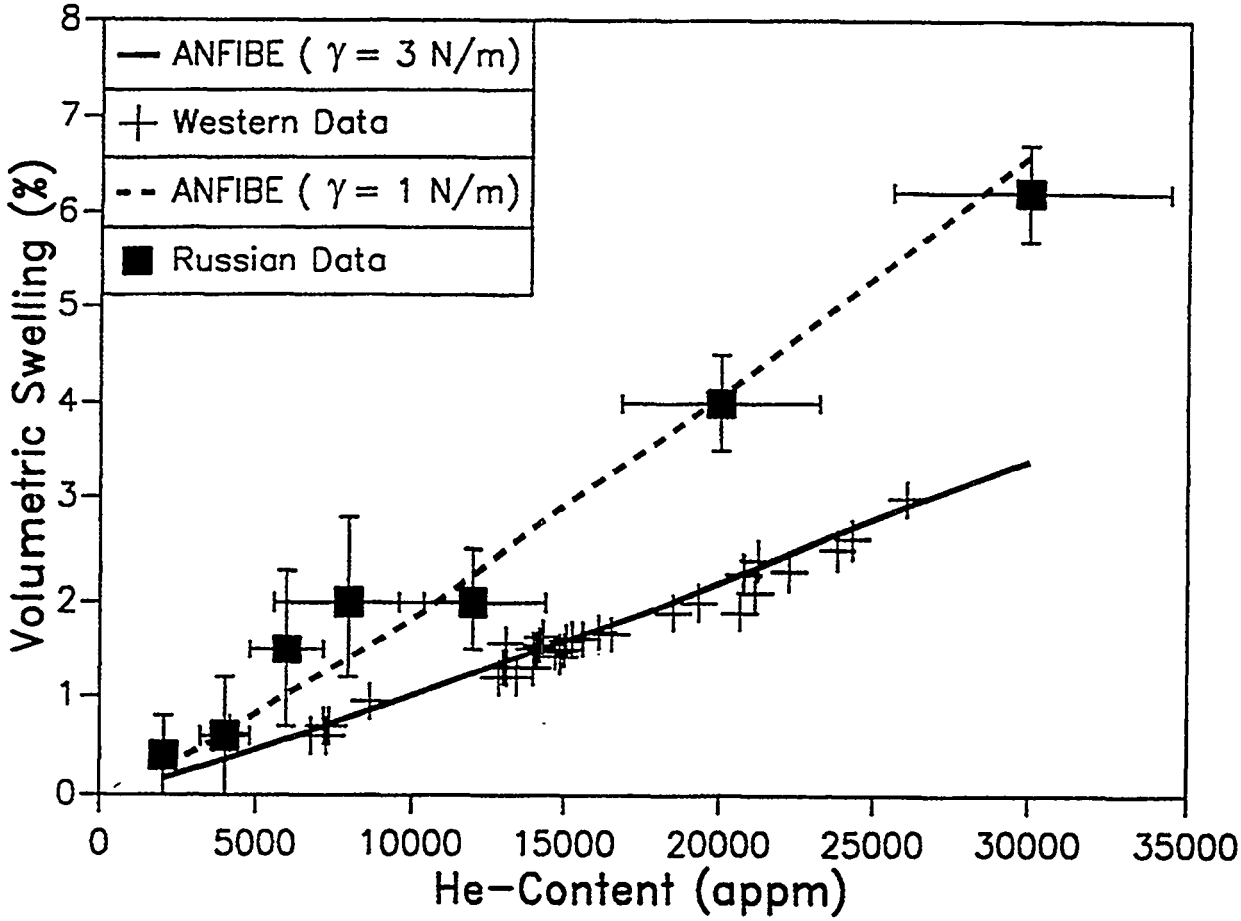

Figure 6: Swelling of Western and Russian beryllium irradiated at temperatures below 100 °C as a function of helium content [2-11].

A likely reason for this behaviour is that, due to its quite poor quality (i.e. high impurity content) the Russian beryllium has a surface tension which is lower than that of the Western, more modern one.
Fig. 6 shows that the Russian experimental data agree quite well with the ANFIBE predictions based on the surface tension values shown in Fig. 2. At these low temperatures the thermal creep doesn't play any role.
Swelling increases at low temperatures almost linearly with the gas content, as expected from theoretical considerations. At low irradiation temperatures, in fact, when the mobility of the vacancies and interstitials is very low and the gas atoms are practically immobile in the lattice, helium cannot migrate to the grain boundaries where it could coalesce to form big intergranular bubbles, which causes the departure from linearity in swelling behaviour.
On the contrary, the situation is quite different for the samples irradiated at high temperatures (up to 970 °C) and at fast neutron fluences up to 10^{26} m^{-2} [11] for which, due to both the rapid coalescence of the gas bubbles and the reduction of the mechanical strength of the material, one should expect a non-linear increase of the swelling with the gas content and the influence on creep strength due to the impurity content (i.e. Al, Mg) in beryllium must also be taken into account.

Fig. 7 shows the volumetric swelling as a function of the irradiation temperature for the Russian beryllium [11] at different fast neutron fluences as compared with the predictions of ANFIBE. In this case a creep law taking into account the possible presence of liquid phases at the grain boundaries has been used as shown in Fig. 3. The agreement between the experimental data and the ANFIBE predictions is also here quite good.

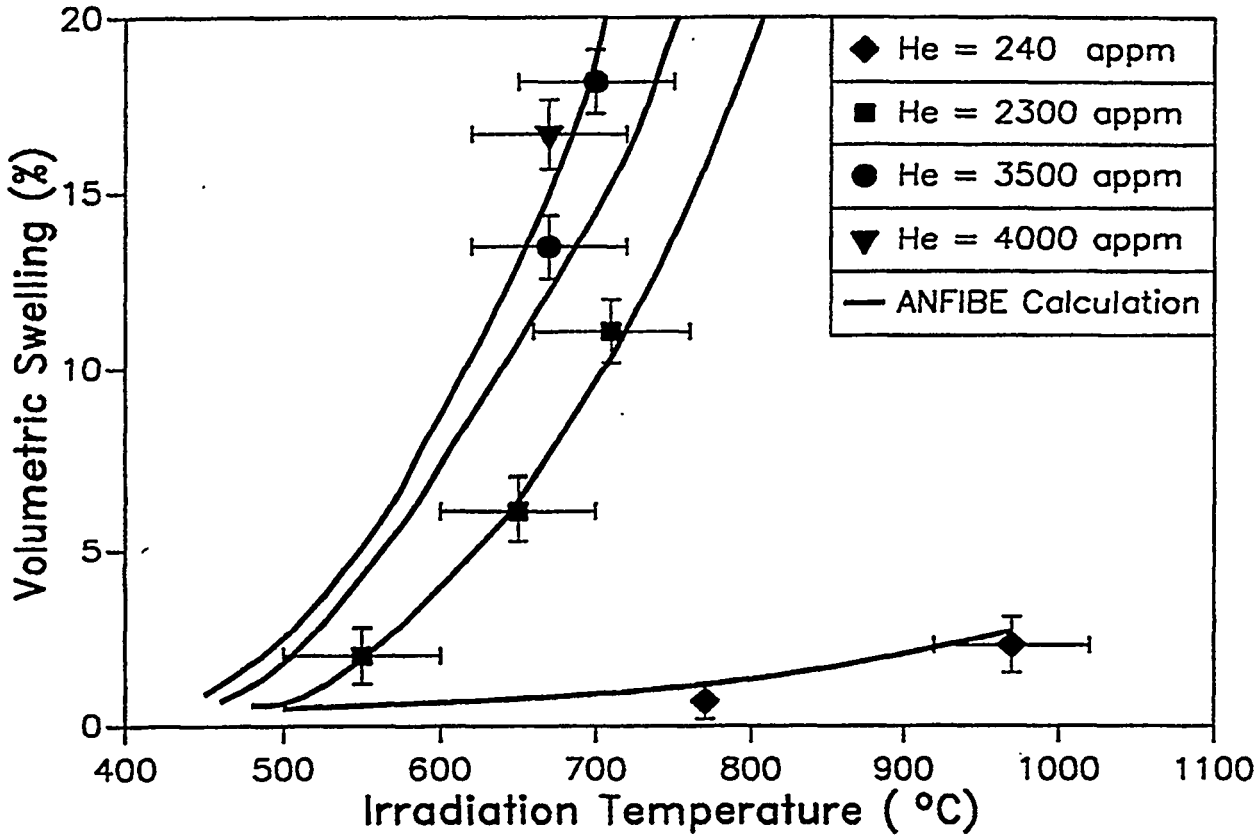

Figure 7: Comparison of calculated and experimental swelling for Russian beryllium irradiated at high temperatures and high fluences [10-11].

5. CONCLUSIONS

An important factor controlling the swelling behaviour of beryllium under neutron irradiation is the impurity content which can strongly affect the material properties.

Beryllium irradiation experiments carried out in different fission reactors at temperatures ranging from 50 to 970 °C and at neutron fluences up to $5.0 \cdot 10^{26}$ m^{-2} (E_n>0.8-1 MeV), with helium contents up to 26100 appm were compared with the predictions of the computer code ANFIBE.

Two sets of data have been selected: the first one named *Western* refers to Western beryllium produced quite recently (end of the seventies), whilst the second one, named *Russian* refers to relatively old (early sixties) Russian beryllium containing a higher impurity rate than the Western one. The comparison between calculated and experimental swelling data shows that:

1. The swelling of Russian beryllium irradiated at low temperature (T<100 °C) is systematically higher than that of the Western and more modern one. This behaviour has to be attributed to the fact that the old Russian beryllium has a relatively high amounts of impurities in comparison with Western beryllium. This fact causes a decrease of the surface tension thus determining a reduction of the mechanical strength of the material which opposes the deformation of the metal under the thrust of the helium-bubble overpressure.

2. The swelling of Russian beryllium irradiated at high temperature and, at the same time, at high neutron fluence is much higher than that of the Western beryllium. This is likely due to the fact that some impurities (i.e. Al, Mg, Si) can form, due to their practical insolubility in beryllium, low-melting phases which are in the liquid form at temperature higher than 650-700 °C. Once these liquid phases are formed on the beryllium grain boundaries they act as a cavity so causing a pronounced grain boundary sliding and an accelerated creep rate. The enhancement of the thermal creep rate and, at the same time, the decrease of the surface tension due to the presence of impurities, will determine a strong increase of the swelling for high irradiation temperature.

ACKNOWLEDGMENTS

This work was performed in the framework of the Forschungszentrum Karlsruhe Nuclear Fusion Project and is supported by the European Communities within the European Fusion Technology Program.

REFERENCES

[1] F. Scaffidi-Argentina, "Modellierung des Schwellens und der Tritium-Freisetzung von bestrahltem Beryllium", FZKA Report 5633 (to be published).

[2] D.L. Baldwin and M.C. Billone, "Diffusion/Desorption of Tritium from Irradiated Beryllium", Journal of Nuclear Materials 212-215 (1994) 948-953.

[3] M.C. Billone et al., "Tritium and Helium Behaviour in Irradiated Beryllium", Fusion Technology 19 (1991) 1707-1714.

[4] L. Sannen et al., "Helium Content and Swelling of Low Temperature Irradiated/Post-Irradiated Annealed Beryllium", CEN/SCK Report FT/Mol/93-07.

[5] J.M. Beeston, "Properties of Irradiated Beryllium: Statistical Evaluation", EG&G Idaho Report, TREE-1063 (1976).

[6] J.M. Beeston et al., "Comparison of Compression Properties and Swelling of Beryllium Irradiated at Various Temperatures", Journal of Nuclear Materials 122-123 (1984) 802-809.

[7] E. Koonen, "Study on Irradiation Effects and Swelling of Irradiated Beryllium", CEN/SCK Report, Reactor Safety Analysis BR2 Department (1989).

[8] J.M. Beeston et al., "Gas Retention in Irradiated Beryllium", EG&G Idaho Report, EGG-FSP-9125 (1990).

[9] V. Levy, "Rapport Final du Contrat SBB-BS1", CEA Report, Centre d'Etudes de Saclay, N.T. SRMA 92-1955 F.A 3591-532 (1992).

[10] G.A. Sernyaev, "Beryllium Swelling and Spontaneous Cracking under Low Temperature Irradiation", SF Nikiet Internal Report.

[11] G.A. Sernyaev, "Beryllium Swelling in High-Temperature Neutron Irradiation. Main Structure Factors Role", SF Nikiet Internal Report.

[12] G. Caglioti et al., "Surface Energy for Brittle Fracture in Metals from Phonon Frequencies", Journal of Applied Physics, Vol. 42 No. 11 (1971) 4271-4276.

[13] J. Barnes and G.B. Reddings, "The Behaviour of Helium Atoms Injected into Beryllium", Journal of Nuclear Energy 10 (1959) 32-35.

[14] V.K. Kumirov, "The measurement of the Surface Tension of Some Pure Metals in the Solid State", Materials Science and Engineering 60 (1983) L23-L24.

[15] R. Swalin, "Thermodynamics of Solids", John Wiley and Sons, Inc., NY, 1962, p.181.

[16] D.A. Porter and K.E. Easterling, "Phase Transformations in Metals and Alloy", Van Nostrand Reinhold (UK) Co. Ltd., 1981, p.113.

[17] D.E. Dombrowski, Brush-Wellman, Private Communication (1992).

[18] Ullmann's Encyclopedia of Industrial Chemistry, Vol. A4, Weinheim, 1985, p.12.

[19] M.C. Billone and W.T. Grayhack, "Summary of Mechanical Properties Data and Correlations for Li_2O, Li_4SiO_4, $LiAlO_2$ and Be", ANL/FPP/TM-218 Report, Argonne National Laboratory, 1988.

[20] M.C. Billone, Private Communication (1992).

[21] D. Webster and D.D. Crooks, "Factors Influencing the Creep Strength of Hot Pressed Beryllium", Metallurgical Transaction 6A (1975) 2049-2054.

[22] D. Webster and D.D. Crooks, "Creep Mechanisms in Beryllium", Metallurgical Transaction 7A (1976) 1307-1315.

[23] R.V. Hesketh, "Proc. of the International Conference on Solid State Physics and Research with Accelerators", BNL-500883(C-52) (Physics-TID-4500), Brookhaven National Lab., September 1967, p. 389.

TRITIUM RELEASE FROM NEUTRON IRRADIATED BERYLLIUM: KINETICS, LONG-TIME ANNEALING AND EFFECT OF CRACK FORMATION

F. Scaffidi-Argentina, H. Werle
Forschungszentrum Karlsruhe, Institut für Neutronenphysik und Reaktortechnik
Postfach 3640, D-76021 Karlsruhe, F.R.G.

ABSTRACT

Since beryllium is considered as one of the best neutron multiplier materials in the blanket of the next generation fusion reactors, several studies have been started to evaluate its behaviour under irradiation during both operating and accidental conditions.
Based on safety considerations, tritium produced in beryllium during neutron irradiation represents one important issue, therefore it is necessary to investigate tritium transport processes by using a comprehensive mathematical model and comparing its predictions with well characterized experimental tests.
Because of the difficulties in extrapolating the short-time tritium release tests to a longer time scale, also long-time annealing experiments with beryllium samples from the SIBELIUS irradiation have been carried out at the Forschungszentrum Karlsruhe. Samples were annealed up to 12 months at temperatures up to 650 °C. The inventory after annealing was determined by heating the samples up to 1050 °C with a He+0.1 vol% H_2 purge gas.
Furthermore, in order to investigate the likely effects of cracks formation eventually causing a faster tritium release from beryllium, the behaviour of samples irradiated at low temperature (40-50 °C) but up to very high fast neutron fluences ($0.8\text{-}3.9 \cdot 10^{22}$ cm^{-2}, $E_n \geq 1$ MeV) in the BR2 reactor has been investigated. Tritium was released by heating the beryllium samples up to 1050 °C and purging them with He+0.1 vol% H_2. Tritium release from high-irradiated beryllium samples showed a much faster kinetics than from the low-irradiated ones, probably because of crack formation caused by thermal stresses in the brittle material and/or by helium bubbles migration.
The obtained experimental data have been compared with predictions of the code ANFIBE with the goal to better understand the physical mechanisms governing tritium behaviour in beryllium and to assess the prediction capabilities of the code. Good agreement between calculated and experimental data has been found.

1. INTRODUCTION

Solid breeder blankets of fusion reactors require beryllium as neutron multiplier to achieve adequate tritium breeding. In the fast neutron field of the blanket, helium and tritium is produced in beryllium. Therefore, besides compatibility with other blanket materials, helium-induced swelling and tritium retention are of concern.

Although the tritium production rate in beryllium is two to three order of magnitude smaller than that in the breeder ceramic, because of the slow release at typical blanket temperatures [1], the inventory in beryllium might become large during the DEMO blanket lifetime (≈3 years) and is therefore a safety concern.

The produced tritium can diffuse through the lattice and/or be captured by structural traps such as intragranular helium bubbles, closed porosity, grain boundaries, etc.. If tritium is trapped in a helium-filled bubble, it follows the fate of the bubble and will be released only if the bubble is vented into an open porosity network, through which the gas can escape with effectively no activation energy. On the other hand, because beryllium of commercial purity always contains some oxide inclusions (which tend to collect at grain boundaries where they form globular phases), beryllium oxide can react with tritium to form beryllium hydroxide which is energetically stable with respect to single tritium atoms. Tritium chemically bound in form of beryllium hydroxide at oxide inclusions requires a sufficiently high thermal energy to be released. In fact, under the action of heating, beryllium hydroxide may dissociate and tritium in atomic form can be re-injected into the lattice. Tritium in excess of what the lattice can dissolve either diffuses through the lattice and escape from the specimen or is captured by gas bubbles, depending on the present global bubble density and size. Due to the two different tritium trapping mechanisms in beryllium, the release kinetics will be thus different depending on gas bubble density and size, and on irradiation or annealing temperature.

Therefore, release kinetics of neutron-generated tritium of two types of beryllium samples (SIBELIUS and MOL) has been studied. For beryllium samples which were in contact with breeder ceramic during irradiation, a second type of tritium inventory, due to implantation from the ceramic, was observed. Because it is difficult to extrapolate the short-time kinetics data to time scales comparable to the blanket lifetime, also long-time annealing experiments (up to 12 months at temperatures up to 650 °C) have been performed. With the MOL samples, which were irradiated up to very high fast neutron fluences of $3.9 \cdot 10^{22}$ cm^{-2} (DEMO blanket $\leq 2.5 \cdot 10^{22}$ cm^{-2}), also effects of crack formation on tritium release were observed.

To describe the irradiation behaviour of beryllium the computer code ANFIBE has been developed [2]. The experimental results have been compared with the ANFIBE predictions with the goal to better understand the mechanisms governing tritium transport and to assess the prediction capabilities of the code.

2. EXPERIMENTS

2.1. Samples and irradiation conditions

The beryllium pellets (8 mm ∅ × 2 mm) for the SIBELIUS irradiation [3] were made by the Brush-Wellman (specification B-26, arc cast, BeO≤300 ppm). The structure is characterized by grains as large as 2 mm and some intergranular cracks; a cold worked layer resulting from machining is observed on the

surface; the density determined from the masses and dimensions varied between 1.79 and 1.82 g/cm^3 and was in the average 1.805 g/cm^3 (98% theoretical density) [4]. The SIBELIUS irradiation was performed 1990 in the SILOE reactor at CEN Grenoble to a fast ($E_n \geq 1$ MeV) neutron fluence of $6 \cdot 10^{20}$ cm^{-2}. The irradiation temperature was 550 °C, except for capsule 1, where it was 270 °C. Whole, fresh pellets, but also smaller samples made from pellets that were previously used for metallographic investigations were studied. The previously used pellets were cleaned and axially cut to quarters of pellets.

The second type of beryllium samples (type MOL) were provided by CEN Mol [5,6]. The samples were made from cylindrical bars (15 mm ∅ × 100 mm) fabricated by Kawecki Berylco Industries by vacuum hot pressing of impact attritioned powder of 100 mesh at least (grade S-200 E). The average grain size amounts to 10-13 μm. The specific BeO content is < 2%, the bulk density corresponds to 99.5% of the theoretical density. The bars have been irradiated at 40-50 °C in the BR2 reactor to a fast ($E_n \geq 1$ MeV) neutron fluence of 0.8, 2.8, $3.9 \cdot 10^{22}$ cm^{-2}. After irradiation the bars were ultrasonically treated to remove the outer oxide layer. Then they were rinsed with water and dried. Appropriate samples were cut from the bars. A cutting method which did not severely heat the samples was used to prevent release of contained gases. During the cutting it was experienced that the irradiated material was rather brittle [5].

2.2. Facilities and procedures

The main characteristics of the tritium release facilities are: the sample chamber is connected by a short, heated line (≈300 °C) to a Zn-reductor (≈390 °C). The reductor transforms any tritium water to tritium gas. This avoids problems with tritium water absorption and allows quantitative tritium measurements. The tritium activity of the purge gas is measured with an ionization chamber and/or a proportional counter. The released tritium inventory is determined by integrating the measured release rate over the time.

Two tritium release facilities have been used: a first series of experiments have been performed in the hot cell facility, where the maximum sample temperature was restricted to 900 °C. It turned out that this temperature is not sufficient to release all tritium. Therefore, in a second series of experiments most of the samples were heated to 1050 °C. By heating some samples to even higher temperatures, it has been checked that essentially all tritium is released at 1050 °C within several hours.

For the tritium release investigations, the samples were purged with high-purity He+0.1 vol% H_2. Two heating procedures were applied: either linear ramps with 5 °C/min or a stepwise temperature increase.

For the long-time annealing studies, the quarters of pellets from the SIBELIUS irradiation have been used. The samples were inserted at definite positions in a tube furnace to achieve the desired annealing temperatures of 380, 450, 550 and 650 °C and were purged with 5 l/h high purity He. After removal from the annealing furnace, the residual tritium inventory was determined by purging and heating the samples up to 1050 °C in the tritium release facilities.

2.3. Results and discussion

Release kinetics

It is expected that if beryllium is in direct contact with breeder ceramic during irradiation, a fraction of the 2.74 MeV tritons (range in ceramic ≈40μm) produced in the ceramic is implanted into the surface layer of beryllium, leading to an additional inventory which was estimated to be several times larger than the neutron-produced one. This has been confirmed by the measured tritium release of SIBELIUS pellets which were in contact with ceramic during irradiation (Fig. 1). Pellet 6 of capsule 1 was irradiated at 270 °C and contained a high implanted inventory (total specific inventory 4100 MBq/g), which is released already at 500 °C (Fig. 1 top). For the other two pellets (pellet 15 of capsule 2 and pellet 15 of capsule 5), which were irradiated at 550 °C, the implanted tritium was evidently released already during irradiation (total specific inventory 1500-1600 MBq/g) and the neutron-generated tritium is released only above 600 °C.

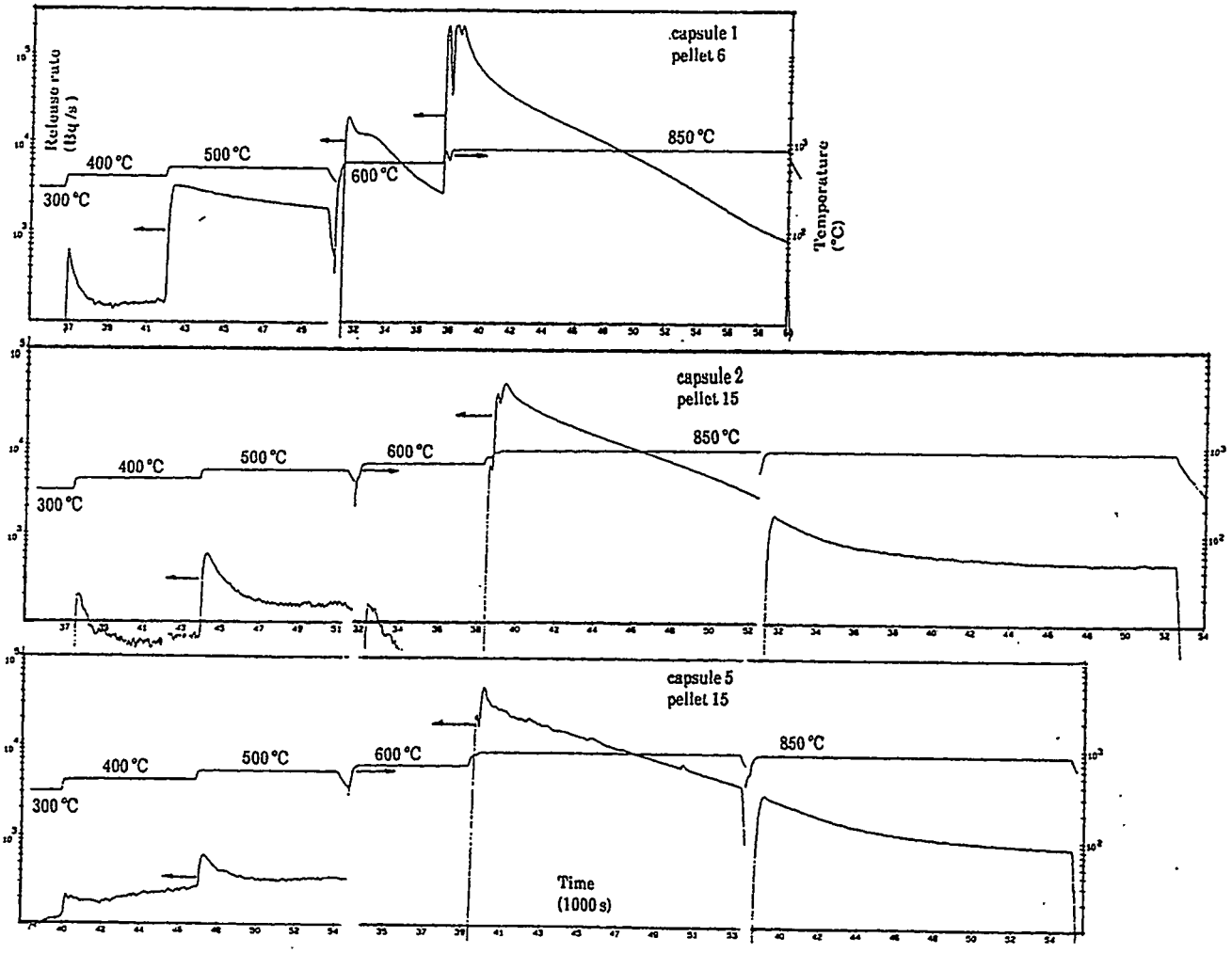

Figure 1: SIBELIUS beryllium samples, whole pellets: release of implanted (top) and neutron-generated tritium (center, bottom).

In Fig. 2 tritium release of not-annealed quarters of SIBELIUS pellets irradiated at 270 °C is shown. Sample 1-3.1 (1 capsule no. - 3 pellet no.. 1 quarter no.) was not, sample 1-5.1 was in contact with ceramic during irradiation, but contained only a small implanted inventory, because the bulk is released during cleaning and cutting of the pellets. The release starts to increase with temperature above about 600 °C. At 850 °C it initially decreases fast, but achieves a nearly constant value after several hours, indicating a remarkable residual inventory, which is confirmed by the 1050 °C runs during which the residual inventories of 15-40% are released.

In Fig. 3 tritium release from the MOL samples 110A-9c, irradiated with the lowest fast fluence ($0.8 \cdot 10^{22}$ cm^{-2}) is shown. Similar as for the SIBELIUS samples, the release starts to increase above about 600 °C, but decreases very slowly at 850 °C. Correspondingly, only a small fraction (11%) of the tritium is released at 850 °C, the bulk (83%) is released at 880 °C and the residual 6% at 1050 °C. The behaviour at 880 °C is very surprising: at constant temperature, normally the release rate decreases monotonically with the time, whereas here, after several hours, it starts to increase to a maximum and finally decreases again. After the maximum, strong oscillations of the release rate are observed. A similar behaviour has been previously observed by Baldwin and Billone [7] for beryllium irradiated at 75 °C. During heating at constant temperature, after a time lag of 2 to 4 hours a burst release of tritium was seen. Details are given in Tab. 1.

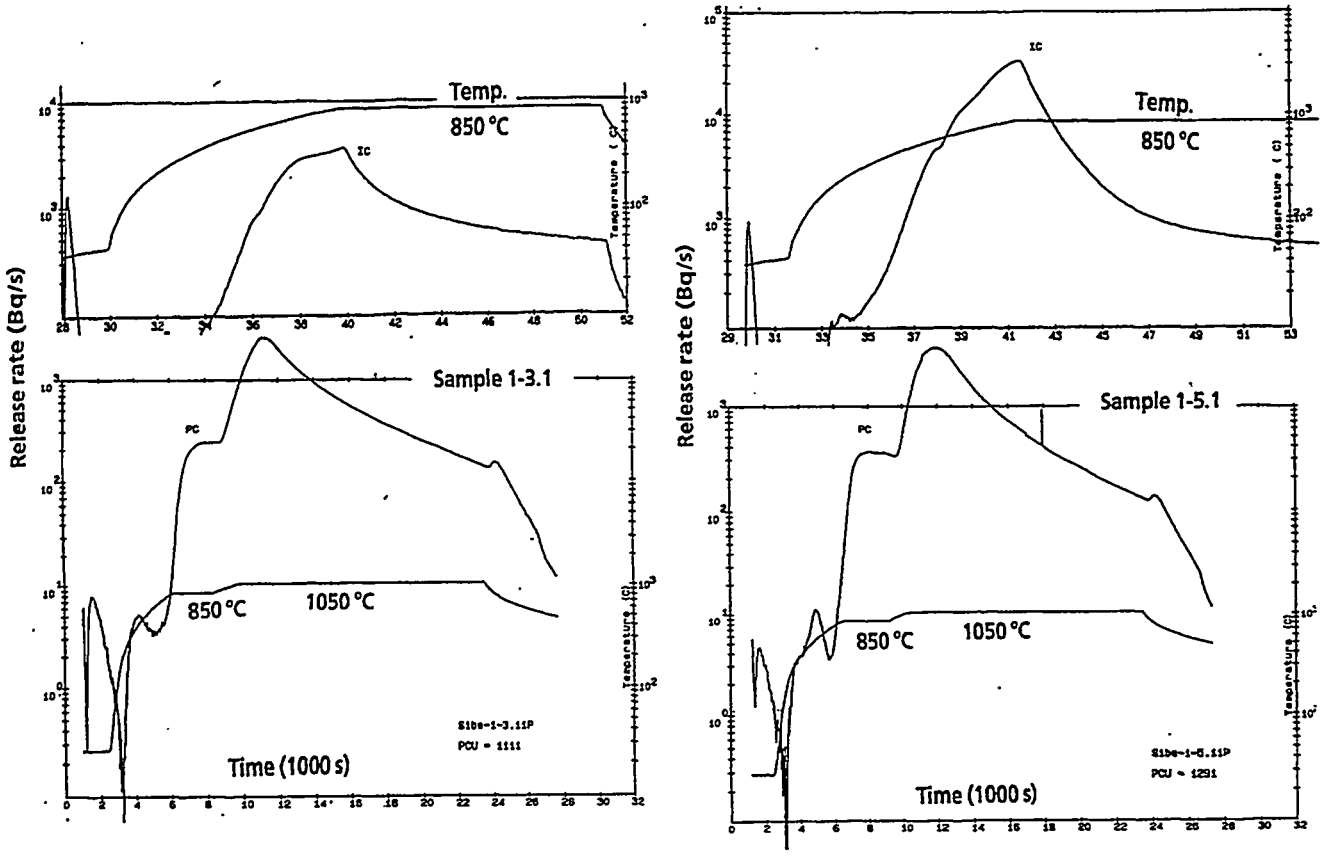

Figure 2: SIBELIUS beryllium samples, not-annealed quarters of pellets: release of neutron-generated tritium.

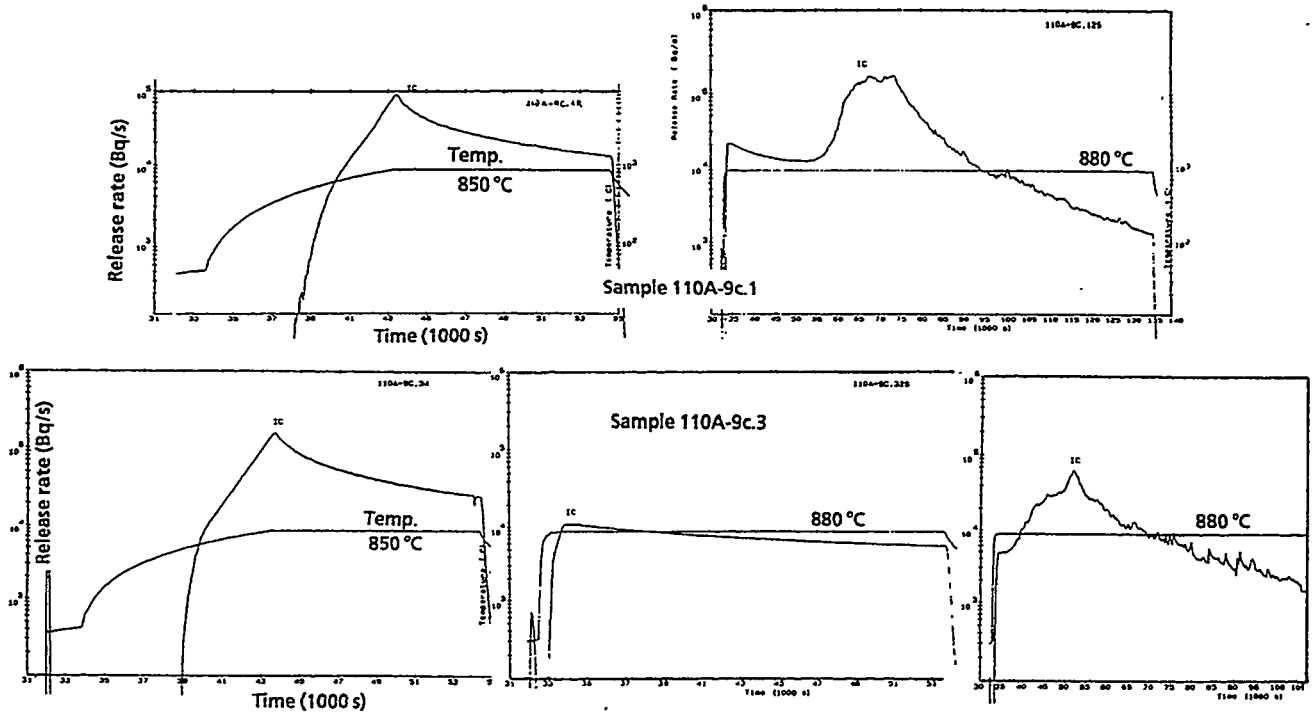

Figure 3: MOL beryllium samples 110A-9c (fast fluence $0.8 \cdot 10^{22}$ cm^{-2}): release of neutron-generated tritium.

Sample density (% of the theoretical)	81%	99%	100%
Fast fluence, $E_n \geq 1$ MeV [cm^{-2}]	$2.6 \cdot 10^{21}$	$2.6 \cdot 10^{21}$	$5.0 \cdot 10^{22}$
Temperature of burst release [°C]	600	900	600

Table 1: Burst release temperature for various beryllium samples observed by Baldwin and Billone [7].

Their explanation, that this burst release is due to the migration of helium bubbles which leads to the formation of interconnected grain-edge tunnels to the sample surface, looks very reasonably.
Tritium release of the highly irradiated MOL samples 110A-9a (fast fluence $2.8 \cdot 10^{22}$ cm^{-2}) and 137A-22b (fast fluence $3.9 \cdot 10^{22}$ cm^{-2}) is much faster than that of weakly irradiated samples 110A-9c and of the SIBELIUS samples, as is clearly shown in Fig. 4. Release drops fast at 850 °C and correspondingly essentially all tritium (94-96%) is released at this temperature. Also in contrast to samples 110A-9c, no burst release was observed. An explanation which is consistent with the fast

release is that in this highly irradiated samples the formation of the interconnected grain-edge tunnels occurs already during irradiation. The different kinetics is also demonstrated in Tab. 2, where the fractional release at different temperatures is given.

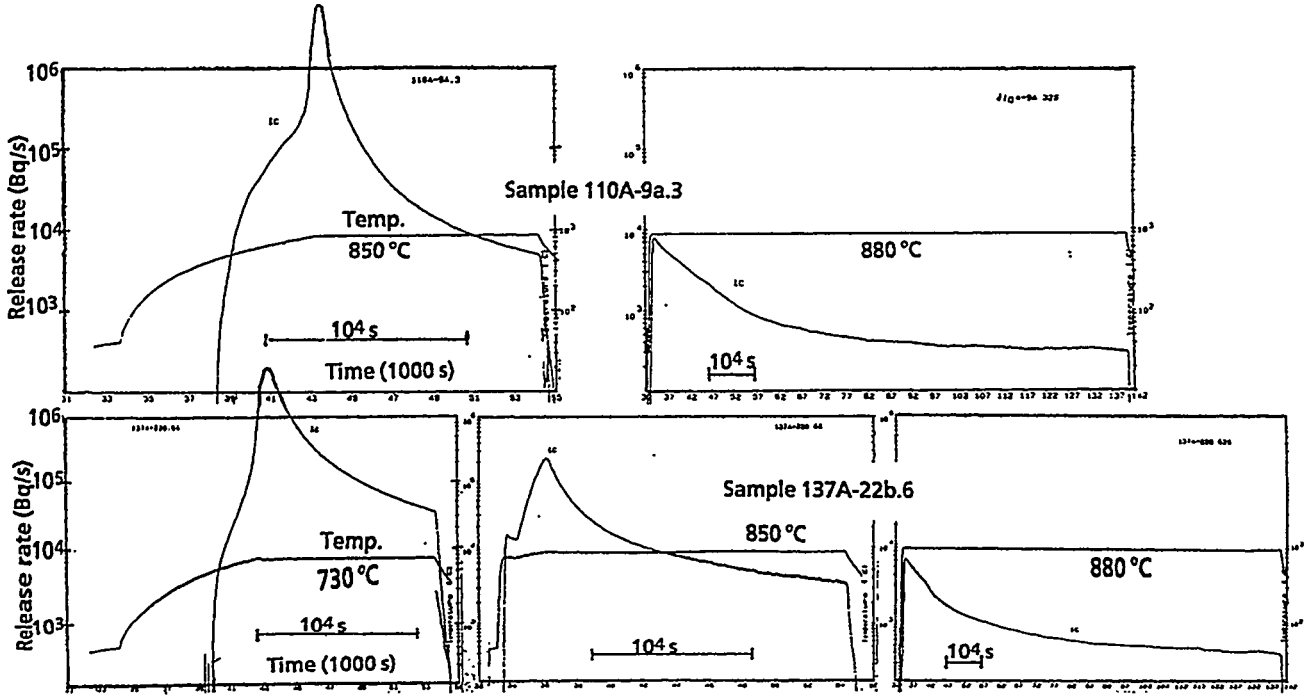

Figure 4: MOL beryllium samples 110A-9a (fast fluence $2.8 \cdot 10^{22}$ cm^{-2}) and 137A-22b (fast fluence $3.9 \cdot 10^{22}$ cm^{-2}): release of neutron-generated tritium.

Temperature [°C]	SIBELIUS samples not-annealed, quarters of pellets			MOL samples		
	1-3.1	1-5.1	2-11.2	110A-9c.3	110A-9a.2	137A-22b.6
850	0.59	0.85	0.58	0.11	0.94	0.96
880	—	—	—	0.94	0.96	0.97
1050	1.0	1.0	1.0	1.0	1.0	1.0

Table 2: Fractional tritium release for SIBELIUS and MOL beryllium samples.

Long-time annealing (SIBELIUS samples, quarters of pellets)

The residual specific inventory after annealing is shown as function of annealing time with the annealing temperature as parameter in Fig. 5. Tritium release is very slow below 400 °C and moderately fast between 450 and 550 °C. At 650 °C, the inventory decreases pretty fast to several percent during the first six months, but afterwards it remains essentially constant.
The data of Fig. 5 have been roughly fitted by straight lines - although at 650 ° C the decrease is not exponential - and tritium residence times have been determined (Fig. 6), which correspond to the time at which the inventory has decreased to 37% (1/e) of the initial value.
Although due to both experimental data scattering and not-exponential decrease, the uncertainty of the residence times in Fig. 6 is quite large, to our knowledge no other data on long-time tritium release from beryllium are available for fusion blanket predictions. From Fig. 6 it can be seen that at temperatures below about 400 °C, essentially all produced tritium is retained in beryllium.

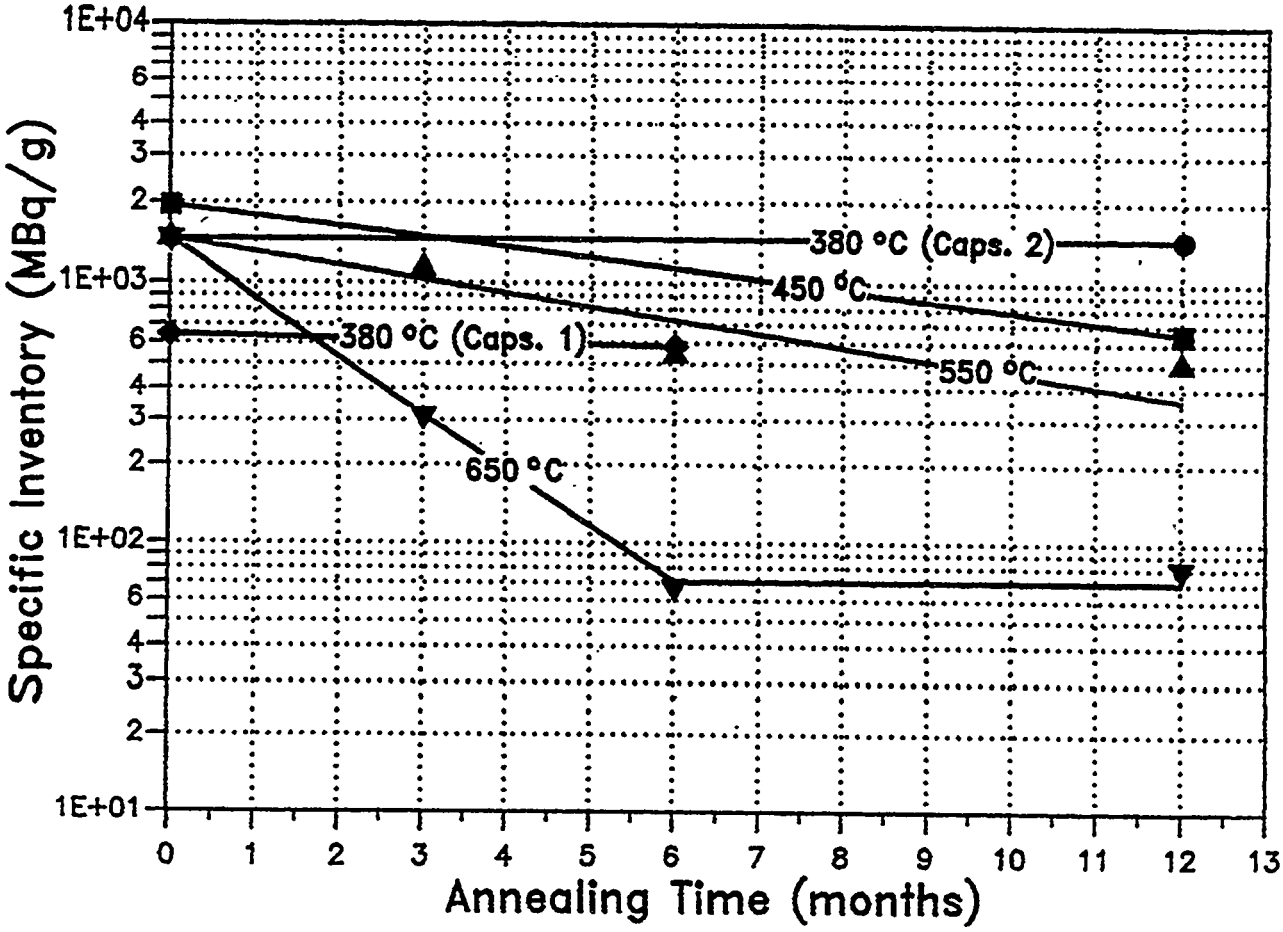

Figure 5: Residual specific inventory vs. annealing time for neutron-generated tritium in beryllium, parameter annealing temperature (SIBELIUS samples, quarters of pellets).

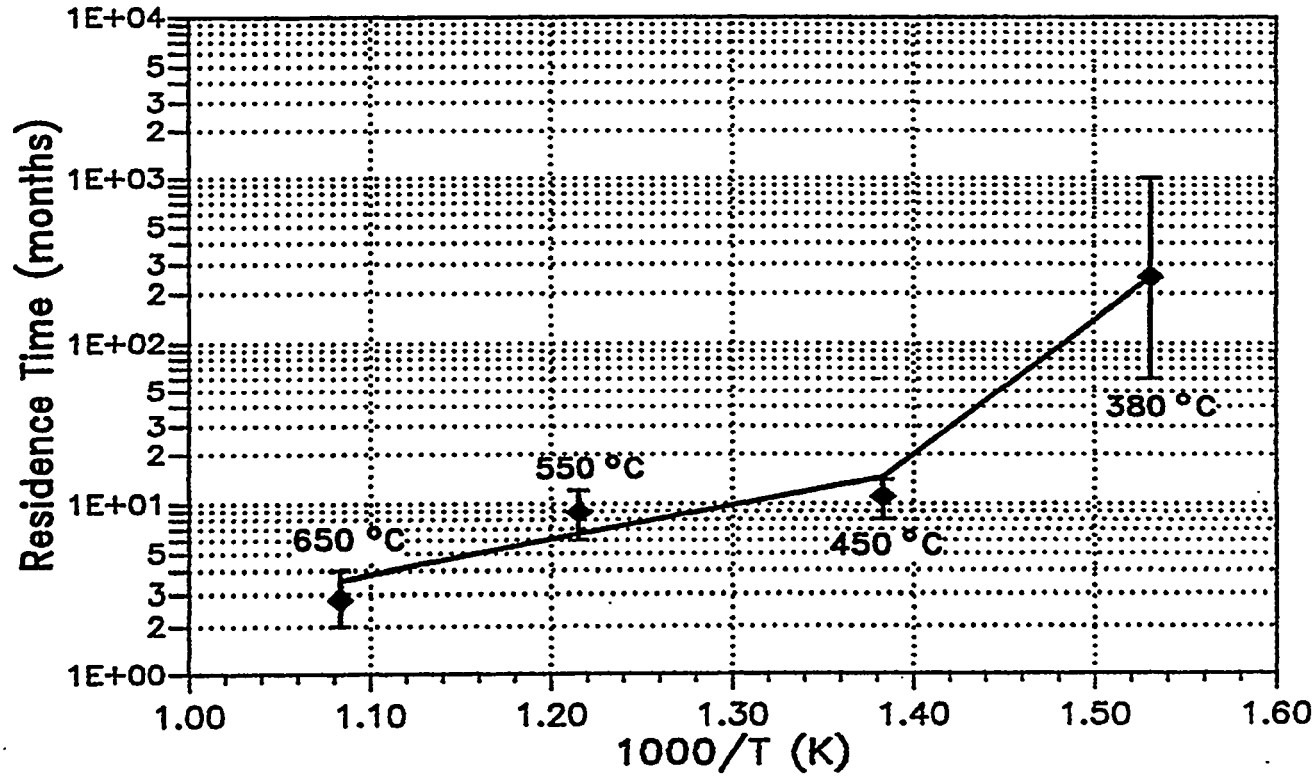

Figure 6: Residence time vs. annealing temperature for neutron-generated tritium in beryllium (SIBELIUS samples, quarters of pellets).

3. COMPARISONS WITH ANFIBE PREDICTIONS

In order to better understand the physical mechanisms governing tritium release behaviour in beryllium, as well as to generate confidence in the results provided by the code ANFIBE and to assess its prediction capabilities, it was necessary to compare the calculated results with a large number of reliable experimental data as described in [2].

Samples 2-13 and 5-11/13 of the SIBELIUS series, both irradiated at 550 °C, and successively annealed at 550 and 650 °C respectively up to 12 months has been taken as reference for long-time annealing calculations with the ANFIBE code. Although both samples were, during irradiation, in contact with ceramics and ANFIBE cannot yet take into account the effects of implanted tritium, they were in any case chosen due to the fact that, in a similar way as for samples 2-15 and 5-15, in both cases essentially all implanted tritium, but only a small fraction of the neutron-generated tritium was released during the irradiation at high temperature.

A comparison in terms of fractional tritium release as a function of the annealing time between experimental data and predictions of ANFIBE is shown in Figs. 7 and 8. The agreement between calculated and experimental data is satisfactory. The predicted residence time of neutron-generated tritium is about 6 months for sample 2-13 (annealing temperature 550 °C) and 2 months for sample 5-11/13 (annealing temperature 650 °C) respectively. These values are in reasonable agreement with the experimental results shown in Fig. 6.

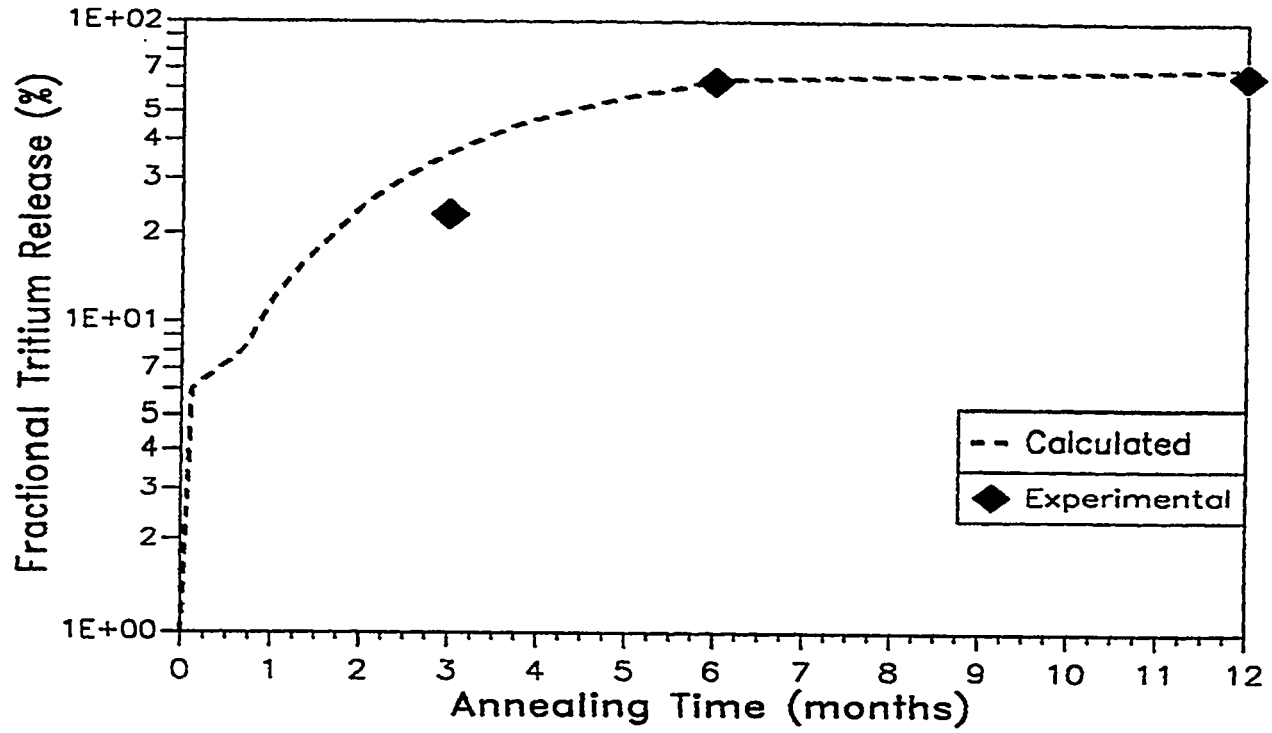

Figure 7: Comparison of calculated and measured (SIBELIUS sample 2-13) fractional tritium release during annealing at 550 °C as a function of time.

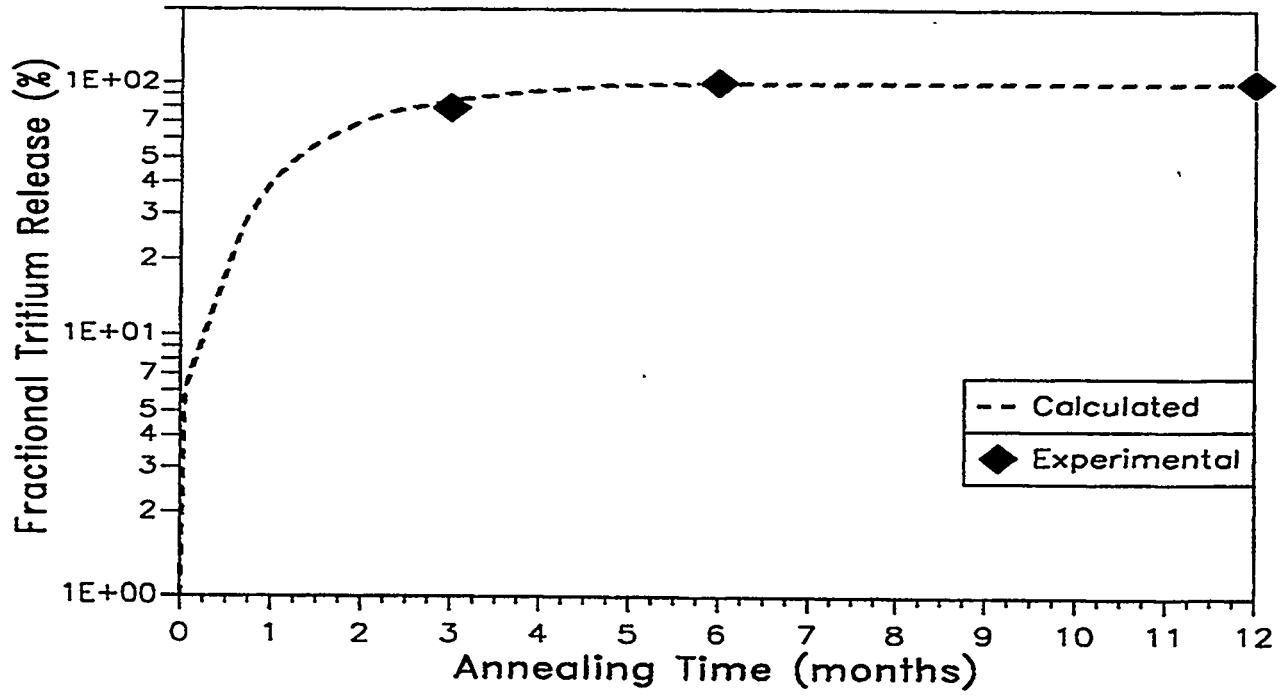

Figure 8: Comparison of calculated and measured (SIBELIUS sample 5-11/13) fractional tritium release during annealing at 650 °C as a function of time.

In order to investigate the possible crack formation eventually causing an increased tritium release from beryllium, the behaviour of two samples both irradiated at low temperature but at very different fast neutron fluence in the BR2 reactor and successively out-of-pile annealed at high temperature has been investigated.

In the first case the behaviour of the sample 110A-9c.3 of the MOL series (fast fluence $0.8 \cdot 10^{22}$ cm^{-2}) was investigated. As previously pointed out, the in-pile irradiation was followed by a temperature ramp with a slope of about 5 °C/min from room temperature up to 850 °C. As shown in Fig. 9, the tritium release rate has a rapid increase during the temperature ramp and then it tends to slowly decrease as the annealing temperature remains constant. The comparison between calculated and experimental data shows in this case a good agreement.

On the contrary, for the sample 110A-9a.3, which was irradiated with a fast neutron fluence of $2.8 \cdot 10^{22}$ cm^{-2} and successively out-of-pile annealed up to 850 °C in the same way as the previous one, a sharp peak is observed in the experimental tritium release rate curve during the temperature ramp probably because of microcracks formation. Due to the higher neutron fluence, in fact, the beryllium specimens has become more brittle than in the previous case and consequently it easily cracked under thermal stresses. A comparison between the calculated and the experimental tritium release is shown in Fig. 10. Since ANFIBE doesn't account yet for the effect of the microcracks, the code prediction cannot be, in this case, in good agreement with the experimental data as for sample 110A-9c.3.

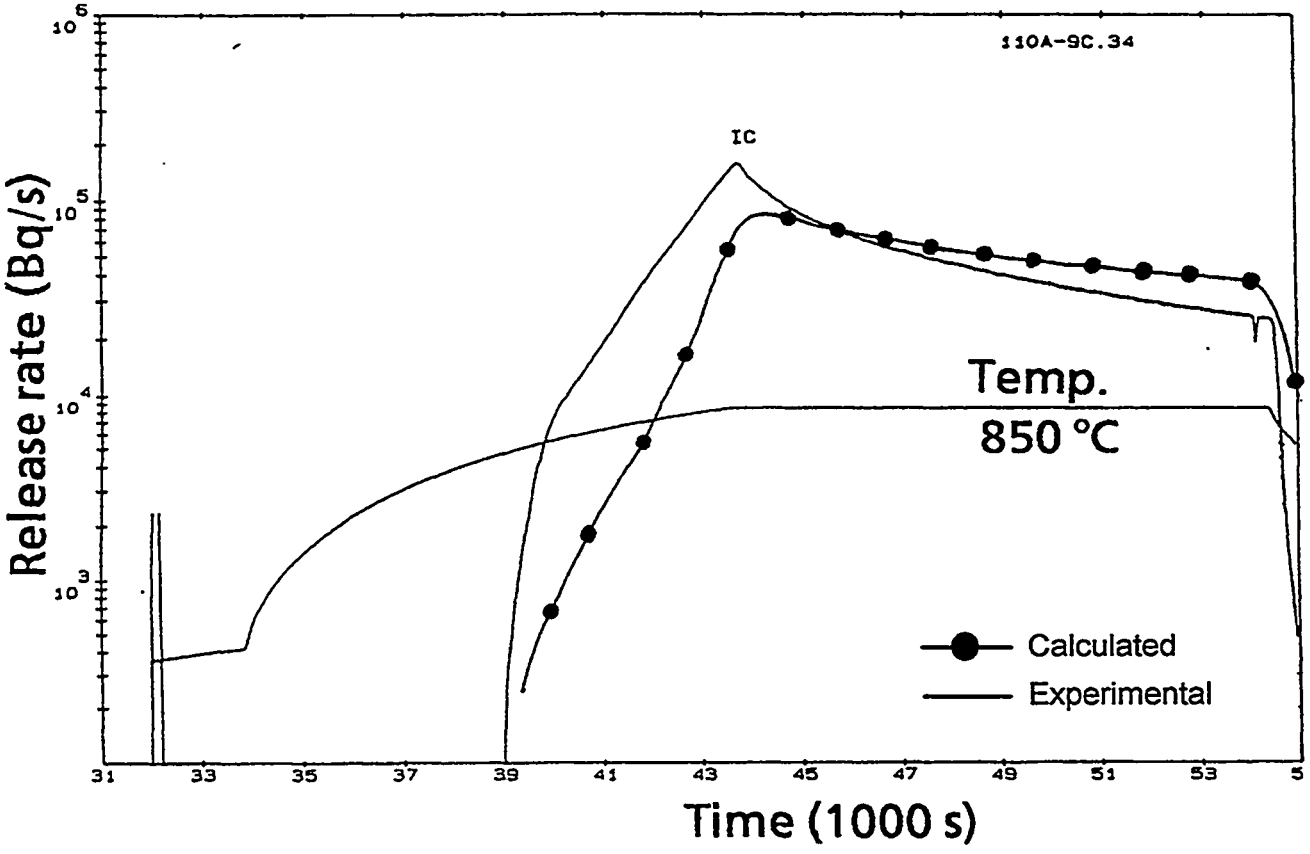

Figure 9: Comparison of calculated and measured tritium release rate as a function of time for moderately irradiated beryllium (fast fluence $0.8 \cdot 10^{22}$ cm^{-2}, MOL sample 110A-9c.3).

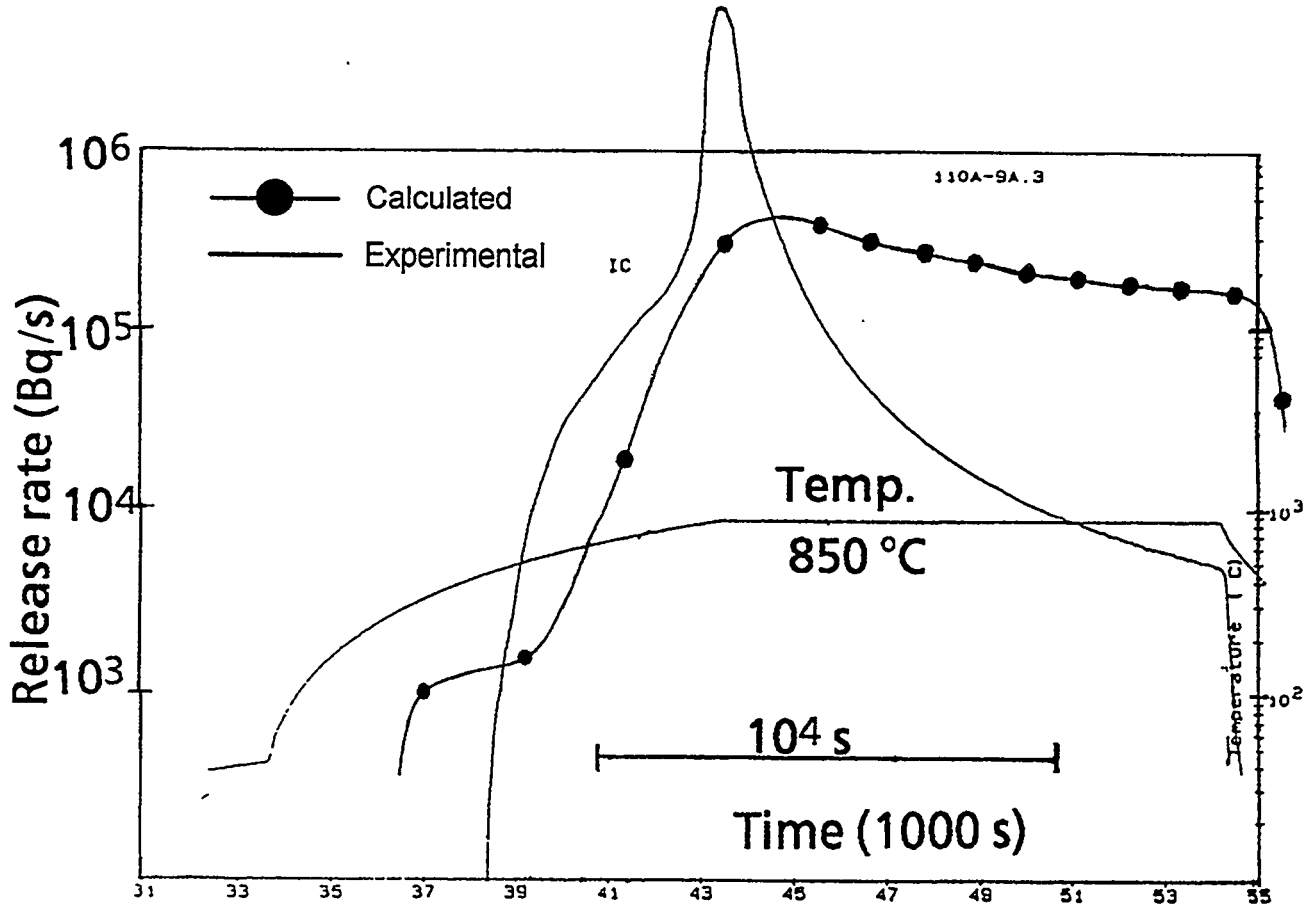

Figure 10: Comparison of calculated and measured tritium release rate as a function of time for highly irradiated beryllium (fast fluence $2.8 \cdot 10^{22}$ cm^{-2}, MOL sample 110A-9a.3).

4. CONCLUSIONS

In the present work both stepped and ramp annealing experiments were done to investigate tritium release behaviour from irradiated beryllium. Tritium release kinetics from two types of beryllium samples (SIBELIUS and MOL) has been studied. Comparison of the experimental data with the prediction of code ANFIBE was also performed with the goal to better understand the mechanisms governing tritium transport and to assess the prediction capabilities of the code.

According to previous studies, it was found that the release of neutron-generated tritium in beryllium is very slow if compared with ceramics. Furthermore, the present work indicates that for beryllium which is in direct contact with breeder ceramic during irradiation, a fraction of the 2.74 MeV tritons (range in ceramic ≈40μm) produced in the ceramic is implanted into the surface layer of beryllium, thus leading to an additional inventory which was estimated to be several times larger than the neutron-produced one. Analysis of samples from the SIBELIUS series indicates that pellets irradiated at relatively low temperature (270 °C) retain, during irradiation, most of the implanted and essentially all the neutron-generated tritium. On the contrary, pellets irradiated at 550 °C, seem to release all the implanted tritium

already during irradiation, while the neutron-generated tritium is released only after annealing at temperatures above 600 °C.
Long-time annealing of beryllium samples from the SIBELIUS series indicates that tritium release is very slow below 400 °C and moderately fast between 450 and 550 °C, while at 650 °C the inventory decreases fast during the first 6 months and then remains essentially constant as confirmed by ANFIBE calculations too.
Beryllium samples from the MOL series irradiated with the lowest fast fluence ($0.8 \cdot 10^{22}$ cm^{-2}) show, in a similar way as for the SIBELIUS samples, a release which starts to increase above about 600 °C, but decreases very slowly at 850 °C. Correspondingly, only a small fraction (11%) of the tritium is released at 850 °C, the bulk (83%) is released at 880 °C and the residual 6% at 1050 °C. On the other hand, a surprising behaviour was observed at 880 °C: during heating at constant temperature, after a time lag of several hours a burst release was observed, probably due to migration of helium bubbles leading to the formation of interconnected grain-edge tunnels to the sample surface. With other samples irradiated up to very high fast neutron fluences of $3.9 \cdot 10^{22}$ cm^{-2}, a much faster tritium release than in the case of weakly irradiated samples was observed. Comparison of experimental data with ANFIBE predictions indicates that this effect is due to microcracks formation during the out-of-pile heating phase. This is confirmed by the fact that highly irradiated beryllium from the MOL series showed a rather brittle behaviour during the cutting phase of the samples.
Although, at this stage, not all the mechanisms governing the release of tritium in irradiated beryllium have been fully understood, comparison of the code predictions with experiments indicate that, for the cases considered so far, the most important phenomena were accounted for by ANFIBE. However, to further improve the availability of the code predictions, in-pile experiments at high temperatures and, at the same time, high fast neutron fluences are clearly required.

ACKNOWLEDGMENT

The authors thank L. Dörr, T. Eberle, J. Lebkücher and A. Weisenburger for performing the experiments.
This work was performed in the framework of the Forschungszentrum Karlsruhe Nuclear Fusion Project and is supported by the European Communities within the European Fusion Technology Program.

REFERENCES

[1] W. Dienst, D, Schuld, H. Werle, "Tritium Release of Li_4SiO_4, LiO_2 and Beryllium and Chemical Compatibility of Beryllium with Li_4SiO_4, LiO_2 and Steel (SIBELIUS Irradiation)", KfK Report 5109, 1992.

[2] F. Scaffidi-Argentina, "Modellierung des Schwellens und der Tritium-Freisetzung von bestrahltem Beryllium", FZKA Report 5633 (to be published).

[3] N. Roux et al., "The SIBELIUS Experiment: Study of the Irradiation Behaviour of Beryllium/Ceramics and Beryllium/Steel Compacts.", J. Nucl. Mater. 179-181 (1991) 827-830.

[4] N. Roux et al., "Compatibility Behaviour of Beryllium with $LiAlO_2$ and $LiZrO_2$ Ceramics with 316L and 1.4914 Steels in SIBELIUS", J. Nucl. Mater 191-193 (1992) 168-172.

[5] L. Sannen, "Characterization of Irradiated Beryllium", CEN Mol Report FT/Mol/92-01, July 1992.

[6] L. Sannen, Ch. de Raedt, "The Effects of Neutron Irradiation on Beryllium", Proceedings of the SOFT-17 Conference, Rome, 1992.

[7] D.L. Baldwin, M.C. Billone, "Diffusion/Desorption of Tritium from Irradiated Beryllium", J. Nucl. Mater. 212-215 (1994) 948-953.

DEVELOPMENT OF RADIATION RESISTANT GRADES OF BERYLLIUM FOR NUCLEAR AND FUSION FACILITIES

I.B.Kupriyanov, V. A.Gorokhov, G.N.Nikolaev

State Scientific Center of Russian Federation VNIINM(A.A.Bochvar All-Russia Research Institute of Inorganic Materials)
123060, Russia, Moscow, P.O.Box 369, VNIINM

V.N.Burmistrov

State Scientific Center of Russian Federation NIIAR
433510, Russia, Dimitrovgrad-10

R&D results on beryllium with high radiation resistance obtained recently are described in this report. The data are presented on nine different grades of isotropic beryllium manufactured by VNIINM and distinguished by both initial powder characteristics and properties of billets, made of these powders. The average grain size of the investigated beryllium grades varied from 8 to 26 μm, the content of beryllium oxide was 0.9 - 3.9 wt.%, the dispersity of beryllium oxide - 0.04 - 0.5 μm, tensile strength -- 250 - 650 MPa.

All materials were irradiated In SM - 2 reactor over the temperature range 550 - 780°C. The results of the investigation showed, that HIP beryllium grades are less susceptible to swelling at higher temperatures in comparison with hot pressed and extruded grades. Beryllium samples, having the smallest grain size, demonstrated minimal swelling, which was less than 0.8 % at 750°C and Fs = $3.7 \cdot 10^{21}$ cm^{-2} (E>0.1 MeV). The mechanical properties, creep and microstructure parameters, measured before and after irradiation, are presented.

1. INTRODUCTION

Beryllium is under the consideration as a main candidate material for plasma facing components of ITER. One of the main requirements for such components is a resistance to thermal cyclic loading under neutron irradiation conditions. Therefore, to create suitable beryllium it is necessary to develop methods of increasing the thermal strength and radiation resistance of existing beryllium grades. The earlier concept of the development of beryllium with high radiation resistance, allowed to formulate requirements to metal structure, providing for suitable properties. The main of them are small grain size, high content and dispersity of beryllium oxide, which has to be distributed at the grain boundaries[1]. Carring out of these requirements increases the nucleation number and stability of gas bubbles, improves the creep resistance, diminishes the brain boundary slipping and increases the high-temperature strength. Finally, all this factors lead to swelling decrease.

For several recent years authors have been conducting the investigations on tile properties of different grades of beryllium before and after irradiation. Some results of these investigations were presented at SOFT-18 [1]. The new data, obtained recently, compared with those, presented earlier, are described in this report. Thus, the report presents the data on swelling, results of tensile and creep tests and microstructure data on swelling results of tensile and creep tests and microstructure

parameters of nine different grades of isotropic beryllium, manufactured by VNIINM and distinguished both initial powder characteristics and properties of the billets, made from these powders.

2. MATERIALS AND EXPERIMENTAL PROCEDURE

Nine grades powder beryllium were manufactured and tested, among them one grade of porous beryllium with 3 vol.% of porosity - THP-56P. Six beryllium grades were prepared out of cast beryllium powder (THP-56, THP-56P, THP-40, TIP-30, TIP, TRR) and three grades were obtained out of distillate beryllium (DIP-30, DIP, DRR). Five beryllium grades (TRR, DRR, TIP, DIP, DIP-30), having a fine-grained microstructure, which is dispersion-reinforced with oxide beryllium inclusions, fit almost all requirements mentioned above.

All beryllium grades are described by the following characteristics: average grain size (a.g.s.), beryllium oxide content (C_{BeO}), dispersity of particles of beryllium oxide (a.o.s.) and compacting method. The characteristics of beryllium grades being investigated are presented in Table. 1.

To evaluate a stability of stricture and mechanical properties during prolonged operating period, six grades of beryllium (TIP, DIP, TRR, DRR, TIP-30, DIP-30) were exposed to annealing at 650 and 750°C for 1000 hours. Within the error limits no change were revealed in the density, grain size and second fases stability. Tensile and compressive test results indicated, that on the whole the mechanical properties do not change due to annealing for all tile materials. The scatter in the data of 2 - 8 % seems to be connected with certain structure inhomogeneity of tile samples investigated.

All materials were irradiated in high flux channels of SM-2 reactor in leaktight capsules. Neutron flux density (E>0.1 MeV) was $(3.2 - 3.6)\cdot\cdot 10^{14}$cm^{-2}s^{-1} and that of thermal neutron was $(3.0 - 5.1)\cdot 10^{14}$cm^{-2}s^{-1}. Irradiation was performed up to the maximum fluence of fast neutrons of $3.7\cdot 10^{21}$cm^{-2} and to that of thermal neutrons $5.4\cdot 10^{21}$ cm^{-2}. Table 2 summarizes the irradiation parameters of tile materials.

3. EXPERIMENTAL RESULTS AND DISCUSSION

3. I. SWELLING

Fig. 1 shows the experimental curves of the beryllium swelling versus irradiation temperature. According to Fig. 1 and Table 1, beryllium swelling reduces with the grain size decrease and with the oxide content and dispersity increase. HIP beryllium grades are less susceptible to the swelling at higher temperature compared with hot pressed grades and the porous beryllium, that is connected with the higher creep resistance of the HIP beryllium [2].

It should be noted, that the differences in swelling between beryllium grades TIP, DIP, TRR and DRR (corresponding data placed in the hatched field of Fig. 1, curves 1 - 4), were less, than it was expected from the differences in grain size, oxide content, mechanical properties and creep resistance. At first sight this fact contradicts earlier experimental results and to the generally accepted opinion, that the structural elements mentioned above have a considerable effect on the swelling at temperatures above 600°C and fluences more than $5 - 10^{20}$ cm^{-2} [3]. By X-ray analysis and transmission electron microscopy (TEM) it was revealed, that in these beryllium grades the gas atoms, formed during irradiation, were dissolved in the solid solution (>95 %), and only a small part of them precipitated in the form of gas bubbles. This fact indicates, that beryllium grades under consideration are in the beginning of swelling, when the importance of structural factors are not

significant. It is expected, that with the increase of fluence or irradiation temperature tile swelling rates of TRR, DRR grades will be less, than those of TIP and DIP grades. Tile creep test results confirm this assumption indirectly (Table 3).

Fig. 2 presents tile data of swelling inhomogeneity versus a distance from tile irradiated surface. These data were obtained by the density measurements of tile samples, cut out of the bulk beryllium block along the neutron flux (F_s) direction at various depths from the outer surface. The maximum depth was of 50 mm. According to Fig. 2, the higher total swelling and tile higher irradiation temperature, the larger swelling inhomogeneity is. This effect is connected with the properties of beryllium to scatter and to slow down neutrons, resulting in inhomogeneities of tile production of transmutation elements along the neutron range. Fig. 3 presents the variation of beryllium density as a function of helium content for the DIP grade samples after irradiation. Swelling inhomogeneities should be taken into account when designing beryllium elements, because they call cause additional alternate stresses, which can lead to inhomogeneous deformation of beryllium elements and even to their failure.

3.2. RESULTS OF TENSILE TEST

Fig. 4 and 5 show the effect of irradiation on mechanical properties of beryllium. Tests were performed at 20, 550, 650 and 750°C. All the irradiated materials suffered a significant decrease of tensile strength, yield strength (15 - 50 %) and elongation (65 - 100 %). However, after the irradiation the tensile strength and yield strength values of the most stable against swelling beryllium grades (TRR, DRR, TIP, DIP) conform to initial strength characteristics of the most of commercial grades. The results of investigation showed, that the materials with higher initial strength properties are less susceptible to swelling (Fig. 1, 4, and 5).

3.3. RESULTS OF CREEP TESTS

Table 3 presents creep test results most stable against swelling beryllium grades before and after irradiation. Creep rate of TIP and DIP grades is higher, than that for TRR and DRR grades. Tills difference seems to be connected with grade size and oxide content effect on the creep resistance [2]. After the irradiation at 750°C with fluence $2.4 \cdot 10^{21}$ cm^{-2} tile creep rate is 2 - 5 times higher.

CONCLUSION

High-temperature neutron irradiation results in significant changes in physical and mechanical properties of beryllium. To minimize these changes, one needs to affect such structural parameters as grain size, content and dispersity of beryllium oxide.

New method of development of beryllium with high radiation resistance allowed to produce beryllium grades with higher size stability under the irradiation. Beryllium grades with the smallest grain size show minimal swelling of less than 0.8 - 1.0 % after the irradiation with fluence $3.7 \cdot 10^{21}$ cm^{-2} at 750°C.

After the irradiation the tensile strength and yield strength values of the most stable against swelling beryllium grades TRR, DRR, TIP, DIP conform to initial strength characteristics of the most of commercial grades.

REFERENCES

[1] I.B.Kupriyanov, V.A.Gorokhov, A.M.Khomutov, Manufacturing and Some Properties of Beryllium with High Radiation Stability, presented at the 18 th SOFT, 1994.

[2] Beryllium: Science and Technology, Edited by D.Webster, D.Floyd, Plenum Press, New York 1979.

[3] V.P.Goilsev, G.A.Sernyaev, Z.I.Chechetkina,, Radiation Material Science of Berylllum, Minsk, Science and Engineering, 1977.

Table I

Characteristics of beryllium grades

Parameters of material	Materials								
	TRR	DRR	TIP	DIP	DIP-30	TIP-30	THP-40	THP-56	THP-56P
a.g.s., μm	8-9	8-9	13-14	13-14	18	20	18	25	26
C_{BeO}, % wt.	3.2	3.9	1.4	2.0	2.2	2.1	1.8	0.9	0.9
a.o.s., μm	0.04	0.04	0.04	0.04	0.04	0.05	0.4	0.5	0.6
Compact-ing method	HIP[a)]	HIP[a)]	HIP[a)]	HIP[a)]	HIP[a)]	HIP[a)]	HP[b)]	HP[b)]	HP[b)]

a) hot isostatic pressing, b) hot pressing

Table II

Irradiation parameters of beryllium

Neutron fluence, cm^{-2}	Materials			
	THP-40 THP-56 THP-56P	TIP-30 DIP-30	TIP DIP	TRR DRR
$F_S \cdot 10^{21}$ (E>0.1 MeV)	1.8-2.6	2.0-2.7	2.4-3.7	2.4-3.7
$F_{th} \cdot 10^{21}$ (E<0.68 eV)	3.3-5.1	2.1-2.6	3.4-5.4	3.4-5.4

Table III

Creep rate of beryllium before and after irradiation with $F_S = 2.4 \cdot 10^{21} cm^{-2}$ (E>0.1 MeV) at 750°C

		Secondary creep rate, s^{-1}			
Material	Condition	T = 650°C		T = 750°C	
		σ = 15 MPa	σ = 25 MPa	σ = 15 MPa	σ = 25MPa
DIP	initial	$5{,}5 \cdot 10^{-9}$	$3{,}6 \cdot 10^{-9}$	$2{,}6 \cdot 10^{-8}$	$2{,}1 \cdot 10^{-7}$
	irradiated				$5.7 \cdot 10^{-7}$
TIP	initial	$1.2 \cdot 10^{-8}$		$4.3 \cdot 10^{-8}$	$2.0 \cdot 10^{-7}$
	irradiated			$<0.9 \cdot 10^{-7}$	
TRR	initial				$4.6 \cdot 10^{-8}$
	irradiated			$<0.9 \cdot 10^{-7}$	$2.5 \cdot 10^{-7}$
DRR	intial				$4.3 \cdot 10^{-8}$
	irradiated				

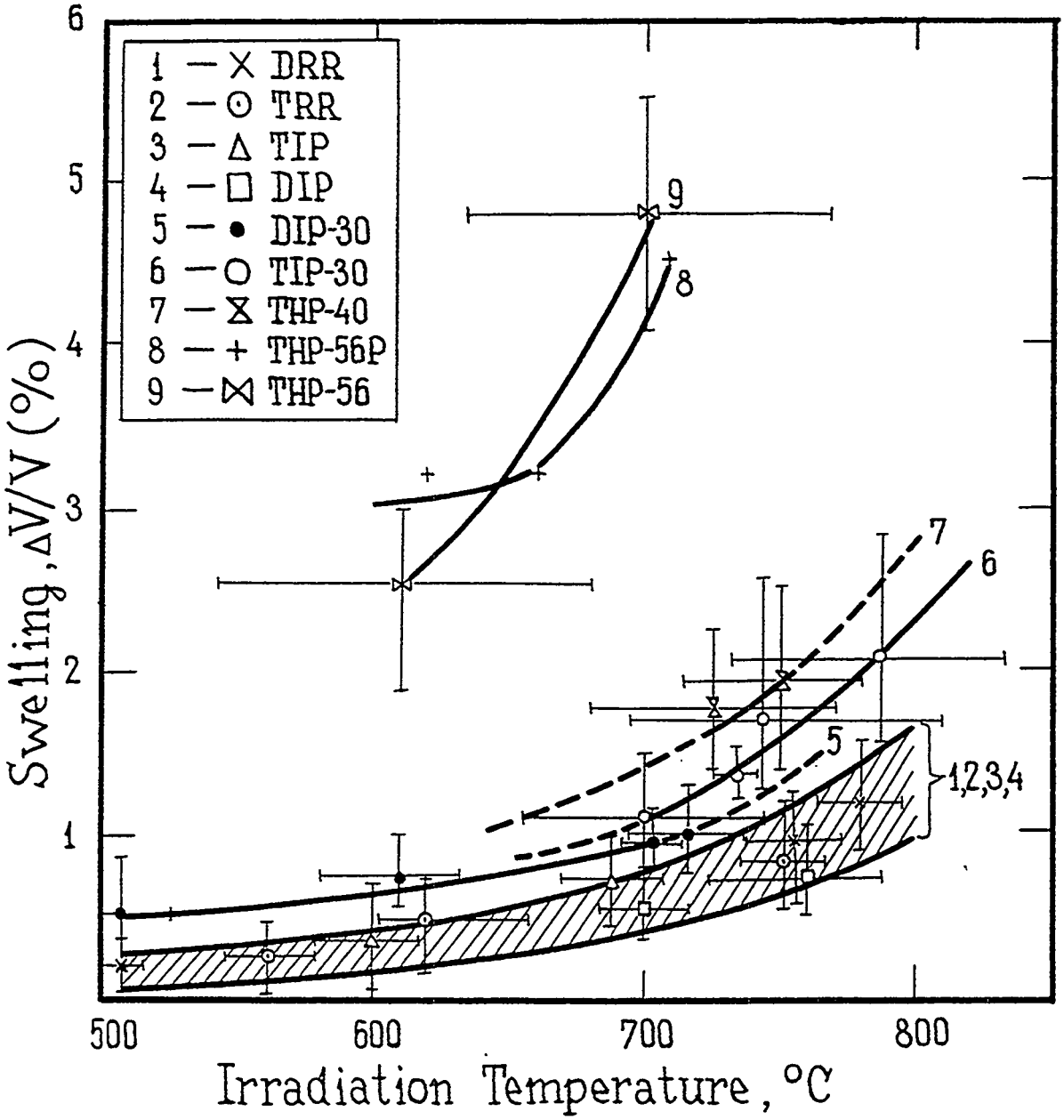

Figure 1. Swelling of beryllium vs irradiation temperature

(1-6) - HIP beryllium, (7-9) - HP beryllium. Neutron fluences (E>0.1) : (1-4) - $3.7 \cdot 10^{21} cm^{-2}$, (5-6) $2.7 \cdot 10^{21} cm^{-2}$, (7-9) - $10^{21} cm^{-2}$.

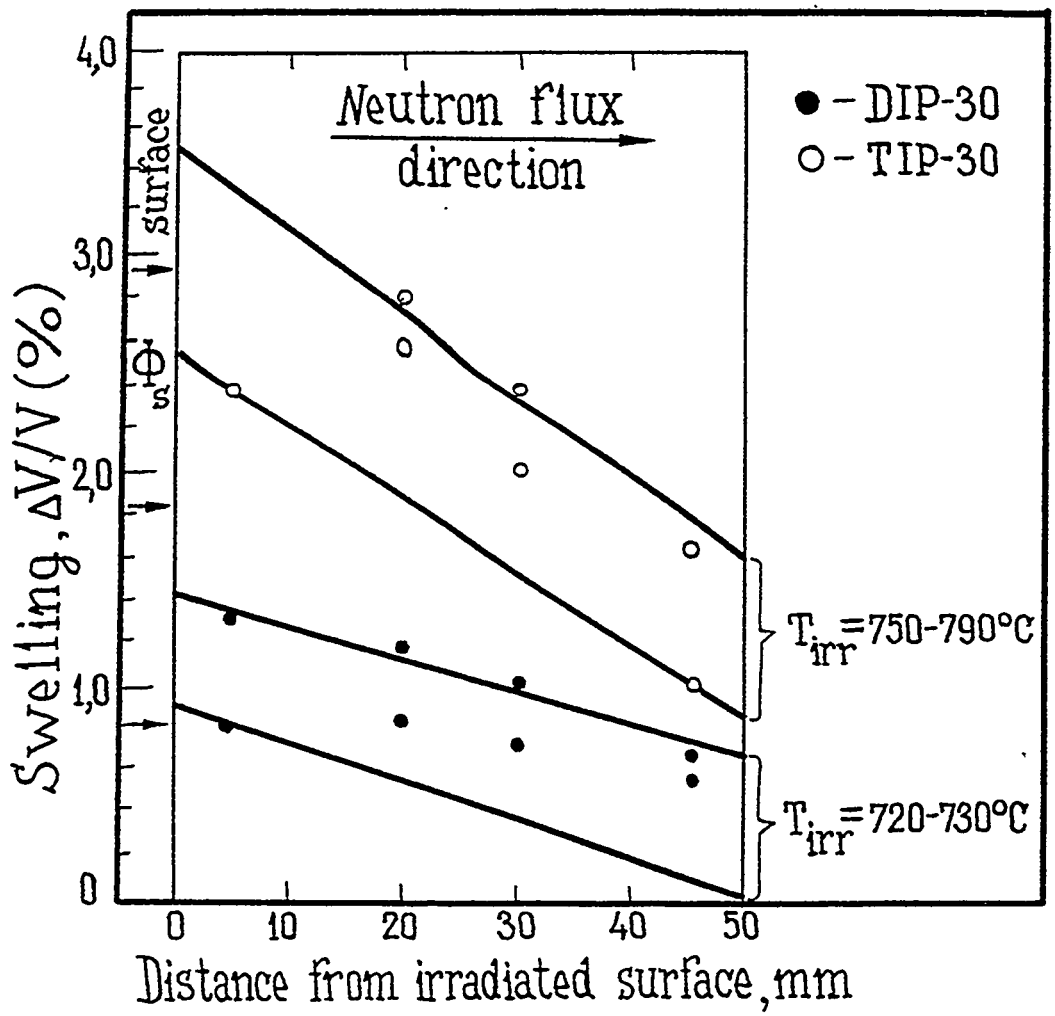

Figure 2. Inhomogeneity of beryllium swelling vs a distance from the irradiated surface

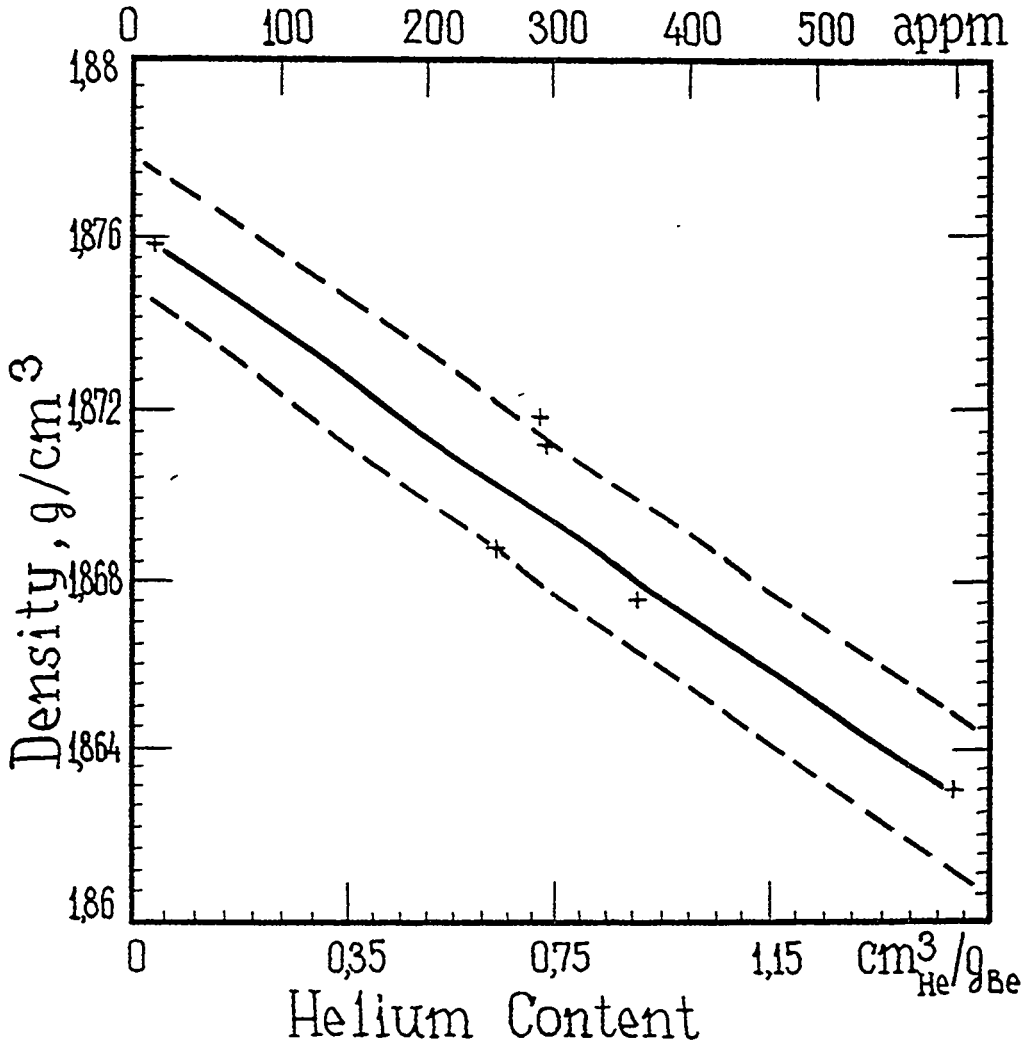

Figure 3. Beryllium density as a function of helium content

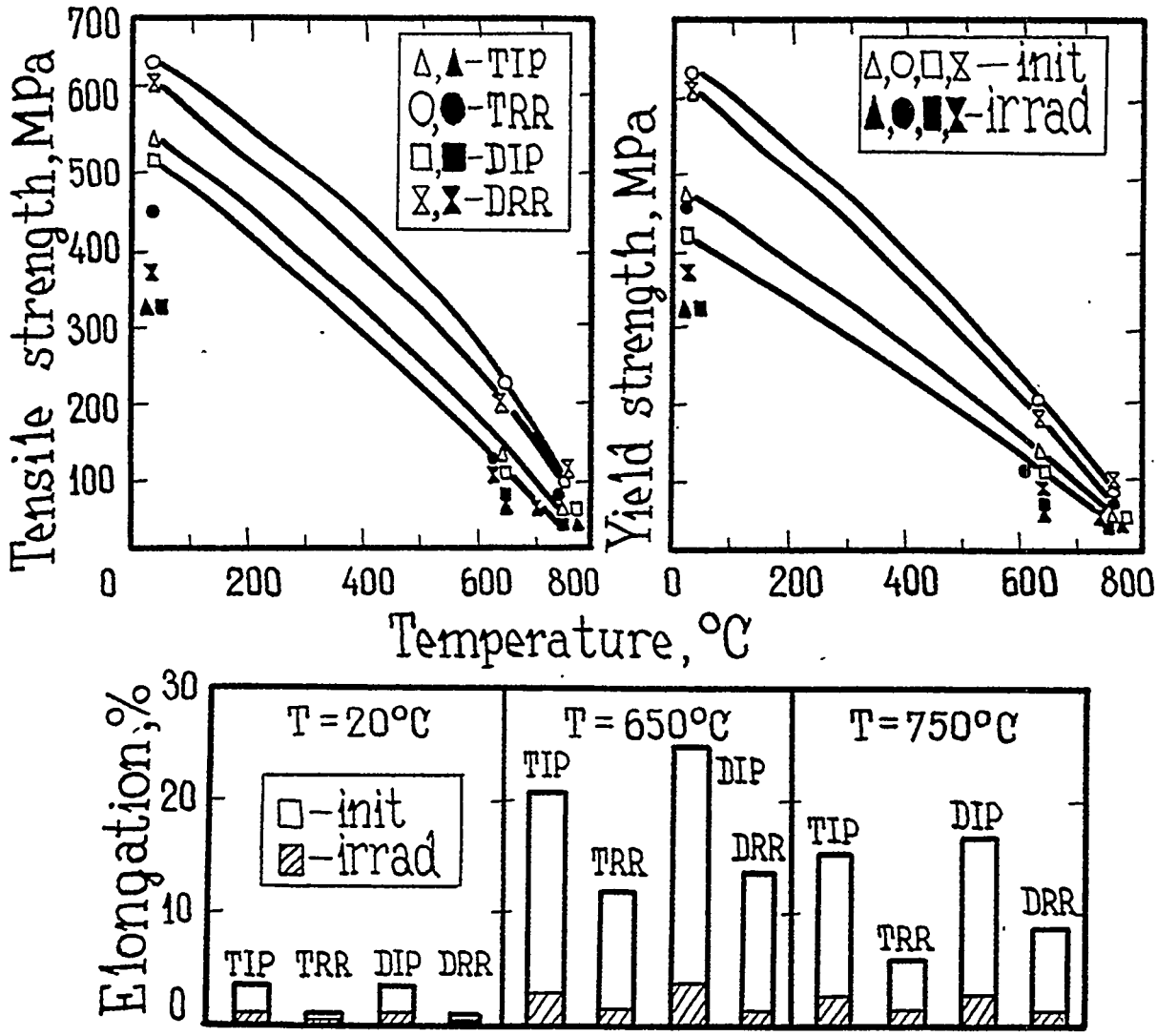

Figure 4. The effect of irradiation with fluence $2.4 \cdot 10^{21} cm^{-2}$(E>0.1 MeV) at 750°C on mechanical properties of beryllium

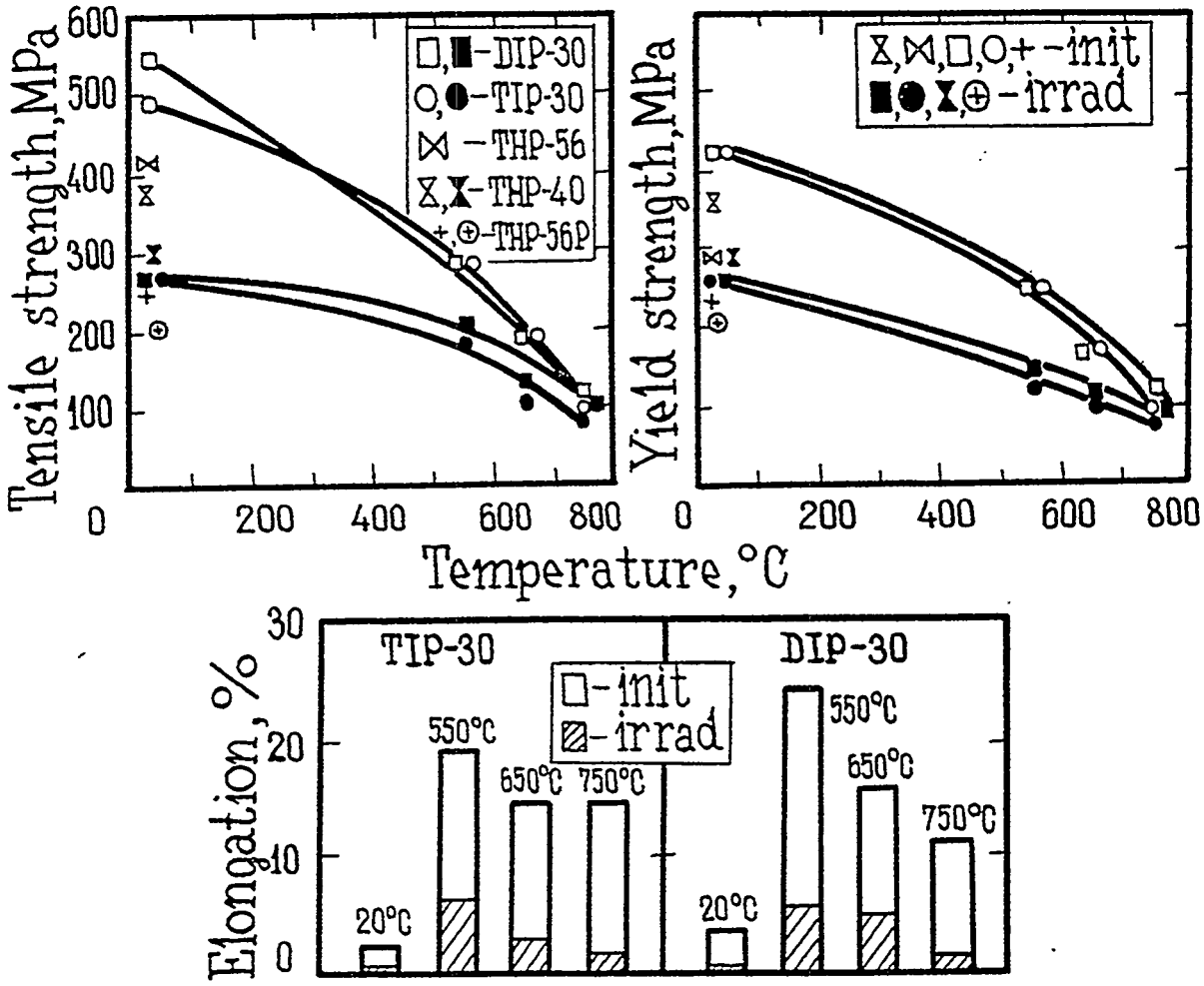

Figure 5. The effect of irradiation with fluence $2.0 \cdot 10^{21} cm^{-2}$ (E>0.1MeV) at 700°C on mechanical properties of beryllium

Reprocessing technology development for irradiated beryllium

H.Kawamura[a], K.Tatenuma[b],
Y.Hasegawa[b] and N.Sakamoto[a]

[a] *Japan Atomic Energy Research Institute, Oarai Research Establishment, Oarai-machi, Higashi Ibaraki-gun, Ibaraki-ken 311-13, Japan*

[b] *KAKEN Co. Mito Institute, Hori-cho 1044, Mito-city, Ibaraki-ken 310, Japan*

Abstract

At present, beryllium is under consideration as a main candidate material for neutron multiplier and plasma facing material in a fusion reactor. Therefore, it is necessary to develop the beryllium reprocessing technology for effective resource use. And, we have proposed reprocessing technology development on irradiated beryllium used in a fusion reactor.

The preliminary reprocessing tests were performed using un-irradiated and irradiated beryllium.

At first, we performed beryllium separation tests using un-irradiated beryllium specimens. Un-irradiated beryllium with beryllium oxide which is a main impurity and some other impurities were heat-treated under chlorine gas flow diluted with Ar gas. As the results, high purity beryllium chloride was obtained in high yield. And it appeared that beryllium oxide and some other impurities were removed as the unreactive matter, and the other chloride impurities were separated by the difference of sublimation temperature on beryllium chloride.

Next, we performed some kinds of beryllium purification tests from beryllium chloride. And, metallic beryllium could be recovered from beryllium chloride by the reduction with dry process.

In addition, as the results of separation and purification tests using irradiated beryllium specimens, it appeared that separation efficiency of Co-60 from beryllium was above 96%. It is considered that about 4% Co-60 was carried from irradiated beryllium specimen in the form of cobalt chloride. And removal efficiency of tritium from irradiated beryllium was above 95%.

1. Introduction

At present, Beryllium is under consideration as a main candidate material for neutron multiplier and plasma facing material in a fusion reactor. Therefore, it is necessary to develop the beryllium reprocessing technology for effective resource use.

We have proposed reprocessing technology development on irradiated beryllium used in a fusion reactor. Concept of beryllium reprocessing in fusion applications is shown in Fig.1. This reprocessing process consists of beryllium separation step from activated nuclides as the impurities in the beryllium, beryllium purification step from recovered beryllium compounds and fabrication step of metallic beryllium. And, the development of beryllium reprocessing technology in this study was shown in Fig.2. In beryllium separation tests from activated nuclides, the recovery of high purity beryllium chloride was performed using chlorine gas. And in beryllium purification tests with dry and wet process, the reduction of beryllium chloride was performed.

2. Experiments

2.1 Specimens

Used specimens for this reprocessing technology development were hot pressed beryllium (disk and block) made by NGK INSULATORS, LTD. and flaky beryllium. The results of chemical analysis on the hot pressed beryllium specimen are shown in Table 1. The purity of the beryllium specimen was about 99 wt%. And, the main impurity was beryllium oxide.

Irradiated beryllium specimens were used for the separation and purification tests. These have been irradiated in JMTR with total fast neutron fluence of 4.5×10^{20} n/cm^2.

2.2 Procedure

The concept of beryllium separation from radioactive isotopes as the impurities in specimen is shown in Fig.3. Used beryllium is heat treated at 450-550°C in quartz tube under chlorine gas flow diluted with Ar gas. Beryllium chloride is generated by the reaction of beryllium with chlorine, it is trapped and recovered. And radioactive isotopes such as Co-60 are separated as residue, tritium chloride is also trapped and separated. In this study, at first, beryllium separation tests using un-irradiated beryllium specimens were performed.

And, some kinds of purification tests from beryllium chloride was performed with wet and dry processes.

The concept of beryllium purification by wet process is shown in Fig.4. In this process, reduction tests of beryllium chloride with two kinds of reducing agents, that is, liquid polysilane and $LiAlH_4$.

The concept of beryllium purification by dry process is shown in Fig.5. In this process, beryllium chloride was decomposed by heating above 1400°C in order to recover metallic beryllium. The experimental apparatus for dry process on beryllium purification is shown in Fig.6. Beryllium chloride which is reaction product with chlorine gas was heated with a SiC filament. And, decomposed matters were trapped by filter (quartz-wool) and recovered.

The experimental apparatus for beryllium separation tests using irradiated beryllium specimen is shown in Fig.7. In this test, separation efficiency of Co-60 was decided with the measurement of γ spectrum on irradiated beryllium specimen before treatment, residue and recovered beryllium chloride after treatment. And removal efficiency of tritium from irradiated beryllium specimen was measured.

And, the experimental apparatus for beryllium purification tests with dry process using irradiated beryllium is shown in Fig.8. In this test, yield of recovered metallic beryllium, separation efficiency of Co-60 on generated matters by decomposition of beryllium chloride and removal efficiency of tritium from irradiated beryllium were evaluated.

3.Results and discussion

In beryllium separation tests using un-irradiated beryllium specimens, beryllium with beryllium oxide and some impurities were heat-treated under chlorine gas flow diluted with Ar gas. And, powder with white fine crystal of beryllium chloride was recovered. Recovery as beryllium chloride, that is, reaction rate of beryllium was above 99%. As the results, it appeared that high purity beryllium chloride was recovered in high yield. Beryllium oxide and some other impurities were removed as the unreactive matter, and the other chloride impurities were separated by the difference of sublimation temperature from beryllium chloride.

And in beryllium purification tests from beryllium chloride with wet process, metallic beryllium was not recovered. From the results of X-ray diffraction, it appeared that the matter after treatment contained beryllium oxide and residue of reducing agents.

As for the beryllium purification tests with dry process, micro particles of beryllium were recovered by decomposition of beryllium chloride. SEM photograph of deposited micro particle was shown in Fig.9. As shown in this figure, these particles were very fine. And, their amount was variable. This result is presumed to be caused by instability of contact between beryllium chloride gas and SiC filament.

In beryllium separation tests using irradiated beryllium specimens, reaction rate of beryllium was above 99%. And, it appeared that separation efficiency of Co-60 from beryllium was above 96% from the results of the measurement on γ spectrum, removal efficiency of tritium from irradiated beryllium was above 95%.

In beryllium purification tests with dry process using irradiated beryllium, reaction rate of beryllium was above 99%. And, yield of recovered metallic beryllium was not stable. Therefore, stability of contact between beryllium chloride gas and SiC filament is necessary. Separation efficiency of Co-60 from beryllium was above 96%, removal efficiency of tritium from irradiated beryllium was above 99%.

4. Conclusions

We have started reprocessing technology development on irradiated beryllium used in a fusion reactor for effective resource use. The obtained results were as follows.

- As the results of beryllium separation tests using un-irradiated beryllium specimens, high purity beryllium chloride was obtained in high yield. Recovery as beryllium chloride, that is, reaction rate of beryllium was above 99%. And it appeared that beryllium oxide and some impurities were removed as the unreactive matter, and the other chloride impurities were separated by the difference of sublimation temperature from beryllium chloride. Additionally in the tests using irradiated beryllium specimens, separation efficiency of Co-60 from beryllium was above 96%. It is considered that residual about 4% Co-60 was carried from irradiated beryllium specimen in the form of cobalt chloride. And, removal efficiency of tritium from irradiated beryllium was above 95%.

- As the results of some beryllium purification tests, metallic beryllium was recovered from beryllium chloride by the reduction with dry process, that is, thermal decomposition method using a SiC filament. However, yield of recovered metallic beryllium was variable. Therefore, it is considered that the improvement for stability of thermal decomposition is necessary. Additionally in the tests using irradiated beryllium specimens, separation efficiency of Co-60 from beryllium was above 96%, removal efficiency of tritium from irradiated beryllium was above 99%.

Reference

[1] A.T. Balaban, E.Barabas and C.Mantescu, Rev. Chim. Acad. Rep. Populaire Roumaine, 8 (1963) 139.

[2] J.R.Saunders Jr, J.C.Ashby and J.H.Carter II, J. Am. Chem. Soc., 90 (1968) 6385 .

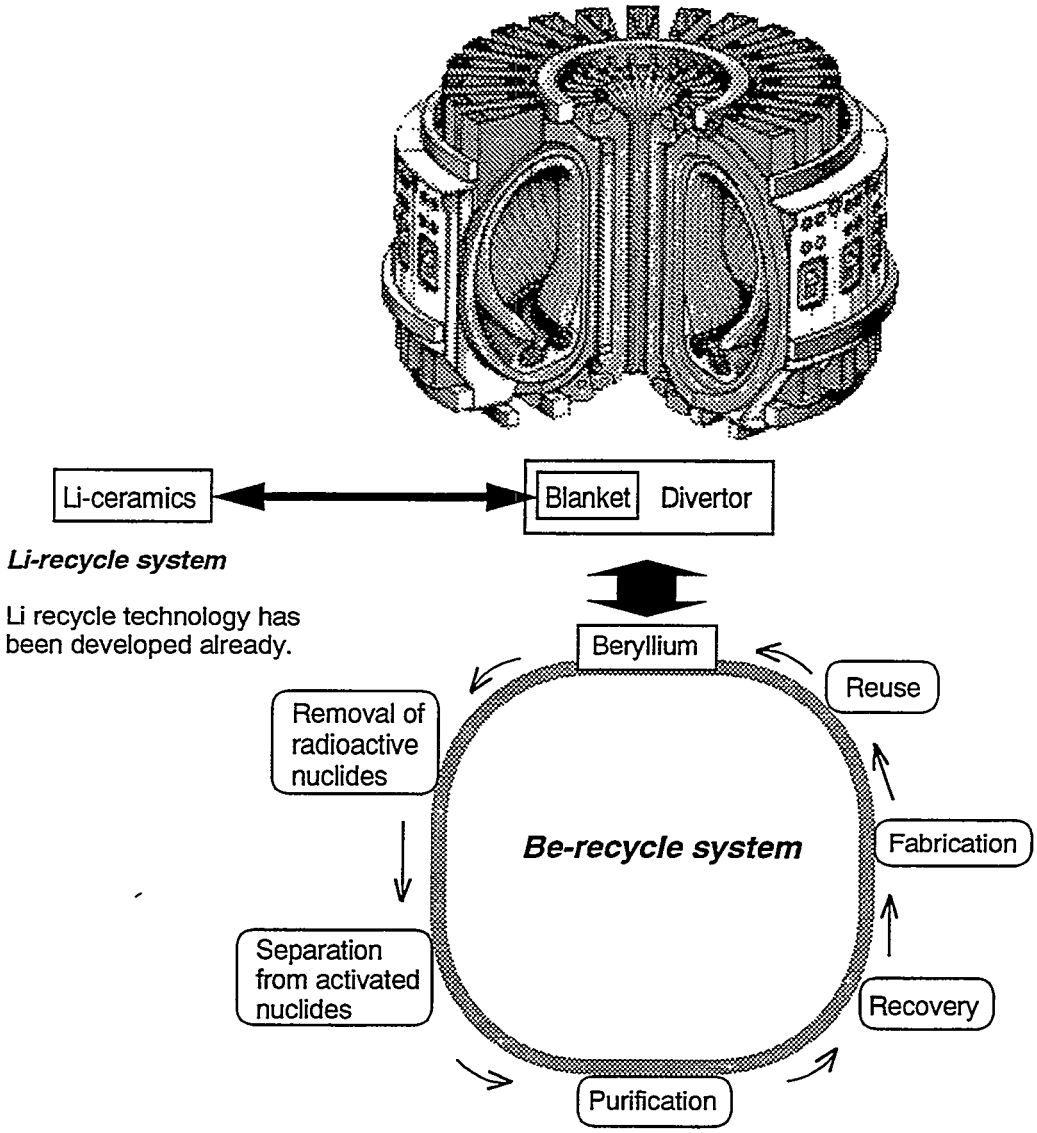

Fig. 1 The concept of beryllium reprocessing in fusion apprications

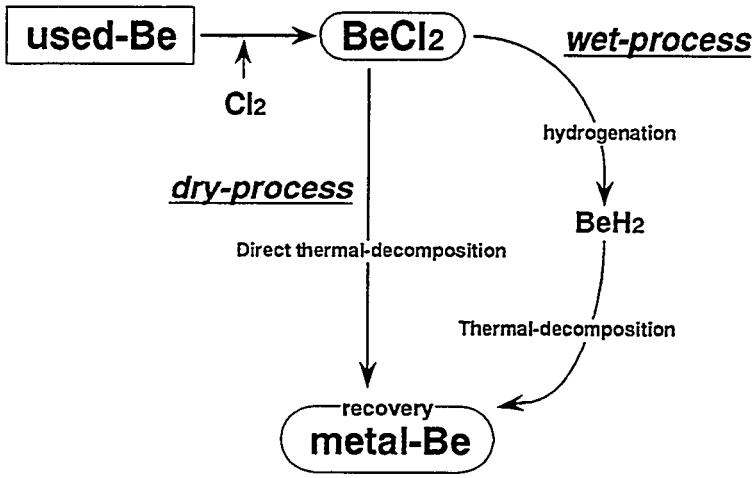

Fig. 2 The development of beryllium reprocessing technology in this study

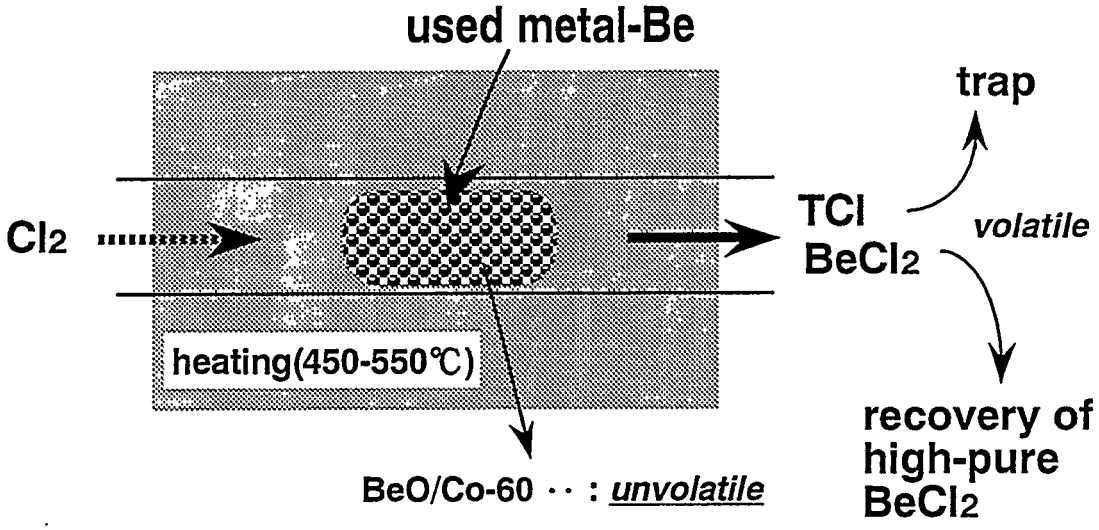

Fig. 3 The concept of beryllium separation

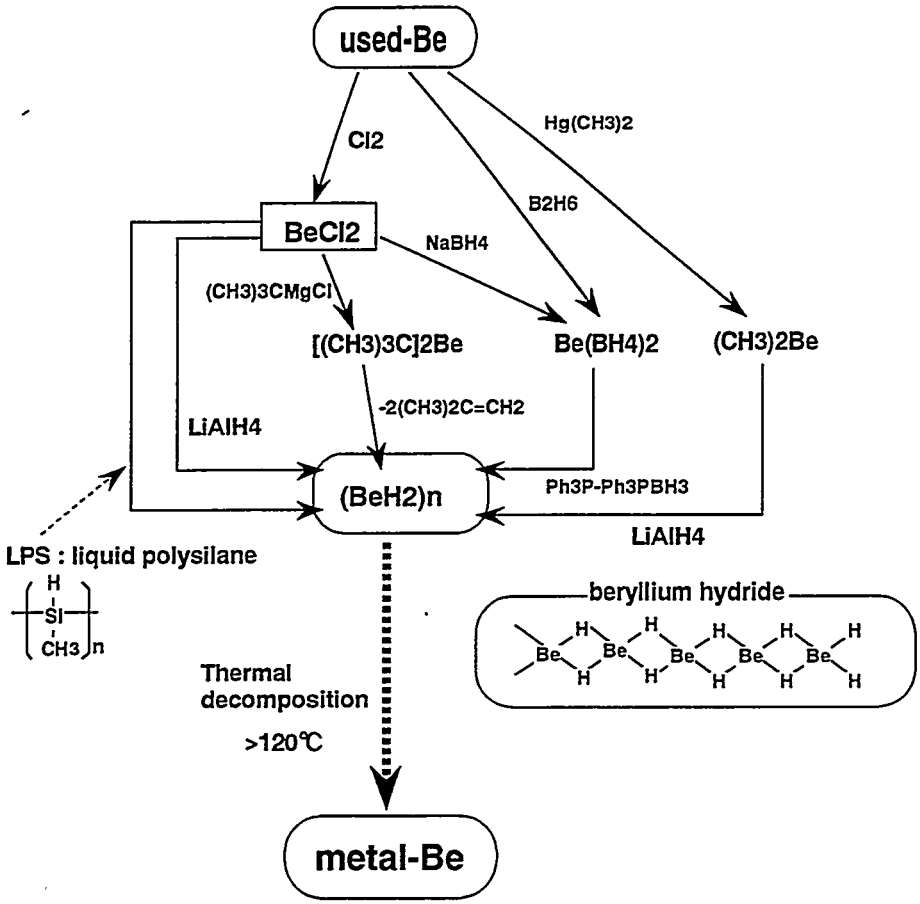

Fig. 4 The concept of beryllium purification by wet process

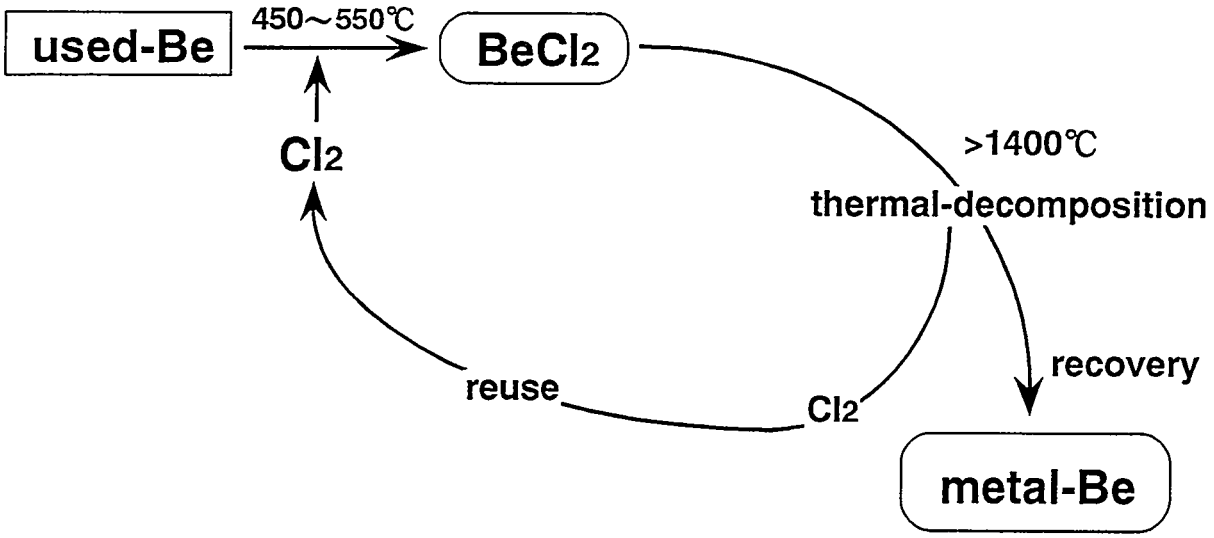

Fig. 5 The concept of beryllium purification by dry process

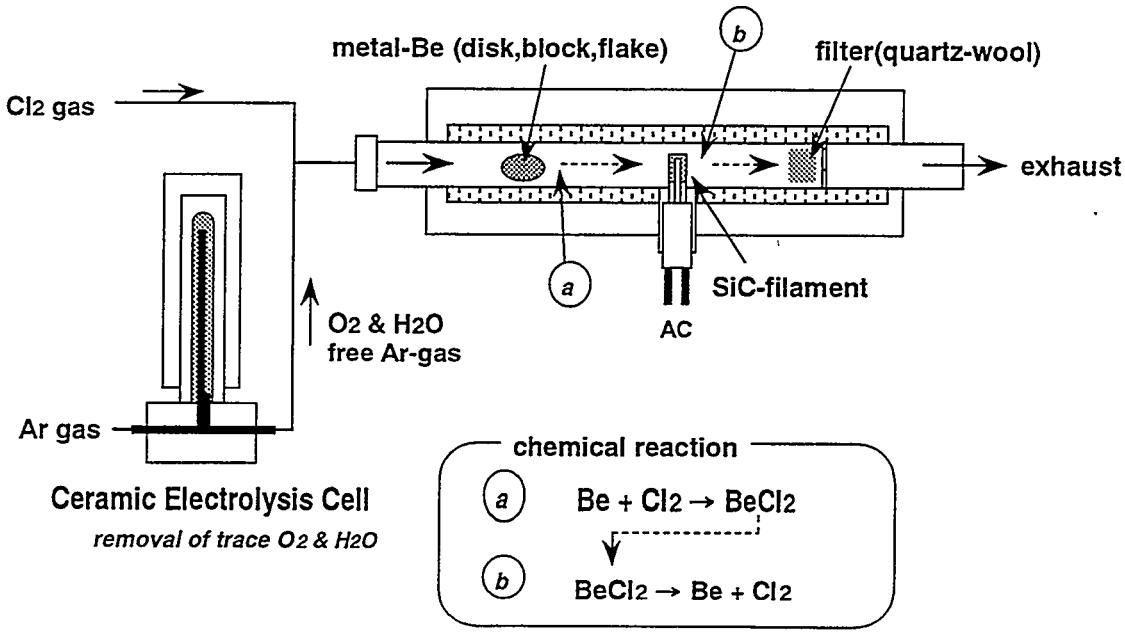

Fig. 6 The experimental apparatus for dry process on beryllium purification

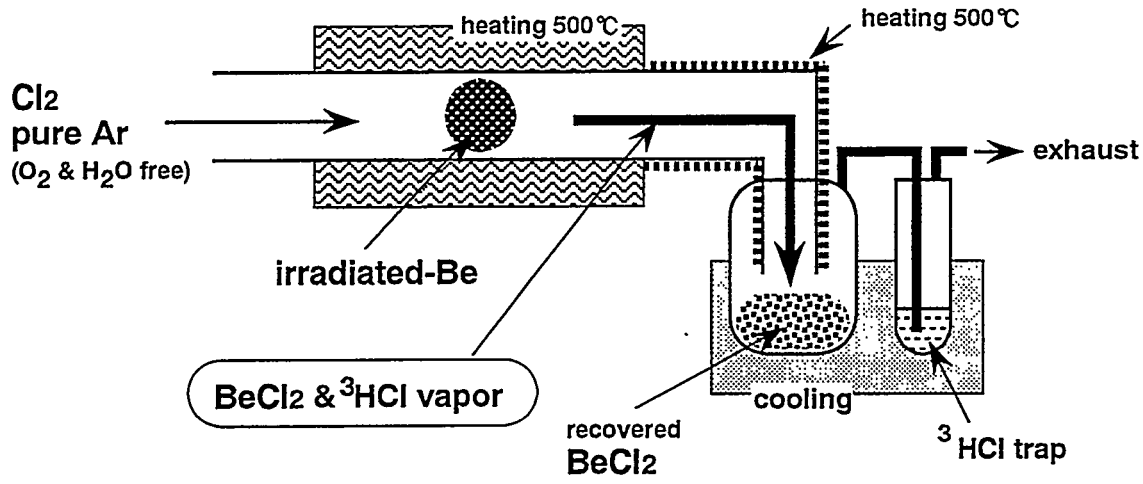

Fig. 7 The experimental apparatus for beryllium separation tests using irradiated beryllium specimens

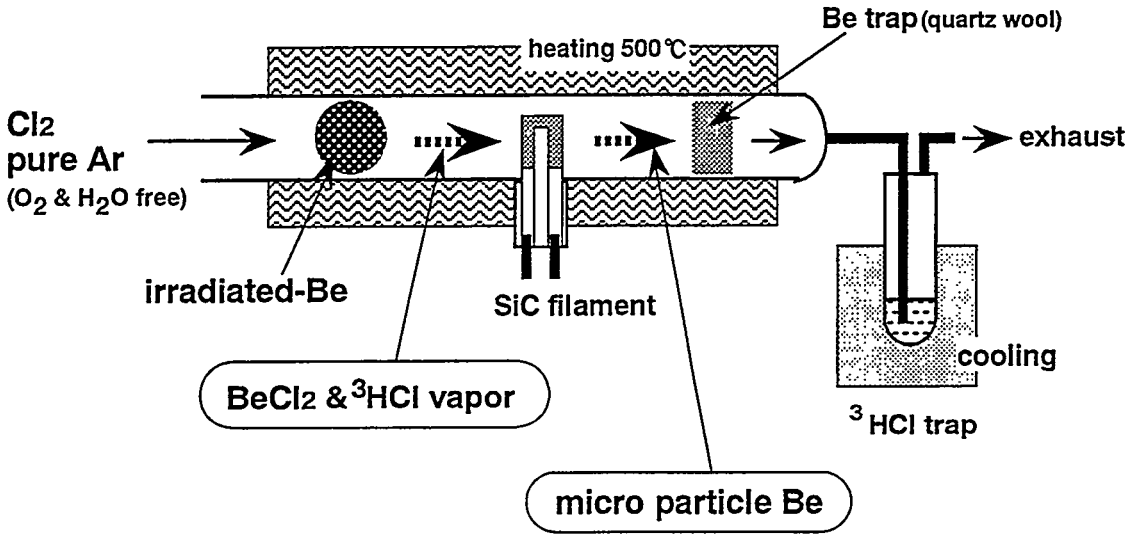

Fig. 8 The experimental apparatus for purification tests using irradiated beryllium specimens

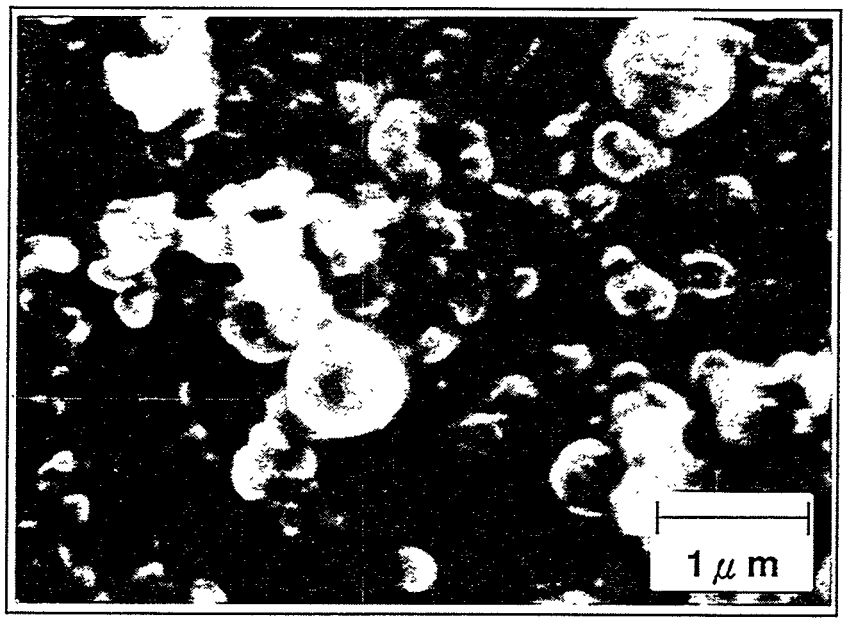

Fig. 9 SEM photographs of deposited micro particle

New facility for post irradiation examination of neutron irradiated beryllium

Etsuo Ishitsuka and Hiroshi Kawamura

Japan Atomic Energy Research Institute, Oarai Research Establishment, Oarai-Machi, Higashi Ibaraki-Gun, Ibaraki-Ken 311-13, Japan.

Abstract

Beryllium is expected as a neutron multiplier and plasma facing materials in the fusion reactor, and the neutron irradiation data on properties of beryllium up to 800 °C need for the engineering design. The acquisition of data on the tritium behavior, swelling, thermal and mechanical properties are first priority in ITER design. Facility for the post irradiation examination of neutron irradiated beryllium was constructed in the hot laboratory of Japan Materials Testing Reactor to get the engineering design data mentioned above. This facility consist of the four glove boxes, dry air supplier, tritium monitoring and removal system, storage box of neutron irradiated samples. Beryllium handling are restricted by the amount of tritium ;7.4 GBq/day and ^{60}Co;7.4 MBq/day.

1. Introduction

Utilization of beryllium as a neutron multiplier and plasma facing materials was planned in the ITER. However, data base concerning neutron irradiated beryllium is not sufficient. For example, the effects of grain size, impurities and produced helium on neutron irradiation behavior were not clear [1] , and the data on thermal properties of neutron irradiated beryllium are still few data. Recently, some reports [2-6] on the swelling or tritium behavior have been presented. However, unknown factor just like as the surface effects and so on also may be still exist. From these reasons, beryllium irradiation studies in the ITER activity continued in this some year.

Facility for the post irradiation examination (PIE) of neutron irradiated beryllium was constructed in the hot laboratory of Japan Materials Testing Reactor (JMTR) to get the engineering data, and was named "Beryllium PIE facility". The most parts of this facility was already established, and a one glove box for mechanical test will be established in October 1995.

2. Beryllium PIE facility

2.1 Out line

Beryllium PIE facility is established in the room of JMTR hot laboratory, and shown in Fig. 1. This facility consists of the four glove boxes, dry air supplier, tritium monitoring and removal system, storage box of neutron irradiated samples. Arrangements of these equipment is shown in Fig. 2. Glove box No. 5 (GB-5) for mechanical test will be established in October 1995.

2.2 Glove box and attached facility

Ventilation system is shown in Fig. 3. When the tritium concentration of glove boxes is low as the normal mode (V1 and V3 open, V2 and V4 close), the dry air of under 10% humidity is supplied in the each glove box, and supplied air flows one thorough, and exhausted by blower into the stuck. If the tritium concentration of glove boxes is very high, V1 and V3 automatically close, V2 and V4 open by the signal of tritium process monitor. The dry air flows closed mode, and released tritium in the glove boxes is removed by tritium removal system.

Characteristics of beryllium PIE facility is shown in Table 2. Dry air supplier is shown in Fig. 4, and consists of compressor, filter, heat-less dryer and mist separator. Mist separator is dust trap, and heat-less dryer have two molecular sieve of alternately playback type.

Glove box system is shown in Fig. 5. Each glove boxes have temperature and pressure monitor, and pressure is maintained by the flow balance of exhaust blower and dry air supplier. The design value of leak rate for glove boxes is under the 0.1 vol%/h, and measured leak rate is 0.006 vol%/h.

Tritium removal system is shown in Fig. 6. The air in glove boxes circulate by the blower of tritium removal system. Released tritium gas is converted in water component by Pt catalyst, and tritium water component is trapped molecular sieve of alternately playback type. Trapped tritium is stored in drain storage for solidification. Pressure of closed mode is maintained in under pressure (about -30 mmH_2O) by the pressure keeping valve.

Storage box has 30 pits that surrounded Pb shield in the lower part storage box. Neutron irradiated beryllium samples keep in metal O ring sealed container, and storage in pit. Tritium getter containers are stored in the upper part of storage box.

3. Equipments in glove box

3.1 Apparatus or tritium release

The new typed apparatus for measuring tritium release ration from neutron irradiated beryllium with the function of pulse mode heating were developed by using the infrared ray furnace in order to simulate the pulse mode heating of tritium breeder blanket of the fusion reactor [7]. This apparatus was installed in the glove box No. 1, and is shown in Fig. 8. This apparatus consists of a carrier gas supplying system, a beryllium heating system, a tritium measuring system and a tritium removing system.

Heating system is shown in Fig. 8. The infrared ray furnace was used in beryllium heating system because it is possible rapid heating and cooling, and is possible compact design to install in glove box. Heat up and cool down rates were measured using beryllium disk (10 mm diameter and 1.4 mm thickness) sample and alumina crucible, and are shown in Fig. 9. Minimum time of rapid heating up to 1015 °C is about 119 s and maximum heating rate reached at 1000 °C/min under helium sweep gas condition. The maximum temperature is depended on the crucible materials because of the differences for infrared ray absorption. The conversion efficiency of the gaseous water by ceramic electrolysis cell for the tritium measurement part is above 99.99 %. The pulse mode heating of the tritium breeder and neutron multiplier materials of the blanket could be demonstrate by using this apparatus. Vacuum heating apparatus also combined to tritium release, and tritium and helium measurement are possible.

3.2 Apparatus for beryllium reprocessing

Reprocessing of neutron irradiated beryllium is important on the effective utilization of beryllium resources and decreasing of nuclear waste. Reprocessing study of neutron irradiated beryllium started from the last year, and preliminary interesting data were obtained. These data will be present in this work shop. Apparatus for beryllium reprocessing will be designed using these obtained data, and will be install in glove box No. 2 on 1996.

3.3 Apparatus for thermal constant measurement

Apparatus for the thermal constant measurement with the laser flush method was installed in the glove box No. 4, and is shown in Fig. 10. This apparatus consists of a Nd glass laser, an electric furnace, InSb infrared ray sensor, a vacuum system and a tritium removal system. Nd glass laser is equipped out of glove box because of maintenance, and a leaser light is led in the glove box by the light guide fiber. Thermal constant measurement is possible under the condition of RT.-1300 °C in vacuum ($< 1\times10^{-7}$ Torr).

3.4 Apparatus for mechanical tests

Glove box No. 5 for measuring the tensile strength, bending strength and compression strength twill be constructed on October 1995. Then the apparatus of mechanical tests from room temperature to 700°C under the vacuum condition ($< 1\times10^{-5}$ Torr) will be installed up to the middle of 1996.

4. Conclusion

Beryllium PIE facility was constructed in the hot laboratory of JMTR to get the engineering data for the fusion reactor developments. This facility will contribute to the acquisition of data on swelling, mechanical and thermal properties, tritium and helium behavior of the neutron irradiated beryllium.

References

[1] D.S. Gelles et al., J. Nucl. Mater. 212-215 (1994) 29.

[2] D.L. Baldwin et al., J.Nucl.Mater., 179-181 (1991) 329.

[3] D.L. Baldwin and M.C. Billone, J.Nucl.Mater. 212-215 (1994) 948.

[4] M. Dálle Donne et al., J. Nucl. Mater. 212-215 (1994) 954.

[5] S.Cho et al., J.Nucl.Mater. 212-215 (1994) 961.

[6] E. Ishitsuka et al., Fusion Technology 1994, 2 (1995) 1345.

[7] E. Ishitsuka et al., "Development of tritium release apparatus using pulse mode heating" in fifth topical meeting on tritium technology in fission fusion and isotopic applications, Belgirate, Lake Maggiore, Italy, 28 May-3 June (1995) .

Table 1 Maximum activity for treatment

Nuclide	Maximum activity	
	per day	per year
^{3}H	7.40 GBq (200mCi)	670 GBq (18 Ci)
^{10}Be	5.55 kBq	505 kBq
^{60}Co	7.40 MBq	673 MBq

Table 2 Characteristics of beryllium PIE facility

Apparatus	Function	Specifications	
Dry air supplier	• Mist separator • Heatless dryer	0.3mm95% trap Humidity : <10%	
Glove box	• Temperature and pressure monitor	Pressure : -10~-50 mmH2O Leak rate : <0.1vol%/h	
Tritium removal system	• Pt catalyst • Molecular sieve	Flow rate : 25m^3/h Removal efficiency : >99%	
Tritium process monitor	• Nude type IC	3.7×10^{-2}~3.7×10^{2} Bq/cm^3	
Exhaust blower	• Invertor control	Flow rate : 25m^3/h	
Storage box	• Pb sheald	Strage capacity/ year	^{3}H : 670 GBq (18Ci) ^{10}Be: 505 kBq ^{60}Co: 673 MBq

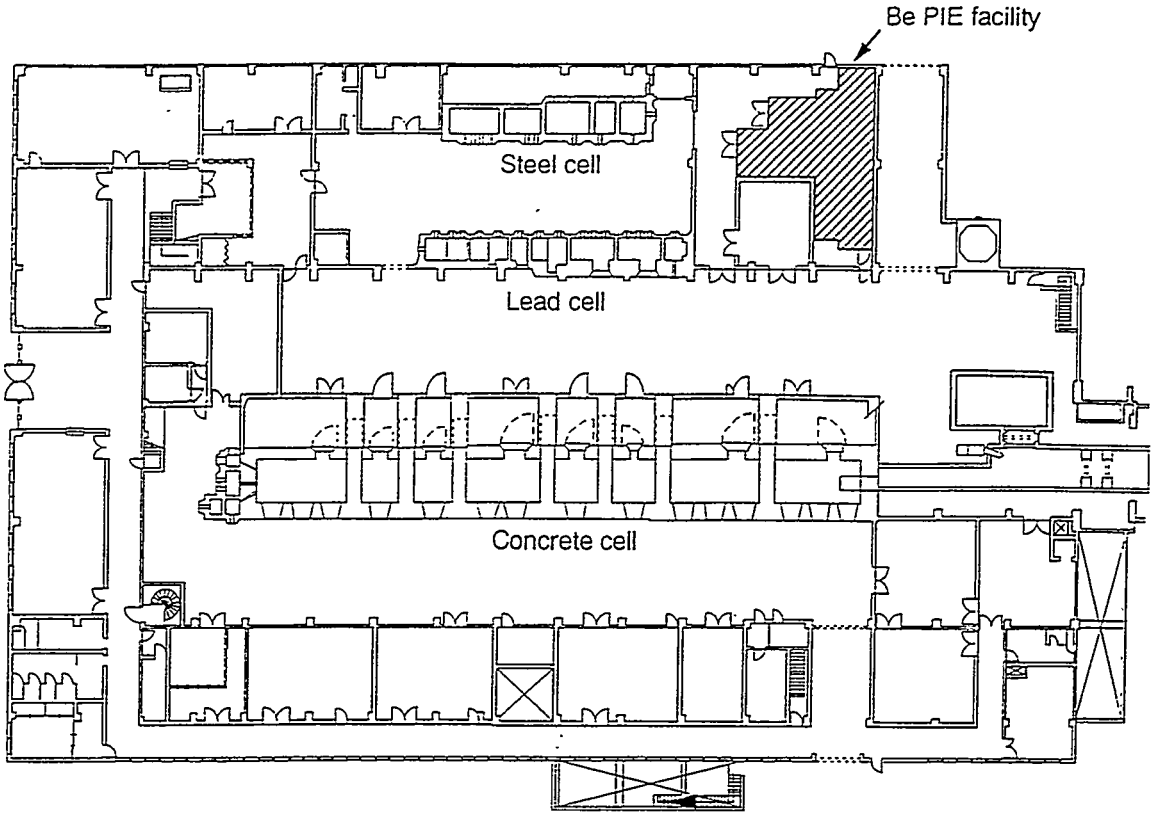

Fig. 1 Be PIE facility in JMTR Hot Laboratory.

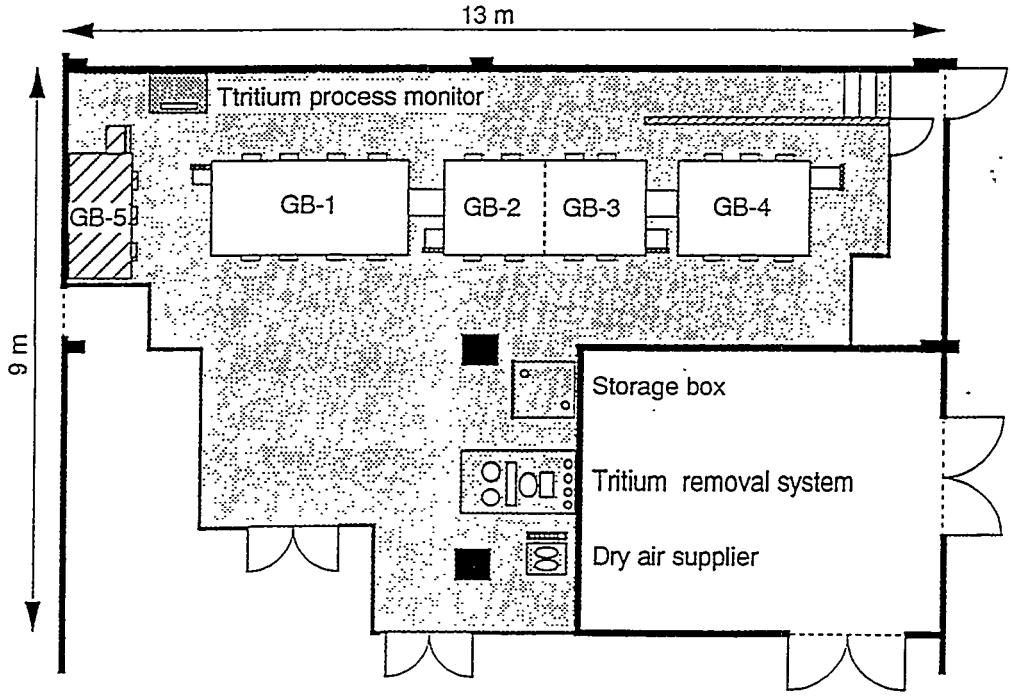

Fig. 2 Out line of beryllium PIE facility.

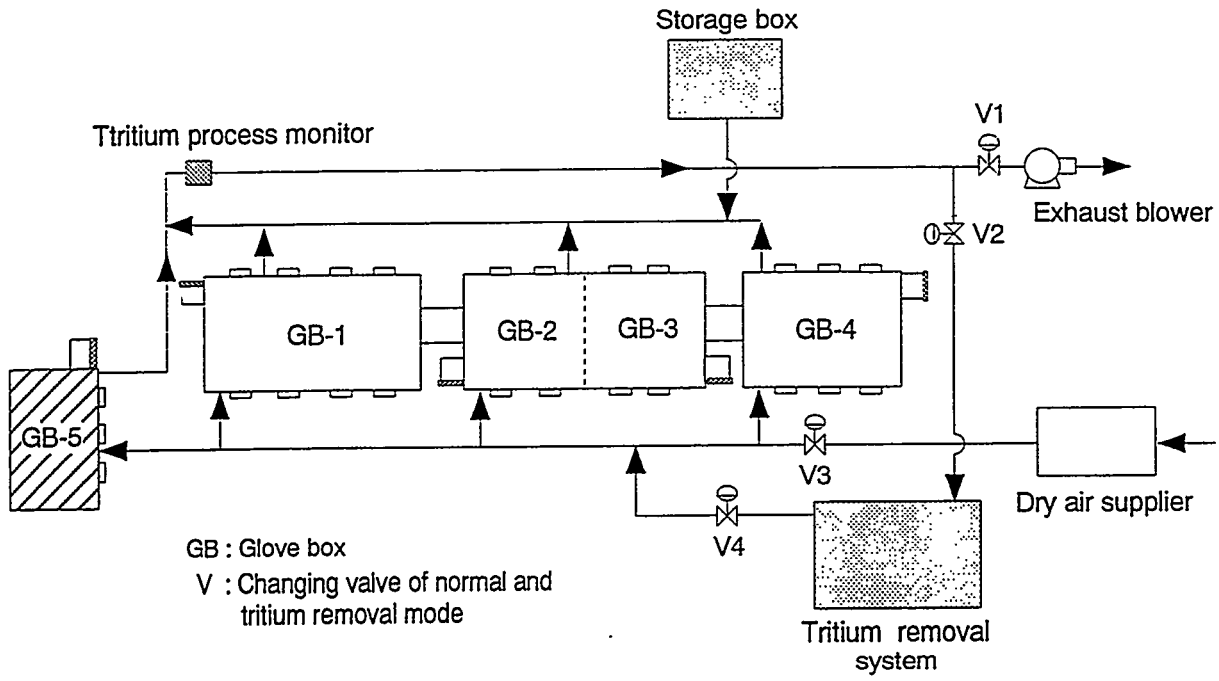

Fig. 3 Ventilation system of beryllium PIE facility.

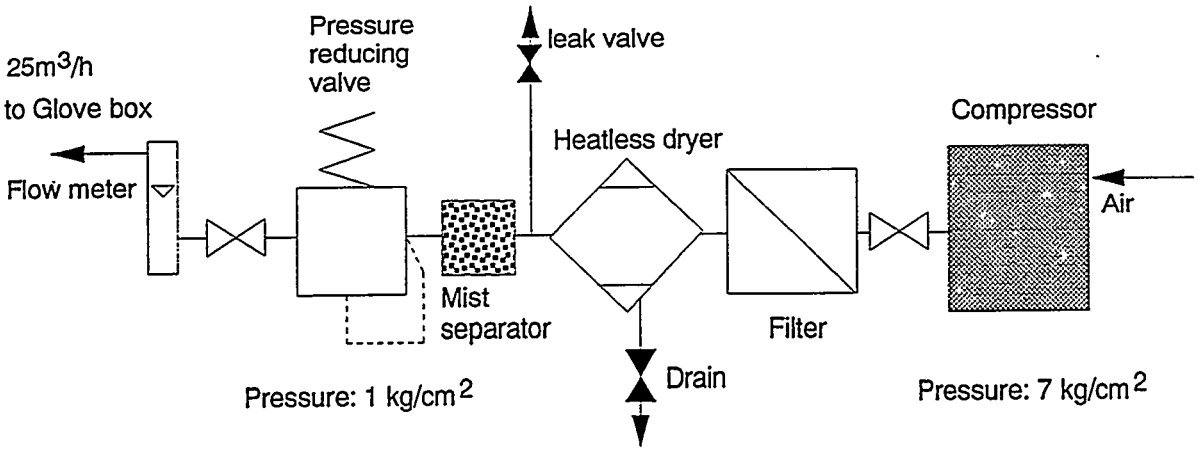

Fig. 4 Dry air supplier.

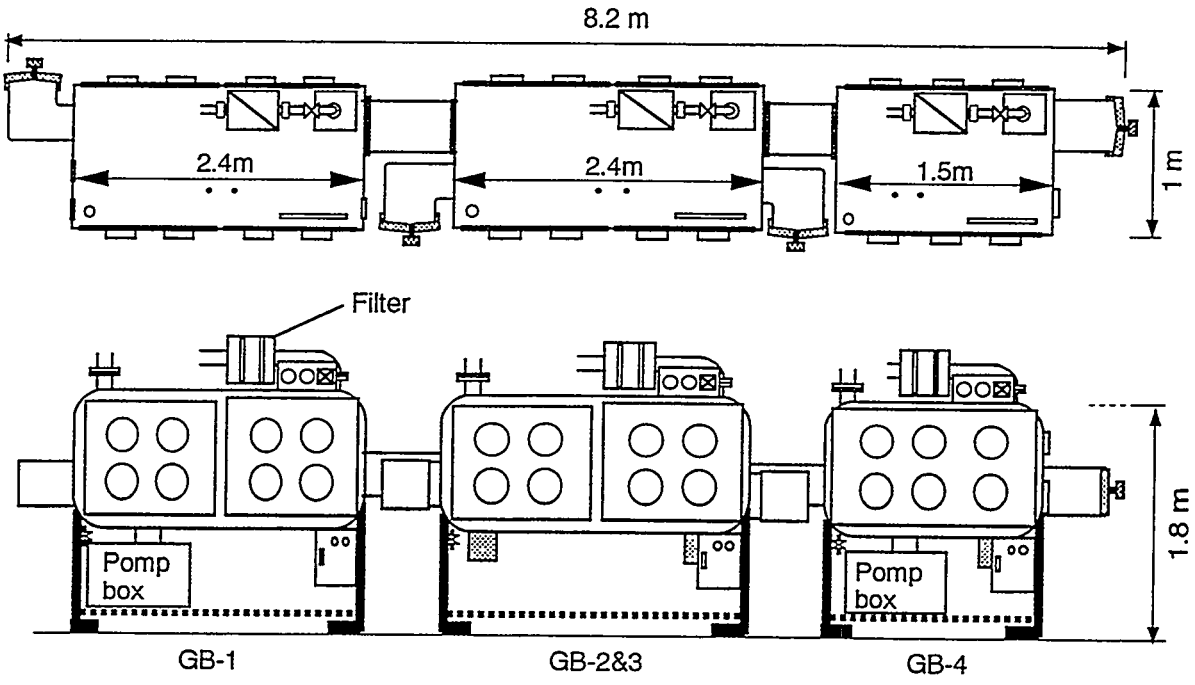

Fig. 5 Glove box system.

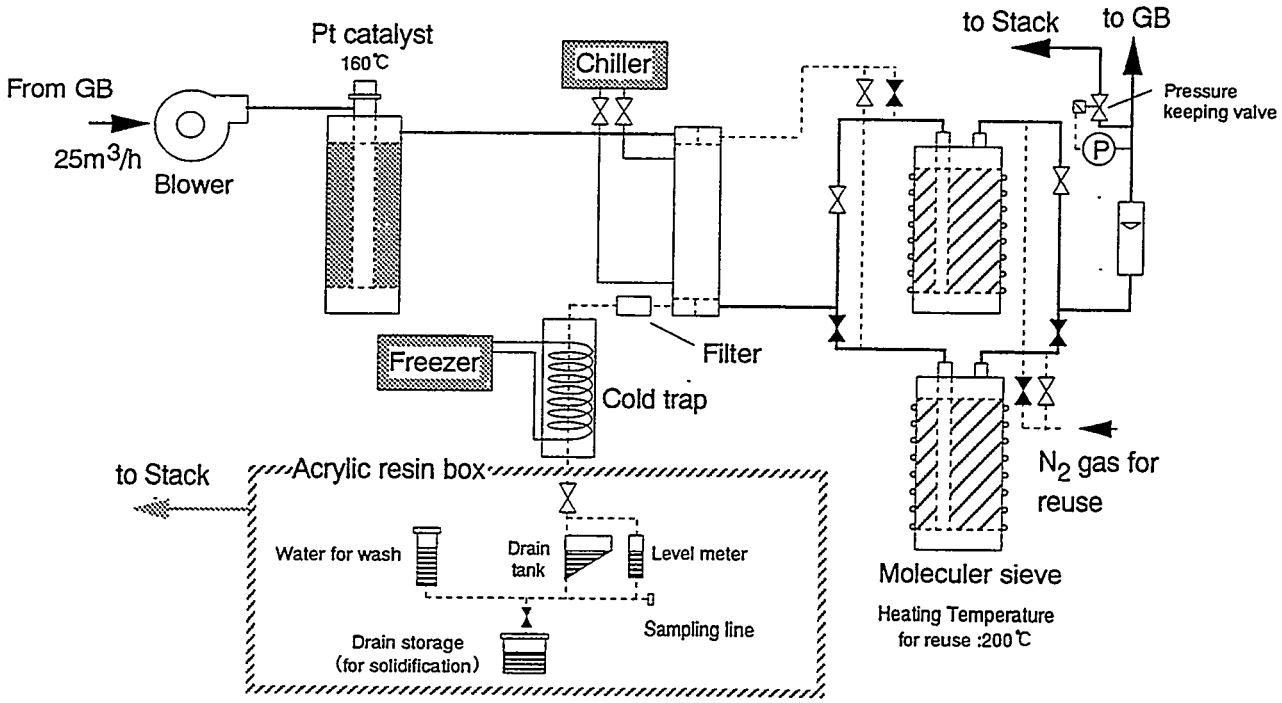

Fig. 6 Tritium removal system.

IC :Ionization Chamber, CEC:Ceramic Electrolysis Cell

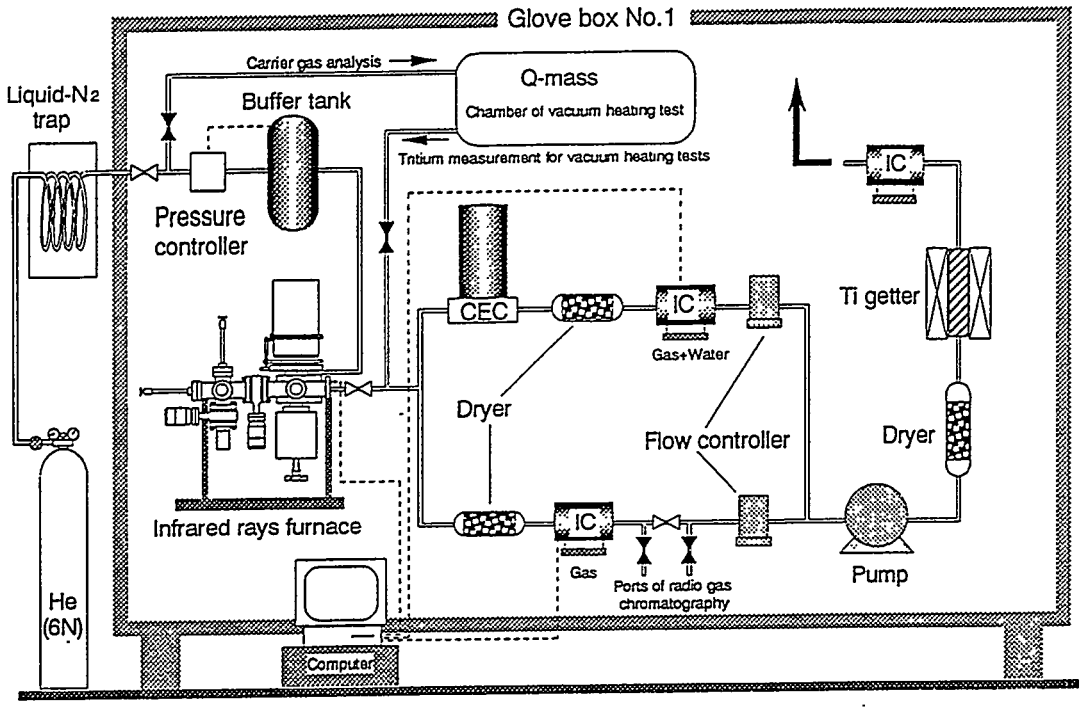

Fig. 7 Tritium release apparatus in glove box No.1.

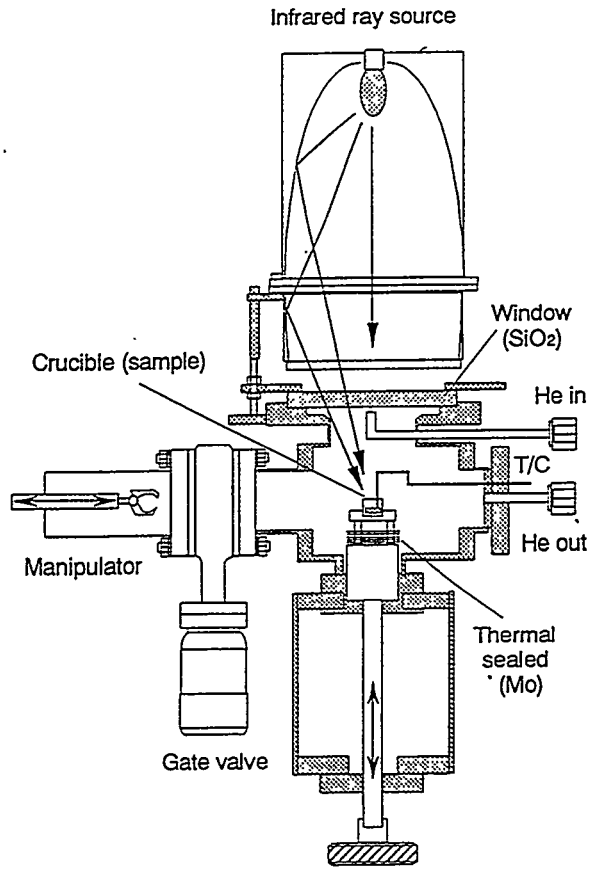

Fig. 8 Heating system of tritium release apparatus.

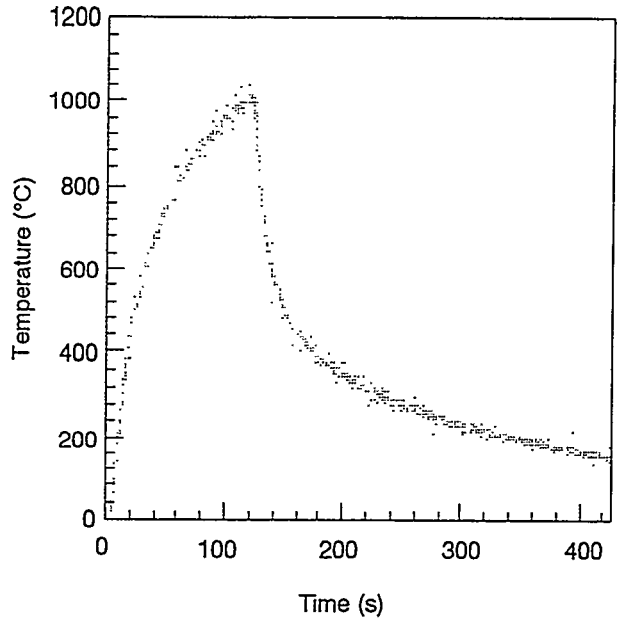

Fig. 9 Heating and cooling rate of beryllium disk sample.

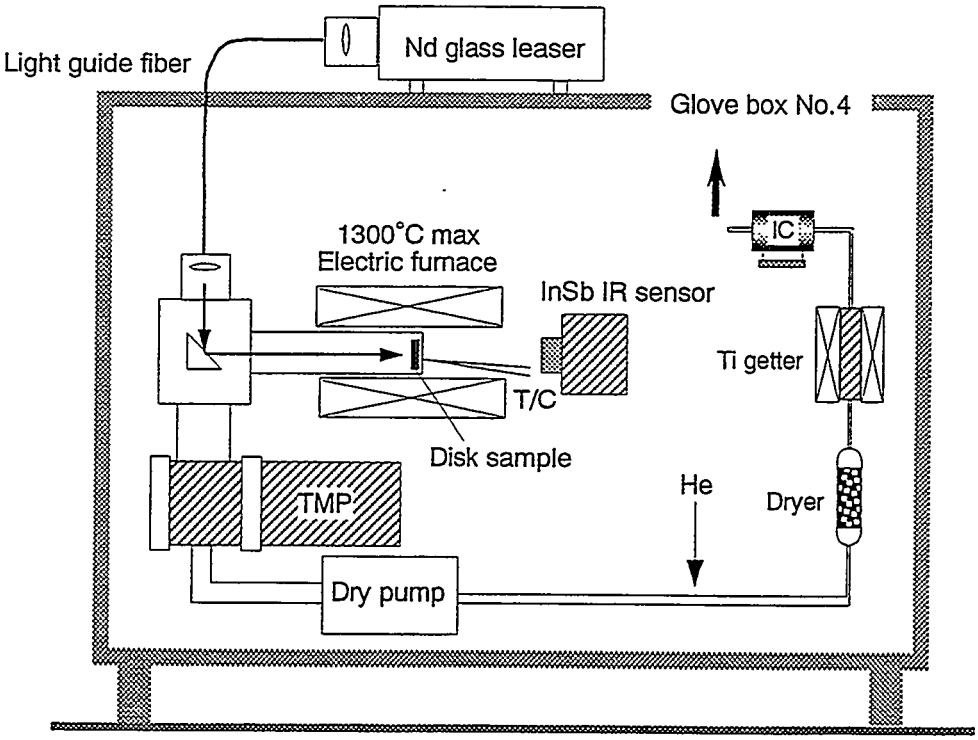

Fig. 10 Leaser flush apparatus in glove box No.4.

New electron beam facility for irradiated plasma facing materials testing in hot cell

N.Sakamoto[a], M.Akiba[b] and H.Kawamura[a]

[a] *Japan Atomic Energy Research Institute, Oarai Research Establishment, Oarai-machi, Higashi Ibaraki-gun, Ibaraki-ken 311-13, Japan*

[b] *Japan Atomic Energy Research Institute, Naka Research Establishment, Naka-machi, Naka-gun, Ibaraki-ken 311-01, Japan*

Abstract

Since plasma facing components such as the first wall and the divertor for the next step fusion reactors are exposed to high heat loads and high energy neutron flux generated by the plasma, it is urgent to develop of plasma facing components which can resist these.

Then, we have established electron beam heat facility ("OHBIS", Oarai Hot-cell electron Beam Irradiating System) at a hot cell in JMTR (Japan Materials Testing Reactor) hot laboratory in order to estimate thermal shock resistivity of plasma facing materials and heat removal capabilities of divertor elements under steady state heating. In this facility, irradiated plasma facing materials (beryllium, carbon based materials and so on) and divertor elements can be treated.

This facility consists of an electron beam unit with the maximum beam power of 50kW and the vacuum vessel. The acceleration voltage and the maximum beam current are 30kV (constant) and 1.7A, respectively. The loading time of electron beam is more than 0.1ms. The shape of vacuum vessel is cylindrical, and the mainly dimensions are 500mm in inner diameter, 1000mm in height. The ultimate vacuum of this vessel is 1 x 10^{-4}Pa.

At present, the facility for thermal shock test has been established in a hot cell. And performance estimation on the electron beam is being conducted. Presently, the devices for heat loading tests under steady state will be added to this facility.

1. Introduction

Since plasma facing components such as the first wall and the divertor for the next step fusion reactors are exposed to high heat loads[1] and high neutron flux generated by the plasma, it is urgent to develop plasma facing components which can resist these. In the development of plasma facing components, it is necessary to estimate the lifetime and the heat removal capabilities of these components which is dependent on the neutron irradiation. The electron beam heat facility for estimation on neutron activated materials was requested[2].

Then, electron beam heat facility ("OHBIS") have established in a hot cell in JMTR hot laboratory in order to estimate thermal shock resistivity of plasma facing materials and heat removal capabilities of divertor element under steady state heating. In this facility, irradiated plasma facing materials (beryllium, carbon based materials and so on) and divertor elements can be treated. This facility can simulate both conditions, that is, high heat flux on plasma disruption and steady state heat flux during normal operation of nuclear fusion reactor.

2. New electron beam facility

Therefore, irradiated plasma facing materials and divertor elements for testing will be activated, heat loading tests with electron beam heat facility must be done using the remote manipulators in a hot cell. This electron beam heat facility has been established in a hot cell in JMTR hot laboratory. This facility is shown schematically in Fig.1. Detailed parameters of this facility are listed in Table 1. It consists of the electron beam unit with the maximum beam power of 50kW and the vacuum vessel which is made of stainless steel. The electron beam unit is placed on the vacuum vessel. The acceleration voltage and the maximum beam current of the electron beam unit are 30kV (constant) and 1.7A, respectively. The loading time of electron beam is more than 0.1ms. Therefore, short time electron beam loading for the simulation of disruption is possible. The electron beam can be deflected with a frequency of 1kHz in X-Y direction with an amplitude of ± 150mm (a rectangular shape) by deflection controller. The shape of the vacuum vessel is cylindrical, and the mainly dimensions are 500mm in inner diameter, 1000mm in height. The wall thickness of the vacuum vessel is 4 mm. The ultimate vacuum of this vessel is about 1×10^{-4}Pa.

At present, the facility for thermal shock test has established in a hot cell. A flange on the side of the vacuum vessel is used for introducing the rotary table. The eleven specimens can be placed on the rotary table in the outside of vacuum vessel using the remote manipulators. The specimen maximum dimensions are $^{w}25$mm x $^{d}25$mm x $^{h}30$mm. And, the rotary table is carried to the inside with an air cylinder, to the electron beam loading position with X-Y moving system. Electron beam is generated in a dummy pot, and it is moved to a specimen in 0.1ms by deflection controller. After electron beam loading to a specimen, the rotary table is rotated, and next specimen is carried to the electron beam loading position. Therefore, continuous electron beam loading is possible.

As performance estimation on the electron beam, many calorimetric measurements using the calorimeter with four kinds of chips (beryllium, graphite, oxygen free copper and tungsten) are being conducted. The concept of the calorimeter is shown in Fig.2. The chips were loaded with electron beam. And, the heat flux was calculated from the value of elevated temperature of the chips. The value of elevated temperature was measured with K-type thermocouple of 0.5mm in diameter. The heat flux with beam current is shown in Fig.3. In the case of beryllium, the heat flux increased with increasing of the beam current until 0.8A. But, when the beam current exceeded 0.8A, the heat flux decreased with increasing of the beam current. It is considered that there was the effect of vapor from a dummy pot on the profile of heat flux. Maximum heat flux to beryllium was 1050MW/m^2 at the beam current of 0.8A. On the other hand, in the case of graphite, maximum heat flux was 700MW/m^2 at the beam current of 0.9A. And profile of heat flux in X and Y directions using calorimeter chips made of beryllium and graphite are shown in Fig.4 and Fig.5, respectively. From these results, it appeared that half width of focused electron beam is about 3-4mm in diameter.

Presently, the devices for heat loading test under steady state will be added to this facility. In heat loading test under steady state, actively cooled divertor elements are inserted in a vacuum vessel. And the cone-shaped sealing are used for holding them. This development of sealing techniques allowed the active cooling of specimens. And, the cooling circuit is used, its flow rate of the water coolant was up to 100 l/min with a maximum pressure of 2MPa. The following devices will be considered for measurement of the temperatures, released gases and so on.

- a pyrometer for point measurements of temperatures on the surface of divertor elements
- an infra-red camera system
- a high speed video camera for visual monitoring of a test
- a gas analysis system with a quadrupol mass spectrometer
- a tritium measurement system with a ion chamber

3. Testing items

In order to estimate the heat removal capabilities and determine the life time of plasma facing components, heat loading tests with electron beam will be performed with this facility. Testing items of heat loading test are thermal shock test and heat loading test under steady state.

3.1. Thermal shock test

Samples for this test are plasma facing materials and joined component between plasma facing materials and heat sink material. In this test, electron beam is generated in a dummy pot. After electron beam becomes stable, it is moved to specimen in 0.1ms by deflection controller, the specimen is loaded with electron beam for the prescribed time.

The estimation items after electron beam loading on thermal shock test are as follows.

- weight loss of the specimen by electron beam loading
- characterization of the specimen surface after electron beam loading
- melting distance from the specimen surface by electron beam loading

Especially, from weight loss of the specimen by electron beam loading, the lifetime of plasma facing materials is estimated.

3.2. Heat loading test steady state

Samples for this test are divertor elements. They are held in the vacuum vessel, cooled actively with water coolant. And, in order to simulate the loading conditions in normal operation, electron beam loading for 30s will been applied on upper surface of divertor elements.

The estimation items after electron beam loading which is being considered are as follows.

- heat removal capabilities of divertor elements under electron beam loading
- characterization of the specimen surface after electron beam loading
- weight loss of the specimen by electron beam loading
- deformation of the specimen by electron beam loading
- damage on joining interface of the specimen by electron beam loading
- temperature distribution on specimen surface under electron beam loading
- temperature increasing on the joining interface by electron beam loading
- gas release of tritium and other gases under electron beam loading

4. Conclusions

The electron beam heat facility ("OHBIS") has been established in a hot cell in JMTR hot laboratory in order to estimate thermal shock resistivity of plasma facing materials and heat removal capabilities of divertor element under steady state heating.

This facility consists of an electron beam unit with the maximum beam power of 50 kW and the vacuum vessel. The acceleration voltage and the maximum beam current are 30kV and 1.7A, respectively. The shortest loading time is 0.1ms. This enabled the simulation of disruptions. The current facility is for thermal shock test. From the results of performance estimation on the electron beam, maximum heat flux to beryllium in the current facility was 1050MW/m^2 at the beam current of 0.8A. And half width was about 3-4mm in diameter. Presently, the devices for heat loading tests under steady state will be added to this facility.

References

[1] K. Nakamura, et al., J. Nucl. Mater. 212-215(1994)1201.
[2] J. Linke, et al., Evaluation of cooling concepts and specimen geometries for high heat flux tests on neutron irradiated divertor elements, Proc. 3rd International Symposium on Fusion Nuclear Technology, Los Angeles(1994).

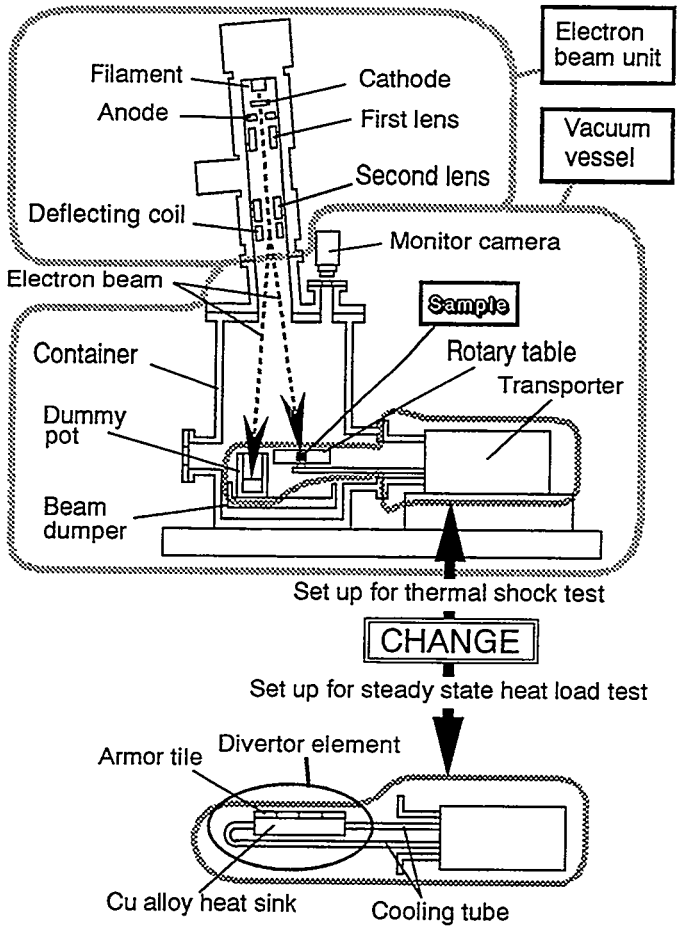

Fig.1 Schematic of OHBIS

Table 1 Detailed parameters of OHBIS

Electron Gun	Power Density	≦2.5GW/m^2 *
	Beam Power	≦50kW
	Beam Potential	30kV
	Beam Current	≦1.7A
	Beam Shape	circle
	Beam Scanning	Sin wave, ≦ 1kHz, ± 150 mm in X,Y
	Exposure Time	≧ 0.1 ms
	Moving Time	≧ 0.1 ms
Work Chamber	Vacuum	< 1×10^{-4} Pa
Sample	Material	Beryllium, CFC etc.
	Shape	Cube
	Dimensions	≦ $25\times25\times^{h}30$ mm^2

* : calculated value at φ5mm in dia. of E.B.

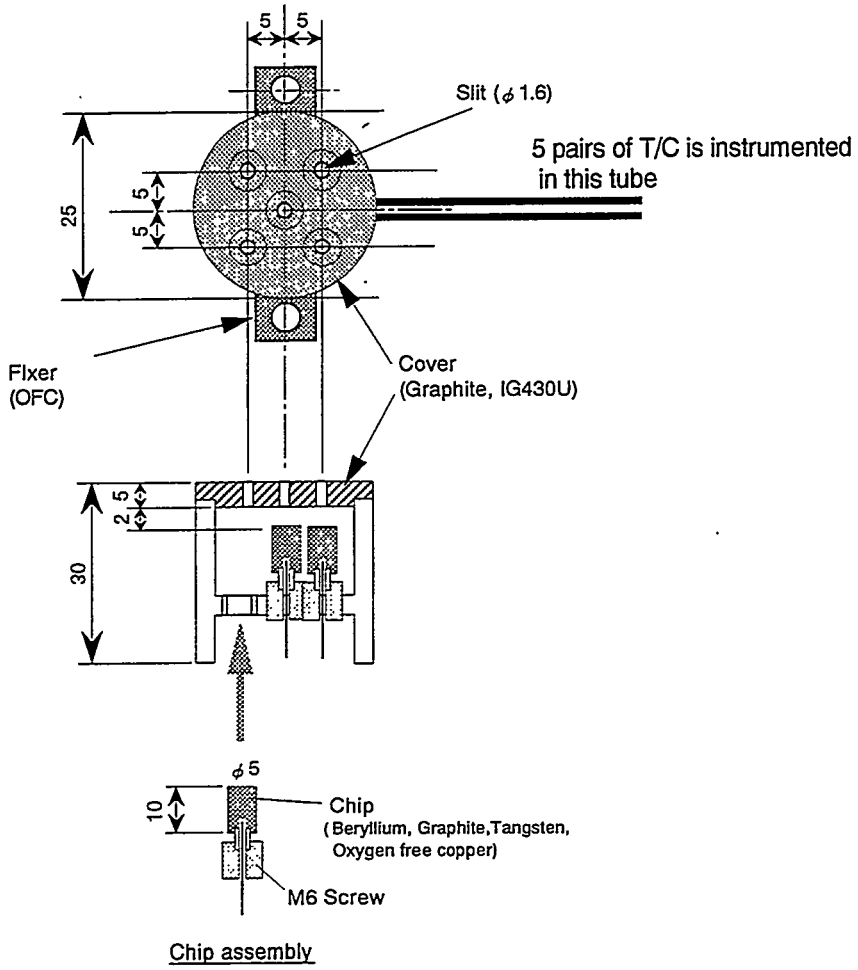

Fig.2 The concept of the calorimeter

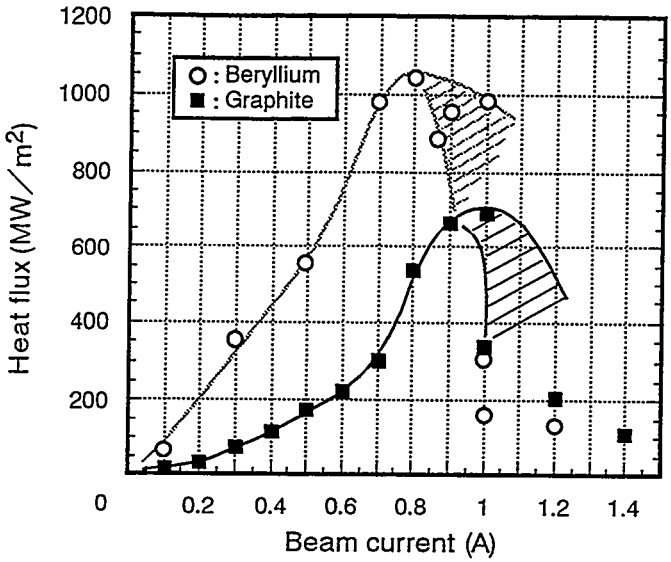

Fig.3 The heat flux with beam current

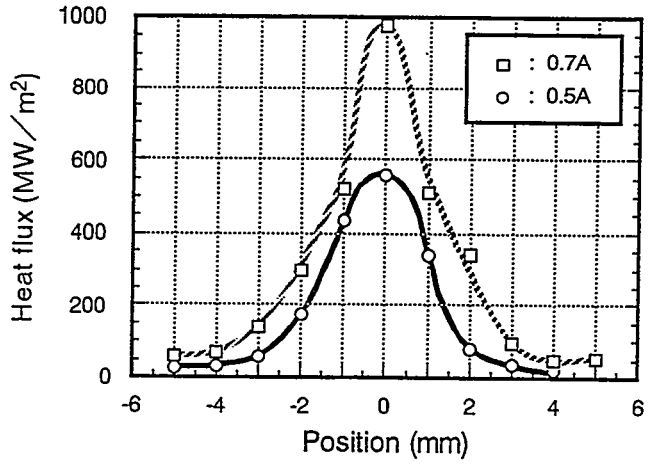

Fig.4 The plofile of heat flux in X and Y directions using calorimeter chips made of beryllium

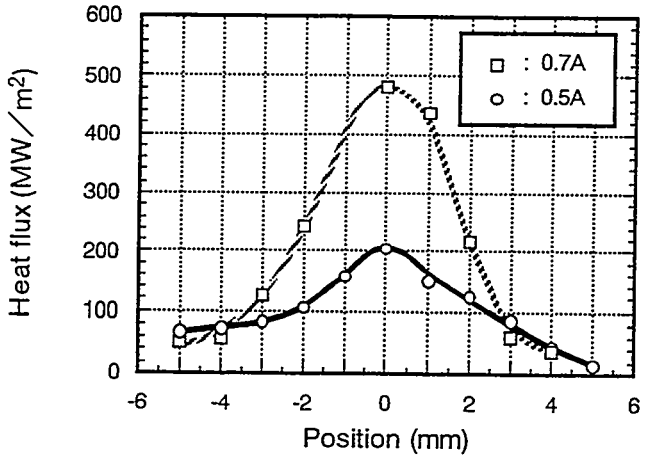

Fig.5 The plofile of heat flux in X and Y directions using calorimeter chips made of graphite

Experimental Investigation of the Energy and Temperature Dependence of Beryllium Self-Sputtering

S.N. Korshunov, M.I. Guseva, V.G. Stoljarova

RRC "Kurchatov Institute"
Kurchatov sq. 1, Moscow 123182, Russian Federation

The low-Z metal beryllium is considered as plasma facing material (PFM) for the ITER. It is expected that operation temperature range of beryllium PFM will be (670 - 1070) K. While experimental Be-sputtering data bases exist for H^+, D^+ and He^+-ions, the self-sputtering yields of Be have only been estimated by computer simulation.

In this paper we report the experimental results on the energy and temperature dependence of the beryllium self-sputtering yield (S^s). The energy dependence of S^s in the energy range (0.5 - 10.0) keV was measured at 670 K. The self-sputtering yield of Be attains its maximal value at the ion energy of 1.5 keV, being equal to (0.32 ± 0.03) at./ion. Comparison of the experimental results and theoretical prediction shows a good agreement for energy dependence of S^s. The temperature dependence of S^s in the temperature range (370-1070) K was obtained for 0.9 keV Be^+ - ions. The value of S^s is not changed up to 870 K. It sharply increases at the temperatures above 870 K, attaining the value of 0.75 at./ion at 1070 K.

1. Introduction

Due to a number of technological properties and, first of all, due to a low atomic number, beryllium and graphite materials are considered to be the main candidate for the first wall plasma facing components (PFCS) at the physical ITER stage [5]. The experimental sputtering erosion data, particularly, the self-sputtering yields of that candidate materials are needed to provide important supporting information for modelling and for estimating the erosion lifetime of PFCS, determined by the net erosion rate.

At present, the peculiarities of sputtering for different graphite varieties have been studied well experimentally. Beryllium, however, is much less investigated. While experimental sputtering yields exist for beryllium irradiated with hydrogen, deuterium and helium ions [1], the energy and temperature dependence of the beryllium self-sputtering yield are only estimated using computer simulation [2,3]. One should note that the calculated data for beryllium self-sputtering fitted with Bohdansky formula [2] differ from a corresponding values fitted with Eckstein's [3] revised of that formula within a factor of two. Therefore , it's very important to obtain the experimental data on beryllium self-sputtering.

In the present work the experimental results on energy and temperature dependence of beryllium self-sputtering yield are presented.

2. Experimental procedure

The main difficulty of the experimental beryllium self-sputtering investigation is the problem of Be^+-ions generation. The metal beryllium was used as a charge material in the high temperature ion source, surrounded with a liner to reduce the Be contamination of the system. However, as the experiments have shown, beryllium actively interacts with graphite and high-melting metals (W, Mo, Ta) at the temperature about 1500 K, which is necessary for the discharge ignition in the vapors of beryllium. As a result, a graphite crucible in the ion source was replaced by the Be oxide crucible. The irradiations with beryllium ions were performed in the chamber of a 180°-separation implanter. Be^+-ions were extracted from the plasma of the ion source and accelerated in the energy range of (0.5-10) keV (without application of a breaking potential to the target area). The beryllium ion current from the source was equal 25 mA. While working on the beryllium high temperature ion source, the necessary safety precautions were taken. The fluence of the singly charged ions was determined by current integrator with an accuracy of 1%. It was chosen such as to yield a collected charge equivalent to an ion mass of about 1.5×10^{-4} kg. The temperature of the beryllium specimens was controlled by means of a platinum-iridium thermocouple. The water cooling of the unirradiated side of the sample was provided and Be samples during ion irradiation were in a temperature regime between 370 K and 1070 K.

The beryllium self-sputtering yields, defined as sputtered atoms per incident ion, were obtained by the weight change method. The loss or gain of target material due to the ion irradiation was determined by an ultramicrobalance with an accuracy of 10^{-6} kg. The uncertainty of the sputtering yield data is estimated to be 10%, this resulting from the mass and current measurements.

A commercial powder-compacted beryllium of TShP-type containing 98.7 wt.% - Be, 0.9 wt.% - O, 0.2 wt.% - Fe and 0.2 wt.% other metals, C and N was used in the experiments. The Be-targets were in form of circles with a diameter of 10^{-2}m and a thickness of about 1.5×10^{-3}m. Before irradiation the beryllium sample surfaces were polished with diamond paste and then electrical polishing was used. Before and after irradiation by Be^+-ions beryllium surface structure was examined in a JEOL scanning electron microscope.

3. Experimental results and discussion

The energy dependence of beryllium self-sputtering yield for the temperature of a target at the level of 670 K is shown in Fig. 1; TRIM.SP calculated data for beryllium self-sputtering fitted with Eckstein revised [3] Bohdansky formula [2] are also shown. The agreement between experimental and calculated data is sufficiently suitable. This can also conclude from the Table I, in which the calculated [2,3] and measured values of beryllium self-sputtering yield as function of ion energy are given for easer look up. The following fit parameters for self-sputtering yield calculation are used in ref. [2] and [3]: $E_{th}^s = 35$ eV and $E_{th}^s = 23$ eV, $Q = 0.94$ at./ion and $Q = 0.77$ at./ion, respectively. Therefore, the comparison of the experimental and calculated data shows that the threshold energy of Be self-sputtering is near to 23 eV. Fig. 2 shows the energy dependence of beryllium self - sputtering yield in comparison with that for carbon [1]. Comparing the self-sputtering yield curves for beryllium and carbon, one sees that the sputtering yields for carbon are larger than for beryllium. As can be seen from Fig. 2, the sputtering threshold energy of beryllium is lower than for a carbon.

Roth et.al. [4] have investigated the angular dependence of Be self-sputtering at ion energy 1 keV. For normal incidence the measured in [4] self-sputtering yield ($S^s = 0.3$ at./ion) is close to our

result (See Table I).

The experimental self-sputtering yield of beryllium as a function of the temperature for an ion energy of 0.9 keV is shown in Fig. 3 (curve 1). Curve 2 illustrates the calculated temperature dependence of beryllium self-sputtering yield from the paper [1]. As seen in Fig. 3 the experimental self-sputtering yield does not depend on surface temperature up to temperature region between 770 K and 870 K when the thermal sublimation process is expected to be dominating in the erosion yield. At temperatures above 870 K the irradiation of beryllium with energetic Be^+-ions leads to radiation enhanced sublimation. In such a case there is typically a steep increase in the sputtering yield with increasing of temperature. It attains the value of 0.75 at./ion at 1070 K. Extrapolation of the experimental curve $S = f(T)$ to the value of $S^s = 1$ at./ion shows that operating temperature above 1170 K for beryllium PFCs of a reactor is not safe. The comparison with corresponding data for self-sputtering of carbon (Fig. 4) shows that "carbon catastrophe" ($S^s = 1$ at./ion) takes place at higher temperature of about 1500 K than "beryllium catastrophe" - $T \geq 1170$ K.

4. Conclusion

1. The experimental energy dependence of beryllium self-sputtering yield for normal incidence is in a good agreement with Eckstein et. al. [2] calculation.
2. Below 770 K the self-sputtering yield is not changed and sharply increases at temperature above 870 K, attaining the value of 1 at/ion at temperature about 1170 K for ion energy 0.9 keV.
3. Comparison of the self-sputtering yields of beryllium and carbon shows that at temperature below 770 K for ion energy below 10 keV the values for beryllium are lower than for carbon including sputtering threshold energy.
4. From the viewpoint of self-sputtering threshold energy and operating temperature carbon as plasma facing material has an advantage in comparison with beryllium.

References

[1] J. Roth, "Erosion and impurity production of C and Be: a comparison", J. Nucl. Mater. 145- 147 (1987) 87.

[2] G. Standenmaier, J. Roth, R. Behrisch et. al., "Trapping of deuterium implanted in carbon and silicon: a calibration for particle-energy measurements in the plasma boundary of TOKAMAKS", J. Nucl. Mater. 84 (1979) 149.

[3] W. Eckstein, C. Garcia-Rosales, J. Roth, W. Ottenberger, "Sputtering Data", Max-Planck-Institut fur Plasmaphysik, Report IPP 9/82 (1993).

[4] E. Hechtl, J. Roth, W. Eckstein, C. H. Wu, "Experimental investigation of the angular dependence of Be self-sputtering", J. Nucl. Mater. 220-222 (1995) 883.

[5] M. Guseva, V. Gureev, B. Kolbasov et. al., "Hydrogen behaviour in vanadium alloys and beryllium", Russian Research Centre "Kurchatov Institute", 93R&D, ETA, RF, Nl-1 Moscow, 1994.

Table I

Calculated [2,3] and measured values of Be self-sputtering yield

E, keV	S^s, at./ion Bohdansky [2]	S^s, at./ion Eckstein [3]	$S^s_{exp.}$, at./ion
0.1	0.16	0.078	-
0.5	0.43	0.232	0.22
1.0	0.50	0.260	0.30
2.0	0.56	0.253	0.32
3.0	0.43	0.263	0.27
5.0	0.34	0.227	0.23

Figure captions

Fig. 1. Energy dependence of beryllium self-sputtering yield at temperature 670 K:

• • • - experimental points

——— - calculated curve [3].

Fig. 2. Energy dependence of beryllium and carbon self-sputtering yields:

1 - experimental (•••) and calculated [3] data for beryllium

2 - experimental data [1] for carbon

Fig. 3. Experimental (1) and calculated (2) [1] temperature dependences of beryllium self-sputtering yield at ion energy 0.9 keV and 1 keV, respectively.

Fig. 4. Temperature dependences of beryllium (curve 1) and carbon (curve 2) [1] self-sputtering yields at ion energy 3 keV.

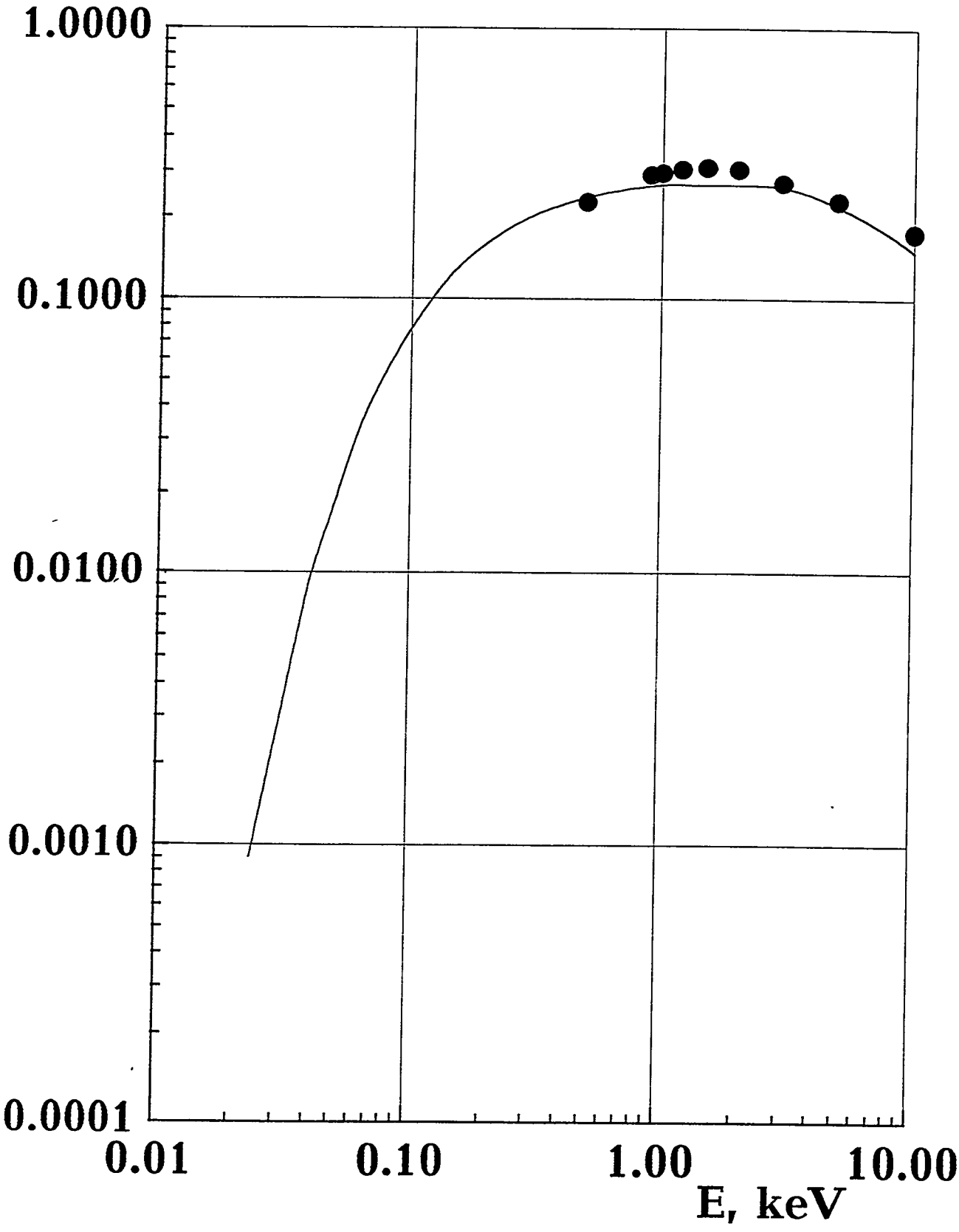
S, atom/ion
1.0000
0.1000
0.0100
0.0010
0.0001
0.01
0.10
1.00
10.00
E, keV

Fig. 1.

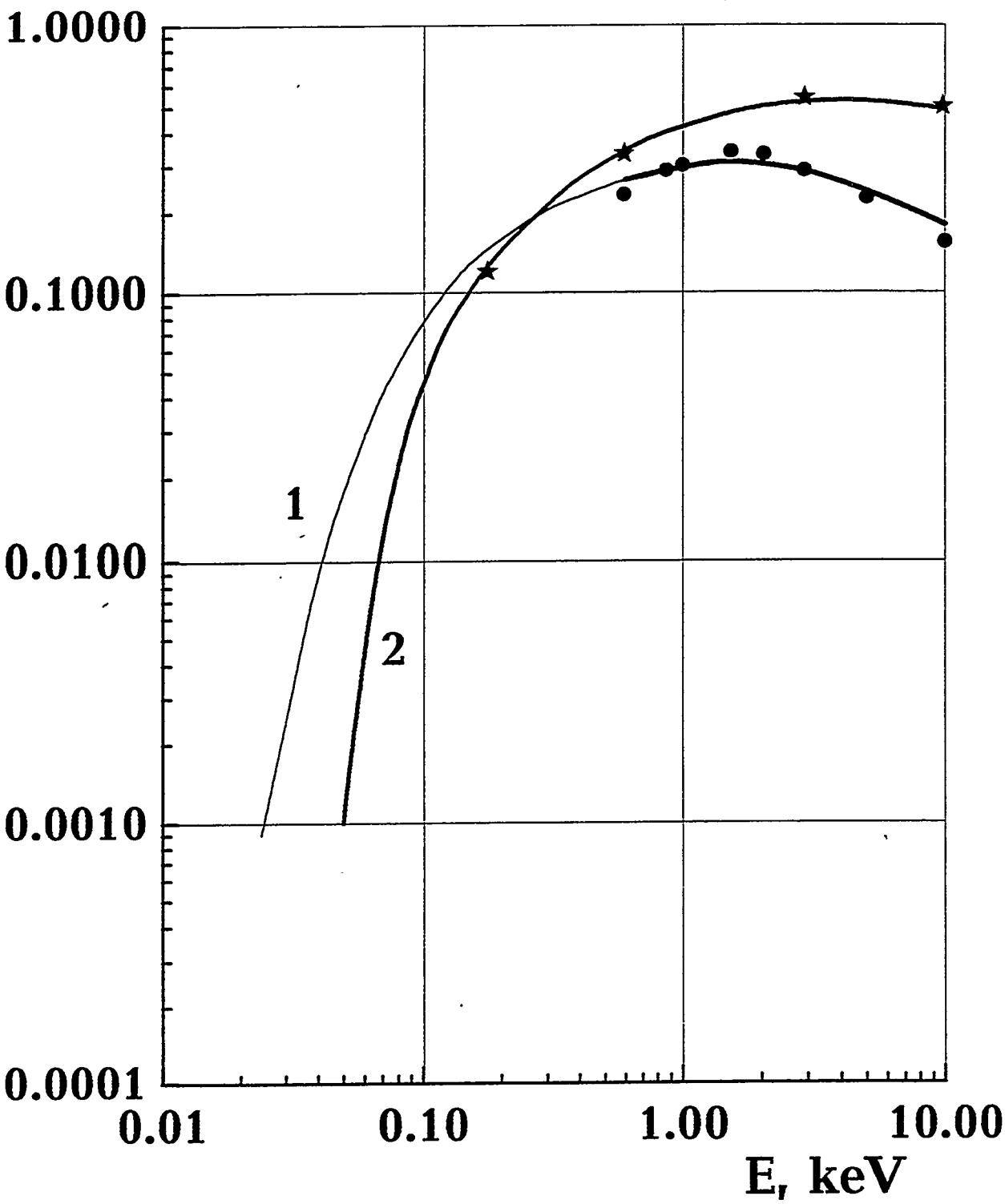
S, atom/ion
1.0000
0.1000
0.0100
0.0010
0.0001
0.01
0.10
1.00
10.00
E, keV
1
2

Fig. 2.

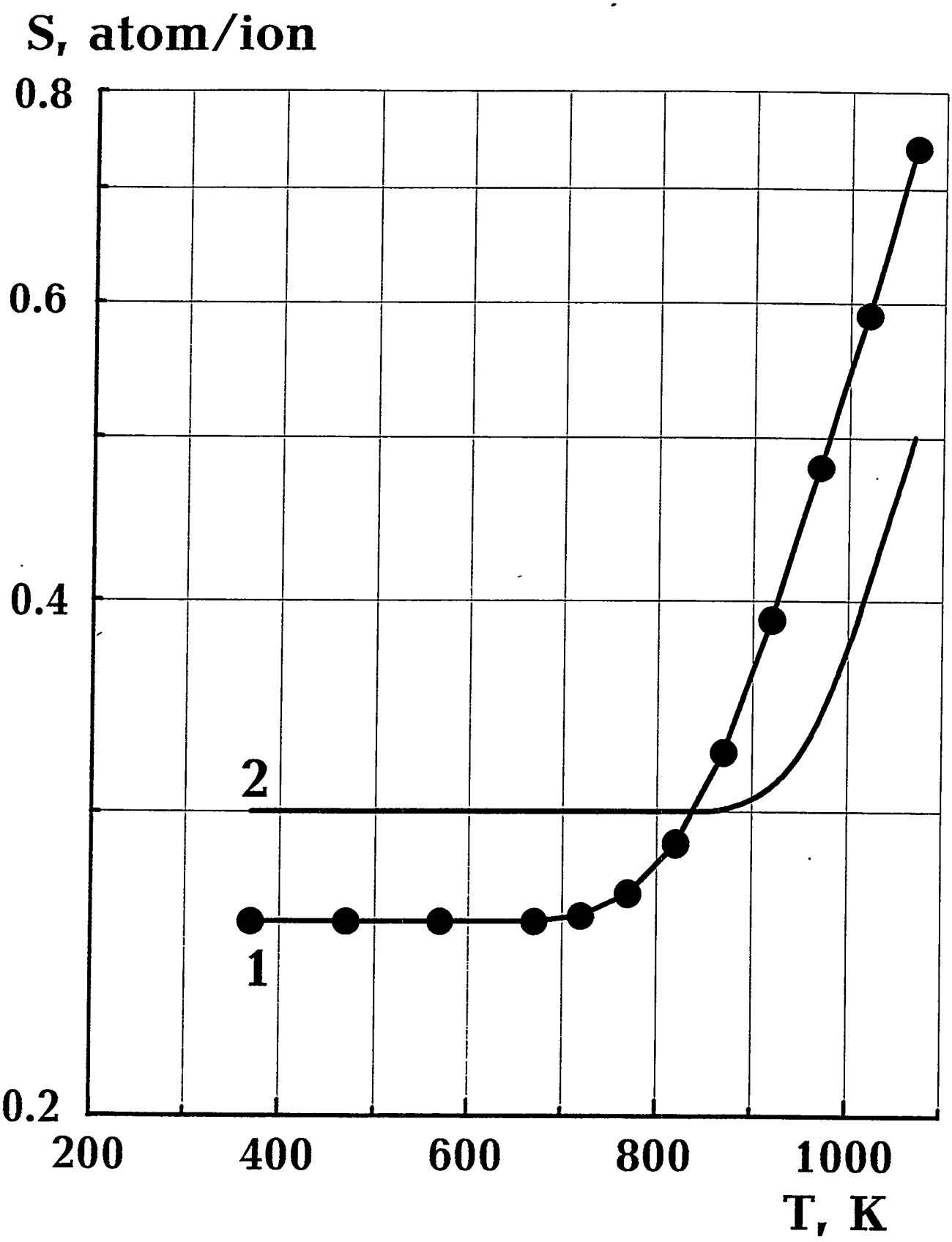

Fig. 3.

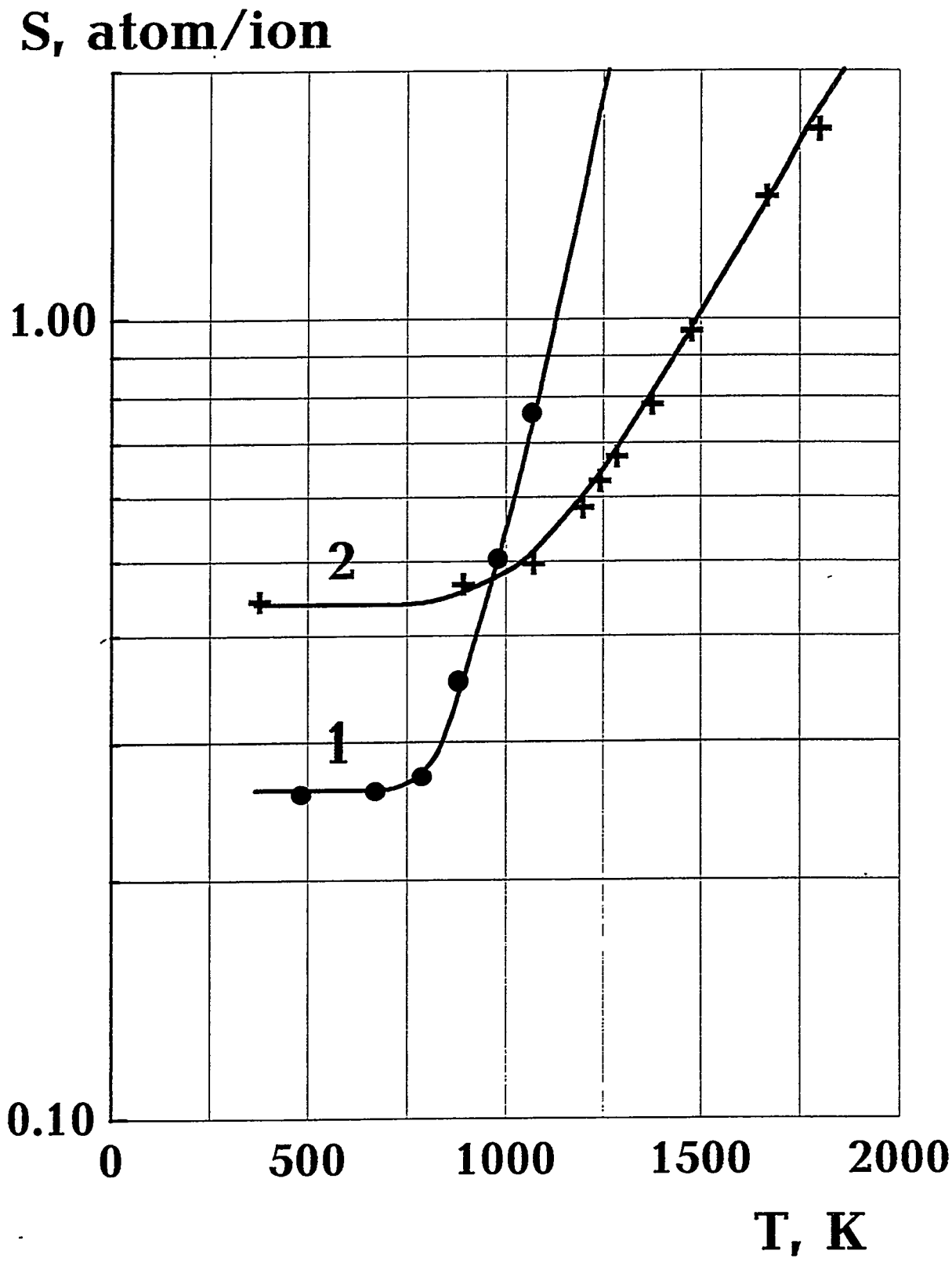

Fig. 4.

GAS SWELLING AND DEUTERIUM DISTRIBUTION IN BERYLLIUM IMPLANTED WITH DEUTERIUM IONS*

V.N.Chernikov, V.Kh.Alimov, A.P.Zakharov

Institute of Physical Chemistry of the Russian Academy of Sciences
Leninsky pr. 31, Moscow 117915, Russian Federation

ABSTRACT

An extensive TEM study of the microstructure of Be TIP-30 irradiated with 3 and 10 keV D ions up to fluences, Φ, in the range from 3×1020 to 8×10^{21} D/m^2 at temperatures, T_{irr} = 300 K, 500 K and 700 K has been carried out. Depth distributions of deutertum in the form of separate D atoms and D_2 molecules have been investigated by means of SIMS and RGA methods, correspondingly.

D ion irradiation is accompanied by blistering and gives rise to different kind of destructions depending mainly on the irradiation temperature. Irradiation with D ions at 300 K leads to the formation of tiny highly pressurized D_2 bubbles reminiscent of He bubbles in Be. Under 3 keV D ion irradiation D_2 bubbles ($\overline{r_b} \approx 0.7nm$) appear at a fluence as low as 3×10^{20} D/m^2. Irradiation at 500 K results in the development, along with relatively small facetted bubbles, of larger oblate gas-filled cavities accumulating most of injected D atoms and providing for much higher gas swelling values as compared to irradiation at 300 K. The increase of Φ and/or T_{irr} to 700 K causes the further coarsening of large cavities which are transformed into sub-suface labyrinth structures. D and He ion implantation leads to the enhanced growth of porous microcrystalline layers of c.p.h.-BeO oxide with a microstructure which differs considerably from that of oxide layers on electropolished surfaces of Be. Based on the analysis of experimental data questions of deuterium reemission, thermal desorption and trapping in Be have been discussed in detail.

1. INTRODUCTION

For beryllium as a candidate plasma-facing material for ITER (1) questions of interaction with hydrogen isotopes are of primary importance. Deuterium and tritium will be introduced into Be directly from plasma; besides, tritium will be generated in the bulk as a result of nuclear reactions. It is well documented that Be has a very high chemical affinity to oxygen and is allways covered with a thin and firm oxide film (2). Hydrogen has a very low solubility in Be (3,4) and does not chemisorb onto its surface (5).

Wampler studied in (6) the retention of deuterium implanted into Be. He has shown that under conditions of isochronal annealing implanted deuterium escaped from specimens in two steps at high fluences and in one step at low fluences. With taking

*Work supported by the US DOE under Contract LC-8102 with SNLA.

into account the results of his more recent investigations performed in (7) Wampler concluded that D atoms were trapped by radiation vacancies and could be retained inside bubbles in molecular form. A broad gas desorption maximum (around 650 K) was attributed to the dissociation of D-V complexes and to permeation of D atoms from gas-filled cavities, while the nature of the first desorption maximum (at about 400 K) was less clear. Möller at al. (8) reported data on the reemission of deuterium from Be under 10 keV D ion implantation at irradiation temperatures, $T_{irr} \leq 920$ K. At low fluences and $T_{irr} \leq 720$ K the reemission rate was either low or absent. But at fluences, $\Phi \approx \Phi_r = 3\times10^{21}$ D/m^2 it demonstrated a relatively abrupt increase. Such a behavior of reemission curves was not discussed. Recent results of Anderl at al. (9) on deuterium transport through Be under 1 keV D ion injection pointed out that the trapping of D atoms in a radiation modified layer played a significant role in deuterium permeation, reemission and retention. But, up to now the information on the microstructure of Be irradiated with hydrogen ions was very poor.

The aim of this work was the obtaining of a detailed information on the near-surface microstructure of Be implanted with D ions at different temperatures with a view to understand the nature of deuterium traps in Be and to follow their evolution on the fluence increase. On this basis it was tempting to clear up peculiarities of thermal desorption and reemission of implanted deuterium.

2. EXPERIMENTAL

TIP-30 type beryllium was used manufactured by hot isostatic pressing, containing about 2.2 wt.% of BeO and with the mean grain size of 20 μm (10). A micrograph of original Be made in a transmission electron microscope (TEM) is presented in Fig.1 which shows BeO precipitates found mainly on grain boundaries.

Conditions of D ion implantation of Be specimens studied in TEM are summarized in Table I. The implantation was fulfilled with 3, 9 and 10 keV D ions in a special UHV facility (11). For comparison, a few specimens were implanted with 5 keV He ions at 300 K and 500 K. After irradiation a part of specimens subjected to a back-thinning procedure (12) was studied by TEM. Another part of implanted specimens was used for SIMS and RGA (residual gas analysis) measurements performed in the same UHV set up simultaneously in the course of the Ar ion sputtering of the surface. Calibrated SIMS signal dependent on the depth was related to the concentration of separate D atoms present in the matrix, while corrected in a certain way RGA signal was attributed to the concentration of deuterium in molecular form (11).

The microstructure of Be was investigated in TEM EM-400T operated at 120 kV. Deuterium content in cavities visible in TEM was determined using RGA data. Estimations of gas pressure inside bubbles were fulfilled by employing Yurichev' equasion of state (EOS) for hydrogen (13).

Figure 1. Microstructure of as-received TIP-30 beryllium. Black spots are mostly BeO metallurgical precipitates.

3. EXPERIMENTAL RESULTS AND DISCUSSION

D-ion implantation of Be up to $\Phi \geq 2\times10^{21}$ D/m^2 leads to the blistering at all temperatures. Typical micrographs of blisters made by TEM after irradiation with 3 keV and 10 keV D ions are demonstrated in Fig.2.

3.1 T_{irr} = 300 K

Very small cavities are formed in Be due to D-ion implantation at T_{irr} = 300 K which is illustrated in Fig.3. Under 3 keV D ion irradiation cavities with the mean radius, r_b of 0.7 nm appear at a fluence as low as 3×10^{20} D/m^2. Fluence increase leads to the growth of the mean cavity size and to the formation of microchannels. The influence of the ion energy is less pronounced.

Concentration profiles of deuterium in atom and molecular form in Be implanted with 3 keV D ions up to the above minimal fluence are demonstrated in Fig.4. They say that injected D atoms are trapped in the ion stopping zone both as separate atoms and also in molecular form. Taking into account a very low solubility of deuterium in Be at 300 K the above cavities were assigned as D_2 gas-filled bubbles. The comparison of RGA data with our TEM data made it possible to estimate the average volume density

Table I. Conditions of D-ion implantation and post-implantation annealing of TIP-30 Be specimens studied by TEM.

D ion energy, E (keV)		3		10		
Mean projected range, R_p (nm) and straggling, σ (nm)		60 13		150 20		
Ion flux, j ($D/m^2 \cdot s$)		$(1.1\text{-}1.2)\times10^{18}$		$(2.8\text{-}3.0)\times10^{19}$		
Fluence, Φ (D/m^2)		3×10^{20}	3×10^{21}	2×10^{21}	4×10^{21}	8×10^{21}
Irradiation temperature, T_{irr} (K)	300	+[1)]	+[2)]	+	+	-
	500	+	-	+	+	+
	700	-	-	+	+	-

[1]) Also after annealing in vacuum at 560 K and 690 K for 10 min
[2]) Also after annealing in vacuum at 440 K for 10 min

Table II. Gas bubble parameters in Be implanted with 3 keV D and 5 keV He ions

Bubble parameters averaged over the near-surface layer	Fluence, Φ (ion/m^2)/Implantation temperature, T_{irr} (K)			
	3-keV D ions		5-keV He ions	
	3×10^{20}/300 K	3×10^{21}/300 K	3×10^{21}/300 K	3×10^{21}/500 K
Radius, r_b (nm)	0.7	1.1	1.0	0.8
Volume density, c_b (m^{-3})	4.0×10^{24}	3.3×10^{24}	4.0×10^{24}	4.6×10^{24}
Gas swelling, S (%)	0.6	1.8	1.7	1.0
Volume density of gas atoms inside bubbles, n (at/nm^3)	140	170	-	-
Innder gas pressure, p_g (GPa)	4.0	6.0	-	-
Foil thickness, t_f (nm)	80	60	50	65

of gas atoms inside bubbles and, using Yurichev' EQS for hydrogen, the average inner pressure of molecular deuterium therein (Table II). For two selected fluences the

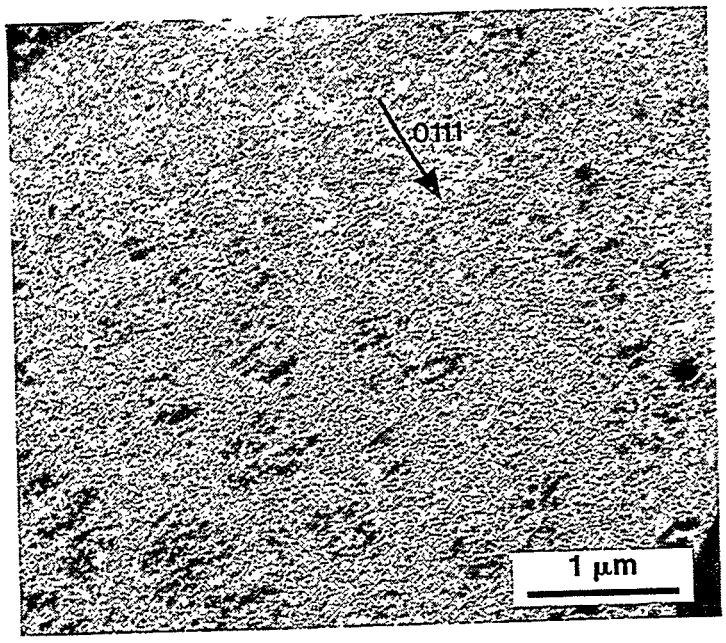

(a)

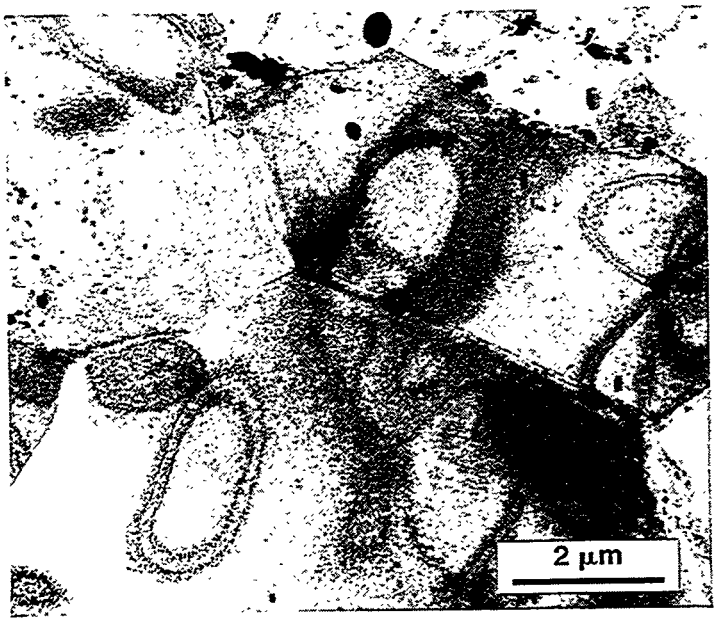

(b)

Figure 2. TEM image of blisters on Be after irradiation at 300 K with: (a) 3 keV D ions up to $\Phi = 3\times10^{21}$ D/m^2 (dark field) and (b) 10 keV D ions up to $\Phi = 2\times10^{21}$ D/m^2 (bright field).

calculated pressures appeared to be of 4 and 6 GPa which is comparable to equilibrium values (9 and 6 GPa, correspondingly). It is to be noted that parameters of deuterium

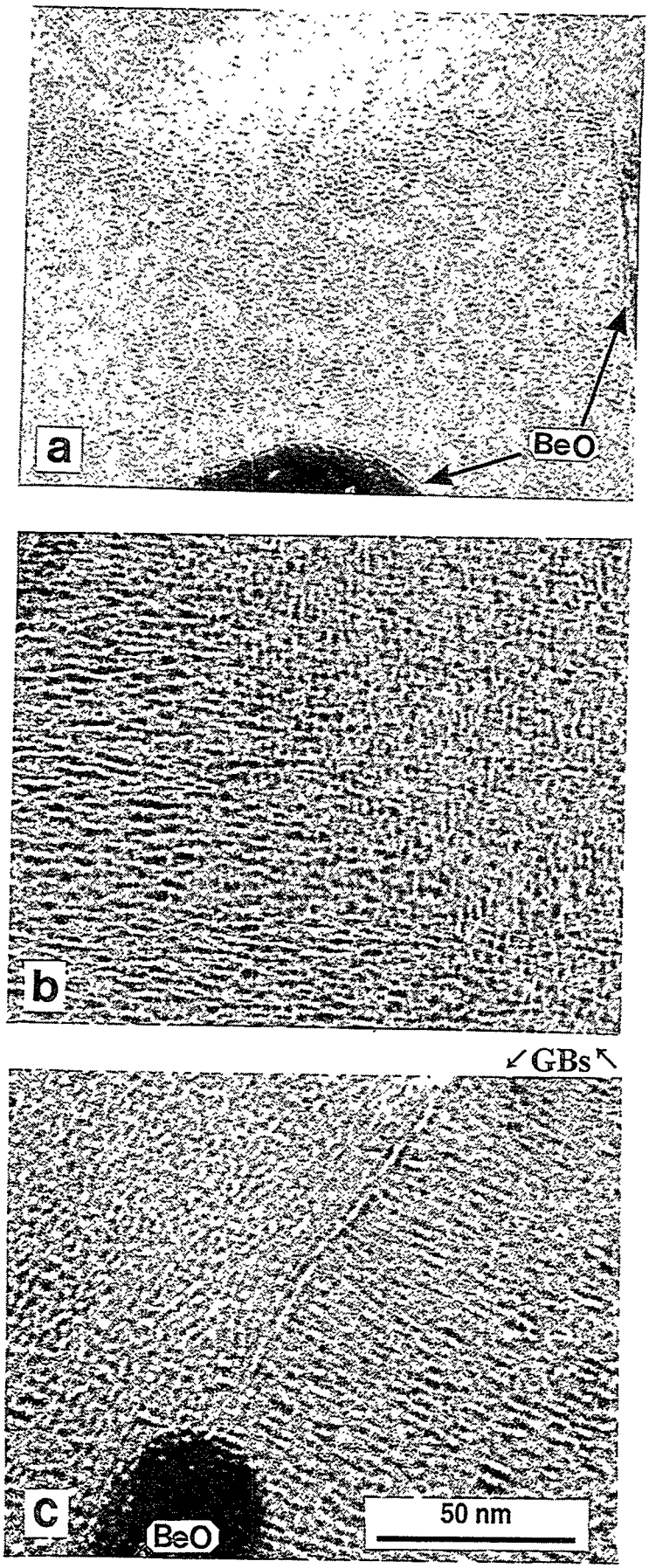

Figure 3. Deuterium bubbles after irradiation at 300 K with 3 keV D ions to fluences: a) 3×10^{20} D/m^2 and b) 3×10^{21} D/m^2, and with 10 keV D ions to a fluence 4×10^{21} D/m^2

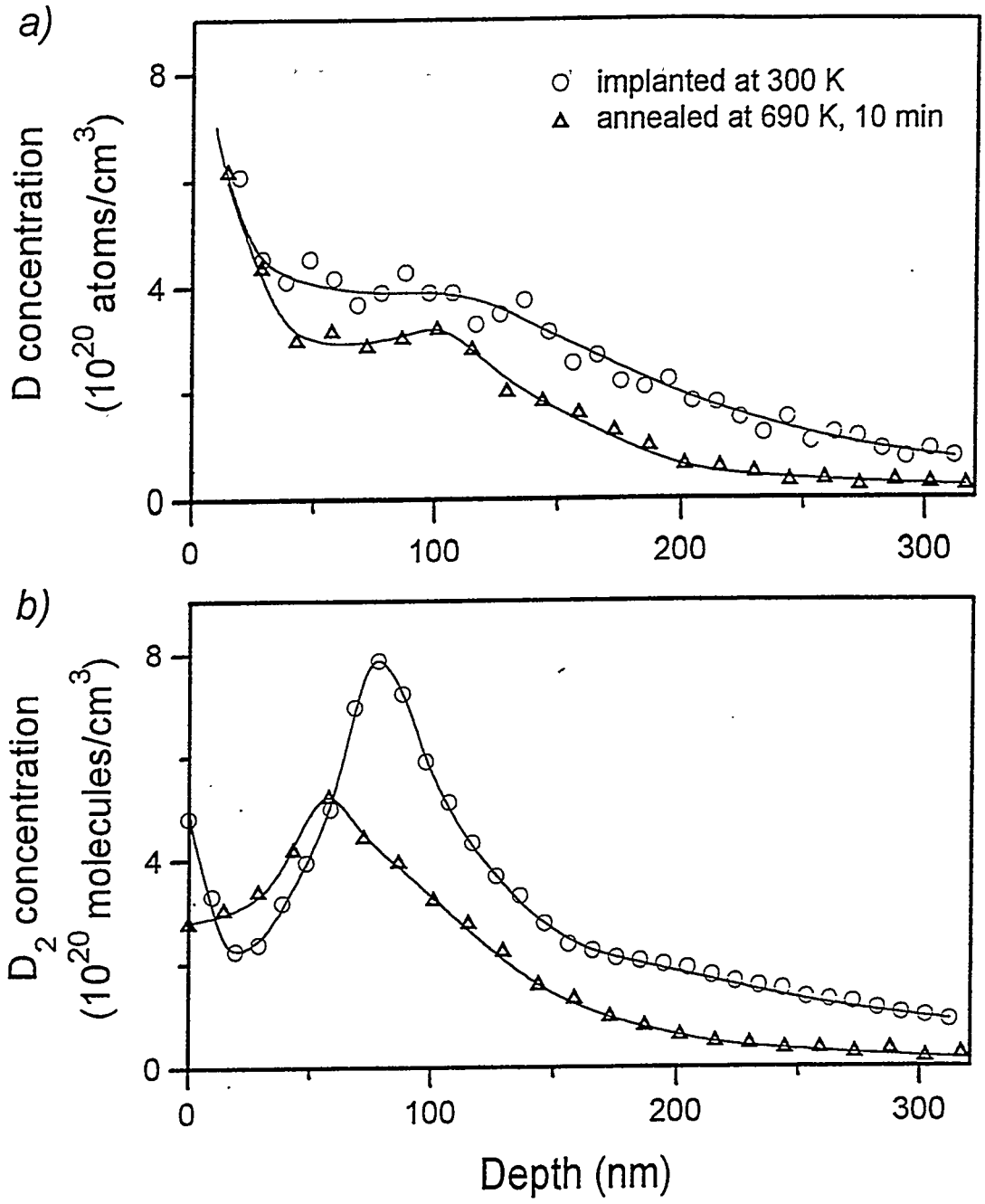

Figure 4. Depth distributions of deuterium in Be implanted at 300 K with 3 keV D ions up to $\Phi = 3\times10^{20}$ D/m^2 and subsequently annealed at 690 K for 10 min (on the basis of SIMS a) and RGA b) data).

bubbles are close to those of helium bubbles in Be manifesting a similarity of the behaviour of deuterium and helium in this metal.

Concentration profiles of atomic and molecular deuterium in Be implanted with 9 keV ions at 300 K up to different fluences are shown in Fig 5 (11). Comparison of these profiles for the lowest fluence, $\Phi = 1.5\times10^{20}$ D/m^2 allows to estimate a minimal concentration of separate D atoms in the matrix sufficient for the onset of the appearance of D_2 gas bubbles. It is about 1 at.% which is of the same order as a concentration of injected He atoms necessary for the onset of He bubble formation in different metals (14). At $\Phi \approx 2\times10^{21}$ D/m^2 both D_2 and D concentration profiles reach their maxima (of 6.5 and 1.6 at.%, correspondingly). Under the further fluence increase the flattening of both kindes of deuterium distributions at the above saturation levels takes place towards the surface. In turn, TEM data give good grounds to believe that at these concentrations of deuterium D_2 bubbles (even though in part) get interconnected forming narrow channels clearly recognizable in Fig.3b and c.

It is reasonable to explain an abrupt reemission of implanted deuterium at $\Phi \approx \Phi_r$ (8) by a partial gas escape from a zone containing channels due to their touching the outer surface being a result of this zone estension under ion injection. At higher fluences the reemission rate remains relativly high (more than 0.5) which is clear: in the presence of a network of open channels thermalized D atoms escape from the metal much more easily comparing to the case when a channel containing zone is either detached from the surface or absent.

3.2. Annealing experiments

For low fluences Wampler observed the onset of the gas release at about 650 K (6). According to his model implanted D atoms are trapped in vacancies forming D-V complexes which are stable and immobile up to dissociation temperature, $T^D \approx 650$ K (7). We have made the following to check it. Two Be specimens were irradiated up to $\Phi = 3\times10^{20}$ D/m^2 and, hence, contained very small D_2 bubbles (Fig.3a). One of these specimens was annealed at 560 K and the other at 690 K (somewhat lower and higher than T^D) for 10 min. At both temperatures separate D atoms and free vacancies are highly mobile in Be matrix (7). No changes in bubble appearance were observed in a specimen annealed at a lower temperature. That is any processes of bubble coarsening were suppressed which was indicative of the immobilization of radiation vacancies at $T_{ann} \geq 560$ K, probably, by D atoms. On the other hand, the annealing at a higher temperature led to a considerable bubble development which is clearly noticeable when comparing Figs.6 and 3a and was accompanied by some losts of implanted deuterium (Fig.4). It meant the appearance in the matrix at $T_{ann} \leq 690$ K of both freely migrating vacancies providing for bubble coarsening and mobile D atoms escaping in part out of the specimen. All these observations say in favour of Wampler's model on the D atom coupling with vacancies and the formation of immobile D-V complexes which are stable up to about 650 K.

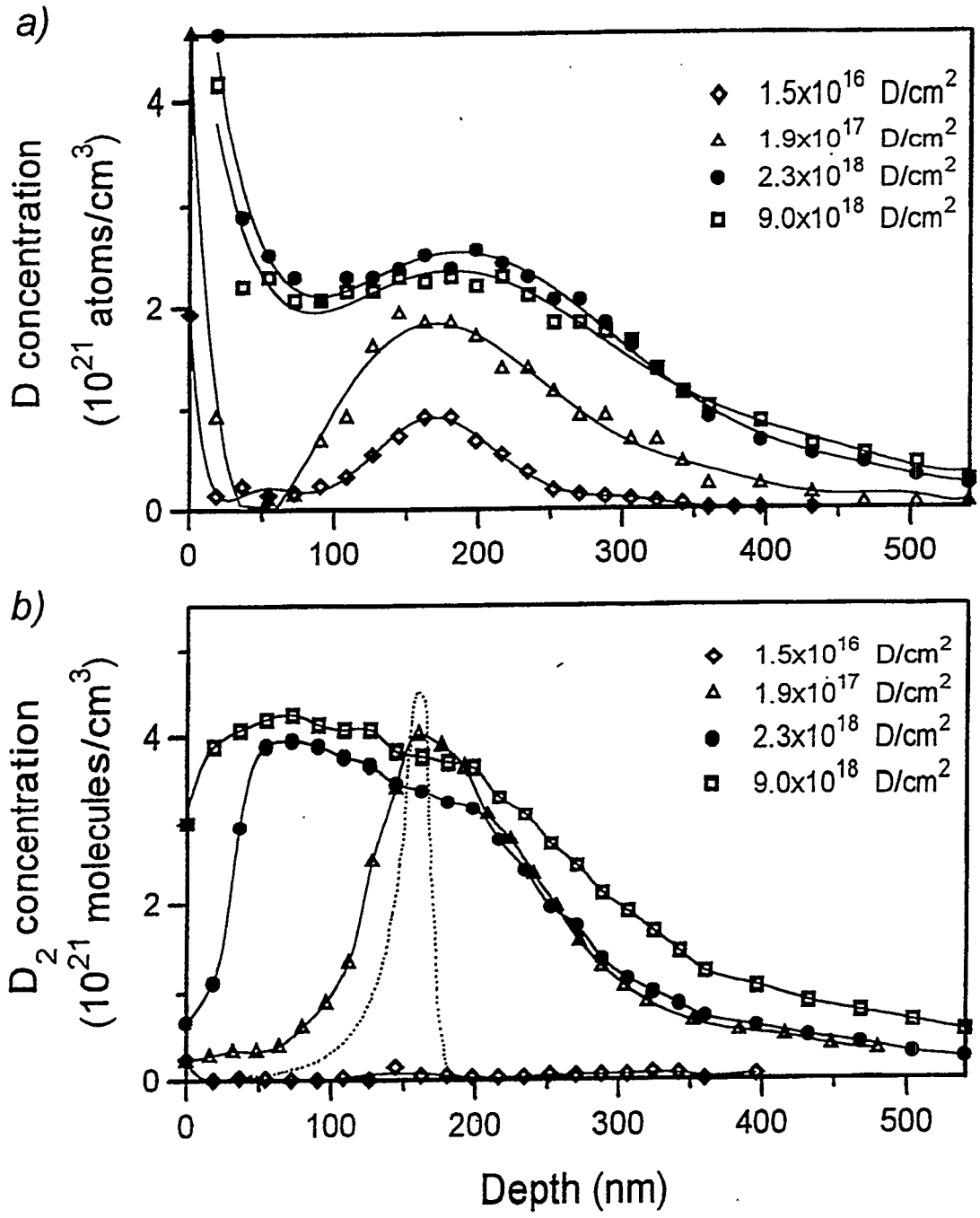

Figure 5. Depth distributions of deuterium in Be implanted at 300 K with 9 keV D ions up to fluences indicated. Dotted curve in b) is a result of TRIM calculation.
Figure 6. Deuterium bubbles after irradiation at 300 K with 3 keV D ions up to $\Phi = 3\times10^{20}$ D/m^2 and subsequent annealing at 690 K for 10 min; on b) a grain boundary is shown.

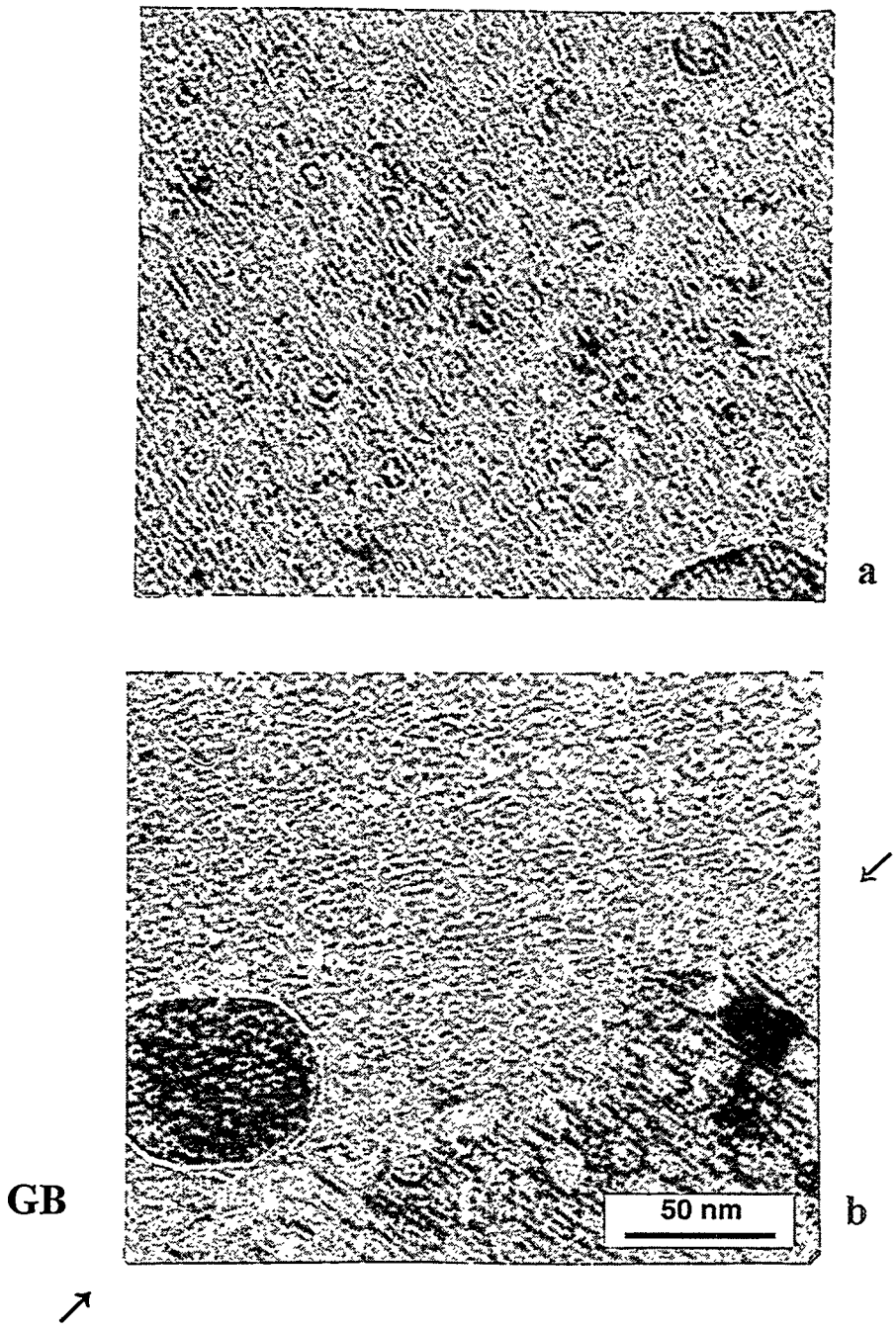

Figure 6

The major part of deuterium implanted up to high fluences is released in a first narrow peak centered around 400 K (6,8,15). We attempted a comparison of bubble and channel appearance in specimens implanted with 3 keV D ions at 300 K up to 3×10^{21} D/m^2 before and after annealing at 440 K for 10 min. No essential differences were observed. It meant that during annealing any processes of bubble/channel coarsening or rupture were of minor importance. A conclusion was made that the main reason of the first thermal desorption maximum was a desorption of deuterium from the walls of channels which were opened or on the verge of their opening to the surface. It explains some peculiarities, in particular, a narrowness of the desorption maximum in question, agrees fairly well with the experimentaliy determined value of deuterium desorption temperature from a clean Be surface (450 K) (5) and predicts the independence of this temperature on the D ion energy which was noticed in (6).

Thus, one can conclude, that distributions of separate D atoms in Be (Figs.4a and 5a) are made up of D atoms trapped in vacancies, absorbed on bubble walls and, probably, bound to and within BeO metallurgical precipitates, similar to the capturing of D atoms by Al_2O_3 inclusions studied in (16). Also, D atoms are accumulated in the surface oxide (see p.3.4). Long tails of D_2 and D concentration profiles seem to be a result of thermal migration of D atoms into the bulk followed by trapping in microdefects and oxide inclusions.

3.3. T_{irr} =500 K and 700 K

The development of the microstructure at T_{irr} = 500 and 700 K has much in common. An example of cavities in Be implanted with 3 keV D ions at 500 K is presented in Fig.7. No doubts that there are D_2 gas bubbles. Indeed, neutron irradiation of TIP-30 Be at the same temperatures and up to the same damage levels can not produce such a high volume increase (10). At T_{irr} =500 K all relatively small bubbles are facetted; they are prisms with their axes along the hexagonal axis of the matrix. A character of the gas porosity is strongly dependent on the grain orientation relative to the entrance surface and is also a function of the distance to the surface. The latter means that small and facetted bubbles are formed in a matrix layer at depths of less than (0.4-0.5)$\cdot\overline{R_p}$, while in a depth range (0.5-1.0)$\cdot\overline{R_p}$ are developed large and oblate cavities and channels. The latter are shown at the very beginning of their development in Fig.7a. They are rather two- than three-dimensional and, according to our estimations, D_2 pressure in them lays between 0.3 and 1.0 GPa.

3.3.1. T_{irr} = 500 K

A series of micrographs in Fig.8 demonstrates the microstructure evolution under D ion irradiation at 500 K with the fluence. Small facetted bubbles are mainly located near the suface (see also Fig.7b). Large light areas are coarse, oblate and flattened-out

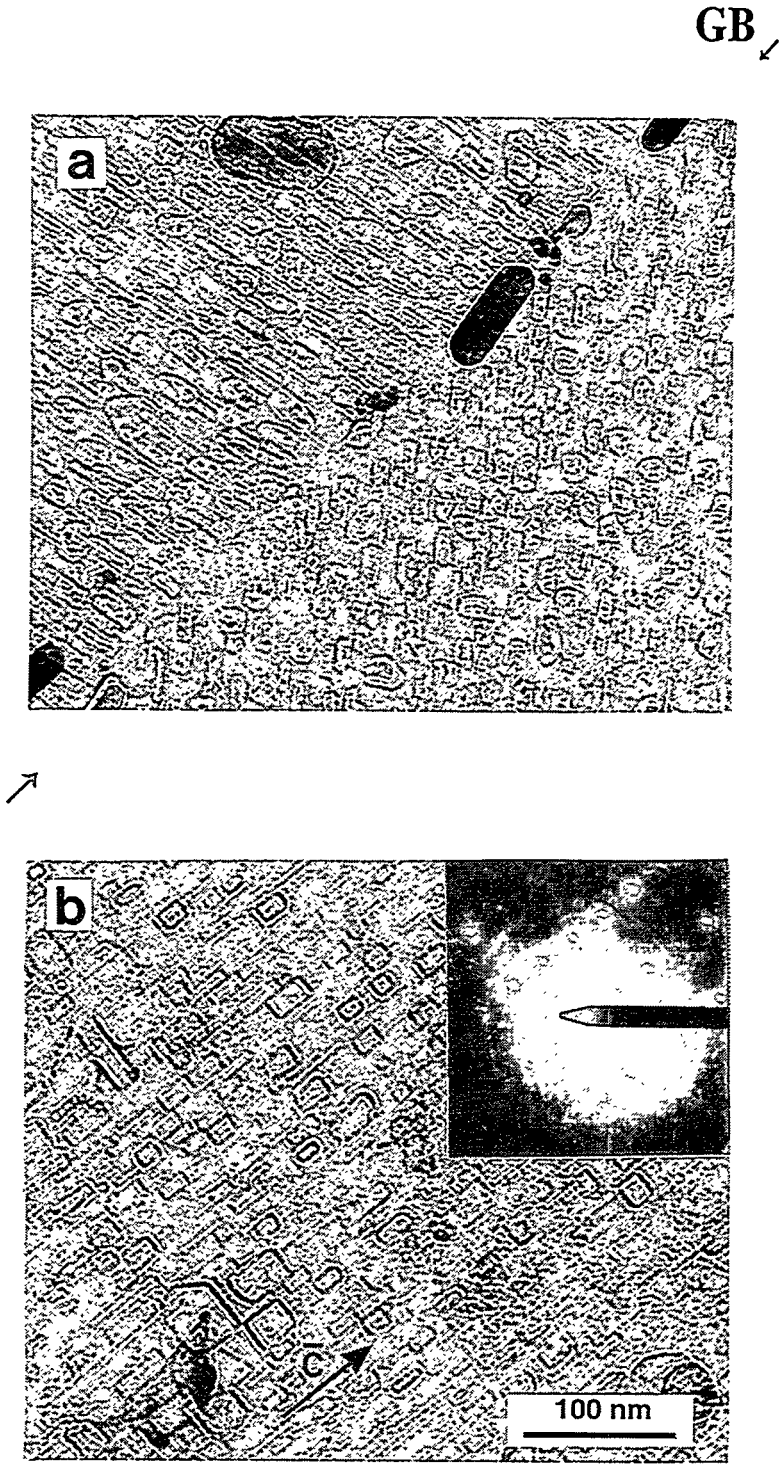

Figure 7. Deuterium bubbles after irradiation at 500 K with: a) 3 keV D ions up to $\Phi = 3\times10^{20}$ D/m^2; a grain boundary is shown along a diagonal of a micrograph ($t_f \approx 60$ nm); b) 10 keV D ions up to $\Phi = 4\times10^{21}$ D/m^2 ($t_f \approx 50$ nm); SADP (on the insert) reveals a direction of the hexagonal axis.

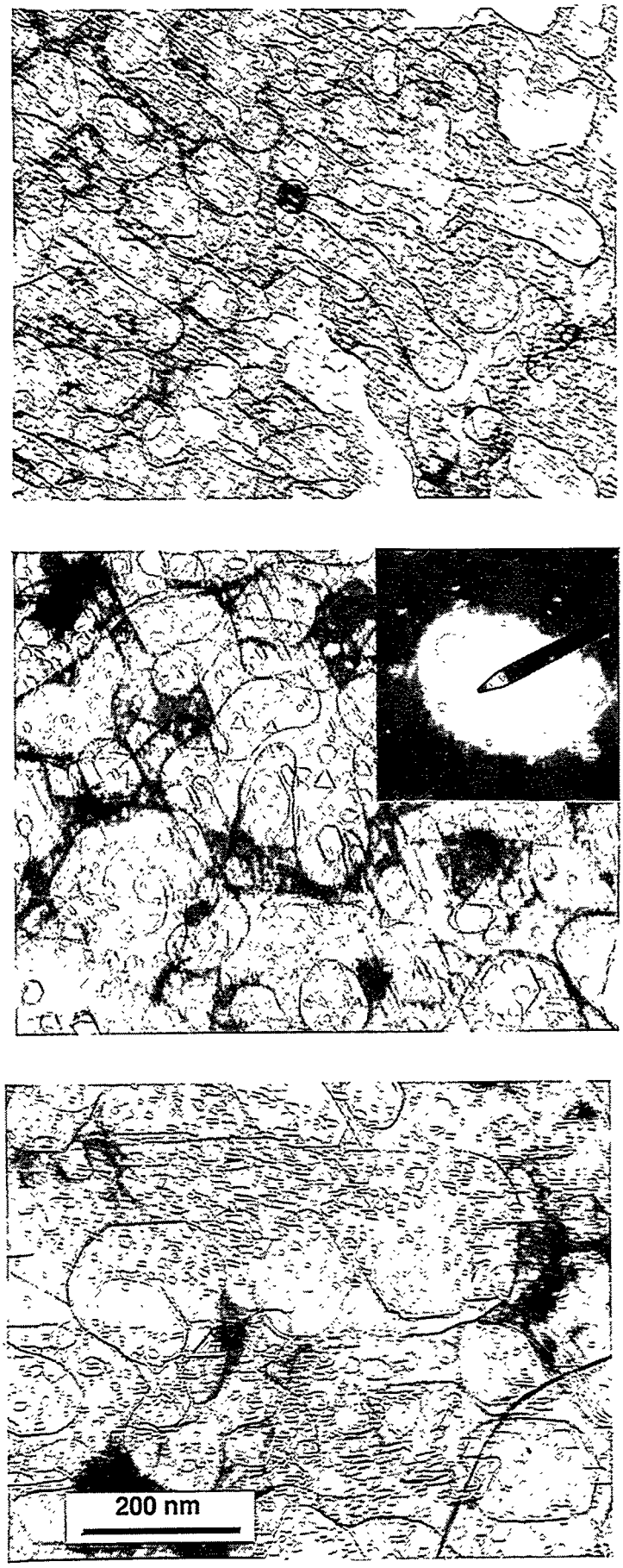

Figure 8. Deuterium bubbles and large cavities after irradiation at 500 K with 10 keV D ions up to: a) 2×10^{21} D/m^2, b) 4×10^{21} D/m^2 and c) 8×10^{21} D/m^2; grains on b) and c) are close to the basal orientation.

cavities at a depth of $\overline{R_p}$. Their height is about 5 times less than their width. Estimations show that the main part of impanted deuterium comes to rest in these cavities, while the remainder resides in small separate bubbles and leaves a specimen by outdiffusion avoiding any trapping and giving rise to a noticeable gas reemission (8). TEM data give good grounds to relate a steep reemission increase at $\Phi \geq \Phi_r$ to uncovering of large and partly interconnected gas-filled cavities. With the further fluence increase (similar to the case of D ion irradiation at 300 K) the escape of implanted and thermalized D atoms into vacuum is facilitated considerably due to the presence near the surface of coarse and open porosity which means a highly desintegrated near-surface layer with a lot of paths short-circuiting the inner layers with the outer surface. Obviously, at higher fluences the further formation and development of bubbles will cease. One can expect, that under steady state conditions, with a reemission rate of 1.0, a certain compromise will be attained between a degree destructions in the near-surface layers (surface roughness) and a level of gas swelling due to D_2 bubbles.

Let us return to bubbles near the surface formed as a result of radiation damage in the presence of D atoms in the matrix. Deuterium pressure in them, calculated as D_2 pressure in spherical bubbles of equivalent volume ($r_b = 5$ nm, = 1.2 GPa), is close to equilibrium and these bubbles are responsible for about 3% gas swelling near the surface. If the gas inside bubbles is now assumed to be in equilibrium with D atoms in the surrounding matrix and using the Shapovalov equation for the solubility of H_2 in Be, one can estimate the minimal value of deuterium concentration in the matrix equal to about 100 appm. A strong orientation dependence of bubble habit is, eventually, a consequence of compressive stresses which build up near the surface due to the presence of interstitial dislocation defects (see below).

What is the origin of a great difference in bubble appearance after D ion implantation at 500 K and at 300 K? Seemingly, the main reason is a considerable difference in vacancy mobility at these temperatures. In contrast to 500 K vacancies are practically immobile in Be at room temperature (7), hence, all diffusion limited processes of coarsening are suppressed. At the same time, Kamada et al. (17) observed in Al, a generally accepted analog of Be, very large cavities after H ion implantation at T_{irr} as low as 300 K. But this stems from the fact that vacancies in Al are highly mobile even at room temperature (18).

At T_{irr} = 300 K the behavior of implanted D and He atoms in Be has much in common which is manifested by their competition for trapping sites under condition of simultaneous ion injection (19) and by a similarity of D_2 and He bubble parameters listed in table II.The main reason for this is, obviously, a very low solubility of both gases in Be at 300 K: On the other hand, the increase of T_{irr} up to 500 K does not influence parameters of He bubbles in Be, while parameters of D_2 bubbles change significantly (Table II). To our mind, this results from a higher binding energy between vacancies and He atoms in comparison with D atoms and, probably, from a substantial

mobility increase of D atoms at 500 K as compared to that of He atoms which remain practically immobile (20). The role of the chemical activity of deuterium in D_2 bubble nucleation and development can not be excluded (21). In particular, when compared with the results of He ion irradiation, the formation of channels at T_{irr} = 300 K under D ion irradiation is much more pronounced which is, probably, facilitated by deuterium adsorbtion onto bubble walls.

3.3.2. T_{irr} = 700 K.

A general view and detailed micrographs of the near surface microstructure of Be implanted with 10 keV D ions at 700 K are presented in Fig.9. Here, the thickness values of near-surface layers with small facetted bubbles and of underlying layers with large gas-filled cavities are higher than those in specimens irradiated with D ions of the same energy at 500 K. Mean sizes of bubbles and cavities are also higher comparing to those for T_{irr} = 500 K. The coalescence of large cavities leads to the development of flattened-out and interconnected channels forming extended labyrinth structures which differ considerably in different grains. For a fluence of 2×10^{21} D/m^2 local values of the gas swelling reach more than 50%. With the use of corresponding D_2 concentration profiles for 9 keV D ions (11) the mean inner pressure of deuterium in the volume of labyrinths can be roughly estimated as less than 50 MPa. Obviously, the main part of implanted deuterium accumulates in labyrinth channels under consideration. At all appearance, the interaction of labyrinth branches with the outer surface leads to the onset of a steep reemission of accumulated gas observed in (8). The estimated stationary concentration of deuterium buried at a temperature considered in gas-filled bubbles and cavities in a surface layer of (0.5-1.0) μm in thickness is of the order of (0.5-1.0) at.%.

The creep rate of TIP-30 Be at 700 K is very low. So, the main mechanism of the development of large cavities is a gas-driven free vacancy absorption which is also valid for the irradiation at 500 K. Differences in the microstructure development and retention /reemission kinetics of deuterium at T_{irr} = 700 K compared to 500 K are a higher vacancy mobility and a higher solubility of deuterium in Be.

The shape of small facetted and large oblate gas cavities which are formed in Be at T_{irr} = 500 and 700 K strongly depends on the grain orientation relative to the surface (Figs.7 and 9). Eventually, it seems to be a concequence of compressive stresses which are build up near the surface of anysotropic Be due to the formation of interstitial dislocation defects (12). The stresses may affect processes of gas cavity nucleation and growth in an indirect way (22).

3.4. Surface Oxide

The electrpolished surface of Be is covered with a qusiamorphous layer of hexagonal oxide BeO of 2-3 nm in thickness. Typical micrographs of an oxide film on Be surface after D ion implantation are presented in Fig.10. Three main effects are

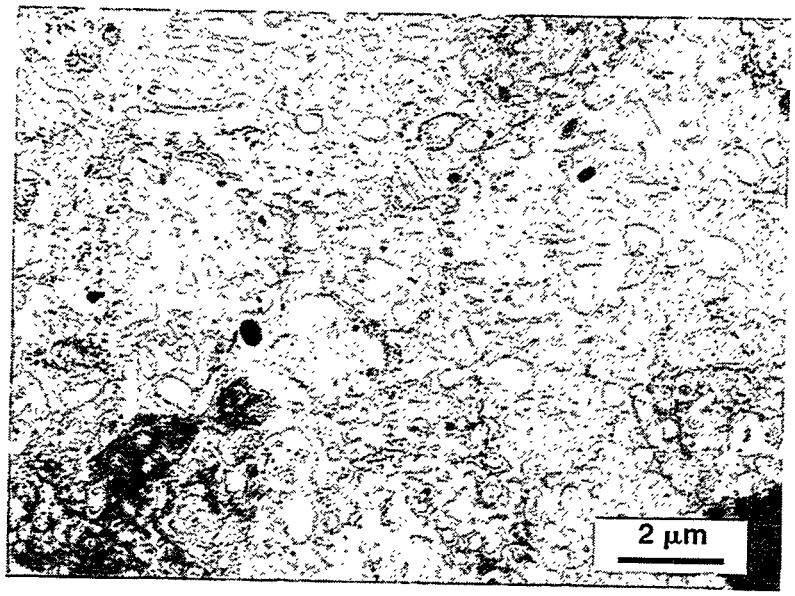

a

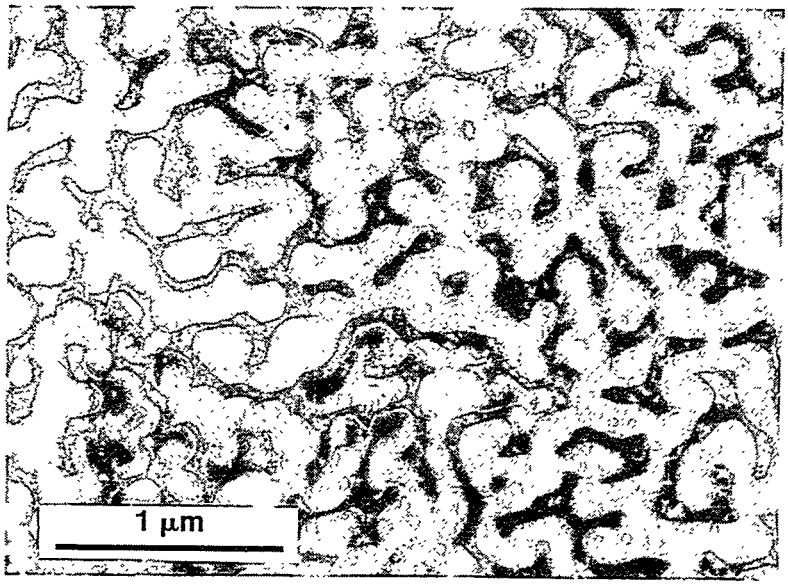

b

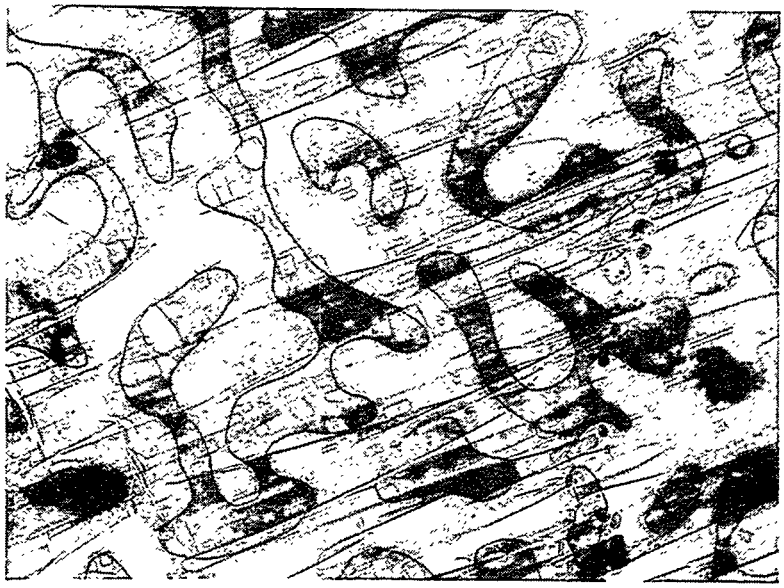

c

Figure 9. Deuterium bubbles and labyrinths of oblate interconnected channels after irradiation at 700 K with 10 keV D ions up to 2×10^{21} D/m^2: a) viewing field covers some grains, low magnification; b) surface plane of the grain is close to (0001); c) surface plane of the grain is nearly parallel to c axis ($t_f \approx 450$ nm).

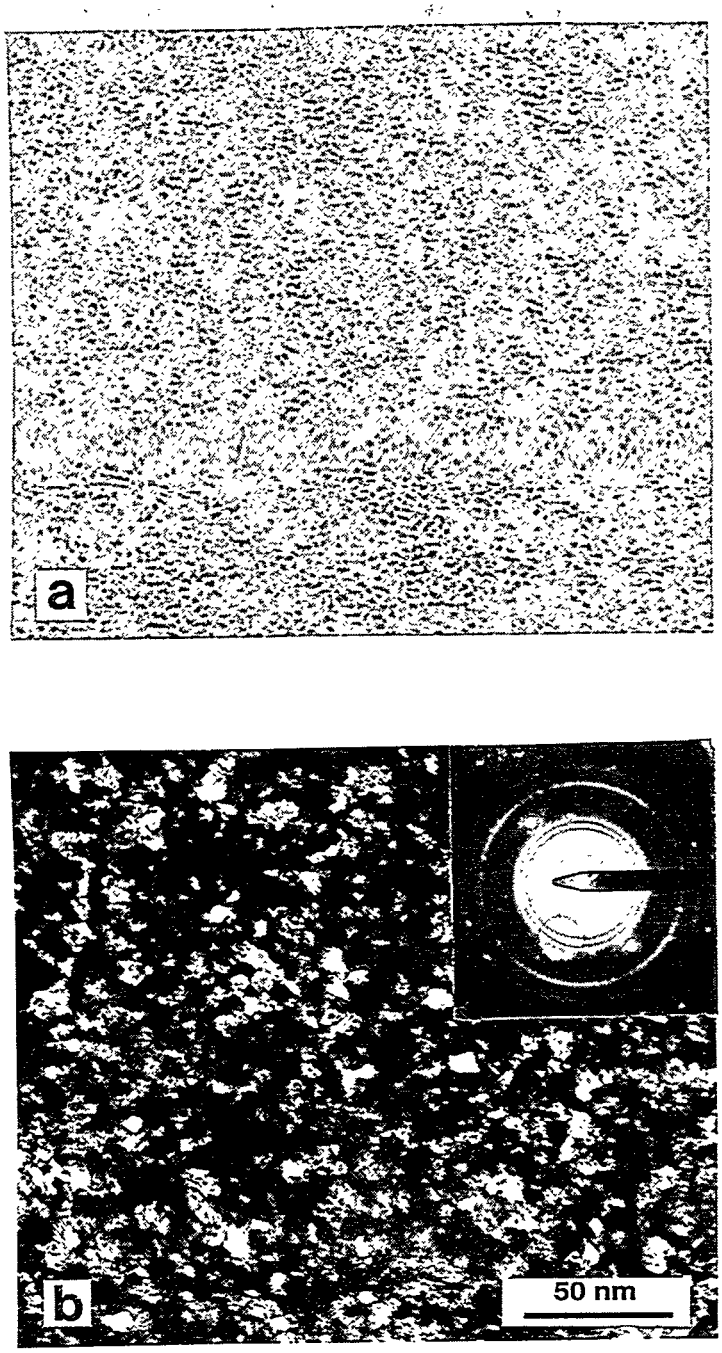

Figure 10. Surface oxide film of 40 nm in thickness after 3 keV D ion irradiation at 300 K up to $\Phi = 3\ 10^{21}$ D/m^2: a) bright field, b) dark field imaged in arcs of two strongest diffraction rings {100} and {101} of BeO (see insert). On the insert is SADP with BeO diffraction rings and Be diffraction reflections from a metal island in orientation close to the basal one.

displayed under D ion implantation in no dependence on the irradiation temperature. First, the thickness of the BeO film grows considerably which points to the radiation-enhanced oxidation. In particular, the thickness of BeO film in Fig.10 is of 40 nm. But, with the fluence increase, at about $\Phi \leq 1\times10^{22}$ D/m^2, the film thickness saturates. Second, the microstructure of this oxide - also hexagonal BeO - is not quasiamorphous but microcrystalline with the average crystal size of 7 nm. Third, small cavities from 1.0 to 2.5 nm in size and with a volume density of 1×10^{24} m^{-3} are formed in the oxide resulting in its free volume increase up to (2-4)%. Implantation with He ions leads to the similar results.

In contrast to a conclusion of Langly (23) who explained the enhanced growth of BeO film by a radiation-induced diffusion of Be atoms followed by the reaction with oxygen on the surface, we consider this saturating process as a penetration of absorbed O atoms deep into the near surface layer of Be due to successive impacts with energetic D atoms throughout the ion stopping zone. Comparative analysis of relevant D atom and D_2 molecule distributions (in Figs.4 and 5) says that deuterium is retained in the surface oxide mainly in the form of separated D atoms. Cavities in BeO may be filled with deuterium up to relatively low pressures ($\leq$ 60 MPa).

4. Main Conclusions

It has been shown that the implantation of Be with 3 to 10 keV D ions in a temperature range 300-700 K leads to the formation of deuterium-filled bubbles and cavities. Resulting gas porosity accumulates most of the injected gas before the reemission starts.

At T_{irr} = 300 K tiny bubbles (r_b = 0.7-1.2 nm) of a high volume density ($c_b \geq 3\times10^{24}$ m^{-3}) are formed with the inner gas pressure values near equilibrium ($\geq$ 5 GPa). The reaching in the ion stopping zone of a total deuterium concentration of (7-8) at.% triggers the formation of channels which extends with a fluence increase towards the surface. The interaction of channels with the surface leads to channel opening which gives rise to the onset of an abrupt deuterium reemission. In addition to the accumulation of D atoms inside bubbles in the molecular form, they are adsorbed on the walls of bubbles and channels. D atoms are trapped also in vacancies (in D-V immobile complexes dissociating at about 650 K), within the surface oxide and by means of bonding to and within BeO metallurgical inclusions. In the quasistationary state under irradiation with 10 keV D ions ($\Phi \geq 5\times10^{22}$ D/m^2) the total concentration of deuterium trapped in the near-surface layer of (300-400) nm in thickness is not less than about 8 at.%. Deuterium bubbles formed at T_{irr} = 300 K are very reminiscent of He bubbles formed in Be under equivalent implantation conditions.

In contrast to T_{irr} = 300 K, D ion irradiation at 500 K and 700 K leads to the appearance, along with relatively small bubbles, of large and oblate gas-filled cavities and channels located within a wide depth gap at a depth of more than $\overline{R_p}$. Labyrinths of flattened-out wide and branching channels are developed at 700 K. Large cavities

and channels accumulate the major part of injected deuterium and provide for much higher values of gas-induced swelling. Their interaction with the surface gives rise to a steep increase of the implanted gas reemission. At T_{irr} = 700 K the total quasistationary concentration of deuterium buried in gas bubbles and cavities over a near-surface layer of (0.5-1.0) μm in thickness reaches (0.5-1.0) at.%.

At all irradiation temperatures D ion implantation of Be gives rise to the formation on its surface of microcrystalline ($d_{cr} \approx 7$ nm) layers of c.p.h.- BeO oxide. Their thickness tends to saturate at fluences, $\Phi \leq 1\times10^{22}$ D/m^2 at a level of 50 nm. Surface oxide contains tiny cavities (r_c = 1.0-2.5 nm) and curved channels. The most part of deuterium retained in BeO layers (up to 3-4 at.%) is in the form of separate D atoms, probably, chemically bound to O atoms.

Considering the application of Be as a first wall material in ITER an assessment seems to be necessary of gas bubble formation in the bulk due to the neutron radiation damage in the presence of dissolved hydrogen isotoipes originating from plasma.

ACKNOWLEDGEMENTS

The authors would like to thank Dr.I.B.Kupriyanov (A.A.Bochvar ARSRIIM, Moscow) for supplement of TIP-30 Be and taking part in specimen preparation, Mr. A.V.Markin for the fulfillment of Be specimen annealing, as well as Dr.A.E.Gorodetsky and Mr.S.L.Kanashenko for valuable discussions.

REFERENCES

1. ITER Conceptual Design, Interim Report, IAEA/ITER/DS/7 (IAEA, Vienna, 1990); M.C.Billone, M.Dalle Donne and R.G.Macaulay-Newcombe. Status of Beryllium Development for Fusion Applications. 3-rd Int.Symp.on Fus. Nucl. Technol., UCLA, 27 .06-1.07.1994 - to be published.

2. K.L.Wilson, R.A.Causey, W.L.Hsu, B.E.Mills, M.F.Smith and J.B.Whitley, Beryllium - a better tokamak plasma-facing material?, J.Vac.Sci.Technol. A8(3) (1990) 1750; K.L.Wilson, R.Bastasz, R.A.Causey, D.K.Brice, B.L.Doyle, W.R.Wampler, W.Möller, B.M.U.Scherzer and T.Tanabe, Trapping, detrapping and release of implanted hydrogen isotopes, Supplement to Nuclear Fusion 1(1991) 31.

3. W.A.Swansiger, Summary abstract: Tritium solubility in high purity beryllium, J.Vac.Sci.Technol. A4 (1986) 1216.

4. V.I.Shapovalov and Yu.M.Dukelskii, On the phase diagram of Be-H system, Russ.Metallurgy No.5 (1988) 210.

5. V.Lossev and J.Küppers, Interaction of hydrogen atoms with beryllium (0001) surfaces, J.Nucl.Mater. 196-198 (1992) 953.

6. W.R.Wampler, Retention and thermal release of deuterium implanted in beryllium, J.Nucl.Mater. 122&123 (1984) 1598.

7. R.Wampler, Trapping of deuterium in beryllium, J.Nucl.Mater. 196-198 (1992) 981.

8. W.Möller, B.M.U.Scherzer and J.Bohdansky, Retention and release of deuterium implanted into beryllium, IPP-JET Report No.26 (1986).

9. R.A.Anderl, M.R.Hankins, G.R.Longhurst, R.J.Pawelko and R.G.Macauley-Newcombe, Hydrogen transport behavior of beryllium, J.Nucl.Mater. 196-198 (1992) 986.

10. I.B.Kupriyanov, V.A.Gorokhov and A.M.Khomutov, Manufacturing and some properties of powder beryllium with high radiation stability, Proc.18-th Symp.Fus.Technol. (Aug.22-26, 1994, Karlsruhe, Germany) - to be published.

11. V.Kh.Alimov, V.N.Chernikov and A.P.Zakharov - to be published in J.Nucl.Mater.

12. V.N.Chernikov, A.P.Zakharov and A.A.Pisarev, Electron-microscopic investigation of defects in molybdenum irradiated with 15 keV D_2^+ ions, Izv.Akad. Nauk SSSR, Ser.Phys. 44 (1980) 1210 (in Russian).

13. I.A.Yurichev, Equation of state and thermodynamic properties of normal hydrogen within a temperature interval (200-700) K and over the pressure range (10-100) MPa, Teplofizika 17 (1979) 1187 (in Russian).

14. A.G.Zaluzhny, Yu.N.Sokursky and V.N.Tebus, Helium in Reactor Materials (Energoatomizdat, Moscow,1988) p.89 (in Russian).

15. H.Kawamura, E.Ishituka, A.Sagara, K.Kamada, H.Nakata, M.Saito and Y.Hutamura, Retention of deuterium implanted in hot-pressed beryllium, J.Nucl.Mater. 176&177 (1990) 661.

16. S.M.Myers and D.M.Follstaedt, Trapping of deuterium in oxygen-implanted aluminum, J.Nucl.Mater. 145-147 (1987) 322.

17. K.Kamada, A.Sagara, H.Kinoshita and H.Takahashi, Microstructural change and hydrogen behaviour in implanted metal, J.Nucl.Mater. 155-157 (1988) 427.

18. S.Z.Bockstein, Diffusion and Structure of Metals (Metallurgiya, Moscow, 1973) p.92 (in Russian).

19. A.E.Pontau, W.Bauer and R.W.Conn, He pumping in the presence of an H beam, J.Nucl.Mater. 93&94 (1980) 564.

20. P.Jung, Diffusion and retention of implanted helium in beryllium, J.Nucl.Mater. 202 (1993) 210.

21. A.E.Gorodetsky, A.P.Zakharov and V.N.Chernikov, Hydrogen trapping during swelling of steel, Atomnaya Energiya 61 (1986) 183 (in Russian).

22. V.N.Chernikov and H.Ullmaier, Helium porosity in near-surface layers of metals during post-implantation annealing - to be published.

23. R.A.Langley, Interaction of implanted deuterium and helium with beryllium: radiation enhanced oxidation, J.Nucl.Mater. 85&86 (1979) 1123.

Investigation of the Ion Beryllium Surface Interaction

M.I. Guseva[1], A.Yu. Birukov[1], V.M. Gureev[1], L.S. Daneljan[1], S.N. Korshunov[1], Yu.V. Martynenko[1], P.S. Moskovkin[1], Yu.A. Sokolov[1], V.G. Stoljarova[1], V.S. Kulikauskas[2], V.V. Zatekin[2]

[1]RRC "Kurchatov Institute" Kurchatov sq. 1, Moscow 12182, Russian Federation
[2]M.V. Lomonosov University Moscow, Russian Federation

The self-sputtering yield of the Be was measured. The energy dependence of the Be self-sputtering yield agrees well with that calculated by W. Eckstein et. al. Below 770 K the self-sputtering yield is temperature independent; at $T_{irr.} > 870$ K it increases sharply. Hot-pressed samples at 370 K were implanted with monoenergetic 5 keV hydrogen ions and with a stationary plasma (flux power ~ 5 MW/m^2). The investigation of hydrogen behavior in beryllium shows that at low doses hydrogen is solved, but at doses $\geq 5x10^{22}$ m^{-2} the bubbles and channels are formed. It results in hydrogen profile shift to the surface and decrease of its concentration. The sputtering results in further concentration decrease at doses $> 10^{25}$ m^{-2}.

1. Introduction

Beryllium has been considered as plasma facing material for the ITER, because its low atomic number, thermal, mechanical and nuclear properties are suitable. It is expected that the operation temperature range of the .first wall and diverter is (670-1070) K. In the ITER diverter physical sputtering is one of the factors limiting its lifetime. While experimental sputtering data bases exist for H^+, D^+ and He^+-ions, the self-sputtering yields of beryllium have only been estimated by computer simulation [1,2]. The other principal problem of the material selection for the ITER first wall and diverter plates is the tritium inventory in them. One should note that a great number of studies was done on the hydrogen isotope retention, diffusion, remission in the graphite materials, meanwhile the similar experimental data on beryllium are rather scarce and contradictive. According to a number of studies [3,4], the concentration of graphite implanted hydrogen is about 0.4 H/C, meanwhile the content of hydrogen in beryllium, according to the data by different authors, is essentially different: from (0.31-0.36) D/Be [5,6] to 1.4 D/Be [7].

In this work the experimental results on the energy and temperature dependence of beryllium self-sputtering yield and the results of the hydrogen distribution profile study at the ion energies 5-6 keV in beryllium under high irradiation fluences ($5x10^{22}$ m^{-2} - $1.5x10^{25}$ m^{-2}) of ion and plasma fluxes at the temperature of 370 K are presented.

2. Experimental technique

A commercial powder-compacted beryllium of TShP-type containing 98.7 wt.% - Be, 0.9 wt.% - O, 0.2 wt.% - Fe and 0.2 wt.% other metals, C and N was used in experiments. Before irradiation the Be sample surfaces were polished with diamond paste and then electrical polishing was used.

The irradiation of beryllium targets was performed in the chamber of a 180°- implanter. Be^+-ions were extracted from the plasma of the ion source and accelerated in the energy range of (0.5-10)

keV (without application of a breaking potential to the target area). The beryllium self-sputtering yields were obtained by the weighting technique. The microbalance sensitivity was 10^{-9}/kg. The temperature dependence of self-sputtering yield was investigated using 0.9 keV Be^+-ions in the temperature range from 470 K to 1070 K.

The beryllium samples were irradiated to 5 keV monoenergetic Hl- ions in 180°-implanter and high-power (5 MW/m^2) hydrogen stationary plasma in the SAPPHIRE facility. The temperature of the specimens was controlled by means of a thermocouple. The water cooling of the unirradiated side of the sample was provided and the sample temperature during plasma exposition was 370 K. The water expense was calculated and was equal 75 ml/s. The ion and plasma irradiation regimes of the beryllium samples are given in Table I.

The H^+-ion distribution profile studies were done by the methods of secondary ion mass-spectrometry (SIMS) at the "A-DIDA" - facility and by the elastic recoil technique (ERD). The depths of ion beam sputtered craters generated during an analysis were measured with a Sloan Instruments Dektak profilometer. In difference from the purely-surface SIMS-analysis (under which one needs a consequtive etching of layers by Ar^+- ions), the ERD technique is not destructive one, allowing one to register all nuclei located in the layer under the analysis thickness which determined by the stopping power of material and by the geometry of the experiment. In our experiments the analysing He^+-ion beam with the energy 2.2 MeV in the Van-de-Graaf accelerator was incident on the sample under study at the angle $\alpha = 15°$ to its surface, the recoil protons were registered with a semiconducting detector at the angle 30° to the initial direction of He^+-ions. The energy spectrum of hydrogen recoil nuclei was registered for finding the hydrogen ion distribution profile. In order to produce the absolute values of concentration the measurements with a standart calibration sample having uniformly-distributed hydrogen in it were done. A thin lavsan film having the structure $C_{10}H_8O_4$ was used as a reference unit. Computed spectra were fitted to each experimental grazing angle spectrum using a data processing program taking account of the energy resolution power of the method. After irradiation and after SIMS-analysis the samples were examined in a JEOL scanning electron microscope.

3. Experimental results and discussion

3.1. Investigation of energy dependence of beryllium self-sputtering yield

The energy dependence of beryllium self-sputtering yield at the target temperature of 670 K is shown in Fig. 1. The self-sputtering yield attains a maximal value ($S^s_{max} = 0.32 \pm 0.03$ at./ion) at the ion energy 1.5 keV, then it's monotonously reduced with the further energy rise. The computer simulation data for Be self-sputtering [1,2] are also shown in Fig. 1. Agreement between experimental and calculated data is quite good.

Fig. 2 shows the energy dependence of Be self -sputtering yield in comparison with that for graphite [8]. As seen in Fig. 2, in the all investigated energy range the self-sputtering yields for graphite are higher than for beryllium.

3.2. Investigation of the temperature dependence of beryllium self -sputtering yield

Fig. 3 illustrates the beryllium self -sputtering yield data in the temperature range from 370 K to 1070 K at ion energy 0.9 keV. As seen in Fig. 3 the self-sputtering yield is not changed up to 770

K. At the irradiation temperature $T_{irr} > 870$ K it sharply increases with the temperature rise attaining the value of 0.75 at./ion at 1070 K. The extrapolation of the curve $S = f(T)$ to the value of $S^s = 1$ at./ion shows that operating temperature $T \geq 1170$ K for Be first wall in the reactor is not safe. Comparing with corresponding data for self-sputtering of graphite shows that "carbon catastrophe" (S^s=1 at./ion) takes place at sufficiently higher temperature T - 1500 K due to the process of radiation enhanced sublimation of graphite.

Curve 2 in Fig. 3 is the calculated dependence $S^s = f(T)$ of Be self-sputtering yield from paper [8]. A comparison of the measured and calculated temperature dependence shows that the sharp increase of sputtering yield is observed at the temperature on 100 K lower in the case of experimental curve $S^s = f(T)$.

3.3. Hydrogen retention in beryllium

The experimental results obtained from the hydrogen distribution profile in beryllium by ERD and SIMS methods are summarized in Table II.

The hydrogen distribution profiles for the samples No. 1 and 2 are given in Fig. 4. A reduction in the integral concentration of implanted hydrogen (See, Table II) and a shift of the distribution profile towards the surface with the fluence growth are rather unexpected.

The similar effect of a reduction in the accumulated hydrogen and an effect of the hydrogen distribution profile shift towards the surface is observed under exposure of beryllium samples No. 3, 4, 5 within the stationary intense hydrogen plasma (Fig. 5) in plasma SAPPHIRE device.

Thus the received results allow one to conclude that the maximal amount of accumulated hydrogen in Be (3.6×10^{21} m^{-2}) is observed under the smallest fluence under study -5×10^{22} m^{-2} which is close to the hydrogen saturation fluence for the ions with the energy of 5 keV [6]. Hydrogen concentration of 16 at.% in the implanted layer is obtained and it is reduced to 4 at.% with the fluence growth to 1.5×10^{25} m^{-2}.

The comparison between the hydrogen distribution profile in the sample No. 2, measured by SIMS (curve 3), and by ERD (curve 2) is made in Fig. 4. As seen in Fig. 4 and in Table II, a noticeable difference in the absolute values of concentrations and in hydrogen atom distributions in depth produced by two different techniques is observed. According to the SIMS - measurements, the maximum hydrogen concentration of 1.25×10^{27} m^{-3} is 18.8 times lower and its integral concentration is about of 50 times lower than the results of the ERD-analysis (2.35×10^{28} m^{-3}) in the same sample (No. 2). For SIMS-method the distribution maximum (curve 3) is upon the surface, and the whole profile is essentially narrower than the distribution profile measured by the ERD-technique (curve 2).

Investigations of hydrogen profiles and the microstructure of beryllium surface after hydrogen ion implantation give us the following picture of hydrogen behavior in beryllium.

At low fluences hydrogen is dissolved in beryllium and diffuses in the target. It follows from the fact, that the profile width is sufficiently broader than the width of the profile calculated by TRIM code [9]. One can estimate hydrogen diffusion coefficient assuming

$$D = \Delta x^2/4t \qquad (1)$$

where Δx - $x_{1/2} - R_p$, $x_{1/2}$ is the depth at half width of profile, R_p is projected range of the ions, t is the time of diffusion. If we take t equal to irradiation time a fluence $\phi = 5 \times 10^{22}$ m^{-2} the diffusion

coefficient $D = 3x10^{-16}$ m^2/s.

The other estimate one can obtain if assume that the equilibrium between implantation and diffusion of hydrogen to the surface is established. Then D x grad (N) = j, where N is hydrogen concentration. Assuming grad (N) = N_{max}/R_P, one obtains

$$D = j \times R_P/N_{max} \qquad (2)$$

This estimate gives $D = 5x10^{-16}$ m^2/s. The both estimates are similar. But at high enough fluence the hydrogen bubbles are formed in the implantation layer, hydrogen atoms are trapped by the bubbles and do not diffuse out of the implantation layer. It can take place at fluence lower than $5x10^{22}$ m^{-2}, then time t in estimate (1) will be lower and the value of D higher. The both estimates coincide if one assumes that the profile broadening stops at fluence $3x10^{22}$ m^{-2}.

The same more lower diffusion coefficient follows from the experiment at low current density (0.25 A/m^2). Authors [10] observed that at fluence 10^{21} m^{-2} about 90% of implanted hydrogen is trapped within beryllium target whereas at $\phi = 10^{22}$ m^{-2} only 20% of it is trapped. We believe that at $\phi = 10^{21}$ m^{-2} there is not equilibrium between implantation and out-diffusion. This equilibrium is reached at $\phi=10^{22}$m^{-2}, when the diffusion front came to the surface. It means

$$D = R_P^2/4t \qquad (3)$$

Taking R_P = 105 nm, t ϕ/j = 670 s (in accordance with experiment [11], ion energy equals 10 keV), we obtain $D = 3.7x10^{-18}$ m^2/S.

Our estimates give the diffusion coefficient about three order of magnitude lower than that obtained from film penetrating [11]. It is a result of surface layer modification during the ion bombardment. We believe that many radiation defects created by ions work as virtual traps for hydrogen atoms and decrease their mobility.

At some fluence ϕ_1 the probability of hydrogen atom trapping by the bubble $4\pi DN_bR_b$ (N_b is bubble concentration, R_b is bubble radius) becomes equal to that of diffusion out of the implantation layer $D/\Delta R_P^2$. At that condition $47\pi N_bR_b\Delta R_P^2 = 1$ implanted hydrogen does not diffuse out of implantation layer, the profile broadening stops, hydrogen diffused previously beyond the implantation layer diffuses partly to the bubble and partly to the deeper layers and hydrogen concentration at the depth higher than $R_P+\Delta R_P$ decreases with fluence increase. The decrease of the hydrogen concentration at x = 100 nm (the maximum of mobile hydrogen is situated near 100 nm) is described by following

$$N(100\ nm,t) = N(100\ nm,0) \times (\Delta x^2/4Dt)^{1/2} \qquad (4)$$

One can estimate the diffusion coefficient from (4) comparing N(100nm) at fluences $\phi=5x10^{22}2$ m^{-2}-and $\phi=10^{23}2$ m^{-2}- $\Delta x=x_{1/2}$ -100nm. We obtain by this way $D = 2x10^{-16}$ m^2/S - the value of the diffusion coefficient in implanted layer. It means that the defects (virtual traps) also diffuse beyond the implanted layer.

The further fluence increase results in bubble growth and coalescence and so way channels are created. The channels give an additional way to release of hydrogen from the target. It gives the decrease of hydrogen concentration from $2.4x10^{28}$ m^{-3} at $\phi = 10^{23}$ m^{-2} to $1.6x10^{28}$ m^{-3} at $\phi = 2.3x10^{23}$ m^{-2}.

The following concentration decrease occurs at fluence $\phi = R_pN/S$ (N is the number of atoms in volume unit, S - sputtering yield), when the layer with the depth R_p is sputtered. Then continuous channels from the surface to depth about R_p are formed and hydrogen release is enhanced.

In case of the SIMS analysis, in the process of subsequent removal of layers by Ar^+ - ion sputtering the bubbles and channels reach the surface and hydrogen escapes. Fig. 6 illustrates the evolution of the microrelief of Be specimen (No.3, Table I) after hydrogen plasma exposure and subsequent SIMS analysis (Ar^+-ions sputtering). In according with depth distribution results (0.5-3) μm pores are observed on the surface. Comparison of the experimental data produced by SIMS and ERD - techniques allows also one to make the conclusion that about 95 at.% of the trapped hydrogen atoms is located within the bubbles and only 5 at.% of them - in a solution. The obtained results are in qualitative agreement with the data from [5] in accordance with which hydrogen two traps are observed in beryllium.

The hydrogen atom distribution profiles in Be (Sample No.2) are compared with those in graphite MPG-8 Type under the same irradiation conditions in Fig. 7. A more than 10 times lower concentration of hydrogen is retained in beryllium than in graphite. The maximum concentration reached is $5x10^{28}$ at/m^3 in graphite and $2.35x10^{28}$ at/m^3 in beryllium. Hydrogen depth profile characterized by very narrow subsurface depths. As noted above such an effect can be provided by the hydrogen out-diffusion from the Be surface layer. The ratio H/C = 0.4 and H/Be = 0.16. In principle, these results are also in an agreement with the data from [5].

3.3. Beryllium microstructure after ions and plasma irradiation.

The scanning electron micrographs of the surface of beryllium after exposition in plasma SAPPHIRE devices at different fluences are shown in Fig. 8. At the fluence of $2.3x10^{23}$ m^{-2} the plasma was etching grain boundaries (Fig. 8a). The grain diameter of the beryllium specimens is found to be 20-40 μm. Significant surface damage is observed after fluence $7.7x10^{23}$ m^{-2} (Fig. 8b). This twinning defects are distributed fairly uniform over the surfaces of the grain and grain boundaries of the specimens. At higher fluences ($1.2x10^{24}$ m^{-2}) cones are observed (Fig. 8c). With the further fluence increase up to $1.5x10^{25}$ m^{-2} the average cone size grows up to 10 μm in height. The cones have developed from small agglomerations of BeO on the surface. This results are in agreement with experiments by D. Mattox and D. Sharp [12].

Conclusions

1. The experimental energy dependence of beryllium self-sputtering yield for normal incidence is in a good agreement with Eckstein et. al. calculation [1].
2. Below 770 K the self-sputtering yield does not change and sharply increases at temperature above 870 K attaining the value of 1 at./ion at 1170 K.
3. The comparison of the hydrogen profiles measured by SIMS, ERD and calculated by using of TRIM code [7] shows as follows. At fluences $\phi < 5x10^{22}$ m^{-2} the hydrogen is dissolved in beryllium and can easy to diffuse. The diffusion coefficient $D = (4 \pm 1)x10^{-16}$ m^2/s. The hydrogen bubbles are formed at fluences $\phi > 5x10^{22}$ m^{-2}. The hydrogen is trapped at the bubbles and does not leave the implantation region with the thickness $R_p+\Delta R_p$, The hydrogen, previously diffused into the deeper layers, diffuses back to the bubbles and to the more deeper

layer. Hence the hydrogen concentration at $x>10^{-7}$m decreases. At the fluences $\phi>(2\div3)x10^{23}m^{-2}$ the bubbles join, form the channels, part of which has the exit to the surface. It results in the additional way of the hydrogen release and the hydrogen concentration decrease from $N = 2.35x10^{28}$ m^{-3} to $N = 1.6x10^{28}$ m^{-3}. At the fluences $\phi > 10^{25}$ m^{-2} the sputtered layer exceed the implantation depth, the continuous channels are formed through the implanted layer and hydrogen release increases. As a result the hydrogen concentration decreases down to $N = 8x10$ m^{-3}

References

[1] W. Eckstein, C. Garcia-Rosales, J. Roth, W. Ottenberger, "Sputtering Data", Max-Planck-Institut fur Plasmaphysik, Report IPP 9/82 (1983).

[21 G. Standenmaier, J. Roth, R. Behrisch et. al., "Trapping of deuterium implanted in carbon and silicon: a calibration for particle-energy measurements in the plasma boundary of TOKAMAKS" J. Nucl. Mater. 84 (1979) 149.

[3] B.L. Doyle et. al., J. Nucl. Mater. 103-104 (1981) 513.

[4] Report on the US-USSR Exchange 11.3 for 1990 Workshop on Advanced Plasma Facing Materials and Disruption Response Ed. by K.L. Wilson SAND 90-8252 (1990).

[5] W.R. Wampler, J. Nucl. Mater. 122-123 (1984) 1598.

[6] H. Kawamura et. al., "Retention of deuterium implanted in hot-pressed beryllium", J. Nucl. Mater. 176-177 (1990) 661.

[7] R.A. Langley, "Retention of hydrogen in beryllium"', J. Nucl. Mater. 85-86 (1979) 1123.

[8] J. Roth, "Erosion and impurity production of C and Be: a comparison", J. Nucl. Mater. 145-147 (1987) 87.

[9] J.F. Ziegler, J.P. Biersack, "The Stopping and Range of Ions in Solids" (Pergaman Press, New York, 1985).

[10]I.P. Chernov, Yu.P. Cherdanzev, V.G. Mironchik et. al. "Hydrogen behavior in beryllium", XXIV Mejnazionalnoe Soveshanie, M.V. Lomonosov University (1994).

[11]F. Reiter, K.S. Forcey, G. Gervasini, EUR 15217 EN.

[12]D.M. Mattox, D.J. Sharp, " Influence of surface morphology on low energy hydrogen ion erosion yields of beryllium", J. Nucl. Mater. 80 (1979) 115.

Figure captions

Fig. 1. Experimental (curve 1) and calculated (curve 2) [1] energy dependence of beryllium self-sputtering yield at temperature 670 K.

Fig. 2. Energy dependences of Be and C self-sputtering yields:
1 - experimental (•••) and calculated [1] data for beryllium
2 - experimental data [8] for carbon

Fig. 3. Experimental (1) and calculated (2) [8] temperature dependences of Be self-sputtering yield at ion energy 0.9 keV and 1 keV, respectively.

Fig. 4. ERD-distribution profiles of hydrogen in beryllium after H^+-ions implantation with the energy 5 keV at 370 K for two fluences (j = 2×10^{20} $m^{-2}s^{-1}$): 1 - 5×10^{22} m^{-2}; 2 - 10^{23} m^{-2};
3 - SIMS-depth distribution of hydrogen for fluence 10^{23} m^{-2},
4 - TRIM computer simulation for hydrogen in beryllium,
5 - TRIM computer simulation for vacantion in beryllium.

Fig. 5. Hydrogen depth distribution in Be after exposure in hydrogen plasma at 370 K under heat loading about 5 MW/m^2 at the fluences (j = 4×10^{21} $m^{-2}s^{-1}$):
1 - 2.3×10^{23} m^{-2}, 2 - 1.2×10^{24} m^{-2}, 3 - 1.5×10^{25} m^{-2}.

Fig. 6. Microstructure of Be surface (sample No 3) after plasma exposure and subsequent SIMS analysis (Ar^+-ions sputtering).

Fig. 7. Hydrogen depth distribution in Be (1) and in graphite (2) after ion implantation with the energy 5 keV at 370 K
($\phi = 10^{23}$ m^{-2}; j = 2×10^{20} m^{-2} s^{-1}).

Fig. 8. Microstructure of Be surface after irradiation by hydrogen plasma in SAPPHIRE device at different fluences:
a - $2.3\times10^{23}m^{-2}$, b - $7.7\times10^{23}m^{-2}$, c - $1.2\times10^{24}m^{-2}$,
d, e - $1.5\times10^{25}m^{-2}$.

Table I

Regimes of the beryllium samples irradiation with monoenergetic H^+- ion fluxes and high-power hydrogen stationary plasma

Sample, N	W, MW/m^2	E, KeV	J, $m^{-2}s^{-1}$	ϕ, m^{-2}	Remarks
1	0.15	5	1.8×10^{20}	5×10^{22}	Monoenergetic ion beam
2	0.15	5	- " -	10^{23}	Monoenergetic ion beam
3	4.8	6	4.8×10^{21}	2.3×10^{23}	Plasma
4	4.8	6	- " -	1.2×10^{24}	Plasma
5	4.8	6	- " -	1.5×10^{25}	Plasma

Table II

Experimental results obtained from the hydrogen distribution profile in beryllium by ERD and SIMS methods

Sample, N	Method of analysis	N, H/Be	N, at/m^2	$N_{max.}$ at/m^3	Remarks
1	ERD	0.16	3.6×10^{21}	2.2×10^{28}	monoenergetic ion beam
2	ERD	0.16	2.6×10^{21}	2.35×10^{28}	monoenergetic ion beam
2	SIMS	0.014	5.1×10^{19}	1.25×10^{27}	monoenergetic ion beam
3	ERD	0.09	2.2×10^{21}	1.6×10^{28}	plasma
4	ERD	0.09	1.7×10^{21}	1.6×10^{28}	plasma
5	ERD	0.04	1.2×10^{21}	8×10^{27}	plasma

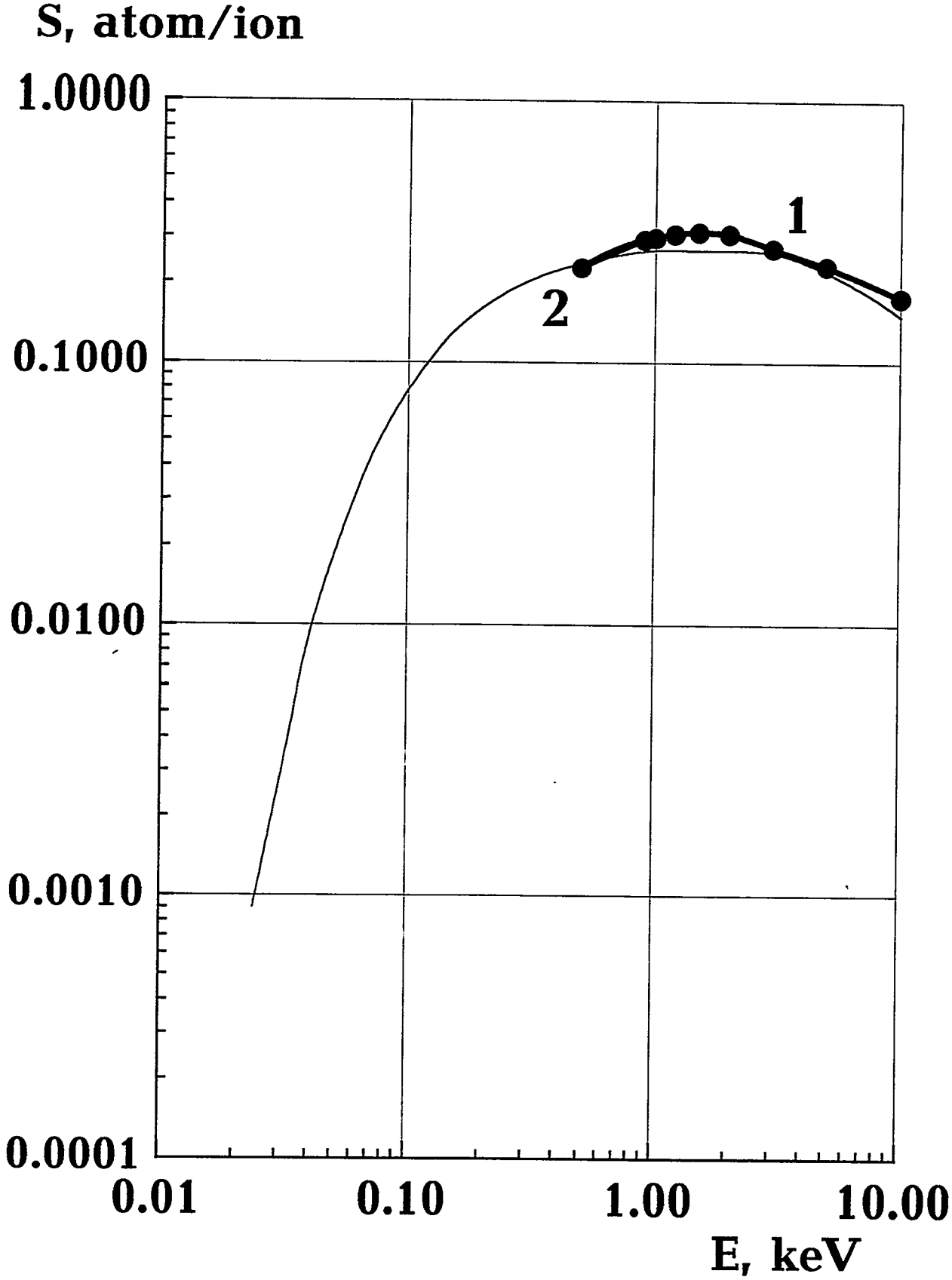
S, atom/ion
1.0000
0.1000
0.0100
0.0010
0.0001
0.01
0.10
1.00
10.00
E, keV
1
2

Fig. 1.

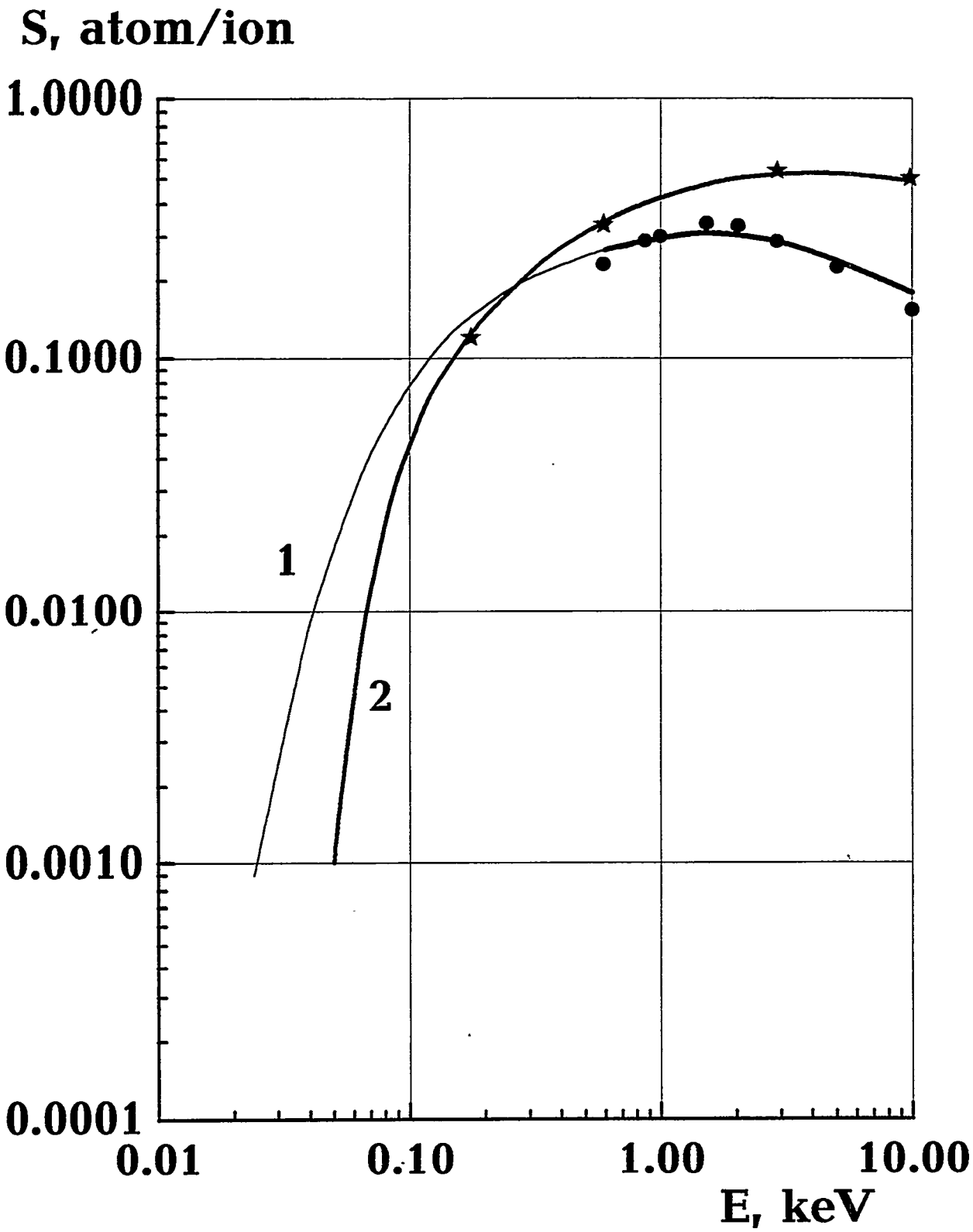
S, atom/ion
1.0000
0.1000
0.0100
0.0010
0.0001
0.01
0.10
1.00
10.00
E, keV
1
2

Fig. 2.

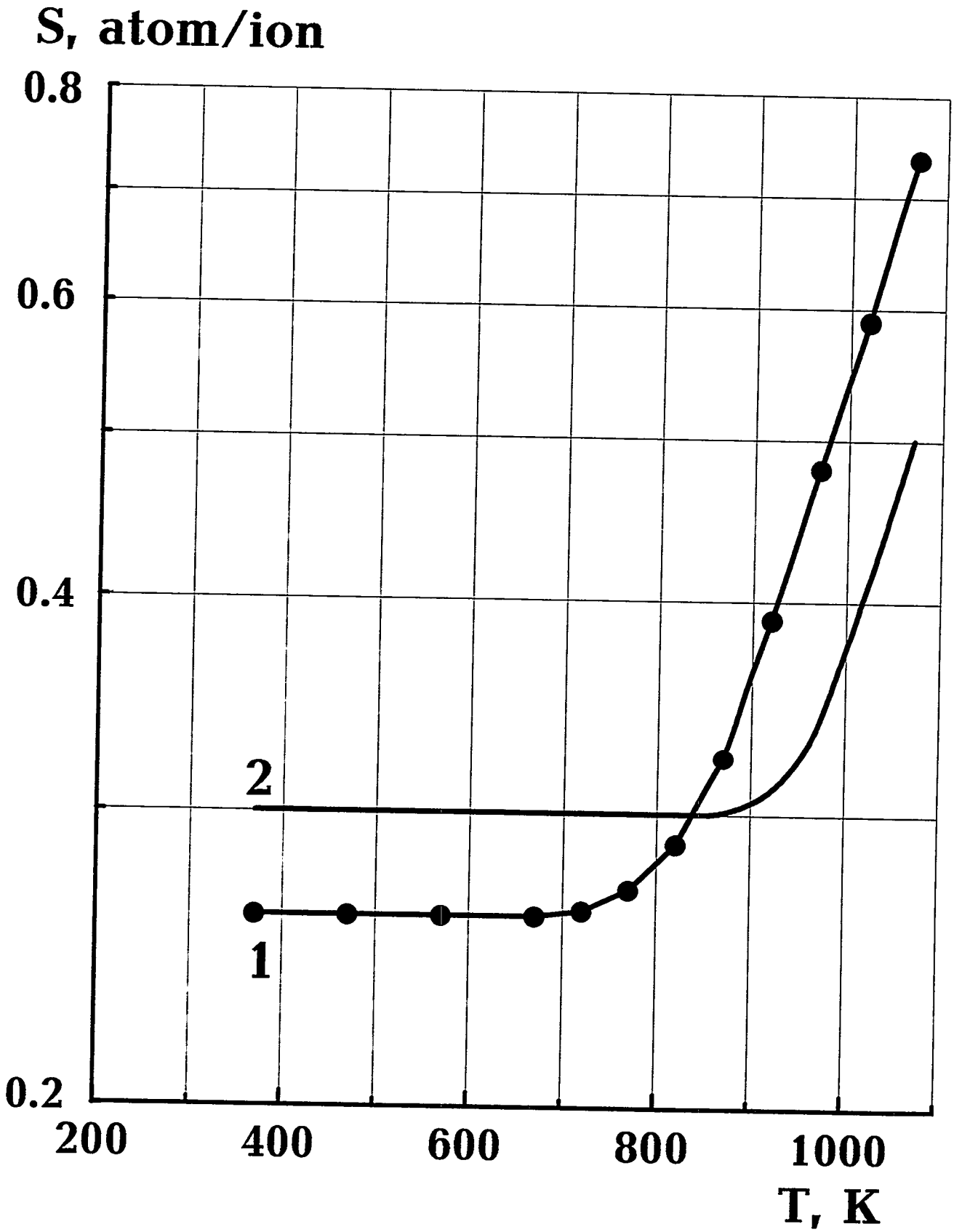

Fig. 3.

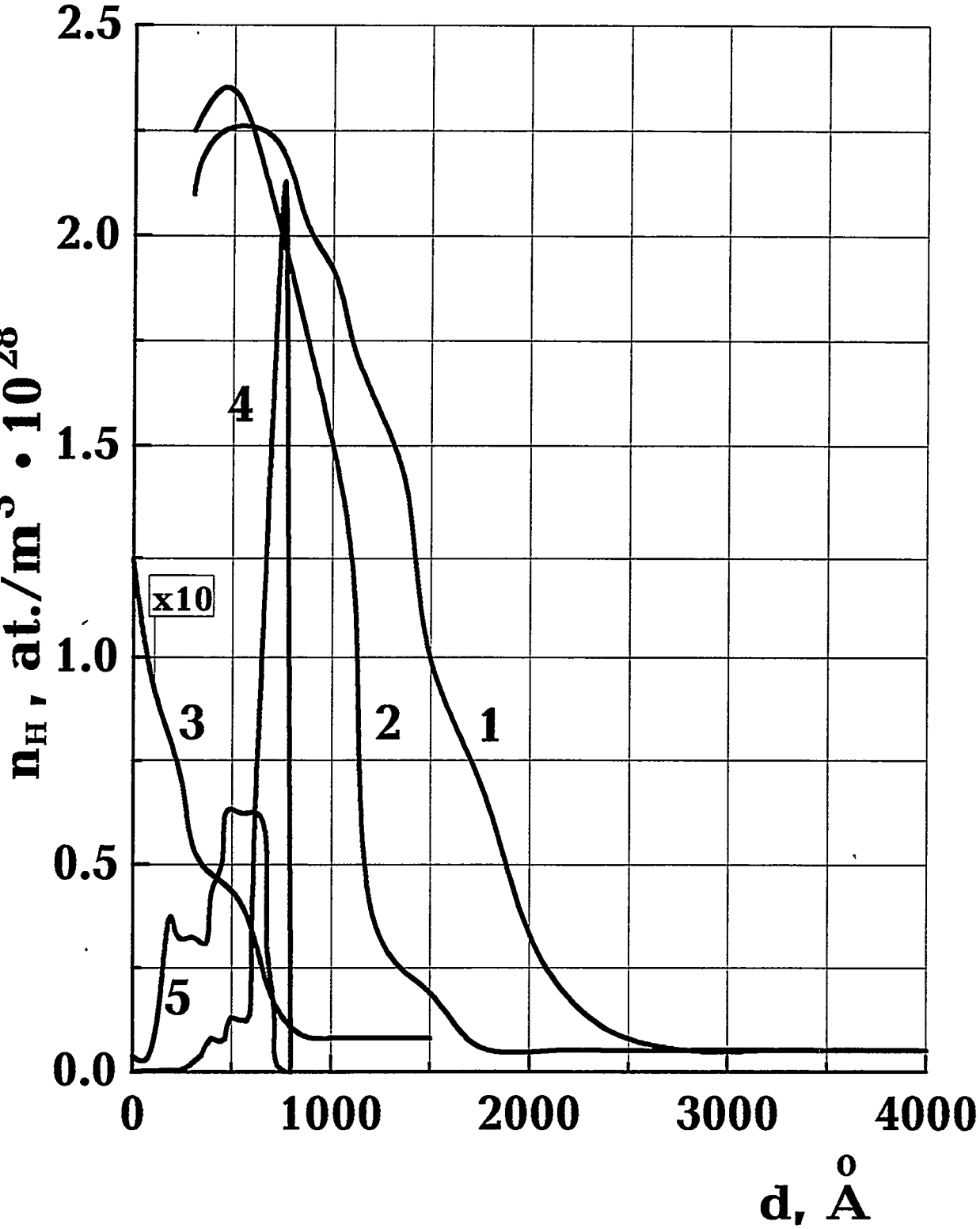

Fig. 4.

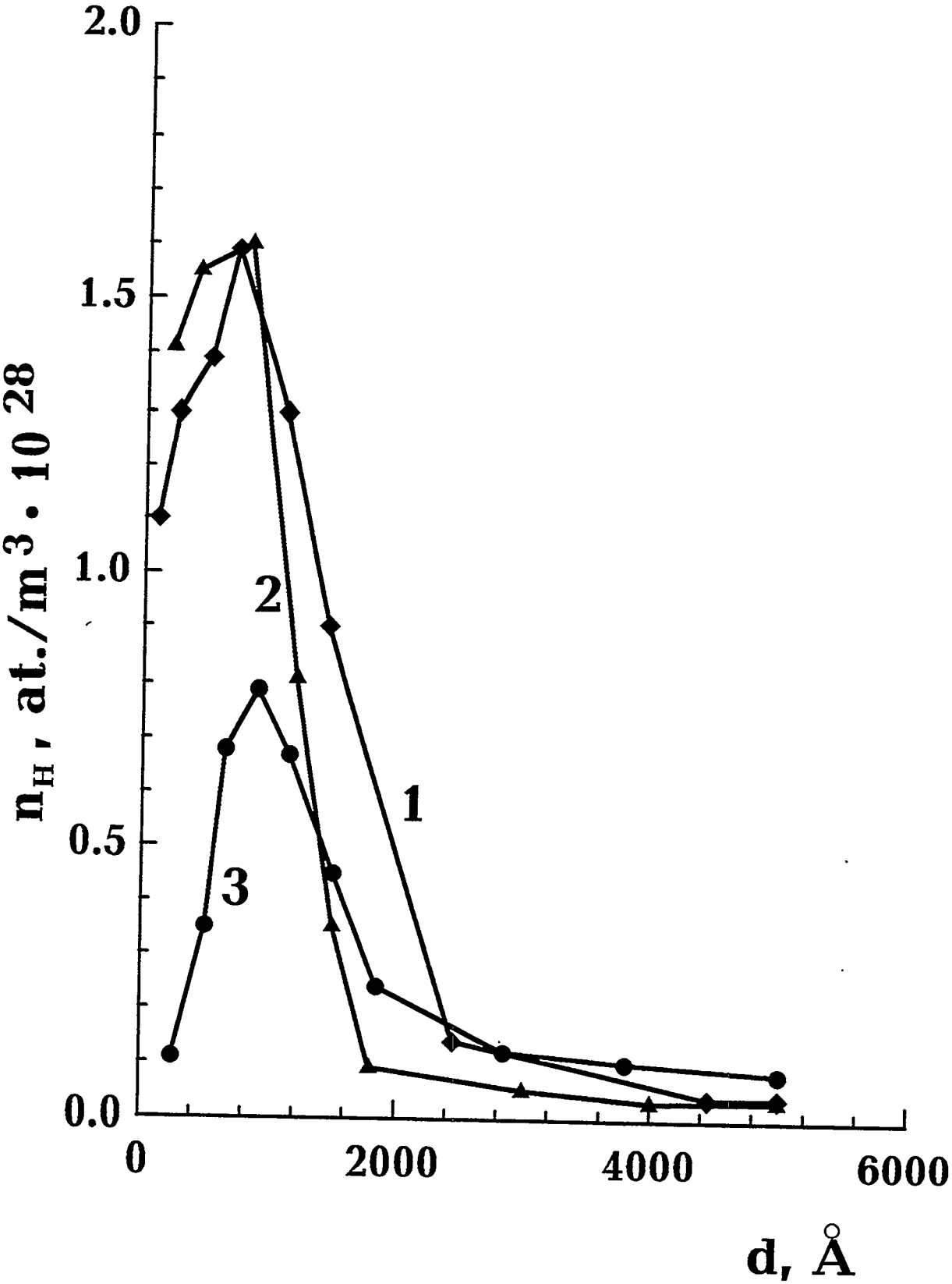

Fig. 5.

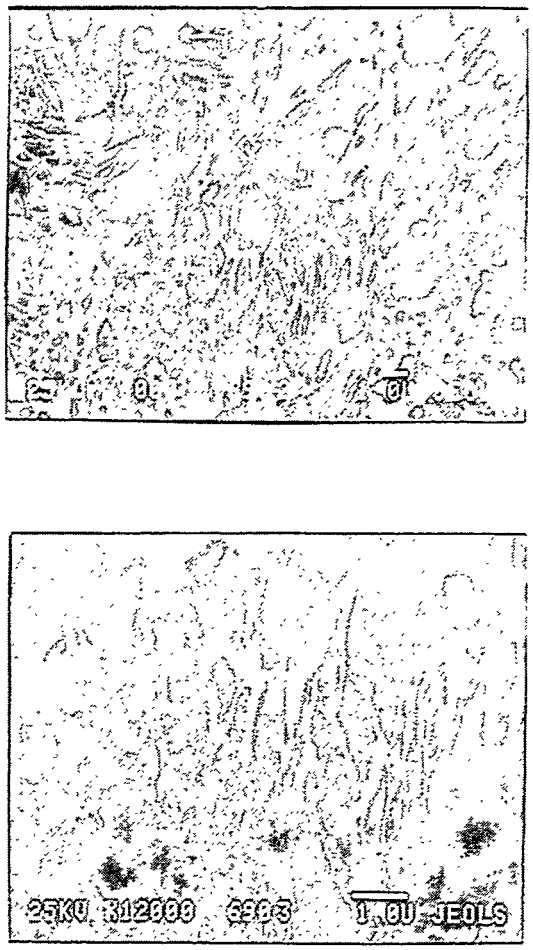

Fig. 6.

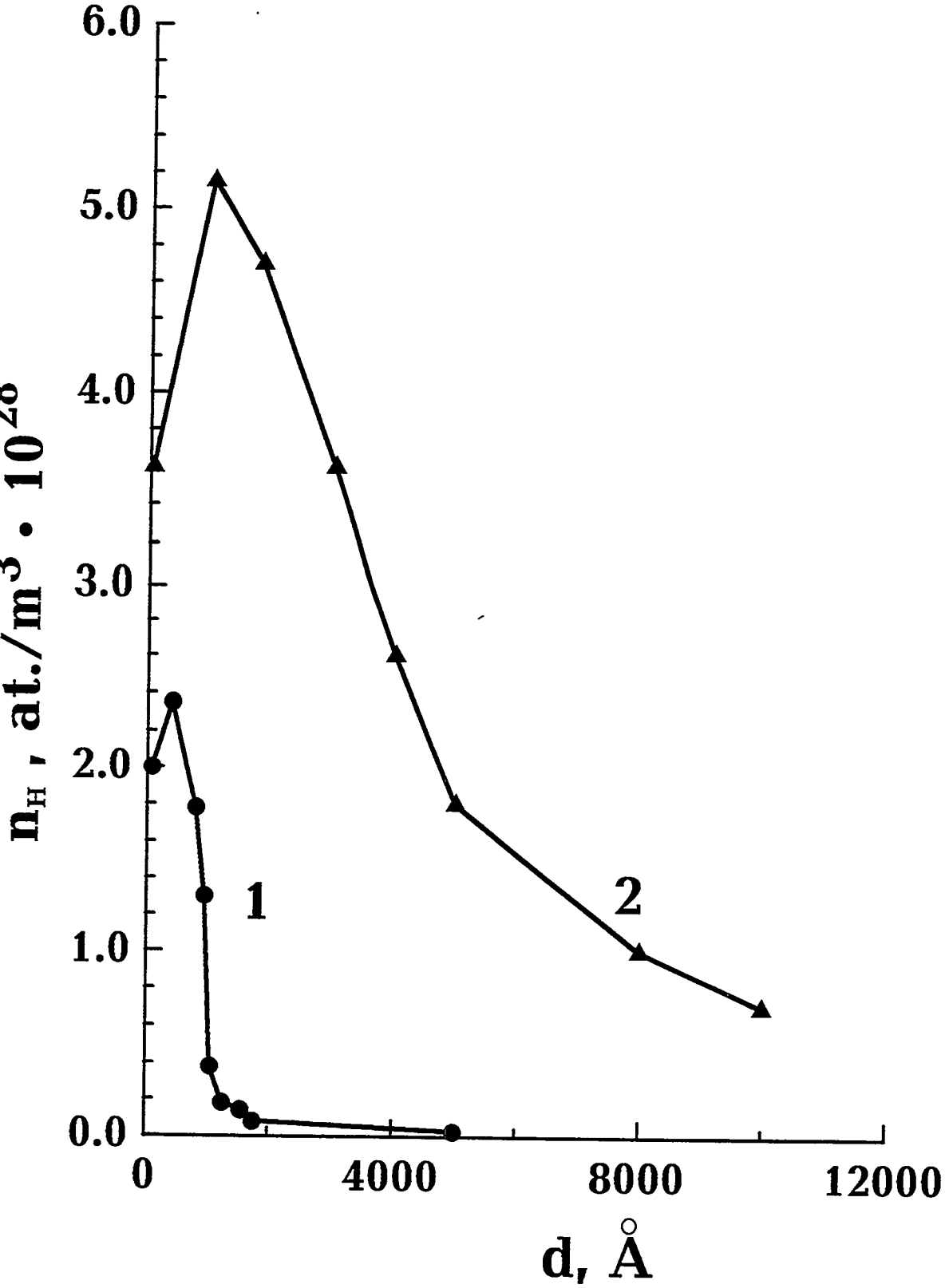

Fig. 7.

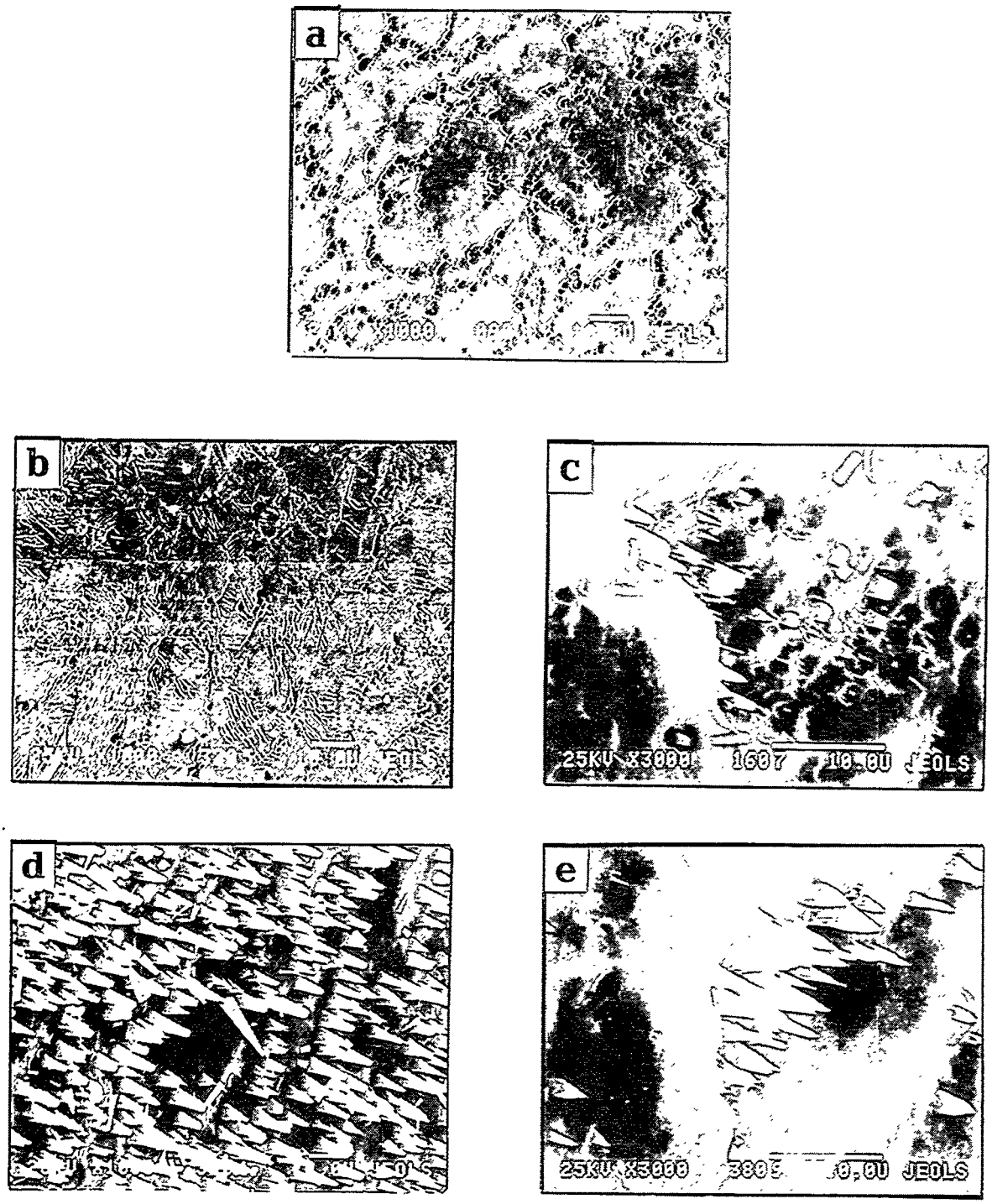

Fig. 8.

THERMAL DESORPTION OF DEUTERIUM IMPLANTED INTO BERYLLIUM*)

Andrey V.Markin, Vladimir N.Chernikov, Sergey Yu.Rybakov, Andrey P.Zakharov

Institute of Physical Chemistry of the Russian Academy of Sciences
Leninsky pr. 31, Moscow 117915, Russian Federation

Abstract

By means of TDS measurements it is shown that the desorption of deuterium from Be implanted with 5 keV D ions to fluences, Φ, from 1×10^{20} D/m^2 to 1×10^{21} D/m^2 proceeds in one high temperature stage B, while at $\Phi \geq 1.2\times10^{21}$D/m^2 one more stage A is added. The desorption maximum A is narrow and consists of two peaks A_1 and A_2 at about 460 K and 490 K, respectively. Peak A_1 is attributed to the desorption of deuterium from the walls of opened channels formed under D ion implantation. Peak A_2 is a consequence of the opening of a part of closed bubbles/channels to the outer surface. The position of maximum B shifts noticeably and nonsteadily on the fluence in a range from 850 to 1050 K. The origin of this maximum is the liberation of D atoms bound at vacancy complexes discussed previously by Wampler. The dependence of T_m(B) on the fluence is governed by the interaction of freely migrating D atoms with partly opened or fully closed gas cavity arrangements which are created under temperature ramping, but differently in specimens implanted with D ions to different fluences.

1. Introduction

Beryllium is considered as a candidate plasma-facing material and neutron multiplier for the ITER [1]. The interaction of beryllium with hydrogen is of great interest with regard to safety requirements and fuel balance. Some codes are available for estimations of tritium inventory in fusion reactor components, permeation into the coolant and ejection in case of accidents [2,3]. But, all the same, there is a lack of consistent data on hydrogen solubility, diffusion and interaction with defects which gives no grounds for reliable prognoses.

*) Work supported by the US DOE under Contract LC-8102 with SNLA

The most complete data on energetic of hydrogen trapping in Be have been derived from the experiments on the thermal desorption of implanted deuterium. In Ref.[4] it was shown by means of the nuclear reaction analysis method (NRA) that after irradiation up to a fluence $\Phi \approx 10^{20}$ D/m^2 the release of deuterium under conditions of isochronal annealing occurs in one stage at about 700 K. After irradiation to $\Phi > 10^{21}$ D/m^2 one more low temperature stage of the gas release appears around 400 K. Based on the analysis of these data it was deduced that two types of traps for D atoms, with detrapping energies, E^D, of 1 and 1.8 eV, are created in Be under D ion irradiation.

More recently, Wampler showed in [5] that the high-temperature stage of thermal desorption is due to deuterium detrapped out of vacancies, but only at low fluences of $\leq 2\times10^{19}$ D/m^2. At $\Phi \geq 2\times10^{20}$ D/m^2 D_2 bubbles were assumed to be developed in the ion stopping zone either under ion implantation or during post-implantation annealing. Subsequent to detrapping from vacancies D atoms were supposed to be recaptured by D_2 bubbles which could explain a shift of the maximum of the thermal desorption rate towards higher temperatures experimentally observed in [5].

Similar experimental results were obtained in [6] when investigating D ion implanted Be by means of the thermal desorption spectroscopy (TDS). It was noted that at $\Phi \approx 6\times10^{20}$ D/m^2 the position of the high temperature desorption maximum depended on the irradiation temperature. A low-temperature stage of deuterium release appearing at high fluences was related in [6] to the detrapping of implanted deuterium from inner surfaces formed, presumably, as a result of small bubble interconnection. On the other hand, as it has been shown in [7] making use of elastic recoil detection technique (ERD), the low-temperature thermal desorption stage was not observed at all provided that specimens implanted up to $\Phi = 2.8\times10^{22}$ D/m^2 were simply exposed in vacuum for 14 hours at 300 K. Concentration profiles of deuterium remaining in these specimens next to such an exposure and those in similar specimens subjected to the annealing at 420 K for 2 min just after irradiation were practically identical. By the authors' opinion, a part of deuterium implanted at 300 K remained mobile and did not interact with any trapping sites.

Having in view to get a more clear understanding of the nature of traps retaining deuterium in Beryllium we have carried out TDS measurements on Be implanted with 5 keV D ions within a range from 1×10^{20} to 4×10^{21} D/m^2. Fine structure of the thermal desorption maximum around 400 K was of special concern. Thermal desorption (TD) spectra related to D ion implanted Be were compared with those related to Be implanted with helium ions. Changes in the microstructure resulted from D ion implantation and post-implantation annealing of Be were monitored by transmission and scanning electron microscope (TEM and SEM) methods.

2. Experimental

Beryllium grade TIP-30 manufactured by hot isostatic pressing with 2.2 wt.% of BeO was used. The samples were plates polished mechanically and electrochemically and annealed in vacuum of 10^{-5} Pa at 1100 K for 3 min. Making use of electron probe microanalysis it was shown that the thickness of the oxide layer on the surface of such specimens was (4-6) nm and did not increase significantly during further implantation and heating.

Implantation with 5 keV D ions and subsequent TDS measurements were carried out in a special UHV system with a background pressure of 10^{-6} Pa. The ion flux in the beam hitting the specimen surface within the limits of the spot of 1 mm in diameter was $(1\text{-}3)\times10^{18}$ D/m^{2}s. New areas on the surface of a plate-specimen were chosen for different implantation-heating runs. Temperature ramping with the heating rate of 4 K/s was achieved by electron bombardment. For the temperature registration and regulation a Pt-Rh thermocouple spot-welded to Be plate-samples was used. The gas release during heating was monitored by a calibrated quadrupole mass-spectrometer.

The investigation of microstructure in the near-surface layers was performed by means of TEM using a set of TIP-30 Be specimens subjected to implantations and annealings under relevant conditions. Specimens were examined in EM 400T electron microscope operated at 120 kV. For more details the reader is refered to [8]. The surface morphology was studied optically and by SEM.

3. Experimental results

TD spectra of deuterium from Be implanted with 5 keV D ions up to fluences, Φ , from 1×10^{20} to 4×10^{21}D/m^2 are shown in Fig.1. At low fluences ($\Phi \leq 1\times10^{21}$ D/m^2) deuterium escapes from Be in a high temperature, broad desorption maximum B. When increasing Φ from 1×10^{20} to 1×10^{21} D/m^2 the position of this peak, T_m(B), shifts from about 850 K to 1050 K, while under further fluence increase T_m(B) decreases gradually.

At high fluences ($\Phi \geq 2\times10^{21}$ D/m^2) new narrow desorption maximum, A appears at $T_m \cong$ 470 K. The latter consists, in fact, of two peaks A_1 and A_2 at $T_m(A_1)\cong$460 K and $T_m \cong$ 490 K, respectively (Fig.1). The above positions of peaks $A_{1,2}$ along the temperature axis do not depend while their amplitudes depend remarkably on irradiation temperature and fluence (Fig.2). The total population of A is of 7×10^{16} D/m^2 at $\Phi=2\times10^{21}$ D/m^2 and of 1×10^{21} D/m^2 when Φ is doubled. In contrast to [7] both the shape and the amplitude of peaks $A_{1,2}$ are the same in specimens investigated both just after implantation and after post-implantation exposure at a room temperature for as long as 20 hs (before TDS measurements).

As it was shown by SEM, a smooth surface of specimens implanted up to $\Phi=(1\text{-}3)\times10^{20}$ D/m^2 remained unchanged after heating up to 1100 K. In case of specimens implanted up to $\Phi \geq 1\times10^{21}$ D/m^2 their further heating to ≥900 K resulted in the appearance on their surface of small dark holes of (0.1-0.3) μm in size. D ion implantation at 300 K to $\Phi \geq 2\times10^{21}$ D/m^2 led to blistering with blister diameters in a range (0.6-1.5) μm.

Specimens implanted with 3 keV D ions up to 3×10^{21} D/m^2 were analyzed in TEM before and after post-implantation annealing at 440 K for 10 min [8]. It was shown that the ion implantation alone led to the formation of tiny D_2 bubbles ($r_b \approx 1.1$ nm; $c_b \geq 3\times10^{24}$ m^{-3}) which were, even though in part, interconnected, forming narrow channels. Bubbles and channels with the same parameters and similar channels were also found in implanted specimens after annealing at 440 K.

TD spectra of helium from Be implanted with 8 keV He ions up to fluences in a range from 1×10^{20} to 4×10^{21} D/m^2 are shown in Fig.3. Helium desorption is absent after implantation to 1×10^{20} D/m^2 in the whole range of annealing temperature (up to 1100 K). In specimens implanted

up to $\Phi = 1\times10^{21}$ D/m^2 it originates only at > 900 K. At $\Phi \geq 2\times10^{21}$ D/m^2 TD spectra consist of two broad maxima. The population of the first maximum, around 420 K, is about 5 %. Starting from 680 K to 1100 K about 50 % of implanted helium escapes in the second desorption stage, while the another 50 % is shared between a fraction which is reemitted and that remains in the specimen.

It's appropriate to note that the changes in the surface morphology of Be specimens implanted with He ions due to post-implantation temperature ramping are similar to those described for specimens implanted with D ions.

4. Discussion

In general two stages of deuterium release from the D ion implanted Be observed in the present study are in agreement with both TDS data of Möller et al. [6] and data reported by Wampler in [4]. We have succeeded in showing that the low temperature desorption maximum A consists, actually, of two narrow peaks A_1 and A_2 and followed their evolution with Φ and T_{irr}. Below, making use of our TEM/SEM data and recent results on the microstructure of D implanted Be reported in [8], we discuss changes in the shape and position of both main desorption maxima A and B.

Let us note that differences in the values of desorption temperatures $T_m(A_1)$ and $T_m(B)$ cited in [4-8] and the present work are explained by using different annealing procedures.

4.1. Desorption maximum A

The comparison of the microstructure of Be specimens implanted with 3 keV D ions up to $\Phi = 3\times10^{21}$ D/m^2 before and after post-implantation annealing at 440 K for 10 min shows that this annealing does not introduce any new defects noticeable by TEM and does not alter the appearance of existing bubbles/channels. In [8] it was taken as an argument to consider the escape of deuterium in the desorption maximum A as D_2 desorption from the walls of a network channels opened to the outer surface. In the following, based on our precise TDS data, we show that after

implantation to fluences in a range from 1×10^{21} to $\geq4\times10^{21}$ D/m^2, where splitting of the maximum A occurs, the above assumption made in [8] is not quite exhaustive.

4.1.1. Peak A_2

The fluence $\Phi = 1.2\times10^{21}$ D/m^2 at which peak A_2 (right shoulder of maximum A) appears first (Fig.2b) correlates well with a fluence at which, according to [8], a zone of interconnected but still closed gas bubbles (that is inner channels) originates within the ion stopping range. It is appropriate to note that under similar irradiation conditions up to the above fluence the authors of [6] did not register any signs of deuterium reemission. Let us remind that the onset of reemission is attributed to the opening (rupture) of pressurized D_2 bubbles/channels due to their further development under ion irradiation as a result of a successive pressure increase therein which leads, eventually, to their interaction with the outer surface [8]. Obviously, bubble/closed channel arrangements in Be implanted at 300 K to $\Phi = 1.2\times10^{21}$ D/m^2 are on the verge of their mechanical stability. Under conditions of a subsequent temperature ramping this stability can be failed (through partial opening of those defects to the surface) followed by some gas evolution in the peak A_2. So, in a way, a medium heating of an implanted Be specimen is equivalent to an additional D ion implantation at a lower temperature. The interchangeability (in certain limits) of fluence and post-implantation heat treatment is not surprising when dealing with inert gases. In [9] it was noted in relation to He bubble development within the He ion stopping range of f.c.c. Cu and Ni.

Near equilibrium D_2 filled bubbles with the mean radius, r_b, of 1 nm produced in Be by D ion implantation at 300 K are characterized by the inner pressure of 6 GPa [8]. The heating up to about 500 K will lead, according to EOS for H_2 [10], to the increase of the gas pressure therein by as low as some percent. It's doubtful that such a pressure rise could be the main reason of the opening of gas-filled bubbles when reaching a temperature $T_m(A_2) \leq 500$ K. To our mind, the conclusion made in [5] on the absence of D atoms chemisorbed onto walls of D_2 bubbles in Be seems to be not quite correct. Actually, the process of deuterium bubble development includes a non-equilibrium stage of D atom expulsion from the matrix onto the wall surface of a gas bubble.

Having in mind the value of the experimentally measured desorption temperature, T_d, of H_2 from a clean Be surface which is about 450 K [11], one cannot exclude the presence of chemisorbed D atoms onto the walls of gas cavities in question. The existence of chemisorbed D atoms is in accord with the fact that a considerable concentration of separate D atoms is always available within the ion stopping zone of D ion implanted Be [8]. Thus, one more source of the pressure rise inside D_2 bubbles due to heating up to $T \geq T_d$ and, namely, deuterium desorbing from the bubble walls has to be considered. With taking it into account a rough estimation related to the same D_2 bubbles (r_b = 1 nm) under the same heating conditions shows that the pressure increase therein will be of tens percent, which seems to be enough for bubble opening.

The independence of $T_m(A_2)$ on both Φ and T_{irr} (Fig.2), in other words, a strict difference between $T_m(A_2)$ and T_d equal to (40-50) K makes us sure that the desorption of deuterium from the bubble/closed channel walls during temperature ramping is a main reason for the subsequent bubble/channel rupture followed by a partial deuterium escape in the peak A_2. Obviously, corresponding changes in the microstructure are very small, and only the application of special TEM techniques can make them visible.

4.1.2. Peak A_1

An excellent correlation between $T_d \cong 450$ K [11] and $T_m(A_1) \cong 460$ K (Fig.1,2) together with our data on the microstructure of D ion implanted Be both before and after annealing at 440 K lead to an obvious conclusion on the nature of the peak A_1. It relates to the direct desorption of deuterium into vacuum from the walls of bubbles and channels which have been opened in the course of the preceding ion implantation.

The ratio of the peak A_1 population to that of peak A_2 (P_1/P_2) grows rapidly with the fluence (Figs.1,2). It says that under ion implantation in a relevant fluence range the degree of bubble and channel interconnection increases considerably, creating within the ion stopping range a dense network of fine open paths which provide for a growing reemission rate and are characterized by a large surface area suitable for adsorption of a large amount of D atoms expelled from the matrix of Be.

The fact that under the increase of the irradiation temperature from 360 K to 440 K at constant $\Phi = 2\times10^{21}$ D/m^2 the ratio P_1/P_2 decreases to zero says *apriori* that D ion implantation at 440 K does not create open cavity arrangements, while forming closed gas-filled cavities which get opened because of the pressure rise at about $T_m(A_2)$ (see p.4.1.1). TEM data in [8] on the appearance and depth distribution of D_2 cavities in Be implanted with D ions at 500 K are in favor of this proposal.

With regard to deuterium escape from Be at 300 K [7] (see Introduction) one has to emphasize that in the present work we failed to reproduce it. It seems to be natural. Using the frequency factor in the equation for the desorption rate from [11] one can show that chemisorbed deuterium remains on the surface of Be for as long as more than about one month. A possible explanation of a result reported in [7] is isotope exchange of chemisorbed deuterium with water vapor as a major component of vacuum vessel atmosphere.

4.1.3. Comparison of deuterium and helium desorption spectra

As it was noticed in [8], parameters of D_2 bubbles and conditions of their appearance in Be at 300 K are very reminiscent to those of He bubbles. In the frames of the present work the TD spectra of implanted He were shown to resemble those of implanted deuterium (Fig.3). In more detail helium desorption spectra will be discussed elsewhere. For the present, let us note only that the nature of the first low temperature desorption maximum of helium seems to be the same as that of the deuterium desorption maximum A. If so, the absence of any splitting of it looks quite natural in the absence of adsorption of inert gases onto the metal surface. Then further, with a high degree of confidence the first helium desorption maximum can be considered as an analog of the peak A_2 in TD spectra of deuterium.

4.2. Desorption maximum B

Wampler in [5] and Chernikov et al. in [8] have brought (weighty) argument(s) that the desorption maximum of deuterium from D ion implanted Be at $T_m(B)$ around 900 K was attributed to the dissociation of vacancy clusters incorporating D atoms. It means that at $T \geq 900$ K the

concentration of free D atoms in Be matrix increases considerably. But the outgassing of a specimen is retarded due to recapturing of migrating D atoms by D_2 bubbles, from which deuterium has to redissolute before escaping out of the sample. The latter process depends on the gas pressure inside bubbles or their mean size provided the pressure in these bubbles is equilibrated by the surface tension. It means that at given temperature capturing is stronger in larger bubbles.

So, the position of maximum B, $T_m(B)$, is determined by the volume density of gas-filled cavities, their size and the integrity of the cavity containing layer adjacent to the surface. According to conclusion made in Ref.[8] the formation of D_2 bubbles which appears at $\Phi = (1\text{-}2) \times 10^{20}$ D/m^2 is very reminiscent of the formation of the He bubbles in Be. On the other hand, the volume density of helium bubbles which are formed in metals during post-implantation annealing is proportional to the implanted gas content [12]. With taking these remarks into account one can suggest the following explanations to the shifts of $T_m(B)$ as a function of the fluence.

The increase of the fluence in the interval $1\times10^{20} \le \Phi < 1\times10^{21}$ D/m^2 leads under the temperature ramping to the increase of both the volume density of D_2 bubbles and their mean radius (the latter implies a pressure decrease therein). It is clear also that the coarsening of bubbles during heating will proceed more intensive in specimens irradiated to higher fluences compared to those irradiated to lower ones. At the same time it will not cause yet any disintegrations in the surface layer. All this can explain the shift of $T_m(B)$ from 850 up to $\approx$1050 K in the fluence range considered (Fig.1).

At $\Phi \ge 1\times10^{21}$ D/m^2 channels extending to the outer surface and their further gradual coarsening under temperature ramping open the additional way for the outgassing of implanted specimens. Besides, such an evolution of the near surface microstructure is accompanied by the build up of new opened surfaces suitable for the recombination of D atoms which additionally accelerates the desorption D_2 molecules into vacuum. The resulting disintegrations can not be cured under heating which is evident from our SEM data (dark holes). Obviously, the higher the fluence the higher is the degree of disintegrations in the near surface layers. The latter seems to be

the main reason for the shift $T_m(B)$ to lower temperatures with the fluence increase in a range $\Phi \geq 1\times10^{21}$ D/m^2.

Möller et al. [6] studying Be specimens implanted with 1 keV D ions up to $\Phi < 1\times10^{21}$D/m^2 at T_{irr} = 300, 520 and 720 K have shown that the desorption of implanted deuterium from them occurs in one stage at $T_m(B)$ in a range from 680 to 850 K increasing with the increase of T_{irr}. The presence of only one desorption maximum results from a relatively low fluence and, eventually, manifests the absence of the open porosity. The growth of $T_m(B)$ with T_{irr} is related to both the different appearance of corresponding arrangements of closed cavities in specimens considered [8], and decreasing amounts of gas accumulated in them at higher T_{irr} due to progressing reemission [6].

5. Summary

1. Thermal desorption of deuterium from Be implanted with 5 keV D ions proceeds in one stage at fluences, Φ, from 1×10^{20} D/m^2 to 1×10^{21} D/m^2 and in two stages at $\Phi \geq 1.2\times10^{21}$ D/m^2.

2. The low temperature desorption maximum A is relatively narrow and consists of two peaks A_1 and A_2 at $T_m(A_1) \cong 460$ K and $T_m(A_2) \cong 490$ K, respectively. Their positions along the temperature axis do not depend, while their amplitude depend remarkably on irradiation temperature and ion fluence.

3. The high temperature desorption maximum, B, shifts noticeably and nonsteadily on the fluence in a range from 850 to 1050 K.

4. It was shown that, the largest at high fluences, peak A_1 is attributed to the desorption of deuterium from the walls of the dense network of thin and opened channels. An additional peak A_2 originates as a consequence of uncovering of closed bubbles/channels in the very vicinity of the outer surface and/or into the volume of neiboughring channels opened to the surface. The driving force of this process seems to be the pressure rise inside closed microvolumes due to deuterium desorption from their walls occurring at $T_m(A_2) > T_d \cong 450$ K (the desorption temperature of deuterium from Be surface [11]).

5. The origin of desorption maximum B at $T_m(B)$ = (950±50) K is the liberation of D atoms bound at lower temperatures at immobile and stable vacancy complexes proposed by Wampler in [5]. Shift of $T_m(B)$ versus fluence to higher temperatures is due to the retarding of freely migrating in the matrix D atoms within the volume of closed cavities which are transformed at temperature ramping differently in specimens implanted with D ions to different fluences. The development of disintegrations in the near-surface layers under further fluence increase is a main reason for the reverse shift of $T_m(B)$.

Acknowledgment

The authors are very grateful to Dr. A.E.Gorodetsky and Dr. S.L.Kanashenko for valuable discussions.

References

1. ITER Conceptual Design, Interim Report, IAEA/ITER/DS/7 (IAEA, Vienna, 1990).

2. G.R.Longhurst, D.F.Holland, J.L.Jones, and B.J.Merrill, "TMAP4 User's Manual", EGG-FSP-10315, INEL(June 12,1992).

3. M.Dalle Donne, F.Scaffidi-Argentina, C.Ferrero, C.Ronchi, Modelling of swelling and tritium release in irradiated beryllium, J.Nucl.Mater. 212-215 (1994) 954.

4. W.R.Wampler, Retention and thermal release of deuterium implanted in beryllium, J.Nucl.Mater. 122&123 (1984) 1598.

5. W.R.Wampler, Trapping of deuterium in beryllium, J.Nucl.Mater. 196-198 (1992) 981.

6. W.Möller, B.M.U.Scherzer and J.Bohdansky, Retention and release of deuterium implanted into beryllium, IPP-JET Report No.26 (1986).

7. H.Kawamura, E.Ishituka, A.Sagara, K.Kamada, H.Nakata, M.Saito and Y.Hutamura, Retention of deuterium implanted in hot-pressed beryllium, J.Nucl.Mater. 176&177 (1990) 661.

8. V.N.Chernikov, V.Kh.Alimov, A.V.Markin and A.P.Zakharov, Gas swelling and related phenomena in beryllium implanted with deuterium ions, J.Nucl.Mater. to be published.

9. V.N.Chernikov and H.Ullmaier, Helium porosity in near-surface layers of metals during post-implantation annealing - to be published.

10. I.A.Yurichev, Equation of state and thermodynamic properties of normal hydrogen within a temperature interval (200-700) K and over the pressure range (10-100) MPa, Teplofizika 17 (1979) 1187 (in Russian).

11. V.Lossev and J.Küppers, Interaction of hydrogen atoms with beryllium (0001) surfaces, J.Nucl.Mater. 196-198 (1992) 953.

12. H.Ullmaier, Helium in metals, in: Landolt-Börnstein, vol.III/25, Atomic Defect in Metals (Springer-Verlag, Berlin, 1991) p.400.

Figure captions

Fig.1. Thermal desorption spectra of deuterium from TIP-30 Be implanted with 5 keV D ions at 300 K.

Fig.2. Fine structure of low temperature desorption maximum vs irradiation temperature, T_{irr}, and ion fluence, Φ.

Fig.3. Thermal desorption spectra of helium from TIP-30 Be implanted with 8 keV He ions at 300 K.

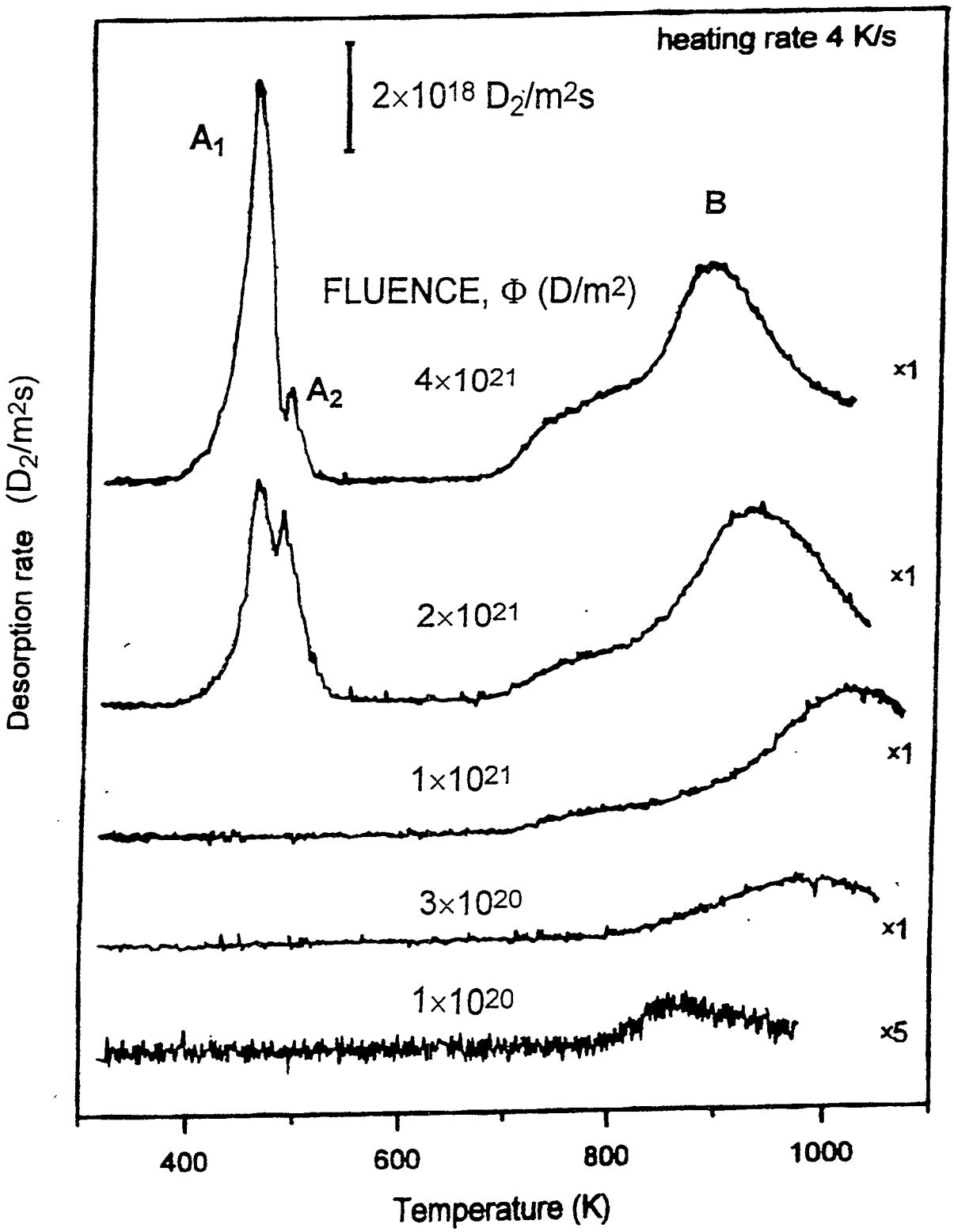
heating rate 4 K/s
2×10^18 D2/m2s
A1
A2
B
FLUENCE, Φ (D/m2)
4×10^21
2×10^21
1×10^21
3×10^20
1×10^20
x1
x1
x1
x1
x5
Desorption rate (D2/m2s)
400
600
800
1000
Temperature (K)

Figure 1

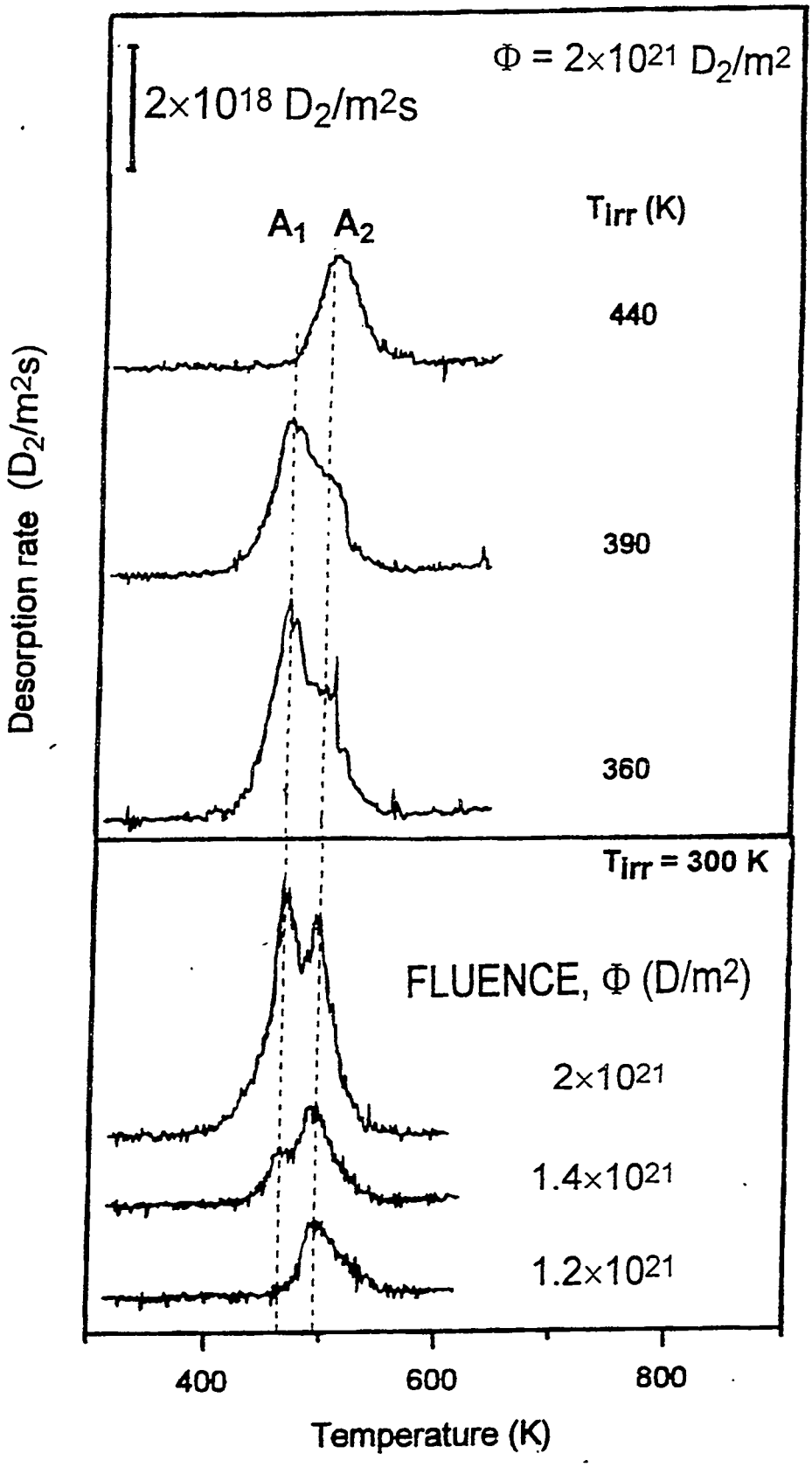
Φ = 2×10^21 D2/m2
2×10^18 D2/m2s
A1 A2
Tirr (K)
440
390
360
Tirr = 300 K
FLUENCE, Φ (D/m2)
2×10^21
1.4×10^21
1.2×10^21
Desorption rate (D2/m2s)
400
600
800
Temperature (K)

Figure 2

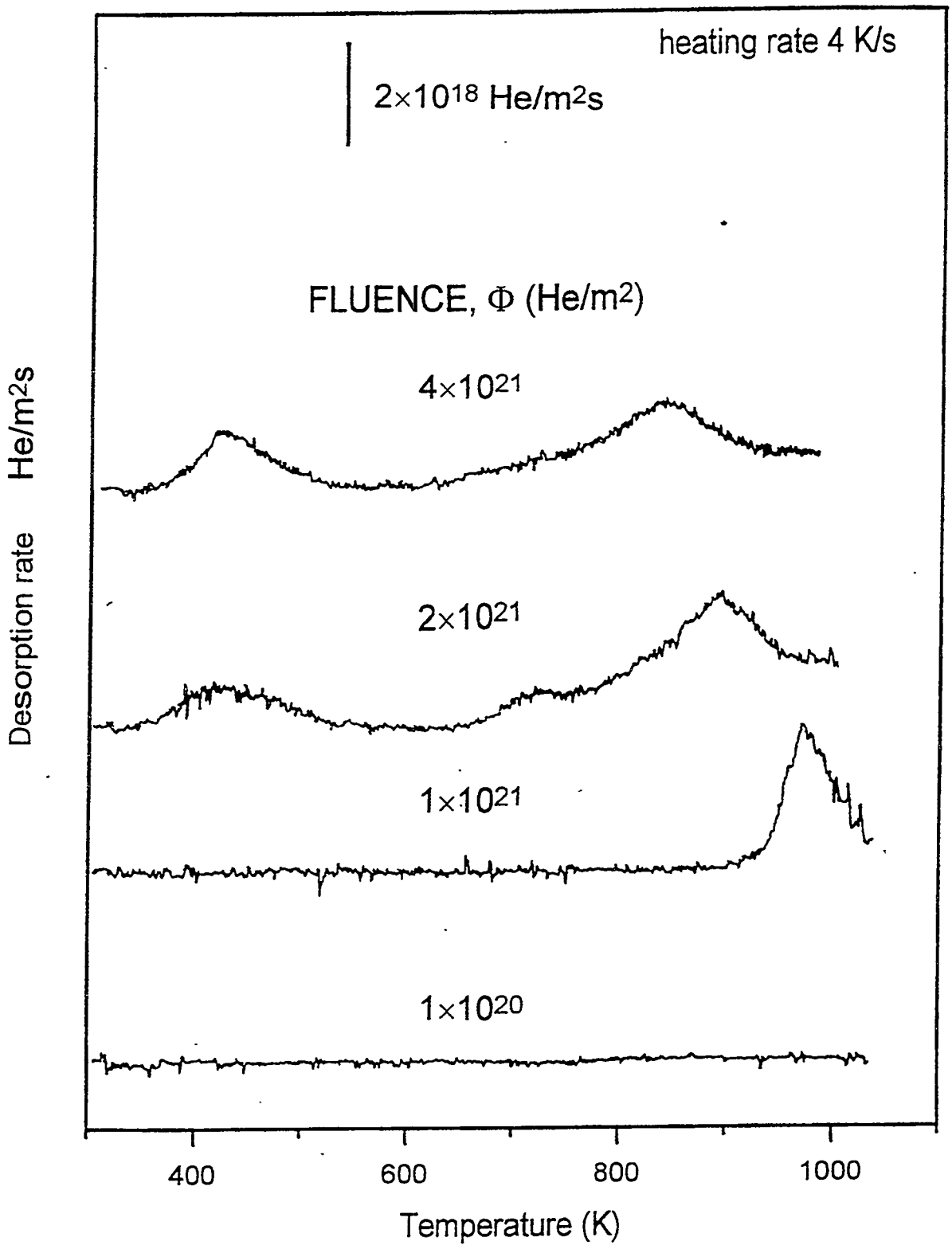
heating rate 4 K/s
2×10¹⁸ He/m²s
FLUENCE, Φ (He/m²)
4×10²¹
2×10²¹
1×10²¹
1×10²⁰
Desorption rate He/m²s
400
600
800
1000
Temperature (K)

Figure 3

RECOMMENDED DESIGN CORRELATIONS FOR S-65 BERYLLIUM*

M. C. Billone
Fusion Power Program
Energy Technology Division (Bldg. 212)
Argonne National Laboratory, Argonne, IL 60439
Telephone: (708)252-7146
Fax: (708)252-4798
E-Mail: mike_billone@qmgate.anl.gov

ABSTRACT

The properties of tritium and helium behavior in irradiated beryllium are reviewed, along with the thermal-mechanical properties needed for ITER design analysis. Correlations are developed to describe the performance of beryllium in a fusion reactor environment. While this paper focuses on the use of beryllium as a plasma-facing component (PFC) material, the correlations presented here can also be used to describe the performance of beryllium as a neutron multiplier for a tritium breeding blanket.

The performance properties for beryllium are subdivided into two categories: properties which do not change with irradiation damage to the bulk of the material; and properties which are degraded by neutron irradiation. The irradiation-independent properties described within are: thermal conductivity, specific heat capacity, thermal expansion, and elastic constants. Irradiation-dependent properties include: yield strength, ultimate tensile strength, plastic tangent modulus, uniform and total tensile elongation, thermal and irradiation-induced creep strength, He-induced swelling and tritium retention/release.

The approach taken in developing properties correlations is to describe the behavior of dense, pressed S-65 beryllium -- the material chosen for ITER PFC application -- as a function of temperature. As there are essentially no data on the performance of porous and/or irradiated S-65 beryllium, the degradation of properties with as-fabricated porosity and irradiation are determined from the broad data base on S-200F, as well as other types and grades, and applied to S-65 beryllium by scaling factors. The resulting correlations can be used for Be produced by vacuum hot pressing (VHP) and cold-pressing(CP)/sintering(S)/ hot-isostatic-pressing(HIP). The performance of plasma-sprayed beryllium is discussed but not quantified.

1. Introduction

Beryllium is being considered as a plasma-facing component (PFC) material for ITER. The specific type of beryllium chosen for the PFC application is S-65 beryllium, which is characterized by < 1 wt.% BeO content, < 1800 wppm (Al+Mg+Si) content, and $\leq$ 20 μm

*Work supported by the Office of Fusion Energy, U. S. Department of Energy under Contract W-31-109-Eng-38.

grain size. The product is made by Brush Wellman by both vacuum hot-pressing (VHP) and cold-pressing (CP)/sintering (S)/hot-isostatic-pressing (HIP). The designation "B" or "C" which follows the label S-65 refers to Brush Wellman internal quality control specifications and has no significance with regard to properties of the final product.[1] The product form for the PFC application will probably be VHP or CP/S/HIP tiles which are about 5-mm thick. Plasma-sprayed Be is also being considered for fabrication. In either case, it is planned to use plasma-spray techniques to repair sputtered Be layers *in situ.* Thus, the properties of both pressed and plasma-sprayed Be are of interest.

There are essentially no data available on porous and/or irradiated S-65 Be in either the pressed or plasma-sprayed product form. The material has been irradiated in European test programs, but the samples have not yet been analyzed. However, there is a large fission reactor data base for dense and porous S-20OF Be, which allows a higher maximum BeO content (1.5 wt.%). In practice there is some overlap between S-20OF and S-65 Be in that the actual BeO content of a particular lot of S-20OF may be as low as 0.9 wt.% BeO. Because of this similarity and because of the absence of irradiation data for S-65 Be, the irradiation behavior of S-200F, as well as other grades of Be, is used to predict the behavior of S-65 Be.

Based on the anticipated ITER operating conditions for a lifetime fluence of 1 MW•a/m^2, the operating ranges for the PFC Be are: $100 \leq T \leq 600°C$, $\leq$ 3000 appm He, $\leq$ 60 appm tritium, and $\leq$ 7 dpa. The He, tritium and neutron damage levels all scale with first-wall fluence if higher design lifetimes (e.g., 3 MW-a/m2) are desired. Because the He/dpa ratio for Be is so much higher than for other first-wall metals, the He content and distribution in Be tends to determine swelling and mechanical performance. Thus, swelling and mechanical performance parameters are correlated to He content in this work, as opposed to the traditional approach of correlating to neutron damage in dpa for steels, copper alloys, and vanadium alloys.

The correlations presented here for thermal-mechanical performance parameters apply to pressed (both VHP and CP/S/HIP) Be. The properties are correlated to as-fabricated (p) and He-generated ($\Delta V/V_o$) porosity fraction, temperature (T in K) and He content (C_{He} in appm). It is very difficult to characterized plasma-sprayed Be because of the wide ranges of porosity content and distribution, grain and particle sizes, shapes and distributions, and post-spray heat treatments. The designer should be aware of the fact that the plasma-sprayed layer of Be which replaces the sputtered layer will have significantly different properties than the original layer. Also, any heat treatment used in the tile-repair may affect the properties of the base metal if the temperature is high enough (e.g., > 600°C).

The thermal properties presented in this work are thermal conductivity (k in W/m•K), specific heat capacity (C_p in kJ/kg•K), and thermal expansion ($\Delta L/L_o$ in %). These properties are relatively independent of the particular grade of Be. Also, with the exception of possible He-induced swelling effects on conductivity, they are considered to be independent of irradiation. Mechanical properties considered are Young's modulus (E in GPa), Poisson's ratio (μ), yield strength (S_y in MPa), plastic tangent modulus (E_p in Gpa),

ultimate tensile strength (S_{ut} in Mpa), uniform elongation (UE in %), total elongation (TE in %), thermal creep (e_c^{th}), irradiation creep (e_c^i) and He-induced swelling ($\Delta V/V_o$ in %). Tritium retention performance is also summarized. The elastic constants (E and μ) are considered to be independent of irradiation, while the remaining parameters are assumed to vary according to the accumulated He concentration. There are three survey-type references used for developing the recommended correlations: Billone, et al.,[2] Billone, Dalle Donne and Macaulay-Newcombe,[3] and Barabash.[4] Primary sources are referred to in the cases of newer data or to resolve conflicting viewpoints in the three survey references.

2. Irradiation-Independent Properties

The following properties are considered to be independent of irradiation as far as neutron damage to the material bulk is concerned. For those properties which depend on porosity (p), either as-fabricated or He-induced, a porosity dependent term is included in the correlation.

2.1 Thermal Properties

The thermal conductivity, specific heat capacity and thermal expansion recommended by Billone, et al.[2] for Be are:

$$k = 291 f_p (1 - 1.650\times10^{-3}T + 1.464\times10^{-6}T^2 - 5.125\times10^{-10}T^3) \quad (1)$$

where $$f_p = (1-p)(1+3.7p^2)^{-1} \quad (1a)$$

$$C_p = 2.432(1+2.643\times10^{-4}T - 2.924\times10^{-4}T^{-2}) \quad (2)$$

and

$$\frac{\Delta L}{L_o} = 8.43\times10^{-4}(1+1.36\times10^{-3}T - 3.53\times10^{-7}T^2)(T-298) \quad (3)$$

The thermal conductivity correlation is based on data up to 700° C. The data are relatively insensitive to the specific type or grade of Be. Although the S-65 data[5,6] were not used to develop the correlation, the correlation matches the data to within 0.6% on the average between room temperature and 700° C. Extrapolation beyond the data base should give reasonable results. Use of the correlation for ITER design analysis involves interpolation within the data set. The heat capacity correlation is based on data up to the melting temperature of Be and applies to all types and grades of Be. It matches the specific data set[5,6] for S-65 Be to within 2% which is also well within experimental error. Similarly, the thermal expansion correlation is based on data up to the melting temperature of Be. It matches the specific data set[5,6] for S-65 Be to within 0.7%.

2.2 Elastic Constants

There are two basic experimental techniques for determining Young's modulus and Poisson's ratio: dynamic techniques involving either sonic or vibration methods or static techniques based on tensile stress-strain data. The dynamic techniques give a more accurate measurement of the elastic constants, which should be dependent on the strength of interatomic bonds and relatively insensitive to impurities and fabrication techniques. Also, based on dynamic determinations of Young's moduli for a large number of metals, the decrease with temperature is generally $< 25\%$ from room temperature up to the melting temperature. Static (really slow strain rate) tensile-tests suffer from a precision/calibration problem at the very low elastic strains. Also, as temperature increases, the apparent Young's modulus determined from tensile tests decreases quite rapidly with temperature, possibly due to other deformation mechanisms (e.g., creep). The tensile-test results can be as much as an order of magnitude low as compared to the true Young's modulus. This perhaps explains the wide variation in reported Young's modulus values with BeO content, microstructure and strain rate. Figure 1 shows the dynamic data,[3,4] the recommended correlations and the static S-65 data[6] for very dense Be.

The recommended correlations for Young's modulus (E in GPa) and Poisson's ratio (g) are:

$$E = 300\exp(-4.574p)[1-2.016\times10^{-4}(T-293)] \quad (4)$$

$$\mu = 0.08 \pm 0.02 \quad (5)$$

The porosity dependence is based on the large number of data points for VHP and CP/S/HIP S-200 Be with as-fabricated porosities in the range of 0 to 0.3 (30%) at 20° C and 370° C. It can also be used to describe the effects of He-induced swelling on the Young's modulus.

3. Irradiation-Dependent Properties

3.1 Tensile Yield Strength

Tensile yield strength (i.e., stress at 0.2% plastic strain) data have been reviewed for unirradiated, dense, powder-metallurgy- produced S-65 Be[5,6], S-200E Be[5,6], S-200F Be[7] and various grades of Be containing ≤ 2 wt.% BeO[8,9]. Figure 2 shows the comparison between the recommended correlation for S-65 Be, the data for S-65 Be and the data for all grades of S-200 Be. The correlation which was obtained by fitting the S-65 data is:

$$S_{yto} = 272 f_p[1-7.675\times10^{-4}(T-293)-3.393\times10^{-7}(T-293)^2] \quad (6)$$

where $f_p = \exp(-3.23p)$ based on HP and CP/S/HIP data for S-200F Be.[2,3]

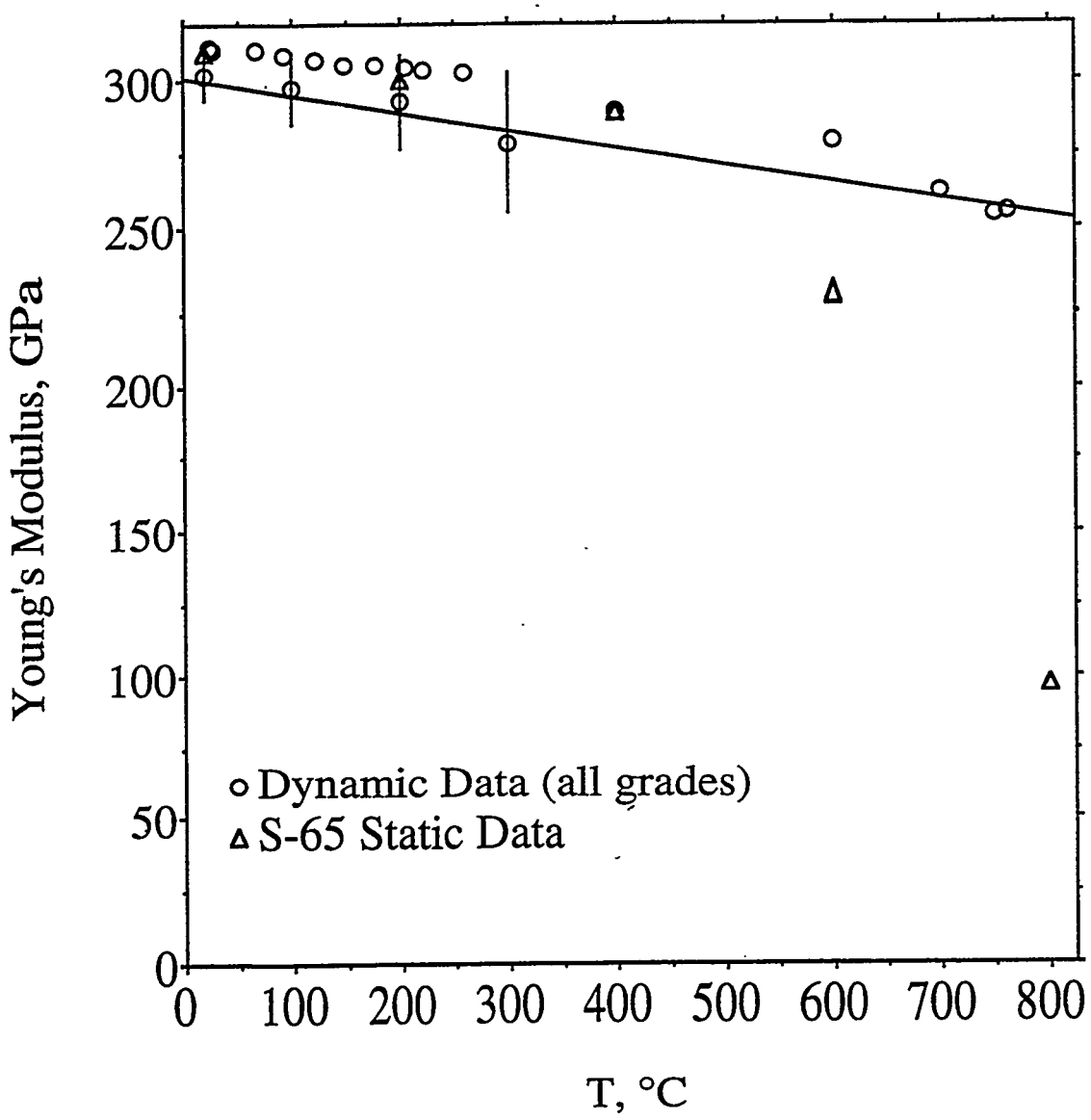

Figure 1. Comparison of the recommended correlation and the dynamic data (all grades) and static data (S-65) for the Young's modulus of dense beryllium.

In terms of irradiation effects on yield stress, most stress/strain tests on irradiated material have been conducted in compression because of the low tensile ductility of irradiated Be. The increase in compressive yield stress with He content is characterized for these tests and used to scale the tensile yield behavior. For S-200 Be irradiated in EBR-II at about 470° C and postirradiation tested at 450° C, the compressive yield strength increased from about 180 MPa to 294 MPa.[10] The irradiated samples contained about 1600 appm He. Assuming a square-root dependence of yield strength on He content to get the saturation of hardness with irradiation which has been observed gives:

$$S_{yc}/S_{yco} = 1 + 1.6 \times 10^{-2} (C_{He})^{0.5} \qquad (6a)$$

In the absence of well-characterized tensile data on Be irradiated and tested at the same

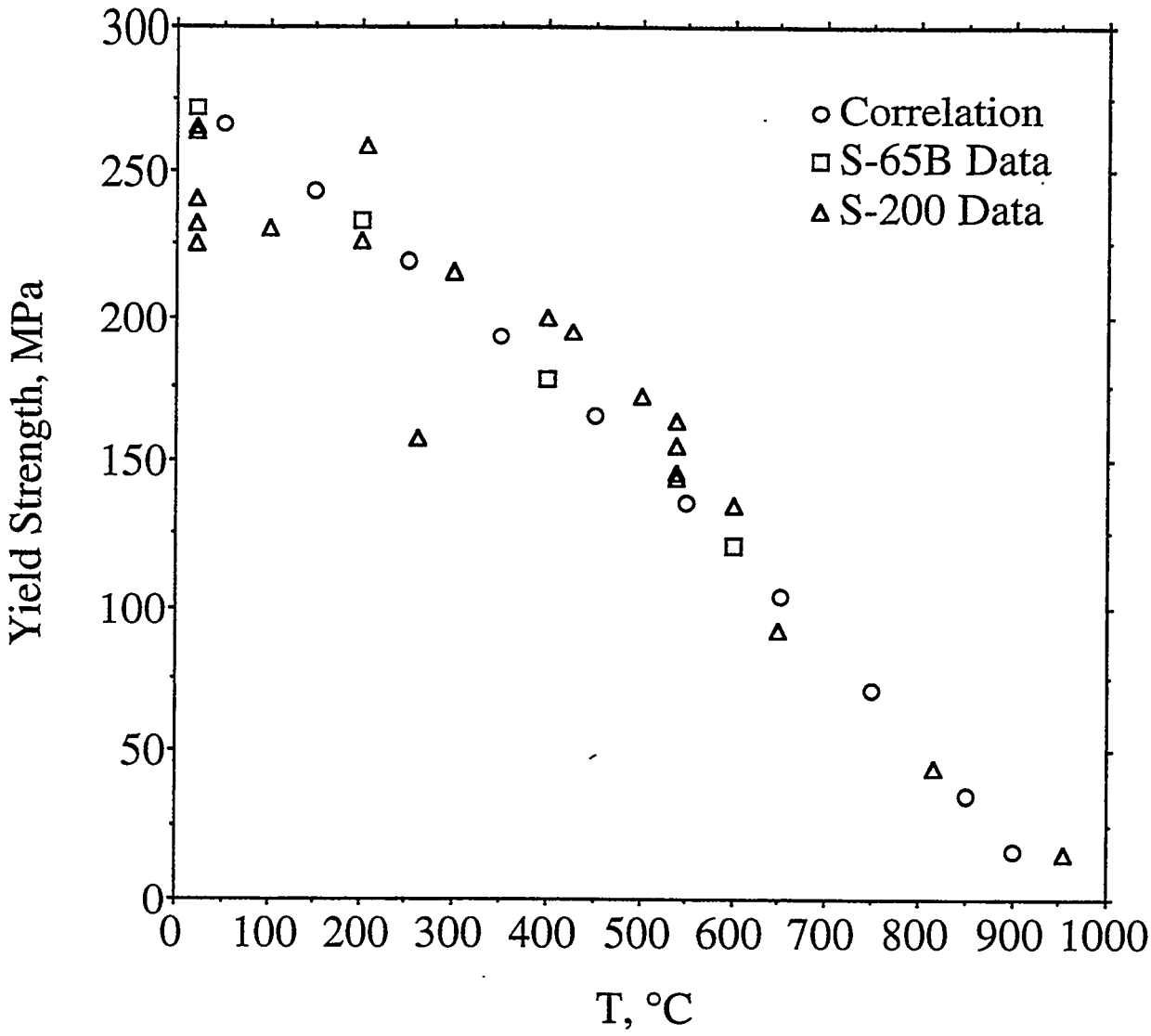

Figure 2. Recommended correlation and data for the tensile yield strength of unirradiated, dense, pressed S-65 and S-200 grades of Be.

temperature, it is assumed that Eq. 6a holds for tension as well as compression and that the irradiation effect is temperature independent up to the ITER-relevant temperature limit of 600° C. The recommended correlation for the irradiation effects on tensile yield strength is

$$S_{yt} = \left[1 + 1.6 \times 10^{-2} \left(C_{He}\right)^{0.5}\right]^{\prime} S_{yto} \qquad \textbf{(6b)}$$

It should be mentioned that annealing of the irradiated samples in Ref 10 at 900° C and then testing at 500° C reduced the compressive yield strength down to levels of 100 - 200 Mpa. Thus, the irradiation effects on yield strength are somewhat reversible.

Also, irradiation and testing at lower temperatures (20 - 1OO° C) will most likely generate

higher yield strength values than would be calculated by Eq. 6b. Based on the work of Beeston et al.,[11] the compressive yield strength of 97%-dense CIP/S/HIP Be was 216 MPa before irradiation and 930 MPa after irradiation at 75° C to 872 appm He. This gives an irradiated-to-unirradiated ratio of 4.3, while Eq. 6a gives a ratio of only 1.5. However, Eq. 6b is still recommended for ITER design analysis because the tests were conducted at a temperature characteristic of the average-to-maximum range for ITER PFC Be and the He content corresponds to about 0.5 MW-a/m^2.

3.2 Ultimate Tensile Strength

The treatment of the ultimate tensile strength (S_{ut}) parallels that of the tensile yield strength. The references are also the same. The recommended correlation for unirradiated S-65 Be is

$$S_{uto} = 438 f_p \left[1 - 8.9\times10^{-5} 9T - 293) - 3.83\times10^{-6}(T-293)^2 + 3.7\times10^{-9}(T-293)^3\right] \quad (7)$$

where $f_p = \exp(-4.733\ p)$ based on room-temperature data for VHP and CIP/S S-20OF Be. Figure 3 shows the comparison of Eq. 7 and the S-65 data, as well as various lots of S-200 Be. Notice that S-65 Be tends to have higher ultimate tensile strength values for T $\leq$ 400° C, but the strength of S-65 Be is comparable to the S-200 grades at > 400° C.

For the EBR-II-irradiated S-20OF Be, the ultimate compressive strength increased from about 250 MPa for unirradiated material at 450° C to an average of 340 MPa for material irradiated at about 470° C to an average of 1600 appm and tested at 450° C. The irradiation effects on ultimate compressive, as well as tensile, strength are assumed to be

$$S_{uc} = \left[1 + 9.0\times10^{-3}(C_{He})^{0.5}\right] S_{uco} \quad (7a)$$

and

$$S_{uc} = \left[1 + 9.0\times10^{-3}(C_{He})^{0.5}\right] S_{uto} \quad (7b)$$

Annealing at 900° C for 1 hour reduced the S_{uc} values for the irradiated samples to those of the unirradiated samples.

Low temperature ATR irradiation of S-20OF Be to 872 appm He increased the room-temperature S_{uc} values from 310 MPa to 982 MPa. This factor of 3.2 increase is higher than the value of 1.3 predicted by Eq. 7a, again indicating a temperature effect on the irradiation hardening. Until this temperature effect is characterized over a wider range of temperatures, Eq. 7b is recommended for ITER design analysis because the data set on which the equation is based is closer to the anticipated operating conditions for PFC Be.

While engineering values of yield strength for Be are within the scatter of the data for both tension and compression, the engineering ultimate strength is often lower in tension than in compression. The specimen in the tensile test undergoes thinning and necking prior to cracking, while the compressive specimen undergoes "barreling" prior to cracking. If the

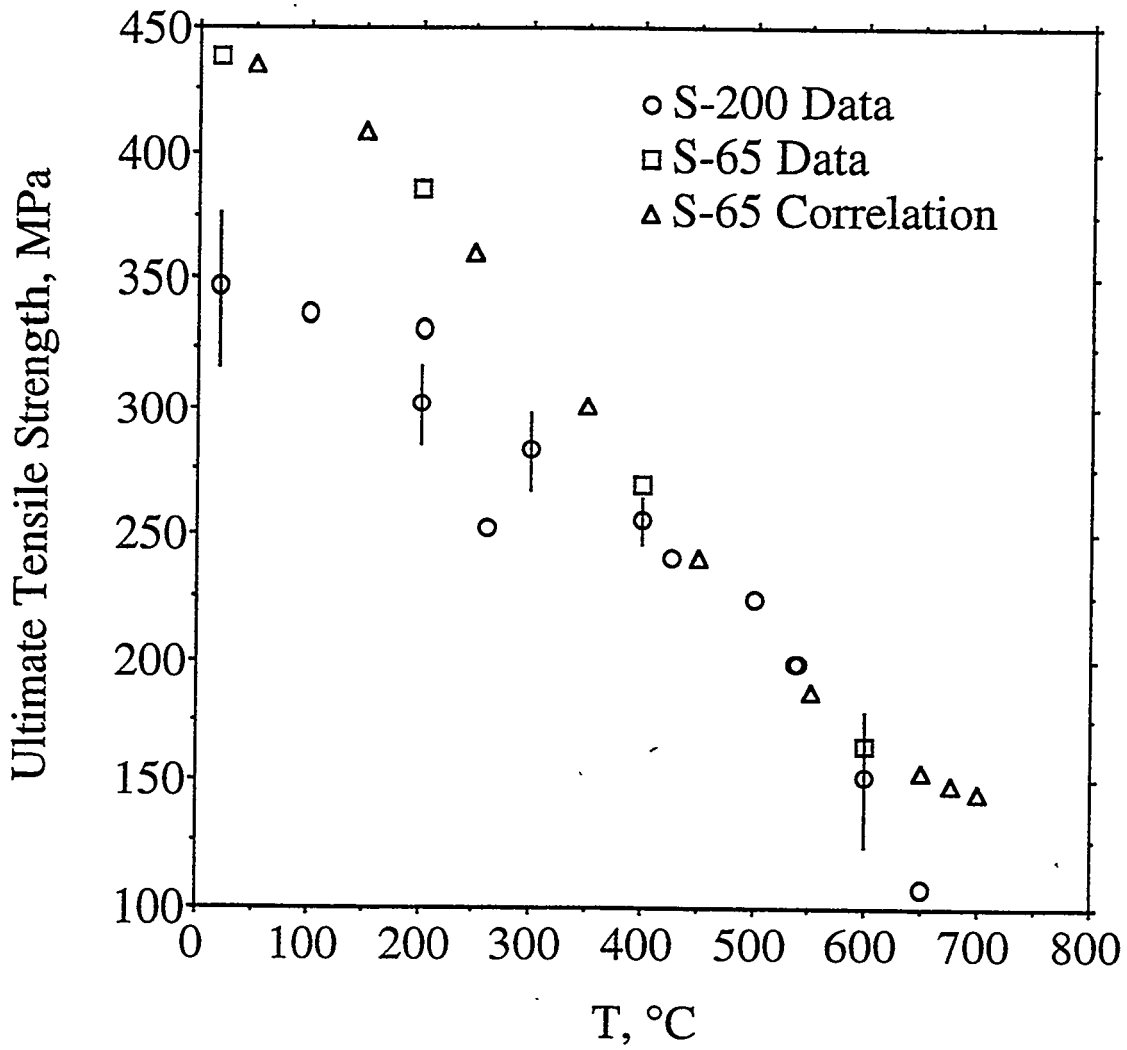

Figure 3. Recommended correlation and data for the ultimate tensile strength of unirradiated, dense S-65 beryllium. The data for various grades of S-200 Be are also shown.

tension and compression data are converted to true stress-strain values, then the plastic behavior of Be is essentially the same in tension and compression. The apparent difference in behavior based on graphs of engineering stress-strain is primarily a geometric, and not a material, effect. This is important in defining a plastic tangent modulus for bi-linear modeling, which is done in the next section.

3.3 Plastic Tangent Modulus

A bi-linear representation of the engineering stress-strain behavior is recommended for ITER design analysis. In the elastic regime, the uniaxial stress (s)-strain (e) behavior is given by: $e = s/E$. In the bi-linear representation, this equation is used for $s < S_y$. For

$s \geq S_y$, the constitutive equation for the bi-linear model is: $e = s/E + (s - S_y)/F_p$, where E_p is the plastic tangent modulus. With E given by Eq. 4 and S_y given by Eqs. 6 and 6b, it remains to specify E_p.

Beeston[12] has published some engineering tensile stress-strain curves for unirradiated, dense VHP S-200 Be. Approximate values of the tangent modulus in the plastic strain range of 0.2 to 0.7% are 7 GPa at 20° C, 4.4 GPa at 427° C, 2.9 GPa at 538° C and about 0 at 826° C. An approximate linear fit to these data is:

$$E_{po} = 7.0\left[1 - 1.0\times10^{-3}(T-293)\right] \tag{8}$$

For similar material irradiated in EBR-II at about 470° C to about 1600 appm He, the post-irradiation tangent modulus between 0.2% and 0.4% compressive strain was 26 GPa for a test temperature of 450° C and 15 GPa for a test temperature of 550° C. Thus, a crude approximation for the tangent modulus as a function of temperature and He content is

$$E_p = 7.0\left[1 + 0.41\left(C_{He}\right)^{0.5}\right]\left[1 - 1.0\times10^{-3}(T-293)\right] \tag{9}$$

3.4 Tensile Ductility

It is very difficult to find uniform elongation data for beryllium. Generally, total elongation is quoted in the literature. Sometimes, total elongation, uniform elongation and uniform ductility are used as interchangeable terms, and it is not clear what data are being presented. It is assumed in this review, that, unless otherwise specified, all data refer to total elongation. The tensile ductility (euo) of unirradiated S-65 Be[5,6] can be correlated to temperature and as-fabricated porosity according to:

$$E_{uo} = (4.2 \pm 1.2\%)\exp(-8.0p)\left[1 - 2.0384\times10^{-2}(T-293) + 2.7244\times10^{-4}(T-293)^2 - 3.836\times10^{-7}(T-293)^3\right] \tag{10}$$

where the porosity dependence is based on data for S-200 Be.[3]

Although no data are available for irradiated S-65 Be, the tensile ductility of S-200 Be drops to about 0.2% after modest irradiation in a fission reactor, while the compressive ductility decreases to about 0.6%. Beeston, et al.[10] report an average compressive uniform elongation of 0.4% for S-200 Be irradiated in EBR-II at about 470° C to about 1600 appm He and post-irradiation tested at 450° C and 550° C. The unirradiated compressive ductility for these samples was about 30%. This value decreased to 14% for samples with irradiation/test temperatures of 470/450 ° C. Annealing at 900° C for one hour restored the ductility back to the unirradiated value. Thus, a crude scaling of ductility with He content can be expressed by:

$$e_u = e_{uo}\left[1 + 2.86\times10^{-2}\left(C_{He}\right)^{0.5}\right]^{-1} \tag{10a}$$

3.5 Thermal and Irradiation Creep

The thermal (e_c^{th} in absolute units) and irradiation (e_c^i in absolute units) of Be have been expressed as functions of porosity (p in absolute units), temperature (T in K), effective stress (s in MPa), time (t in s) and neutron damage (D in dpa) as: [3]

$$e_c^{th} = 0.751(1-p^{2/3})^{-3.6}\exp(-2.60\times10^4/T)s^{3.6}t \quad (11)$$

and

$$e_c^{i} = 3.2\times10^{-6}(1-p^{2/3})^{-1}sD \quad (12)$$

The thermal creep of Be tends to decrease with increasing grain size and BeO content and increase with increasing impurity levels of Al, Mg, and Si.[13] At about 980° C, increasing the (Al + Mg + Si) content from 100 wppm to 1000 wppm resulted in an increase of a factor of 9 in the stress required to produce a creep rate of 10^{-4} s^{-1}. Above 1000 wppm (which includes S-65 Be), the creep rate is relatively insensitive to the levels of these impurities. At higher temperatures, the creep rate of Be varies inversely with grain size. However, in the temperature range of 650-760° C, this trend was reversed in high purity Be. For medium purity Be (1 wt.% BeO and 760 wppm Al+Mg+Si), the creep rate was insensitive to grain size in the relevant range of 10 to 50 μm. As these specifications are close to those of S-65 Be, it is recommended that a grain size dependence not be included in Eq. 11.

Crook and Webster[13] report a steady-state thermal creep rate of 10^{-8} s^{-1} at 649° C and 10 MPa. Under these conditions, Eq. 11 predicts a creep rate of 1.7 x 10^{-9} s^{-1}. Thus, the measure thermal creep rate is a factor of 7 times higher than what is predicted by Eq. 11. While this may seem large to the designer, it should be emphasized that scatter in thermal creep data is generally quite large and that predictions within an order of magnitude are considered adequate. Thus, in the absence of specific thermal creep data for S-65 Be, Eq. 11 is recommended for ITER design analysis.

The irradiation creep correlation represented by Eq. 12 is based on only one data point at 43° C under low dpa and He generation conditions. Thus, the data base is inadequate for validation of the correlation.

3.6 Helium-induced Swelling

The effects of as-fabricated porosity on swelling and irradiation temperature on swelling are not well characterized. Most data are based irradiation at temperatures < 100° C followed by postirradiation anneals from 1 to 24 hours. Also, it has only been within the past five years that the He content in the irradiated samples has been characterized well enough to allow the volumetric swelling (in %) to be correlated to annealing temperature and helium content. Billone et al.[2,3] have proposed a correlation to match the ATR irradiation and post-irradiation annealing data of S-200F Be:

$$\Delta V/V_o = 1.15\times10^{-4} C_{He}\left[1+9.49\times10^{-5} C_{He}^{0.5} T^{1.5}\exp(-3940/T)\right] \quad (13)$$

The data base includes He contents up to 26,000 appm and annealing temperatures up to 500°C for one hour. However, with the exception of a few immersion density measurements, most of the data are actually length change measurements. The axial strains are multiplied by three to obtain an estimate of volumetric strain. Also, He content was measured for only a few high bum-up samples.

Sannen et al.[14,15] have performed extensive studies of the helium content and swelling of BR2-irradiated Be. Samples were irradiated at 60°C up to He contents of 20,000 appm He. One and 24 hour anneals were performed at temperatures in the range of 200 - 800°C. Also, data consisted of both length and diameter change measurements which give a more accurate reading of volumetric swelling than simple length measurements. They used the following correlation to represent their data:

$$\Delta V/V_o = 1.19\times10^{-4} C_{He}\left[1+A\,C_{He}(T-293)^4\right] \quad (14)$$

where A = 1.01 x 10^{-12} for 1-hour anneals and A = 1.31 x 10^{-12} for 24-hour anneals.

In deciding which correlations to use for ITER analyses, an independent data set is required to validate the correlations. At present, the only data set available for validation of in-reactor swelling is the EBR-II data set.[10] The problem with using this data set is that the He measurements were made after compression-testing samples to failure. Some He may have been released in the fracture of these samples, perhaps giving rise to the low He (in appm) to fluence [in 10^{22} n(E>1 MeV)/cm^2] ratio of 1540. Figure 4 is a comparison between Eqs. 13 and 14 and the EBR-II swelling data for the He range of 1000 - 2000 appm and 427 - 487°C.

The correlations tend to underpredict the data for measured swelling in the range of 0.2 - 0.9%, with the Billone correlation (Eq. 13) giving slightly better agreement with the data than either of the Sannen correlations. However, the validity of the comparison of correlations to data depends on the relevance of the He measurements in the EBR-II samples after post-irradiation fracturing to the He contained in the specimens during irradiation. Clearly, what is needed for validation of correlations for ITER application is another set of data for Be irradiated at temperatures from 400 - 600°C with well-characterized He contents in the range of 3000 - 9000 appm.

In choosing a design correlation for ITER for calculation of Be swelling during normal operation, as well as over-heating events, it is useful to compare Eqs. 13 and 14 to determine which correlation is an upper bound. The comparison between the Billone correlation (Eq. 13) and the Sannen correlation (Eq. 14) based on the 24-hour anneals is shown in Fig. 5 for 3000 appm He (I MW•a/m^2) and 9000 appm He (3 MW•a/m^2). The agreement between the correlations is quite good for temperatures < 450°C. In the range of 450 - 600°C and for higher temperatures, Eq. 13 is an upper bound to Eq. 14. Thus, the

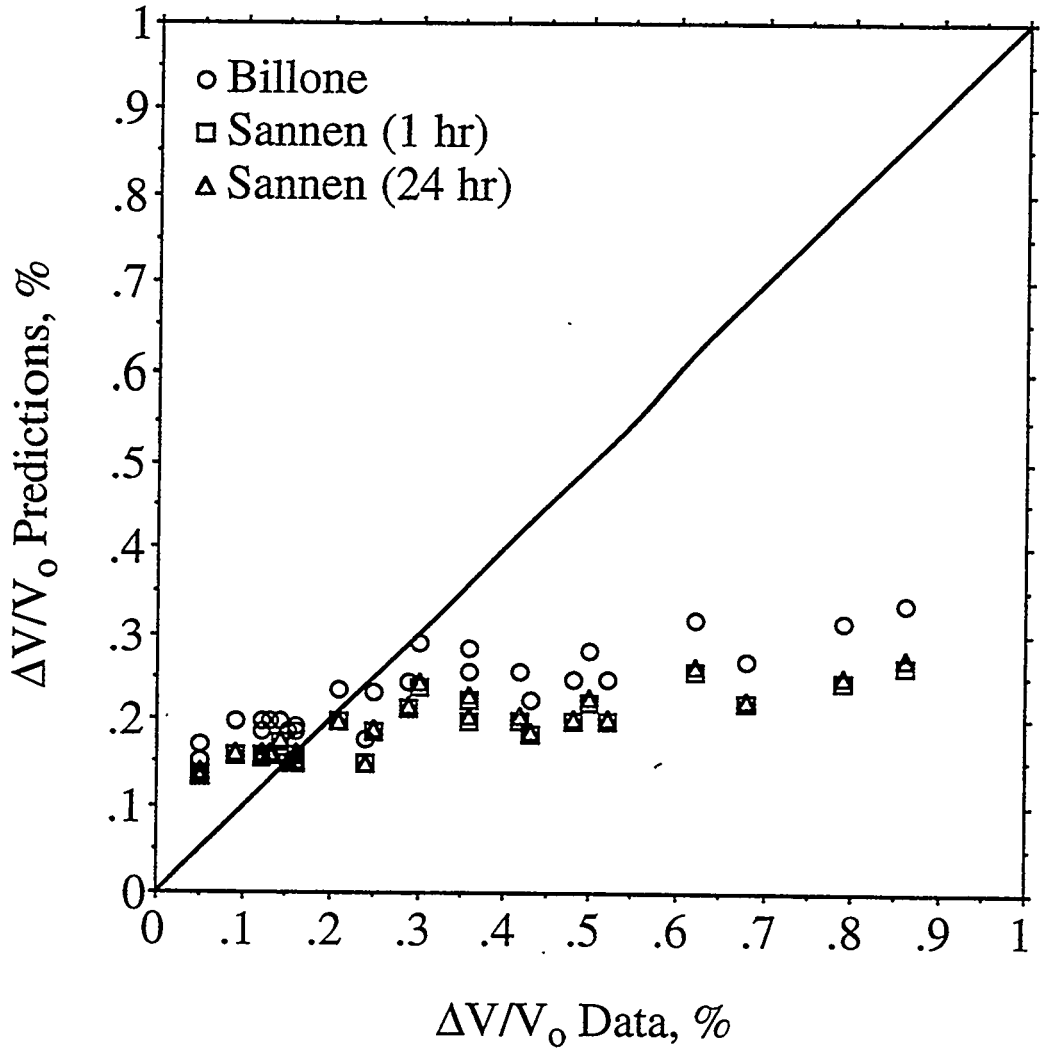

Figure 4. Comparison of the EBR-II swelling data and the swelling correlations of Billone et al.[2,3] (based on 1-hour anneals) and of Sannen[15] (based on 1- and 24-hour anneals). The EBR-II data are for temperatures of 427 - 487°C and He contents of 1000 - 2000 appm.

Billone correlation is recommended for ITER design analysis. There is very good confidence in using this correlation to predict the swelling of Be under normal operating conditions for $T \leq 400°C$ and for overheating events of < 24-hour duration up to 800°C. However, it remains to demonstrate that the correlation is either a best fit or an upper bound for normal operating temperatures of 400 - 600°C up to He contents of 9000 appm. Such a validation requires the generation of new data.

In using Eq. 13 to estimate the degradation of properties with swelling porosity, it is important to convert the results of Eq. 13 from percent values to fractional values for use in Eqs. 1a, 4, 6, 7, and 10 - 12. Also, the designer should be aware of the fact that the

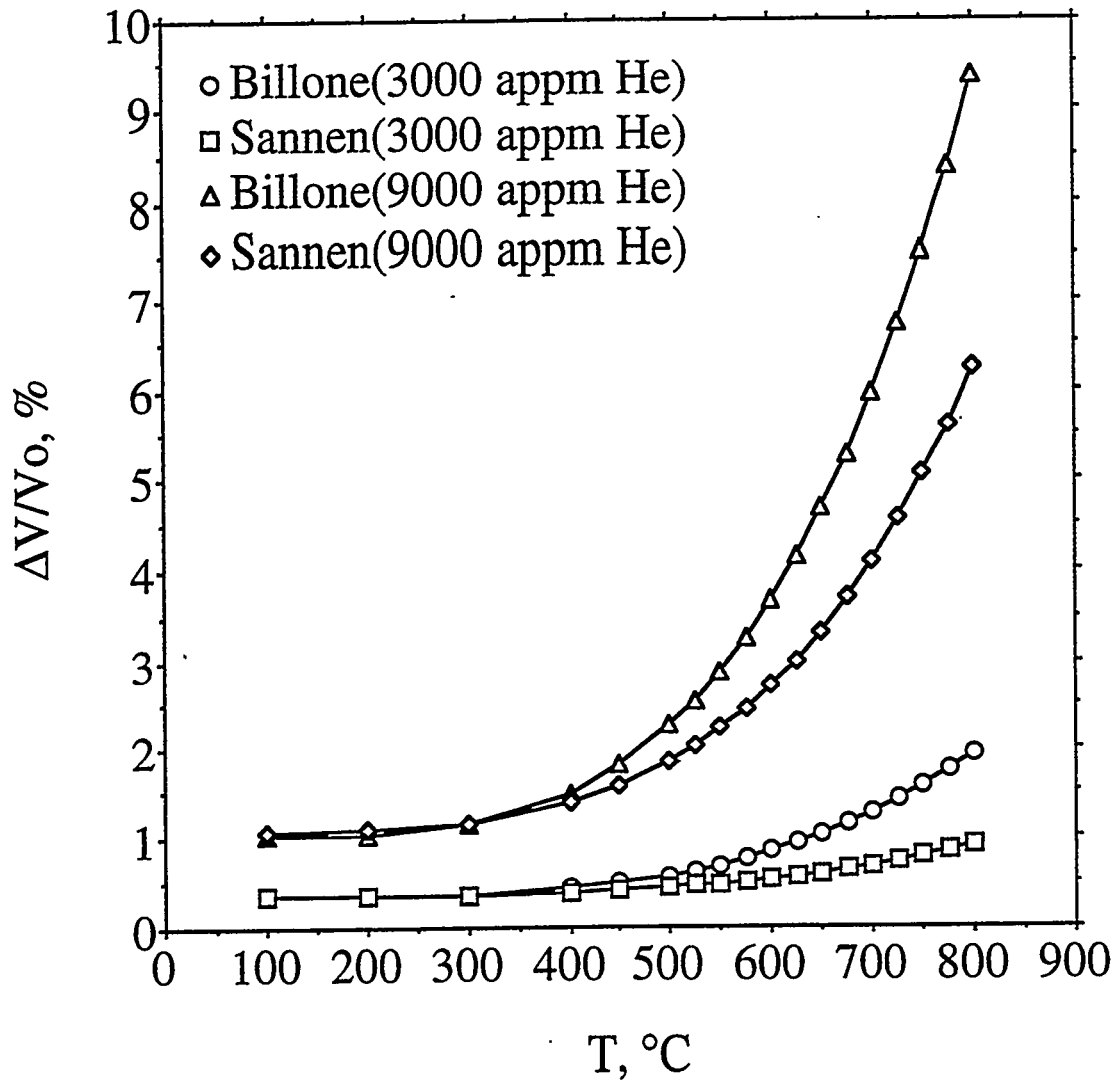

Fig. 5 . Comparison of the Billone et al.[2,3] and the Sannen et al.[15] correlations for He-induced swelling in S-20OF Be at 3000 appm He (1 MW•a/m^2 for ITER PFC) and 9000 appm He (1 MW•a/m^2 for ITER PFC).

swelling of Be with as-fabricated porosity has not yet been characterized due to a lack of data in this area.

4. Tritium Retention

There are no data on tritium retention/release from S-65 Be. Also, there are no relevant data for on-line tritiumrelease. Most of the available data are for pressed S-20OF Be and cast Be based on post-irradiation annealing studies. Table I summarizes the tritiumretention/release data gathered so far.[2,3,16,17] The most recent data set is from the SIBELIUS experiment.[17] It appears that as-fabricated porosity, as well as He-induced

swelling, enhances tritium release. No simple design correlation has been found to match these data sets. However, KfK has developed the ANFIBE code to predict tritium, as well as He, behavior in Be.[3] In the absence of a design correlation, the designer may use the data directly from Table 1 to estimate tritium inventory in Be.

Table 1. Summary of tritiuma nd helium retention in beryllium irradiated at low temperature (except for SIBELIUS) and post-irradiation annealed at high temperature. Fast (E > 1 MeV) fluence is in units of 10^{22} n/cm^2.

Initial Density %TD	Fab. Form	Fluence/ Irr. T, °C	Tritium/He appm	Anneal T °C	Anneal t Hours	Retained Tritium %	Ref.
100	HIP	5.0 ± 0.3/ 75	2530/ 26100	300 400 500 600 700	20-114 142-170 99-669 148-202 17	99.99 99.75 99.4 10 ~0	2
99.6	CIP/S	0.26/ 75	71.8/ 872	300 400 500 600 700 750 800 850 900	355 307 365 381 319 24 24 24 24	99.905 99.45 96.7 90.3 73.5 71.6 66.8 57.6 3.6	1
98	Arc-Cast	0.061/ 550	3.8/ 140	550 550 650 750 850 850	Irrad. 24 24 24 24 24	??? 99.95 89.1 47.0 9.4 0.3	17
80.9	CIP/S	0.26/ 75	55.3/ 733	300 400 500 600	386 335 318 435	96.8 62.0 11.0 1.0	2

5. Discussion

As stated in the introduction, the correlations presented in this work apply to vacuum hot-pressed and/or cold-pressed/sintered/hot-isostatic-pressed Be. In cases for which baseline data for 100% dense, unirradiated, pressed S-65 Be are available, correlations are developed for the performance of this material as a function of temperature. Porosity-dependent and He-dependent terms are developed based on data for pressed S-200 Be, with an emphasis on S-20OF material. These terms are then applied to the S-65 Be correlations.

It is difficult to characterize the performance of plasma-sprayed Be. Without post-spray heat treatment, the thermal conductivity of plasma-sprayed Be tends to be significantly lower, particularly in the spray direction, from what is obtained from Eqs. 1, la. Optimization of particle size, shape and purity, along with spraying techniques, have led to densities as high as 95% and thermal conductivities as high as 70% of what is predicted by Eqs. 1, la. The mechanical properties of plasma-sprayed Be are quite poor in terms of ductility and strength. Post-spray heat treatments, which may not be practical for ITER applications, have resulted in strengths and ductilities even higher than for pressed Be.

Given that plasma-spraying is an evolving art and given the near-impossibility of characterizing plasma-sprayed Be as a class of materials independent of specific data for a specific technique, it is recommended that the designer use the properties of pressed Be for the design analysis. If problems arise in the performance of pressed Be, then the designer should be aware that these problems will only get worse for plasma-sprayed Be. Exceptions to this are in the areas of Be/copper/steel mechanical interaction where the plasma-sprayed Be may be too weak to exert much force on the other layers, and tritium retention and He-induced swelling for which the plasma-sprayed Be may release more tritium and He than a corresponding pressed Be.

References

1. D. E. Dombrowski, personal communication, Brush Wellman, Inc., Nov. 8, 1994.

2. M. C. Billone, W. Dienst, T. Flament, P. Lorenzetto, K. Noda and N. Roux, "ITER Solid Breeder Blanket Materials Database," Argonne National Laboratory report ANL/FPP/TM-263, November 1993.

3. M. C. Billone, M. Dalle Donne and R. G. Macaulay-Newcombe, "Status of Beryllium Development for Fusion Applications," *Fusion Engineering & Design 27* (1995) 179-190.
4. V. Barabash, "Data on Be Thermomechanical Properties for Plasma Facing Components Design Evaluation," Version 2, ITER Garching Joint Work Site, June 16, 1994.

5. M. F. Smith, R. D. Watson, J. B. Whitley and J. M. McDonald, "Thermomechanical Testing of Beryllium for Limiters in ISX-B and JET," *Fusion Technology 8* (1985) 1174-1182.

6. R. D. Watson and J. B. Whitley, "Thermal Fatigue Tests of a Prototype Beryllium Limiter for JET," *Nuclear Engineering & Design/Fusion 4* (1986) 49-60.

7. W. J. Haws, "Characterization of Beryllium Structural Grade S-200F," Brush Wellman Technical Memorandum TM-778, May 27, 1985.

8. G. E. Darwin and J. H. Buddery, *Beryllium,* Academic Press, New York (1960) pp 179 - 198.

9. B. King, "Mechanical Properties," Chapter 7 in H. H. Hausner (ed.), *Beryllium, Its Metallurgy and Properties,* University of California Press, Los Angeles (1965) pp. 206-221.

10. J. M. Beeston, L. G. Miller, E. L. Wood and R. W. Moir, "Comparison of Compression Properties and Swelling of Beryllium Irradiated at Various Temperatures," *Journal of Nuclear Materials 122 & 123* (1984) 802-809.

11. J. M. Beeston, G. R. Longhurst and R. S. Wallace, "Mechanical Testing of Irradiated Beryllium," in G. R. Longhurst (ed.) "Beryllium Technology Workshop, EG&G report EGG-FSP-10017, December 1991.

12. J. M. Beeston, "Beryllium Metal as a Neutron Moderator and Reflector Material," *Nuclear Engineering & Design 14* (1970) 445-474.

13. D. Webster and D. D. Crooks, "Factors Influencing the Creep Strength of Hot Pressed Beryllium," *Metallurgical Transactions A, 6A* (1975) 2049-2054.

14. L. Sannen and Ch. De Raedt, "The Effects of Neutron Irradiation on Beryllium," *Fusion Technology 192* (1993) 1474-1478.

15. L. Sannen, Ch. De Raedt, F. Moons and Y. Yao, "He-Content and Induced Swelling of Neutron-Irradiated Beryllium," Fusion Engineering & Design (1995) to be published.

16. D. L. Baldwin and M. C. Billone, "Diffusion/Desorption of Tritium from Irradiated Beryllium," *Journal of Nuclear Materials 212-215* (1994) 848-953.

17. D. L. Baldwin, "Tritium Release Behavior of Sibelius Beryllium," Proceedings, International Workshop on Ceramic Breeder Blanket Interactions, held at UCLA Los Angeles, USA, June 22 - 24, 1994, C. E. Johnson (ed.), Argonne National Laboratory, 307-323.

METALLOGRAPHIC ANALYSIS AND STRENGTH INVESTIGATION OF DIFFERENT BE-CU JOINTS IN THE TEMPERATURE RANGE RT-3500C

A.A. Gervash[1], R.N. Giniatouline,[1] I.V. Mazul[1], A.A. Ganenko[2]
L.S. Gitarskij[3], V.S. Sizenev[3], D.A. Davydov[4]

[1] Efremov Research Institute, 189631, St. Petersburg, Russia
[2] CRISM "Prometey", 193167, St. Petersburg, Russia
[3] SIA "Composite",141070, Kaliningrad, Russia
[4] Bochvar Institute, 123060, Moscow, Russia

The goal of this work is to estimate the strength and structure of different Be-Cu joining techniques. Brazing, diffusion bonding and joint rolling methods were chosen as ITER Be-Cu joint method candidates.

Selected for ITER application Be-Cu joints were produced as technological plates (30-50 mm x 50-100 mm x thickness). AR samples for further investigations were cutted out from initial technological plates. To compare mechanical strength of selected Be-Cu joints tensile and shearing tests of chosen candidates were carried out in the temperature range RT - 350 °C. The metallographic analysis of Be-Cu crosssection was also done. Preliminary results of these ests as well as metallographic analysis data are presented. The industrial possibilities of producing required for ITER full scale Be-Cu joints are discussed.

Introduction

One of the main requirement for ITER divertor target technology is to provide reliable joint between Be coatings and copper alloy heat-sink stricture. It takes a very long time and heavy expenses to carry out full-scale investigation of all Be/Cu joining techniques. That is why it looks reasonable to develop rather simple comparative methods to estimate a quality of different joints and select the best Be/Cu candidates for detailed investigation in ITER application. The Russian approach is to start the investigation of Be/Cu joints producing the potential divertor elements (not separate samples) - bimetallic Be/Cu technological plates (see fig. 1). Bimetallic Be/Cu technological plate as initial state for further investigations allows:

To demonstrate the industrial (device) possibilities of each selected Be/Cu joint methods

To produce all necessary samples for different experiments by cutting out from uniform technological plate

To demonstrate the possibilities of cutting, machining etc. of technological plate producing the different samples

Thus a number of technological plates for further investigations were produced by different

techniques used (see fig. 2 and table 1.).

Methods of Be/Cu joining

Brazing

The brazing of the technological plate was carried out with Ag-based brazing alloy(Ag=63%, In 1-2%). The surfaces of Be and Cu were cleaned, etched and vacuum brazed at temperature 760°C. The cross-section of Ag brazed joint is shown on fig. 5. The technological plate produced by this method remained intact through considerably handling including cutting out and machining during the test sample preparation.

In regard to the concerns of Ag transmutation to Cd (under the neutron influence) we plan the so-called "Cd experiment". We prepared Ag based brazing alloy with Cd. The goal of forthcoming experiment is to measure the own vapour pressure of Cd in this brazing alloy. Our future plans with Ag based brazing alloy win be strongly depended on Cd experiment results.

Diffusion bonding

Be and Cu surfaces were preliminary cleaned and etched. Diffusion bonding was carried out in vacuum. The bonding pressure was increased up to plastic deformation in copper appearance. Then pressure was kept at temperature 720°C during 5 - 7 min. The cross-section of diffusion bonded zone is given on fig. 6. The bimetallic technological plates produced by this method remained intact during cutting out and following machining for test samples preparation.

Joint rolling

This work started in two directions:

joint rolling in vacuum

joint rolling in inert gas atmosphere

The current results show the same properties of joint rolled plates produced in vacuum and inert gas atmosphere. Thus it was decided to continue the investigations using vacuum joint rolling facility. Thus the several joint rolled technological plates were produced for further investigations. The cross-section of this type of joint is given on fig. 7. The plates remained intact during test samples preparation and attempt of bending this plate (see fig. 4).

Explosion bonding.

The result of the first attempt of explosion Be to Cu is shown on fig. 3. The Be plate cracked due to twice bending during explosion process. The attempts to explode Cu on Be plate limits the thickness of exploded Cu plate. The technological plate produced by this method failed during cutting out for cross-section sample preparation. Some additional industrial problems resulted finishing investigations in that direction.

Bonding by HIP method.

In the main this method was observed for Be/Cu tube divertor element application. The container for Be/Cu bimetallic tube joint was manufactured. The HIP technique parameters were chosen. As result two Be/Cu tube joint samples were produced. These samples remained intact through handling and bending attempts. To decrease the intermetallic formation V alloy diffusion barrier was used.. This method is very expensive. That is why it was decided not to continue (at least now) investigations of this type of bonding.

Tensile and shear testing experimental details.

The Russian Team point of view is to create the real ITER conditions for testing. The main of these conditions are cyclic high heat loading and neutron flux. However for some traditional estimations and calculations the mechanical properties of Be/Cu joints are required. With that aim tensile and shear Be/Cu joint testing at temperatures RT., 350°C was carried out.

To cutting out the samples for tensile and shear tests the technological plates produced by different methods were used. The general view of the tensile and shear samples and schemes of test loading are given on fig. 8, 9. The device for tensile and shear tests of Be/Cu joints at temperatures RT., 350°C was manufactured and tested. The tensile and shear experiments were carried out using standard mechanical testing machine with grip velocity of I mm/min.

Results and discussion

The main results of tensile and shear testing of different Be/Cu joints at temperatures RT., 350°C are presented in tables II., III. and given in fig. 11. It should be signed that brazed, diffusion bonded and joint-rolled samples successfully passed cutting out and machining treatment stages.

The detailed analysis of microstructure tested types of Be/Cu joints will be done. At present we can see that brazed, diffusion bonded and joint-rolled samples were metallurgical bonded and remained intact trough cutting out and machining. The defectless zone (lack of brazing alloy, bonding fine cracks, voids etc.) were not found on the samples cross-sections.

The static (not cyclic) increasing of testing temperature up to 350°C did not lead to changes in tensile and shear strength of Be/Cu joints.

At least two factors could influence on the spread in values of tensile and shear strength from sample to sample:

- rather small number of samples for testing
- possibility appearance of defects in brittle Be and on the bond tine of Be/Cu sample during preparation stages

No doubt it takes more samples for each point of experiment as well as high precision during machining of samples to obtain accuracy in tensile and shear values. Nevertheless on the first stage of Be/Cu joints investigations this experiment allowed to select brazing, diffusion bonding and joint rolling techniques as candidates for further study for ITER. In particular device were developed and samples were cut out from brazed, diffusion bonded and joint-rolled technological plates for simultaneous comparative cyclic HHF test of selected Be/Cu joints (including irradiated Be/Cu joints).

Conclusion

In regard to Be/Cu joining techniques some progress was made in the producing of different technological plates as initial structure for all types of Be/Cu joint tests. The device was developed and mechanical strength testing was carried out for different Be/Cu joints.

The tensile and shear strength of tested joints does not depend on static temperature increasing up to 350°C.

The detailed metallography of tested types of Be/Cu joints is necessary for selected techniques optimization.

It takes more samples for each point of experiment to obtain accuracy in tensile and shear values.

In whole the industrial possibilities of manufacturing of Be/Cu joints were estimated and the most suitable technologies (brazing, diffusion bonding and joint-rolling were selected for further investigations.

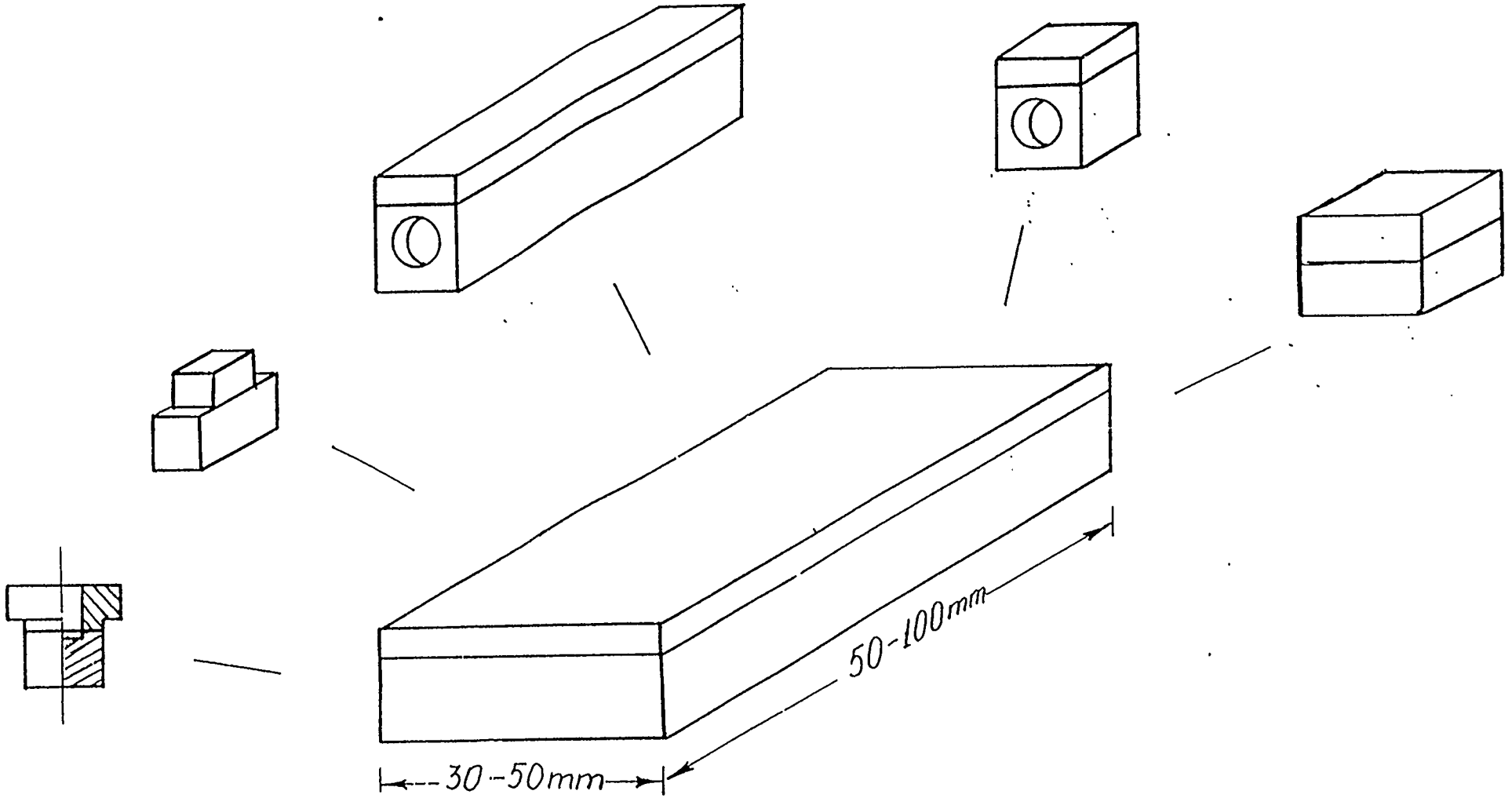

Fig. 1 Be/Cu technological plate

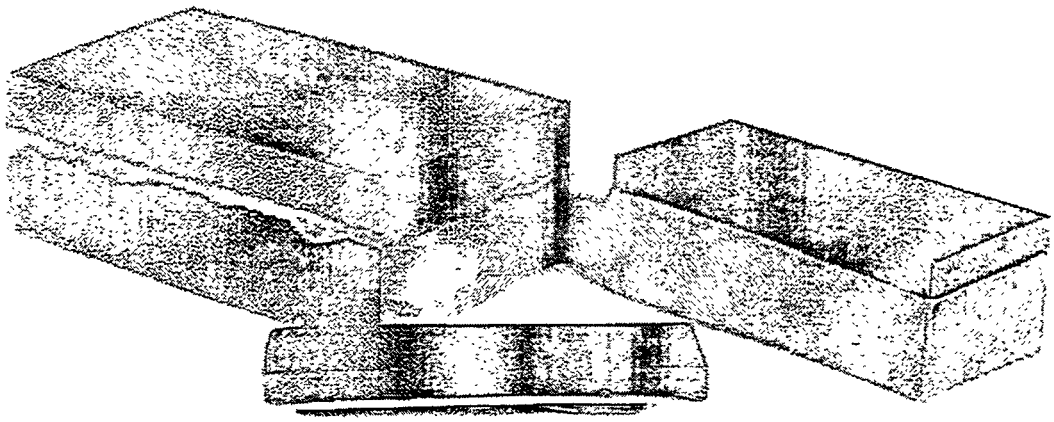

Fig. 2 Be/Cu technological plates

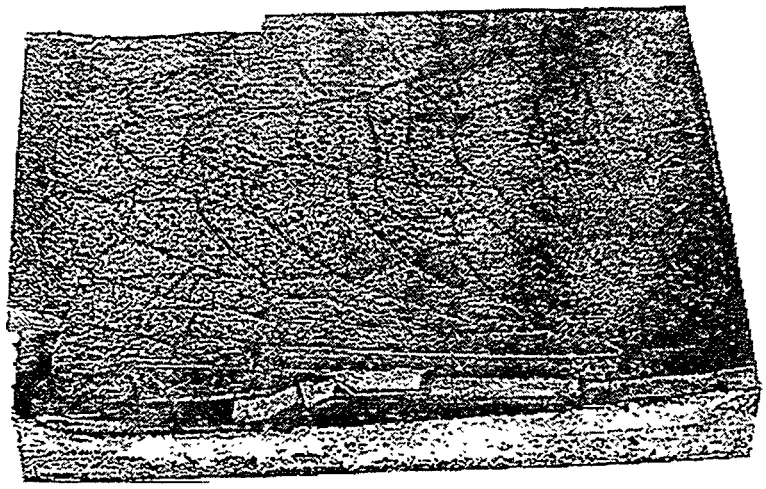

Fig. 3 Explosion welded Be/Cu technological plate

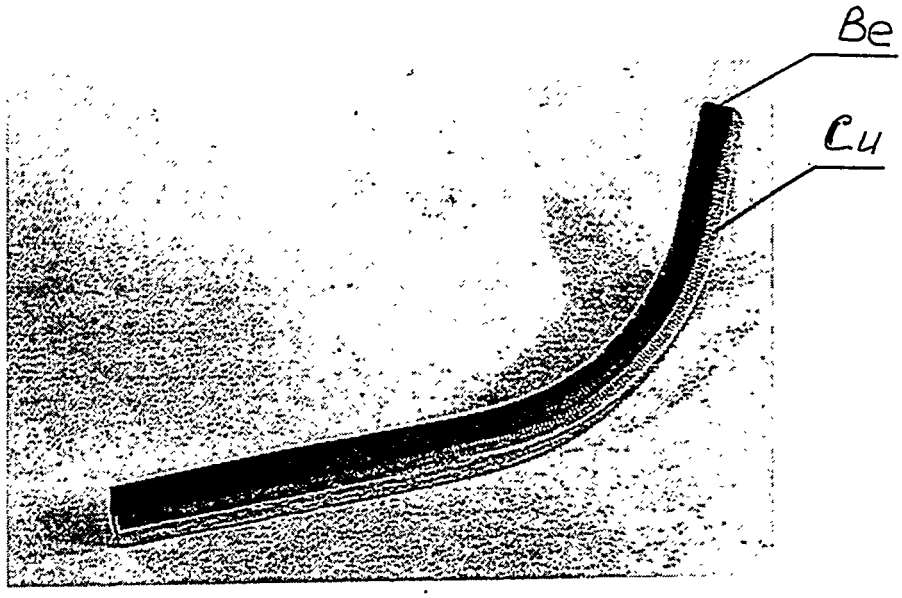

Fig. 4 Bending tested joint-rolled Be/Cu strip

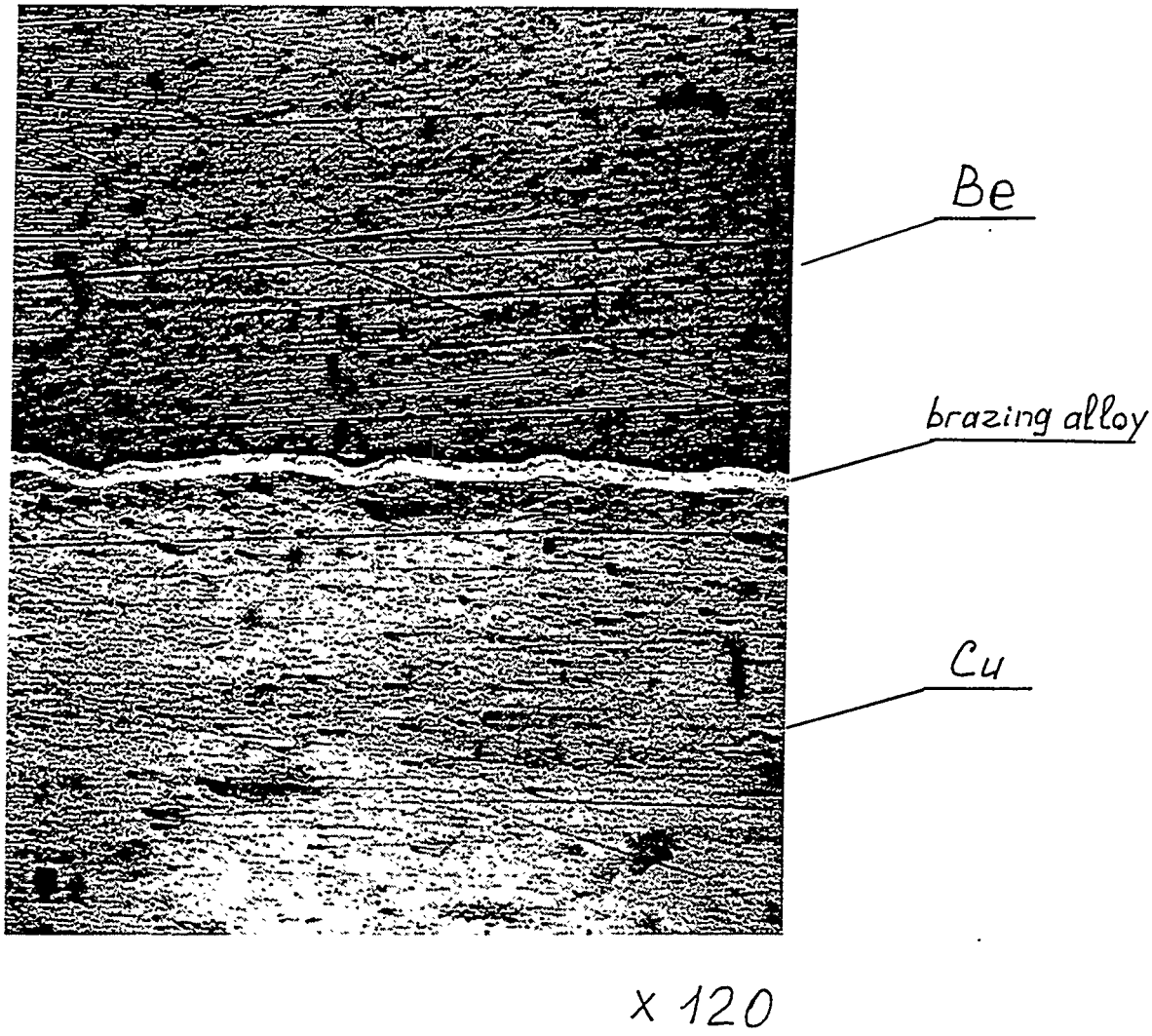

Fig. 5 **Cross-section of brazed Be/Cu joint**

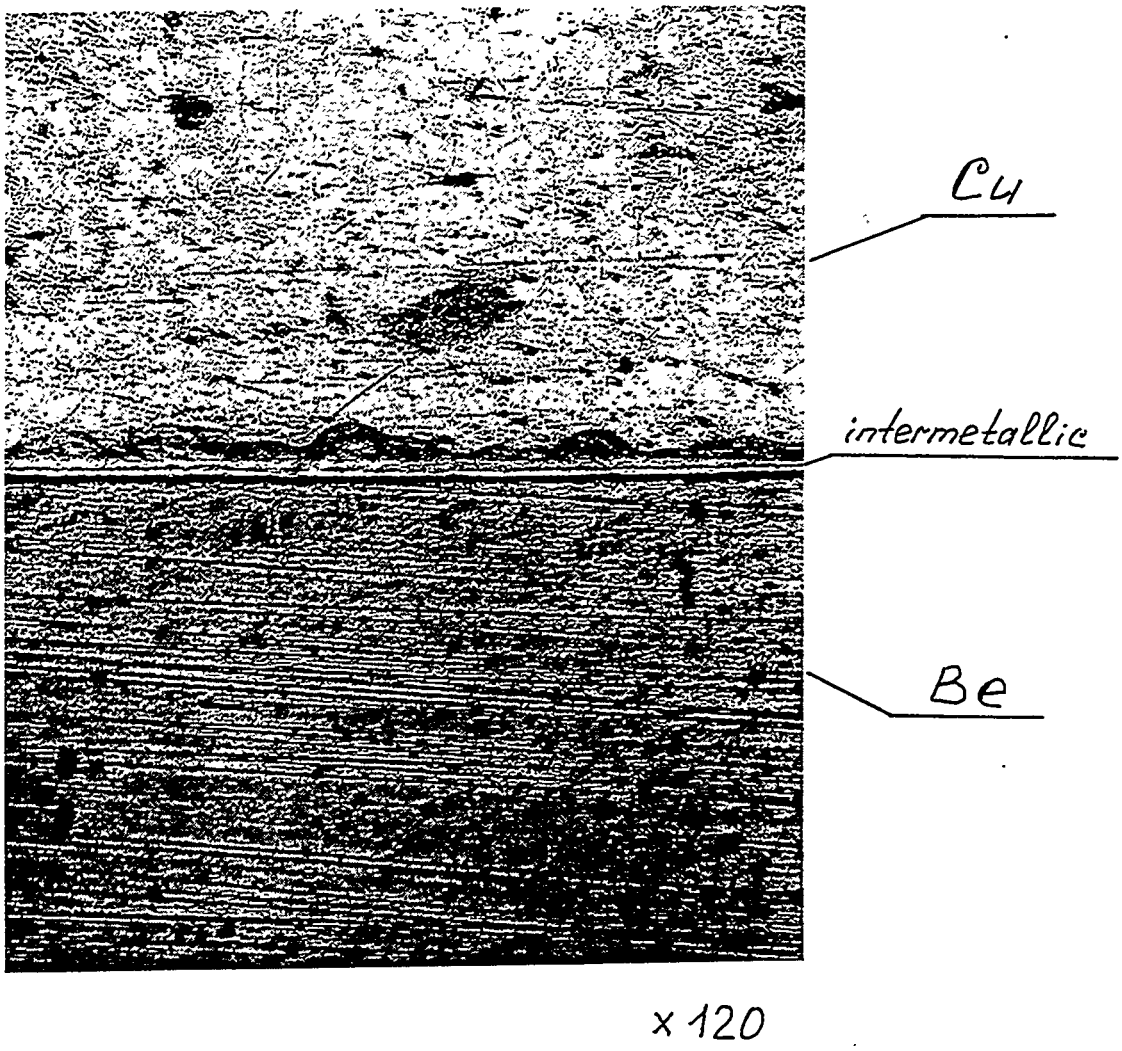

Fig. 6 **Cross-section of diffusion bonded Be/Cu joint**

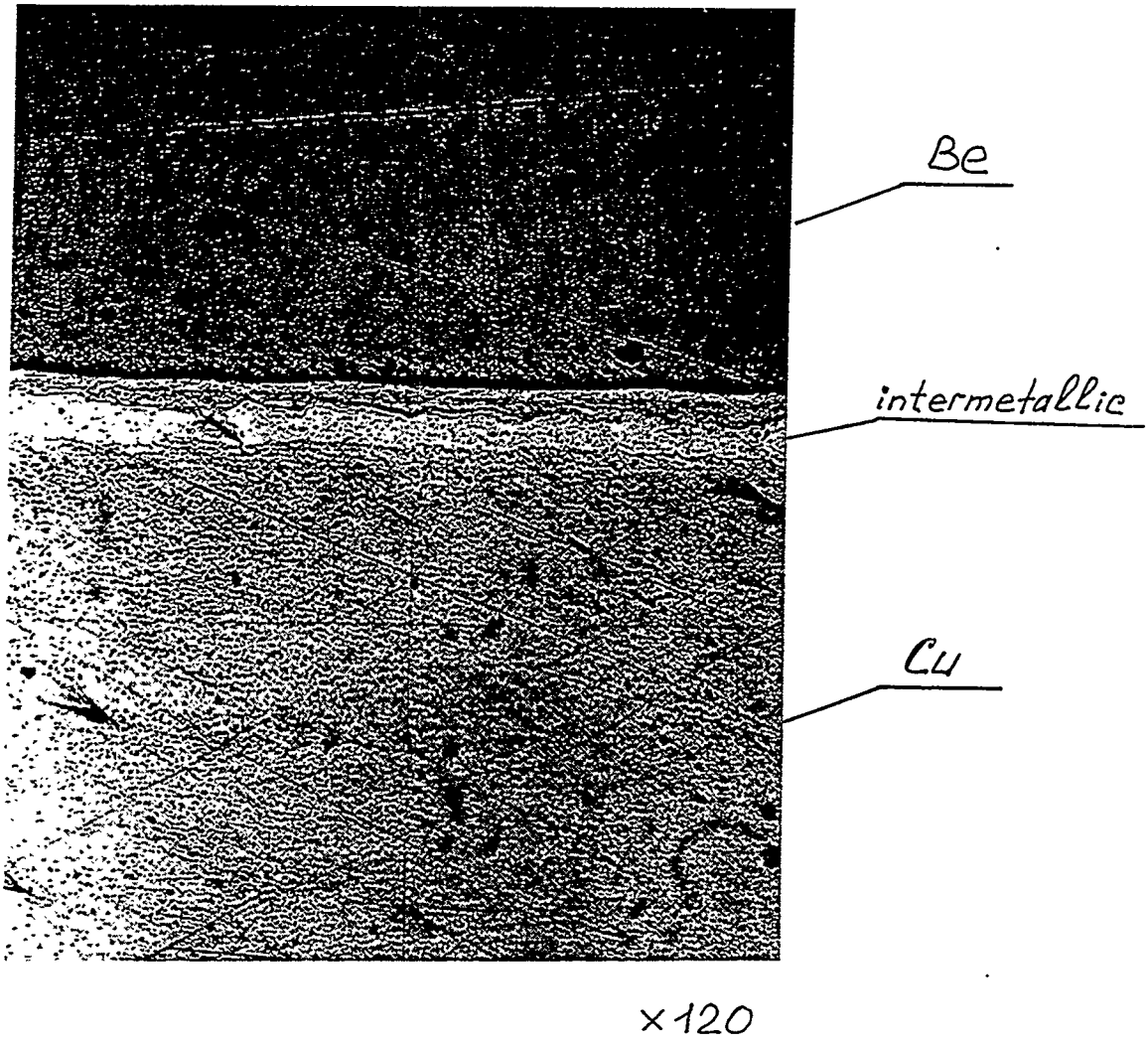

Fig. 7 Cross-section of joint-rolled Be/Cu joint

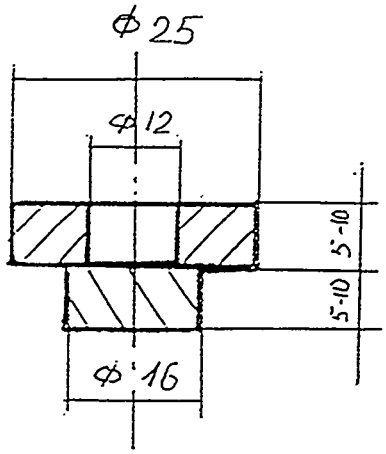

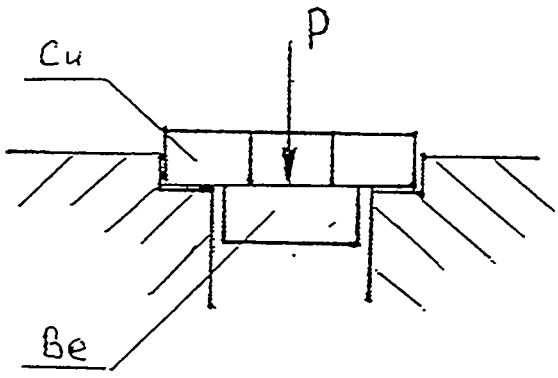

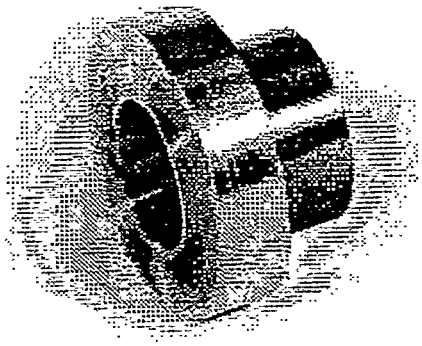

Fig. 8 Sample for tensile testing of Be/Cu joints

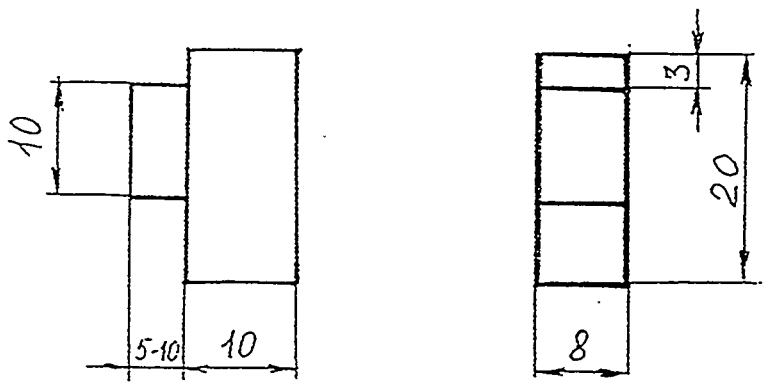

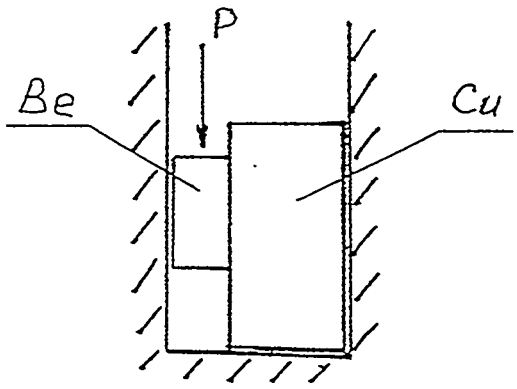

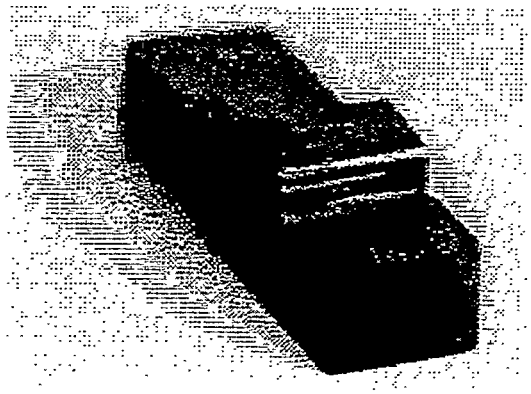

Fig. 9 Sample for shear testing of Be/Cu joints

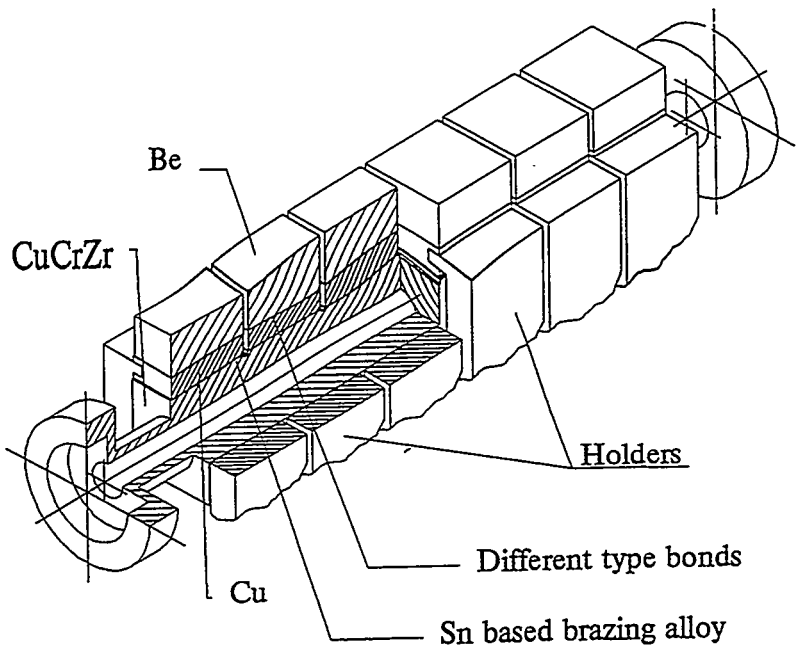

Fig. 10 Mock-up for comparative HHF testing of different Be/Cu joints

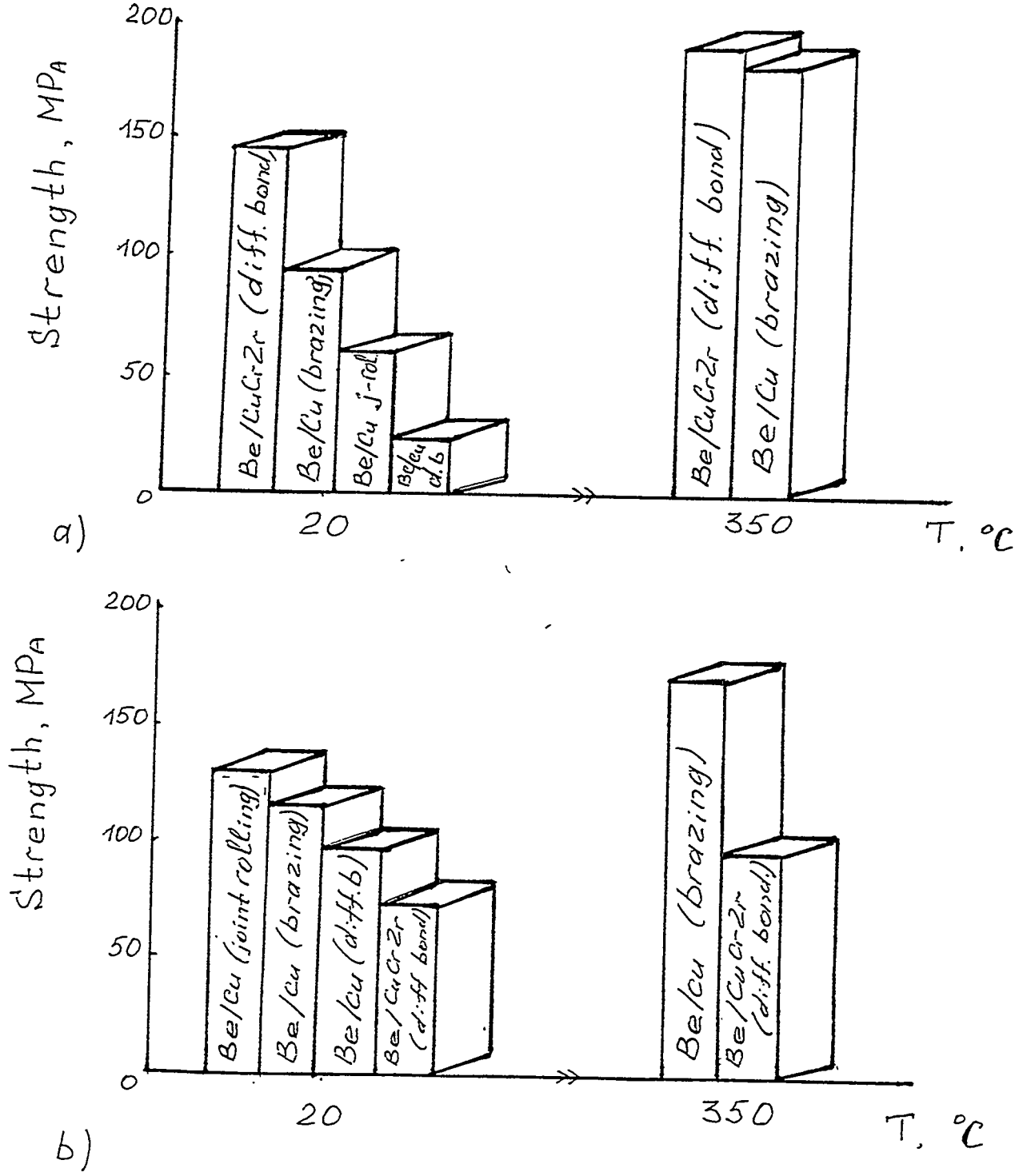

Fig.11 **Tensile (a) and shear (b) strength results for different types of Be/Cu joints**

Methods of joining	Surface preparation	Joining parameters	Dimensions of Be/Cu plates	Comments
Brazing (Ag-based brazing alloy)	Cleaning and etching	Ag-based brazing alloy (Ag=63%, In=1-2%) vacuum brazing at T=760°C	Several plates (50 x 100 x thickness)	"Cd experiment" to test Ag transmutation to Cd concerns
Diffusion bonding	Cleaning and etching	T=720°C P~up to plastic deformation in Cu appearance t=300-400 seconds	Several pieces (30 x 40 x thickness)	Partial warpage of Be/Cu bonded surface
Joint-rolling	Cleaning and etching	T=800°C thickness reduction ~30%	Several strips (30 x 100 x thickness)	Successful attempt of bending
Explosion welding	Cleaning and etching	T=700°C Ar atmosphere	Several plates	Collection of cracks in Be
HIP	Cleaning and etching	T=820°C P=145 MPa t=3600 seconds	Two tube samples	Samples remained intact trough bending attempts

Table I. **Russian Be/Cu joining techniques**

#	Bonded materials	Method of joining	Testing temp. °C	Tensile strength MPa	Damage zone	Comments
1	Be/Cu	Brazing	20	81	through brazing alloy	brittle fracture
2	Be/Cu	Brazing	20	103	through brazing alloy	brittle fracture
3	Be/Cu	Brazing	350	125	through brazing alloy	mainly brittle fracture
4	Be/Cu	Brazing	350	212	through Cu	ductile failure of Cu
5	Be/CuCrZr	Diff. bonding	20	188	through Be	brittle fracture
6	Be/CuCrZr	Diff. bonding	20	103	through Be	brittle fracture
7	Be/CuCrZr	Diff. bonding	350	191	through Be	brittle fracture
8	Be/Cu	Diff. bonding	20	-		was failed after machining
9	Be/Cu	Diff. bonding	20	-		was failed after machining
10	Be/Cu	Diff. bonding	20	21	through Be/Cu bond line	brittle fracture
11	Be/Cu	Joint rolling	20	53	through Be/Cu bond line	brittle fracture
12	Be/Cu	Joint rolling	20	70	through Be/Cu bond line	brittle fracture

Table II. **Results of Tensile Testing of Be/Cu Samples**

#	Bonded materials	Method of joining	Testing temp. °C	Shear srength MPa	Zone of destroying	Comments
1	Be/Cu	Brazing	20	72	through brazing alloy	brittle fracture
2	Be/Cu	Brazing	20	123	through brazing alloy	brittle fracture
3	Be/Cu	Brazing	350	126	through Cu	ductile failure of Cu
4	Be/Cu	Brazing	350	213	through Cu	ductile failure of Cu
5	Be/CuCrZr	Diff. bonding	20	43	through Be	crack in Be
6	Be/CuCrZr	Diff. bonding	20	103	through Be	crack in Be
7	Be/CuCrZr	Diff. bonding	350	107	through Be/Cu bond line	brittle fracture
8	Be/CuCrZr	Diff. bonding	350	82	through Be/Cu bond line	was failed after machining
9	Be/Cu	Diff. bonding	20	75	through Be/Cu bond line	was failed after machining
10	Be/Cu	Diff. bonding	20	152	through Be/Cu bond line	brittle fracture
11	Be/Cu	Joint rolling	20	1233	through intermetallic	brittle fracture
12	Be/Cu	Joint rolling	20	141	through Cu	ductile failure of Cu

Table III. **Results of Shear Testing of Be/Cu Samples**

Preliminary characterization of interlayer for Be / Cu functionally gradient materials

- Thermophysical properties of Be / Cu sintered compacts -

N.Sakamoto and H.Kawamura

Japan Atomic Energy Research Institute, Oarai Research Establishment, Oarai-machi, Higashi Ibaraki-gun, Ibaraki-ken 311-13, Japan

ABSTRACT

At present, beryllium is under consideration as a main candidate material for plasma facing components of ITER, because of its many advantages such as low Z, high thermal conductivity, low tritium retention, low activation and so on . Among the different divertor design options, the duplex structure where the beryllium armor is bonded with heat sink structural materials (DS-copper, Cu-Cr-Zr and so on) is under consideration. And plasma facing components will be exposed to high heat load and high neutron flux generated by the plasma. Therefore, it is necessary to develop the reliable bonding technologies between beryllium and heat sink structural materials in order to fabricate plasma facing components which can resist those. Then, we started the bonding technology development of beryllium and copper alloy with FGM (functional gradient material) in order to reduce thermal stress due to the difference of thermal expansion between beryllium and copper alloy.

As the interlayers for FGM, eleven kinds of sintered compacts in which the mixing ratio of beryllium powder and oxygen free copper powder is different, were fabricated by the hot press / HIP method. The dimension of each compact is 8mm in diameter, 2mm in thickness. Then, thermal diffusivity and specific heat of these compacts were measured by laser flash method, and thermal conductivity was calculated from those values.

From metalographical observation, it became clear that the sintered compacts of mixture of beryllium powder and copper powder contain residual beryllium, copper and two kinds of intermetallic compounds, $Be_2Cu(\delta)$ and $BeCu(\gamma)$. From the results of thermal characterization, thermal diffusivity of interlayers increased with increase of copper containing ratio. And, specific heat gradually decreased with increase of copper containing ratio. Then, the thermal conductivity of main sintered compact at 400°C calculated from those values is shown as follows, ~100W/m/K in pure Be compact, ~170W/m/K in Be10%-Cu90% compact and ~230W/m/K in pure Cu compact.

1. Introduction

At present, beryllium is under consideration as a main candidate material for plasma facing components of ITER, because of its many advantages such as low Z[1], high thermal conductivity, low tritium retention, low activation and so on. Among the different divertor design options, the duplex structure where the beryllium armor is bonded with heat sink structural materials (DS-copper, Cu-Cr-Zr and so on) is under consideration. And plasma facing components will be exposed to high heat load[2] and high energy particles generated by the plasma. Therefore, it is necessary to develop the reliable bonding technologies between beryllium and heat sink structural materials in order to fabricate plasma facing components which can resist those. Then, we started the bonding technology development of beryllium and copper alloy with FGM (functional gradient material) to reduce thermal stress due to the difference of thermal expansion between beryllium and copper alloy. Concept of divertor mock-up using FGM is shown in Fig.1.

As the interlayers for FGM, eleven kinds of sintered compacts in which the mixing ratio of beryllium powder and oxygen free copper powder is different, were fabricated by the hot press / HIP method. The dimension of each compact is 8mm in diameter, 2mm in thickness. Then, thermal diffusivity and specific heat of these compacts were measured by laser flash method, and thermal conductivity was calculated from those values.

2. EXPERIMENTS

2.1 SPECIMENS

As the interlayers for FGM, eleven kinds of sintered compacts in which the mixing ratio of beryllium powder and oxygen free copper powder is different, were fabricated by the hot press / HIP method. Detailed manufacturing method of Be/Cu sintered compacts is shown in Fig.2. At first, beryllium powder and oxygen free copper powder were mixed by mechanical mixing process, and mixture powder was sintered with hot press and hot isostatic press methods. Then, sintered blocks was cutting to disk shape. Mixture matrix of those powder was shown in Fig.2. The dimension of each compact is 8mm in diameter, 2mm in thickness. These sintered compacts were made by NGK INSULATORS, LTD..

2.2 PROCEDURE

In this study, thermal diffusivity and specific heat of these compacts were measured by laser flash method, and thermal conductivity was calculated from those values in order to characterize them as interlayers of joined components between beryllium and copper alloy used in the divertor components. The concept of measurement equipment is shown in Fig.3.

3.RESULTS AND DISCUSSION

At first, as the results of metalographical observation, it became clear that the sintered compacts of mixture of beryllium powder and copper powder contain residual beryllium, copper and two kinds of intermetallic compounds, $Be_2Cu(\delta)$ and $BeCu(\gamma)$. SEM image on a 50at.%Be-50at.%Cu compact is shown in Fig.4 for one example.

The results of measurement on thrmal diffusivity and specific heat of interlayers, and of thrmal conductivity with caluculation from those values are shown in Fig. 5, 6 and 7. From these results, it appeared that thermal diffusivity of interlayers increased with increase of copper containing ratio. And, specific heat gradually decreased with increase of copper containing ratio. And the tendency on thermal conductivity was similer to thrmal diffusivity. Particularly, thermal conductivity on interlayers which contains above 50at.%Cu is higher than 100at.%Be. Therfore, these interlayers have advantage to apprication as FGM interlayers.

4. Conclusions

In this study, thermal diffusivity and specific heat of these compacts were measured by laser flash method, and thermal conductivity was calculated from those values in order to characterize them as interlayers of joined components between beryllium and copper alloy used in the divertor components. The obtained results are as follows.

--From metalographical observation, it became clear that the sintered compacts of mixture of beryllium powder and copper powder contain residual beryllium, copper and two kinds of intermetallic compounds, $Be_2Cu(\delta)$ and $BeCu(\gamma)$.

--From the results of thermal characterization, thermal diffusivity of interlayers increased with increase of copper containing ratio. And, specific heat gradually decreased with increase of copper containing ratio.

From these results, thermal designs of Be/Cu alloy joined compacts using Be/Cu sintered compacts as FGM interlayer became possible.

Presently, thermal expansion tests will be performed in order to estimate thermal stress at joining interface.

REFERENCE

[1]D.W.Doll et al., J.Nucl.Mater.,85&86(1979)191.
[2] K. Nakamura, et al., J. Nucl. Mater. 212-215(1994)1201.

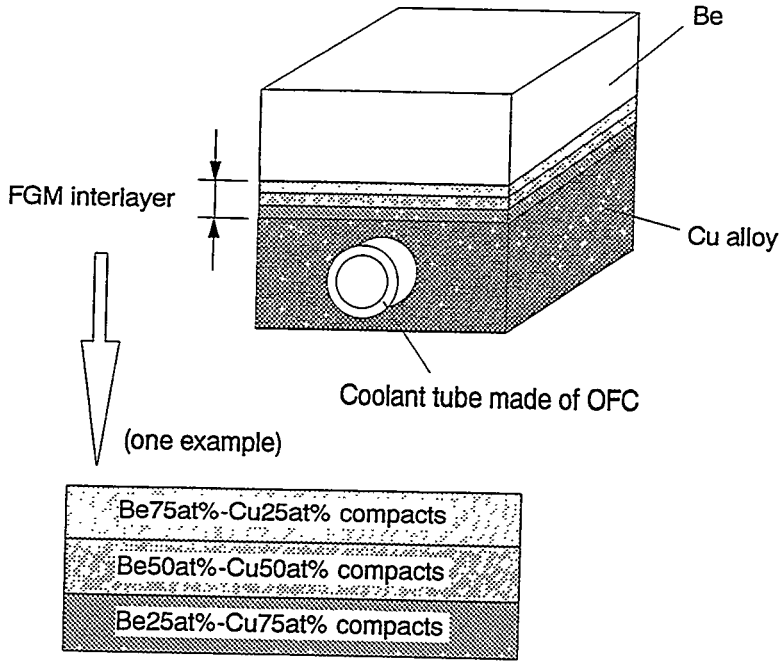

Fig. 1 Concept of divertor mock-up using FGM .

＊1 : Mixture matrix (at%)

	1	2	3	4	5	6	7	8	9	10	11
Be	100	90	80	70	60	50	40	30	20	10	0
Cu	0	10	20	30	40	50	60	70	80	90	100

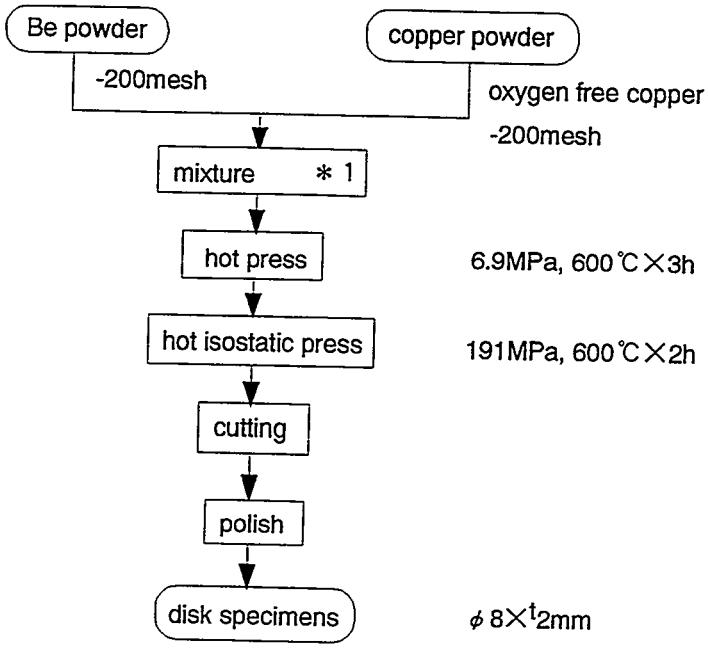

Fig. 2 Manufacturing method of Be/Cu sintered compacts.

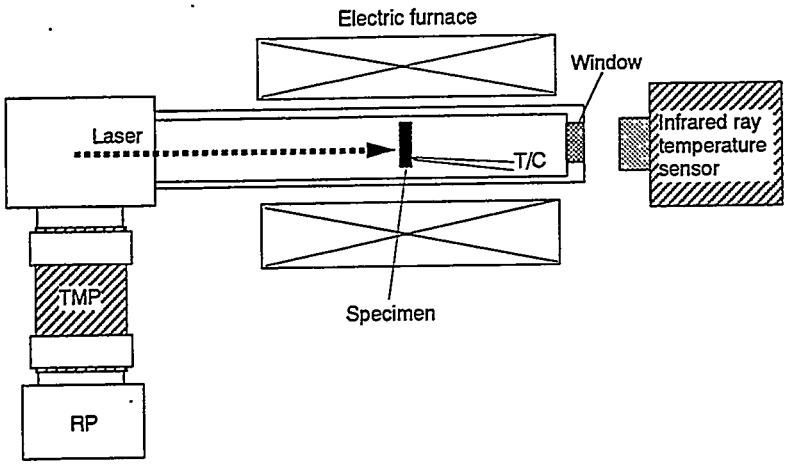

Fig. 3 Measurement method on thermophysical properties.

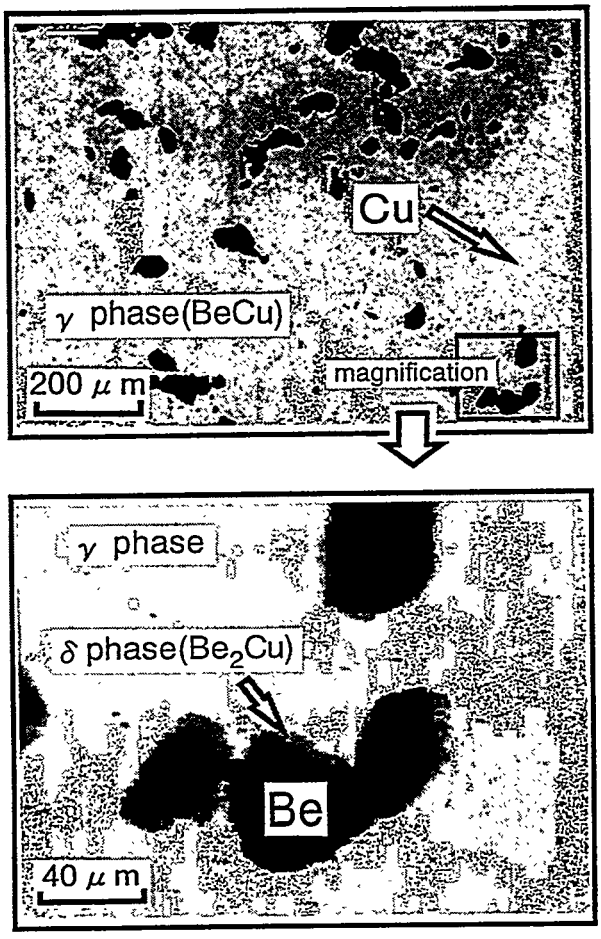

Fig. 4 SEM photograph of 5 at%Be-50at%Cu compact.

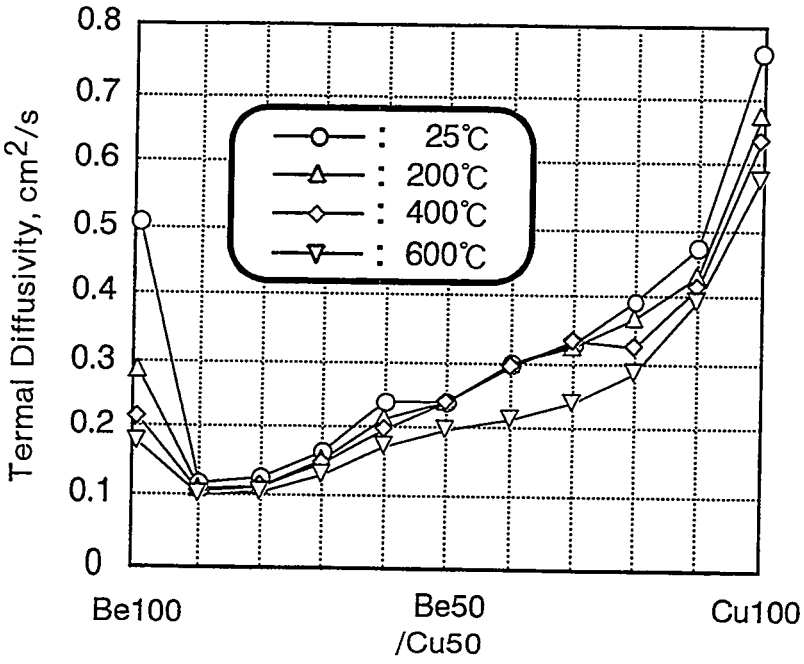

Fig. 5 Thermal diffusivity of Be/Cu sinterd compacts.

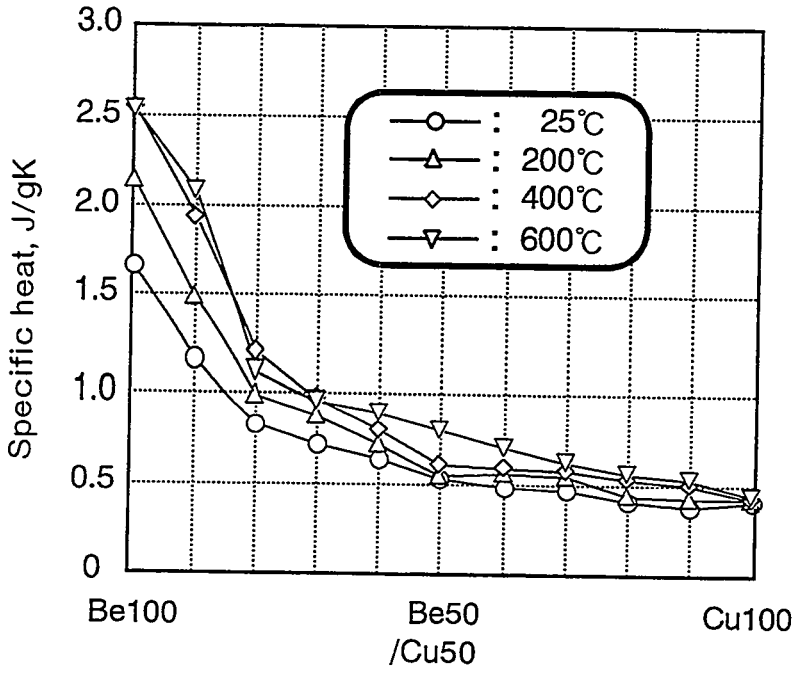

Fig. 6 Specific heat of Be/Cu sinterd compacts.

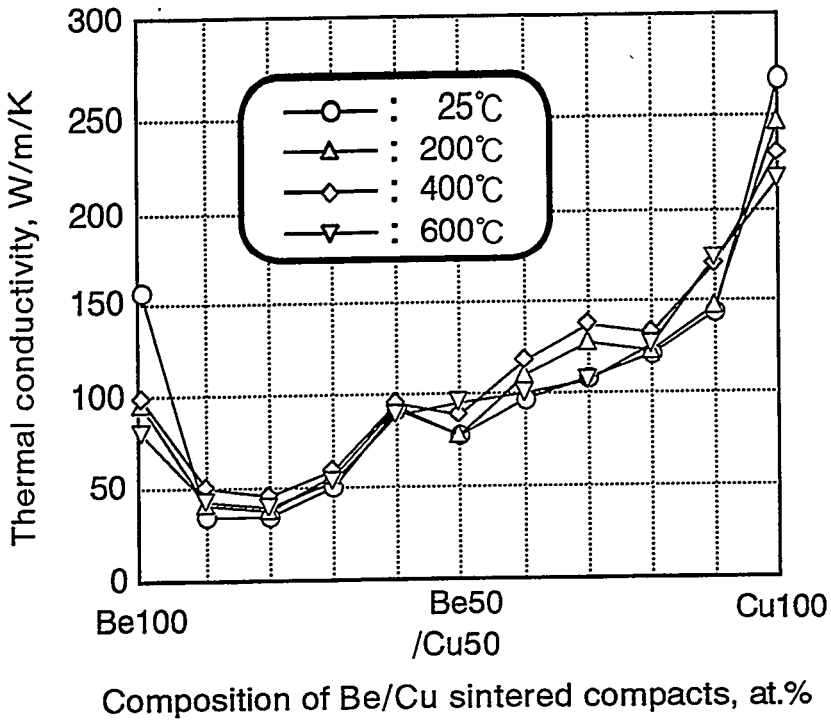

Fig. 7 Thermal conductivity of Be/Cu sinterd compacts.

MANUFACTURING AND THERMOMECHANICAL TESTING OF ACTIVELY COOLED ALL BERYLLIUM HIGH HEAT FLUX TEST PIECES

N.N.Vasiliev, Yu.A.Sokolov, G.E.Shatalov, A.G.Zimelev
(Kurchatov Institute),
Yu.Ya. Kurochkin ("KOMPOZIT"),
J.M.Bezmozgy, A.G.Chernjagin ("ENERGIA").

1. Introduction.

One of the problems affiliated to ITER high heat flux elements development is a problem of interface of beryllium protection with heat sink routinely made of copper alloys. To get rid of this problem all beryllium elements could be used as heat receivers in places of enhanced thermal loads. In accordance with this objectives four beryllium test pieces of two types have been manufactured in "Institute of Beryllium" for succeeding thermomechanical testing. Two of them were manufactured in accordance with JET team design (fig. 1); they are round "hypervapotron type" test pieces. Another two ones are rectangular test sections with a twisted tape installed inside of the circular channel (fig. 2). Preliminary stress-strain analysis have been performed for both type of the test pieces. Hypervapotrons have been shipped to JET where they were tested on JET test bed [1]. Thermomechanical testing of pieces of the type of "swirl tape inside of tube" have been performed on Kurchatov Institute test bed.

Chosen beryllium grade properties, some details of manufacturing, results of preliminary stress-strain analysis and ther-

momechanical testing of the test pieces "swirl tape inside of tube" type are given in this report.

2. Some properties of DShP-56 beryllium.

Distilled DShP-56 metal-ceramic beryllium grade was chosen as material of the test pieces.

Table 1. *Chemical composition of DShP-56 beryllium grade (weight percent)*

Fe	Al	Si	Ti	Mg	Mn	Cu	C	O	Ni
0.045	0.004	0.008	0.036	0.005	0.003	0.002	0.088	1.1	0.004

Table 2. *Assured mechanical properties of DShP-56*

	RT	100°C	200°C	300°C	400°C	500°C	600°C
E, GPa	298	298	298	289	~280	~270	~250
σ_Y,MPa	269	258	218	186	163	146	100
σ_u,MPa	425	402	320	269	235	194	125
δ_5, %	3.8	8.2	25.7	39.6	38.8	21.4	22.0
ψ, %	5.6	11.5	36.4	61.8	62.9	57.0	35.1

Fatigue Characteristics Of Metal-Ceramic Beryllium TshP-56

σ_a(RT): 160 MPa (smooth specimen);
110 (specimen with ring notch).

3. Some features of manufacturing

3.1. Work pieces actually used: beryllium tubes.

3.2. Method used for joining of machined details (Be+Be; Be+SS): brazing (silver-copper alloy).

3.3. Special electrochemical treatment was used for elimination of microcraks generated by machining.

3.4. Special coating of 10 μm thickness was deposited on inner surface of the test pieces in order to prevent any interaction beryllium with cooling water.

4. Preliminary Stress Analysis.

4.1.Objective: to assess stresses/strains levels caused by the thermomechanical testing.

4.2. Codes Actually Used Here: COSMOS/M for transient thermal analysis and FEM 3D code "SPRUT" for nonlinear analysis of the stress/strain problem (in steady state approximation).

4.3. Some Results Of The Analysis (test pieces with swirl tapes, steady-state incident heat load of 5 MW/m^2): actual strains (up to 1% at some points) exceed elastic ones very much, that would mean very serious problems in respect to surviving of the hypervapotron in case of cyclic mode of testing.

5. Testing.

5.1. Beryllium compatible test bed "SPRUT-2" was used for the thermomechanical testings of the test pieces. *"SPRUT-2"* is a device with plasma discharge supported by electron beam. During the testings only electron beam was used as source of surface heat load.

Main parameters of the electron beam gun of the *"SPRUT-2"* device:

- electron beam current — up to 2A;
- acceleration voltage — up to 10kV;
- cooling of test piece — by distilled water, $p \leq 0.6$ Mpa, $G \leq 2$ kg/s;

The test bed is located at RRC "Kurchatov Institute".

5.2. Instrumentation. Acoustic emission method was used for monitoring of the test pieces integrity as well as detection of start of boiling of cooling water during the testing processes. Because previously there were no experience to use such system for beryllium destroying some calibrating experiments were performed with beryllium samples. Besides that, parameters of cooling water (pressure and temperatures, flow rate) was monitored also. Power parameters of electron beam gun have been determined beforehand and were controlled during experiments.

5.3. Modes of the testing performance. Following modes of experiments were performed during the testing:

- smooth increasing (during ~ 100 s) of thermal load up to nominal level of 5 MW/m^2 with following its abrupt;
- smooth increasing (during ~ 100s) of thermal load up to nominal level of 5 MW/m^2; steady-state regime during 300 s; abrupt of the thermal load.

- cyclic mode of loading (10 cycles): thermal load increasing up to nominal level during 6s; steady-state regime upon nominal level of thermal load during 20 s; abrupt of the thermal load during 7 s; dwell time between cycles was 30s;

- 101 cycles with parameters the same as in previously item.

6. Results of the testing.

Main result of the testing is that no any symptoms of the test piece disintegration were observed.

7. CONCLUSION.

In our opinion a rather important result of the studying is that experience of using of acoustic emission method for diagnostic of integrity of HHF test piece during testing was obtained. It could be not excluded that such experience will be useful for designers of ITER plasma facing components. Sensors can receive information concerning conditions of beryllium protection of PFC through acoustic wave gides and be located far away from places with high level of radiation (on back plate for example). Such investigations could be performed using "SPRUT-2" test bed more carefully if it would be interesting for ITER designers.

8. Reference.

[1]. H.D.Falter, D.Ciric, E.B.Deksnis et. al. Test Report: Actively cooled Beryllium Vapotron. JET-TN(94)), 1994.

9. List of Pictures.

Fig. 1. Hypervapotron (JET design).

Fig. 2. Test piece with swirl tape.

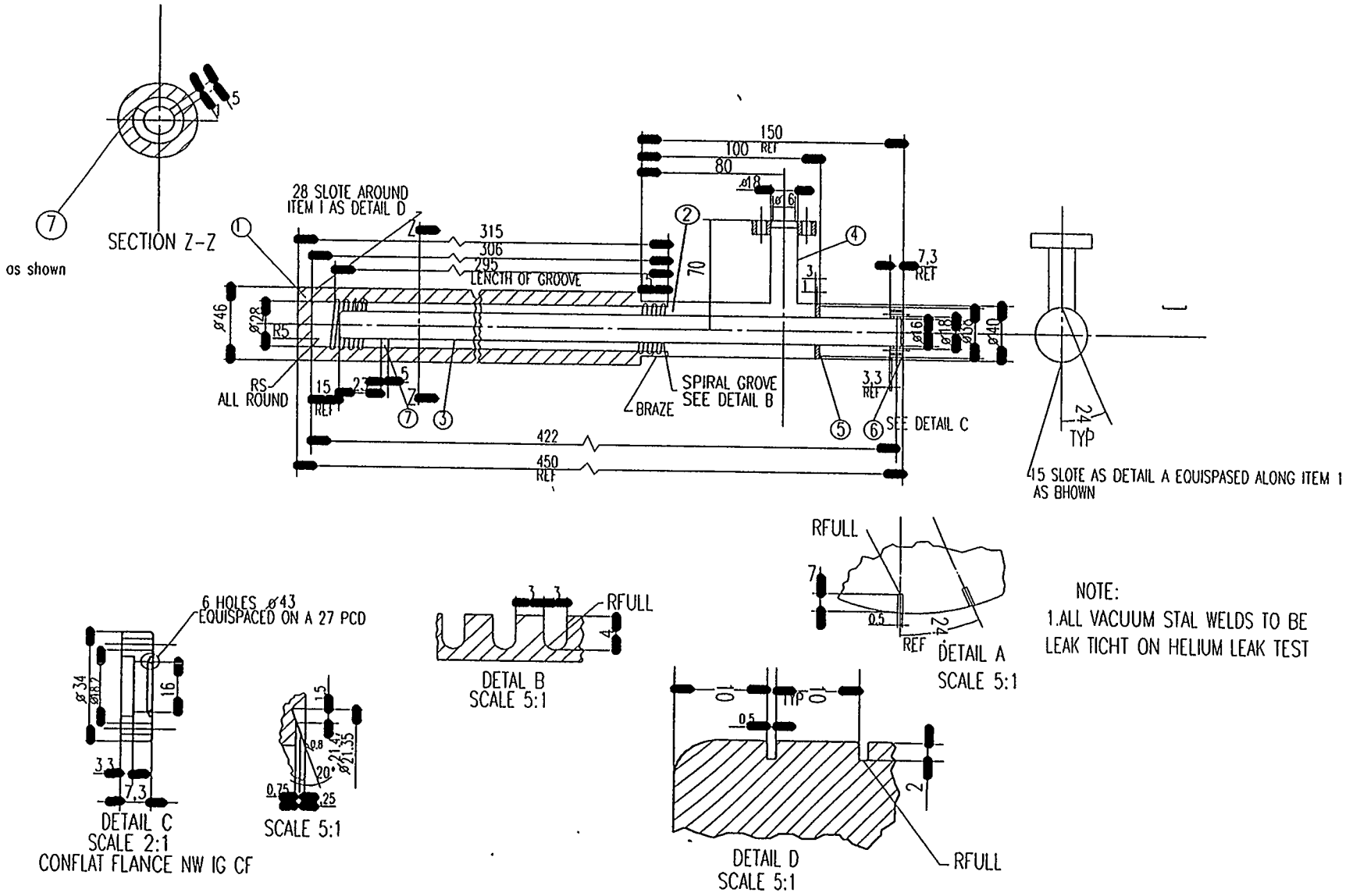
SECTION Z-Z
os shown
28 SLOTE AROUND ITEM 1 AS DETAIL D
315
306
295
LENGTH OF GROOVE
150
100 REF
80
70
7.3 REF
RS ALL ROUND
SPIRAL GROVE SEE DETAIL B
BRAZE
SEE DETAIL C
422
450 REF
TYP
15 SLOTE AS DETAIL A EQUISPASED ALONG ITEM 1 AS BHOWN
6 HOLES ø43 EQUISPACED ON A 27 PCD
DETAIL C
SCALE 2:1
CONFLAT FLANCE NW IG CF
SCALE 5:1
RFULL
DETAL B
SCALE 5:1
DETAIL A
SCALE 5:1
DETAIL D
SCALE 5:1
NOTE:
1.ALL VACUUM STAL WELDS TO BE LEAK TICHT ON HELIUM LEAK TEST

70
5Δ1
450
72
Ø36
0.5
0.5
10
0.5
5
10
0.5
□40

ATTENDEES

Organization	Name	E-Mail	Fax
Argonne National Laboratory ET/Bldg 212 9700 Cass Avenue Argonne, I L 60439	Billone, Michael C.	mike_billone@qmgate.anl.gov	708-252-4798
ASRIIM 5 Rogov Street, Box 369 123060 Moscow Russian Federation	Kuprianov, I. B.	postmaster@VNIINM402.msk.su	7-095-925-5972 7-095-925-2896
Battelle Pacific Northwest Laboratory Richland, WA	Baldwin, David L	dl_baldwin@pnl.gov	509-367-1279
Brush Wellman Inc. 17876 St. Clair Ave. Cleveland, OH 44110	Dombrowski, Dave M.	None	216-481-5480
CEA Cadarache 13108 St. Paul Lez Durance France	Boisset, Laurence	boisset@MACADAM.cea.fr	33-4225-7287
Efremov Reseach Institute P. O. Box 42 189631 St. Petersburg Russian Federation	Mazul, Igor Gervash, Alexander Guiniatouline, R. E.	mazul@al4.niiefa.spb.su gerv@al4.niiefa.spb.su grn@al4.niiefa. spb.su	812-314-33-60 812-314-33-60 812-314-33-60
Forschungszentrum Juelich GmbH IWE-1 D-52425 Juelich, Germany	Linke, Jochen M. Roedig, Manfred	j.linke@kfa-juelich.de m.roedig@kfa-juelich.de	49-2461-613699 49-2461-616464
Idaho National Engineering Laboratory P. O. Box 1625 Idaho Falls, ID 83415	Longhurst, Glen R. Smolik, Galen R.	gxl@inel.gov grsl@inel.gov	208-526-0528 208-526-0690
Institute Beryllium SIA "Komposit" Kaliningrad City 141070 Pionerskaya Moscow Region Russian Federation	Kurochkin, Yu. Ya. Sizenev, Victor. Vygovskij, Yevgenij		7-095-512-4934 7-095-230-7404

Organization	Name	E-Mail	Fax
Institut fur Neutronenphysik und Reaktortechnik Postfach 3640 D-76021 Karlsruhe Germany	Dalle Donne, Mario Scaffidi-Argentina, Francesco	inr0d9@ucla.hdi.kfk.d400.de inr0d9@ucla.hdi.kfk.d400.de	49-7247-824874 49-7247-824874
Institue of Physical Chemistry Russian Academy of Sciences Leninsky Prospekt 31 117915 Moscow Russian Federation	Chernikov, Vladimir. N.	zakharov@surface.phyche.msk.su	7 095 335-17-78
ITER Garching Joint Work Site Boltzmannstrasse 2 85748 Garching Germany	Barabash, Vladimir Tanaka, Shigeru	barabav@sat.ipp-garching.mpg.de tanakas@sat.ipp-garching.mpg.de	49-89-3299-4163 49-89-3299-4163
JAERI Oarai Research Establishment Oarai-Machi, Higashi Ibaraki-Gun Ibaraki-Ken 311-13 Japan	Kawamura, Hiroshi Ishitsuka, Etsuo Sakamoto, N.	kawamura@vax001.naka.jaeri.go.jp	81-292-64-8480 81-292-64-8480 81-292-64-8480
JET Joint Undertaking Abbingdon, Oxfordshire OX14 4DD U. K	Deksnis, Ed B. Pick, Michael A.	ebd@jet.uk map@jet.uk	44 1235 465373 44 1235-465373
K-Tech International 7000 SW Hampton St. Suite 101Portland, OR 97223	Howard, Charles	p00143@psilink.com	503-624-0735
Institute of Nuclar Fusion Russian Research Center Kurchatov Institute Kurchatov Sq. 46 123182 Moscow Russian Federation	Kolbasov, Boris N. Kurochkin, Yu. Ya Vasiliev, N. N.	vasiliev@qq.nfi.kiae.su vasiliev@qq.nfi.kiae.su vasiliev@qq.nfi.kiae.su	095-943-00-73 095-943-00-73 095-943-00-73
Lawrence Livermore National Laboratory	Hanafee, James.E.	hanafee1@llnl.gov	510-422-0049
Chemistry & Materials Science Department P.O. Box 808, L-352 Livermore, CA 94550	Torres, Sharon. G.	torres4@llnl.gov	510-422-0049

Organization	Name	E-Mail	Fax
Los Alamos National Laboratory P.O. Box 1633, MS-G770 Los Alamos, NM 87545	Abeln, Steve Castro, Richard G. Jacobson, Loren A Stanek, Paul	abeln@lanl.gov rcastro@lanl.gov jake@mustang.mst6.lanl.gov pstanek@lanl.gov	505-667-5268 505-667-5268 505-667-5151 505-667-5268
Manufacturing Sciences Corporation Rocky Flats, CO	Floyd, Dennis	None	303-233-2993 303-9665731
McDonnel Douglas Aerospace MC 106 7211 P.O. Box 516 St. Louis, MO 63166	Davis, John W.	davis@lllsrv.mdc.com	314-234-4506
Minatom Office of Fusion Energy Moscow, Russian Federation	Korzhavin, Victor M.	vas@itef.msk.su	7-095-239-22-38
Naval Air Warfare Center Code 4342 - MS08 Warminster, PA 18974	London, Gil	None	215-441-1773
NGK Metals Corporation P. O. Box 13367 Reading, PA 19612-3367	Lilley, Eugene A.		610-921-5358
Sandia National Laboratory P.O. Box 5800, MS-1129 Albuquerque, NM 87185-1129	Odegard, Ben Watson, Robert D.	odegard@ca.sandia.gov rdwatson@pmtf.sandia.gov	510-294-3410 505-845-3130
SRIETP of Kazakh State University	Shestakov, V.	itervova@ietp.alma-ata.su	7-327-2-50-62-88
Versuchtechnik Indertasch 4a 76277 Karlsruhe, Germany	Goraieb, Ancieto A.	None	49-7247-2-25-13

AUTHOR INDEX

2ND IEA INTERNATIONAL WORKSHOP ON
BERYLLIUM TECHNOLOGY FOR FUSION

September 6-9, 1995, Jackson Lake Lodge, Wyoming, USA

The attached material was presented at the 2nd IEA International Workshop on Beryllium Technology for Fusion, but due to technical difficulties, it was not available in time for inclusion in the report of the proceedings. It is furnished separately as an addendum.

Operational Aspects of Using Beryllium - Safety and Decontamination

M. A. Pick and A. D. Haigh

JET Joint Undertaking, Abingdon, OX14 3EA, UK

Abstract

After more than six years of operational experience working and handling beryllium, JET is now in a position to work efficiently and easily with the imposed procedural, organisational and facility-wise requirements associated with the large scale use of beryllium. It is, however, clear that the use of beryllium requires a large additional commitment both in the form of additional facilities as well as man-power, ultimately leading up to a substantial additional financial burden. This paper outlines this additional effort and what impact it has on the design, operation and maintenance of a large scale machine such as JET or ITER.

1. Introduction

As beryllium and most of its compounds are considered toxic, their use is governed by a number of statutory instruments, regulations and recommendations. These are associated with the control of the work place; storage; control of discharges; personal protection of the work force; medical supervision of the work force; reporting of injuries, diseases and occurrences; classification, packaging, labelling and shipment; insurance. Many of these requirements are to be seen simply as additions to those regulations already implemented in an industrial site such as JET. JET, as any future large fusion machine site, already implements the requirements associated with the Ionising Radiation Regulations due to the induced radiation and the use of tritium. Although there are differences in the regulations throughout the countries of the world, the example of JET and the impact the use of beryllium has had there, serves as a good example. The requirements will differ only slightly were the experiment to be sited elsewhere. The application of the appropriate regulations brings with it the setting up of a variety of facilities, installations and procedures. It is these areas which will be discussed in some detail below.

2. Implementation of Regulations

2.1 General

At JET the implications and recommendations have been formulated in an internal document entitled: Code of Practice for the Safe Use of Beryllium at the JET Laboratory (1).

According to the Code of Practice beryllium should be manipulated in enclosed areas only. Where this is not possible, a local exhaust ventilation system equipped with filtration of a specified high standard is provided for processes likely to generate dust or fumes. Areas in which beryllium is manipulated are clearly marked as **Beryllium Controlled Areas** and access to these areas is strictly controlled. There are large Beryllium Controlled Areas at JET where routine work is performed on beryllium or beryllium contaminated equipment. If beryllium is manipulated in an area not normally designated a Beryllium Controlled Area then a temporary Beryllium Controlled Area is established. Local Rules to regulate work activities, personnel entry, exit and discipline, are associated with each of the Beryllium Controlled Areas. All the possible hazards associated with each separately identifiable job, normally laid down in the form of an Assembly Procedure, are assessed by way of a Safety Assessment which is circulated to a series of prescribed Safety Assessors and attached to the Procedure.

Any person expected to manipulate beryllium at JET must become a Beryllium Worker. To obtain that designation the person must undergo a full medical examination and be declared medically fit for beryllium work. He must attend an induction course in beryllium safety at JET and be trained in the use of all applicable safety equipment including being trained to operate in a full pressurised suit.

2.2 Exposure Limits and Standards

The principal risk associated with the use of beryllium is the inhalation of dust or fumes. These may be generated by processes in which beryllium is manipulated or they may be re-suspended from contaminated surfaces. For these reasons limits have been set on the airborne dust concentration and the surface concentration of 2 mg m^{-3} and 100 mg m^{-2} respectively. This airborne dust concentration limit was first adopted by the American Atomic Energy Commission in 1949 and is recognised throughout the European Union and other western countries. These are the Occupational Exposure Limits (OEL) in use in the UK (2,3).

In JET a Beryllium Controlled Area (BeCA) is set up whenever a Safety Assessment of a job to be undertaken states that 0.2 mg m^{-3} airborne contamination or 10 mg m^{-2} surface contamination is likely to be reached or exceeded. A Respiratory Protection Zone (RPZ) is established at JET whenever the airborne beryllium concentration is expected to reach or exceed 1mg m^{-3}. No person is allowed into these areas unless they are wearing the type of respiratory protection equipment prescribed by Health Physics. A

Beryllium Controlled Area may be an entire room or the inside of a piece of equipment such as the JET torus itself, a temporary enclosure such as a PVC tent or 'Isolator' or even a barriered off area.

2.3 Monitoring

The monitoring of the above outlined limits on airborne and surface contamination is performed by the Health Physics group.

As there is as yet no reliable and legally accepted form of real-time beryllium monitoring, this is carried out by drawing measured volumes of air through a filter paper over a known period of time and measuring the amount of beryllium on the paper by using an Absorption Spectrometer.

Both routine and special air monitoring programmes are undertaken. The routine samples provide information on the general conditions in all areas and indicate whether the performance of all control procedures and facilities is adequate.

Surfaces are monitored by taking dry smear samples of the surface and determining the amount of beryllium in the smear, as with the airborne beryllium samples.

The chemical analysis work on the samples and the absorption spectrometer are carried out in the **Analysis Laboratory.**

2.4 Personal Protection

When working with beryllium all personnel must wear some degree of personal protection. This ranges from the minimum requirement of disposable coveralls, overshoes and gloves, through a range of intermediate levels of protection using different ori-nasal or respiratory protection, to the maximum protection of a full pressurised suit. The respiratory protection to be used is specified by Health Physics.

All respiratory protection equipment is worn only once. If not of the disposable type this equipment is subsequently cleaned and sanitised. This is done in a specialised **Suit Cleaning Facility.**

2.5 Waste Management

The disposal of solid beryllium waste, solid radioactive waste, mixed waste and the disposal of contaminated liquids is covered by a series of formal JET Waste Management Procedures.

The Environmental Protection Act and the Radioactive Substance Act impose a legal duty on the operator to ensure that waste materials are appropriately classified and disposed of by authorised disposal routes. JET deals with a variety of authoritative bodies including the National Rivers Authority, Her Majesty's Inspectorate of Pollution and the local District Council. JET is periodically inspected by the disposal authorities and final recipients of JET waste, and also makes its own visits to the recipient sites.

Solid beryllium is sent either for controlled burial at an authorised land fill site, or, if radioactive, it is disposed of at the UK national radioactive waste repository in Sellafield, Cumbria. The Waste Management Group collects, sorts, samples, processes and dispatches waste using the JET **Waste Handling Facilities**, Fig 1.

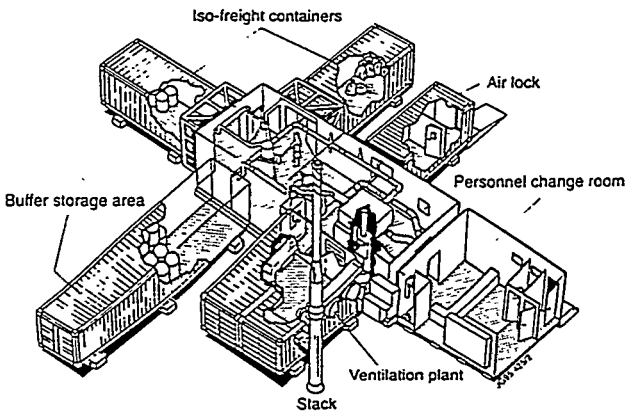

Fig.1: The JET Waste Handling Facility

2.6 Procedures

A very large number of Procedures and Working Rules have been developed which govern all aspects of the work with beryllium. They include, amongst others, the following:

Procurement, Receipt and Issue of Beryllium
Work Permit and Safety Assessment

Packaging, Labelling And Transport of Beryllium
Storage of Beryllium
Beryllium Controlled Areas and Local Rules
Respiratory Protection Zones
Removal of Temporary Enclosures (Isolators and Tents)
Cleaning
Transfer of Materials from Beryllium Controlled Areas
Waste Disposal
Incident Procedures i.e. Accidental Release, Injury, Fire etc.
Radioactive Beryllium

3. Facilities

The following is a list of the main facilities which have been required to be established at JET. The list shows the equipment associated with each of the facilities as well as the number of staff required to man the units during shutdown periods.

3.1 Torus Access Cabin

This Cabin, Fig 2, allows entrance to the JET vessel through the main horizontal port at the 6m level. It contains all the support and communications equipment required for pressurised suits as well as the dressing and washing facilities. It also contains all the services required to enable the in-vessel work.

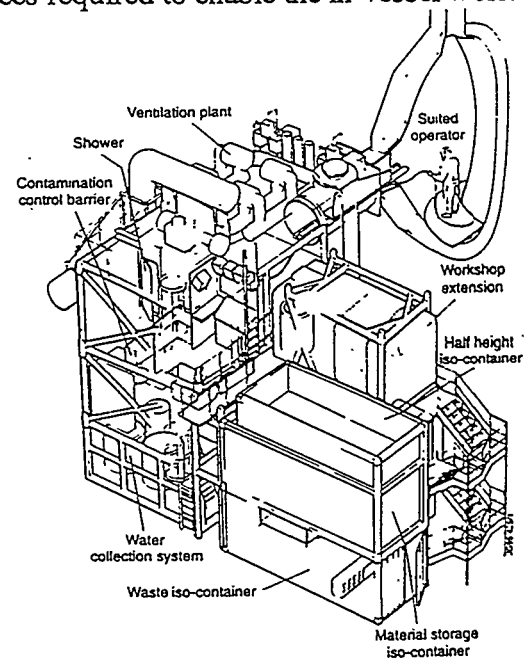

Fig.2: The JET Torus Access Cabin

Equipment:

Contamination control barrier
Ventilation system
Breathing air supply system
Pressurised suit dressing room
Shower
Ex- to in-vessel communications systems - audio\video
JET access and operations box, extensions to storage and workshop areas
In-vessel services -
power distribution
welding power supply
compressed air
water
hydraulics
cryogenic CO_2 blasting
boron carbide water jet grit blasting
Posting facilities
ISO-container docking

Staffing (assuming 2 shift operation):

In-Vessel Operators in suits 12 to15
(3 entrances x 4 or 5)
Engineers/Supervisors 6
Suit support staff 7 to 8

3.2 Boom Access Facility

This facility permits access to the vessel for the boom as well as for personnel at the Octant 5 main horizontal port.

Equipment:

Contamination control barrier
Ventilation system
Breathing air supply system
Pressurised suit dressing room
Shower
Ex- to in-vessel communications systems - audio/ video
JET access and operations area, extensions to storage areas
In-vessel services -
power distribution
welding power supply
compressed air
water
hydraulics
Posting facilities
ISO-container docking

Staffing (assuming 2 shift operation):

In-Vessel Operators in suits 9
(3 entrances x 3)
Remote Handling Boom Operators 4
Suit support staff 7

3.3 Beryllium Handling Facilities

These facilities, Fig 3, are designed to enable decontamination, assembly, inspection and repair work to be performed on components.

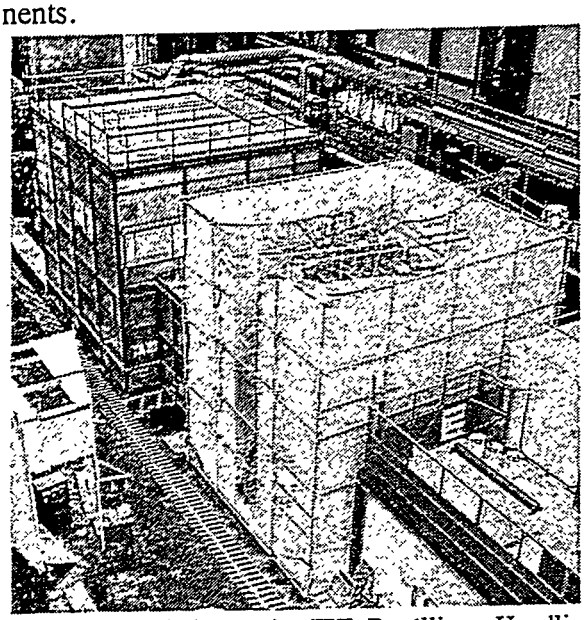

Fig.3: Two of the main JET Beryllium Handling Facilities are shown located in the Assembly Hall of JET. The upper one is a fixed, permanent facility with an in-built 5 m^2 access port in the roof. The lower facility is a temporary facility which is basically a large supported tent. This also permits large components to be entered whilst supported from the roof crane

Equipment:

Contamination control barrier
Ventilation system
Breathing air supply system
Pressurised suit dressing room
Shower
Communications systems - audio/ video
Small beryllium workshops
Decontamination systems -
water wash (high pressure)
boron carbide water jets
ultrasonic cleaning baths
Services -
power distribution
welding power supply
compressed air
water
ISO-container docking
5 m^2 bagging port in roof
Monitored discharge stack

Staffing (assuming 2 shift operation):

Suit support staff 6
Operators in suits 8 (2 x 4)
Non-suited staff 5

3.4 Beryllium Suit Cleaning Facility

This facility is used to clean and disinfect and inspect used pressurised suits and respirators and to keep a stock of clean equipment ready for use in the various facilities. The full stock includes 350 full suits, 80 half suits, 150 respirators and several thousand disposable suits. The throughput of the facility allows 18 to 20 full pressurised suits to be cleaned per day. This is the usual number of suits required for use during a normal working day in the JET vessel.

Equipment:

Contamination control barrier
Ventilation system
External decontamination bath for suits
Internal disinfection bath for suits
Ultrasonic baths for respirators, etc.

Staffing:

Suit cleaning 4
Inspection and issue 3

3.5 Waste Handling Facility

Designed to collect, sort, sample, process, pack and dispatch Be contaminated and radioactive waste, Fig 1.

Equipment:

Contamination control barrier (emergency shower)
Ventilation system and monitored discharge stack
ISO-container docking stations for waste in, waste out

Waste drum compactors
Glove box inspection station
cutting/size reduction room
Buffer store

3.6 Beryllium Analysis Laboratory

Designed to quantitatively measure beryllium contamination of swabs and filters.

Equipment:

Contamination control barrier
Ventilation system
Fume cupboards
Atomic absorption spectrometry
Chemical laboratory facilities

Staffing:

8 on shifts

3.7 Isolator and Tent Manufacturing, Suit Repair Facility

PVC cutting and welding and test equipment
Staffing: 3 Operators

3.8 Transfer and Storage Facilities

ISO container park with ventilated extracts
Standardised transfer and docking facilities using ISO containers
Liquid effluent holding and discharge tanks

3.9 In-Vessel Training Facility

In 1994, an In-Vessel Training Facility was built as a realistic full-scale replica of four octants of the inside of the JET vessel and all of the important aspects of the in-vessel components, Fig 4. This facility has three main uses:

- The provision of adequate training for in-vessel workers. The work in the vessel, in which the background radiation levels is increasing as the number of high performance plasmas increases, is performed by workers wearing pressurised suits with limited visibility and three pairs of gloves. To remain within JET's self imposed radiation exposure limit, a large number of trained fitters, engineers, welders and inspectors are required. The facility is used to train in-vessel personnel in the conditions that await them and to allow them to practice the procedures just prior to their actually going into the vessel. This ensures that all in-vessel work can be done correctly, safely, efficiently and with the absolute minimum of radiation exposure.

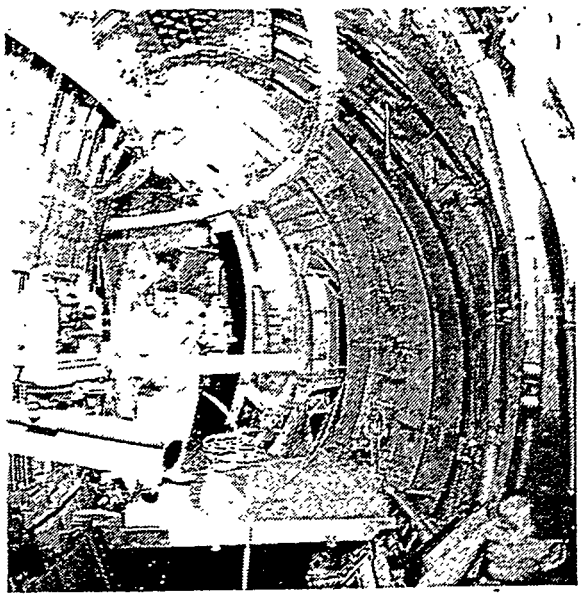

Fig.4: The In-Vessel Training Facility showing an inspector wearing a pressurised half-suit being trained in the use of a theodolite to position in-vessel components

- To check the details of new components, develop and test all new installation procedures, handling and installation tools, new in-vessel flooring, and interface problems in order to ensure that the Mark II divertor can be installed to the desired accuracy and within the boundary conditions prevailing.

- For remote handling operations trials. The preparation of equipment and operators for the fully remote exchange of the tile carriers includes the fullscale testing and proving of each individual task both under normal operating conditions and under failure case conditions. All of these trials will be performed within the facility. The facility has incorporated into it a full-scale space frame representation of all in-vessel

components considered to potentially offer a manoeuvring, viewing or access constraint under fully remote conditions.

Equipment:

Suit training facility
In-vessel mock-up of all hardware
Configuration control
Installation trials
In-vessel procedures training
Remote handling trials and procedure tests

4. Decontamination

A detailed examination of a wide variety of possible decontamination techniques was carried out to identify a method which; could be used to safely remove beryllium containing layers from the surface of the inside of the JET machine; would be compatible with subsequent plasma operations i.e. would not introduce unwanted high Z impurities onto the material; would not damage the surface, and would cause little waste disposal problems. Such a method was identified in the wet abrasive blasting using boron carbide grit (4). The method uses a high pressure water jet and a separate vacuum recovery and hydro cyclone system to recover the grit. The method was used successfully to decontaminate the inside of the JET vessel from a layer of tritium containing beryllium and to thereby allow the vessel to be reclassified from a Class 3 Respiratory Protection Zone where the use of pressurised suits is mandatory to a class zero Respiratory Protection Zone where no respiratory protection at all is required, Fig 5. This method of decontamination can be applied to particular smaller components which either require to be worked on or which need to be disposed of easily. It has therefore been included in the equipment available in one of the fixed Beryllium Controlled Areas.

A second method, blasting the vessel walls with a cold jet of carbon dioxide pellets, was successfully investigated and employed in the vessel The mechanical and thermal shock of the blast embrittles and dislodges a contaminating film, which can then be removed by vacuuming (5).

Fig.5: An in-vessel operator wearing a full pressurised suit and using the 100 bar boron carbide grit water gun to clean the JET vessel

5. Conclusions

The use of beryllium in a large fusion device implies a substantial effort in terms of infrastructure, facilities, organisation and manpower. Many, but not all, of the requirements can be regarded as an extension of the requirements already necessary for a facility operating with tritium. This paper describes the situation at JET where beryllium has been used on a large scale and very substantial work has been performed on heavily beryllium contaminated components both inside and outside the JET vessel. Any future machine in which beryllium is planned to be used should consider integrating the requirements into the organisation and the design of the facility and buildings right from the start.

Acknowledgements

The authors wish to acknowledge the contributions to the work by a very large number of members of the JET Team, Special emphasis is made to the contributions of the Health Physics and Safety Group, the Waste Management Group, and the First Wall Installation Group,

References

(1) Code of Practice for the Safe Use of Beryllium at the JET Laboratory, JET-SR(89)02

(2) EH40, Occupational Exposure Limits, Health and Safety Executive, HMSO Publication ISBN 0-11-88-20-80 Annual

(3) EH13, Beryllium - Health and Safety Precautions 1977 HMSO, ISBN 0-11-88-30-38 4

(4) Decontamination of the JET Vacuum Vessel from Beryllium and Tritium, S M Scott et al. 17th Symposium on Fusion Technology, Rome, September 1992

(5) Decontamination of the JET Vacuum Vessel Using the CO_2 Pellet Blasting (cold jet) Technique. S M Scott et al. International Symposium on Decontamination & Decommissioning, Knoxville, April 1994